Proceedings of the International Congress of the Mexican Hydrogen Society XVI, Querétaro, México, 2016

September 26 - 30, 2016

In Honor of Professor Oumarou Savadogo

INFORMACIÓN LEGAL

PROCEEDINGS OF THE INTERNATIONAL CONGRESS OF THE MEXICAN HYDROGEN SOCIETY DERECHOS DE AUTOR Y DERECHOS CONEXOS, **Año 3, No. 3, 2016**, es una publicación anual editada por la Sociedad Mexicana del Hidrogeno A. C., Calle Monte Bello No. 108, Col. Colinas del Padre, C. P. 98085, Zacatecas, Zacatecas, México, Teléfono (614) 4394815, Editor responsable: Alejandro López Ortiz., **ISSN: 2448-7120**, otorgado por el Instituto Nacional del Derecho de Autor.
Responsable de la última actualización de este Número, Dr. Alejandro López Ortiz, Cordillera de Guanacaste, 6435, Frac. Cordilleras, C.P. 31124, Chihuahua, Chihuahua, México, teléfono (614) 4394815, correo electrónico lalejan@gmail.com, fecha de última modificación, 8 de septiembre 2016.

This conference will address important aspects of the hydrogen technologies, from fundamentals, applications, policies and environmental aspects.

Topics will include but are not limited to:

- Hydrogen Production, Storage and Applications
- Direct Oxidation Fuel Cells
- Fuel Cells Components and Stacks
- Modelling and Design
- Renewable Energy Systems
- Control and Power Conditioning
- Policies, Economy and Market Strategies
- Codes, Standards and Safety Issues
- Nanostructured Materials
- Environmental Aspects

Congreso Internacional de la Sociedad Mexicana del Hidrógeno 2016

Chairs Committee:

Conference Chair: Dr. Gonzalo Macias-Bobadilla

Publication Chair: Dra. María Lucero Gómez-Herrera

Conference and MHS Treasurer: Dra. Virginia H. Collins-Martínez

Technical Program Chair: Lic. María Guadalupe Arredondo-Ramírez

Information Contact: Ing. Carlos Miguel Torres-Hernández

SMH Committee:

President: Dr. Sergio Miguel Durón Torres

Vice-President: Dr. Alejandro López Ortiz

Secretary: Dra. Beatriz Escobar Morales

Congreso Internacional de la Sociedad Mexicana del Hidrógeno 2016

Invited Speakers

Professor Oumarou Savadogo

Dr. d'État ès Sciences Physiques; Professor in Materials Sciences and Engineering, Electrochemistry and Energy, Polytechnique of Montréal. He earned, a Bachelor in Materials Sciences (DEA Sciences des Matériaux), and a Sciences Doctorate in Physical Sciences (Doctorat d'État) at Institute of Materials Sciences at Caen National University in France and a post-doctoral fellow at Laboratory of Interfacial Electrochemistry of National Science Research Centre at Bellevue in France. He joined the Materials Engineering Programme at Polytechnique Montréal, Canada as a Senior Scientist and Professor. He is the founder of the Laboratory of New Materials for Electrochemistry and Energy. The laboratory was founded from CFI (Canadian Foundation for Innovation) funding. He is the founder and the Editor of the Journal of New Materials for Electrochemical Systems and the Chairman of the International Symposium of New materials for Electrochemical Systems. E-mail:osavadogo@polymtl.ca: web: http://www.newmaterials.polymtl.ca. He is responsible of the two graduate programmes: Renewable energies, and Energy and Sustainable Development at Polytechnique Montreal. He is responsible of the course: Electrochemistry and Applications; Efficiency of Energy Resources; Electrochemical Energy and Applications; Energy storage. He graduated over 70 PhD and Master Students. His research activities are on new materials for thin films and dye sensitize solar cells, lithium batteries, PEM and Microbial Fuel Cells, redox flow batteries, solid alkaline fuel cells, biomaterials and corrosion of materials. He is the initiator and the Director of the project: Creation of the Institute of Solar Cell Technology (an Engineering School on Solar Cell Technologies) for the eight countries of the West African Economic and Monetary Union (2013—2018). He was also the initiator and the Director of the project: Applied Solar Cell Technologies to Burkina Faso (205-2011). These Projects are supported by the Canadian Government and Polytechnique Montréal. web: http://www.institut-tsa.org. He is the authors and coauthor of over 200 published papers in per-review journals and 6 patents.

PhD. Michel Cassir

Michel Cassir is Professor at Chimie-Paris Tech and group leader of “Interfaces, Electrochemistry, Energy” (I2E). He obtained a Ph.D. of the University of Paris VI, France. He was a professor 9 years at the National University of Mexico (UNAM). He was head of the Laboratory “Electrochemistry, Chemistry of Interfaces & Modeling for Energy”. His expertise covers electrochemistry, molten salts, solid oxides, separation techniques, thin layers and nanotechnology. His main activities are dedicated to high temperature fuel cells (MCFC, SOFC), batteries, catalysis and sensors. He gave more than 300 conferences in scientific events (80 invited conferences) and authored 235 scientific peer-reviewed publications, proceedings & book chapters.

Dr. Benito Serrano

Maximum Academic Degree: Doctor of Philosophy in Engineering Science. Level in the Research National System (SNI): National Researcher, level I. Professor with the category “PROMEP”. In México.

Congreso Internacional de la Sociedad Mexicana del Hidrógeno 2016

XVI International Congress of the Mexican Hydrogen Society

Sponsors

GENERAL INDEX

GENERAL INDEX

GENERAL INDEX

GENERAL INDEX

GENERAL INDEX

GENERAL INDEX

GENERAL INDEX

Platinum nanoparticles supported on different substrates for ORR: electrolyte medium effect

A. Camacho Ramírez[1], J. Donato Moreno[1], I. Galindo Esquivel[1], R. Fuentes-Ramírez, B. Ruiz Camacho[1]
[1]Departamento de Ingeniería Química, Universidad de Guanajuato, División de Ciencias Naturales y Exactas, Noria Alta s/n, Col. Noria Alta, 36050 Guanajuato, Gto México
beatriz.ruiz@ugto.mx

***Abstract*—Nanoparticles of platinum supported were prepared by a simple method of synthesis. The salt precursor of platinum (H_2PtCl_6) was reduced to metallic state using sonication equipment. Carbon Vulcan and xerogel carbon were used as support of platinum nanoparticles. Pt/C and Pt/C-XG were obtained at room temperature with not consecutive thermal treatment. The synthesized materials were characterized by scanning and transmission electron microscopy techniques. Cyclic voltammetry and linear voltammetry were also carried out in acid and alkaline electrolytes to investigate the effect of the electrolyte in the oxygen reduction reaction (ORR). According to TEM results, Pt nanoparticles with less of 20 nm shows a better dispersion onto the carbon Vulcan compared to dispersion obtained in xerogel carbon. Both materials exhibit electrochemical properties to carry out the ORR. However, in acid medium the kinetic of both materials as cathode catalysts is higher compared to the alkaline electrolyte. The number of electrons transferred was calculated by Koutecky-Levich, results show that on Pt/C-XG both electrochemical reactions are carried out, the direct and indirect ORR.**

Keywords—nanoparticles, sonication, oxygen reduction, carbon support, fuel cell.

I. Introduction

A fuel cell is a device that generates electricity by a chemical reaction. Every fuel cell has two electrodes, one positive and one negative, called, respectively, the anode and cathode. The reactions that produce electricity take place at the electrodes. Every fuel cell also has an electrolyte, which carries electrically charged particles from one electrode to the other, and a catalyst, which speeds the reactions at the electrodes [1]. Proton exchange membrane fuel cell (PEMFC) and alkaline fuel cell (AFC) use acid and alkaline electrolytes, respectively.

The electrochemical reactions are carried out in presence of one electrocatalysts that typically is Pt/C Etek. Commercial catalyst has a high cost due to the use of platinum. Currently, one of the most important challenges for PEMFCs in terms of facilitating their widespread commercial use is to improve the performance and durability of the electrocatalyst by developing novel carbon-based catalyst-support materials [2-3]. In addition, is necessary developed new electrocatalyst with high catalytic activity for hydrogen oxidation (anode) and the oxygen reduction reaction (cathode). In terms of durability, the supporting materials should possess a good compromise between the electric conductivity and corrosion resistance. Several approaches to increase the corrosion resistance of electrocatalysts have been studied [4-5]. Different types of carbon structures have been investigated, for example xerogel carbons [6], black carbons [7], nanotubes of carbons [8], etc. The preparation of catalysts is a fundamental step toward obtaining the desired activity, selectivity and lifetime [9]. Several methods of synthesis have been investigated to increase the activity of the conventional Pt/C electrocatalyst for PEMFCs. To improve on the advantages identified in previous research, in this work, we investigate the effect of two substrates of carbon to support platinum nanoparticles obtained by sonication method. Both materials synthesized were tested for the ORR in acid and alkaline medium for possible PEMFC and AFC applications.

II. Materials and Methods

2.1 Materials

Hexachloroplatinic acid (H_2PtCl_6, Sigma-Aldrich) was used as salt precursors of metallic nanoparticles. Carbon vulcan (CV) and xerogel carbon (XGC) were used as support of platinum. Sulfuric acid (H2SO4, Sigma-Aldrich) and potassium hydroxide (KOH, Sigma-Aldrich) were used to prepare the different electrolytes.

2.2 Pt/C and Pt/XGC preparation

The synthesis of nanoparticles supported on carbon was prepared follow the methodology describes by Ruiz-Camacho et al [10]. Two samples were obtained using this methodology: 1) Pt supported on carbon Vulcan (Pt/C) and 2) Pt supported on xerogel carbon (Pt/XGC), respectively. The xero gel carbon was synthesized following the literature [11].

2.3 Physical and electrochemical characterization

Particle size and morphology of samples were obtained with a high resolution transmission electron microscopy (TEM) using a TEM JEOL 1010 field emission operated at 80 kV. Cyclic voltammetry (CV) and rotating disk electrode (RDE) were carried out in a conventional three-electrode cell using a potentiostat/galvanostat Gamry Instruments reference 1000T and a RDE710 rotation speed controller. All the electrochemical reactions were carried out at 25 °C. A platinum mesh was used as the counter electrode, and a standard saturated calomel electrode (SCE = 0.24 V) as reference electrode. A glassy carbon disk with a geometric area of 0.196 cm^2 was used as working electrode. 25 cycles of CV in nitrogen atmosphere at 50 mV s^{-1} was performed in a nitrogen-saturated electrolyte to stabilize the system. The potential range of CV used in acid electrolyte (H_2SO_4 0.5 M) was between 0.05-1.2 V. In the case of alkaline electrolyte (KOH 0.5 M), the electrochemical window was in the interval range of -0.75-0.8 V. Hydrodynamic experiments were recorded at oxygen atmosphere with different speeds: 200, 400, 900 and 1600 rpm at 5 mV s^{-1}. The different potential ranges used in acid and alkaline electrolytes were 1.0 to 0.1 V and from 0.2 to -0.7 V, respectively.

III. RESULTS AND DISCUSION

Fig. 1 shows the TEM image of Pt/C and Pt/XGC electrocatalysts prepared by sonication method. Pt/C exhibits a higher distribution of nanoparticles onto the substrate compared to Pt/XGC. This can be related with the surface charge of the XGC substrate.

Pt/C and Pt/XGC were tested in cyclic and linear voltammetry in two different electrolytes acid (Fig. 2) and alkaline (Fig. 3) electrolytes. Cyclic voltammetry results shows that both materials synthesized exhibits the typical fingerprint of platinum nanoparticles in both electrolytes with different intensity of current density according different substrates. Briefly, Pt samples (Pt/C and Pt/XGC) prepared by sonication exhibits desorption peaks at 0.05–0.3 V/NHE and Pt oxide formation/reduction peaks at 0.85/0.75 V/NHE in acid medium.

The oxygen reduction reaction (ORR) activity in acid and alkaline medium at different rotating speed from 200 to 2500 rpm is presented in Fig. 2 and Fig. 3 for Pt/C and Pt/XGC respectively. The overall current density for the ORR is calculated by:

$$\frac{1}{j}=\frac{1}{j_k}+\frac{1}{j_d} \qquad (1)$$

.

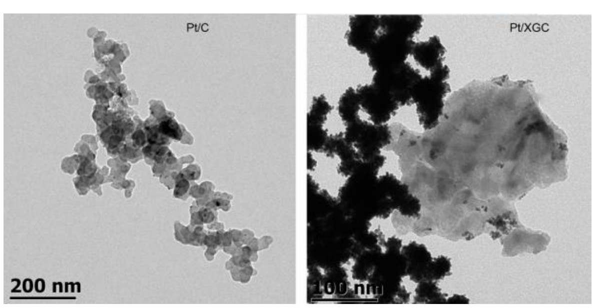

Fig. 1 TEM of Pt/XGC synthetized by sonication

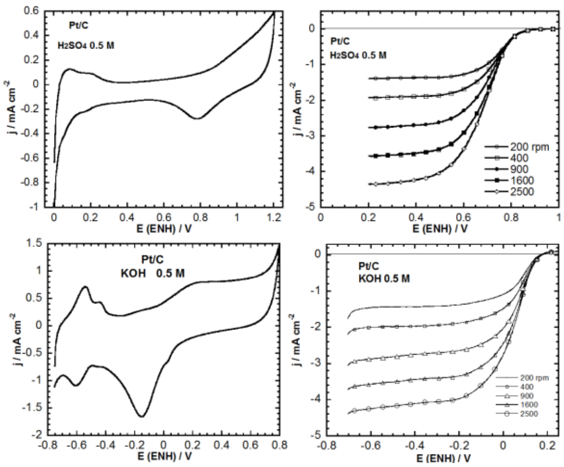

Fig. 2 Cyclic and linear voltammetry of Pt/C in acid and alkaline medium

where j_k is the kinetic density current and j_d is the diffusion-limited density current. An explanation of the increase in the limiting current could be associated with increase of molecular oxygen diffusion through the electrode surface.

Fig. 4 exhibits the inverse current density (j^{-1}) as function of the inverse of the square root of the rotation rate ($w^{-1/2}$), corresponding to Koutecky-Levich (K-L) plot for a) Pt/C and b) Pt/XGC samples at various electrode potentials. The linearity of the K-L plots indicates first-order kinetics with respect to molecular oxygen [12]. Pt/C showed the Koutecky-Levich slope of 9.74 mA^{-1} rpm ^{½} that correspond to the four-electro process transferred, indicating that the ORR on Pt/C follows four-electron path way leading water [13]. However, Pt/XGC exhibits a Koutecky-Levich slope of 20 mA^{-1} rpm ^{½} that correspond to the two electrons transference.

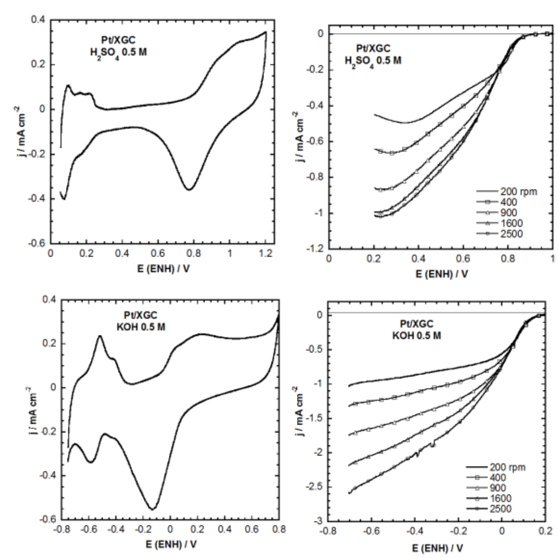

Fig. 3 Cyclic and linear voltammetry of Pt/XGC in acid and alkaline medium

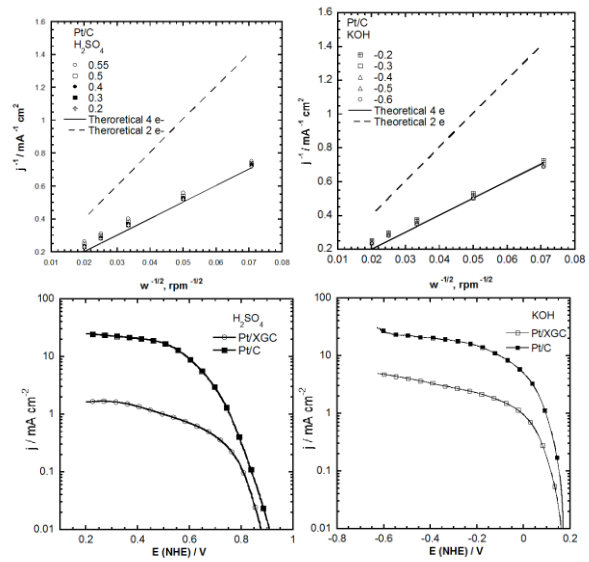

Fig. 4 Koutecky-Levich of Pt/C and Tafel plot comparison of Pt/C and Pt/XGC materials synthesized in both electrolytes.

Table I. Electrochemical parameters of Pt/C and Pt/XGC in acid electrolytes.

Material	**Koutecky-Levich slope (mA^{-1} rpm ^{½})**	**α**	**b (mV dec^{-1})**	**j_k @ 0.85 V/NHE (μA cm^2)**
Pt/C	9.74	0.85	69	75
Pt/XGC	19.02	0.84	70	26

Mass transfer corrected the Tafel plots deduce for RDE on of Pt/C compared to Pt/XGC is presented in Fig. 4 in two different electrolytes. We observed at a higher electrochemical activity of Pt/C than Pt/XGC in both electrolytes.

IV. CONCLUSION

Platinum nanoparticles supported on different substrates (carbon vulcan and xerogel carbon) was synthesized following sonication method. Their electrochemical activity in the ORR reaction was compared in two different electrolytes (acid and alkaline). Pt/C electrocatalyst showed an enhancement of their electrocatalytic activity for the ORR compared with the Pt/XCG catalysts en both electrolytes. The activity changes are related with the physical properties of substrates. A high distribution of Pt nanoparticles is obtained on carbon vulcan compared to xerogel carbon due to the superficial charge.

ACKNOWLEDGMENT

The authors want to express their gratitude to UNAM for the TEM images. We also thank to Universidad de Guanajuato and Promep project (103.5/15/7007) for financial support of this work.

REFERENCES

[1] W. Vielstich, H. Gasteiger, A. Lamm, Handbook of Fuel Cells-Fundamentals Technology and Applications 3-4, 2003.

[2] W. Jung-Ho, L. Kwan-Young, K. Sung, “Fabrication methods for low-Pt-loading electrocatalysts in proton exchange membrane fuel cell systems” J. Power Sources vol. 165, pp 667-677, 2007.

[3] T. Ioroi, Z. Siroma, N. Fujiwara, S. Yamazaki, K. Yasuda, “Sub-stoichiometric titanium oxide-supported platinum electrocatalyst for polymer electrolyte fuel cells”. Electrochem. Comm. vol. 7, pp. 13-188, 2005.

[4] A. Ishihara, Y. Ohgi, K. Matsuzawa, S. Mitsushima, K.-I. Ota, “Progress in non-precious metal oxide-based cathode for polymer electrolyte fuel cell”s. Electrochim. Acta vol. 55, pp 8005-8012. 2010.

[5] X. Zhang, H. Zhu, Z. Guo, Y. Wei, F. Wang, “Sulfated SnO2 modified multi-walled carbon nanotubes – A mixed proton-electron conducting suppor for Pt catalysts in direct ehanol fuel cells”, J. Power Sources vol. 196, pp. 3048 3053, 2011.

[6] N. Job, J. Marie, S. Lambert, S. Brehon-Faby, P.Achard. “Carbons xerogels as catalysts suports for PEM fuel cell cathode”. Energy Conversion and Manangement vol. 49 pp 2461-2470, 2008.

[7] Z. Yang, M.R. Berber, N. Nakashima. “A polymer-coated carbon black-based fuel cell electrocatalyst with high CO-tolerance and durability in direct methanol oxidation”. J. Mater Chem. A vol. 2, pp.18875-18880, 2014.

[8] C. Wang, M. Waje, X. Wang, J.M. Tang, R.C Haddon, Yushan. “Proton exchange membrane fuel cell with carbonnotubes based elctrodes”. Nano Letter. Vol. 4 pp. 345-348, 2004.

[9] B. Ruiz-Camacho, M. A. Valenzuela, J. A. Pérez-Galindo, F. Pola, M. Miki-Yoshida, N. Alonso-Vante, R. G. González-Huerta.”Oxygen Reduction Reaction on Pt/C Catalysts Prepared by Impregnation and Liquid Phase Photo-Deposition”. J. New Mat. Electrochem. Syst. Vo. 13 pp 183-189, 2010.

[10] B. Ruiz-Camacho, O. Martínez Álvarez, H.H. Rodríguez-Santoyo, P.A. López-Peréz, R. Fuentes-Ramírez. Mono and bi-metallic electrocattalysts of Pt and Ag for oxygen reduction reaction synthesized by sonication, Electrochem. Comm, vol. 61 pp 5-9, 2015.

[11] J. Donato Moreno, Síntesis de xerogeles de carbono como soportes de electrocatalizadores de Pt para la reacción de reducción de oxígeno, Tesis de Maestría, en proceso. Universidad de Guanajauto, 2016.

[12] A.J. Bard, L.R. Faulkner, “Electrochemical Methods: Fundamentals and Applications”, John Wiley & Sons, New York, 1985.

[13] Kinoshita K., Electrochemical Oxygen Technology, Wiley, Hoboken, NJ, 1992.

DFT calculations to determine the interaction energy of a Pt cluster with sp2 and sp3 carbon surfaces

C.A. Campos-Roldán[1,2], , N. Alonso-Vante[2], R.G. Gonzalez-Huerta[1*]
[1]Intituto Politécnico Nacional-ESIQIE, Laboratorio de Electroquímica y Corrosión, UPALM, 07738, CDMEX, México
[2]IC2MP, UMR-CNRS 7285, University of Poitiers, 4 rue Michel Brunet, 86022 Poitiers, France
line 4: e-mail address if desired

G. Ramos-Sánchez3, P. B. Balbuena4
[3]CONACYT – Universidad Autónoma Metropolitana-I, San Rafael Atlixco 186, Iztapalapa, Vicentina, 09340 CDMX, México.
[4]Artie Mc. Ferrin Department of Chemical Engineering, Texas A&M University, College Station, TX 77843, USA

Abstract*— Hydrogen technologies such as fuel cells require the use of supported Pt nnanoparticles, the effect of the support is still debatable. In this work, DFT calculations were used to determine the interaction energy of a Pt cluster with sp2 and sp3 carbon diamond-like surfaces as well as with sp3 oxygen terminated surface. The Vienna Ab-Initio Software Package (VASP) was used for all calculations, the sp3 and sp2 domains were simulated as surfaces of graphene and diamond. Pt species were allowed to interact with the sp2 and sp3 surfaces and also with a sp3 oxygen terminated surface. The values of interaction energy confirm that when the cluster interacts with the oxygen terminated and sp3 surfaces most of the charge is kept at the interface thus the charge being transferred to the CO molecule is higher only when the Pt cluster interacts with sp2 domains, on the other cases, the amount of charge transferred is similar to systems where the support is not included. The interaction energy and electronic structure of the platinum cluster presents dramatic changes as function of the support surface chemistry, which also modifies its catalytic properties evaluated by the interaction with CO. The interaction energy was calculated to be 8 fold higher on sp3 and oxidized surfaces in comparison to sp2 domains.

Keywords*— *DFT calculations; Pt cluster; sp2 and sp3 carbon surfaces

I. Introduction

Climate change and global warming have raised concerns about the use of finite non-renewable resources thus speeding up the search of means to harvest renewable energy and using more efficient means to transform it, consequently leading to a more sustainable world [1]. Proton Exchange Membrane Fuel Cell (PEMFC) is considered an ideal power source for mobile and stationary applications. When using hydrogen as fuel and air as oxidant the only sub-product is water; therefore, no contaminants are released at an energy transformation efficiency higher than heat machines [2]. To date PEMFC operates in acidic electrolytes in which the Oxygen Reduction Reaction (ORR) is the limiting step diminishing efficiency and leading to the use of huge platinum loads or else carbon supported Pt-based nanoparticles. Nanoparticulated Pt approaches have resulted in the increase of the utilization of Pt, higher mass activity and thereof reduced Pt loads.

However, the use of carbonaceous supports provides new challenges on the electrode durability; because of, either, the agglomeration of particles or the oxidation of the support itself [3-5]. Nanoparticle agglomeration can be related to the strength of the support-nanoparticle interaction: weaker interaction provides high nanoparticle mobility while strong interaction might be detrimental enhancing the oxidation rates of the support or the nanoparticle itself. On the other hand, the oxidation of the support might be influenced by several factors such as operation voltage, surface chemistry and carbon structure. The effect of the support/nanoparticle interaction has been attributed to the modification of the nanoparticle electronic structure [6]. The modification of the electronic structure of the nanoparticle as results of the interaction with the support has been observed by Density Functional Theory (DFT) [6-8]. DFT simulations have been useful to confirm that the support is capable to modify the nanoparticle electronic structure thus changing the catalytic properties [9,11]. Strong interactions between platinum clusters and sp2 carbon material domains, such as highly oriented pyrolytic graphite (HOPG) [8] multi-walled carbon nanotubes [6] have been reported. However, the effects of the support structure and surface chemistry remain elusive. The ORR activity as well as the stability, and dynamics of the Pt NPs onto the substrate are investigated and the results reported on the basis of the effect of the support structure. In this work theoretical evidences demonstrate the consequences of the interaction strength of Pt nanoparticles with sp2 and sp3 domains toward the oxygen reduction reaction (ORR) in acid medium.

II. Experimental

Periodic DFT calculations were used to elucidate the role of the support on the interaction with platinum. The Vienna Ab-Initio Software Package (VASP) [12-15] was used for all calculations, spin polarized calculations were performed using the projected augmented wave (PAW) pseudopotentials and the PBE exchange correlation functional [16-17]. The sp^3 and sp^2 domains were simulated as surfaces of graphene and diamond, the former as a single 5x5 graphene layer separated by 12 Å vacuum space while the later as (111) diamond surfaces. Pt species were allowed to interact with the surfaces and also with a sp^3 oxygen terminated surface. The surfaces are intended to determine their effects on the limits of the sp^3 and sp^2 domains, intermediate behaviors are expected depending on the support synthesis and treatments.

III. Results And Discussion

DFT simulations were performed in which the effect of the support on the adsorption of a CO molecule was analyzed. The CO was allowed to interact with the cluster in the same site in the unsupported Pt6 cluster and interacting with sp2 and sp3 domains. The interaction energy was calculated as the difference of isolated systems (taking into account the changes in geometry) and the interacting one. Bader charge analysis was performed in order to determine the trends in electron transfer to the CO molecule. Table 1 shows the interaction energy of CO with the cluster and the changes in charge transfer to the CO molecule. Both quantities are modulated by the presence and the nature of the support. In comparison to the interaction on the unsupported cluster, the interaction energy is higher on the oxygen terminated surfaces, and lower on sp2 and sp3 domains. However, the charge transfer follows an interesting trend since the CO receives a higher electron density on the cluster supported on the sp2 domains than on the oxygen terminated and sp3 surfaces, having similar values than the unsupported cluster. A graphical representation of the charge accumulation depletion caused by the interaction with the support is depicted in Figure 1.

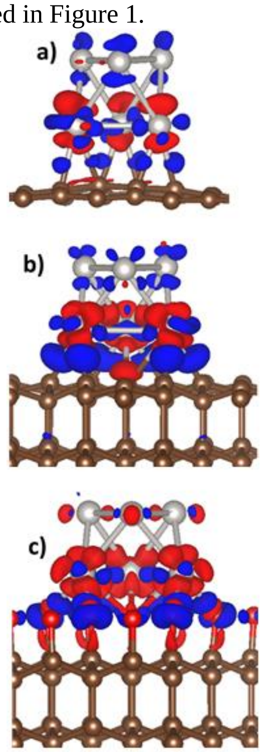

Fig. 1. Electron density accumulation (blue) and depletion (red) iso-surfaces (0.01 $e^{-}/Å^{3)}$ as result of the interaction with the support, a) sp^2 domains, b) sp^3 domains and c) oxygen terminated diamond (111) surfaces. Gray, brown and red spheres represent platinum, carbon and oxygen atoms respectively.

Blue areas represent electron density accumulation while those in red represents depletion. Interesting features are observed in Figure 1, the formation of bonds between the support and the nanoparticle is evident as blue areas appear directly between carbon and platinum atoms. This interaction occurs at expenses of charge depletion of platinum atoms at the interface, comparing sp3 and sp2 domains the higher blue regions at the interface is a direct consequence of an enhanced interaction energy. The interaction with the oxygenated surface is fundamentally different, owed to a strong charge transfer process at the interface characterized by a high electron density accumulation in the oxygen and depletion in the platinum atoms, differently to the interaction with sp3 and sp2 domains, the charge transfer is so extreme than even the platinum atoms located on top of the cluster presents charge depletion areas.

Therefore, the electronic properties of the cluster are very different which is expected to lead to changes in the interaction with reactive molecules, i.e., CO and O2. The values on Table 1 confirms that when the cluster interacts with the oxygen terminated and sp3 surfaces most of the charge is kept at the interface thus the charge being transferred to the CO molecule is higher only when the Pt cluster interacts with sp2 domains, on the other cases, the amount of charge transferred is similar to systems where the support is not included.

Table 1. Properties of CO interaction with the supported clusters as function of the surface chemistry

	Interaction energy / eV	CO charge / excess electrons
Pt	-3.01	-0.09
Pt/sp^2	-2.95	-0.15
Pt/sp^3	-2.92	-0.09
Pt/O-terminated sp^3	-3.18	-0.10

Periodic Density Functional Theory (DFT) calculations were used to elucidate the role of the support on the interaction with platinum. First, a single Platinum atom was allowed to interact with the graphite and diamond surfaces, the goal of this preliminary study is to demonstrate the basic interaction strength and charge delocalization caused by the platinum-support interaction. The modelled surfaces are depicted in Figure 2. In them, the possible interaction sites are identified. In graphene there are three possible sites, bridge (A), top (B), and hollow-type at the center of the hexagon (C), while on the diamond (111) surface we initially simulated three sites corresponding to top (A) in which the Pt lies above a three-fold coordinated C atom, top2 (B) in which the site is above a 4-coordinated carbon atoms and in the space between three A-sites, the C site is a bridge one between two adjacent carbon atoms.

The platinum atom was placed directly above the surface at a distance of ~ 2 Å and then relaxed until the force criteria were reached. On one hand, in the sp2 domains the only stable interaction site corresponds to the bridge one, all other sites irremediably shift to the bridge position, the interaction energy calculated as the energy difference between isolated and interacting systems. The interaction energy (adsorption energy) between Pt and sp2 domains is similar to previous reports [18-19]. On the other hand, for sp3 domains, the relaxation of the Pt on the A and B sites lead to stable configurations; however, on the bridge site the platinum atom was relaxed into a hollow site interacting with three carbon atoms having no carbon atom in the second sublayer. For diamond (111) oxygen terminated surfaces, the interaction directly with on top of an oxygen atom did not result in a stable configuration; however, those interacting in the space formed by three oxygen atoms resulted in a very stable configuration.

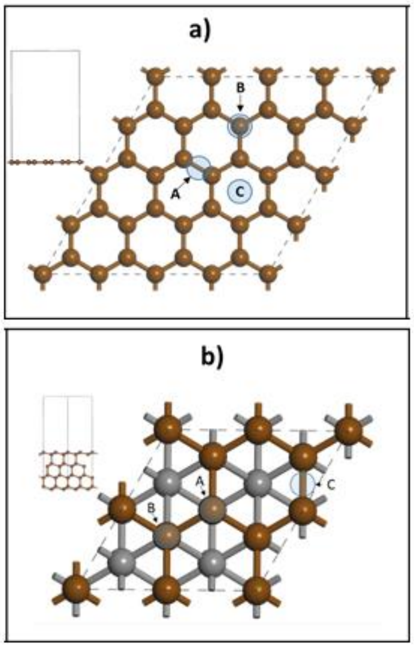

Fig. 2. Models used for sp^3 and sp^2 domains analyses. A) Periodic graphite totally sp^2 carbon, B) diamond 111 surface having sp^3 carbon domains. The letters indicate the site for adsorption, on diamond 111 the first layer is depicted in brown and subsurface layers in gray.

The interaction energy is an important indicator of the stability of the nanoparticle on the support surface. For instance, if the interaction energy is too weak, the mobility of the nanoparticle is very high leading to migration and possible sintering into bigger nanoparticles.

The interaction energy of the single atom is reported in Table 2, the interaction energy of Pt with the sp3 domains is around three times higher than in the sp2 domains on the C site (Figure 2) which is not surprising since the interaction is done directly with three three-fold sp3 coordinated atoms. It is very unlikely that the (111) surface (or any other) is composed of uncoordinated C atoms, according to the experimental procedure, a high number of oxygenated species is expected; therefore, the diamond (111) surface was covered with =O terminal groups. The interaction of the Pt atom with the =O groups is the highest of all the possible sites being slightly higher than the interaction with the pure (111) diamond surface. This indicates that all non-graphitic sites (sp3 domains) which are formed during the synthesis are most likely to serve as anchoring sites for the interaction with positive ions and then as stable sites for the interaction with Pt clusters.

Another important characteristic of the nanoparticle-support interaction is the charge transfer features. In pure covalent systems it is expected the charge being distributed equally between the interacting atoms; however, in mixed covalent-ionic systems there are atoms that donate/receive electron density. Table 2 illustrates that in the sp2 systems the charge being transferred is almost null, while in the sp3 systems the charge transfer is two orders of magnitude higher depending on the site (and therefore on the atom coordination). However, compared to the interaction with oxygenated sites, the previous charge transfer processes are eclipsed by the positive formal charge found in Pt interacting with oxygen terminated surfaces, becoming a true positive ion. The charge transfer is of primordial importance since it modifies the electronic structure of the nanoparticle and in consequence changes its properties, especially those related to the electrocatalytic ones.

The last row of Table 2 shows the results of the interaction energy per Pt atom for a 6-atom cluster interacting with the surfaces. The cluster was relaxed in vacuum and then was allowed to interact with the surface in the most energetically favorable sites determined for the single atom interactions (A for graphene and C for diamond and O-terminated diamond surfaces).

The interaction energy was calculated in a similar way than in previous sections. Interestingly, the trend in interaction energy is reverted, and the higher interaction energy is observed in the sp^2 graphite domains while in diamond (111) surface the interaction energy is slightly weaker. Analyzing the interatomic distances in the nanoparticle/support interphase it is found that the Pt-Pt distance was enlarged from 2.56 Å for the cluster in vacuum to 2.99 Å in sp^3 domains while the interaction with graphene sp^2 domains the distance is only increased to 2.74 Å. The changes in interaction energy thus, can be ascribed to the modification of the cohesive energy in the clusters by the different interaction with the sp^3 domains. Thereafter, the interaction energy calculated, taking into account the geometry changes in the Pt cluster, confirms a higher (5.1 eV) interaction energy with sp^3 domains in comparison to the sp^2 domains. Similarly to the interaction of a single atom with =O sites, the interaction of the cluster with the (111) diamond surface oxygen terminated led to the highest interaction energy in comparison to all other surfaces. Considering the changes in cluster geometry the interaction energy in oxygen terminated surfaces is -10.1 eV which, compared to the interaction with graphene is one order of magnitude higher and around 1.5 times higher than in the (111) diamond surface. Thus the interaction energy is higher on the sp^3 domains which indicates lower nanoparticle mobility.

Table 2. Interaction energy of the Pt atom and Pt_6 with the support and charge transfer properties.

Site	Interaction energy / eV		
	Graphene	Diamond 111	O terminated sp^3
A	-1.69	-4.00	
B	Shift to A	-4.87	-5.28
C	Shift to A	-5.11	-5.17
Pt_6	-1.15	-1.02	-8.65
Site	Platinum charge / excess electrons/atom		
	Graphene	Diamond 111	O terminated sp^3
A	-0.002	-0.06	
B		+0.13	+1.14
C		+0.18	+1.15
Pt_6	+0.13	+0.27	+2.33

However, this statement does not indicate that the interaction of the cluster with sp^3 sites should lead to more stable catalyst in comparison to the interactions with the sp^2 domains, since other factors such as support corrosion or cluster oxidation might take place. The charge transfer properties per atom are in line with the interaction of the single atom. The charge transferred to sp^3 domains is twice that found in graphene, while the charge transferred in oxygenated surfaces is very much like a real ionic interaction. These changes in charge transfer properties are the responsible for the changes in the nanoparticle electronic structure and therefore for the modification of the catalytic activity towards CO and O_2 reactions. Theoretical analysis is consistent with experimentally reported in Pt 4f XPS spectra [20], where Pt 4f peaks of materials prepared by PD present a binding energy down-shift, leaving the photo-deposited materials supported on *f*-CNT (substrate with > sp^2 character) with higher electron density on Pt.

As demonstrated by DFT calculations, the higher electron density on Pt occurs when Pt is deposited on sp^2 domains, i.e. on Pt/*f*-CNT_{PD}. This interaction could be responsible for the limited mobility and agglomeration of platinum nanoparticles through sp^2 domains, saying nothing about carbon nanotubes corrosion resistance. The effect on the stability of Pt/*f*-CNT_{PD} could be related to extended π systems, which can anchor particles, strongly modifying platinum *d*-band properties, therefore, even though the Pt-sp^2 interaction is much weaker than the Pt-sp^3, it is possible to appreciate a coordinating bonding between platinum *d*-orbital and the π–π carbon network, namely sp^2-*d* hybridization [6]. Previous reports [6-8] have demonstrated that the *d*-band density of states (DOS) of atoms with higher electron density, resulting from the interaction between platinum clusters and graphite, has more states near the E_f in comparison to those of the interface Pt atoms having a deficit of electrons.

IV. Conclusions

In this work theoretical evidences demonstrate the consequences of the interaction strength of Pt nanoparticles with sp2 and sp3 domains toward the oxygen reduction reaction (ORR) in acid medium. DFT simulations revealed two different interactions between platinum nanoparticles and carbon sp2 or sp3 nano-domains. The limited mobility of platinum nanoparticles supported onto in-plane extended sp2 nano-domains could be a consequence of the observed electronic density modification of platinum nanoparticles. The presence on the support of mostly sp2 domains augments the durability since re-deposition occurs on sp2 domains. In contrast, the presence of sp3 domains causes the re-deposition of Pt to occur on sp3 sites causing agglomeration. These results provide new avenues for enhancing the stability of platinum nanoparticles supported onto carbon-based materials via engineering their surface chemistry. After the text edit has been completed, the paper is ready for the template..

Acknowledgment

The authors thank the financial support from University of Poitiers. C.A.C.-R. acknowledges financial support from CONACYT-Mexico Nr.: MX-561206.

References

[1] Chen, X.; Li, C.; Grätzel, M.; Kostecki, R.; Mao, S. S., Nanomaterials for renewable energy production and storage. *Chemical Society Reviews* **2012,** *41* (23), 7909-7937.

[2] Steele, B. C.; Heinzel, A., Materials for fuel-cell technologies. *Nature* **2001,** *414* (6861), 345-352.

[3] Antolini, E., Carbon supports for low-temperature fuel cell catalysts. *Applied Catalysis B: Environmental* **2009,** *88* (1–2), 1-24.

[4] Shao-Horn, Y.; Sheng, W. C.; Chen, S.; Ferreira, P. J.; Holby, E. F.; Morgan, D., Instability of Supported Platinum Nanoparticles in Low-Temperature Fuel Cells. *Topics in Catalysis* **2007,** *46* (3), 285-305.

[5] Pinheiro, A. L. N.; Oliveira-Neto, A.; De Souza, E. C.; Perez, J.; Paganin, V. A.; Ticianelli, E. A.; Gonzalez, E. R., Electrocatalysis on Noble Metal and Noble Metal Alloys Dispersed on High Surface Area Carbon. *J of New Mats for Electrochemical Systems* **2003,** *6* (1), 1-8.

[6] Ma, J.; Habrioux, A.; Morais, C.; Lewera, A.; Vogel, W.; Verde-Gomez, Y.; Ramos-Sanchez, G.; Balbuena, P. B.; Alonso-Vante, N., Spectroelectrochemical Probing of the Strong Interaction between Platinum Nanoparticles and Graphitic Domains of Carbon. *ACS Catalysis* **2013,** *3* (9), 1940-1950.

[7] Luo, Y.; Mora-Hernández, J. M.; Estudillo-Wong, L. A.; Arce-Estrada, E. M.; Alonso-Vante, N., Nanostructured palladium tailored via carbonyl chemical route towards oxygen reduction reaction. *Electrochimica Acta* **2015,** *173*, 771-778.

[8] Hofmann, S.; Sharma, R.; Ducati, C.; Du, G.; Mattevi, C.; Cepek, C.; Cantoro, M.; Pisana, S.; Parvez, A.; Cervantes-Sodi, F.; Ferrari, A. C.; Dunin-Borkowski, R.; Lizzit, S.; Petaccia, L.; Goldoni, A.; Robertson, J., In situ observations of catalyst dynamics during surface-bound carbon nanotube nucleation. *Nano Lett.* **2007,** *7* (3), 602-608.

[9] Ewing, C. S.; Veser, G.; McCarthy, J. J.; Johnson, J. K.; Lambrecht, D. S., Effect of Support Preparation and Nanoparticle Size on Catalyst–Support Interactions between Pt and Amorphous Silica. *The Journal of Physical Chemistry C* **2015,** *119* (34), 19934-19940.

Synthesis and Characterization of NiPdPt Alloy Nanoparticles for the Oxygen Reduction Reaction

H. Cruz-Martínez[1,*], M. M. Tellez-Cruz[2], C. A. Ramírez-Herrera[1], P. Calaminici[2], O. Solorza-Feria[2],

[1]Programa de Doctorado en Nanociencias y Nanotecnología, CINVESTAV, Av. Instituto Politécnico Nacional 2508, Col. San Pedro Zacatenco, Delegación Gustavo A. Madero, México D.F. C. P. 07360. *Tel: +52 (55) 5747 3800, ext. 4473; e-mail: hcruzm@cinvestav.mx
[2]Departamento de Química, CINVESTAV, Av. Instituto Politécnico Nacional 2508, Col. San Pedro Zacatenco, Delegación Gustavo A. Madero, México D.F. C.P. 07360.

ABSTRACT

Proton exchange membrane fuel cells (PEMFCs) are electrochemical energy conversion devices which have attracted considerable interest as power sources for mobile and stationary applications. However, their commercialization is severely hampered both by the fact that oxygen reduction reaction (ORR) is slow and by the extremely high cost of platinum. To overcome these disadvantages, Pt-based nanoparticles have been actively explored in recent years due to their outstanding activity for the ORR. Nevertheless, these problems still require further investigations. In this study, we report the synthesis and characterization of NiPdPt (60:20:20 wt%) nanoparticles. In a standard synthesis, $Ni(acac)_2$, $Pd(acac)_2$ and $Pt(acac)_2$ were dissolved in a mixture of benzyl ether, oleylamine and oleic acid. The formed solution was preheated to 130 ºC and 100 mg $W(CO)_6$ was added to the mixture as a source of CO that can promote the formation of {111} facets. Finally, the mixture was kept at 235 ℃ for 30 min. Cyclic voltammetry and rotating disk electrode were employed for electrochemical characterization of NiPdPt/C nanocatalyst. For the phases identification X-ray diffraction (XRD) was used, for compositional analysis energy disperse X-ray (EDX) spectroscopy was employed and scanning transmission electron microscopy (STEM) was used to determine morphology and particle size of NiPdPt/C nanocatalysts. The presence of Ni, Pd and Pt in the synthesized nanoparticles was confirmed by EDX and XRD. STEM micrographs showed homogeneous nanoparticles of 10 nm size. Finally, electrochemical procedures showed that our nanocatalysts exhibit a best activity catalytic than commercial Pt/C for the ORR in acid media.

Keywords: PEMFCs; ORR; Nanoparticles; Physical characterization

Optimization operation of a parabolic trough collector using artificial neural network

O. May Tzuc
Estudiante de Posgrado, Facultad de Ingeniería
Universidad Autónoma de Yucatán
Mérida, México
maytzuc@gmail.com

M. Vázquez Caamal
Estudiante de Posgrado, Facultad de Ingeniería
Universidad Autónoma de Yucatán
Mérida, México
maytzuc@gmail.com

M.A. Escalante Soberanis
Facultad de Ingeniería
Universidad Autónoma de Yucatán
Mérida, México

A. Bassam
Facultad de Ingeniería
Universidad Autónoma de Yucatán
Mérida, México

***Abstract*— The present work describes the thermal efficiency optimization of parabolic trough collectors by combining a model of artificial neural network and computational optimization techniques. A feedforward neural network architecture is trained using experimental database from parabolic trough collector operations. Rim angle, inlet and outlet fluid temperatures, ambient temperature, water flow, direct solar radiation, and wind velocity were used as main input variables within the neural network model to estimate the thermal performance. The optimal operation conditions of parabolic trough collectors are established using the hybridization of optimization technique with neural network model to achieve optimal operation conditions of parabolic trough collector. The result indicated that methodology implemented is a feasible tool for parabolic trough collectors optimization.**

***Keywords*— Renewable energy; solar energy; artificial intelligence; optimization technique**

Catalyst screening for photocatalytic hydrogen production using copper, nickel and titanium oxides core-shell nanostructures

S.P. Ramírez, M.A. Valenzuela, J.A. Wang
Lab. Catálisis y Materiales
ESIQIE-Instituto Politécnico Nacional
Ciudad de México, México
mavalenz@ipn.mx

A.Dalai
Department of Chemical Engineering
University of Saskatchewan
Saskatoon, Canada

***Abstract*—Hydrogen production from the photocatalytic reforming of glycerol has been performed on NiOCuO, CuONiO, $CuOTiO_2$ and $NiOTiO_2$ core-shell nanostructured catalysts under simulated solar light. The catalysts were prepared by precipitation and sol-gel methods and characterized by powder X-ray diffraction (XRD), UV/Vis diffuse reflectance spectroscopy (UV–Vis DRS), scanning electron microscopy (SEM), transmission electron microscopy (TEM) and nitrogen physisorption. According to the results, the highest rates of hydrogen production were obtained with the $CuOTiO_2$ and $NiOTiO_2$. In the first case, after activation of TiO_2 with UV-light the conduction band electrons can be transferred to CuO which is gradually reduced to Cu_2O and Cu favoring the proton reduction to hydrogen. In the second case, the $NiOTiO_2$ presented lower activity than $CuOTiO_2$ due to the conduction band of NiO is more negative than the conduction band of TiO_2, then the reduction process is carried out by both, the TiO_2 and NiO using only UV light. The catalysts containing TiO_2 as a shell showed much higher activity compared with those formulated with only Cu or Ni oxides.**

Keywords*—*sol-gel process; core-shell; photocatalysis; hydrogen production.

I. INTRODUCTION

Hydrogen is the simplest and lightest element on earth, is not an energy source but an intermediate medium for storing and carrying energy. It can be burned or combined with oxygen in a fuel cell without generating CO_2, the only significant emission is water vapor. A variety of feedstock can be use to produce hydrogen; include fossil resources, such as natural gas and coal, as well as renewable resources, such as biomass and water. Several process technologies of hydrogen production are known, like water electrolysis [1-2], coal gasification [3-4], steam reforming of natural gas [5-6], etc. Therefore, recent investigations are focused on finding an efficient and economic method for hydrogen production. Photocatalysts for producing hydrogen has become a topic of international interest and challenge because of their low cost potential and environmentally friendly nature. Photocatalytic hydrogen production can be performed under mild conditions and biomass such as alcohols, glycerol, glucose and sugars can be utilized for sustainable generation of hydrogen. Recently a larger amount of glycerol is produced as a byproduct in biodiesel production so it is desirable to find its application.

Several authors have reported different attempts to improve the photocatalytic efficiency of the semiconductor and retard the electron-hole recombination, such as noble metals deposition [8, 9], metal ion doping [10, 11] and anion doping [12, 13]. Consequently, coupling of semiconductors or metal oxides with different band gaps is good approach to prepare photocatalysts with high activity and good stability. The excited electrons can transfer in coupled semiconductors from the high conduction band to the low one, leading to efficient separation of photogenerated electron-hole pairs [14].

In recent years, the preparation and exploration of core–shell nanoparticles have been demonstrated to possess improved physical and chemical properties for electronics, magnetism, optics, catalysis, and other applications. Numerous studies have shown that the unique structure of core–shell nanoparticles improve their catalytic activity and selectivity. In photocatalysis, core/shell structure plays an important role in the charge separation, transport and utilization during photocatalytic H_2 evolution. For example, Zhang et al. [15] reported that the coupling of CdS and TiO_2 nanorods has a beneficial role in improving charge separation and in the reduction of electron–hole rate recombination, due to excited electrons from CdS nanoparticles can quickly transfer to TiO_2 nanorods and the extension of absorption spectrum into the visible region by TiO_2@CdS core–shell nanorods.

TiO_2 has been deeply studied as a promising candidate to support the future hydrogen economy due to its high catalytic activity, long-term photostability, strong oxidizing power, abundant availability, low-cost, non-toxicity and environmentally friendly nature [16, 17]. It can be activated only under UV light irradiation (380 nm) due to its large band gap energy (anatase 3.2 eV, rutile 3.0 eV). To extend its light absorption into the visible light spectrum and prevent the high rate of photogenerated electron–hole recombination, a core-shell nanostructure is an excellent option to be used. Several semiconductors have been used as sensitizers in core-shell structured because they are capable to transfer electrons to large band gap semiconductors such as TiO_2, for instance Fe_3O_4@TiO_2 [18], Cu_2O@TiO_2 [19], WO_3@TiO_2 [20],

$CdS@TiO_2$ [21], $Fe_3O_4@ZnO@TiO_2$ [22] $ZnS@TiO_2$ [23] and so on showing good result for different applications.

Among low-cost transition metal oxide catalysts are copper and nickel oxide two of the most efficient oxidation catalysts to substitute precious metals. The oxidation state of copper changes between CuO, Cu_2O and Cu, while of nickel changes between Ni_2O_3, NiO and Ni, as a function of temperature and hydrogen partial pressure. The differences in oxygen defects, oxygen holes and oxygen adsorbed species in these oxidation states are thought to be the reason for the high activity and selectivity of these metal oxide catalysts [24]. It is widely recognized that p-type CuO facilitates charge separation and acts as a water reduction site [25]., it also has been regarded as a good active component for the reduction of water under sacrificial condition [26], because it can prevent the recombination between photogenerated electrons and holes and can decrease the energy of the band gand. It can exist in several different forms on TiO_2, depending on the CuO content and catalyst pretreatment conditions. Due to CuO itself is inactive for H_2 production under UV or visible light irradiation, since the conduction band of CuO is more positive than that of the H_2O/H_2 redox potential, this semiconductor has been coupling with TiO_2 and NiO. On the other hand, NiO_x doping onto TiO_2 surface is effective for p-type (NiO_x)–n-type (TiO_2) junction preparation. Such NiO_x-doped TiO_2 catalysts were recently reported to show good performance of photocatalytic degradation of organic compounds [27].

This work presents the results obtained for an efficient photocatalytic hydrogen production in which CuO or NiO (15 wt. %) were introduced as core and TiO_2 as shell. Their performance in photocatalytic H_2 production was evaluated using glycerol/water solution as a model molecule for biomass. For comparative purposes, two other types of core shell NiO@CuO and CuO@NiO catalysts were also synthesized and evaluated. The photocatalytic activity of all samples for hydrogen evolution under UV-Vis irradiation was then compared under the same operation conditions.

II. Materials and Methods

A. Materials

Copper nitrate (98.5%, $Cu(NO_3)_2{\cdot}xH_2O$), nickel nitrate (98.2%, $Ni(NO_3)_2{\cdot}6H_2O$), sodium hydroxide (98%, NaOH), titanium (IV) butoxide (98%, TBOT) and hidroxypropil cellulose (Mw~ 80 000) were purchased from Sigma-Aldrich. Absolute ethanol (99.9%, CH_3CH_2OH) was obtained from J.T Baker. Deionized water (DW) was obtained using millipore purification system. All reagents were used as received without further purification.

B. Preparation of photocatalysts

CuO and NiO nanoparticle synthesis: appropriate amounts of copper or nickel nitrate were dissolved in 20 ml alcohol, separately. Then 1 M NaOH solution was added to the first solution (nickel or copper solution) and it was contained in a 250 ml beaker while the temperature of the new precipitated solution was increased to 80 ºC and maintained under stirring at 600 rpm for 6 h. The solution was keeping under agitation overnight, the precipitates were then washed three times with water to remove the impurities and were dried in an oven at 80 ºC for 12 h. Finally, the two catalysts were ground and the calcination in air was carried out using a muffle furnace at 350 ºC at a rate of 1 ºC/min to obtain CuO and NiO metal oxide nanoparticles.

TiO_2 coating: TiO_2 shell was prepared via sol-gel process [28]. CuO nanoparticles (0.125 g) were dispersed in 5 mL absolute ethanol and this solution was added in a mixture of 0.1 g hydroxypropyl cellulose, 20 mL absolute ethanol and 0.125 mL of deionized water. This mixture was stirred for 30 minutes at 600 rpm then 1 mL titanium (IV) butoxide in 5 mL absolute ethanol was injected, using a syringe pump, into the above solution at a rate of 0.5 mL min^{-1}; while the mixture was stirring at 900 rpm milk white solution was obtained. After injection, the temperature of the resulted solution was increased to 85 °C under reflux and agitation condition for 90 min. The precipitate containing $CuO@TiO_2$ was centrifuged, washed three times with ethanol and redispersed in 5 mL absolute ethanol. The coating procedure was repeated three more times in order to increase TiO_2 thickness layer. Finally, the samples were dried and calcined at 400 °C (1 ºC/min) for 3 h in an air atmosphere. Same procedure was followed for $NiO@TiO_2$ nanostructure preparation however NiO were used as core. A schematic representation of CuO and $NiO@TiO_2$ nanostructures is shown in Fig.1.

CuO and NiO coating: In order to prepare NiO@CuO, 0.125 g of NiO nanoparticles were dispersed in 5 mL absolute ethanol and this solution were added in a mixture of hydroxypropyl cellulose (0.1 g), absolute ethanol (20 mL) and deionized water (0.125 mL). After stirring (30 minutes at 600 rpm) a mixed solution of 0.3 g $Cu(NO_3)_2{\cdot}3H_2O$ in 5 mL absolute ethanol was injected into the above solution at a rate of 0.5 mL min^{-1} while the mixture was stirring at 900 rpm. After injection, the temperature of the resulted solution was increased to 85 °C under reflux and agitation condition for 90 min. The NiO@CuO precipitated, was collected by centrifugation, rinsed three times with ethanol and redispersed in 5 mL absolute ethanol. The coating procedure was repeated three more times. The resulting powder was dried at 80 °C and then calcined in air at 350 °C for 2 h. Same procedure was followed for CuO@NiO nanostructure preparation however 0.3g of $Ni(NO_3)_2{\cdot}3H_2O$ were used as core.

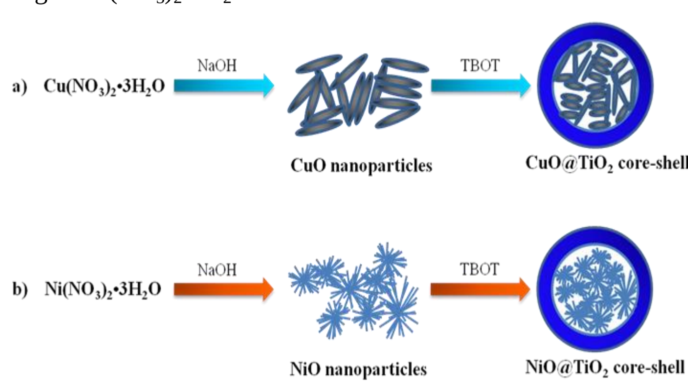

Fig. 1. Scheme of preparation process for a) $CuO@TiO_2$ and b) $NiO@TiO_2$ core-shell structures.

C. Characterization techniques

X-ray Diffraction measurements were carried out on a Rigaku MiniFlex 600 X-ray diffractometer, using $CuK_{\alpha 1}$ radiation (λ=1.5406 Å). The accelerating voltage and the applied current were 40 kV and 15 mA, respectively. The 2θ angular regions from 10º to 100º were explored with a scanning speed of 0.1º in 0.01θ/min in order to obtain the particle size using Scherrer's formula.

For UV–Visible spectroscopy measurements a UV-visible spectrophotometer GBC Cintra 20 was employed and recorded over the range from 200 to 800 nm. The reflection data were converted to absorbance through the standard Kubelka– Munk method.

The scanning electron microscopy images were acquired on a FEI Quanta 3D equipped with X-ray energy dispersive spectrometer (EDS) measurements. SEM was operated at 10 kV while EDS analysis was performed at 30 kV.

The transmission electron microscopy observations of the nanoparticles were done using JSM 7800F JEOL, equipped with EDS measurements. TEM was operated at 15 kV. For TEM images the sample powder was dispersed in isopropyl alcohol by using ultrasonic radiation for 10 min and a drop of the suspension was placed onto the copper-coated grids.

The nitrogen adsorption–desorption isotherms at -196 °C were measured using a gas sorption Quantachrome NovaWin system. Before carrying out the measurements, each sample was degassed at 200 °C for 2 h. Specific surface area determination was performed by using the Brunauer–Emmett–Teller (BET) method. The average pore size and pore volume were calculated by using the Barrett–Joyner–Halenda (BJH) method.

D. Photocatalytic test

The photocatalytic activity for hydrogen evolution was studied in a closed-gas circulation system connected to a autosystem XL Perkin Elmer gas chromatograph equipped with a Carbonxen 1006 PLOT capillary column and a thermal conductivity detector (TCD). The photocatalyst (15 mg) was added in a 20 mL clear glass vial at ambient temperature and atmospheric pressure containing 1.5 ml glycerol and 13.5 ml deionized water, and this was connected to the closed gas circulation system. The suspension was then exposed to a Hg-Xe Newport 66901 (solar simulator) 200 W irradiation lamp at a distance of 17 cm. Before each experiment the suspension was dispersed by an ultrasonic bath for 15 min then the photocatalytic cell was purged with nitrogen for 15 min to eliminate oxygen and other gases. The reaction was studied during 8 h with vigorous agitation (500 rpm) to ensure the uniform irradiation of the suspension. The photocatalytic cell is equipped with gas inlet/outlet lines and sealed with a silicone rubber septum to collect and transfer gaseous products to the analytical system measured.

III. Results and discussion

A. XRD

X-ray diffractograms of pure NiO and CuO prepared by precipitation, and NiO@TiO_2 and CuO@TiO_2 prepared by sol-el method were determined. Fig. 2A illustrates X-ray diffractograms of pure NiO and CuO, peaks at 2θ = 37.2°, 43.3°, 62.9°, 75.4° and 79.4◦ can be well indexed to cubic structure of nickel oxide by referencing to JCPDS (No. 47-1049). All XRD peaks of copper oxide (2θ= 32.5°, 35.4°, 38.7°, 48.7°, 53.5°, 58.3°, 61.5°, 66.2°, 68.1° and 72.4°) well match the monoclinic CuO phase (JCPDS No. 48-1548), demonstrating the formation of well-crystallized CuO nanoparticles. Besides CuO and NiO characteristic peaks, no impurity peaks were detected. The average crystallite size of pure CuO and NiO were estimated from the FWHM of NiO (2 0 0) and CuO (0 0 2) reflections using the Scherrer equation, with values of 3.2 and 5.1 nm, respectively.

The XRD patterns of NiO@TiO_2 and CuO@TiO_2 are shown in Fig. 2B. In both patterns, the peaks at 2θ= 25.3°, 36.6°, 37.8|, 38.6°, 48.0°, 53.9°, 55.1°, 62.7°, 68.8°, 70.3°, 74.1°, 82.2° and 94.2°, are indexed as anatase TiO_2, 21-1272 JCPDS card. The anatase crystallite size were derived from the most intense diffraction peak (1 0 1) at 2θ= 25.3°, with a value of 4.4 nm for NiO@TiO_2 and 4.2 nm for CuO@TiO_2.

XRD patterns of NiO@TiO_2 and CuO@TiO_2 samples are dominated by anatase peaks however small CuO peak at 35.4° (0 0 2) and NiO peak at 43.3° (2 0 0) were also detected. Due to metal oxide loading of NiO and CuO was 15 wt.%, certainly above detection limits, the decrease in the intensity of characteristic peak of NiO and CuO could be tentatively attributed to TiO_2 shell thickness coating [28].

B. UV–Vis DRS

The optical properties of NiO@TiO_2 and CuO@TiO_2 photocatalysts were probed by UV–Vis DRS and converted to the UV-Vis absorption edge energies by the Kubelka–Munk method as shown in Fig.3A and B. It should be pointed out that the DRS of both samples are very similar to that presented of bare TiO_2 which indicates that the presence of NiO or CuO practically did not change the intrinsic properties of TiO_2. As can be seen in Fig. 3B, for NiO@TiO_2 the band gap energy was estimated to be 3.19 eV while, for CuO@TiO_2 was 3.11 eV. Obviously, the presence of CuO caused greater absorption of photons in the visible compared with NiO addition. Usually, the addition of Ag, Cu, Pt toTiO_2 causes changes in the band gap transition to larger values in the wavelength [29,30]., however, our results presented in Fig. 3 demonstrate the stabilization of TiO_2 would be encapsulating the CuO and NiO phases with a minimal chemical interaction. Indeed, it is worth noting that CuO-TiO_2 composites show a dramatic reduction in their band gap energy, with respect to that of bare TiO_2 (E_{bg}= 3.1-3.2 eV), even with very small amounts of CuO [31].

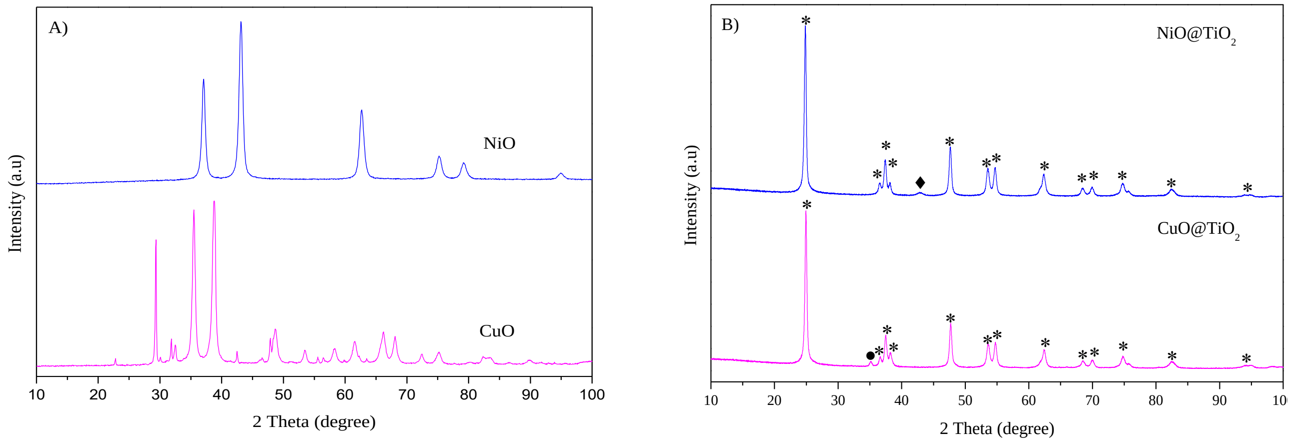

Fig. 2. X-ray diffraction patterns of A) pure cubic NiO and monoclinic CuO B) $NiO@TiO_2$ and $CuO@TiO_2$ calcined at 400 °C, where * represents TiO_2 anatase phase, • CuO monoclinic phase and ♦ NiO cubic phase.

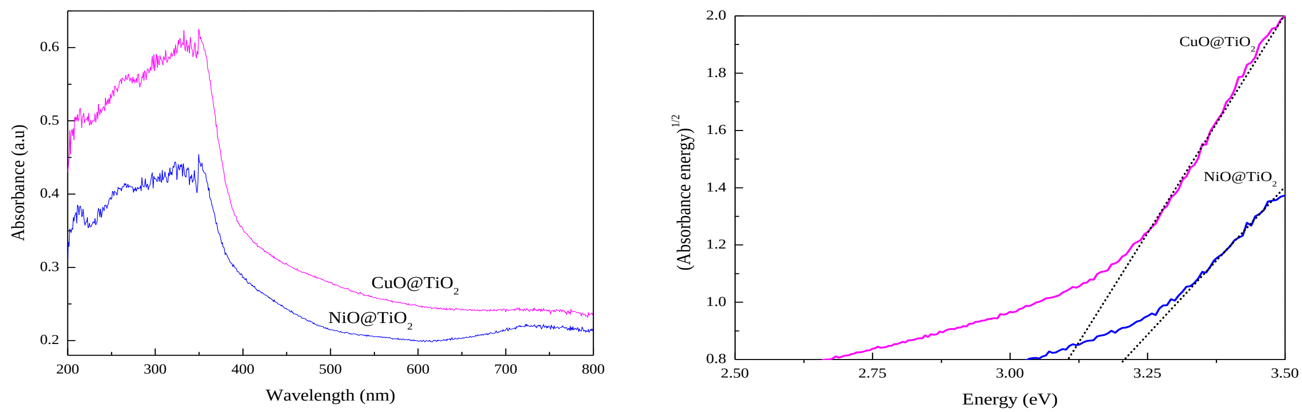

Fig. 3. A) UV-vis spectra measured for $NiO@TiO_2$ and $CuO@TiO_2$ and B) Plot of (adsorbance· energy)$^{1/2}$ versus energy.

C. SEM

The morphology of pure NiO and CuO catalyst powder prepared by precipitation method are shown in Fig.4.

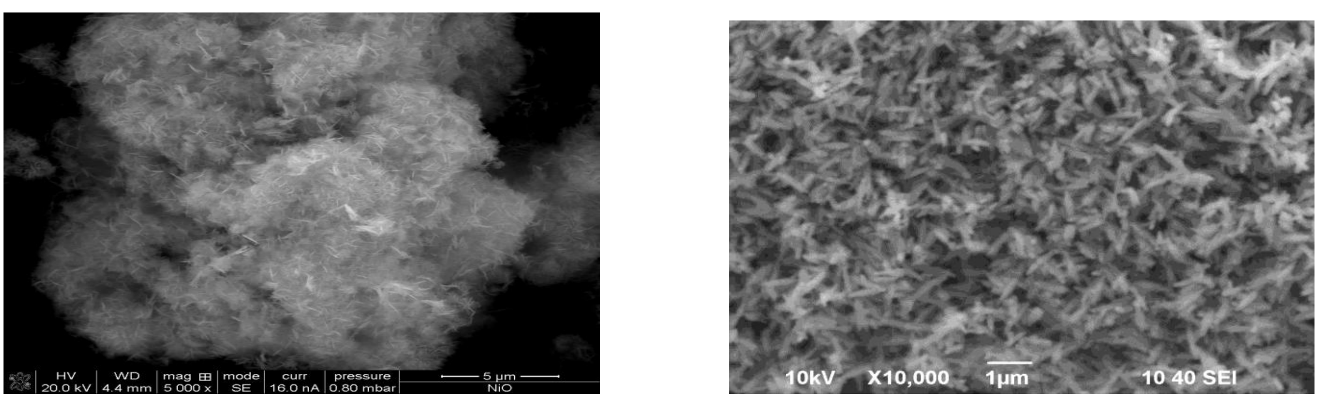

Fig. 4. SEM images of pure A) NiO and B) CuO prepared by precipitation method and calcined at 450°C.

It is clear that SEM images for pure NiO showed an agglomeration of fine nanoparticles forming a dandelion-like structure; on the other hand, a close inspection of micrograph of pure CuO reveals larger nanoparticles with homogeneous morphology and uniform size similar to seeds, these results agreed with those obtained by XRD.

D. TEM

Fig. 5 shows the TEM micrographs of the prepared $NiO@TiO_2$ and $CuO@TiO_2$ photocatalysts after the three shell coating steps. An irregular sized spherical morphology can be observed in both materials.

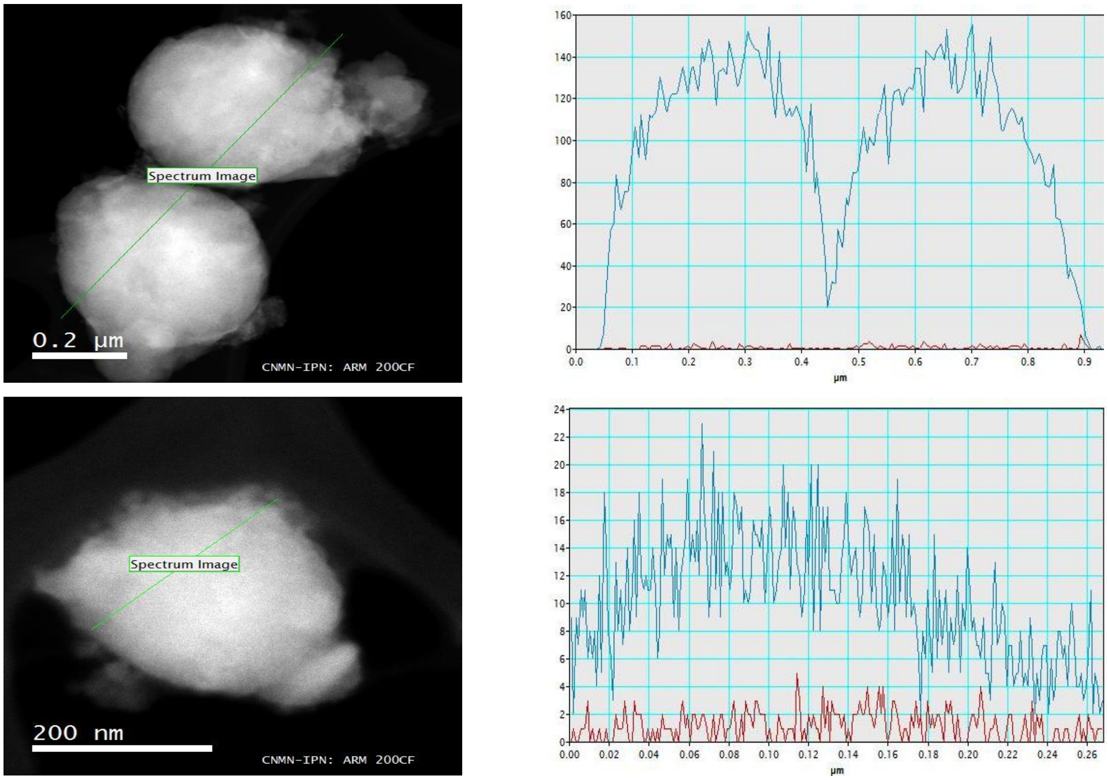

Fig. 5. TEM images (A-B) of $NiO@TiO_2$ spheres 90,000x magnification and $CuO@TiO_2$ spheres 50,000x magnification, respectively and the EDS results (C-D) for $NiO@TiO_2$ and of $CuO@TiO_2$, respectively.

The particle diameter calculated from SEM images is about 400- 500 nm for spherical $NiO@TiO_2$ and $CuO@TiO_2$. TiO_2 rough surface is composed of small spherical anatase TiO_2 crystallites. EDS mounted on the TEM machine was carried out to clarify the compositions of the samples. It was found that $NiO@TiO_2$ sample consists of Ti, Ni and O elements. EDS also showed that $CuO@TiO_2$ is composed of O, Cu and Ti. In both cases it is clear that TiO_2 shell is covering the surface of the core.

E. N_2 physisorption

The surface structural characteristics of $NiO@TiO_2$ and $CuO@TiO_2$ core-shell nanostructures were analyzed by nitrogen sorption isotherm techniques. The measured isotherms belong to type IV isotherm of IUPAC classification with hysteresis loops, which indicates capillary condensation [32] as is common in mesoporous (2-50 nm) materials. Fig. 6 showed the nitrogen adsorption-desorption isotherms of the samples and their surface characteristics are included in Table I.

Examination of Table I shows the pore size distribution for $NiO@TiO_2$ is 50.2 nm while $CuO@TiO_2$ average pore size is 48.2 nm. The BET surface area of $NiO@TiO_2$ and $CuO@TiO_2$ samples was calculated to be 72 m^2/g and 53 m^2/g, respectively. It can see in both samples that the BET surface areas of the photocatalysts are bigger than 50 m^2/g, common surface area for TiO_2 [25, 26], indicating that there is not too much deposition of CuO or NiO particles in TiO_2 surface.

TABLE I. SPECIFIC SURFACE AREA, CRYSTALLITE SIZE, AVERAGE PORE SIZE AND POROUS VOLUME

Catalyst	*Surface area (m^2/g)*	*Crystallite size (nm)*	*Average pore size (nm)/ porous volume (cm^3/g)*
$CuO@TiO_2$	73	4.4	50.2 / 0.09
$NiO@TiO_2$	52	4.2	48.2 / 0.06

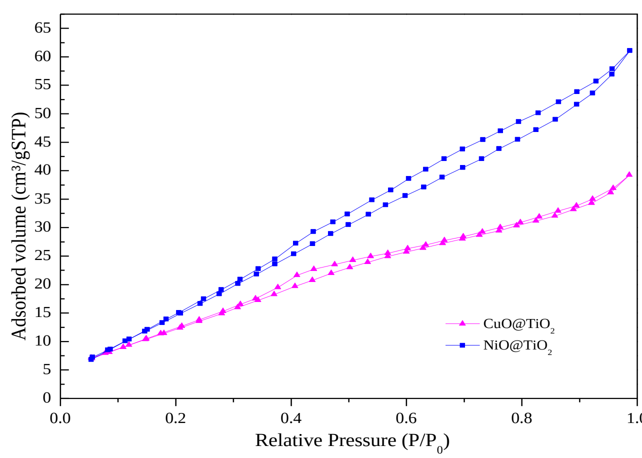

Fig. 6. Nitrogen adsorption/desorption isotherms of sol–gel TiO2 modified samples.

F. *Photocatalytic hydrogen production tests*

The photocatalytic activity of four CuO and NiO catalysts powders for H_2 production from glycerol-water mixtures (90 vol.% glycerol, 10 vol.% H_2O) under simulated solar light at ambient temperature were evaluated (Fig.7). Results of the rates of evolution of H_2 and other gaseous product as CO_2 are presented in Fig. 8 and summarized in Table II. TiO_2 Degussa P25 was used as a reference for the photocatalytic test.

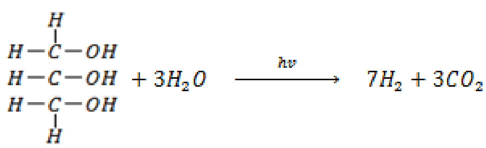

Fig.7. Photocatalytic reaction from aqueous glycerol solution.

The maximum H_2 evolution was 153.8 μmol g^{-1} at 2 h in photocatalytic reaction under the conditions used; CuO core nanoparticles dramatically enhanced the rate of H_2 production. The amount of CO_2 evolved was 20.1 μmol g^{-1}. The photocatalytic activity of NiO@TiO2 photocatalyst was compared, confirming that CuO core is a better candidate than NiO, for solar H_2 production. The CuO@NiO and NiO@CuO catalyst displayed very low photocatalytic activity for H_2 production showing that pure CuO and NiO were not active for the photocatalytic hydrogen production under the test conditions used in this study.

TABLE II. SUMMARY OF PHOTOCATALYTIC ACTIVITY FOR H_2 PRODUCTION OF THE. PHOTOCATALYSTS AFTER 2 H OF IRRADIATION

Catalyst	*H_2 production rate (μmol/ g h)*	*H_2 production rate (μmol/ g h)*
NiO@CuO	6.2	2.2
CuO@NiO	5.3	1.5
CuO@TiO_2	153.8	20.1
NiO@TiO_2	48.1	11.5
TiO_2 P25	13.8	4.2

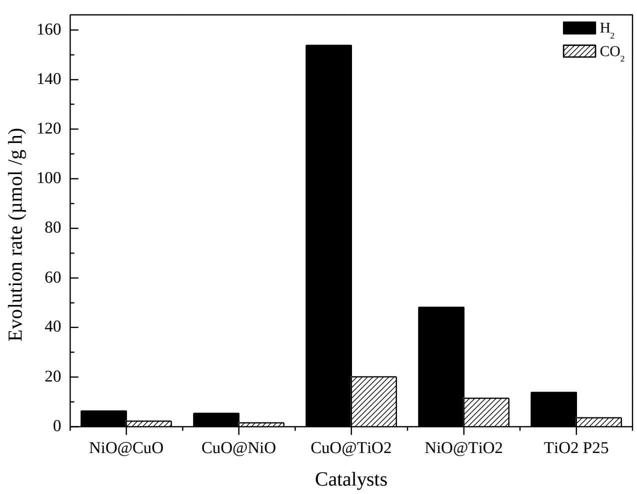

Fig.8. Evolution of H_2 and CO_2 for different photocatalysts in a glycerol-water mixture under visible light irradiation at ambient temperature.

G. *Effect of photocatalyst concentration*

In order to study the photocatalyst concentration effect on the photocatalytic activity of the core-shell spheres and quantify the dependence of hydrogen evolution on photocatalyst concentration, hydrogen production rate were determined as shown in Fig. 9. It can be seen that with the increase of photocatalyst concentration from 0.5 g/L to 2 g/L, the photocatalytic hydrogen production is gradually increased. However, photocatalyst 1 g/L concentration seems to be the optimal level, because to duplicate the suspension does not result in duplicate hydrogen production rate because when photocatalyst concentration is above optical level, the light does not penetrate the suspension due to scattering by the suspended photocatalyst particles, resulting in a decrement in photocatalytic H_2 production.

H. *The stability of NiO@TiO_2 and CuO@TiO_2 core-shell spheres.*

Stability is a main factor to recognize the practical applications for photocatalytic H_2 production. To estimate the photocatalytic stability of CuO@TiO_2 and NiO@TiO_2 spheres, for activity cycles were performed as Fig. 10 showed. In both catalysts, it can be seen that hydrogen production rate gradually decreases with the increase of irradiation time in every cycle. Note that hydrogen production rate was below 50% of initial value after the third cycle, almost with both catalysts, which means that the original nanostructure is not photochemically stable.

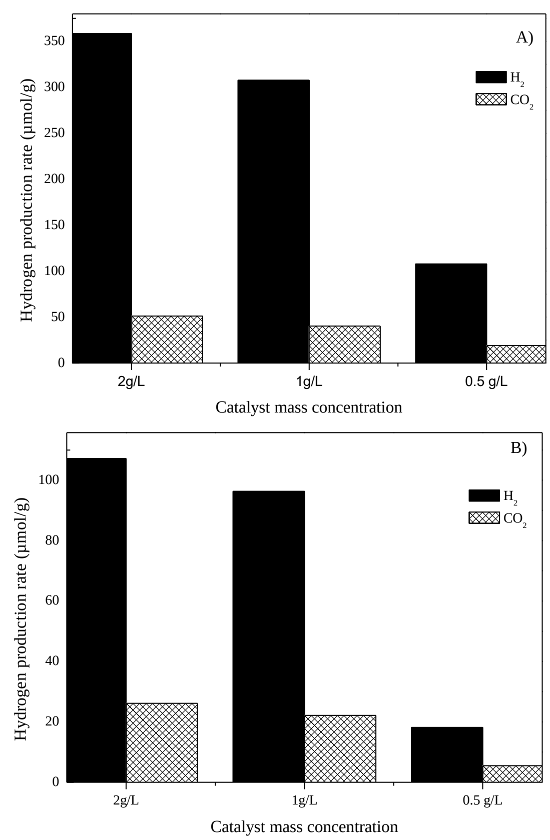

Fig. 9. Hydrogen generation rate of a) CuO@TiO_2 and b) NiO@TiO_2 at different catalyst mass concentration after 2 h of irradiation time.

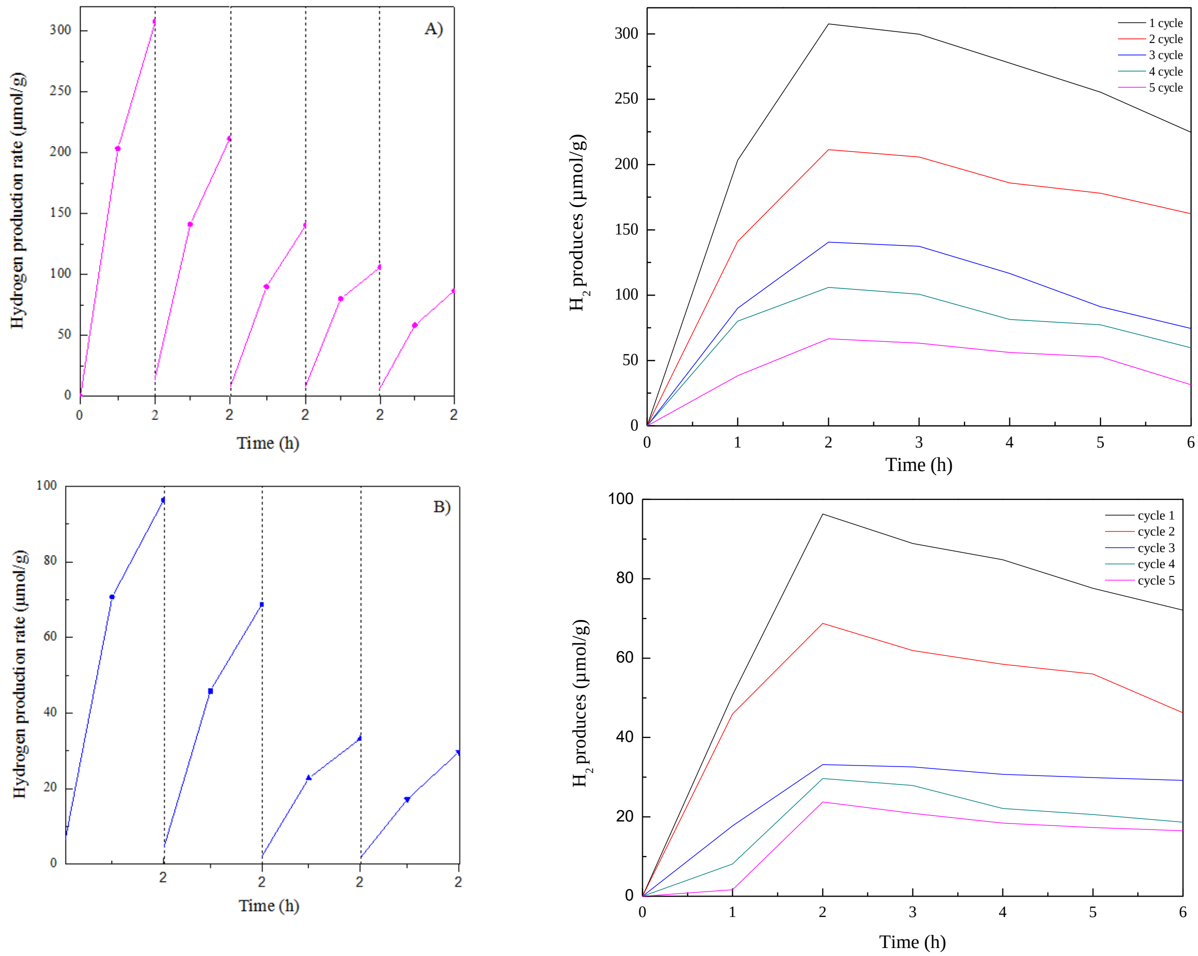

Fig. 10.Time courses of photocatalytic H_2 production over a) CuO@TiO_2 and b) NiO@TiO_2.

Furthermore, there is no significant decrease in the photocatalytic activity after 3 cycles. The experimental results demonstrate that the catalysts exhibit a not very high stable photocatalytic activity and tended to reach the behavior of bare TiO_2.

IV. CONCLUSIONS

CuO and NiO @TiO_2 core-shell spheres were synthesized through a modified sol-gel method. The obtained photocatalytic materials were uniform particles with an average size of 400–600 nm. Pure CuO and NiO displayed very low photoactivity for H_2 evolution, whereas the existence of TiO_2 rich shells linked with CuO or NiO can improve hydrogen evolution efficiently from glycerol aqueous solution. A higher photocatalytic activity was found with the CuO@TiO_2 compared with that of NiO@TiO_2 core-shell spheres. The higher activity of CuO@TiO_2 photocatalyst was explained in terms of electron transfer from photoexcitated TiO2 to the conduction band of CuO as well as photogenerated electrons production after visible light irradiation.

The accumulation of excess electrons in the conduction band of CuO caused a negative shift in the Fermi level of CuO to give the required energy for efficient water reduction as demonstrated in Fig. 11. In addition, core-shell structure played an important role in improving photogenerated carrier transfer and charge separation leading to enhancement of photocatalytic activity.

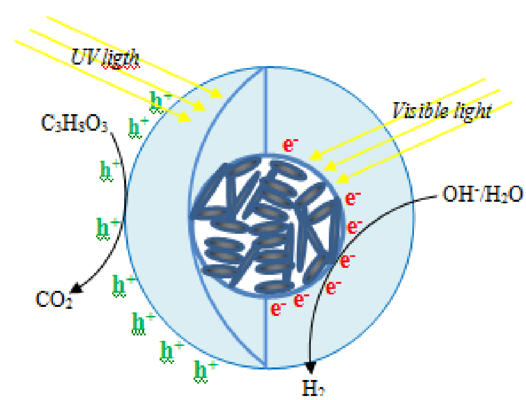

Fig. 11. Proposed photocatalytic hydrogen evolution process over CuO@TiO_2 core-shell spheres

ACKNOWLEDGMENT

Financial support of this work was provided by Instituto Politécnico Nacional. We also thank ESIQIE Catalysis and Materials Laboratory and the support offered by CONACYT-Mexico.

REFERENCES

[1] Stolten D. Hydrogen and fuel cells, fundamentals, technologies and applications. Weinheim: Wiley-VCH 2010.

[2] Grigoriev S, Porembsky V, Fateev V. Pure hydrogen production by PEM electrolysis for hydrogen energy. Int J Hydrogen Energy 2006; vol. 31, pp. 171-5.

[3] Ehsan Mostafavi, Nader Mahinpey, Moshfiqur Rahman , Mohammad Hashem Sedghkerdar, Rajender Gupta. High-purity hydrogen production from ash-free coal by catalytic steam gasification integrated with dry-sorption CO_2 capture. Fuel 2016; vol. 178, pp. 272–282.

[4] Rezaiyan J, Cheremisinoff NP. Gasification technologies: a primer for engineers and scientists. CRC Press; 2005.

[5] J.C. Guevara, J.A. Wang, L.F. Chen, M.A. Valenzuela, P. Salas, A. García-Ruiz, J.A. Toledo, M.A. Cortes-Jácome, C. Angeles-Chavez, O. Novaro. Ni/Ce-MCM-41 mesostructured catalysts for simultaneous production of hydrogen and nanocarbon via methane decomposition. International Journal of Hydrogen Energy 2010; vol. 35, pp. 3509.

[6] V. Kyriakou, I. Garagounis, A. Vourros, E. Vasileiou, A. Manerbino, W.G. Coors, M. Stoukides. Methane steam reforming at low temperatures in a $BaZr_{0.7}Ce_{0.2}Y_{0.1}O_{2.9}$ proton conducting membrane reactor. Applied Catalysis B: Environmental 2016; vol. 186, pp. 1–9.

[7] Wenlong Zhang, Yi Li, Chao Wang, Peifang Wang, Qing Wang. Energy recovery during advanced wastewater treatment: Simultaneous estrogenic activity removal and hydrogen production through solar photocatalysis. Water research 2013; vol. 47, pp. 1480-1490.

[8] P. Wei, et al., Effect of Pt loading and calcination temperature on the photocatalytic hydrogen production activity of TiO2 microspheres, Ceramics International 2013; http://dx.doi.org/10.1016/j.ceramint.2012.12.045.

[9] Guopeng Wu, Tao Chen, Weiguang Su, Guohua Zhou, Xu Zong, Zhibin Lei, Can Li. H_2 production with ultra-low CO selectivity via photocatalytic reforming of methanol on Au/TiO_2 catalyst. International Journal of Hydrogen Energy 2008; vol. 33, pp. 1243 – 1251.

[10] R. Dholam, N. Patel, M. Adami, A. Miotello, Hydrogen production by photocatalytic water-splitting using Cr or Fe-doped TiO2 composite thin films photocatalyst, International Journal of Hydrogen Energy 2009; vol. 34, pp. 5337–5346.

[11] W.Cai, G.Lu, J.He, Y.Lan, The adsorption feature and photocatalytic oxidation activity of $K_{1\_2x}M_xTiNbO_5$ (M=Mn, Ni) for methyl mercaptan in methane, Ceramics International 2012; vol. 138, pp. 3167–3174.

[12] H. Tian, J. Ma, K. Li, J. Li, Hydrothermal synthesis of S-doped TiO_2 nanoparticles and their photocatalytic ability for degradation of methyl orange, Ceramics International 2009; vol. 35, pp. 1289–1292.

[13] R. Asahi, T. Morikawa, T. Ohwaki, K. Aoki, Y. Taga, Visible-light photocatalysis in nitrogen-doped titanium oxides, Science 2001; vol. 293, pp. 269–271.

[14] Xian-Jun Zheng, Yong-Jie Wei, Li-Fang Wei, Bing Xie, Ming-Bao Wei. Photocatalytic H_2 production from acetic acid solution over CuO/SnO_2 nanocomposites under UV irradiation. International Journal of Hydrogen Energy 2010; vol. 35, pp. 1709-1718.

[15] Huimin Jia, Hua Xu, Yan Hu, Yiwen Tang, Lizhi Zhang. TiO_2@CdS core–shell nanorods films: Fabrication and dramatically enhanced photoelectrochemical properties. Electrochemistry Communications 2007; vol. 9, pp. 354–360.

[16] Yaojun Zhanga, Yong Xua, Tuo Li, Yachao Wanga. Preparation of ternary Cr_2O_3–SiC–TiO_2 composites for the photocatalytic production of hydrogen. Particuology 2012; vol.10, pp. 46– 50.

[17] L.Kokporka, et al. Sol–gel synthesized mesoporous assembled TiO_2–ZrO_2 mixed oxide nanocrystals and their photocatalytic sensitized H_2 production activity under visible light irradiation, Materials Science in Semiconductor Processing (2013), http://dx.doi.org/10.1016/j.mssp.2012.12.007i.

[18] Qinghang He, Zhenxi Zhang, Jianwen Xiong, Yuying Xiong, Hua Xiao. A novel biomaterial Fe_3O_4:TiO_2 core-shell nano particle with magnetic performance and high visible light photocatalytic activity. Optical Materials 2008; vol. 31, pp. 380–384.

[19] Xiaodan Su, Jingzhe Zhao, Yunling Li, Yanchao Zhu, Xiaokun Ma, Fang Sun, Zichen Wang. Solution synthesis of Cu_2O/TiO_2 core-shell nanocomposites . Colloids and Surfaces A: Physicochem. Eng. Aspects 2009; vol. 349, pp. 151–155.

[20] W. Smith, Y.P. Zhao. Superior photocatalytic performance by vertically aligned core–shell TiO_2/WO_3 nanorod arrays. Catalysis Communications 2009; vol. 10, pp. 1117–1121.

[21] H.L. Meng, C. Cui, H.L. Shen, D.Y. Liang, Y.Z. Xue, P.G. Li, W.H. Tang. Synthesis and photocatalytic activity of TiO_2@CdS and CdS@TiO_2 double-shelled hollow spheres.Journal of Alloys and Compounds 2012; vol. 527, pp.30– 35.

[22] Fenglong Wang, Jiurong Liu, Xinzhen Wang, Jing Kong, Song Qiu. Synthesis of hollow Fe_3O_4 at ZnO at anatase TiO_2 core–shell structured spheres. Ceramics International 2012; vol. 38, pp.6899–6902.

[23] Sonalika Vaidya, Amitava Patra, Ashok Kumar Ganguli. CdS@TiO_2 and ZnS@TiO_2 core–shell nanocomposites: Synthesis and optical properties Colloids and Surfaces A: Physicochem. Eng. Aspects 2010; vol. 363, pp. 130–134.

[24] Nagi R.E. Radwan, M.S. El-Shall, Hassan M.A. Hassan. Synthesis and characterization of nanoparticle Co_3O_4, CuO and NiO catalysts prepared by physical and chemical methods to minimize air pollution. Applied Catalysis 2007; vol. 331, pp. 8–18.

[25] Wan-Ting Chen, Vedran Jovic, Dongxiao Sun-Waterhouse, Hicham Idriss, Geoffrey I.N. Waterhouse. The role of CuO in promoting photocatalytic hydrogen production over TiO_2. International Journal of hydrogen energy 2013; vol. 38, pp. 1503-1504.

[26] Jiang Wua, Chaoen Li, Xuying Zhao, Qiang Wu, Xuemei Qi, Xiantuo Chen, Tao Hu, Yan Cao. Photocatalytic oxidation of gas-phase Hg^0 by CuO/TiO_2. Applied Catalysis B: Environmental 2015; vol. 176-177, pp. 559–569.

[27] Ruixia Liu, Hiroshi Yoshida, Shin-ichiro Fujita, Masahiko Arai. Photocatalytic hydrogen production from glycerol and water with NiO_x/TiO_2catalysts. Applied Catalysis B: Environmental 2014; vol. 144, pp. 41– 45.

[28] Ilkeun Lee, Ji Bong Joo, Yadong Yin, and Francisco Zaera. AYolk@Shell Nanoarchitecture for Au/TiO_2 Catalysts. Angew. Chem. 2011; vol. 50, pp. 10208 –10211.

[28] E. Grabowska, A.Zaleska, S. Sorgues, M. Kunst, A. Etcheberry, C. Colbeau-Justin and H. Remita. Modification of Titanium(IV) Dioxide with Small Silver Nanoparticles: Application in Photocatalysis, J.Phys. Chem. C, 2013; vol. 117, pp.1955.

[29] E.Kowalska, H.Remita, C.Colbeau-Justin, J.Hupka, J.Belloni. Modification of titanium dioxide with platinum ions and clusters: application in photocatalysis. J.Phys.Chem C. 2008; vol. 112, pp.1124-1131.

[30] Ana L. Luna, Miguel A. Valenzuela, Christophe Colbeau-Justin, Patricia Vázquez, Julia L. Rodriguez, Juan R. Avendaño, Salvador Alfaro, Salvador Tirado ,Adrián Garduño, José M. De la Rosa, Photocatalytic degradation of gallic acid over CuO-TiO_2 mixtures under Vis-LED irradiation, Applied Catalysis A: General 2016; vol. 52, pp. 140–148.

[31] Nadia Riaza, F.K. Chong, Binay K. Dutta, Zakaria B. Man, M. Saqib Khan, Ela Nurlael. Photodegradation of Orange II under visible light using Cu–Ni/TiO_2: Effect of calcination temperatura. Chemical Engineering Journal 2012; vol. 185– 186, pp. 108– 119.

Synthesis and Characterization of Pt_3Fe Alloy Nanoparticles for the Oxygen Reduction Reaction

M.M Tellez-Cruz, M.A. Padilla-Islas. O. Solorza-Feria
Departamento de Química
CINVESTAV,
México City, México
e-mail: mtellez@cinvestav.mx

H. Cruz-Martinez
Programa de Doctorado en Nanociencias y Nanotecnología
CINVESTAV,
Mexico City, México

***Abstract*— Fuel cells offer a potentially more efficient and cleaner source of energy due to their high efficiency as a result of the chemical energy converted directly to electrical energy with low emissions, compared with internal combustion engines and other energy-conversion devices. However, two major technical gaps limit their commercialization: cost and reliability. Currently, the main challenge in the wide spread of fuel cell technology is to decrease the content of Pt in catalysts without losing their performance.**

The synthesis of octahedral nanocatalyst of Pt_3Fe for oxygen reduction reaction (ORR) in acid media is presented. The catalyst was prepared through chemical reduction with the properly amount of oleylamine, oleic acid and precursor salts (Pt $(acac)_2$ and $Fe(acac)_3$), for subsequent dispersion in a carbon matrix (Vulcan Carbon) previously thermally treated. The presence of the alloy Pt_3Fe in the catalyst was proved by XRD. TEM micrographs shown the morphology of the nanoparticles with an average 7-9 nm size. The electrochemical performance of Pt_3Fe/C was evaluated by cyclic voltammetry, CO stripping and rotating disk electrode in $HClO_4$ as electrolyte. Pt_3Fe/C nanocatalyst showed best catalytic activity in terms of mass activity and specific activity than commercially available 20-wt% Pt /C-Etek® catalyst. Therefore, this finding suggests a methodology for producing a carbon supported nanoframe nanocatalyst, which could be used as a cathode electrode in a PEM fuel cell.

Keywords*— *Pt_3Fe alloy; octahedral; ORR catalyst; fuel cells.

I. Introduction

Nowadays there is an urgent concern seeking energy resources or forms of energy conversion which allows replacement of fossil fuels such as gasoline or diesel [1], as well as the energy consumption has increased more than one hundred times since the industrial age [2], the problems of global pollution resulting from the use of such energy sources, have caused serious environmental problems such as global warming [3]. One of the most promising alternatives to solve this problem is the development of fuel cells technologies [4].

Fuel cells for mobile, stationary and transportation applications offer the advantages of high efficiencies result of direct conversion of chemical energy into electrical energy, low emissions when they are compared to internal combustion engines [5-7]. Among the various types of fuel cells, Proton exchange membrane fuel cells (PEMFC) are the that greater attention have captured for mobile, electronic and automotive [8] applications, due to its low operating temperature (between 50 -100 ° C) [9-12].

Even though the above, PEM cells face three major challenges that limit their marketing: performance, cost, and durability of the cells. The reduction reaction of oxygen (RRO) is at least six orders of magnitude slower than the reaction of hydrogen oxidation occurred at the anode [13] [14], which limits their performance [15] . With regard to large amounts of platinum catalyst required to accelerate the cathodic reaction, which results in a high cost for the fuel cell [16]. There are two main problems regarding stability: degradation proton exchange membrane and catalysts [17] [18]; with respect to the catalyst the problem is referred to instability of the metal nanoparticles used to speed RRO and the medium used to disperse the catalyst, since the acid medium of the cell causing corrosion problems in both components. Today most catalysts based on platinum are dispersed in carbonaceous substrates, in which corrosion begins to 0.97 V (NHE) [19], which results in that the nanoparticles migrate from their place and agglomerating and decreasing the electrochemically active surface.

In response to the three challenges mentioned above it has been developed several strategies to try to solve these problems. As efforts to improve cell performance, it has succeeded synthesizing many types of catalysts as alloys of bimetallic and trimetallic based alloys of platinum Pt-M (M= Pd, Cu, Ni, Co, Fe, Y, Mn, Cr, etc.) [20-27]; also it has explored Pt_3M alloys (M=V, Ti, Co, Fe, Ni) [4,28,29] and core-shell structures Pt@M (M=Co, Ni, Cu, Pd, Mo , Fe) [30-38] which showed a marked improvement in the activity toward oxygen reduction reaction compared to pure platinum nanoparticles. Such efforts have also resulted in a decrease in the cost of the catalyst as part of platinum in the catalyst is replaced by a metal lower cost: usually transition elements.

However, the stability is currently the most difficult problem to solve, since as previously mentioned must be optimized not only nanoparticles of the catalyst but also the support material of the catalyst, reason for which recently it been synthesized nanoparticles with various geometric shapes such as octahedral [1,16, 39, 40], truncated octahedral [41-43], cubes [1] [44], icosahedron [44] of various alloys, which have proved extremely stable even after between 4000-30000 potential sweep cycles. And with regard to the strategy followed to achieve an improvement in the stability of the support, is currently studying the strong interaction metal substrate (SMSI) between nanoparticles of Pt and support, in which seeks to use carbon supports with highly ordered structures such as carbon nanotubes, graphene and graphene oxide reduced [45-49].

Motivated by these reasons we decided to carry out the study of the catalytic activity of catalysts Pt_3Fe with octahedral structures supported on carbon Vulcan and study its stability and specific and mass activity for the reduction reaction of oxygen.

II. Experimental

A. Chemicals and materials

Platinum acetylacetonate (II) ($Pt(acac)_2$, 97%) acetylacetonate, Iron (III) acetylacetonate ($Fe(acac)_3$, 99%), oleylamine (70%), oleic acid (90%), ethanol (98%), Hexane (99%), glacial acetic acid (99.7%). All reagents were obtained from Sigma Aldrich and used without purification. Vulcan XC-72R Carbon Cabot was used as support nanoparticles with a previous heat treatment at 500 ° C under nitrogen flow to remove any adsorbed impurities.

B. Synthesis of catalyst

0.37 mmol of $Pt(acac)_2$ and 0.13 mmol of $Fe(acac)_3$ were dissolved in a mixture containing oleic acid and oleylamine in ratio 3:2 v/v. The mixture is purged with N_2 for 30 minutes, then the rises to 240°C and the reaction was kept 30 minutes until completion, then reaction was allowed to cool to room temperature. Subsequently the catalyst was washing with ethanol and hexane.

The catalyst was sonicated in ethanol for one hour. Simultaneously, 175 mg thermally treated Vulcan carbon is dispersed in ethanol. Both solutions were mixed and sonicated for an hour and subsequently magnetic stirring for 12 hours. Once the remaining magnetic stirring the catalyst is centrifuged and added 20 mL of glacial acetic acid and heated at 60 ° C for 30 minutes to clean the catalyst of possible organic residues, allowed to cool and washed with ethanol to remove acid remainder. Finally dried at 120°C in oil bath under N_2 flow for 2 h. The composition relative to the amount of coal was 30:70 Pt3Fe:C.

C. Surface area analysis

The surface area of the heat-treated carbon were measured using the Brunauer–Emmett–Teller analysis (BET, Gemini equipment II-2370, Micromeritics). The sample was degassed at 120 °C for 12 h in vacuum before use.

D. X-ray diffraction (XRD)

The identification of the crystal structure of the catalysts was performed by XRD2, using Brucker equipment (D8Venture), with Mo-Ka (λ = 0.7093 Å) radiation operated at 50 kV and 1 mA, in a range 2Θ 15 ° to 55 °. For the treatment of the data, we were used suite APEXIII.

E. X-ray photoelectron spectroscopy (XPS)

The elemental composition of these materials was determined using a K-alpha X-ray photoelectron spectrometer manufactured by Thermo Fisher Scientific Company. An XPS data analysis was performed using the Thermo Avantage software. XPS measurements were made with Al K-alpha radiation (1486 eV). The X-rays were microfocused at the source to give a spot-focus size of 400 μm in diameter, using lenses in standard mode. The analyser was run in the constant analyser energy (CAE) mode. The pass energy was set to 200 eV for survey scans and 50 eV for high-resolution regions. All XPS data were referenced according to the adventitious C 1s peak (284.6 eV).

F. High-resolution transmission electron microscopy (HRTEM)

Particle size, morphology, and distribution of the nanomaterial were assessed with HRTEM from JEM ARM200F instrument operated at an accelerated voltage of 300 kV.

G. Electrochemical measurements

Prior to the measurements of electrochemical characterization, the catalytic inks were prepared as follows [50]: 10 mg of the corresponding catalyst dispersed in 7 mL of a solution of 20% v/v of isopropanol and 0.05% ionomer Nafion (5% by weight) by sonication at a temperature below 10 ° C for 1 h. 10 uL were placed on a previously polished carbon electrode, the film was dried in air flow to obtain a catalyst loading of 20 $ug_{Pt}cm^{-2}$. Electrochemical measurements were carried out at room temperature (approximately 25°C) in a typical three-electrode cell with 0.1M $HClO_4$ solution was employed as electrolyte. A potentiostat / galvanostat AUTOLAB (Model PGSTAT128N), coupled to a rotating disc electrode (RDE) (Pine Instruments) was used for the electrochemical experiments. A Pt mesh was used as counter-electrode; potentials were determined using a reversible hydrogen electrode (RHE).

The cyclic voltammetry (CV) curves were recorded in a N_2 atmosphere at 50 mV s^{-1} between 0.05 V and 1.2 V for 30 cycles. The ORR polarization curves for the rotating disc electrode (RDE) in an O_2-saturated electrolyte were obtained at 20 mV s^{-1} through a positive sweep between 0.05 V and 1.05 V/RHE at rotation rates of 400, 900, 1600, and 2500 rpm. Additionally, the CO stripping charge was used to determine the electrochemical surface area (ESA). For CO-stripping measurements, the catalyst surface was previously saturated with CO by bubbling it through the electrolyte solution while polarizing the electrode at 0.1 V/RHE for 5 min. Then the remaining CO was purged by flowing N_2 for 10 min before commencing measurement, performed at a scanning rate of 20 mV s^{-1}.

III. Results and Discussion

A. *Surface area analysis*

The determination of the surface area of heat treated carbon Vulcan was performed by analysing BET obtaining a value of 230.1 ± 1.7 m^2 g^{-1}, this value is consistent with that reported in the literature [51]. It is noteworthy that coal only received a heat treatment and non-chemical functionalization (generally made with a oxidizing agent as nitric acid or hydrogen peroxide) as despite functionalization increases the dispersion of the nanoparticles in it, due an interaction of atoms generally oxygen with nanoparticles, also has a negative effect on stability, and present a reduced surface area, resulting from acid penetration into the pores of coal which causes a partial blockage of the pores due to the functional groups or a possible collapse in the pores of coal [52].

B. *X-ray diffraction (XRD)*

Fig. 1 shows the diffraction pattern for the catalyst Pt_3Fe/C, after removal of the background, showing the pattern slightly out of phase right $Pt_{3.2}Fe_{0.8}$ metal phase, indicating the contribution of some other phase in this case the phase contributes maximum diffraction signal is pure platinum, and $Pt_{3.2}Fe_{0.8}$ 96.7% while the remaining 3.3% is pure platinum.

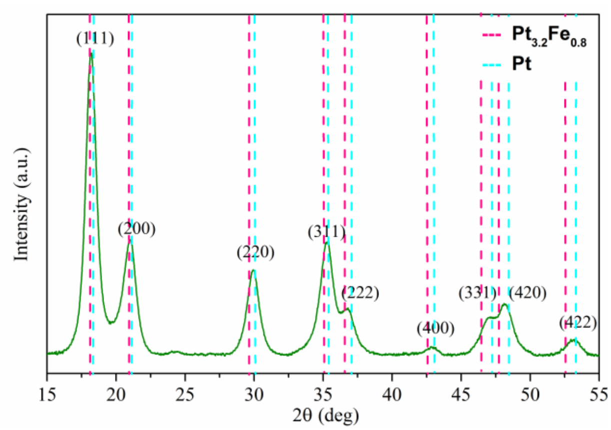

Figure 1. Diffraction patterns for Pt_3Fe/CV

This analysis revealed that this catalyst has a crystallite size of 4.7 nm, with cell parameters of 3.89 Å which corresponds to a (IT, 225) characteristic space group Fm-3m for a cubic structure face-centered, based on the file JCPDF for $Pt_{3.2}Fe_{0.8}$ (00-029-0717), however the cell parameter determined is slightly higher than reported in the card which indicates an lattice expansion in the structure of the catalyst, probably due to the portion of pure platinum which is not alloyed with Fe.

C. *X-ray photoelectron spectroscopy (XPS)*

The surface presence of the species present in the catalyst was determined by X-rays photoelectron spectroscopy. Figure 2 shows spectra's of ultra-high resolutions for zones of Fe 2p and Pt 4f with their respective settings multi-peaks.

Fig. 2 shows a peak at a binding energy of 708.8±0.2 eV which corresponds signal $Fe2p_{3/2}$ for the species of Fe(0) [53] (slightly shifted to energies higher than typical value rreported for Fe (0), probably due to metallic bonding with platinum with its corresponding doublet at 722.0±0.2eV for $Fe2p_{1/2}$. In addition to a contribution of the species Fe (OH)O at 711.8 ± 0.2eV with his double in 724.1 ± 0.2 eV [54]. The absence of oxides may be due to that in the catalyst´s, synthesis was used non-solvent and this allowed oleylamine and oleic acid strongly absorbed to the metal surface protecting to the environment and preventing oxidation.

It is also important to note that there are two intermediate signals between $Fe2p_{3/2}$ and $Fe2p_{1/2}$ signals in all cases, these signals are associated with characteristic satellites to Fe (II) and Fe (III) [55-57].

Regarding the spectra of two signals one Pt4f 71.4 ± 0.2 eV to corresponding $Pt4f_{7/2}$ of Pt-Fe and the doublet ($Pt4f_{5/2}$) at 74.8 ± 0.2 eV [58-60] are observed; and PtO species appears in $Pt4f_{7/2}$ = 72.4 ± 0.2 eV with his double in ($Pt4f_{5/2}$) = 75.8 ± 0.2 eV [61].

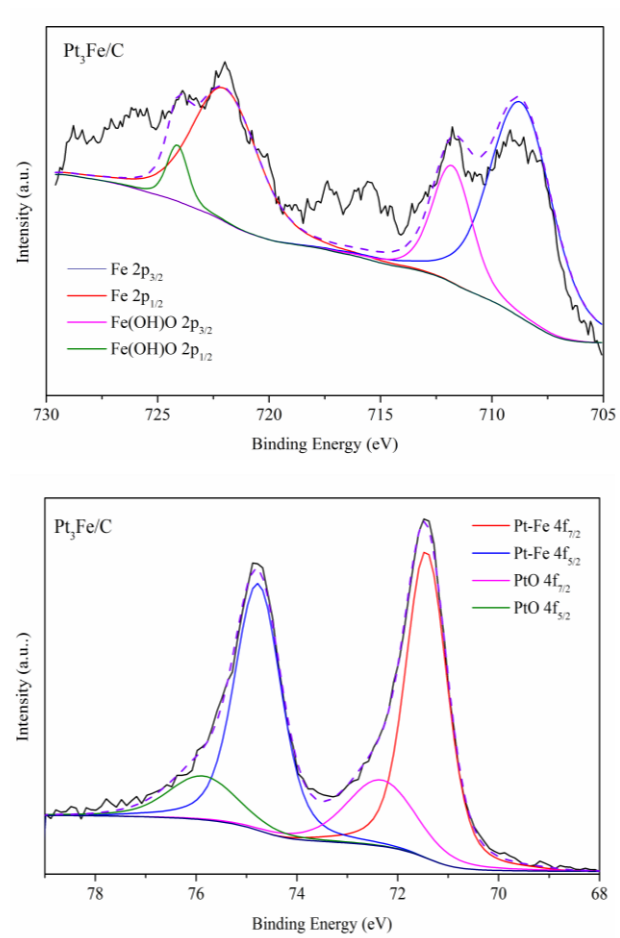

Figure 2. Spectra Fe2p zones (above) and Pt4f (below) with corresponding deconvolution. The solid black line represents the experimental spectrum and the dotted line represents the multipeaks adjustment.

D. *High-resolution transmission electron microscopy (HRTEM)*

Figure 3 shows representative micrographs low and high resolution of nanoparticles to Pt3Fe / C in which one can observe the good homogeneity in the particle size of between 7-9 nm and octahedral shape. It is possible to observe the crystal structure of the catalyst in the high-resolution images.

E. *Electrochemical measurements*

The catalyst was evaluated by cyclic voltamperomtria (Figure 4), noting that no peak was found at low potential to indicate the segregation of iron. Regarding the peak position reduction oxides adsorbed, it can be seen a shift to more positive potentials for catalysts of Pt_3Fe/C (0.78V vs NHE) compared to pure platinum (0.76 V potential vs NHE), i.e., at lower overpotentials, which means that the catalyst Pt_3Fe/C require less energy to reduce such oxides [35], this feature should be reflected in an improvement in the catalytic activity of the catalyst.

$$ESA\ (m^2 g^{-1}{}_{Pt}) = (Q_{CO} / 420\ \mu C cm^{-2} \times L_{Pt} \times A_{geo}) \times 10^5 \qquad (1)$$

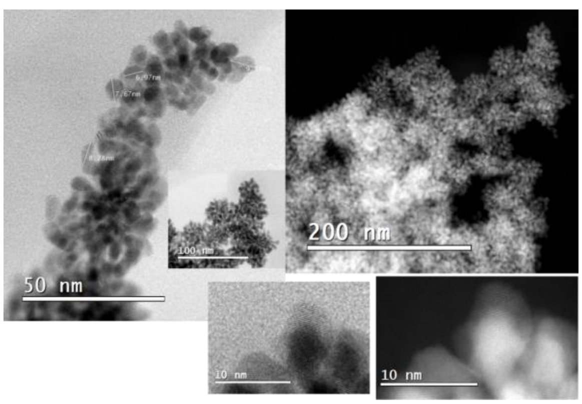

Figure 3. High-resolution STEM micrograph for the Pt_3Fe/C catalyst.

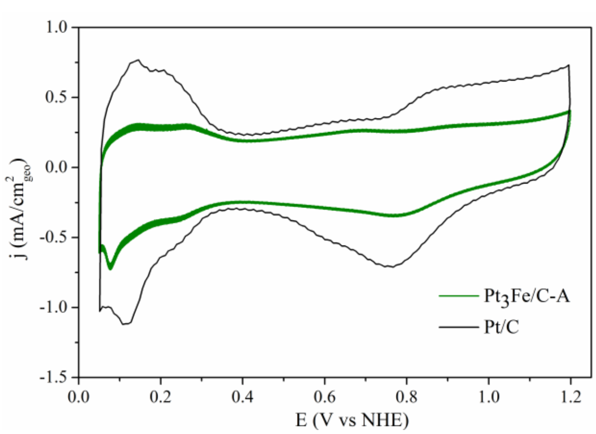

Figure 4. Cyclic voltammograms for Pt_3Fe/C and Pt/C nanocatalyst at 50 mV s^{-1} in 0.1 M $HClO_4$ at room temperature.

The determination of electrochemically active area was done by integrating the area under the curve obtained in the CO-stripping (Figure 5) by Equation 1 [50], it is also important to note that the difference in peak position is related to the nature of the material as well as its crystal structure as shown in recent studies [62].

ESA is where the electrochemically active area in $m^2 g_{Pt}^{-1}$; Q_{CO} is the transferred load to oxidize the pre-absorbed monolayer of CO, 420 μCcm^{-2} is used as conversion factor, L_{Pt} is the platinum loading in $mg_{Pt}cm^{-2}$ and A_{geo} is the geometric electrode area in cm^2, which in our case is 0.196 cm^2.

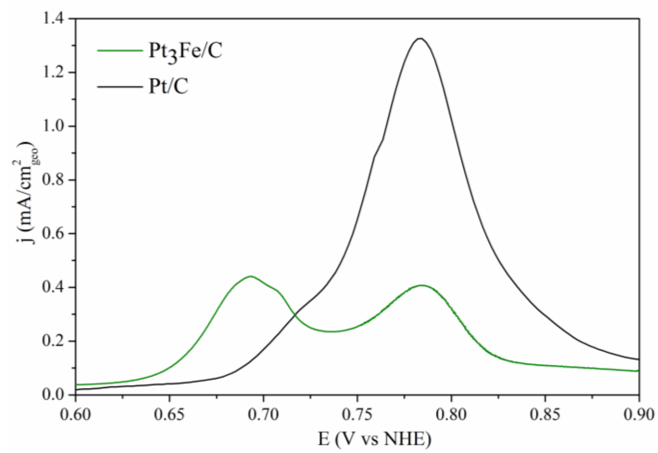

Figure 5. CO stripping voltammograms for Pt_3Fe/C nanoparticles (green line) and Pt/C (black line).

Comparing the electrochemically active areas shown in Figure 6, in which one can see that the catalyst have a lower ESA with respect to the pure platinum which may be due to agglomeration of nanoparticles on the carbonaceous support.

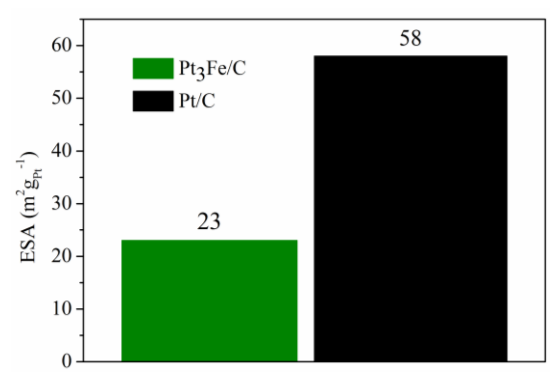

Figure 6. Comparison of electrochemically active area values (ESA) in $m^2 g_{Pt}^{-1}$ for Pt_3Fe/C and Pt/C.

The analysis for the determination of the specific activity and mass and the determination of kinetic parameters was performed by EDR steady state technique. In Figure 7, the polarization curves 1600rpm for Pt_3Fe/C catalyst and its comparison with Pt/C commercial. In this figure, it can be seen as the catalyst Pt_3Fe/C has less of potential for oxygen reduction.

Figure 7 shows the graph of the Tafel slopes previously corrected for mass transportation in a range of 0.85 to 0.95 V vs NHE, kinetic current was obtained by Equation 2 [63]:

$$J_k = J_L \times J / J_L - J \qquad (2)$$

Where J is the current density measured in $mAcm^{-2}_{geo}$, J_L it is the density and diffusion limited current density, Jk is the kinetic current $mAcm^{-2}_{Pt}$. Obtaining values of slope of 92 mV/dec for Pt_3Fe/C close to the value of platinum nanoparticles of 85 mV/dec, which indicates that the transfer of the first electron is the determining step of the reaction [64].

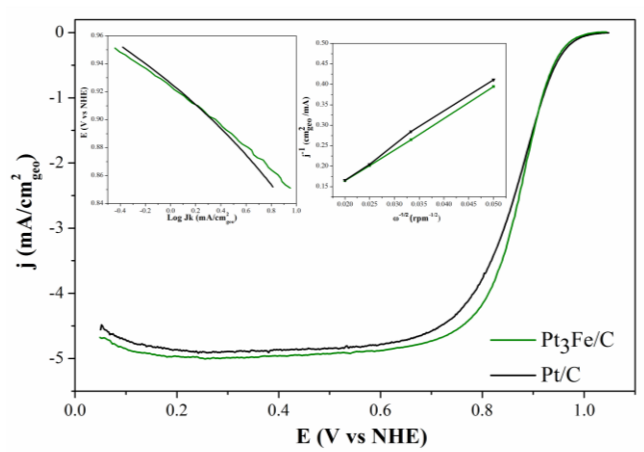

Figure 7. Steady-state polarization curves for the ORR and mass transfer corrected Tafel plot. Koutecky–Levich plots in O_2 saturated 0.1 M $HClO_4$ for Pt_3Fe/C nanoparticles (green line) and Pt/C (black line).

Additionally one can see in Figure 7, the linear relationship between the reciprocal of the current the inverse of the square of the rotation speed indicating that for the catalysts of Pt_3Fe the reduction reaction of oxygen is carried out by a kinetic reaction first order. The value of the reverse slope $B_0 = 11.6\times10^{-2}$ $mAcm^{-2}$ $rpm^{-1/2}$ for the catalyst Pt_3Fe match the calculated theoretical ($B_0 = 12.6\times10^{-2}$ $mAcm^{-2}$ $rpm^{-1/2}$) [65] for the reduction mechanism via four electrons following:

$$O_2 + 4H^+ + 4\,e^- \rightarrow 2\,H_2O \qquad (4)$$

Finally, in Figure 8A can be seen in comparing the values of specific activity, being 2.6 times higher activity for Pt_3Fe/C with respect to Pt/C. While in Figure 8B, it can be seen that the mass activity is practically the same for Pt_3Fe/C and Pt/C.

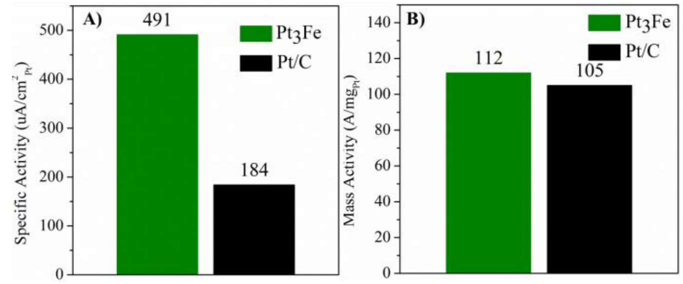

Figure 8. A) Comparison of the specific activities and B) mass activities for Pt_3Fe/C and Pt/C, bars green and black respectively.

IV. Conclusions

It was possible to synthesize nanoparticles with octahedral success in near Pt_3Fe proportion.

It was possible to characterize by X-ray diffraction phases present in the catalysts in addition to determining the crystallite size and cell parameters also were achieved obtain micrographs of low and high resolution with which the uniform size of the nanoparticles is verified. However, it would be important to analyze the composition of nanoparticles by TEM. It was not possible to carry out adequate dispersion of metal nanoparticles on the carbonaceous support, why they should be sought alternative methodologies that allow proper dispersion.

Regarding the support used was possible physical characterization (partial), lacking its electrochemical

Acknowledgment

M.M.T.C. acknowledges CONACYT for the PhD fellowship (number 397722), the grant numbered 245920, and to Laboratorio Avanzado de Nanoscopía Electrónica (LANE). The authors gratefully acknowledge Daniel Bahena Uribe, and Marco Antonio Leyva for their assistance with the HRTEM, and XRD measurements.

References

[1] J. Zhang, H. Yang, J. Fang and S. Zou, "Synthesis and oxygen reduction activity of shape-controlled Pt3Ni nanopolyhedra", Nano letters, vol. 10, pp. 638-644, January 2010.

[2] B. Y. M. Soria, J. I. L. Hurtado, M. D. M. C. Castro and A. C. González, Hidrógeno y pilas de combustible: estado actual y perspectiva inmediata. Asociacion de Ingenieros del ICAI : Universidad Pontificia Comillas, 2010.

[3] X. Cheng, Z. Shi, N. Glass, L. Zhang, J. Zhang, D. Song, et al. "A review of PEM hydrogen fuel cell contamination: Impacts, mechanisms, and mitigation", Journal of Power Sources, vol. 165, pp. 739-756, March 2007.

[4] V. R. Stamenkovic, B. S. Mun, M. Arenz, K. J. Mayrhofer, C. A. Lucas, G. Wang, et al. " Trends in electrocatalysis on extended and nanoscale Pt-bimetallic alloy surfaces", Nature materials, vol. 6, pp. 241-247, February 2007.

[5] S. M. Haile, "Fuel cell materials and components", Acta Materialia, vol. 51, pp. 5981-6000, November 2003

[6] S. Zhang, X. Z. Yuan, J. N. C. Hin, H. Wang, K. A. Friedrich and M. Schulze, "A review of platinum-based catalyst layer degradation in

proton exchange membrane fuel cells", Journal of Power Sources, vol. 194, pp. 588-600, December 2009.

[7] K. E. Martin, J. P. Kopasz and K. W. McMurphy, "Status of fuel cells and the challenges facing fuel cell technology today. In Fuel Cell Chemistry and Operation", American Chemical Society Symposium Series, vol. 1040, pp. 1-13, April 2010.

[8] V. Mehta and J. S. Cooper, "Review and analysis of PEM fuel cell design and manufacturing". Journal of Power Sources, vol. 114, pp. 32-53, February 2003.

[9] U.S.-Department-of-Energy, Fuel Cells A Handbook, West Virginia: EG&G Technical Services, Inc., 2007.

[10] M. S Dresselhaus. and I. L. Thomas, "Alternative energy technologies", Nature, vol. 414, pp. 332-337, November 2001.

[11] M.Winter and R. J. Brodd, "What are batteries, fuel cells, and supercapacitors?",Chemical reviews, vol. 104, pp. 4245-4270, September 2004.

[12] W. Vielstich, H. Yokokawa and H. A. Gasteiger, "Handbook of fuel cells: fundamentals technology and applications". John Wiley & Sons. 2009.

[13] J. Wu and H. Yang. "Platinum-based oxygen reduction electrocatalysts", Accounts of chemical research", vol. 46, pp.1848-1857, June 2013.

[14] L. Carrette, K. A. Friedrich and U. Stimming, "Fuel cells–fundamentals and applications", Fuel cells, vol. 1, pp. 5-39, May 2001.

[15] M. K. Debe, "Electrocatalyst approaches and challenges for automotive fuel cells", *Nature*, vol. 486, pp. 43-51, June 2012.

[16] C. Zhang, S. Y. Hwang, A. Trout, and Z. Peng, "Solid-state chemistry-enabled scalable production of octahedral Pt–Ni alloy electrocatalyst for oxygen reduction reaction", Journal of the American Chemical Society, vol. 136, pp. 7805-7808, May 2014.

[17] R. Borup, J. Meyers, B. Pivovar, Y. S. Kim, R. Mukundan and N. Garland, "Scientific aspects of polymer electrolyte fuel cell durability and degradation" Chemical reviews, vol. 107, pp. 3904-3951, September 2007.

[18] D. Li, H. Lv, Y. Kang, N. M. Markovic and V. R. Stamenkovic, "Progress in the Development of Oxygen Reduction Reaction Catalysts for Low-Temperature Fuel Cells", Annual review of chemical and biomolecular engineering, vol. 7, pp. 509-532, April 2016.

[19] J. H. A. &. A. N. Ma, «The Effect of Substrates at Cathodes in Low-Temperature Fuel Cell.,» Chem Electro Chem, vol. 1, nº 1, pp. 37-46., 2014.

[20] J. Ma, A. Habrioux, and N. Alonso-Vante, "The Effect of Substrates at Cathodes in Low-temperature Fuel Cells", ChemElectroChem, vol. 1, pp. 37-46, December 2013.

[21] T. Toda, H. Igarashi, H. Uchida and M. Watanabe, "Enhancement of the electroreduction of oxygen on Pt alloys with Fe, Ni, and Co", Journal of The Electrochemical Society, vol. 146, pp. 3750-3756, May 1999.

[22] Y. Bing, H. Liu, L. Zhang, D. Ghosh and J. Zhang, "Nanostructured Pt-alloy electrocatalysts for PEM fuel cell oxygen reduction reaction", Chemical Society Reviews, vol. 39, pp. 2184-2202, March 2010.

[23] M. Wakisaka, H. Suzuki, S. Mitsui, H. Uchida and M. Watanabe, "Increased oxygen coverage at Pt-Fe alloy cathode for the enhanced oxygen reduction reaction studied by EC-XPS", The Journal of physical Chemistry C, vol. 112, pp. 2750-2755, January 2008.

[24] M. K. Jeon and P. J. McGinn, "Carbon supported Pt–Y electrocatalysts for the oxygen reduction reaction" Journal of Power Sources, vol. 196, pp. 1127-1131, February 2011.

[25] S. J. Yoo, S. K. Kim, T. Y. Jeon, S. J. Hwang, J. G. Lee, S. C. Lee, "Enhanced stability and activity of Pt–Y alloy catalysts for electrocatalytic oxygen reduction", Chemical Communications, vol. 47, pp. 11414-11416, 2011.

[26] P. Yu, M. Pemberton, and P. Plasse, "PtCo/C cathode catalyst for improved durability in PEMFCs", Journal of Power Sources, vol. 144, pp. 11-20, June 2005.

[27] J. Greeley, I. E. L. Stephens, A. S. Bondarenko, T. P. Johansson, H. A. Hansen, T. F. Jaramillo, "Alloys of platinum and early transition metals as oxygen reduction electrocatalysts" Nature chemistry, vol. 1, pp. 552-556, September 2009.

[28] J. Lai, R. Luque and G. Xu, "Recent Advances in the Synthesis and Electrocatalytic Applications of Platinum-Based Bimetallic Alloy Nanostructures" ChemCatChem, vol. 7, pp. 3206-3228, August 2015.

[29] V. Stamenkovic, T. J. Schmidt, P. N. Ross and N. M. Markovic, "Surface composition effects in electrocatalysis: Kinetics of oxygen reduction on well-defined Pt3Ni and Pt3Co alloy surfaces" The Journal of Physical Chemistry B, vol. 106, pp. 11970-11979, October 2002.

[30] U. A. Paulus, A. Wokaun, G. G. Scherer, T. J. Schmidt, V. Stamenkovic, V. Radmilovic, et al. "Oxygen reduction on carbon-supported Pt-Ni and Pt-Co alloy catalysts" The Journal of Physical Chemistry B, vol. 106, pp. 4181-4191, March 2002.

[31] N. Kristian, Y. Yu, J. M. Lee, X. Liu and X. Wang, "Synthesis and characterization of Co core–Pt shell electrocatalyst prepared by spontaneous replacement reaction for oxygen reduction reaction", Electrochimica Acta, vol. 56, pp. 1000-1007, December 2010.

[32] J. H. Jang, E. Lee, J. Park, G. Kim, S. Hong and Y. U. Kwon, "Rational syntheses of core-shell Fex@ Pt nanoparticles for the study of electrocatalytic oxygen reduction reaction" Scientific reports, vol. 3, pp. 2872, June 2013.

[33] G. Wang, H. Wu, D. Wexler, H. Liu and O. Savadogo, "Ni@ Pt core–shell nanoparticles with enhanced catalytic activity for oxygen reduction reaction" Journal of Alloys and Compounds, vol. 503, pp. L1-L4, July 2010.

[34] H. Zhang, Y. Yin, Y. Hu, C. Li, P. Wu, S. Wei and C. Cai, "Pd@ Pt core− shell nanostructures with controllable composition synthesized by a microwave method and their enhanced electrocatalytic activity toward oxygen reduction and methanol oxidation", The Journal of Physical Chemistry C, vol. 114, pp. 11861-11867, June 2010.

[35] Z. Liu, J. E. Hu, Q. Wang, K. Gaskell, A. I. Frenkel, G. S. Jackson and B. Eichhorn, "PtMo Alloy and MoO x@ Pt Core− Shell Nanoparticles as Highly CO-Tolerant Electrocatalysts" Journal of the American Chemical Society, vol. 131, pp. 6924-6925, May 2009.

[36] J. Zhang, F. H. B. Lima, M. H. Shao, K. Sasaki, J. X.Wang, J. Hanson, et al., "Platinum monolayer on nonnoble metal-noble metal core-shell nanoparticle electrocatalysts for O2 reduction", *The Journal of physical chemistry B*, vol. 1*09*, pp. 22701-22704, November 2005.

[37] D. A. Cantane, F. E. R. Oliveira, S. F. Santos and F. H. B. Lima, "Synthesis of Pt-based hollow nanoparticles using carbon-supported Co@ Pt and Ni@ Pt core–shell structures as templates: electrocatalytic activity for the oxygen reduction reaction", Applied Catalysis B: Environmental, vol. 136, pp. 351-360, June 2013.

[38] M. Neergat and R. Rahul, "Unsupported Cu-Pt core-shell nanoparticles: oxygen reduction reaction (ORR) catalyst with better activity and reduced precious metal content", Journal of the Electrochemical Society, vol. 159, pp. F234-F241, July 2012.

[39] H. Zhu, X. Li and F. Wang, "Synthesis and characterization of Cu@ Pt/C core-shell structured catalysts for proton exchange membrane fuel cell", International Journal of Hydrogen Energy, vol. 36, pp. 9151-9154, July 2011.

[40] C. Zhang, W. Sandorf and Z. Peng, "Octahedral Pt2CuNi uniform alloy nanoparticle catalyst with high activity and promising stability for oxygen reduction reaction", ACS Catalysis, vol. 5, pp. 2296-2300, March 2015.

[41] S. I. Choi, S. Xie, M. Shao, J. H. Odell, N. Lu, H. C. Peng, et al., "Synthesis and characterization of 9 nm Pt–Ni octahedra with a record high activity of 3.3 A/mgPt for the oxygen reduction reaction", Nano letters, vol. 13, pp. 3420-3425, June 2013.

[42] J. Wu, M. Shi, X. Yin and H. Yang, "Enhanced Stability of (111)-Surface-Dominant Core–Shell Nanoparticle Catalysts Towards the Oxygen Reduction Reaction", ChemSusChem, vol. 6, pp. 1888-1892, July 2013.

[43] S. I. Choi, M. Shao, N. Lu, A. Ruditskiy, H. C. Peng, J. Park, et al., "Synthesis and characterization of Pd@ Pt–Ni core–shell octahedra with high activity toward oxygen reduction", ACS nano, vol. 8, pp. 10363-10371, September 2014.

[44] Wu J., J. Zhang, Z. Peng, S. Yang, F. T. Wagner and H. Yang, "Truncated octahedral Pt3Ni oxygen reduction reaction electrocatalysts", Journal of the American Chemical Society, vol. 132, pp. 4984-4985, March 2010.

[45] W. Zhou, J. Wu and H. Yang, “Highly uniform platinum icosahedra made by hot injection-assisted GRAILS method”, Nano letters, vol. 13, pp. 2870-2874, May 2013.

[46] Ma J., A. Habrioux, C. Morais, A. Lewera, W. Vogel, Y. Verde-Gómez, et al., “Spectroelectrochemical probing of the strong interaction between platinum nanoparticles and graphitic domains of carbon”, ACS Catalysis, vol. 3, pp. 1940-1950, July 2013.

[47] X. Wang, W. Li, Z. Chen, M. Waje and Y. Yan, “Durability investigation of carbon nanotube as catalyst support for proton exchange membrane fuel cell”, Journal of Power Sources, vol. 158, pp. 154-159, July 2006.

[48] R. Kou, Y. Shao, D. Wang, M. H. Engelhard, J. H. Kwak, J. Wang, et al., “Enhanced activity and stability of Pt catalysts on functionalized graphene sheets for electrocatalytic oxygen reduction”, Electrochemistry Communications , vol. 11, pp. 954-957, May 2009.

[49] Y. Li, E. Zhu, T. McLouth, C. Y. Chiu, X. Huang and Y. Huang, “Stabilization of high-performance oxygen reduction reaction Pt electrocatalyst supported on reduced graphene oxide/carbon black composite”, Journal of the American Chemical Society, vol. 134, pp. 12326-12329, July 2012.

[50] Y. Garsany, O. A. Baturina, K. E. Swider-Lyons and S. S. Kocha, “Experimental methods for quantifying the activity of platinum electrocatalysts for the oxygen reduction reaction”, Analytical chemistry, vol. 82, pp. 6321-6328, June 2010.

[51] M. Carmo, A. R. Dos Santos, J. G. Poco and M. Linardi, “Physical and electrochemical evaluation of commercial carbon black as electrocatalysts supports for DMFC applications” Journal of Power Sources , vol. 173, pp. 860-866, November2007.

[52] M. M. Tellez-Cruz, M. A. Padilla-Islas, M. Pérez-González and O. Solorza-Feria, “Comparative study of different carbon-supported Fe2O3-Pt catalysts for oxygen reduction reaction” Environmental Science and Pollution Research, pp. 1-11, (in Press) August 2016.

[53] R. V. Siriwardane and J. M. Cook, “Interactions of SO 2 with sodium deposited on silica”, Journal of colloid and interface science, vol. 108, pp. 414-422, December 1985.

[54] N. S. McIntyre and D. G. Zetaruk, “X-ray photoelectron spectroscopic studiesof iron oxides”, Anal Chem , vol. 49, pp. 1521-1529, September 1977.

[55] D. D. Hawn and B. M. DeKoven, “Deconvolution as a correction for photoelectron inelastic energy losses in the core level XPS spectra of iron oxides”, Surface and interface analysis, vol. 10, pp. 63-74, March1987.

[56] R. Steinberger, J. Walter, T. Greunz, J. Duchoslav, M. Arndt, S. Molodtsov, et al. “XPS study of the effects of long-term Ar+ ion and Ar cluster sputtering on the chemical degradation of hydrozincite and iron oxide”, Corrosion Science, vol. 99, pp. 6-75, October 2015.

[57] J. Thiele, N. T. Barrett, R. Belkhou, C. Guillot and H. Koundi, “An experimental study of the growth of Co/Pt (111) by core level photoemission spectroscopy, low-energy electron diffraction and Auger electron spectroscopy” Journal of Physics: Condensed Matte, vol. 6, pp. 5025, 1994.

[58] G. M. Bancroft, I. Adams, L. L. Coatsworth, C. D. Bennewitz, J. D. Brown and W. D. Westwood, “ESCA study of sputtered platinum films”, Analytical Chemistry, vol. 47, pp. 586-588, March 1975.

[59] V. I. Nefedov, Y. V. Salyn, G. Leonhardt and R. Scheibe, “A comparison of different spectrometers and charge corrections used in X-ray photoelectron spectroscopy”, Journal of Electron Spectroscopy and Related Phenomena, vol. 10, pp. 121-124, 1977.

[60] V. I. Nefedov, D. Gati, B. F. Dzhurinskii, N. P. Sergushin and Y. V. Salyn, “X-ray electron study of oxides of elements”, Zhurnal Neorganicheskoi Khimii, vol. 20, pp. 2307-2314., 1975.

[61] V. I. Nefedov, M. N. Firsov and I. S. Shaplygin, “Electronic structures of MRhO 2, MRh 2 O 4, RhMO 4 and Rh 2MO6 on the basis of X-ray spectroscopy and ESCA data”, Journal of Electron Spectroscopy and Related Phenomena, vol. 26, pp. 65-78., 1982.

[62] N. Jung, Y. H. Chung, D. Y. Chung, K. H. Choi, H. Y. Park, J. Ryu, et al., “Chemical tuning of electrochemical properties of Pt-skin surfaces for highly active oxygen reduction reactions”, Physical Chemistry Chemical Physics, vol. 15, pp. 17079-17083., August 2013.

[63] K. J. J. Mayrhofer, Strmcnik, B. B. Blizanac, V. Stamenkovic, M. Arenz, & N. M. Markovic, “Measurement of oxygen reduction activities via the rotating disc electrode method: From Pt model surfaces to carbon-supported high surface area catalysts”, Electrochimica Acta, vol. 53, pp. 3181-3188, February 2008.

[64] N. M. Markovic, T. J. Schmidt, V. Stamenkovic and P. Ross, “Oxygen reduction reaction on Pt and Pt bimetallic surfaces: A Selective Review”, Fuel Cell, vol. 1, pp. 105-116, March 2001.

[65] U. Paulus, T. Schmidt and H. Gasteiger, “Oxygen reduction on a high-surface area Pt:Vulcan carbon catalyst: a thin-film rotating ring-disk electrode study” Journal of Electroanalytical Chemistry, vol. 495, pp. 134–145, January 2001.

Electrocatalysis of NiCu@Pt core-shell nanoparticles for ORR

M. A. Padilla-Islas, M. M. Tellez-Cuz, O. Solorza-Feria
CHEMISTRY DEPARMENT
CINVESTAV
México CDMX.
adrianmapi@gmail.com

H. Cruz-Martinez
Ph.D. Program in Nanoscience and Nanotechnology
CINVESTAV
México CDMX.
hcruzm@cinvestav.mx

***Abstract*— Recent efforts in electrocatalysis have focused on decreasing the Pt content in fuel cell electrocatalysts or replacing it with less expensive materials. Controllable synthesis of non-noble alloys remains a significant challenge. Among core-shell nanoparticles of various combinations, those made of an inexpensive metal core and a noble metal shell has received particular attention associated to the functional and economic advantages that they can provide. A NiCu@Pt catalyst was synthesized for the oxygen reduction reaction, following two-steps methodology: reducing non-noble metals and platinum decoration by galvanic displacement of the bimetallic core. A new synthetic route for catalysts fabrication using a properly amount of oleylamine and oleic acid and precursor salts of non-noble metals, $Cu(acac)_2$ and $Ni(acac)_2$, morpholine borane as a reducing agent is described. The morphology, shape, electronic configuration and methodology of synthesis of alloy nanocrystals, play an important role in catalytic performances. Many methods developed so far in controlling the morphologies of nanocrystals are however limited by the synthesis procedure to attain a specific shape. The oriented crystallographic phases (111) on Pt, favor the coverage of O_2 and the oxygen reduction reaction in acid media. The synthesized NiCu@Pt core-shell Nano frames were characterized with TEM to check the facets, lattice parameter, elemental and particle size distribution, Scanning electron microscope-energy dispersive X-ray analysis provide information of the chemical composition which is in agreement between the estimated and the experimentally produced catalyst. X-ray diffraction shows us a synthesized CuNi alloy with octahedral pattern with less than 10 nm in size, and, cyclic voltammetry, CO stripping and rotating disk electrode techniques conducted to an electrocatalyst with enhanced activity in relation to obtained with Pt alone. Results of the synthesized nanoframe nanocatalyst suggest that this could be used as a cathode electrode in a PEM fuel cell, experiments which are now in route.**

***Keywords*— nanoframes; fuel cells; ORR catalyst.**

I. Introduction

Proton exchange membrane fuel cell (PEMFC) has become a very attractive alternative power source for transportation applications because of its high power density, high energy conversion, high efficiency, and clean utilization [1-2]. However, high cost and low stability are the major problems that hinder the commercialization of PEMFC. Although some progress has been made in developing catalysts, additional drawbacks like low efficiency also restrict the development of PEMFC [3-5]. It is desirable to develop low-Pt content catalysts to improve the utilization of the noble metal and thereby reduce the amount of Pt used in fuel cell electrodes [6-9]. An alternative to reduce costs is a bimetallic non-noble alloys such as cores, in platinum catalysts core-shell type have been widely explored not only because of its low cost and abundant content in the earth's crust, but also its excellent performance in catalytic reactions [9-11]. However, the non-noble alloys controllable synthesis remains a major challenge. Specifically, octahedral, which possess a (111) facet and a large specific surface, and achieved high area-specific and mass ORR activities, demonstrating good promise of the strategy [12-13]. However, one remaining problem of these particular nanoparticle catalysts is their poor stability. The ORR activity, accompanied by fast leaching of Ni element and collapse of particle morphology, decays rapidly, within thousands of potential sweeping cycles. It makes these catalysts insufficient for the long-term operation requirement for real applications Thus, how to improve the stability of the shaped nanoparticles and retain their high activity becomes crucial in the ORR catalyst research [14-15].

II. Experimental

A. Chemicals and materials

Oleyamine (>70%), oleic acid (90%), cupric(II) acetylacetonate ($Cu(acac)_2$, >99%), nickel(II) acetylacetonate ($Ni(acac)_2$, >99%) and borane morpholine complex (95%) were obtained from Sigma-Aldrich. All other solvents and chemicals used were analytical grade. All chemicals were obtained from Sigma Aldrich and used without further purification. Vulcan XC-72R Carbon Cabot was used as support nanoparticles with a previous heat treatment at 500 °C under nitrogen flow to remove any adsorbed impurities.

B. Synthesis of catalyst

In a synthesis of CuNi@Pt/C octahedral, $Cu(acac)_2$, $Ni(acac)_2$ molar relation 1:1 were dissolved in of dibenzyl ether, oleylamine and oleic acid. The formed solution was degassing whit N_2 for 30min subsequently was heated 10°C/min to 240 °C for 30min, followed by the addition of borane morpholine complex. Afterwards, the temperature was kept at 240 °C for 30 min. The reaction was down to 210°C at the time, a Pt $(acac)_2$ was dissolved in 9 ml of oleylamine at 210 ° C the solution was injected to the reaction to give a 80:20 weight percent ratio relative to the non-noble metals and reacted for 30 min the product was precipitated by ethanol, washed three times with a mixture for hexane and ethanol, and then re-dispersed in hexane. Simultaneously a support carbon Vulcan 70:30 weight percent ratios relative to the carbon, and the dispersed catalyst were sonicated 1h and mixed, they were stirred 12h. The catalyst CuNi@Pt/CV was centrifuged and dried at 120 °C under N_2 flow for 2 hrs.

C. X-ray photoelectron spectroscopy (XPS)

The elemental composition of these materials was determined using a K-alpha X-ray photoelectron spectrometer manufactured by Thermo Fisher Scientific Company. An XPS data analysis was performed using the Thermo Avantage software. XPS measurements were made with Al K-alpha radiation (1486 eV). The X-rays were microfocused at the source to give a spot-focus size of 400 µm in diameter, using lenses in standard mode. The analyzer was run in the constant analyzer energy (CAE) mode. The pass energy was set to 200 eV for survey scans and 50 eV for high-resolution regions. All XPS data were referenced according to the adventitious C 1s peak (284.6 eV).

D. X-ray diffraction (XRD)

The identification of the crystal structure of the catalysts was performed by XRD2, using Brucker equipment (D8Venture), with Mo-Ka (λ = 0.7093 Å) radiation operated at 50 kV and 1 mA, in a range 2Ɵ 15 ° to 45 °. For the treatment of the data, we were used suite APEXIII.

E. High-resolution transmission electron microscopy (HRTEM)

Particle size, morphology, and distribution of the nanomaterial were assessed with HRTEM from JEM ARM200F instrument operated at an accelerated voltage of 300 kV.

F. Electrochemical measurements

Prior to the measurements of electrochemical characterization, the catalytic inks were prepared as follows [16]: 10 mg of the corresponding catalyst dispersed in 1.7 mL of a solution of 20% v/v of isopropanol and 0.05% ionomer Nafion (5% by weight) by sonication at a temperature below 10°C for 1 h. 10 uL were placed on a previously polished carbon electrode, the film was dried in air flow to obtain a catalyst loading of 20 $ug_{Pt}cm^{-2}$. Electrochemical measurements were carried out at room temperature (approximately 25°C) in a typical three-electrode cell with 0.1M $HClO_4$ solution was employed as electrolyte. A potentiostat / galvanostat AUTOLAB (Model PGSTAT128N), coupled to a rotating disc electrode (RDE) (Pine Instruments) was used for the electrochemical experiments. A Pt mesh was used as counter-electrode; potentials were determined using a reversible hydrogen electrode (RHE).

The cyclic voltammetry (CV) curves were recorded in a N_2 atmosphere at 50 mV s^{-1} between 0.05 V and 1.2 V for 30 cycles. The ORR polarization curves for the rotating disc electrode (RDE) in an O_2-saturated electrolyte were obtained at 20 mV s^{-1} through a positive sweep between 0.05 V and 1.05 V/RHE at rotation rates of 400, 900, 1600, and 2500 rpm. Additionally, the CO stripping charge was used to determine the electrochemical surface area (ESA). For CO-stripping measurements, the catalyst surface was previously saturated with CO by bubbling it through the electrolyte solution while polarizing the electrode at 0.1 V/RHE for 5 min. Then the remaining CO was purged by flowing N_2 for 10 min before commencing measurement, performed at a scanning rate of 20 mV s^{-1}.

III. RESULTS AND DISCUSSION

A. X-ray diffraction (XRD)

The Fig. 1A and 1B shows XRD pattern for NiCu and NiCu@Pt/C respectivelly, after removing the background. The results reveal that there are defined peaks characteristic diffraction inorganic sample, highlighting that peaks are wide, which allows qualitatively interpret that the catalyst has small crystallite sizes. Fig 1A show the metallic NiCu phase with high crystallinity.

The deduced phase and cell parameters were NiCu(3.566A), which correspond to the Fm-3m (225) space group characteristic of a face-center-cube (FCC) crystal structure based in the PDF chart for NiCu (03-065-9048). For the NiCu@Pt/C nanocatalyst the XRD profile (Fig 1B), the peaks for the NiPt alloy (03-065-9445)are shifted towards higher 2Ɵ angles associated to the (111), (200), (220), (311) and (222) planes, and the peaks for the CuPt (00-048-1549) alloy are shifted towards smaller 2Ɵ angles, these displacements may be because the alloy predominant is the NiCuPt.

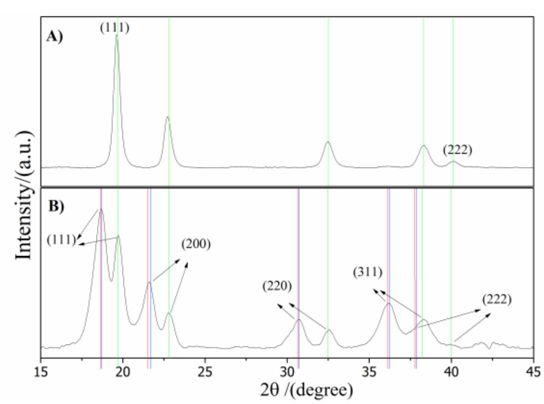

Figure 1. Diffraction patterns for A) NiCu and B) NiCu@Pt. NiCu alloy are represented by green line, NiPt alloy are represented by blue line and CuPt alloy are represented by red line.

B. X-ray photoelectron spectroscopy (XPS)

The surface presence of the species present in the catalyst was determined by X-rays photoelectron spectroscopy. Fig.2 shows the spectra of ultra-high resolution for areas Pt 4f, Ni 2p and Cu 2p

In the spectrum of the Fig. 2A) corresponding to the zone of Pt can be seen that the main peak at 70.9±0.2 eV which could correspond to the signal Pt-Cu [17]. However, it has also reported that the binding energies located at 70.74±0.2 and 71.13±0.2 could correspond to Pt-Co [18].

With regard to the zone Ni2p Fig.2 B), can be observed two peaks, one located at 852.8±0.2 eV and another at 856.4±0.2 eV, the first signal can be assigned to the species of Ni(0) [19-23] it has even been reported the binding energy corresponding to Ni-Cu to 852.6 eV [19, 24] which could be found in our catalyst, reinforcing the phase of Ni-Cu which was found by X-ray spectroscopy. But also you can see another peak at 856.4±0.2 eV which can be attributed to three species, which are very close, which are: 856.5 eV for NiO [22] and $Ni(C_2H_3O_2)_2$ [25, 26] and 856.6 eV for $Ni(OH)_2$ [27]. Species of oxides and hydroxides probably present in the surface of the nanoparticles and $Ni(C_2H_3O_2)_2$ precursor remaining probably used.

Finally in relation to the zone of Cu2p Fig.2 C), the main peak is observed at 932.6 + -0.2eV, the signal can be assigned to Cu (0) [28-30] it has been reported that binding energies for the species Cu-Ni, Cu-Ni-O and Cu2O at 932.60 eV reason for which it is difficult to assign the signal.

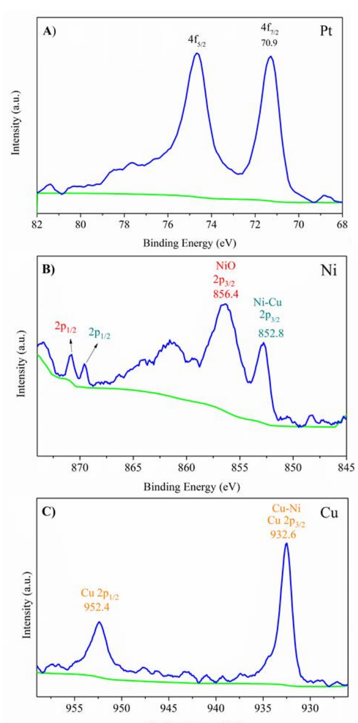

Figure 2. Spectra Pt 4f A), Ni 2p B) and Cu 2p C) zones.

C. High-resolution transmission electron microscopy (HRTEM)

Figure 3 shows the high-resolution transmission electron micrographs in STEM mode for the NiCu@Pt/VC nanocatalyst Fig.3. In a qualitative first approach it was possible to observe by Z contrast the High Angle Annular Dark Field image (HAADF) where brightest atoms associated to Pt phase and gray atoms associated to Ni and Cu Fig.3 B) phase are distributed in a random way inside the nanoparticle suggesting alloy formation between both metals. The particle size distribution allowed to establish an average size in 9 ± 2 nm Fig.3 A). For the trimetallic nanocatalyst NiCu@Pt/VC high resolution micrographs were obtained (Fig. 3A and B).

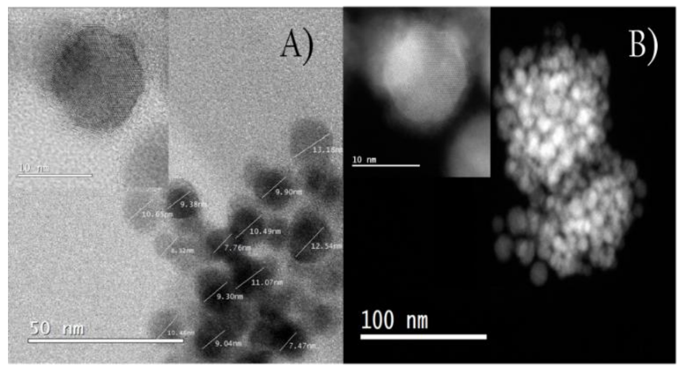

Figure 3. High-resolution STEM micrograph for the NiCu@Pt/C catalyst.

D. Electrochemical measurements

Cyclic voltammogram of NiCu@Pt/C (Fig. 4A) show three different potential regions: a hydrogen underpotential deposition domain (H_{upd}) between 0.05 and 0.35 V/RHE, a potential range between 0.35 and ~0.75 V/ RHE corresponding to a double layer, and a region E > 0.75 V to the onset potential related to OH_{ad} adsorption and oxide formation/reduction of the Pt surface. The wide peak observed above 0.7 V/ NHE was attributed to the quinone/hydro-quinone equilibrium due to the carbon support and corresponds to the OH adsorption area [31]. Regarding the peak position of the reduction adsorbed oxides, can be seen a displacement of the peak to more positive for NiCu@Pt/C catalyst (0.80V vs NHE) compared to pure platinum potential (0.76 V vs NHE), i.e., at lower overpotentials, which means that the catalyst NiCu@Pt/C require less energy to reduce said oxides [32], that characteristic should be reflected in an improvement in the catalytic activity of the three catalysts.

Fig.4 B) shows CO-stripping, used to determine the electrochemical active surface area (ESA) from the normalized curves according to the equation 1 [14].

$$ESA\ (m^2 g^{-1}{}_{Pt}) = (Q_{CO} / 420\ \mu C cm^{-2} \times L_{Pt} \times A_{geo}) \times 10^5 \qquad (1)$$

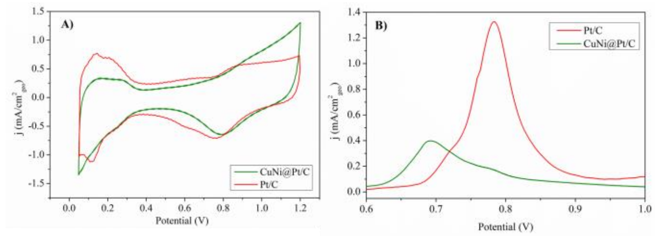

Figure 4. A) Cyclic voltammograms for NiCu@Pt/C (green line) and Pt/C (red line) nanocatalyst at 50 mV s^{-1} in 0.1 M $HClO_4$ at room temperature. B) CO stripping voltammograms for NiCu@Pt/C nanoparticles (green line) and Pt/C (red line).

Comparing the electrochemically active areas shown in Figure 6, in which one can see that the catalyst have a lower ESA with respect to the pure platinum which may be due to agglomeration of nanoparticles on the carbonaceous support.

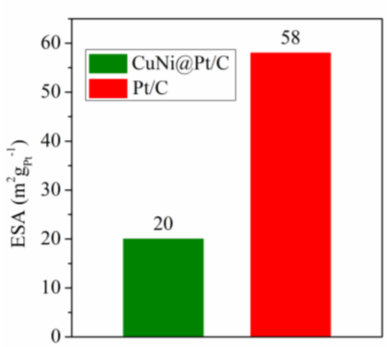

Figure 6. Comparison of electrochemically active area values (ESA) in $m^2 g_{Pt}^{-1}$ for NiCu@Pt/C and Pt/C.

The analysis for the determination of the specific activity and mass and the determination of kinetic parameters was performed by EDR steady state technique. In Figure 7, the polarization curves 1600rpm for NiCu@Pt/C catalyst and its comparison with Pt/C commercial. By starting at 1.05 V and scanning the electrode potential negatively, a mixed kinetic-diffusion control region between 0.85-0.95 V is followed by a defined diffusion-limiting current bellow 0.85 V. The NiCu@Pt/C sample showed half-wave potential of $\Delta E_{1/2}$ = 0.90 V with a positive shift compared with platinum $\Delta E_{1/2}$ = 0.87 V.

Figure 7 shows the graph of the Tafel slopes previously corrected for mass transportation in a range of 0.85 to 0.95 V vs NHE, kinetic current was obtained by Equation 2 [33]:

$$J_k = J_L \times J / J_L - J \quad (2)$$

Where J is the current density measured in $mAcm^{-2}_{geo}$, J_L it is the density and diffusion limited current density, Jk is the kinetic current $mAcm^{-2}_{Pt}$. Obtaining values of slope of 95 mV/dec for NiCuPt/C close to the value of platinum nanoparticles of 85 mV/dec, which indicates that the transfer of the first electron is the determining step of the reaction [34].

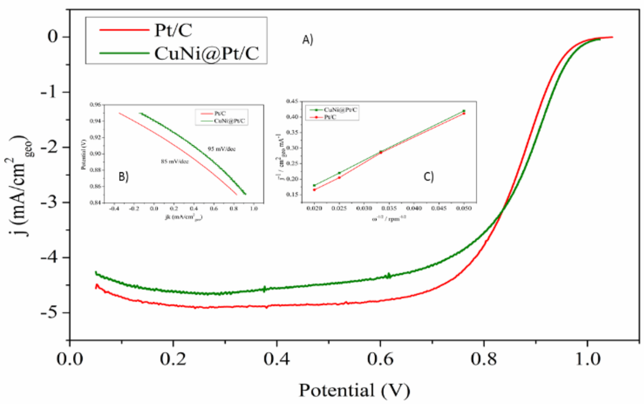

Figure 7. Steady-state polarization curves for the ORR A) and mass transfer corrected Tafel plot B). Koutecky–Levich plots C) in O2 saturated 0.1 M HClO4 for NiCu@Pt/VC nanoparticles (green line) and Pt/C (red line).

Additionally one can see in Figure 7, the linear relationship between the reciprocal of the current the inverse of the square of the rotation speed indicating that for the catalysts of NiCu@Pt/C the reduction reaction of oxygen is carried out by a kinetic reaction first order. The value of the reverse slope $B_0 = 12.5 \times 10^{-2}$ $mAcm^{-2}$ $rpm^{-1/2}$ for the catalyst NiCu@P/Ct match the calculated theoretical ($B_0 = 12.6 \times 10^{-2}$ $mAcm^{-2}$ $rpm^{-1/2}$) [35] for the reduction mechanism via four electrons following:

$$O_2 + 4H^+ + 4e^- \rightarrow 2 H_2O \quad (4)$$

Finally, in Figure 8A can be seen in comparing the values of specific activity, being 2.3 times higher activity for NiCu@Pt/C with respect to Pt/C. While in Figure 8B, it can be seen that the mass activity is less for NiCu@Pt/C, this because the nanoparticles are agglomerated to the carbon matrix.

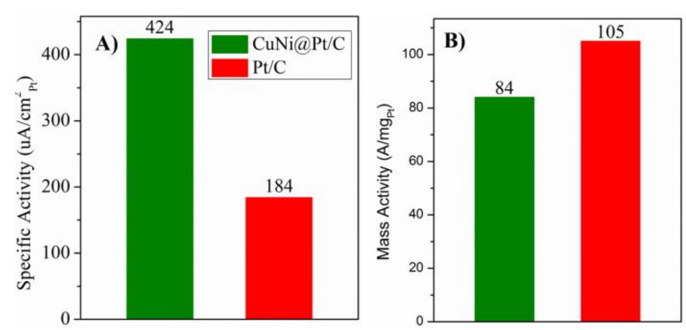

Figure 8. A) Comparison of the specific activities and B) mass activities for NiCu@Pt/C and Pt/C, bars green and red respectively.

IV. Conclusions

We synthesize nanoparticles with preferential ORR facets that promote and demonstrate that the NiCu@Pt/C catalyst is efficient for the ORR, the catalyst has comparable activities with pure platinum despite the complications that I present. Can improve the dispersion of the material and being able to obtain better quality particles, we would increase considerably the activities.

Acknowledgment

M.M.T.C. acknowledges CONACYT for the PhD fellowship (number 397722), the grant numbered 245920, and to Laboratorio Avanzado de Nanoscopía Electrónica (LANE). The authors gratefully acknowledge Daniel Bahena Uribe, and Marco Antonio Leyva for their assistance with the HRTEM, and XRD measurements.

References

[1] J. Wang, B. Li, T. Yersak, D.Yang, Q. Xiao, J. Zhang, & C. Zhang, "Recent Advances in Pt-based Octahedral Nanocrystals as High Performance Fuel Cell Catalysts". Journal of Materials Chemistry A. 2016.

[2] R. M. Arán-Ais, F. Dionigi, T. Merzdorf, M. Gocyla, M. Heggen, R. E. Dunin-Borkowski, & P. Strasser, "Elemental Anisotropic Growth and Atomic-Scale Structure of Shape-Controlled Octahedral Pt–Ni–Co Alloy Nanocatalysts". Nano letters, 15, 7473-7480. October 2015.

[3] V. Beermann, M. Gocyla, E. Willinger, S. Rudi, M. Heggen, , Dunin- R. E Borkowski, & P. Strasser, "Rh-Doped Pt–Ni Octahedral Nanoparticles: Understanding the Correlation between Elemental Distribution, Oxygen Reduction Reaction, and Shape Stability". Nano letters, 16, 1719-1725.February 2016.

[4] S. I. Choi, S. Xie, M. Shao, J. H. Odell, N. Lu, H. C.Peng, & J. Wang, "Synthesis and characterization of 9 nm Pt–Ni octahedra with a record high activity of 3.3 A/mg Pt for the oxygen reduction reaction". Nano letters, 13, 3420-3425. June 2013.

[5] J. Wu, , J. Zhang, Z. Peng, S. Yang, F. T. Wagner, & H. Yang, "Truncated octahedral Pt3Ni oxygen reduction reaction electrocatalysts". Journal of the American Chemical Society, 132, 4984-4985. January 2010.

[6] C. Cui, L. Gan, M. Heggen, S. Rudi, & P. Strasser, "Compositional segregation in shaped Pt alloy nanoparticles and their structural behaviour during electrocatalysis". Nature materials, 12, 765-771. August 2013.

[7] M. K. Carpenter, T. E. Moylan, R. S. Kukreja, M. H. Atwan, , & M. M. Tessema. "Solvothermal synthesis of platinum alloy nanoparticles for oxygen reduction electrocatalysis". Journal of the American Chemical Society, 134, 8535-8542. April 2012 .

[8] Z. Hong, Li Xingwang, F. Wang "Synthesis and characterization of Cu@Pt/C core-shell structured catalysts for proton exchange membrane fuel cell international journal of hydrogen energy" International Journal of Hydrogen Energy 36 9151 9154. July 2011.

[9] S. I. Choi, S. Xie, M. Shao, N. Lu, S. Guerrero, J. H. Odell & Y Xia,. "Controlling the size and composition of nanosized Pt–Ni octahedra to optimize their catalytic activities toward the oxygen reduction reaction". ChemSusChem, 7, 1476-1483. May 2014.

[10] Y. Chen, Z. Liang, F. Yang, Y. Liu, & S. Chen, "Ni–Pt Core–Shell Nanoparticles as Oxygen Reduction Electrocatalysts: Effect of Pt Shell Coverage". The Journal of Physical Chemistry C, 115, 24073-24079. November 2011.

[11] J. Zhang, H. Yang, J. Fang, & S. Zou, "Synthesis and oxygen reduction activity of shape-controlled Pt3Ni nanopolyhedra". Nano letters, 10, 638-644. January 2010.

[12] M. Wang,."Ratio-Controlled Synthesis of CuNi Octahedra and Nanocubes with Enhanced Catalytic Activity". J. Am. Chem. Soc. 137, 14027−1403.October 2015.

[13] C. Zhang, "Octahedral Pt2CuNi Uniform Alloy Nanoparticle Catalyst with High Activity and Promising Stability for Oxygen Reduction Reaction", ACS Catal. 5, 2296−2300. March 2015.

[14] R. Borup, J. Meyers, B. Pivovar, Y. S. Kim, R. Mukundan and N. Garland, "Scientific aspects of polymer electrolyte fuel cell durability and degradation" Chemical reviews, vol. 107, pp. 3904-3951, September 2007.

[15] D. Li, H. Lv, Y. Kang, N. M. Markovic and V. R. Stamenkovic, "Progress in the Development of Oxygen Reduction Reaction Catalysts for Low-Temperature Fuel Cells", Annual review of chemical and biomolecular engineering, vol. 7, pp. 509-532, April 2016.

[16] Y. Garsany, O. A. Baturina, K. E. Swider-Lyons, & S. S. Kocha,. "Experimental methods for quantifying the activity of platinum electrocatalysts for the oxygen reduction reaction". Analytical chemistry, 82, 6321-6328. June 2010

[17] Barrett NT, Belkhou R., J. Thiele, Guillot C. Surf. Sci. 331.

[18] J. Thiele, Barrett N.T., Belkhou R., C. Guillot, Koundi H. J. Phys. Cond link. Matter 6, 5025 (1994); Shuzhong D., Fanhua X., Jingfa D.J. Catal. 109, 170 1988.

[19] K Kishi ., Fujita T.Surf. Sci 227, 107 1990.

[20] Marcus P., Grimal J.M. Corros. Sci 33, 805 1992.

[21] C. L. Bianchi, M. G. Cattania, Villa P.Appl. Surfing. Sci 70, 211 1993.

[22] Mansour A.N. Surfing. Sci. Spectra 3, 221 1994.

[23] Dube C.E., Workie B., S. P. Kounaves, Robbat A., Jr, Aksu M. L., G. Davies and J. Electrochem. Soc. 142, 3357 1995.

[24] Hernnas B., M. Karolewski, Tillborg H., Nilsson A., N. Surf Martensson. Sci. 302, 64 1994.

[25] Nefedov I.V., Zhumadilov E.K., L. Baer Zh. Neorg. Khimii 23, 2113 1978.

[26] L. J. Matienzo, Yin L.I., Grim S.O., W. E. Swartz Inorg. Chem. 12 2762 1973.

[27] K. S. Kim, N. Winograd Surf. Sci. 43, 625 1974.

[28] J. C. Klein, A. Proctor, D.M. Hercules, Black J.F. Anal. Chem 55, 2055 1983.

[29] Anthony M. T., Seah, M.P. Surfing. Interface Anal. 6, 95 1984.

[30] Seah M.P., Smith G.C., Anthony M.T. Surfing. Interface Anal. 15, 293 1990.

[31] J. Maruyama and I. Abe, "Influence of anodic oxidation of glassy carbon surface on voltammetric behavior of Nafion®-coated glassy carbon electrodes", Electrochimica Acta, vol.46, pp. 3381–3386, August 2001.

[32] J. Zhang, F. H. B. Lima, M. H. Shao, K. Sasaki, J. X.Wang, J. Hanson, et al., "Platinum monolayer on nonnoble metal-noble metal core-shell nanoparticle electrocatalysts for O2 reduction", The Journal of physical chemistry B, vol. 109, pp. 22701-22704, November 2005.

[33] K. J. J. Mayrhofer, Strmcnik, B. B. Blizanac, V. Stamenkovic, M. Arenz, & N. M. Markovic, "Measurement of oxygen reduction activities via the rotating disc electrode method: From Pt model surfaces to carbon-supported high surface area catalysts", Electrochimica Acta, vol. 53, pp. 3181-3188, 2008.

[34] N. M. Markovic, T. J. Schmidt, V. Stamenkovic and P. Ross, "Oxygen reduction reaction on Pt and Pt bimetallic surfaces: A Selective Review", Fuel Cell, vol. 1, pp. 105-116, March 2001.

[35] U. Paulus, T. Schmidt and H. Gasteiger, "Oxygen reduction on a high-surface area Pt:Vulcan carbon catalyst: a thin-film rotating ring-disk electrode study" Journal of Electroanalytical Chemistry, vol. 495, pp. 134–145, January 2001.

XVI International Congress of the Hydrogen Mexican Society 2016

Production of renewable fuels from hydrocarbons biosynthesized by *Botryococcus braunii* microalgae: Estimation of thermophysical properties of pure compounds and thermodynamics of hydroprocessing reactions

I. Pala-Rosas[1,*], E. A. de la Rosa-Reyna[2], J. Acuapan-Hernández[3], A. Castro-Agüero[4], A. A. Fragoso-Montes de Oca[1], H. Cruz-Martínez[5].

[1] ESIQIE-SEPI, Instituto Politécnico Nacional, UPALM, Av. Instituto Politécnico Nacional s/n, Col. San Pedro Zacatenco, Del. Gustavo A. Madero, Ciudad de México, México, C.P.07738.

[*]e-mail: ipalar@hotmail.com

[2]Research Institute of Inorganic Chemistry, RENTECH-UniCRE, Chempark Litvínov, Záluží-Litvínov, Czech Republic, C.P. 43670.

[3]Departamento de Biotecnología y Bioingeniería, CINVESTAV, Av. Instituto Politécnico Nacional 2508, Col. San Pedro Zacatenco, Del. Gustavo A. Madero, Ciudad de México, México, C.P. 07360.

[4]Facultad de Ciencias Básicas, Ingeniería y Tecnología, Universidad Autónoma de Tlaxcala, Calzada Apizaquito s/n, Apizaco, Tlaxcala, México, C.P. 90300

[5]Programa de Doctorado en Nanociencias y Nanotecnología, CINVESTAV, Av. Instituto Politécnico Nacional 2508, Col. San Pedro Zacatenco, Del. Gustavo A. Madero, Ciudad de México, México, C.P. 07360.

ABSTRACT

In the last decades, as a result of the concern of the depletion of fossil fuels deposits caused by the high energetic demand and the alarming environmental situation present nowadays, the research and development of technologies have focused their attention on the pursuit of new approaches of sustainable energy production. Among these, biomass derived fuels, such as biodiesel and bioethanol, seem to be promissory options in terms of internal combustion engines. Nevertheless, these technologies still present some drawbacks, mainly, because of the competition between the biofuel production and the alimentary sector, as well as the requirement of large areas of land for the cultivation of raw materials or even deforestation and the generation of waste-waters with dissolved alkalis or acids.

Under this perspective, the cultivation of microalgae offers a potential alternative for the mitigation of green-house gases and the energetic crisis since they can metabolize CO_2 by photosynthesis to produce compounds of different chemical nature; furthermore, microalgae can be cultivated in organic waste-water or eutrophic ones. It is well known that one of the main features of microalgae is the production of substantial amounts of triglycerides, however, the oil generated by *Botryococcus braunii* is remarkable because it is constituted by long-chain hydrocarbons such as triterpenes, alkadienes and/or alkatrienes which can be transformed into gasoline, kerosene and diesel fuels. Nevertheless, the research and use of novel raw materials implies the knowledge of the thermophysical properties of their pure constituent compounds in order to develop further engineering calculations.

In this way, the present work deals with the estimation of critical and thermodynamic properties, by means of group contribution methods, of two long-chain alkadienes with formula $CH_3(CH_2)_7CH{=}CH(CH_2)_{17}CH{=}CH_2$ and $CH_3(CH_2)_7CH{=}CH(CH_2)_{19}CH{=}CH_2$ biosynthesized by race A of *B. braunii*, and with the thermodynamic analysis in terms of heats of reaction, change of Gibbs free energy and equilibrium constants of the characteristic hydroprocessing reactions such as hydrogenation, PCP branching, methyl shift and acyclic β-scission.

Keywords: renewable fuels, *Botryococcus braunii*, thermophysical properties, themodynamic analysis, hydroprocessing.

XVI International Congress of the Hydrogen Mexican Society 2016

3D CFD modeling and experimental validation of a 10-Cell PEM fuel cell stack.

J. Macedo-Valencia[1], J.M. Sierra[1], S. Figueroa-Ramirez[1], M. Meza[1], C. Patiño[1]

[1]Universidad Autónoma del Carmen, Facultad de Ingeniería, Cd. Del Carmen, Campeche, México, 24115.
[*]Tel: +529831235482; e-mail: jmacedov184@hotmail.com

ABSTRACT

A single-phase, three-dimensional model has been implemented to simulate the fluid flow, heat transfer, electrochemical reaction and species transport in a Proton Exchange Membrane Fuel Cell stack with ten single cells connected in series, including the membrane, gas diffusion layers, catalyst layers, flow channels and current collectors. A commercial computational fluid dynamics (CFD) code, Ansys 12.1 ®, was used to solve the numerical model. The results were validated by polarization curves and thermal behavior obtained using a 100W air-cooled PEM fuel cell stack with an active area of 31.2 cm2. The stack surface temperature profiles have been measured using infrared thermographic images and thermocouples. The results show the detailed distributions of the fluid flow and heat transport through each single cells inside the stack. The heat generation from the fuel cell affect the cell temperature, especially in the middle of the stack. Furthermore, this model would be an important step for further proposal of the design of a stack and the proper cooling method.

Keywords: Stack modeling, CFD, PEMFCs, Heat transfer

Preparation and Properties of Polypropylene-Carbon Nanotubes Nanocomposites for Application in Bipolar Plates

C. A. Ramírez-Herrera, J. G. Cabañas-Moreno, O. Solorza-Feria
Centro de Investigación y de Estudios Avanzados del I.P.N.
Cd. de México, México.

J. Pérez-González, A. Flores-Vela
Instituto Politécnico Nacional
Cd. de México, México.

N. Romero-Partida
Industrias Romfer S.A. de C.V
Cd. de México, México.

***Abstract*—Polymer electrolyte membrane fuel cells (PEMFCs) have the potential to play a major role as energy sources for transportation and portable applications because they feature high power density at relatively low operating temperatures. Bipolar plates are a key component of PEMFCs in terms of cost and weight. To date, many different materials for bipolar plates have been investigated and an alternative solution consists in carbon nanotubes (CNTs)-filled polymer nanocomposites which combine the good processability, high corrosion resistance and good mechanical properties of polymers with the excellent electrical and other functional properties of the CNTs. However, a preferential distribution of well dispersed CNTs forming conductive 3D networks is required to successfully exploit their potential. In this work, polypropylene (PP)-multi-walled CNTs (MWCNTs) nanocomposites have been prepared by melt-blending using different loadings (1, 2 and 5 wt.%) of MWCNTs and processing conditions. The microstructure and properties of these nanocomposites have been characterized on molded plates of 1.5 mm thickness. The state of dispersion of the MWCNTs in the polymer matrix is investigated by SEM and optical confocal microscopy and the electrical properties of the nanocomposites are measured in order to find the electrical percolation threshold.**

Keywords*—polymer nanocomposites; carbon nanotubes; electrical properties

Hydrogen Technologies National Laboratory: Advances on design

J.Gutiérrez, H. Laut
Runkel Continuity SC, Coscomate #264, Tlalpan
CP 14050, Ciudad de México, México
Tel: +52 1 (55) 2847 2617; e-mail: jg@runkel.com.mx

R. González-Huerta[1], L. F. Terán Balaguer[2]
1 Instituto Politécnico Nacional-ESIQIE, Lab. Electroquímica y Corrosión, UPALM, CP 07738, Ciudad de México, México

2 Xantronic, Rafael Campoy 811, Col. Pitic, C.P. 83150, Hermosillo-Sonora, México

***Abstract*— Hydrogen Technologies National Laboratory (HTNL) is a service unit, which supports scientific and industrial community to develop greater impact projects in different areas of hydrogen technologies. This National Laboratory will consist of a central laboratory and several associated laboratories. In this work, the HTNL implementation in Mexico is proposed, considering that the central laboratory will be administered by the IPN and associated laboratories will be distributed along the Mexican Republic and institutional infrastructure will be used, e. g. CINVESTAV, CIMAV, UAZ , CICY, IIE, etc., currently developing hydrogen technologies.**

The Central Laboratory is a complex infrastructure designed to provide researchers of necessary elements to get better results. Early planning allows future users to choose proper technologies and offer planners the opportunity to generate integral solutions that ensure the functionality of the HTNL and provide value from the investment. HTNL will focus on developing, integrating, and demonstrating hydrogen production and delivery, hydrogen storage, fuel cell technologies for transportation, stationary, and portable applications, including security and regulations. Projects will range from fundamental research to overcome technical barriers, manufacturing process improvement to enable high-volume fuel cell production, systems analysis to identify the most promising commercialization pathways, and market transformation to support early market deployments.

Advances in HTNL's design includes area planning, technology selection and integration according with current international normative related with lab design, good laboratory practice, hydrogen work areas, hydrogen management, hydrogen storage and any other necessary to this kind on scientific area. It is expected to generate dialogue between the company and researcher to get feedback and improve the proposal.

Keywords*— *Hydrogen Technologies National Laboratory; security and regulations; technology-integration

I. INTRODUCTION

T The first decades of the century begin to build what will be the next energy revolution, which will have to generate the necessary technology to meet the energy needs of the growing world population but also have to meet the requirement of being less polluting than their processors: fossil fuels.

In order to be prepared to face the challenge of generating more energy with less environmental impact, hundreds of scientific organizations, governments and social organizations are working around the multidisciplinary development of different techniques: photovoltaic solar energy, wind energy, batteries and hydrogen as energy carrier able to be converted into chemical or electrical energy.

Mexico is not the exception: there are different research and development groups around the country and the National Commission on Science and Technology (CONACYT for its acronym in Spanish) is working to strengthen them through "National Laboratories" program.

According with CONACyT, a National Laboratory is: "A specialized research unit for scientific development and innovation in key issues these laboratories meet three main functions: Research, human resources training and service delivery."

National Laboratories are established in partnership between institutions in different regions of the country to expand the capacities of scientific and technological research groups.

II. MATERIAL AND METHODS

A. *Conceptual design*

The National Hydrogen Technologies Laboratory aims to be a comprehensive development center to study all parts of the hydrogen value chain. These are:

- Hydrogen production
- Hydrogen storage
- Hydrogen distribution
- Technology associated with hydrogen quality (product purity and raw materials)
- Consumption systems of hydrogen (fuel cells, burners, etc.)

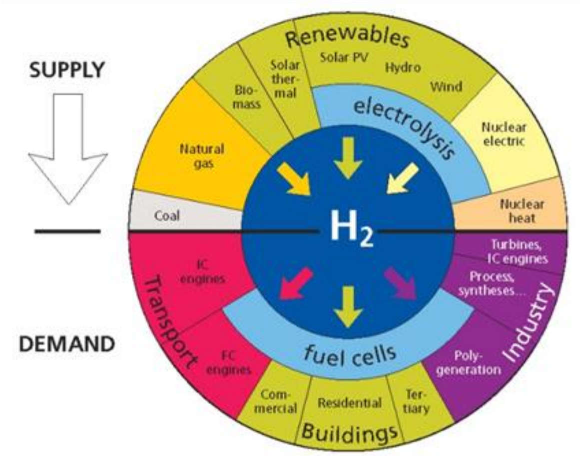

Figure 1. Hydrogen sources and consumption systems

Different laboratories and work areas have been proposed to allow the development of theoretical and practical work, which are summarized in Table 1.

B. Technology selection

Due the amount of investment and expected lifetime of the Hydrogen Technologies National Lab, technology selection is a key issue.

At this moment of the project development most of equipment is not selected yet. When the moment come it will be important to keep in mind some aspects:

- Throughput: As HTNL should be a self-sustainable institution, it will be needed to produce certain income level. That income will come from test and developments sold. As a consequence, HNTL must have enough analytical and working capacity: for sale and research projects.

- Return of investment: It is an economic issue that will define which technology is needed. Investment must be returned as soon as possible. It includes equipment lifetime and technology updates.

- Warranties and maintenances: Longest warranties and minimal maintenances are desirables.

- Calibration and operation qualification: The HTNL will be a reference lab for hydrogen technology, devices and equipment; therefor is mandatory to have calibrated and qualified equipment. It is the only way a lab could trust its results.

- Spare parts: Availability ensured of spare pieces is so important. Another topic related spare parts is: provenance and price.

Architectonical design

The complete HTNL project design includes the workspaces distribution. These spaces should be designed inside to meet the needs of the analytical or manufacturing process for which it is intended. Turn: all the laboratory halls must be distributed according to the general workflow, data-flow and material flow.

All described halls in Table 1 are currently designed according with equipment size, people working inside and occupational safety rules. Figure 2 shows an layout example.

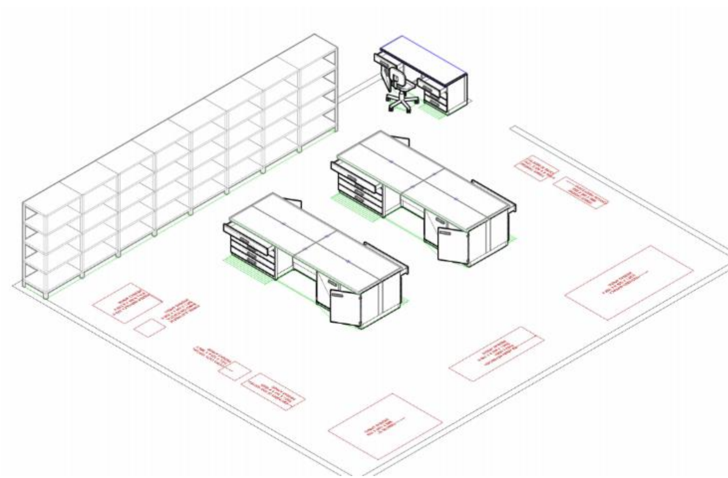

Figure 2. Architectonical layout of Fuel Cell Testing and Characterizing Lab

III. Norms and Standards

Currently hydrogen as an energy carrier is a set of technologies whose development is increasing. As a result, the rules used to design and work with this gas come mainly from the experience in handling it as a chemical substance. However in recent years, some regulatory institutions have begun to develop codes to govern the way in which the hydrogen gas must be used with energy purposes. Table 2 shows the standards currently used for design development HTNL

IV. Conclusion

There are elements such a previous conceptual scope, expertise in scientific facilities designing and online available info that allow to get advances on this project, however coming soon will be researcher's advice and desire the best design guide for Hydrogen Technology National Laboratory.

V. Acknowledgments

This work has been supported by

- Multidisciplinary project IPNSIP 1683 (2015-2016)
- CONACYT: project PEI 231094 (2016)
- Programa de Redes Temáticas/RTH2

Table 1 – Proposed laboratories for HTNL

Laboratory	Objective	Infrastructure	Estimated area
Modeling and Material Simulation Lab	-To design and evaluate by computational methods new materials for fuel cells. -To collaborate with materials synthesis optimization and characterization as well as physicochemical processes.	- Computational workstations (10x) - Specialized software: Materials Studio, ATK, Turbomole, Cosmotherm, Medea, etc. - Printer stations.	65 m^2
Fuel Cell Testing and Characterizing Lab	- To test and characterize fuel cell stacks. - To study every fuel cell component. - To get a new catalytic material behavior in a fuel cell prototype.	-Pressurized gas lines (H2, O2, N2, Zero Air) -PEM-FC test stations (Up to 15 kW) -Potentiostat -Frequency analyzer -Electrochemical impedance measuring device. -FC - stacks assembly equipment -Automatic press for MEAs	80m^2
Electrolyzer Testing and Characterizing Lab	- To test and characterize different kind of electrolysers - To study every electrolyser component. - To improve design characteristics, as well as get more efficient electrolysers.	-Gas chromatograph - Mass spectrometer. -Rotative pump -Electrolyser test station. -Photovoltaic technology to integrate to electrolysis process. -Electrolyser components -Standard electrolyser prototype to test materials. -Hydrogen analizers. -Heat exchangers -Corrosion study equipment	80m^2
Membrane-Electrolyte Assembly Preparation Lab	-To assemble Membrane-Electrode Assemblies. -To synthesize polymeric membranes as alternative to commercial ones.	-Elemental analyser (C,N,H,S) CE Instruments EA 1110 CHNS -Inorganic charges elemental analyser LECO CHNS-932 -Common lab stuff	45 m^2
Hydrogen Storage Lab	-To storage hydrogen gas at 40 psi of pressure (or less) -To storage hydrogen in hydride way.	-Filling system for low capacity tanks. -Low capacity compressor -Hydrogen recirculation pump. -Different capacity tanks. -Different capacity hydride tanks	120 m^2
Power Electronics Lab	-To design and build electronic control systems for hydrogen consumption systems. -To apply a nonlinear control for power converters as well as analyse control algorithms. -To produce electronics for hydrogen chain value devices (electrolysers, fuel cells, power supply systems, etc)	-Oscilloscope -Signal Generator -Power Sources -Computer system in real time	65 m^2
Mechanical Parts Manufacturing Lab	-To design and manufacture mechanical parts for electrolyser and fuel cells	-Numerical milling machine -Workbenchs -Drill press -Vertical saws for metal and plastic tapes	160 m^2

		-Abrasive disc cutter -Electric grinders bank -Hydraulic press type H -Sharpeners for bits -Time controls with electronic contactor -Different mechanical tools	
Prototyping Lab	-To integrate low and medium power prototypes. For example: go.karts, hydrogen utility cars, stationary power-to-gas systems, etc.	-Lift truck -Tools -Work table -CD power supply (MGI integrated) -CD power supply (TIG-AF integrated)	100 m^2

Table 2 – Normative, standards and guidelines for hydrogen infrastructure

Normative or standard	Application
General building codes	
International Building Code (IBC)	General construction requirements for building based on occupancy class
International Fire Code (IFC)/NFPA 1 Uniform Fire Code	Requirements for hydrogen fueling stations, flammable gas, and cryogenic fluid storage
International Mechanical Code (IMC)	Requirements for ventilation for hydrogen usage in indoor locations
International Fuel Gas Code (IFGC)	Requirements for flammable gas piping
Hydrogen Technologies Specific Fire Codes and Standards	
NFPA 2 Hydrogen Technologies Code	Comprehensive code for hydrogen technologies constructed of extract material from documents such as NFPA 55 and 853 and original material
NFPA 55 Compressed Gas and Cryogenic Fluids Code	Comprehensive gas safety code that addresses flammable gases as a class of hazardous materials and also contains hydrogen-specific requirements
NFPA 853 Standard for the Installation of Stationary Fuel Cell Power Systems	Covers installation of all commercial fuel cells including hydrogen PEM fuel cells
Hydrogen Technologies Component, Performance, and Installation Standards	
ASME B31.3 and B31.12 Piping and Pipelines	Piping design and installation codes that also cover material selection
ASME Boiler and Pressure Vessel (BPV) Code	Addresses design of steel alloy and composite pressure vessels
CGA S series	Addresses requirements for pressure relief devices for containers
CGA H Series	Components and systems
UL 2075	Sensors
ISO/TC 197	Hydrogen technologies

REFERENCES

[1] González, Rosa. Laboratorio Nacional de Tecnologías del Hidrógeno, México DF, 2014.

[2] Rivkin, C. Burgess, R. Hydrogen Technologies Safety Guide, NREL Ed, Colorado, USA. 2015.

[3] Flores, J. (2016). Programa de Laboratorios Nacionales. [online] Conacyt.gob.mx. Available at: http://conacyt.gob.mx/index.php/el-conacyt/desarrollo-cientifico/programa-de-laboratorios-nacionales [Accessed 12 Sep. 2016].

Development of an Automatized Manufacturing System of Electrodes for PEM Fuel Cells

M. López[1,*], J. R. Flores[1], L. Albarrán[1], F. Loyola[1], U. Cano[1]

[1]Instituto de Investigaciones Eléctricas. Reforma 113, Col. Palmira, Cuernavaca, Morelos, México, 62490.
[*]Tel: +527773623811; e-mail: manuel.lopez@iie.org.mx

Abstract

Membrane Electrode Assemblies (MEAs) are the core of the Proton Exchange Membrane Fuel Cell (PEMFC) technology. For real applications several MEAs must be stacked to integrate a PEMFC stack. In order to have a good performance and durability of the PEMFC stack, the MEAs must have similar characteristics, because a change in one of them could have a very important impact on the performance of the others and eventually in the stack. The fabrication of the MEAs is a process in continuous development in order to increase its performance and reduce its cost. Several methods have been proposed for the MEAs fabrication, such as painting, decal method, magnetron sputtering, chemical vapor deposition, spraying, and others. In the Hydrogen and Fuel Cells Laboratory of the Electric Research Institute (IIE) an automatized manufacturing system for MEAs fabrication was developed. With this system based in the spraying technology is possible to prepare MEAs for PEMFC or water electrolyzer technologies. The automatized system has an injection subsystem and positioning subsystem. The injection subsystem can apply the catalytic ink on the membrane or diffusor. Whereas that the positioning subsystem enables movement of the nozzle across the area to atomize. More than 400 MEAs of 100 cm2 of active area had been prepared with very good performance and reproducibility using this automatized system. In this work, the characteristics and the operation of the automatized system is presented. Additionally the typical performance of the MEAs fabricated with this system is showed.

Keywords: Manufacturing System, Catalytic Ink, Electrodes, Fuel Cells.

REDUCING TIME AND COST OF THE MANUFACTURING PROCESS OF MEMBRANE ELECTRODE ASSEMBLIES

I. Lorena Albarrán Sánchez[1], *J. Roberto Flores Hernández[1] Tatiana Romero [1] , U. Cano Castillo[1]
[1]IIE, Gerencia de Energías Renovables , Calle Reforma 113, Col. Palmira, 62490, Cuernavaca, Morelos, México
* contact email: jrflores@iie.org.mx

ABSTRACT

Membrane-Electrodes Assemblies (MEA's) are unit cells in a proton exchange membrane fuel cell technology (PEMFC). MEAs performance depends on the process used during their manufacture (painting, decal method, sputtering, chemical vapor deposition, spraying, and others). In the same way each one of the processes mentioned before includes several steps and parameters that must be optimized to prepare the best MEA at a competitive price and with the best possible performance. For some years in-house preparation of MEAs had been made manually employing mechanical equipment developed at the Electrical Research Institute (IIE). The MEAs thus prepared had very good performance and good reproducibility, however, the time employed in their manufacture was very long, with an impact in their cost. To overcome this limitation, the manufacturing process of the MEAs was redesigned by changing parameters of the process such as roughness surface of the membrane, membrane cleaning and activation, spraying the catalytic ink on the membrane vs on carbon paper, etc. MEAs performance and reproducibility was tested and this work presents results obtained during characterization of several MEAs prepared under different parameter conditions. Such changes allowed the reduction of manufacturing time and facilitated MEAs handling for stack integration without compromising performance.

Keywords: Manufacturing process, MEA´s, Electrodes, Fuel Cells.

Enhance Photoactivity of Hydrogen production with mixed oxide: TiO_2-NiO as semiconductor

Alejandro Pérez-Larios[1,2,3*], R. Gomez[2], R. Zanella[3], J. Bedia[4], C. Belver[4].

[1]Universidad de Guadalajara, Centro Universitario de los Altos, Depto. Ciencias Biologicas, Carretera a Yahualica km. 7.5, Tepatitlán de Morelos, Jalisco, México. 47600.
[2]Universidad Autónoma Metropolitana-Iztapalapa, Depto. de Química, Área de Catálisis, Grupo ECOCATAL, Av. San Rafael Atlixco No 189, D.F., México 09340.
[3]Centro de Ciencias Aplicadas y Desarrollo Tecnológico, Universidad Nacional Autónoma de México (UNAM), 04510, Ciudad Universitaria, D.F. México.
[4]Seccion de Ingenieria Quimica, Facultad de Ciencias, Universidad Autónoma de Madrid, Campus Cantoblanco, E-28049 Madrid, Spain.

(*) alarios@cualtos.udg.mx

ABSTRACT

The most studied processes at the present for the hydrogen production are electrochemical, steam reforming of alcohols or hydrocarbons and water splitting. Thus, the water splitting using semiconductors materials had recently acquired great relevance because of the low cost for the hydrogen production. The principle of this technique is based on the photoexcitation of the semiconductor using a UV or visible light sources.
The alternative method of photocatalytic water splitting is promising since it involves the absorption of light to produce hydrogen by irradiating oxide semiconductors. Photocatalytic systems for water splitting may contain sacrificial reagents, as methanol, commonly used in the photocatalytic evolution of H_2 from water, since its hydroxyl group captures photogenerated holes and minimizes the probability of e^-/h^+.
In this study, Titanium dioxide doped with Nickel (1.0, 3.0, 5.0 and 10.0 % wt) by sol-gel method were obtained. The solids were characterized by nitrogen adsorption using adsorption isotherm (BET) and porosity (BJH) method, XRD patterns and UV-Vis spectroscopy. The photoactivity was evaluated using a Pyrex reactor of 200 ml using a solution Methanol-Water (1:1) and 0.1 g of catalyst. A high pressure Hg lamp (with a λ=254 nm, I_o = 2.2 mW/cm^2) encapsulated in a quartz tube was used as source of energy.
The results showed materials with specific surface area among 100 to 180 m^2/g and mesopority characteristics. The XRD patterns show the formation of the crystalline anatase phase. The band gap energy (Eg) for the materials were obtained with UV-Vis spectroscopy, the Eg values were lower than 3.2 eV. In the water splitting evaluation a maxim in the efficient was found at Ni at 10 wt.%. The hydrogen produced was 3000 μmol.

Keywords: Photocatalysis; hydrogen production; sol-gel; Titanium dioxide.

Hydrogen production improved mixed oxide TiO_2-ZrO_2 photocatalyst as semiconductor

Alejandro Pérez-Larios[1,2*], Ricardo Gomez[2].

[1]Universidad de Guadalajara, Centro Universitario de los Altos, Depto. Ciencias Biologicas, Carretera a Yahualica km. 7.5, Tepatitlán de Morelos, Jalisco, México. 47600.
[2]Universidad Autónoma Metropolitana-Iztapalapa, Depto. de Química, Área de Catálisis, Grupo ECOCATAL, Av. San Rafael Atlixco No 189, D.F., México 09340.

(*) alarios@cualtos.udg.mx

Abstract

In this study the synthesis of the semiconductor oxide TiO_2 doped with ZrO_2 varying concentrations was using for hydrogen production. The photocatalysts were characterized by N2 phisisortion studies, scanning electron microscopic-energy dispersive analysis, X-ray diffraction studies, UV-vis and Raman spectroscopy. The anatase phase in these materials showed high superficial area, the studies of UV-Vis absorption showed a diminish in the energy band gap in function of the zirconium content. The Raman spectrum indicates that crystalline structure of TiO_2 was modified for the presence of cerium. In the photocatalytic activity, the materials showed an increase in the hydrogen production, where, the maximum hydrogen production was achieved at 10 wt. % of the zirconium content.
keywords: Hydrogen; photocatalysts; semiconductor; TiO_2; Mixed oxide

I. Introduction (*Heading 1*)

Hydrogen is an attractive alternative sustainable clean energy carrier because of the depletion of fossil fuel reserves and the environmental pollution caused by continuous burning of fossil [1,3]. Hydrogen is currently obtained from nonrenewable natural gas, naphta, heavy oil, methanol, biomass, wastes, coal, petroleum and water, but could be generated from renewable resources such as biomass [4,8]. Water decomposition by means of sunlight mimics photosynthesis by converting water into H_2 and O_2 using inorganic photo-semiconductors that catalyze the water-splitting reaction [9,10]:

$$H_2O \rightarrow \frac{1}{2}O_2 + H_2 \quad (g)$$

Water decomposition using sunlight on semiconductor photocatalysts has attracted intense research interest since the pioneering work on a photo-electrochemical cell conducted [11]. This work has stimulated the research for the overall water splitting reaction using particulate photocatalysts that was first realized in 1980 [12] who reported stoichiometric evolution of hydrogen and oxygen. Since these ground-breaking works, many papers have been published on the impact of different semiconductor materials on photocatalytic water splitting performance [13-14]. These studies clearly prove that the energy conversion efficiency of water splitting is principally determined by the properties of the semiconductors used as photocatalysts. Light-driven water splitting is initiated when a photo-semiconductor absorbs light photons with energies greater than its band gap energy (Eg). This absorption creates excited photoelectrons in the conduction band (CB) and holes in the valence band (VB) of the semiconductor. After that, the second step in photochemical water splitting consists of charge separation and the migration of photogenerated electron–hole pairs from the bulk of the semiconductor towards the reaction sites on the photocatalysts surface. The final step of the photocatalytic process involves the surface chemical reactions. The photo-generated electrons (e^-) and holes (h^+) that migrate to the surface of the photocatalysts without recombination can reduce and oxidize, respectively, water molecules adsorbed onto the surface of the semiconductor to produce gaseous oxygen and hydrogen by the following reactions:

Oxidation: $H_2O + 2h^+ \rightarrow 2H^+ + \frac{1}{2}O_2$

Reduction: $2H^+ + 2e^- \rightarrow H_2$

Overall reaction: $H_2O \rightarrow \frac{1}{2}O_2 + H_2$

This phenomenon explains the slow hydrogen production by photocatalytic water splitting using TiO_2 alone [15,16]. Some oxide in combine with TiO_2 in the formation of mixed oxide is also known to increase photocatalytic performance via inhibiting the recombination of electrons and holes for the evolution of H_2 [17].

It was recently suggested by Verykios and co-workers, that decomposition of organics and H_2-production can be used in tandem [18, 19]. The idea is that H_2-production efficiency is increased by using an electron-donor contaminant (sacrificial reagent), which will ultimately result in enhancement of the H_2 production rate with simultaneous degradation of the organic substrate'' [18]. In the majority of the studies published in the literature, methanol was used as sacrificial reagent [19–23], further examples include the decomposition of various azo-dyes [18], glucose [24], glycerol [25] and formic acid [26], etc.

In the present study we have prepared mixed oxide TiO_2-ZrO_2 photocatalysts using sol-gel method and tested their efficiency for hydrogen generation. Thus, the principal objective of the work is to develop TiO_2-ZrO_2 mixed oxide photocatalysts for hydrogen production from aqueous solution ethanol-water under irradiation with UV-visible light. Characterization of the catalysts was done following standard procedures.

II. Experimental

2.1 Synthesis and Characterization of Materials

The mixed oxide TiO_2-ZrO_2 nanostructures were prepared by the sol-gel method using titanium butoxide (IV) (Aldrich 97%) and their respective salt as precursor: 44 mL of 1-butanol (Aldrich 99.4 %) and 18 mL of distilled wáter containing the appropriate average $C_{20}H_{28}O_8Zr$ (Strem Chemicals 99%), In the preparation of each of the series of obtaining materils with 1.0, 3.0, 5.0 y 10.0 wt %, were mixed and added few drops of HNO_3 to obtain a pH=3 in the solution. 44 mL were prepared butoxide titanium (IV) to add the above solution at 70°C under reflux (with a molar ratio of 8) this solution was mixed under magnetic stirring to form the gel. The gel was dried at 100 °C for 24h and the solid was ground to a fine powder in an agate mortar. The xerogel obtained was calcined at 500° C for 5 h in an air atmosphere with a heating rate of 1°C/min; finally the product was ground again. As a reference the sample of pure TiO_2 was prepared in the same manner described but not added salt as precursors.

2.2 Materials Characterization

2.2.1 Thermal Analysis (TGA)

Thermograms for thermogravimetric analysis (TGA) were determined on a Perkin Elmer Analyse, modelo Diamond TG/DTA instrument. It was operated un der static atmosphere of air, covering the range from room temperature to 800º C with a heating rate of 10 ºC/min. Samples of about 50 mg of dry gel were analized [27].

2.2.2 Energy dispersive X-ray spectroscopy (EDS)

Energy dispersive X-ray spectroscopy, EDS best known, is an analytical technique used for the elemental analysis or chemical characterization of a simple. Analysis were carried out in a JEOL JSM-6390LV Scanning Electron Microscope instrument.

2.2.3 Nitrogen adsorption

Nitrogen adsorption-desorption isotherms were obtained with an automatic Quantachrome Autosorb 3B instrument. Prior to the nitrogen adsorption, all the samples were outgassed overnight at 200° C. The specific surface areas of the samples were calculated from the nitrogen adsorption-desorption isotherms using the BET method, and the mean pore size diameter from the desorption isotherms using the BJH method.

2.2.4 X-ray diffraction

The obtained TiO_2 and TiO_2-ZrO_2 powders were analyzed by X-ray diffraction using a Bruker D-8 Advance apparatus. The diffraction intensity as a function of the diffraction angle (2θ) was measured between 4 and 70°, using a step of 0.03° and a counting time of 0.3 s per step [30,31].

2.2.5 RAMAN Spectroscopy

Raman spectra ewre obtained using a renishaw spectrometer model Invia MicroRaman using 100x objective and as radiation source an argón laser monochromatic with wavelength 514.5 nm wmission corresponding to green light and a power of 25 mW. In the analysis equipment were placed 10 mg of powdered sample of solids. The Raman shift range for analysis was of 0 a 1200 cm^{-1}[30,32].

3.2.6 UV-Visible Spectroscopy by reflactance difusse.

The UV–Vis absorption spectra were obtained with a Cary 100 UV–Vis spectrophotometer (VARIAN) coupled with an integration sphere for diffuse reflectance studies. A sample of MgO with 100% of reflectance was used as a reference. The diffuse reflectance spectrum was obtained and transformed to a magnitude proportional to the extinction coefficient (α) through the Kubelka-Munk function, equation (a):

$$F(R) = \frac{(1-R)^2}{2R} \qquad \text{(a)}$$

Eg value was calculated from the plot of Kubelka-Munk function F(R) vs wavelength of the absorbed light.

2.2.7 Hydrogen production

The schematic reactor system is described in a previous report. The photo-activity for the hydrogen generation was evaluated using a homemade Pyrex reactor of 250 mL containing 200 mL of water-ethanol solution (1:1 vol/vol) and 0.1 g of catalysts. The irradiation was made using a high pressure Hg pen-lamp (with a radiation of 254 nm and intensity of 2.2 mW/cm^2) encapsulated in a quartz tube immersed in the water solution. The amount of hydrogen produced was followed by using a gas chromatograph (VARIAN CP-3800) equipped with a thermal conductivity detector and with a 5A column molecular sieve (30m length, 0.35mm ID and 50 mm OD).

3. Result and discussion

3.1 Thermogravimetric analysis (TGA-DTA)

The principal analysis of thermogravimetric (TGA) of the samples of TiO_2-ZrO_2 (1.0, 3.0, 5.0 and 10.0 wt %) it can show in the figures 2 and 3.

The Fig. 2 and 3shown the lost weight (Tg) and the curves of analysis differential thermal (DTA) of the mixed oxide TiO_2-ZrO_2 without thermal treatment. For the sample with 1 % de Zr in the figure 2 shown the curves of TG at 1 % wt of Zr, where it show a peak endothermic a low temperatures of 80° C, with a lost weight of 1.0 %, that go associates to lost residual water and trapped solvent in the particles. of 80° C to 250° C, 250° C to 270° C, 270° C to 350° C and 350° C to

460° C, it has tree peaks exothermic corresponding to 8.9 %, 10.5 % and 18.42 % of lost weight respectively, that could be atribuirse to the combustion of organic residual strong retained, same that it evidence of calcination of gel. After of 460° C it has a sintering of material that suggest a crystallization to anatase phase [27].

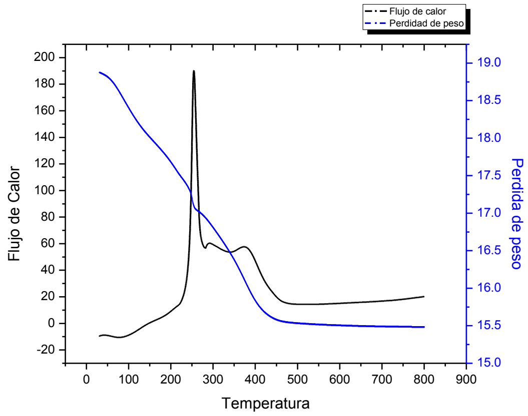

Figure 2. TGA-DTA of mixed oxide of TiO_2-ZrO_2 at 1 %.

Figure 3 show the lost weigth (TG) and the curves of the analysis differential thermal (DTA) of mixed oxide TiO_2-ZrO_2 at 5 % wt. of Zr, without thermal treatment. The curves of TG show the lost endothermic weight to small temperature of 50° C to 100° C it has a peak, with lost weight of 4.76 %, that ranging associated to residual water and trapped solvent in the particles. Of 100° C to 220° C, 220° C to 400° C, it has two exothermic peaks corresponding to 9.0 % and 19.04 % of lost weight respectively that go associated at organic material. After of the 450° C it has a winterization of material that suggest more stability of anatase phase [27].

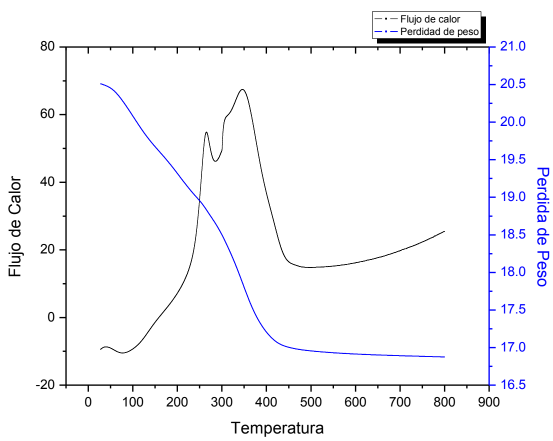

Figura 3. TGA-DTA of mixed oxide TiO_2-ZrO_2 at 10 %.

3.2 Energy Dispersive Spectroscopy (EDS)

Spectra EDS were obtained, which are shown in table 1, it can be seen the presence of ZrO_2, these results can be observed the presence of Zr^{4+}, which is not identifiable by X-ray technique, will be appreciated that the material surface has unevenness, you can also be seen in the micrographs some agglomerates granular appearance. The presence of particles with large unevenness is likely due to the fact that the formation of mixed oxide, in this cases TiO_2-ZrO_2, are in the Surface of TiO_2.

Tabla 1. Elemental Analysis EDS of mixed oxide TiO_2-ZrO_2

Percent	Ti	Zr
1	98.68	1.32
3	96.72	3.28
5	93.42	6.42
10	91.68	8.32

3.3 N_2 Physisorption

The data of the specific áreas of the samples which were calcined at 500° C are reported in table 2. The results show that the specific área by the BET method when the % Zr increases, increased respect to reference of TiO_2 (64 m^2/g). the profiles of the isotherms and the distribution of pore size respectively, we suggest that are type 4 [2], this adsorption isotherm perfectly corresponds to that determined by Hackley and Anderson [3], with hysteresis type 2 (IUPAC), accordingto the classification of de boer [4] which are in solid matrices with uniform pores having capillary condensation and have mesoporous structure and is attributed to the monolayer adsorption data distribution pore size are reported in table 2 (1.0, 3.0, 5.0 and 10.0 % wt of Zr) although wide is unimodal with maximum (4 nm) located in the mesoporous region [5].

Tabla 2. Textural properties, Band gap (Eg) of mixed oxide of TiO_2-ZrO_2.

ZrO_2 (% Wt)	Área (m^2/g)	Pore diameter (nm)	Eg (eV)	Cell Parameters a (nm)	Cell Parameters c (nm)	Cristalite size D (nm)
1.0	91	5.6	3.05	0.56	0.948	7.8
3.0	147	7.7	3.14	0.58	0.956	7.9
5.0	157	7.8	3.20	0.66	0.950	8.7
10.0	138	6.5	3.15	0.78	0.156	9.9
TiO_2	64	6.5	3.20	0.377	0.943	5.7

3.4 X-ray Difracction (XRD)

Figure 4 XRD patterns of the samples of TiO_2 and mixed oxide TiO_2-ZrO_2. XRD patterns show the anatase phase (JCPDD: 21-1272) formed in the TiO_2. Peaks appear in 2Θ=25.4°, 38°, 48°, 54°, 63°, corresponding to the diffraction patterns of (101), (112), (200), (211) and (204) respectively of anatase phase. It has been reported that ZrO_2 peaks does not appear in the present study in 2Θ: 30°, 35°, 50° y 60°, corresponding to the diffraction patterns of (101), (002), (112) and (211). The tetragonal phase of ZrO_2 not appear in the present study [6]. Vishwanathan et al. Has been reported that 10 % by weight does not contribute to any change in morphology in the mixed oxide, as well as high crystallinity in the existing particles [7]. These results suggest that some of Zr^{4+} cations were incorporated within the network of titania, as evidence increase in cell parameter with respect to Zr (Table 2). However, high specific area shown in the mixed oxide is highly likely that the ZrO_2 was sufficiently dispersed to form clusters on the Surface of titania and not detectable by

XRD [8] these data are supported with RAMAN and EDS spectroscopy.

The cristal size, D, of the samples was estimated from half with (β) of the peak 2θ = 25.4° by the Scherrer formula:

$$D = \frac{K\lambda}{\beta \cos\theta}$$

The values are reported in table 2, the cristal size is in the range of nanometers (7.8 to 9.9 nm) which was obtained in all samples.

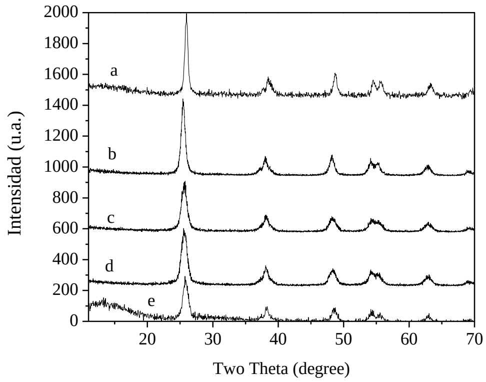

Figure 4. X-Ray diffractograms for mixed oxide TiO_2-ZrO_2

3.5 RAMAN Sepepctroscopy

Figure 5 shows the RAMAN spectra of the samples TiO_2-ZrO_2, with concentrations of Zr^{2+} (1.0, 3.0, 5.0 and 10.0 %). Al peaks are characteristic signs of the anatase phase which has a shift in wavelength of 145 cm^{-1}, 395 cm^{-1}, 513 cm^{-1} and 640 cm^{-1} [9], these peaks correspond to the 5 modes of absorption of this active phase Raman of which overlapped two of the located at 519 cm^{-1} [10], which suggest that the ZrO_2 be embedded in the network of the titania. On the other hand these peaks decrease as the content of Zr^{2+} is increased, indicating a significant decrease in the cristalilinity of the mixed oxide. These result are consistent with XRD, not corresponding to the rutile phase (240 cm^{-1}, 442 cm^{-1} and 606 cm^{-1}) [11] or broquita (450 cm^{-1}, 365cm^{-1}, 320 cm^{-1} and 245 cm^{-1}) [12], where smalls crystal size correspond to smaples with high content of Zr.

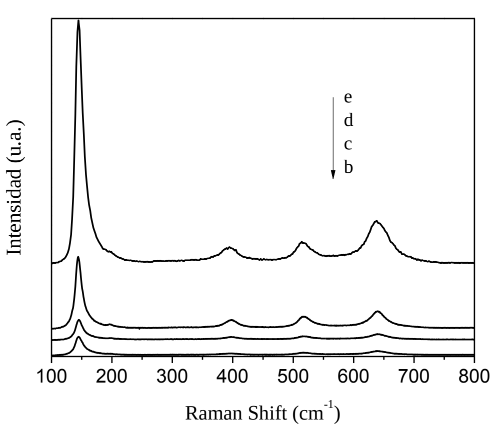

Figura 5. Raman spectra of the simple TiO_2-ZrO_2

3.6 UV-Vis spectroscopy

As to UV-visible spectrum of the sol-gel TiO2 calcined at 500° C (Fig. 6) is observed (at ~ 356 nm) corresponding to electronic transitions of Ti-O-Ti bonds in octahedral coordination absorption. It has been reported [13] that the anatase phase is characterized by an absorption starting near 450 nm with an inflexion near 370 nm accompanied by a plateau between 330 and 230 nm. This signal originates from the charge transfer transition → O2- Ti^{4+} corresponding to the excitation of electrons from the valence band (O2p with character) to the conduction band (with Ti 3d character) [14]. The position of this band with an energy gap of 3.2 eV characterizes in the TiO2 anatase phase as a semiconductor.

The UV-Vis studies were conducted in order to investigate the effect of ZrO_2 in the photophysical properties of TiO_2-ZrO_2 semiconductors. All samples a shift between these wavelengths, which can be attributed to the transitions of the Ti-O electrons TiO_2 nanocrystals TiO_2-ZrO_2 and the results show small bands in the red region (3.05-3.2 eV) for TiO_2-ZrO_2 samples of 1% to 10% by weight of Zr, compared to TiO_2 in anatase phase reference (3.2 eV) (Fig. 6) .

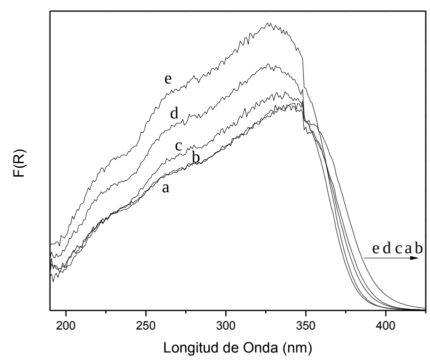

Figure 6. UV-Vis spectra by diffuse reflactance, samples TiO_2-ZrO_2

3.7 Hydrogen Production

In Figure 9, the hydrogen production is shown as a function of irradiation time for samples of TiO_2 and TiO_2-ZrO_2. It can be seen that the formation of hydrogen increases with respect to the weight percent of Zr^{4+}. Hydrogen production for titanium dioxide was 190 mol / h. an important effect of ZrO_2, regarding the content is observed. Forming TiO_2-ZrO_2 to 1% and TiO_2-ZrO_2 to 3% was 387 and 910 μmol/h, respectively, an increase of approximately 100% and for each of the catalysts 500%. H_2 production for TiO_2-ZrO_2 5% was 1600 μmol/h, while the maximum formation was obtained for TiO2-ZrO_2 catalyst 10% to 1,990 μmol/h, Fig. 7 The ZrO2 disappears as the reaction proceeds in the samples d and e (graph 7). These results are very interesting compared when used Au/TiO_2 [16] Pt-TiO_2 [17,18] Ag/TiO_2. [19].

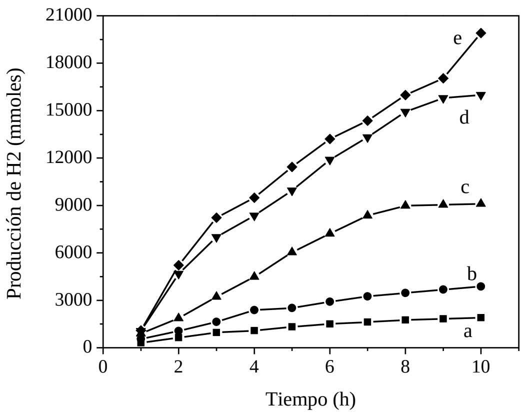

Figure 7. Profile of hydrogen production of mixed oxide TiO_2-ZrO_2

4. Conclusion

This study clearly demonstrates the advantages of the formation of mixed oxides such as ZrO_2-TiO_2, for photocatalytic hydrogen generation. Most TiO_2 parameters such as particle size, surface area, the anatase phase, OH groups on the surface and the thermal stability can be controlled in the formation of the mixed oxides by sol-gel method.

Although high ZrO_2 content of the specific area increases and crystallite sizes suffer the same effect. The photocatalytic activity was good from 5% ZrO_2, this is due to the number of transfers electrons to TiO_2 at ZrO_2. Chemical interactions of Zr-O-Ti in the mixed oxide is a major factor by which a high photocatalytic activity was taken into H_2 production. The study of UV-vis by diffuse reflectance can give strong evidence of changes in the transition states, and there are changes on the surface of oxides, so we suggest that there is a change of CB ZrO_2 of the CB surface of TiO_2 and facilitate the exchange of electrons between them. And preventing recombination of electrons and holes to increase the photocatalytic efficiency of TiO_2. Electron generation proves to be the most important in the photocatalytic activity of the mixed oxides as evidenced by UV-vis analysis after reaction factor.

REFERENCIAS

[1] Gratzel M. Photoelectrochemical cells.Nature 2001;414:338-44.
[2] Rostrup-Nielsen JR. Conversion of hydrocarbons and alcohols for fuel cells. Phys Chem Chem Phys 2001;3:283-8.
[3] Service RF. Hydrogen economy? Let sunlight do the work. Science 2007;315:789.
[4] Cortright RD, Davda RR, Dumesic JA. Hydrogen from catalytic reforming of biomass-derived hydrocarbons in liquid water. Nature 2002;418:964-7.
[5] Woodward J, Orr M, Cordray K, Greenbaum E. Biotechnology: enzymatic production of biohydrogen. Nature 2000;405: 1014-5.
[6] Bard AJ, Fox MA. Artificial photosynthesis: solar splitting of water to hydrogen and oxygen. Acc Chem Res 1995;28:141-5.
[7] Fujishima A, Honda K. Electrochemical photolysis of water at a semiconductor electrode. Nature 1972;238:37-8.
[8] Khan SUM, Al-shahry M, Ingler Jr WB. Efficient photochemical water splitting by a chemically modified n-TiO_2. Science 2002;279:2243-5.
[9] Maeda K, Teramura K, Lu D, Takata T, Saito N, Inoue Y, et al. Photocatalyst releasing hydrogen from water. Nature 2006; 440:295.
[10] Ishikawa A, Takata T, Kondo JN, Hara M, Kobayashi H, Domen K. Oxysulfide $Sm_2Ti_2S_2O_5$ as a stable photocatalyst for water oxidation and reduction under visible light irradiation (λ= 650 nm). J Am Chem Soc 2002;124:13547-53.
[11] Ashokkumar M. An overview on semiconductor particulate systems for photoproduction of hydrogen. Int J Hydrogen Energy 1998;23:427-38.
[12] Meissner D, Memming R, Kastening B. Photoelectrochemistry of cadmium sulfide. 1. Reanalysis of photocorrosion and flatband potential. J Phys Chem 1988;92:3476-83.
[13] J. Jitputti, Y. Suzuki, S. Yoshikawa. Synthesis of TiO_2 nanowires and their photocatalytic activity for hydrogen evolution.
[14] L.S. Yoong, E.K. Chong, B.K. Dutta. Development of copper doped TiO2 photocatalyst for hydrogen production under visible light. Energy 34 (2008) 1652-1661.
[15] Ha SP, Dong HK, Sun JK, Kyung SL. The photocatalytic activity of 2.5 wt.% Cu doped TiO_2 nano powder synthesized by mechanical alloying. J Alloy Compounds 2005;415:51–5.
[16] Ni M, Micheal KH, Dennis YCL, Leung KS. A review and recent development in photocatalytic water-splitting using TiO2 for hydrogen production. Renew Sust Energ Rev 2007;11:401–25.
[17] K. Maeda, H. Terashima, K. Kase, K. Domen. Nanoparticulate precursor route to fine particles of TaON and ZrO2-TaON solid solution and their photocatalytic activity for hydrogen evolution. App. Catal. A: Gral. 357 (2009) 206-212.
[18] Patsoura A, Kondraides DI, Verykios XE Appl Catal B 64 (2006) 171.
[19] Patsoura A, Kondraides DI, Verykios XE Catal Today 124 (2007) 94.
[20] Sreethawong T, Suzuki Y, Yoshikawa S C R Chimie 9 (2006) 307.
[21] Dubey N, Rayalu SS, Labhsetwar NK, Devotta S Int J Hydrogen Energy 33 (2008) 5958.
[22] Yin S, Sato T. J Photochem Photobiol A 169 (2005) 89.
[23] Khan MA, Akhtar MS, Woo SI, Yang O-B. Catal Commun 10 (2008) 1.
[24] Fu X, Long J, Wang X, Leung DYC, Ding Z, Wu L, Zhang Z, Li Z, Fu X. Int J Hydrogen Energy 33 (2008) 6484.
[25] Daskalaki VM, Kondarides DI (in press) Catal Today. 144 (2009) 75-80.
[26] Chen T, Wu G, Feng Z, Hu G, Su W, Ying P, Li C. Chin J Catal 29 (2008) 105.
[27] Xu Q., Anderson M. A., *J. Am. Ceram. Soc*. **77** (1994) 1939
[28] Brunauer S., Deming L. S., Deming W. E., Teller E., *J. Am. Chem. Soc*. **62** (1940) 1723.

[29] Hackley V. A., Anderson M. A., Spooner S., *J. Mater. Res*. **7** (1992) 2555
[30] de Boer J. H., van den Heuvel A., Linsen B. G., *J. Catal*. **3** (1964) 268
[31] Bosch G. P., Domínguez J. M., Zénith J., Rouffignac E., Guzmán O.,Tejeda J., "Técnicas Experimentales en la Caracterización de Catalizadores", Series Científicas IMP, México (1986).
[32] Dzwigaj S., Louis C., Breysse M., Cattenot M., Bellière V., Geantet C., Vrinat M., Blanchard P., Payen E., Inoue S., Kudo H., Yoshimura Y., *Appl. Catal.* B **41** (2003) 181.

Study of the Dynamics of a Four-module Fuel Cell Stack to be Integrated in a Hybrid Electric Power Plant of a Utility Vehicle

Tatiana Romero*, J. Roberto Flores, I. Lorena Albarrán, Félix Loyola and Ulises Cano

Instituto Nacional de Electricidad y Energías Limpias, Gerencia de Energías Renovables. Cuernavaca, México
*contact email: tromero@iie.org.mx

Abstract— A four-module PEM fuel cell stack was electrochemically characterized prior to its incorporation to a hybrid power plant of an electrical utility vehicle. The 3 kW fuel cell stack, comprised of 4 units of 100 membrane electrode assemblies (MEAs) in an open-cathode and air-cooled configuration, was characterized in order to identify its optimum operational parameters. The open cathode configuration is a common approach to reduce parasitic loads and increase energy efficiency in fuel cells; however, the forced convection derives frequently to internal dehydration. Voltage reversal caused by lack of reactants, many times due to dehydration at the reaction sites (membrane-electrode interface) is a common failure source for this kind of configuration especially at high current demands. Therefore, water management becomes crucial for preventing fuel cell´s performance decrease and permanent failure. Subsequently, a smart water management strategy had to be established prior to the power plant integration into the vehicle for the fuel cell´s performance to be guaranteed during the vehicle duty cycle.

For this purpose, a testing protocol was established for testing each module based on linear voltammetries, electrochemical impedance spectroscopy and thermal images in order to observe cell´s voltage and resistance as indicators of internal hydration, reactants concentration, and heat distribution during the stack operation. Polarization curves were obtained for each module and from them, the point (voltage, current, temperature and air vent) for steady operation was identified as the recommended condition for nominal performance during the fuel cell operation in the hybrid power plant of the electrical vehicle.

Keywords: PEMFC stacks, open cathode, air cooled, dynamics, voltage reversal

Computational analysis of the machining and design parameters in the flow conditions of the electrodes in the PEM Cells

David Guillermo Huérfano Delgado
School of Engineering and Science
ITESM, Campus Estado de México
Cd López Mateos, Méx.
A0137081@itesm.mx

Héctor Morano Okuno
School of Design, Engineering and Architecture
ITESM, Campus Estado de México
Cd López Mateos, Méx.
hector.morano@itesm.mx

Abstract— **In this paper is shown a comparative analysis of the effect of the machining angle through the simulations of non-isothermal multidimensional fields flow though electrodes for proton exchange membrane (PEM) cell. Different designs of channel (coil, parallel and pin-type), positions of the inlet feed gas, just as the effect of curvature machined into different sections of the channels according to some relevant aspects as the relation between the channel dimensions were used. The analysis is flux performed to determine: pressure load losses, gas distribution, gas velocity in the electrode and the residence time. The research was developed using computer-aided design (CAD) and computational fluid dynamics (CFD) software application, the results were compared with experimental data in the literature.**

Keywords— PEM fuel cells; electrode modeling; fluid dynamics; CFD

Microwave-assisted green synthesis of Ag-Pd and Fe-Pd nanoparticles supported on SiC and Al_2O_3 for zinc sulfate decomposition.

O. Soto[1], V. Ramos[1], D. Chávez[1]

Universidad Autónoma de Chihuahua, Circuito Universitario s/n,
Campus II, Chihuahua, Chihuahua, México, 31170.
Tel. +52 (614) 236 6000; e-mail: a257569@uach.mx

ABSTRACT

This work focuses on the synthesis of Ag-Pd and Fe-Pd nanoparticles supported on SiC and Al_2O_3 as a catalytic material for the zinc sulfate decomposition in the sulfur-ammonium thermochemical cycle. This cycle involves a high temperature reaction for the oxygen production step: a metal sulfate decomposition. To reduce the high energy requirements of this particular step, catalysts are introduced to lower the reaction temperature.

Pd catalysts in nanometric scale are one of the most used materials for this purpose. However, the main disadvantages of palladium are its scarcity and high cost. To counteract the previous, the use of Pd-based alloys is being widely investigated. Additionally, it has been reported that the use of Ag and Fe to form Pd-based alloys significantly enhances the catalytic activity.

The synthesis consists in a microwave-assisted method using nutshell extract as chemical reductant and stabilizing agent. Glycerol is used as solvent, its high boiling point (290 °C) will allow to carry the synthesis at higher temperature with respect to aqueous medium (100 °C). The synthesized materials are thermally treated to remove all organic and solvent residues. Finally, the catalytic material is characterized by the BET technique, scanning electron microscopy (SEM), X-ray fluorescence (XRF), transmission electron microscopy (TEM), x-ray diffraction (XRD) and thermogravimetric analysis (TGA). The catalytic performance is evaluated by calorimetric techniques such as the TGA, and differential analysis calorimetry (DSC) coupled to a mass spectrometer (MS).

Preliminary results shows evidence of the presence of the desired materials.

Keywords: Glycerol, microwave assisted synthesis, nanoparticles, nutshell extract, sulfur-ammonium cycle.

1. INTRODUCTION.

Hydrogen is a promising alternative for producing sustainable energy. It has the potential to replace the use of fossil fuels, which are responsible of climate change due to high emissions of greenhouse gases such as CO_2. [1]

Basically there are three ways to produce hydrogen from solar energy: electrochemical, photochemical and thermochemically. [2] Thermochemical cycles, which main objective is the dissociation of the water molecule through a series of chemical reactions at different temperatures, have the potential to produce hydrogen with high efficiency in a large scale process. [3]

Since the early 1970s there have been more than 400 thermochemical cycles for hydrogen production. Among them, a class of cycles known as thermochemical cycles sulfur family has received special attention. [4]

The sulfur-ammonium cycle is a promising technology for the large-scale production of chemical energy from solar energy. It consists of two stages: first, hydrogen production followed by oxygen production described by next equations.

$$SO_3\,(g) + 2NH_3\,(g) + H_2O\,(l) \longrightarrow (NH_4)_2SO_3\,(ac) \quad \textbf{(1)}$$

$$(NH_4)_2SO_3\,(ac) + H_2O\,(l) \longrightarrow (NH_4)_2SO_4\,(ac) + H_2\,(g) \quad \textbf{(2)}$$

$$(NH_4)_2SO_4\,(ac) \longrightarrow 2NH_3\,(g) + H_2SO_4\,(g) \quad \textbf{(3)}$$

$$H_2SO_4\,(l) \longrightarrow SO_2\,(g) + H_2O\,(g) + ½\,O_2\,(g) \quad \textbf{(4)}$$

[5]

The first step for hydrogen production consists in reactions 1 and 2. In the reaction 1, the ammonia and sulfur dioxide are chemically absorbed in water to produce ammonium sulfite. In reaction 2, hydrogen is produced by a photocatalytic process in which the $SO3^{2-}$ ions are oxidized to $SO4^{2-}$. Oxygen production, where solar thermal energy is used for oxygen production, consists in reactions 3 and 4.

For the sulfuric acid requires highly expensive materials to withstand the corrosive nature of this compound at high temperatures are required. As an alternative the introduction of a metal oxide in the reaction has been proposed. Metal oxide are capable of reacting with sulfate ammonia to produce the corresponding metal sulfate by a catlyzed thermal reaction with energy obtained from solar radiation as shown in (3'). Successively, the formed sulfate is decomposed by the same thermal energy from solar radiation, producing sulfur dioxide and oxygen as described in (4'). [6].

$$y(NH_4)_2SO_4 + M_xO_y \longrightarrow M_x(SO_4)_y + 2y\,NH_3 + y\,H_2O \quad \textbf{(3´)}$$

$$Mx(SO4)y \longrightarrow MxOy + y\,SO2 + Y/2\,O2 \quad \textbf{(4´)}$$

The decomposition of metal sulfate formed requires temperatures above 900 ° C. To reduce the high energy requirements of this particular step, catalysts are introduced to lower the reaction temperature. For this purpose, a variety of catalysts have been tasted such Pt [7-9], Pd [10], Cu [11-13], Fe [14] supported primarily on alumina, silica and silicon carbide due to their known thermal stability.

Microwave assisted synthesis is characterized by a rapid and uniform heating of the reaction medium [15] propitiating homogeneous nucleation with shorter reaction times, small sizes of nanoparticles (nm), monodispersity and high purity with respect to the traditional methods of synthesis. [16]

Stabilizing agents, reducers and the reaction medium are three key factors for an efficient metal nanoparticles synthesis. Most commonly used stabilizing agents for the synthesis of metal nanoparticles, such as thiols, triphenylphosphine and / or polyvinylpyrrolidone are toxic, difficult to obtain and they minimizes the utility of nanoparticles. Moreover, most of the reducing agents reported includess sodium borohydride (NaBH4), which is potentially hazardous to the environment. [17]

The use of plant extracts such as *Aloe Barbadensis Miller* plant [18], *Camellia sinensis* [19], *Azadirachta indica* [20], *Macrotyloma uniflorum* [21] as reducing agents and reactive stabilizers for the green synthesis of nanoparticles has been widely investigated.

.

It has also been found that the biosynthesis of silver nanoparticles by an assisted microwave method using plant extracts such as *Biophytum sensitivum* [22], *Aerva lanata* [23] and nutshell [24] as reducing agents and stabilizers is a viable method for an easy and fast synthesis.

This work focuses in the synthesis and characterization of Ag-Pd and Fe-Pd nanoparticles supported on SiC and Al_2O_3 by a microwave-assisted method using nutshell extract as chemical reductant and stabilizing agent, glycerol as solvent and evaluate their performance for zinc sulfate decomposition.

2. MATERIAL AND METHODS.

2.1. Support pretreatment.

The required amount of gamma alumina nano powder purchased from Sigma Aldrich was treated at 500 °C in a tubular furnace to remove impurities. A functionalization pretreatment was made for SiC purchased from sigma Aldrich; this consisted in mixing and heating sulphuric acid and SiC (50% wt) for 30 minutes at 110 °C in a CEM-Discover microwave, using 50 mL of acid per gram of solid. After functionalization time, the mixture was separated by filtration and the recuperated solid was rinsed with distilled water until pH 7 before drying overnight at 80 °C.

2.2. Extract and precursor preparation.

1.5 g of milled nutshell (40 mesh) and 30 mL of distillated water in a round flask and heated by microwave for 10 minutes at 80 °C while stirring. The resulting product was filtrated and stored for later use.

$PdCl_2$, $AgNO_3$ and $Fe(NO_3)_3$ 1mM solutions were used as precursors. For this, the required amount of salt was putted in a volumetric flask and graduated at 100 mL with glycerol.

2.3. *Ex-situ* nanoparticles synthesis.

In a microwave vial, 1 mL of $PdCl_2$ and 1 mL of $AgNO_3$ or Fe $(NO_3)_3$ according to the desired alloy were added. After, two milliliters of extract and 3 mL of glycerol were added.

This mixture was heated by microwave at 180 °C during 1 minute. The above process was carried five times and the product of the synthesis was putt in a flask with the required amount of support (Al_2O_3 or SIC) to obtain a metal load of 7%. The mixture was stirred during 1h and centrifuged to separate the solid. Finally, the solid was dried in a vacuum oven and calcinated at 500 °C during 10h

3. RESULTS AND DISCUSSION.

The adsorption isotherms of BET analysis performed on alumina and silicon carbide before and after the pretreatment are represented in Figure 1. Decrease on superficial area for both materials can be observed: alumina decrease from 475.832 m²/g to 220.946 m²/g and silicon carbide from 27.740 m²/g to 5.285 m²/g after pretreatment.

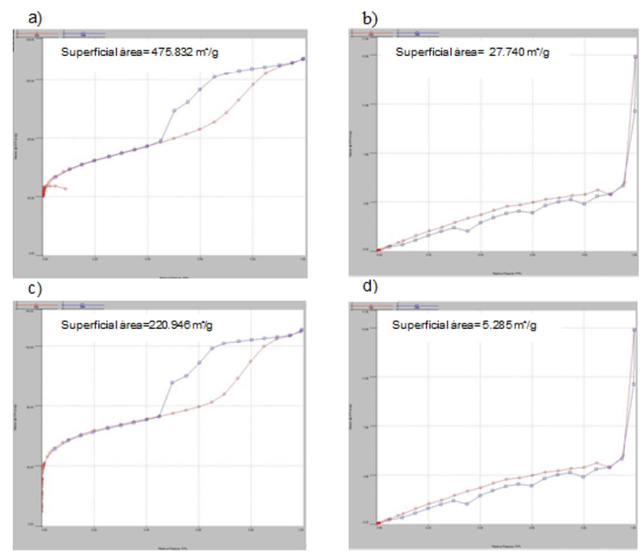

Figure 1.BET adsorption isotherms: a) Al_2O_3 not pretreated, b) SiC not pretreated, c) Al_2O_3 pretreated and c) SiC pretreated.

The Al_2O_3 and PdAg/ Al_2O_3. XRD patterns are presented in Figure 2. Diffractograms show an evident change in patterns before and after the synthesis process. The appearance of a broad and poorly defined peak in the region of 20 and 30 2 theta, it´s attributed to the high organic load from the nutshell extract (C). Moreover, we can see some diffraction peaks at 38.10, 44.8, 65.6 and 78.58 which are between of the representative peaks for an fcc structure of palladium and a fcc structure of silver. [25] and [26] With the above, the signals obtained in the XRD can be attributed to both metals alloy. However, this analysis also shows an incomplete precursor reduction that can be caused by an insufficient amount of reducing agent or reaction time.

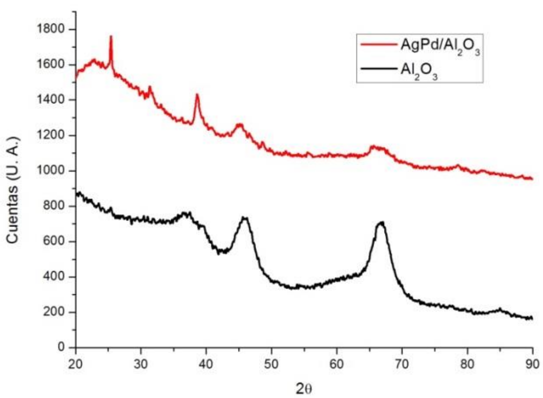

Figure 2. Diffraction pattern of PdAg/ Al_2O_3 catalyst and Al_2O_3 support.

To determinate the material morphology, a scanning electron microscopy (SEM) was made (Figure 3), the results obtained shows a spherical morphology for AgPd/ Al_2O_3 and FePd/ Al_2O_3 systems. On the other hand, an irregular morphology was found for silver palladium and iron palladium over silicon carbide materials. Moreover, an elemental analysis by EDS (figure 3) was also made. The results evidence the presence of silver and palladium or iron and palladium depending on the kind of material system.

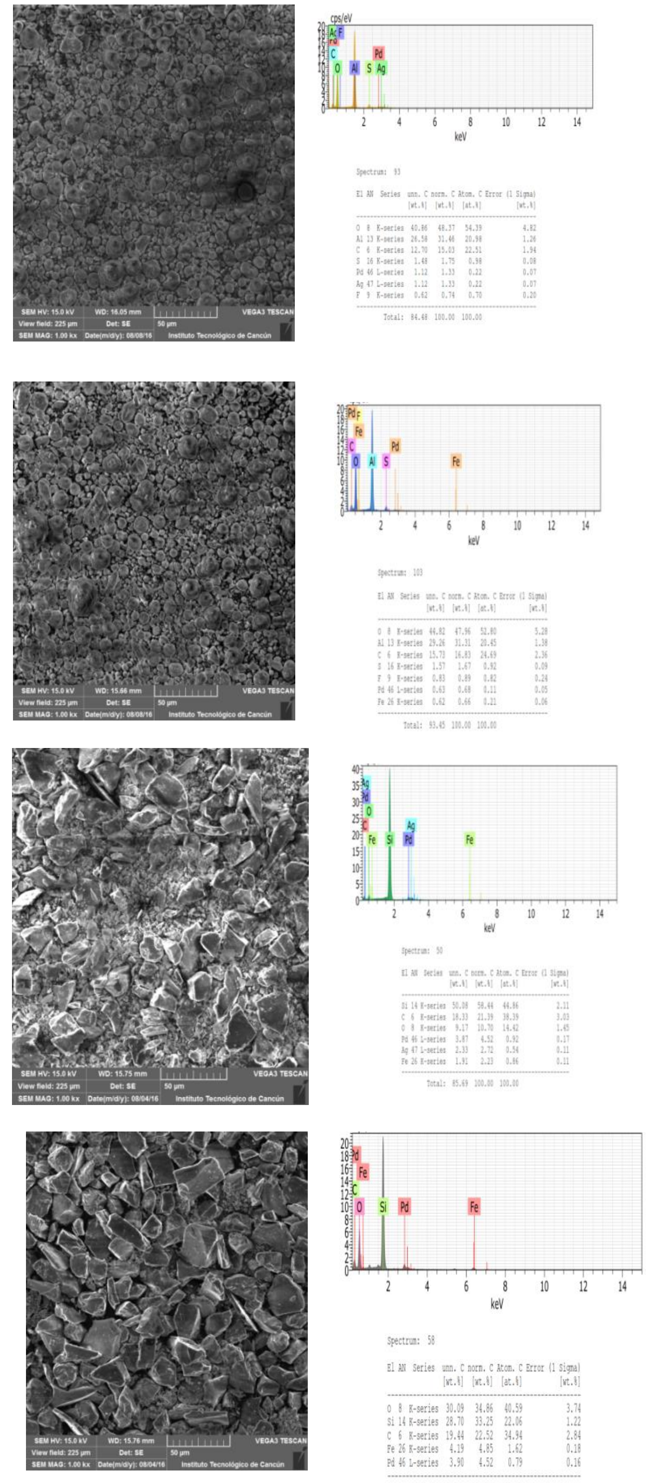

Figure 3. Scanning electron microscopy (SEM) and elemental analysis by EDS for: a) AgPd/Al_2O_3, b) FePd/ Al_2O_3, c) AgPd/SiC and FePd/SiC.

A semi-quantitative X-ray fluorescence analysis was carried out with the purpose to know the amount of metal loads over the catalytic support. The Figure 4 shows the results of this analysis for silver palladium and iron palladium over alumina and sustain the results obtained by EDS elemental analysis.

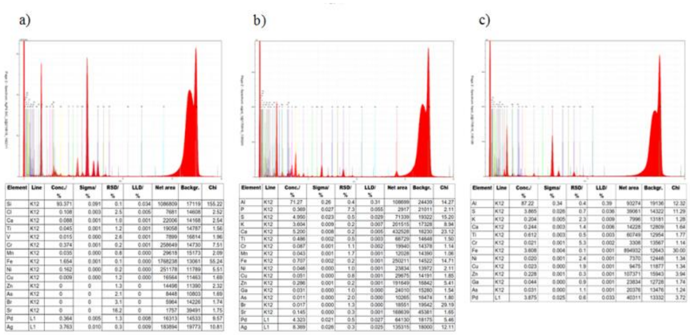

Figure 4. XRF spectra and catalysts composition: a) AgPd/SiC, b) AgPd/Al_2O_3 and c) FePd/ Al_2O_3

Although this analysis confirms the presence of the desired metals, the amount of them is not the expected in all the cases. It can be attributed to a low efficacy of the impregnation method or insuffisent time of metal impregnation.

4. CONCLUSIONS.

Ag-Pd and Fe-Pd nanoparticles supported on SiC and Al_2O_3 were synthetized by a microwave-assisted method using nutshell extract as chemical reductant and stabilizing agent using glycerol as solvent. The analyzes confirm the presence of Ag and Pd in AgPd/ Al_2O_3 and Ag/ SiC catalysts and Fe and Pd in FePd/ Al_2O_3 and FePd/Sic catalysts.

Proposed work for the future:

- Continue the synthesis and characterization of the proposed.
- Evaluate the performance of the synthesized materials as catalysts for zinc sulfate decomposition.

5. REFERENCES.

1. Abanades, S., Charvin, P., Flamant, G. y Neveu, P. (2006). Screening of wáter-splitting thermochemical cycles potentially attractive for hydrogen production by concentrated solar energy. *Energy*. 31, 2805 - 2822.
2. Steinfeld, A. (2005). Solar thermochemical production of hydrogen- a review. Solar *Energy*. 18, 603-615.
3. Roeb, M., Thomey, D., de Oliveira, L., Sattler, C., Fleury, G., Para, F.,…, Ferrato, M. (2013). Sulphur based thermochemical cycles: Development and assessment of key components of the procces. *INTERNATIONAL JOURNAL OF HYDROGEN ENERGY*. 38: 6197 – 6204.
4. Mao, L., T-Raissi, A., Huang, C. y Muradov, N. (2011). Thermal decomposition of $(NH_4)_2SO_4$ in presence of Mn_3O_4. *INTERNATIONAL JOURNAL OF HYDROGEN ENERGY*. 36: 5822 – 5827.
5. Wesley, L. (2013). A Continuous Solar Thermochemical Hydrogen Production Plant Design. (A Thesis submitted in

partial satisfaction of the requirements for the degree Master of Science). University of California, San diego.
6. Tizzoni, A., Corsaro, N., D´Ottavi, C., Liccocia, S., Sau, S. y Tarquini, P. (2015). Oxygen production by intermediate metal sulphates in sulphur based thermochemical watter splitting cycles. *INTERNATIONAL JOURNAL OF HYDROGEN ENERGY*. 40: 4065 – 4083.
7. Banerjee, A., Pai, M., Tewari, R., Raje, N., Tripathi, A., Bharadwaj, S. y Das, D. (2015). A comprehensive study on Pt/Al2O3 granular catalyst used for sulfuric acid decomposition step in sulfur- iodine thermochemical cycle: changes in catalyst structure, morphology and metal-support interaction. *Aplied Catalysis B: Environmental*, 162, 327-337.
8. Everson , R,., Stander, B., Neomagus, H., Van Der Merwe, A., le Grange, L. y Tietz M. (2015). Sulphur trioxide decomposition with supported platinum/palladium on rutile catalyst: 1reaction kinetics of catalyst pellets. *INTERNATIONAL JOURNAL OF HYDROGEN ENERGY*, 40, 85-94.
9. Seong-Sheol, N., Seoung, L., Yong, S. y Kwang, J. (2014). Sulfuric acid decomposition on the Pt/n-SiC catalyst for SI cycle to produce Hydrogen. *INTERNATIONAL JOURNAL OF HYDROGEN ENERGY*, 40, 2493- 2499.
10. Barbarossaa, V., Bruttib, S.,Diamantia, M.,Sau S., DeMaria, G. (2006). Catalytic thermal decomposition of sulphuric acid in sulphur–iodine cycle for hydrogen production. *INTERNATIONAL JOURNAL OF HYDROGEN ENERGY*, 31, 883–890.
11. Abimanyu, H., Kwang-Deog, J., Ki-Won, J., Jinsoo, K. y Kye, Y. (2008). Preparation and characterization of Fe/Cu/Al2O3- Composite granules for SO3 decomposition tos assist Hydrogen production. *Aplied Catalysis A: General*, 343, 134-141.
12. Kawada, T., Yamashita, H., Zheng, Q. y Machida, M. (2014). Hydrothermal synthesis of CuV2O6 suported on mesoporous SiO2 as SO3 decomposition catalyst for solar thermochemical Hydrogen production. *INTERNATIONAL JOURNAL OF HYDROGEN ENERGY*, 39, 20646-20651.
13. Nagaraja, B., Jung, K. y Yoo, K. (2009). Synthesis of Cu/Fe/Ti/Al2O3 Composite Granules for SO3 Decomposition in SI Cycle. *Catal Lett*, 128, 248–252.
14. Giaconia, A., Salvatore, S., Felici, C., Tarquini, P., Karagiannakis, G., Paykoura. C.,… Sattler, C. (2011). Hydrogen production via sulfur-based thermochemical cycles: part 2 performance evaluation of Fe2O3-based catalyst for the sulfuric acid decomposition step.
15. Siby, M. y Beena, M. (2014). Microwave-assisted facile synthesis of silver nanoparticles in aqueous médium and investigation of their catalytic and antibacterial activities. *Journal of Molecular Liquids*, 197: 346-352.
16. Wang, H., Xu, J., Zhu, J. y Chen, H. (2002). Preparation of CuO nanoparticles by microwave irradiation. *Journal of Crystal Growth*, 244: 88-94.
17. Peng, H., Yang, A. y Xiong, J. (2013). Green, microwave-assistedsynthesis of silver nanoparticles using bamboo hemicelluloses and glucose in an aqueous médium. *Carbohydrate Polimers*, 91: 348-355.
18. Chandran, S., Chaudhary, M., Pasricha, R., Ahmad, A. and Sastry, M. (2006), Synthesis of Gold Nanotriangles and

Silver Nanoparticles Using *Aloevera* Plant Extract. *Biotechnol Progress*, 22: 577–583.

19. Vilchis, A., Sánchez, V., Camacho, M., Gómez, R., Camacho, M. y Arenas, J. (2008). Solventless synthesis and optical properties of Au and Ag nanoparticles using Camellia sinensis extract. *Materials Latters*, 62: 3103- 3015.
20. Shankar, S., Rai, A., Ahmad, A. y Sastry, M. (2004). Rapid synthesis of Au, Ag and bimetallic Au core-Ag Shell nanoparticles using Neem (Azadirachta indica) leaf broth. *Journal of Colloid and Interface Science*, 275:496-502.
21. Vidhu, V., Aromal, S. y Philip, D. (2011). Green synthesis of silver nanoparticles using Macrotyloma uniflorum. *Spectrochimica Acta Part A*, 83: 392-397.
22. Siby, J. y Beena, M. (2015). Microwave-assisted Green synthesis of silver nanoparticles and the study on catalytic activity in the degradation of dyes. *Journal of Molecular Liquids*, 204: 184-191.
23. Siby, J. y Beena, M. (2015). Microwave-assisted facile Green synthesis of silver and gold nanocatalysts using the leaf extract of Aerva lanata. *Spectrochimica Acta Part A: Molecular and Biomolecular Spectroscopy*, 136: 1371-1379.
24. Casas Hidalgo, Ana Isabel. Aprovechamiento de la Cáscara de Nuez para la Obtención de Electrocatalizadores bimetálicos basados en paladio. Tesis (Ingeniero Químico). Chihuahua, Chihuahua, Universidad Autónoma de Chihuahua, Facultad de Ciencias Químicas.
25. Wang, Y., Sheng, M., Yang, H., Jiang, S. and Li, C. (2010). Electro catalysis of carbon black- or activated carbon nanotubes-supported Pd-Ag towards methanol oxidation in alkaline media. *INTERNATIONAL JOURNAL OF HYDROGEN ENERGY* 35: 10087-10093.
26. Siby, J. and Beena M. (2015). Microwave-assisted green synthesis of silver nanoparticles and the study on catalytic activity in the degradation of dyes. *Journal of Molecular Liquids.* 204: 184-191.

Synthesis and sulfonation of graphene oxide as catalyst support for fuel cell electrodes

D. Morales-Acosta, J. A. Rodríguez-González, S. Fernández-Tavizón, N.M. Sánchez-Padilla, R. Benavides
Centro de Investigación de Química Aplicada
Saltillo, Coahuila, México
diana.morales@ciqa.edu.mx

D. Flores-Oyervides
Facultad de Ciencias Químicas, Universidad Autónoma de Coahuila, México

***Abstract*— The chemical reduction of oxygen functionalities on graphene oxide (GO) sheets produces RGO with a partially restored structure. Otherwise, the covalent functionalization of rGO surface with -SO_3H groups can lead to a significant increase in hydrophilicity of rGO as support material improving the nano-catalyst dispersion. In this study, sulfonic-functionalized graphene oxide (SGO) was prepared for the development of electrodes. GO was synthesized by a modified Hummers method using graphite powder as starting material. The GO synthetized material was chemically and thermally reduced and subsequently sulfonated by means of two sulfonating agents. The influence of reduction and sulfonation methods on physicochemical properties of RC-GOS and RT-GOS were evaluated by XRD, FT-IR and Raman techniques. Electrochemical behavior of both materials as modified glassy carbon electrode (GCE) was investigated in K_3FeCN_6 solution as reference redox system. Our results demonstrate that thermal reduction improves the electrochemical properties of GO, while the electrochemical behavior of both sulfonated materials is controlled by an electron transfer process.**

Keywords*— Reduced graphite oxide; Sulfonation; fuel cell electrodes.

I. Introduction

Graphene (G) is considerate as the next-generation material. This material promises enhanced improvement in several fields of materials science. G has 2-dimensional sheet of sp^2 carbon network, which resembles a honeycomb structure, has attracted enormous attention from the scientific community due to their mechanical, optical, thermal and electrical conductivity properties [1]. The oxidation of graphite-to-graphite oxide (GO) and consequent reduction to chemically reduced graphene oxide (CR-GO) is the most relevant method towards large scale production of graphene materials with new opportunities to develop graphene as a material for energy storage, electronic and electrical devices [2].

GO can be synthesized from oxidation and exfoliation of graphite via oxidative through several methods as Staudenmaier, Hofmann, Hummers and Tour [3–5]. GO, produced by oxidation and exfoliation of graphite, is hydrophilic and electrically insulating because a large number of oxygen-containing functional groups (hydroxyl, carboxyl and epoxy groups) are bonded with carbon atoms[2,5,6]. In order to recover the electrical conductivity of graphene, GO should be reduced to graphene-like sheet, named reduced GO, by partially removing the oxygen-containing functional groups and recovering the sp2carbon atoms [6–9]. Reduced graphene oxide (RGO) is considered to be a chemically converted graphene due to the residue functional groups and the defects. During the reduction of GO to RGO is necessary to recover the conjugated network and electrical conductivity properties. Therefore, the reduction of GO is definitely a key topic, and different reduction processes result in different properties that in turn affect the final performance of materials or devices composed of RGO. The reduction of GO by chemical or thermal routes has widely been accepted to prepare RGO[6–8]. Chemical compounds as hydrazine and borohydride, are widely recognized as strong reducing agents and used for the chemical reduction of GO (CR-GO) [7,9–11]. The thermal reduction of GO (T-GO) is a more complex process because of the thermal energy induced multistep removal processes of intercalated H_2O molecules and oxide groups of carboxyl, hydroxyl, epoxy group, producing various defects by consuming the carbon backbone of GO and the eventual releases of H_2O, CO_2, and CO.

So, both chemical or thermal reduction of GO can be able to restore the graphitic network in the basal plane of RGO, however this process lead to the aggregation of graphene sheets, diminishing its procesability. The above, can be inhibited by covalent or non-covalent functionalization, so that intrinsic properties of graphene can be retained [12,13]. Non-covalent functionalization include the adsorption of polymers and aromatics species via π-π staking and van der Walls interactions [14], while the covalent functionalization includes the formation of new chemical bonds between the atoms native to RGO/GO and the guest functional groups [13]. For instance, the incorporation of sulfonic acid functional groups (-SO_3H) into GO/RGO structure is well known and emerged as a powerful strategy to produce promising materials in catalysis and energy applications [15,16]. However, the sulfonation chemistry of GO/RGO materials has developed only recently and continues to expand for diverse applications [16,17]. The sulfonating agent that has been evaluate include fumic sulfuric acid, cholorosulfonic acid, ammonium sulfate, sulfuric acid and 4-Benzenediazonium [16]. Particularly for fuel cells application, the sulfonation of carbon-supported catalyst as mixed electronic and protonic conductors and has been proved to be an efficient strategy to increase the triple-phase boundary (TPB) [18]. Moreover, the covalent functionalization of RGO surface with $-SO_3H$ groups can lead to a significant increase in hydrophilicity of RGO as support material improving the nano-catalyst dispersion [19].

In this study, sulfonic-functionalized graphene oxide (SGO) was prepared for the development of electrodes. The influence of two-different sulfonating agents on CRGO and TRGO in the electrochemical properties was evaluated. The sulfonated materials (S1CR-GO, S1CR-GO, S1TR-GO and S1TR-GO) were physicochemical characterized by XRD, FT-IR and Raman techniques. Electrochemical behavior of sulfonated materials as modified glassy carbon electrode (GCE) was investigated in K_3FeCN_6 solution as reference redox system.

II. Experimental

Graphene oxide (GO) was synthetized from graphite powder by modified Hummers method. Briefly, graphite powder and H_3PO_4 were mixed together under ultrasonic stirring followed by the addition of concentrate H_2SO_4 under ultrasonic stirring during 30 min. The mixed was input in ice-bath to keeping the temperature less than 10°C, followed of the gradual addition of $KMnO_4$ under constant stirring. The mix solution was heated until 35 °C during 30 min. The resulting solution was diluted by adding of 46 mL of deionized water under vigorous stirring for 48 hrs. To ensure the complete reaction with $KMnO_4$, the suspension was further treated with of H_2O_2 solution (at 30% v/v). Finally, the mixture was centrifuged and washed with H_2O and methanol until to adjust the pH~7. The brownish-dark carbon sludge was dried and graphene oxide sheets were then obtained. To reduce GO, GO sheets was dispersed in deionized water by sonication during 30 min. Then $NaBH_4$ in solution was added. CR-RG solution was filtrated and rinsed with water and finally dried in a vacuum oven at 60°C. For thermal reduction, GO sheets was treated under temperature conditions at 260 °C during 5 min, then TR-GO was obtained. The sulfonation of CR-G was then carried out with aryl diazonium salt of sulfanilic acid in ice bath for 2 h under stirring conditions, the resulting mix was let at room temperature maintaining stirring. The final solution was filtered, washed and dried, then the S1CR-GO was obtained. In the second method, the sulfuric acid was used as sulfonation agent. The CR-GO sheets was mix with concentrate sulfuric acid at 150 °C during 15 h under stirring conditions, then the solution was filtered, washed and dried in order to obtain S2CR-GO. Both procedures were followed for T-GO in order to obtain S1TR-GO and S2TR-GO using aryl diazonium salt of sulfanilic acid and sulfuric acid, respectively.

X-ray diffraction (XRD) measurements were carried out using an X-pert MPD Phillips diffractometer equipped with a curved graphite monochromator and CuKα radiation (Kα=1.5406 Å), at 43 kV and 30 mA. Raman micro-analysis was performed in a confocal µsurf explorer microscope (HORIBA) equipped with a 532 laser. The Raman spectra were recorded with the spectral resolution of 5 cm^{-1}, over the 600-4000 cm^{-1} range. FT-IR analysis of the GO and sulfonated RGO materials were performed in a Nicolet 550 infrared spectrometer coupled with a continuum microscope (Thermo Electron Corporation, UK), with a nominal resolution of 4 cm^{-1} using the ATR technique. Spectra were recorded over 600-4000 cm^{-1} range. Each spectrum is the average of 32 individual scans. The experimental spectra were mathematically evaluated using OMNIC (Thermo Nicolet).

The electrochemical behavior of the GO and sulfonated-RGO materials were evaluated by recording the cyclic voltammograms of modified glassy carbon electrode (GCE), in presence of 10 mM $K_3Fe(CN)_6$ and 0.1 M KCl as support electrolyte in a Biologic (SP-300) potentiostat/galvanostat. A platinum wire was used as counter electrode and a Silver/Silver Chloride (3M NaCl, Ag/AgCl=0.225 V/SHE) as the reference electrode, although all potentials in the manuscript are referred to the Standard Hydrogen Electrode (SHE). A bare GCE with a cross-sectional area of 0.0706 cm^2 was used as an ink-type working electrode. The catalytic ink for working electrodes was prepared by ultrasonic mixing of 1 mg of the corresponding GO material, 500 µL of isopropyl alcohol and 5 µL of Nafion in order to form a colloidal suspension. An aliquot of 10 µL of the solution was dispersed onto the glassy carbon disc and dried at room temperature. Bare GCE and GCE modified with RC-GO and TR-GO and sulfonated RC-GO and TR-GO were used for the electrochemical measurements.

III. Results and Discussion

The XRD patterns of graphite, graphene oxide (GO), reduced graphene oxide synthesized by chemical reduction of exfoliated and intercalated graphite oxide (CR-GO) and reduced graphene oxide synthesized by thermal reduction of exfoliated and intercalated graphite oxide (TR-GO) are shown in figure 1. In the figure, it shows the progressive phase changes from graphite to GO, followed of both GO chemical and thermal reduction process. The pattern of Graphite shows two peaks located at 2θ= 26.5° and 54.5° corresponding to graphite (002) and (004), respectively. The sharp peak has an interlayer spacing d_{002}= 0.33 nm, which is characteristic of graphitic materials. Through the chemical oxidation process, a shift of C(002) peak at 2θ below of 10° with interlayer spacing d_{002}= 1.23 nm indicates that the stacked layers of graphite have been expanded by the incorporation of oxygenated functional groups such hydroxyl, carboxyl and epoxy groups and some other structural defects, resulting in GO. These groups facilitated the hydration and exfoliation of GO in aqueous and alcoholic medium.

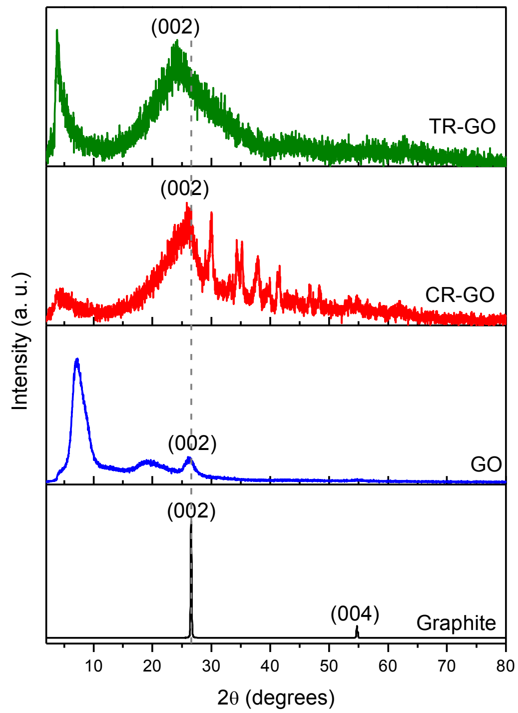

Fig. 1. XRD patterns of graphite (Gr) and graphene oxide (GO), chemical reduced graphene oxide (CR-GO), thermal reduced graphene oxide (CR-GO).

After chemical and thermal reduction process, the hydrophilicity of GO sheet gradually decreased, leading to an irreversible agglomeration of reduced graphene oxide (CR-GO and TR-GO). The broad peak at 2θ= 26.3° and 2θ= 24.2° in the XRD patterns for CR-GO and TR-GO, respectively, indicating a random packing of graphene sheets in the R-GO. This peak corresponds to (002) plane with d_{002}= 0.34 nm for RC-GO and d_{002}= 0.37 nm RT-GO, respectively. This peak is due to the removal oxygen-groups that got into the graphite gallery during intercalation process. The above confirms the reduction process to GO to R-GO.

The Raman spectra of graphite and graphene oxide (GO), chemical reduced graphene oxide (CR-GO), thermal reduced graphene oxide (CR-GO) are presented in Fig. 2. Raman spectrum of graphite is also included. Raman spectroscopy analysis provide information from structural properties of graphene-based materials and the presence of defects on the graphene carbon network. The spectra of grahite shows two bands located at 1350 and 1570 cm^{-1} corresponding to D and G bands, respectively. The G-band is the higher intensity and corresponds to the sp^2 bonded carbon, which is characteristic of the graphitic materials, while the D-band corresponds to the breathing mode of sp^2 carbon. The relative intensity ratio of

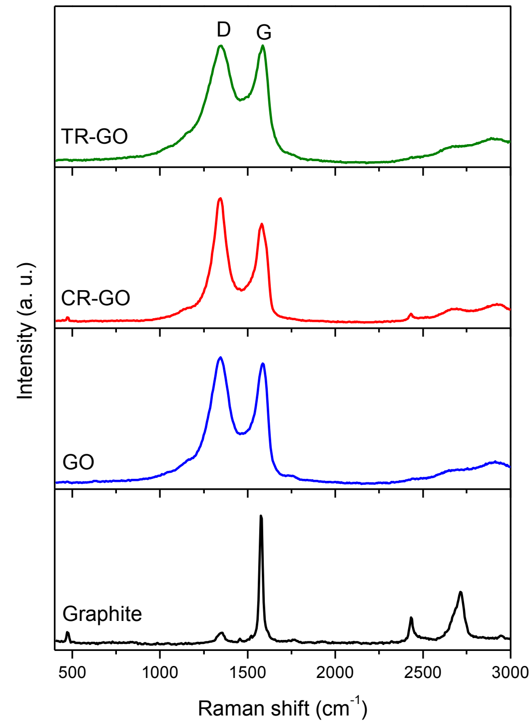

Fig. 2. Raman spectra of graphite (Gr) and graphene oxide (GO), chemical reduced graphene oxide (CR-GO), thermal reduced graphene oxide (TR-

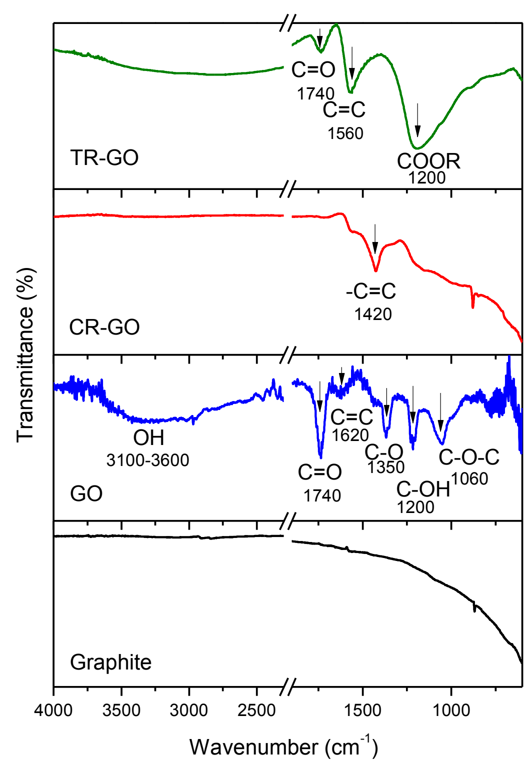

Fig. 3. FT-IR spectra of graphite, and graphene oxide (GO), chemical reduced graphene oxide (CR-GO), thermal reduced graphene oxide (TR-GO).

the D and G bands (I_D/I_G ratio) is proportional to the number of defect sites in the graphitic carbon. For Graphite and GO I_D/I_G ratio increase from 0.13 to 1.03 indicating that, a high number of defects has been introduced in GO structure. As GO is reduced by sodium borohydride and thermal process, a diminution in I_D/I_G ratio in the order of 1.03, 1.06 and 1 for GO, TR-GO and CR-GO, respectively suggesting that the oxygen groups was partially removed.

In order to identify the oxygen moieties formed during oxidation of graphite and its subsequent reduction, FT-IR analysis were carried out, and their spectra are shown in figure 3a. In FTIR spectrum of graphite no bands are observed. Infrared spectra of as-synthesized GO indicate contributions from various oxygen functional groups. GO shows dominant peaks at 1060, 1,200, 1,350, 1,620, 1,740, and 3100-3,600 cm^{-1}. The peak at 1,060 cm^{-1} corresponds to a stretching vibration from the C-O-C bonds of epoxy or alkoxy groups. The peak at 1,200 cm^{-1} is attributed to C-OH bonds, while the peak centered at 1,350 cm^{-1} is assigned to C-O group. The adsorption band at approximately 1,620 cm^{-1} corresponds to the C=C bonding of aromatic rings within the GO carbon skeleton structure, and the band at 1740 cm^{-1} correspond to C=O.
After reduction process, both CR-GG and TR-GO spectra show that these bands for oxygen functional groups of GO has been significantly reduced and some of them disappeared entirely. The spectral information of CR-GO suggests an increase of sp^2-conjugated domain density in the carbon backbone, which overlaps with the possible contributions from carboxylates (COO^-) at 1420 cm^{-1}. For TR-GO, it is possible to observe that the band intensity corresponding to C=O group is low, and two new absorption bands appeared at 1560 and 1200 cm^{-1}. The first one, may be attributed to the C=C stretch vibration of graphene sheets (sp^2 hybridization of carbon atoms), while the second one can be due to ester group, produced by the reaction between carboxylic and alcohol groups.

Figure 3b shows the FT-IR spectra of sulfonated CR-GO and TR-GO through sulfuric acid (S1) or aryl diazonium salt of sulfanilic acid (S2). As comparative, the spectra of both CR-GO and TR-GO are also included. After sulfonation at S1CR-GO and S2CR-GO (fig. 3b), the peak at 1420 cm^{-1} (-C=C) is clearly attenuated, and the increased of C=C stretching vibration peak is observed, suggesting an increased in the sp^2 hybridization of carbon atoms after sulfonation process. The peaks between 1240-1020 cm^{-1} correspond to S=O group for both S1CR-GO and S2CR-GO materials, confirming the presence sulfonic acid group ($-SO_3H$). Depending of the sulfonating agent used, some differences in the intensity of these bands are observed, suggesting a distinct interaction

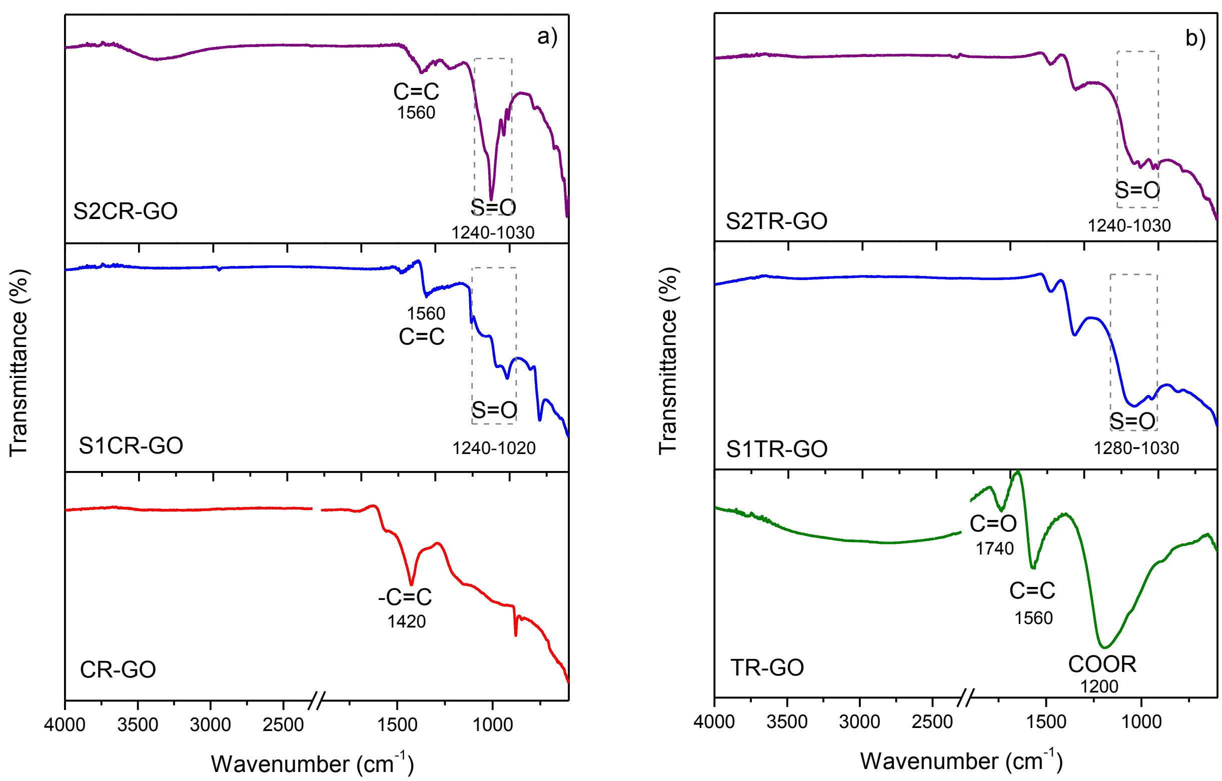

Fig. 4. FT-IR spectra of sulfonated chemical reduced graphene oxide (a), sulfonated thermal reduced graphene oxide (b) by two sulfonation methods. As comparative CR-GO and TR-GO are also included.

with reduced-GO surface. For S1TR-GO and S2TR-GO materials, the incorporation of sulfonic acid group is also confirmed by the peaks recorded between 1280-1030 cm^{-1}.

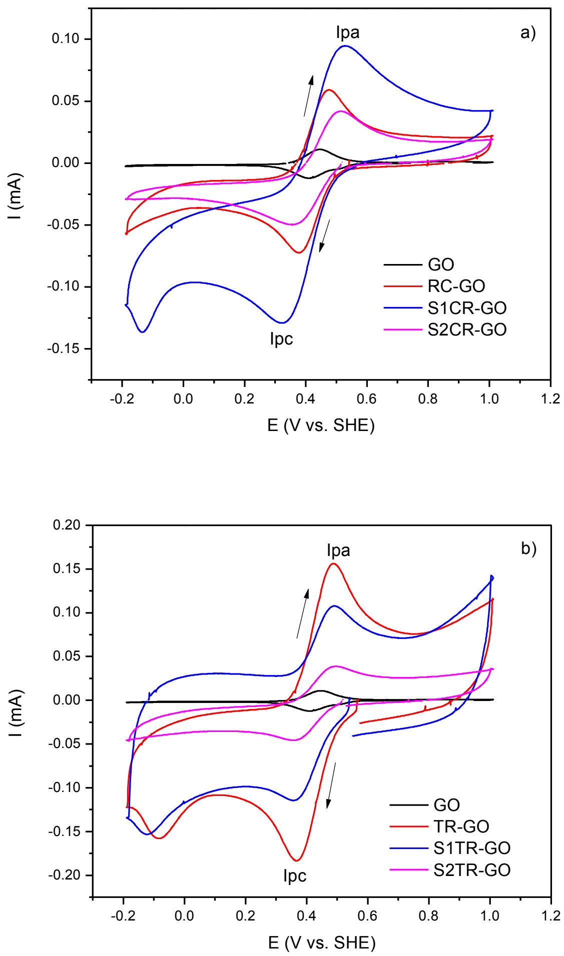

Fig. 5. Cyclic voltammograms at GCE modified with CR-GO and TR-GO sulfonated using sulfuric acid (S1) or aryl diazonium salt of sulfanilic acid (S2) in 0.1 M KCl containing 10 mM K3[Fe(CN)6] at 20 mV s^{-1}.

The electrochemical properties of the GCE using sulfonated thermally and chemically reduced GO materials were investigated in the presence of 0.1 M KCl and 10 mM $K_3[Fe(CN)_6]$ and the CVs response are shown in Fig. 5. As comparative, CR-GO, CR-GO and GO response are also included. The ferri/ferrocyanide redox couple is often used as a standard probe to monitor the charge transport within the modified electrode. A pair of peaks corresponding to the redox reaction are recorded at all GCE modified electrodes. For reduce GO electrodes (CR-GO and TR-GO), it is observed that the redox current response towards the ferricyanide ion was higher than GO, suggesting the recovering the sp^2carbon atoms promoted during the chemical and thermal process. For sulfonated chemical reduced materials, some differences are observed depending of sulfonating agent used. For instance, S1CR-GO electrode (Fig. 4a) display higher I_{pa} and I_{pc} values than those observed for RGO sulfonated by aryl diazonium salt of sulfanilic acid (S2CR-GO). The peak potential separation ΔE_p (E_{pa}-E_{pc}), was estimated for S1CR-GO and S2CR-GO modified GCE to be 20 and 17 mV, respectively. These results suggest that S1CR-GO electrode can act as superior electron transfer medium and thereby enhance the electron transfer efficiently compared to S2CR-GO and CR-GO. For sulfonated TR-GO, both S1TR-GO and S2TR-GO electrodes reached lower current intensities than TR-GO, indicating a decrease in charge transport properties. The above results indicate that the sulfonic acids groups produced by sulfuric acid during the reaction modified the surface modifying the interaction electrode-ferri/ferrocyanide system.

The Fig. 6a shows a comparative between both S1QR-GO and S1TR-GO electrodes, where slight differences are observed. S1TR-GO shows a higher redox current density an lower ΔE_p values. Regarding to the electrochemical mechanism that takes place on the surface of S1TR-GO, it was evaluated the

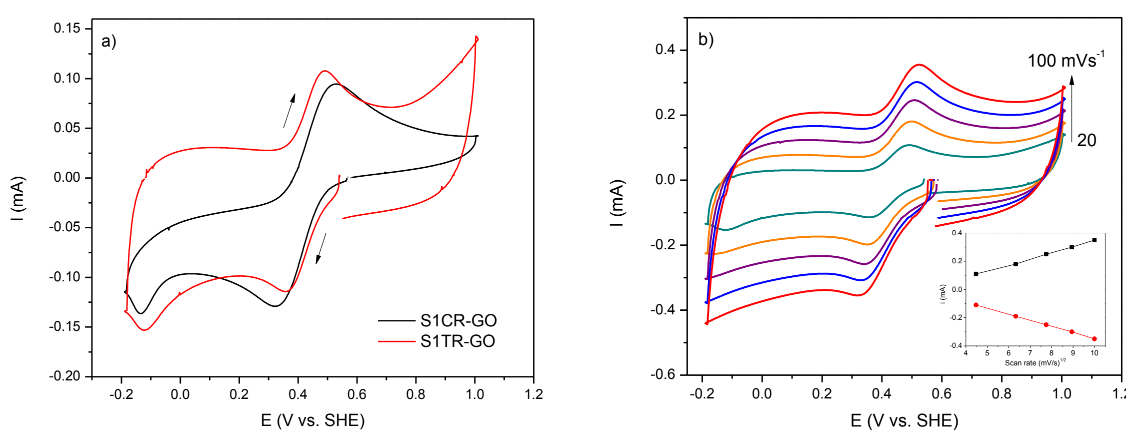

Fig. 6. Comparative CVs between GCE modified with S1CR-GO and S1TR-GO in 0.1 M KCl containing 10 mM $K_3[Fe(CN)_6]$ at 20 mV s^{-1} (a). CV of S1TR-GO as a function of scan rate (10–100 mV/s) and inset shows variation of current as function of square root of scan rate indicating a diffusion controlled process.

relationship of anodic and cathodic peak currents as a function of the square root of the scan rate (ν½) (inset Fig. 4b), both parameters are proportional at the scan rates values studied (20-100 $mV \cdot s^{-1}$). The redox peak potential is found to be shifted (anodic peak potential toward positive and cathodic peak potential toward negative) as the scan rate increases indicating a diffusion control process.

CONCLUSIONS

GO was successful synthetized by hummers method. The reduced GO. The structural defects and oxygen functional groups presence were confirmed by Raman and FT-IR measurements. It has been proved that the effect thermal and chemical reduction of GO plays an important role in the sulfonated resulting material. During TR process the C=O and COOR moieties are retained. Among of two sulfonation methods, the R-GO materials sulfonated with sulfuric acid showed better electrochemical properties. S1CR-GO electrode showed superior electron transfer activity compared to CR-GO demonstrating an enhanced of electrochemical properties. However, S1TR-GO recorded higher I_{pa} and I_{pc} and lower ΔE_p values than S1TR-GO. The good linear relationship observed at S1TR-GO indicated that this electrode is electroactive under diffusion-controlled.

ACKNOWLEDGEMENTS

The authors are grateful to the National Council of Science and Technology (Conacyt) through the Bilateral Brasil-Mexico, 259010, 270214 projects. Authors also are grateful to National Laboratory of Graphene Materials (LNMG), to J.A. Mercado-Silva and R. Rangel-Ramirez to the facilities provided for the use of some of its installations.

REFERENCES

[1] A.K. Geim, K.S. Novoselov, The rise of graphene., Nat. Mater. 6 (2007) 183–191. http://www.ncbi.nlm.nih.gov/pubmed/17330084.

[2] S.K. Srivastava, J. Pionteck, Recent Advances in Preparation, Structure, Properties and Applications of Graphite Oxide, J. Nanosci. Nanotechnol. 15 (2015) 1984–2000. doi:10.1166/jnn.2015.10047.

[3] D.C. Marcano, D. V. Kosynkin, J.M. Berlin, A. Sinitskii, Z. Sun, A. Slesarev, et al., Improved synthesis of graphene oxide, ACS Nano. 4 (2010) 4806–4814. doi:10.1021/nn1006368.

[4] L. Sun, B. Fugetsu, Massive Production of Graphene Oxide from Expanded Graphite, Sci. Direct. 109 (2013) 207–210. doi:10.1016/j.matlet.2013.07.072.

[5] J.M. Tour, Pristine Graphite Oxide, (2011).

[6] W. Gao, Graphite Oxide:Structure,Reduction and Applications, 2012.

[7] C.K. Chua, M. Pumera, Reduction of graphene oxide with substituted borohydrides, J. Mater. Chem. A. 1 (2013) 1892. doi:10.1039/c2ta00665k.

[8] S.H. Huh, Thermal Reduction of Graphene Oxide, Eng. Technol. (2010) 73–90. doi:10.5772/14156.

[9] C.K. Chua, M. Pumera, Chemical reduction of graphene oxide: a synthetic chemistry viewpoint., Chem. Soc. Rev. 43 (2014) 291–312. doi:10.1039/c3cs60303b.

[10] S. Stankovich, D.A. Dikin, R.D. Piner, K.A. Kohlhaas, A. Kleinhammes, Y. Jia, et al., Synthesis of graphene-based nanosheets via chemical reduction of exfoliated graphite oxide, Carbon N. Y. 45 (2007) 1558–1565. doi:10.1016/j.carbon.2007.02.034.

[11] H.J. Shin, K.K. Kim, A. Benayad, S.M. Yoon, H.K. Park, I.S. Jung, et al., Efficient reduction of graphite oxide by sodium borohydride and its effect on electrical conductance, Adv. Funct. Mater. 19 (2009) 1987–1992. doi:10.1002/adfm.200900167.

[12] W. Gao, The chemistry of graphene oxide, Graphene Oxide Reduct. Recipes, Spectrosc. Appl. (2015) 61–95. doi:10.1007/978-3-319-15500-5_3.

[13] V. Georgakilas, M. Otyepka, A.B. Bourlinos, V. Chandra, N. Kim, K.C. Kemp, et al., Functionalization of Graphene: Covalent and Non-Covalent Approaches, Derivatives and Applications, Chem. Rev. 112 (2012) 6156–6214. doi:10.1021/cr3000412.

[14] H. Bai, Y. Xu, L. Zhao, C. Li, G. Shi, Non-covalent functionalization of graphene sheets by sulfonated polyaniline, Chem. Commun. (2009) 1667–1669.

[15] D. He, Z. Kou, Y. Xiong, K. Cheng, X. Chen, M. Pan, et al., Simultaneous sulfonation and reduction of graphene oxide as highly efficient supports for metal nanocatalysts, Carbon N. Y. 66 (2014) 312–319. doi:10.1016/j.carbon.2013.09.005.

[16] B. Garg, T. Bisht, Y.-C. Ling, Graphene-Based Nanomaterials as Heterogeneous Acid Catalysts: A Comprehensive Perspective, Molecules. 19 (2014) 14582–14614. doi:10.3390/molecules190914582.

[17] G. Zhao, L. Jiang, Y. He, J. Li, H. Dong, X. Wang, et al., Sulfonated graphene for persistent aromatic pollutant management, Adv. Mater. 23 (2011) 3959–3963. doi:10.1002/adma.201101007.

[18] C.Y. Du, T.S. Zhao, Z.X. Liang, Sulfonation of carbon-nanotube supported platinum catalysts for polymer electrolyte fuel cells, J. Power Sources. 176 (2008) 9–15. doi:10.1016/j.jpowsour.2007.10.016.

[19] T.F. Hung, B. Wang, C.W. Tsai, M.H. Tu, G.X. Wang, R.S. Liu, et al., Sulfonation of graphene nanosheet-supported platinum via a simple thermal-treatment toward its oxygen reduction activity in acid medium, Int. J. Hydrogen Energy. 37 (2012) 14205–14210. doi:10.1016/j.ijhydene.2012.07.027.

XVI International Congress of the Hydrogen Mexican Society 2016

Evaluation of an internal combustion engine enriched by Oxyhydrogen gas generated by an Alkaline electrolyzer

M. Horcasitas-Verdiguel[1], I. Trujillo-Olivares[1], R. G. González-Huerta[2], J. M. Sandoval-Pineda[1],

[1]ESIME-IPN UA, Sección de posgrado, Av. de las Granjas 682, C.P. 02250, México, D.F.
[*]Tel: +525557296000; e-mail: hove_lenuma@hotmail.com
[2]ESIQIE-IPN, Laboratorio de Electroquímica y Corrosión, UPALM, 07738, México D.F.

ABSTRACT

This paper focuses on the methodology for the design of an alkaline electrolyzer and the coupling process in diesel engines combustion cycle. Therefore, hydrogen produced by water electrolysis can be utilized, along with fossil fuels, as an additive for transportation, reducing parameters such as pollutants CO and CO_2 with the general objective of abating automotive emissions. At present, one of the main problems of alkaline electrolysis concerns its manufacture and assembly, as a high-efficiency electrolyzer requires a design that allows for controlling parameters such as the electrical current, gas outlet, level of electrolyte, corrosion and sealing system.With gas generation technology Oxyhydrogen by alkaline electrolysis, the application of the methodology and appropriate manufacturing can be reached to develop a more efficient reactor in all its features and a better design.

Keywords: alkaline electrolyzer; fuel; Hydrogen; Oxyhydrogen; combustion.

XVI International Congress of the Hydrogen Mexican Society
2016

Hydrogen storage in Ca-coated Nanotorus: A DFT Theoretical Study

E. López[1], Y. Peña[1], G. González[1], F. Castillo[2], J. Díaz[3], A. García[1], L. Zamudio[4]

[1]Universidad Autónoma de la Ciudad de México, Fray Servando Teresa de Mier, México, D. F, 06080.
[*]Tel: +525551349804 Ext. 11110; e-mail: elopezc_h@hotmail.com
[2]Escuela Superior de Física y Matemáticas del Instituto Politécnico Nacional Unidad Adolfo López Mateos, México, D .F, 07738.
[3]Centro de Investigación en Ciencia Aplicada y Tecnología Avanzada, Instituto Politécnico Nacional Legaria, México, D. F.
[4]Instituto Mexicano del Petróleo, Eje Central Lázaro Cardenas Norte, México, D. F., 07730.

ABSTRACT

One of the obstacles to overcome in science and technology of hydrogen and fuel cells is hydrogen storage in solid state materials. Currently, nanostructures of carbon in form of fullerenes and nanotubes have been studied as solid state materials for storage of hydrogen, however, they do not meet the industry requirement yet. In this work, we evaluate a nanostructure of carbon in form of nanotorus C_{120} decorated with Ca atoms in order to design a new solid state material for hydrogen storage. Nanotorus is formed by pentagonal, hexagonal and heptagonal rings with 120 carbon atoms, these characteristics are suitable for putting one Ca atom next to pentagonal and hexagonal rings, where transition metal atoms distributed uniformly over the surface were shown to bind copious amounts of hydrogen in a quasi-molecular form through a novel mechanism where the adsorbed H_2 molecule donates electrons to the unfilled d-orbitals of the transition metals atoms which in turn back donate the electron to the antibonding orbital of the H_2 molecule. The metodology allowed to obtain binding energies, gravimetric density, analysis of the effect of H insertion on the absorption of H_2, and the study of thermodinamic stability of C120-Ca system. Calculations were done with DFT theory and molecular mechanics and dynamics simulations. The functional GGA-PW91 and basis set DND were used in this work.

Keywords: Nanotorus; hydrogen storage; DFT

Precursor effect on graphene oxide properties for fuel cell applications

N.C. Luna-Comparan, R. Benavides, D. Morales-Acosta
Procesos de Transformación de Plásticos, Materiales Avanzados
Centro de Investigación de Química Aplicada
Saltillo, Coahuila, México
diana.morales@ciqa.edu.mx

***Abstract*—Fuel cells are devices used for clean energy, which have been increasing their use nowadays. Electrodes, as cell components can be improved by using different materials, such as graphene oxide (GO). The oxidation of graphite through the modified Hummers method is the most used, however the physicochemical characteristics of the graphite influence the final material. In this work, GO was synthesized by a Hummers modified method. Graphite powder and graphite flakes were used as precursors, H_3PO_4 as pre-oxidative treatment and KMnO4 as the oxidizing agent. The structural properties of GO_f and GO_p were carried out by XRD, Raman and FT-IR techniques. Diffractions patterns show differences depending on the used precursor. The FT-IR results confirmed the presence of oxygen-groups and Raman spectroscopy shows an enhanced in I_D/I_G ratio. The electrochemical characterization was performed by cyclic voltammetry with K_3FeCN_6 solution as reference redox system. GO_p is a potential material to be used for both in anodes or cathodes, and for membranes as well in fuel cells**

***Keywords*— graphene oxide; fuel cells.**

I. Introduction

The proton exchange membrane fuel cell (PEMFC) is one of the key technologies for generating clean energy, reducing emissions of greenhouse gases [1]. Fuel cells (FCs) are electrochemical devices that directly convert chemical energy stored in the fuel [2]. The FCs are composed for a proton exchange membrane (PEM) as electrolyte and two electrodes (anode and cathode) [3]. To improve the performance of fuel cells components, novel carbon materials can be integrated as improve the long-life performance of these devices [4,5]. Graphene oxide (GO), it is a material with hydrophilic nature and colloidal stability in aqueous environments. In addition, it has thermal and mechanical stability, easy mass production from low-cost, good processability, flexible structure, dimensional stability, and suitable conductivity after reduction process [6–8]. The GO is a bulk solid made from oxidation of graphite through processes that modification the basal planes and increase the interlayer spacing distance by oxygen- groups introduction that modified its surface [7,9]. GO can be synthesized by several methods as Staudenmaier, Hofmann, Hummers and Tour methodologies that constitute chemical strategies used towards large scale production [7]. Among of the Hummers method is the most extensively used for GO production, and several variations of this method have been introduced to enhance the degree of oxidation and exfoliation of graphite oxide during oxidation process. Hummers method includes the use of KMnO4, $NaNO_3$ and H_2SO_4 in graphite oxidation, however, a modification of this procedure exchange $NaNO_3$ by H_3PO_4, increasing the quantity of $KMnO_4$ and varying the H_2SO_4/H_3PO_4 volume ratio in a 9:1, which it produced more intact graphitic basal planes [10,11]. The aforementioned can be improves the efficiency of the oxidation process [11].

Another important issue, is the carbon precursor type, because it can influence the oxidization reaction and final characteristics of GO produced. For instance, the graphite particle size has an important effect during exfoliation process, affecting the position of the functionalities produced. Then, the oxidation reaction becomes more difficult with both large sizes graphite and high crystallinity [10], and the resulting GO is largely variable in terms of surface properties or structural features. The differences between final product of GO can be establish since the reaction conditions and graphitic material [7].

In this work, GO was synthesized from two distinct graphite precursor: graphite flakes and graphite powder with similar crystalline structure through modified Hummers method. The effect of precursor in the structural and electrochemical properties of the obtained GO was evaluated.

II. Material and Methods

The GO was synthesized from graphite by modified Hummers method [11]. Graphite powder was added to H_3PO_4 and this solution was sonicated during 30 minutes. After the required quantity, H_2SO_4 was added to above solution and the outcome was placed in a cold bath until the temperature was below to 10 °C under vigorous magnetic stirring.

Once the temperature was reached, $KMnO_4$ was slowly added and when the solution became stabilized, the cold bath was removed. Then the temperature was increased to 35°C, the resulting solution was maintaining under magnetic stirring followed by the addition of water. Finally, H_2O_2 were added after continuous stirring during 60 hours. The resulting powder of GO was washed and centrifuged several times until neutral pH was reached and finally it was dried at 80 °C for 24 hours The same methodology was employed for graphite flake.

III. CHARACTERIZATION

The GO synthetized materials were characterized using various analytical methods such as X-ray diffraction analysis (XRD), Fourier transform infrared (FT-IR), Raman spectroscopy and cyclic voltammetry (CV). XRD of powders were -acquired using a Rigaku Ultima IV diffractometer equipped with D/teX Ultrahigh-speed position sensitive detector system with a curved graphite monochromator using CuKα radiation (Kα=1.5406 Å), at 40 Kv and 44 mA. The FT-IR spectra of the samples were carried out on a Thermo Scientific NICOLET iS5 with accessory iD7 ATP. Spectra were recorded over 600-4000 cm^{-1} range. Each spectrum is the average of 32 individual scans and the experimental spectra were mathematically evaluated using OMNIC. Raman spectroscopy was performed in a confocal usurf explorer microscope (HORIBA) equipped with a 532 laser, 100- 400 cm^{-1} range and acquisition time of 10 s.

The electrochemical behavior of the GO materials by recording the cyclic voltammograms of GO modified glassy carbon electrode (GC), in presence of 10 mM $K_3Fe(CN)_6$ and 0.1 M KCl as support electrolyte in a Biologic (SP-300) potentiostat/galvanostat. A platinum wire was used as counter electrode and a silver/silver chloride (3M NaCl, Ag/AgCl=0.209 V/SHE) as the reference electrode, although all potentials in the manuscript are referred to the Standard Hydrogen Electrode (SHE). A bare glassy carbon electrode (GCE) with a cross-sectional area of 0.0706 cm^2 was used as an ink-type working electrode. The catalytic ink for working electrodes was prepared by ultrasonic mixing of 10 mg of the corresponding GO material, 1000 µL of isopropylic alcohol and 5 µL of Nafion in order to form a colloidal suspension. An aliquot of 20 µL of the solution was dispersed onto the glassy carbon disc and dried at room temperature. Bare GCE and GCE modified with GCE-GO_p and GCE-GO_f were used for the electrochemical measurements.

IV. RESULTS AND DISCUSSION

Synthesis of GO was achieved by using graphite in concentrated acid as H_3PO_4 in the presence of an oxidizing agents like H_2SO_4 and $KMnO_4$. The GO was decorated with oxygen functional groups on both sides of the plane.

Fig. 1 shows the XRD pattern of GO_f synthesized by modified Hummers method using graphite flakes as carbon precursor. As reference, the XRD of graphite flakes precursor was also included. Graphite flakes displays a main diffraction peak observed at 2θ =26.41° corresponding to (002) plane and d_{002}=0.337 nm. On conversion to GO, the peak of GO is observed at 2θ =10.87° with d-spacing of 0.812 nm, while the (002) peak become broader and slightly displaced to higher appear at 2θ =26.61° with d_{002}=0.334 nm, in addition. This indicated that the synthesized GO_f was not completely oxidized. XRD pattern of GO synthesized from graphite powder is shown in Fig. 2. The interlayer distance increases from 0.859 nm in relation with the graphite precursor d=0.336 nm. The increased observed, this is the result of the expansion caused by the incorporation of water and oxygen functional groups during the oxidation process.

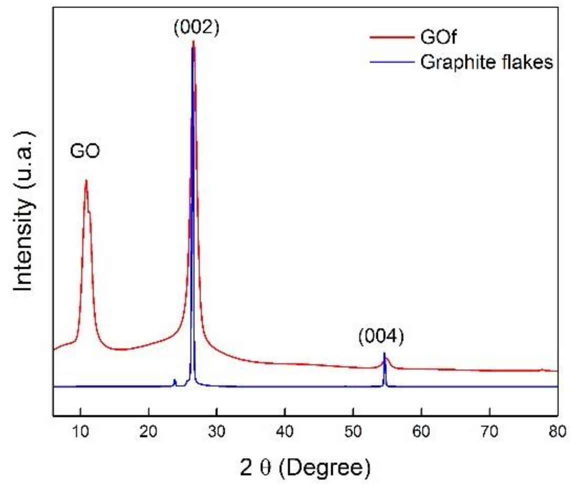

Fig. 1 XRD spectra of Graphite flakes as precursor.

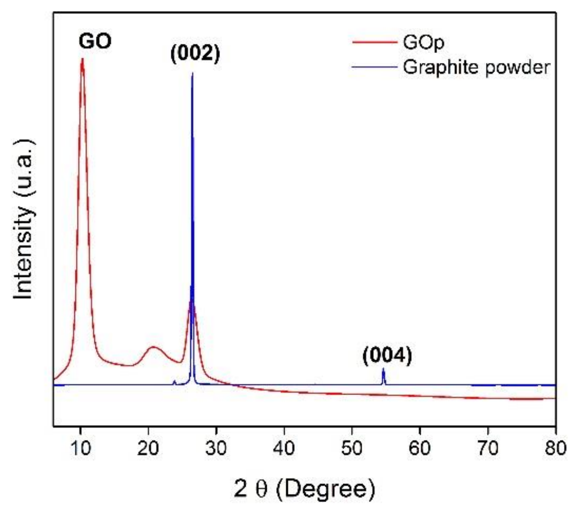

Fig. 2 XRD spectra of Graphite powder as precursor.

Raman spectroscopy is a non-destructive technique that is used to obtain structural information about carbon-based materials. The Fig. 3 shows Raman spectrum of GO_f and GO_p. For both GO materials, the G and D bands are observe. The spectrum of GO_p shows two bands located at 1347 and 1582 cm-1 corresponding to D and G bands, respectively [12]. The D-band is the highest intensity corresponds to the breathing mode of sp2 indicating the carbon lattice distortion to the sp2 bonded carbon, while the G-band is characteristic of the graphitic materials. For GO_f both D and G bands are slightly displaced towards higher values (D band at 1354 cm^{-1} and G band at 1595 cm^{-1}), besides the D-band intensity is lower than compared to G-band. The relative intensity ratio of the D and G bands (I_D/I_G ratio) is proportional to the number of defect sites in the graphitic carbon. For GO_p the ID/IG ratio is higher (I_D/I_G =1.1) compared to GO_f (I_D/I_G =1). These results demonstrate that GO_p has more disorder in its structure, which means GO_p is more oxidized than GO_f.

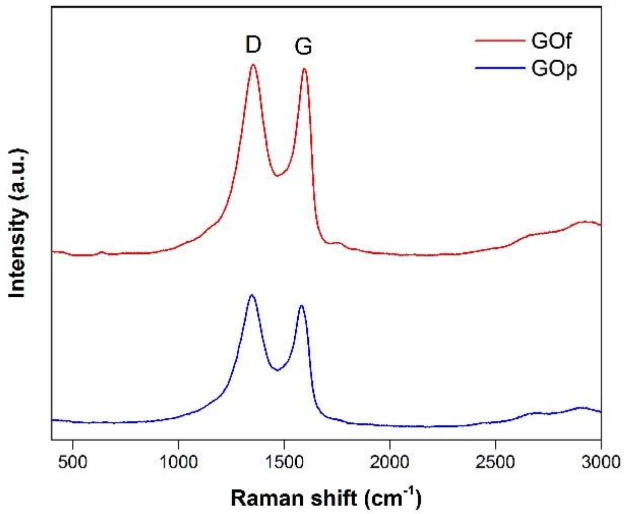

Fig. 3 Raman spectrum of GO_p and GO_f.

The oxidation of graphite by modified Hummer's method resulted in the formation of hydroxyl, carboxyl and epoxide groups. The FT-IR analysis was used to identify the functional groups produced on the surface of GO. For the samples of GO_f (Fig. 4) and GO_p (Fig. 5), diverse peaks are identified. The FT-IR spectra of GO_p shows a broad peak between 3000-3600 cm^{-1} that it was generated from the stretching vibrations of -OH from COOH, C-OH, and H_2O. Both absorption peaks at 1716 cm^{-1} and 1725 cm^{-1} correspond to the stretching vibrations of carbonyl groups, while the stretching vibration of C=C is observed at 1622 cm^{-1} and 1627 cm^{-1}, epoxy group is depict at 1223 cm-1 and 1221 cm-1, and finally the peaks at 1053 cm^{-1} and 1174 cm^{-1} correspond to the stretching vibration of C-O of carboxylic acid [10,12–14]. For GO_p the same bands are observed, although of distinct intensity. For instance, the lower OH band intensity suggest a minor formation of oxygen groups.

The electrochemical behavior (Fig. 6) of the synthesized GO materials was determined by recording the cyclic voltammograms of GCE-GO_p and GCE-GO_f modified GC electrodes, in presence of 10 mM $K_3Fe(CN)_6$ containing 0.1 M KCl. The ferri/ferrocyanide redox couple is often used as a standard probe to monitor the charge transport within the modified electrode. A pair of redox peaks corresponding to the redox reaction of $Fe(CN)_6^{3-}/Fe(CN)_6^{4-}$ was observed at all electrodes. Two main features to analyses in a cyclic voltammograms are the peak current and the peak separation.

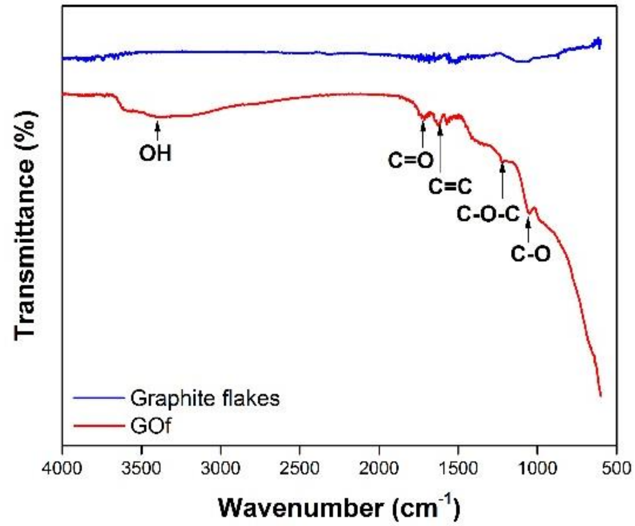

Fig. 4 FT-IR spectrum of GO_f and Graphite flakes.

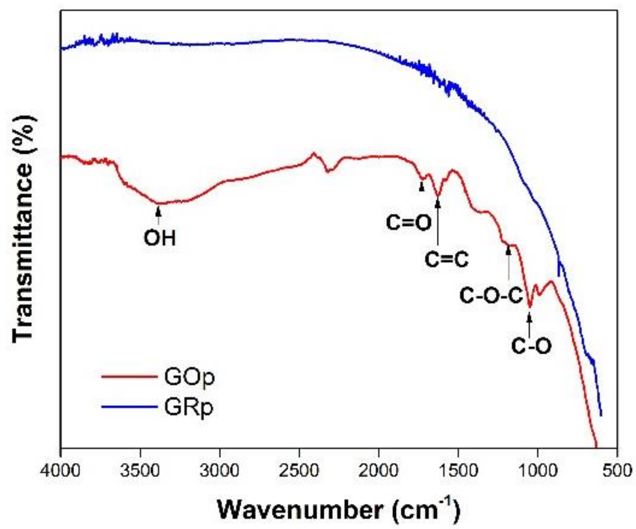

Fig. 5 FTIR spectrum of GO_p and Graphite powder.

Both GO electrodes show diminished peak currents compared to the unmodified GCE, however differences exists between their CV profiles. For instance, the GCE-GO_p shows peaks with low peak currents and reversible peaks, while the GCE-GO_f shows sharper redox peaks. These results demonstrates that the charge transfer from the $Fe(CN)_6^{3-}/Fe(CN)_6^{4-}$ to the GCE-GO_f modified surface decreases due to electrostatic repulsion from the intrinsic functional groups as epoxide, hydroxyl and carbonyl/carboxyl of GO and ferri/ferrocyanide system. Hence, the increase in the charge transfer in the presence of $Fe(CN)_6^{3-}/Fe(CN)_6^{4-}$ for GCE-GO_p indicates the formation of GO with higher functional groups.

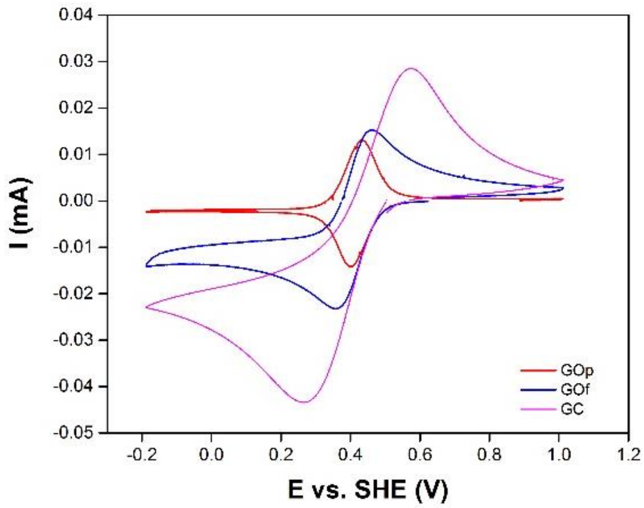

Fig. 6 Cyclic voltammograms at GCE and GCE modified with GO-p and GO-f in 0.1 M KCl containing 10 mM $K_3[Fe(CN)_6]$ at 20 mV s^{-1}.

V. CONCLUSIONS

GO was synthesized by a Hummers modified method, where graphite powder and graphite flakes were used as precursors to obtained GO_p and GO_f, respectively. The XRD, Raman spectroscopy and FT-IR spectroscopy confirm the oxidation of both precursors to obtain GO, being GO_p the material with the highest oxidation degree.
The electrochemical evaluation confirmed the formation of functional groups mainly for GO_p, where the charge transfer diminished due to electrostatic repulsion from the intrinsic functional groups as epoxide, hydroxyl and carbonyl/carboxyl of GO.

ACKNOWLEDGMENT

The authors are grateful to the National Council of Science and Technology (Conacyt) through the 259010, 270214 and bilateral Mexico-Brazil projects. NCLC is thankful to Conacyt for the PhD scholarship, to SMH and XVI International Congress of the Mexican Hydrogen Society for the fellowship to assistance to the congress. Authors also are grateful to National Laboratory of Graphene Materials (LNMG), to J.A. Mercado-Silva, R. Rangel-Ramírez, B. Puente and S. Fernández to the facilities provided for the use of some of its installations.

REFERENCES

[1] A.B. Stambouli, Fuel cells: The expectations for an environmental-friendly and sustainable source of energy, Renew. Sustain. Energy Rev. 15 (2011) 4507–4520. doi:10.1016/j.rser.2011.07.100.

[2] A.S. Abdulkareem, A. S. Afolabi, N. Fungura, T. Mokrani, C. Mateescu, The Realities and Economic Benefit of the Utilization of Fuel Cells as an Alternative Source of Energy: A Review, Energy Sources, Part B Econ. Planning, Policy. 10 (2015) 404–411. doi:10.1080/15567249.2011.557684.

[3] S. Mekhilef, R. Saidur, A. Safari, Comparative study of different fuel cell technologies, Renew. Sustain. Energy Rev. 16 (2012) 981–989. doi:10.1016/j.rser.2011.09.020.

[4] I. Nicotera, C. Simari, L. Coppola, P. Zygouri, D. Gournis, S. Brutti, et al., Sulfonated Graphene Oxide Platelets in Na fi on Nanocomposite Membrane : Advantages for Application in Direct Methanol Fuel Cells, J. Phys. Chem. C. 118 (2014) 24357−24368. doi:dx.doi.org/10.1021/jp5080779.

[5] V. Parthiban, S. Akula, S.G. Peera, N. Islam, A.K. Sahu, Proton Conducting Nafion-Sulfonated Graphene Hybrid Membranes for Direct Methanol Fuel Cells with Reduced Methanol Crossover, Energy & Fuels. (2015) acs.energyfuels.5b02194. doi:10.1021/acs.energyfuels.5b02194.

[6] E. Bakangura, L. Wu, L. Ge, Z. Yang, T. Xu, Mixed matrix proton exchange membranes for fuel cells: state of the art and perspectives, Prog. Polym. Sci. (2016). doi:10.1016/j.progpolymsci.2015.11.004.

[7] A.J. Dhifaf, L. Neus, K. Kostas, Synthesis of few-layered, high-purity graphene oxide sheets from different graphite sources for biology, 2D Mater. 3 (2016) 14006. doi:10.1088/2053-1583/3/1/014006.

[8] J. Sun, N. Yang, Z. Sun, M. Zeng, L. Fu, C. Hu, et al., Fully Converting Graphite into Graphene Oxide Hydrogels by Preoxidation with Impure Manganese Dioxide, ACS Appl. Mater. Interfaces. 7 (2015) 21356–21363. doi:10.1021/acsami.5b06008.

[9] A. Bianco, H.M. Cheng, T. Enoki, Y. Gogotsi, R.H. Hurt, N. Koratkar, et al., All in the graphene family - A recommended nomenclature for two-dimensional carbon materials, Carbon N. Y. 65 (2013) 1–6. doi:10.1016/j.carbon.2013.08.038.

[10] L. Sun, B. Fugetsu, Massive Production of Graphene Oxide from Expanded Graphite, Sci. Direct. 109 (2013) 207–210. doi:10.1016/j.matlet.2013.07.072.

[11] D.C. Marcano, D. V. Kosynkin, J.M. Berlin, A. Sinitskii, Z. Sun, A. Slesarev, et al., Improved synthesis of graphene oxide, ACS Nano. 4 (2010) 4806–4814. doi:10.1021/nn1006368.

[12] L. Shahriary, A. a. Athawale, Graphene Oxide Synthesized by using Modified Hummers Approach, Int. J. Renew. Energy Environ. Eng. 2 (2014) 58–63.

[13] D.C. Lee, H.N. Yang, S.H. Park, W.J. Kim, Nafion/graphene oxide composite membranes for low humidifying polymer electrolyte membrane fuel cell, J. Memb. Sci. 452 (2014) 20–28. doi:10.1016/j.memsci.2013.10.018.

[14] T. Kuila, S. Bose, A.K. Mishra, P. Khanra, N.H. Kim, J.H. Lee, Chemical functionalization of graphene and its applications, Prog. Mater. Sci. 57 (2012) 1061–1105. doi:10.1016/j.pmatsci.2012.03.002.

Effect of functionalization of ordered mesoporous carbon as support in cathodes for fuel cells

N.M. Sánchez-Padilla[a,c], D. Morales-Acosta[a], S.M. Montemayor[b], R. Benavides[a]
[a]Procesos de Transformación de Plásticos,
[b]Materiales Avanzados
Centro de Investigación de Química Aplicada
Saltillo, Coahuila, México
sagrario.montemayor@ciqa.edu.mx

F.J. Rodriguez-Varela[c,d]
[c]Programa de Sustentabilidad de los Recursos Naturales y Energía,
[d]Programa de Nanociencias y Nanotecnología
Cinvestav Unidad Saltillo
Ramos Arizpe, Coahuila, México
javier.varela@cinvestav.edu.mx

***Abstract*— In this work, a comparative study of the effect of functionalization of ordered mesoporous carbon (OMC) as support in catalytic activity for the Oxygen Reduction Reaction (ORR) is presented and compared to that commercial Pt/C ETEK catalysts. OMC were obtained via organic-organic self-assembly. The resulting OMC were functionalized by two different methods (with methanol-OMC-AF1 and mixture of acids-OMC -AF2). The catalysts were prepared via impregnation-reduction (Pt/OMC-AF1 and Pt/OMC-AF2). The different OMC functionalization is confirmed by FT-IR spectroscopy. BET analysis confirms the mesoporous structure of the support, with pore size close to 4 nm and a surface area of 532 m^2 g^{-1}. The XRD patterns of the catalysts show the formation of metallic Pt with crystallite size below 10 nm. The electrochemical measurements were carried out with cyclic voltammetry in acid media for ORR and the catalytic activity of the materials. The catalyst prepared with OMC functionalized with methanol as support (Pt/OMC-AF1) leads to a significant shift on the onset potential to higher anodic values (50 mV) compared to Pt/C ETEK. The mass and specific activities were also calculated. A threefold increase of these activities are observed for Pt/OMCaf1 which deliver 0.003 A $mg^{-1}_{Pt@0.9V}$ versus 0.001 A $mg^{-1}_{Pt@0.9V}$. The results underlining the efficiency of OMC as support by enhance the catalytic activity of Pt for the ORR.**

Keywords*— fuel cells; ordered mesoporous carbon; catalyst; oxygen reduction reaction

I. INTRODUCTION

Oxygen reduction reaction (ORR) plays a critical role in fuel cells technologies. Platinum (Pt) in nanoparticles are the most used material to catalyze this reactions. However, the cost and the scarcity of this precious metal limits the commercialization of fuel cells. In order to decrease the use of Pt, the nanoparticles are commonly supported in materials with high surface area.

Carbon blacks, especially Vulcan XC-72, are the most commonly used supports for Pt and Pt-based alloys catalysts, due to their high surface area and high electrical conductivity. Vulcan is composed of extensively agglomerated nanosized carbon particles, in a morphology that includes broad pore size distribution in the micropore (mostly) and mesopore ranges [1]. On this context, ideal supports should also offer high corrosion resistance and a mesoporous structure that enhances the interaction of the catalyst nanoparticles with the reactants, thus maximizing the triple-phase boundary (TPB) to facilitate electron transfer resulting in better fuel cell performances [2].

Ordered mesoporous carbon (OMC) has a higher surface area (600-650 m^2 g^{-1}), higher resistance to corrosion and bigger pores than Vulcan [3]. The porous structure is a determining factor related to electrochemical performance. Also, the electrolyte diffusion and the catalytic activity can be tuned trough the pore size adjustment [4].

Mainly, carbon materials as support has a hydrophobic behavior, which become a drawback at the time of the synthesis resulting in agglomeration of the nanoparticles. Functionalization of the support is an important key to achieve a good dispersion of Pt in the surface of the carbon material, where strong acids are the most commonly used functionalization agents. The use of soft chemical agents as methanol it has not been extensively studied [5]. In this work, we synthesized Pt nanoparticles supported in OMC functionalized with two different chemicals agents in order to evaluate the effect of the functionalization on the performance of Pt/OMC cathodes in acid media and compared to commercial Pt/C ETEK.

II. EXPERIMENTAL

OMC was synthesized via self-assembly in aqueous phase using a mixture of resorcinol/formaldehyde (1:3 molar ratio) as carbon precursors. Pluronic F127 triblock copolymer was used as the template to promote the formation of a hexagonal mesostructure. First, formaldehyde and Na_2CO_3 were mixed under stirring conditions. Afterwards, resorcinol were added to initiate the pre-polimerization maintaining stirring conditions. After 2 hours, a solution containing 6.4 g of Pluronic F127 and the required amounts of ethanol and water were adjusted continuing with magnetic stirring for 1 hour. Finally, 8 mL of 1 M HCl were added to the mixture. After condensation, the polymer gel phase was let at room temperature for 12 hours followed by drying at 80 °C for 24 h. Finally, the carbonization of the orange resin was carried out at 900 °C for 3 h with a heating rate of 1 °C min^{-1} under N_2 atmosphere, in a tubular furnace.

The resulting OMC were functionalized by means of two different procedures: using a soft chemical agent (methanol, named OMC-AF1) and with acid mixture (HNO3:H_2SO_4, named OMC-AF2). To obtain OMC-AF1, the support was dispersed in a 4 M methanol solution, then the temperature was raised to 80 °C for 5 hours. The solution was filtered, washed and the resulting material was dried. The same procedure was followed for OMC-AF2 using a mixture HNO_3:H_2SO_4 1 M.

The Pt/OMC catalysts with a nominal ratio of 20:80 (%wt) were prepared via impregnation-reduction method. Briefly, H_2PtCl_6•H_2O were dispersed during 1 hour on OMC and subsequently reduced by $NaBH_4$ solution. The resulting solution was filtered, washed and dried.

The electrodes were prepared from catalytic ink as follows: the catalysts powder were dispersed in isopropanol and Nafion (5 µL) by ultrasound to form an ink with catalyst loading of 10 mg mL^{-1}. Then, an aliquot of 10 µL of catalytic ink were deposited onto glassy carbon disk (0.196 cm^2 geometrical area), previously polished until mirror-finished surface. After drying, the working electrodes were obtained.

The catalytic activity was measured in a WaveDrive (Pine Inst.) bipotenciostat connected to a RDE (Pine Inst.) in a electrochemical cell. A Pt wire was used as counter electrode, while Ag/AgCl serve as reference. All experiments were carried out in acidic media (0.5 M H_2SO_4). After 40 cycles at 50 mV s^{-1} cyclic voltammetry (CV) activation and CV profile at 20 mV s^{-1}, the ORR activity was measured at different rotation rates (400 until 2000 rpm) in a O_2-saturated electrolyte. CV was carried out to test the activity at 5 mV s^{-1}.

III. Results and Discussion

The specific surface areas of OMC was determined according to the Brunauer-Emmett-Teller (BET) method in the relative pressure range of 0.05-0.3. The specific surface of the chemically modified OMC was obtained from an analysis of the desorption branch of N_2 isotherms. As shown in Fig. 1, the isotherm of the OMC correspond to type IV, which is characteristic of mesoporous structures. The specific surface area of the support was 532 m^2 g^{-1}. The pore diameter calculated exhibits a material having mesopores ranging from 3 to 16 nm (inset) with an average size of 4.6 nm and pore volume of 0.61 cm^3 g^{-1}.

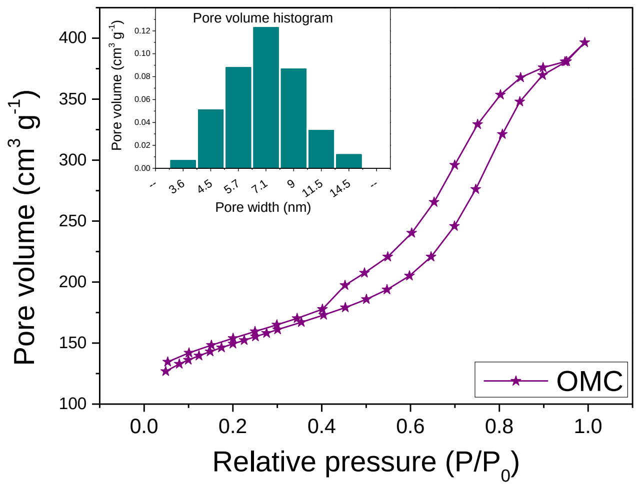

Fig. 1. N_2 adsorption-desorption isotherms of OMC.

In order to corroborate the functionalization, FT-IR spectroscopy were carried out. Figure 2 shows the spectra of the supports before and after two ways of functionalizations. Slight differences can be noticed. While OMC without functionalization barely present two bands (1570 and 1100 cm^{-1}) associated to C-C stretching, OMC-AF1 and OMC-AF2 show an intensification of the same two bands, which suggests an effect of the functionalization agents. It is noteworthy that OMC-AF2 shows higher intensification than OMC-AF1.

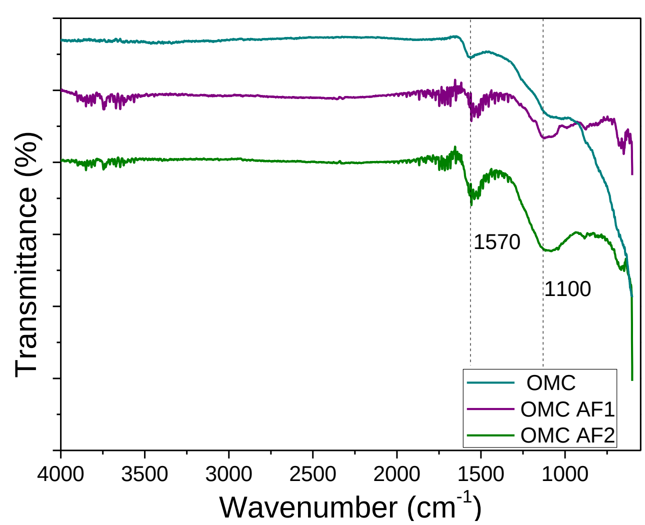

Fig. 2. FT-IR spectra of OMC before and after functionalization.

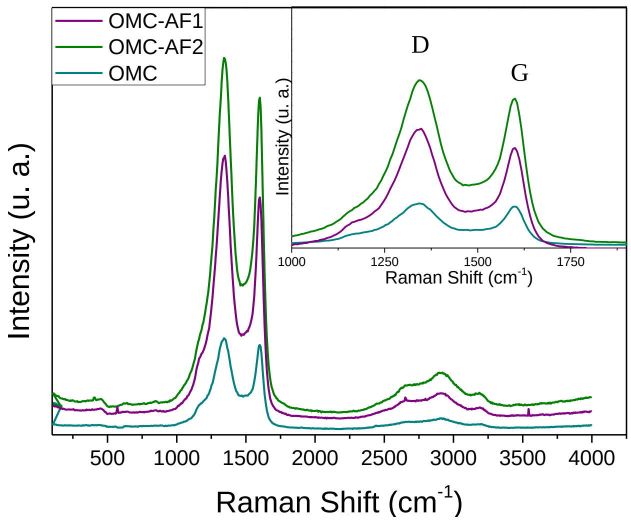

Fig. 3. Raman spectra of OMC before and after functionalization.

Raman spectroscopy could be used to analyze the structural damage in carbon structures and also provides direct information about covalent functionalization. Fig. 3 shows the Raman spectra for OMC, OMC-AF1 and OMC-AF2. The three characteristics bands are present in the three samples: D-band (~1340 cm^{-1}) which reveals the non-crystalline sites and disorder of the carbon, G-band (~1590 cm^{-1}) that provide information about the high degree order (sp^2 hybridization) and 2D-band is an overtone of the D-band [6]. The intensity ratio of D- and G- band (I_D/I_G) could provide information about the effect of functionalization of OMC. While the I_D/I_G ratio for OMC was 0.98, for OMC-AF1 was 1.26 and for OMC-AF2 was 1.02. This increasing ratio is linked to an increment in the disorder of the material which is directly related to the functionalization (rehibridization sp^2 to sp^3) [7], being the higher value for the OMC functionalized with methanol.

Fig. 4 shows the diffraction patterns obtained for Pt/OMC-AF1 and Pt/OMC-AF2 catalysts. A broad peak near to 25° 2θ associated to the plane (002) of graphite present in OMC is observed. The other principal peaks located at 39, 46, 67, 81 and 86°, correspond to (111), (200), (220), (311) and (222)

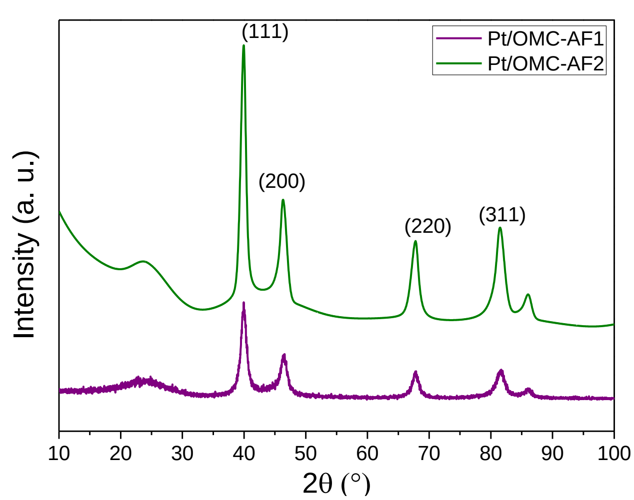

Fig. 4. XRD pattern for Pt/OMC-AF1 and Pt/OMC-AF2.

planes of metallic Pt with single face-centered-cubic (fcc) structure (Pt JCPDS 4-0802). The average crystallite size of the two catalysts was calculated from difractograms using the Scherrer equation applied to (220) peak, which were estimated in 7.8 and 8.3 nm for Pt/OMC-AF1 and Pt/OMC-AF2, respectively.

Fig. 5 compare the electrochemical response of the Pt/OMC-AF1 and Pt/OMC-AF2 catalysts in 0.5 M H_2SO_4. As comparative, a commercial catalyst (Pt/C ETEK) was also included. The typical voltammetric curve of Pt in acid media for the three catalysts is observed, where three regions are recorded: (I) Hads/des, (II) double layer and (III) oxides formation/reduction regions. However, both Pt catalysts supported in OMC show a wide double layer related with a higher capacitive current associated with the higher surface area of the support [8]. There are also notable differences between Pt/OMC-AF1 and Pt/OMC-AF2, the catalyst supported in OMC functionalized with acids exhibits a lower oxide formation/reduction region compared to Pt/OMC-AF1. The electrochemical surface area (ECSA) was calculated from the density charge associated to the hydrogen desorption

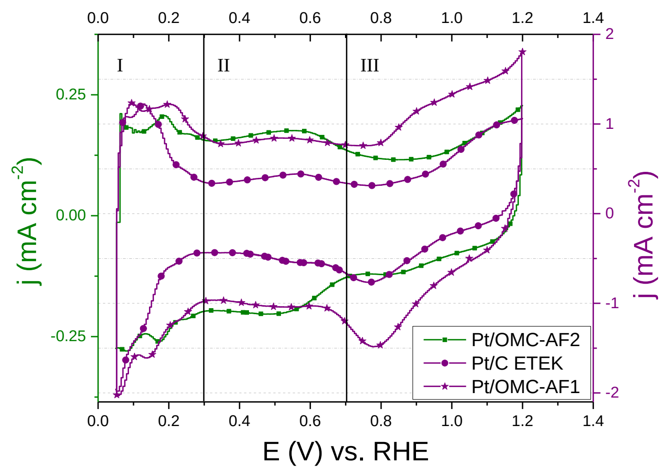

Fig. 5. CVs of Pt/OMC-AF1, Pt/OMC-AF2 and Pt/C ETEK in N_2 saturated 0.5 M H_2SO_4. Scan rate 20 mV s^{-1}.

region. The ECSA obtained for Pt/C ETEK catalyst (27.5 m^2 g$^{-1}_{Pt}$) was slightly larger than that obtained for Pt/OMC-AF1 (22.8 m^2 g$^{-1}_{Pt}$) and significant larger than Pt/OMC-AF2 (22.8 m^2 g$^{-1}_{Pt}$). The differences observed between both Pt catalysts supported on OMC, may be related to to poor dispersion of Pt nanoparticles promoted by a lower oxygen-groups formation during functionalization procedure.

The catalytic performance for the ORR of Pt/C ETEK is shown in Fig. 6. The onset potential (E_{ORR}) is near to 0.8 V vs. RHE while the current density at 0.8 and 0.1 V vs. RHE ($j_{RRO}^{0.8\,V}$ and $j_{RRO}^{0.1\,V}$ respectively) are -0.04 and -5.7 mA cm^{-2}. These parameters serve as a reference to compare the performance of the Pt supported in OMC. Koutecký-Levich plots of Pt/C ETEK at different potentials is presented in the same figure. The experimental plots shows linearity and parallelism to the theoretical 4 electrons (4 e$^-$) slope, which means that the ORR is taking place via 4 electrons transfer mechanism.

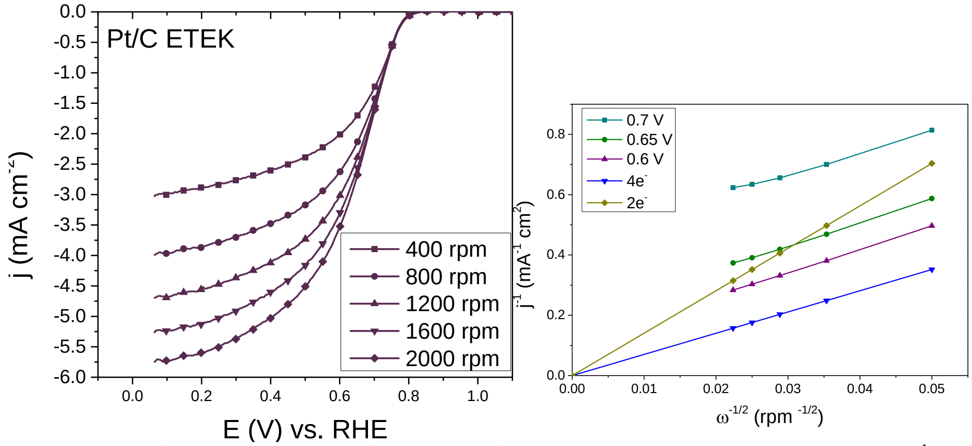

Fig. 7. Polarization curves of the ORR and Koutecký-Levich plots for Pt/C ETEK in 0.5 M H_2SO_4. Scan rate 5 mV s^{-1} in O_2 saturated.

The polarization curves of the ORR for Pt/OMC-AF1 and Pt/OMC-AF2 at different rotation rates are shown in Fig. 7a and 7b, respectively. The polarization curves for both catalysts reveal three distinguishable potential regions: kinetic (E > 0.8 V), mixed (0.6 < E < 0.8) and diffusion controlled (E < 0.6 V). For Pt/OMC-AF1, the E_{ORR} is 0.85 V vs. RHE, the $j_{RRO}^{0.8\,V}$ and $j_{RRO}^{0.1\,V}$ are -0.25 and -3.3 mA cm^{-2} $j_{RRO}^{0.8\,V}$, respectively. These values are bigger than the recorded for Pt/OMC-AF2, where E_{ORR} value is 0.8 V vs. RHE while $j_{RRO}^{0.1\,V}$ are -0.04 and -2.6 mA cm^{-2}, respectively. In the Koutecký-Levich analysis, the experimental plots shows parallelism to the theoretical 4 electrons (4 e$^-$) slope, which suggests that the ORR taking place at these catalysts approaches a 4 electrons transfer mechanism.

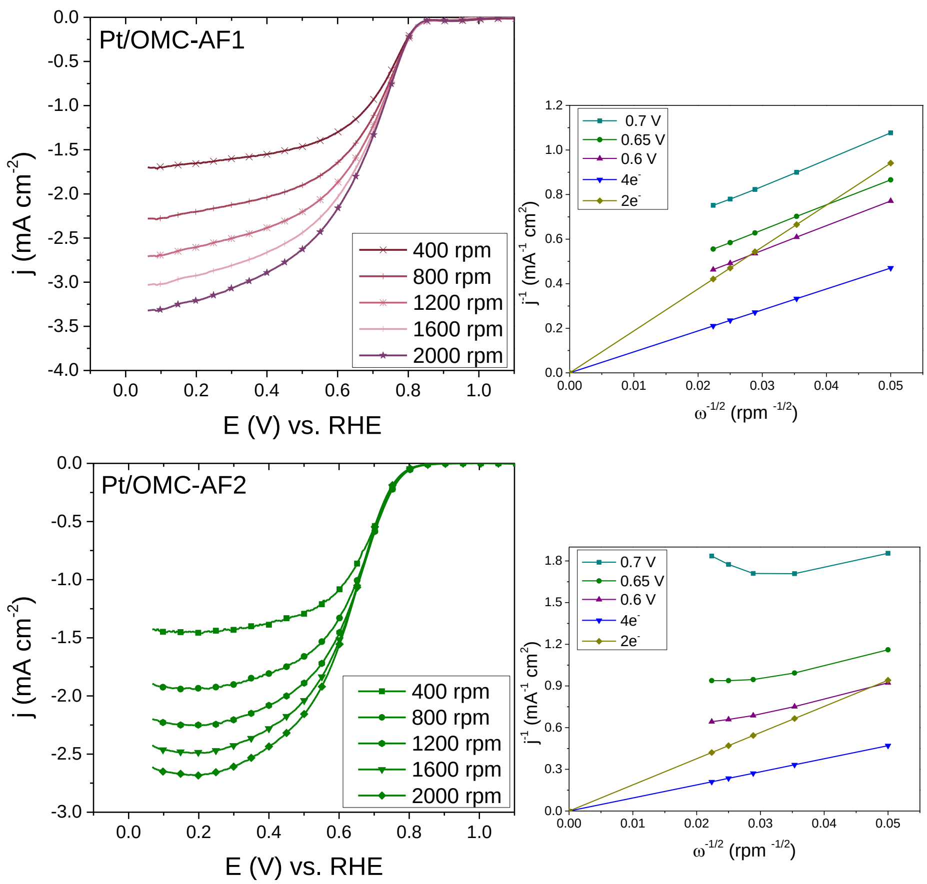

Fig. 6. Polarization curves of the ORR and Koutecký-Levich plots for a) Pt/OMC-AF1 and b) Pt/OMC-AF2 in 0.5 M H_2SO_4. Scan rate 5 mV s^{-1} in O_2 saturated.

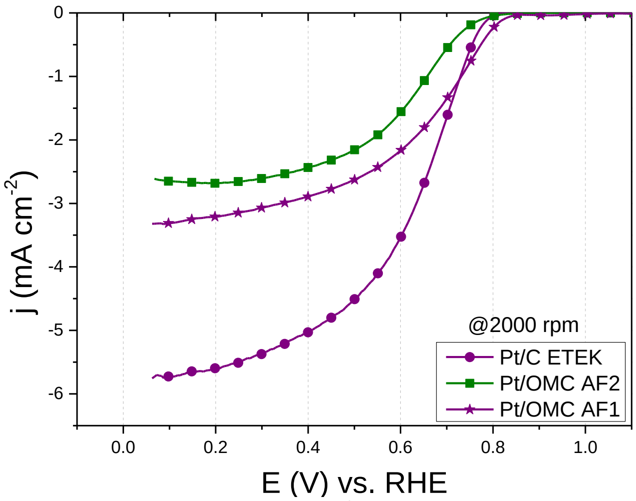

Fig. 8. Polarization curves @2000 rpm for Pt/C ETEK, Pt/OMC-AF1 and Pt/OMC-AF2 in 0.5 M H_2SO_4. Scan rate: 5 mV s^{-1}.

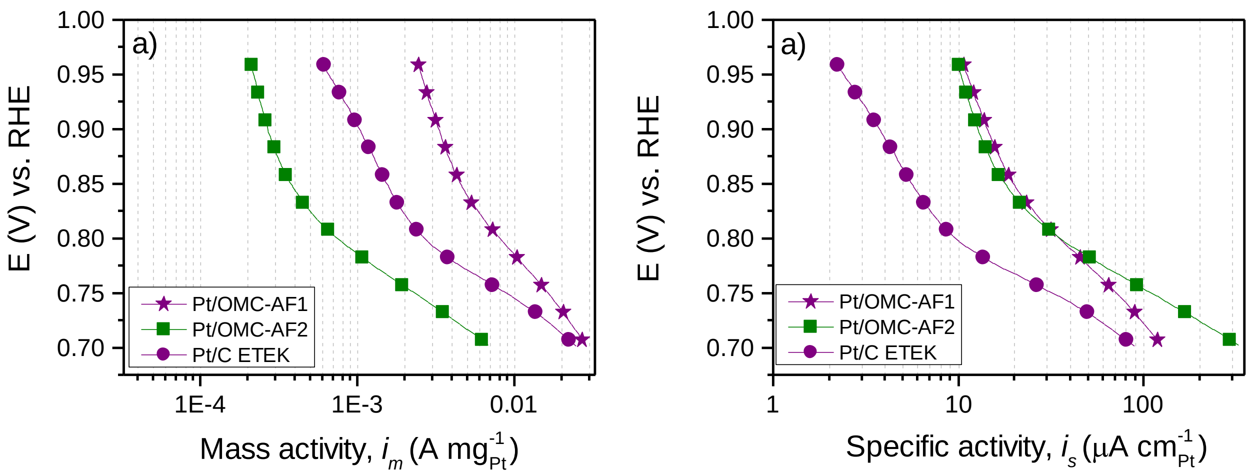

Fig. 9. (a) Mass and (b) specific activity plots of the ORR on Pt/OMC-AF1, Pt/OMC-AF2 and Pt/C ETEK catalysts in 0.5 M H_2SO_4 saturated with O_2. ω=2000 rpm.

As a comparison, the polarization plots at ω = 2000 rpm for the three cathodes are presented in Fig. 8. The performance on both Pt/OMC catalysts are comparable to that observed for Pt/C ETEK. Pt/OMC-AF1 shows a higher onset potential (50 mV) than the commercial cathode proving that the OMC is a good alternative as support that could be attribuited to the regular pores in OMC that might be responsible of a high utilization of Pt. Also, the mesoporous structure could maximize the TPB that result in a higher electron transfer. However, the current densities delivered by as-synthetized cathodes are smaller than ETEK. This could be attributed to a poor dispersion of the nanoparticles in the OMC.

Fig. 9 shows the mass (a) and specific (b) activities plots of the ORR in the three cathodes. The ORR current data used in such plots is that of Figure 7 (ω = 2000 rpm). From the results in both plots it can be observed that Pt/OMC-AF1 shows a higher mass and specific activity than Pt/C ETEK, proving the enhance of the catalytic activity of Pt due to the OMC support. A threefold increase of these activities are observed for Pt/OMC-AF1 which deliver 0.003 A $mg^{-1}_{Pt@0.9V}$ versus 0.001 A $mg^{-1}_{Pt@0.9V}$.

IV. CONCLUSSIONS

Two catalysts Pt/OMC were successfully synthetized. It has been proved that the effect of the functionalization of the carbon support plays an important role in the catalytic activity of the resulting material. Also, the results underlining the efficiency of OMC as support by enhance the catalytic activity of Pt for the ORR.

ACKNOWLEDGEMENTS

The authors are grateful to the National Council of Science and Technology (Conacyt) through the 252079, 241526, 252003, 259010, 270214 projects. NMSP is thankful to Conacyt for the master scholarship, to SMH and XVI International Congress of the Mexican Hydrogen Society for the fellowship to assistance to que congress. Authors also are grateful to National Laboratory of Graphene Materials (LNMG), to J.A. Mercado-Silva, R. Rangel-Ramírez, B. Puente and S. Fernández to the facilities provided for the use of some of its installations.

REFERENCES

[1] Soboleva T, Zhao X, Malek K, Xie Z, Navessin T, Holdcroft S. On the Micro-, Meso-, and Macroporous Structures of Polymer Electrolyte Membrane Fuel Cell Catalyst Layers. Appl Mater interfaces. 2010; 2: 375-384.

[2] E. Antolini. Carbon supports for low-temperature fuel cell catalysts. Appl Catal A Gen. 2009; 88:1-24.

[3] S.H. Joo, C. Pak, D. You, et al. Ordered mesoporous carbons (OMC) as supports of electrocatalysts for direct methanol fuel cells (DMFC): Effect of carbon precursors of OMC on DMFC performances. Electrochim Acta. 2006; 52: 1618-1626.

[4] J. Tang, J. Liu, N.L. Torad, T. Kimura, Y. Yamauchi. Tailored design of functional nanoporous carbon materials toward fuel cell applications. Nano Today. 2014; 9: 305-323.

[5] W.J. Pech-Rodríguez, D. González-Quijano, G. Vargas-Gutiérrez, J.I. Escalante-García, F.J. Rodríguez-Varela. Electrochemical Characterization of Pt Nanocatalysts Supported on Functionalized Vulcan XC-72 for the EOR. ECS Trans. 2014; 61: 11-18.

[6] D. Morales-Acosta, F.J. Rodríguez-Varela, R. Benavides, Template-free synthesis of ordered mesoporous carbon: Application as support of highly active Pt nanoparticles for the oxidation of organic fuels, Int. J. Hydrogen Energy. 2016; 41: 3387–3398.

[7] S. Karimifard, M.R. Alavi Moghaddam, Enhancing the adsorption performance of carbon nanotubes with a multistep functionalization method: Optimization of Reactive Blue 19 removal through response surface methodology, Process Saf. Environ. Prot. 99 (2016) 20–29.

[8] A. Kaur, I. Singh, J. Kumar, C. Bhatnagar, S.K. Dixit, P.K. Bhatnagar, et al., Enhancement in the performance of multi-walled carbon nanotube: Poly(methylmethacrylate) composite thin film ethanol sensors through appropriate nanotube functionalization, Mater. Sci. Semicond. Process. 31 (2015) 166–174.

Catalytic activity of Pt/GO-Fe_3O_4 for oxygen reduction reaction

N.M. Sánchez-Padilla[a], L.F. Vieira[a], R. Benavides[a], J. A. Rodríguez-González[b], S. Fernández-Tavizón[b], J.A. Mercado-Silva[b], D. Morales-Acosta[a,*]

[a] Departamento de Procesos de Transformación de Plásticos, [b] Laboratorio Nacional de Materiales Grafénicos
Centro de Investigación de Química Aplicada
Saltillo, Coahuila, México
diana.morales@ciqa.edu.mx

***Abstract*— Fuel cells are promising devices to be used as new energy sources. Recently, graphene oxide (GO) have attracted the attention to be used as alternative support. The latter due to good activity towards oxygen reduction reaction (ORR) enhancing the catalytic activity of Pt. However, some efforts need to be carried out to improve its processability. In this work, a study of the catalytic activity for the ORR of Pt/GO-Fe_3O_4 is presented. The GO was obtained via modified Hummer's method from graphite powder and partially reduced with NaBH4 solution. Reduced graphene oxide (rGO) was recovered by using magnetite (Fe3O4) nanoparticles. The rGO-Fe_3O_4 was used as support for Pt nanoparticles (Pt/GO-Fe_3O_4), deposited via impregnation-reduction using NaBH4 as reducing agent. The support was physicochemical characterized by XRD and FT-IR, while the catalyst obtained by XRD and electrochemical techniques. The results showed the oxidation of graphite onto GO and the formation of metallic Pt. The Pt/GO-Fe_3O_4 catalytic activity for ORR was evaluated by means of cyclic voltammetry in acid media and compared with Pt/C. The electrochemical results showed that GO increase the catalytic activity of Pt and such characteristics were attributed to the enhanced dispersion achieved in the GO used as support.**

Keywords*— fuel cells; graphene oxide; catalyst; oxygen reduction reaction.

I. INTRODUCTION

Platinum (Pt) nanoparticles are the most used metal as the active material in electrodes for fuel cells technologies. However, it has a high cost. In order to decrease the amount of this noble metal, improve the catalytic activity and selectivity in the reactions, new support materials are needed. Graphene (G) materials has recently received significant attention due to great potential. Owing to its unique properties as high conductivity, surface area and stability [1] it could be used as support in fuel cells electrodes [2].

G can be synthetized through chemical routes using graphite as the starting material [3]. Some of these chemical techniques involves the oxidation of the precursor to obtain graphene oxide (GO), which are G sheets with some functional groups covalently bonded to the carbon and involves the rehybridization sp^2 from G to sp^3 in GO [4], which confers it hydrophilic character. As the GO is formed by single or few layer G, the dispersion of these are good enough to form colloidal solutions which can help to prepare nanoparticles with high dispersibility. Its electrical conductivity is lower than G but can be improved through a reduction process (which creates reduced graphene oxide, rGO). However, during this process, the GO sheets can be strongly stacked which can reduce the catalytic activity of the final material. An approach to help to minimize this stacking is the use of a second material as Fe_3O_4.

Moreover, recently Fe_3O_4 has been studied as co-catalysts for fuel cell applications showing good results [5]. Also, there are reports that use some oxides (in combination with carbon) as support, which have been demonstrated to improve the Pt-support interactions [6]. In this work, a catalyst of Pt supported in GO-Fe_3O_4 was synthesized and characterized in order to evaluate the effect of support in its performance as cathode in acid media.

II. EXPERIMENTAL

GO was synthetized by modified Hummers method. Typically, graphite powder was dispersed in concentrated mixture H_2SO_4:H_3PO_4 (9:1 volume ratio) and sonicated for 30 minutes. Then, the dispersion was placed in an ice bath and $KMnO_4$ (3:1 mass ratio respect graphite) were slowly added. The temperature were raised to 35 °C for 30 minutes. The reaction was cooled to room temperature and water was added (1.5:1 volume ratio respect volume of the acid mixture) and continuous stirring for 48 hours. To stop the reaction, a 3 % H_2O_2 solution was added. The resulting solution was centrifuge, washed with water and ethanol to neutral pH and dried.

The Pt/rGO catalysts were prepared via impregnation-reduction method. First, GO was dispersed in water (0.2 mg mL^{-1}) and placed in an ultrasonic bath for 1 hour. Then, H_2PtCl_6•H_2O were magnetically stirred by 2 hours on GO-dispersion and subsequently reduced by $NaBH_4$ solution. In order to facilitate the recovery of the catalyst, Fe_3O_4 nanoparticles were added to the solution to obtain Pt/rGO-Fe_3O_4. The resulting solution was filtered, washed and dried.

The electrode was prepared from catalytic ink as follows: the catalyst powder was dispersed in isopropanol and Nafion (5 μL) by ultrasound to form an ink with catalyst loading of 10 mg mL^{-1}. Then, an aliquot of 10 μL of catalytic ink was deposited onto glassy carbon disk (0.196 cm^2 geometrical area), previously polished until mirror-finished surface. After drying, the working electrodes were obtained.

The catalytic activity was measured in a WaveDrive (Pine Inst.) bipotenciostat connected to a RDE (Pine Inst.) in an electrochemical cell. A Pt wire was used as counter electrode, while Ag/AgCl serve as reference. All experiments were carried out in acidic media (0.5 M H_2SO_4). After 40 cycles at 50 mV s^{-1} cyclic voltammetry (CV) activation and CV profile at 20 mV s^{-1}, the ORR activity was measured at different rotation rates (400 until 2000 rpm) in a O_2-saturated electrolyte. CV was carried out to test the activity at 5 mV s^{-1}. Tolerance to methanol in ORR was measured adding the alcohol in three concentrations (0.1, 0.25 and 0.5 M) into the electrochemical cell and testing at 2000 rpm under oxygen bubbling.

III. Results and Discussion

Fig. 1 show the experimental diffraction patterns from the graphite precursor (a), the powder as obtained by modified Hummers method, or GO (b), GO-Fe_3O_4 (c) and the catalyst Pt/rGO-Fe_3O_4 (d). The graphite precursor (Fig. 1a) shows two peaks at 26.5 and 54.62 °2θ, related to the (002) and (004) planes of graphite (JCPDS 41-1487) with an interlayer spacing (d-spacing) of 0.34 nm. For GO sample (Fig. 1b), a shift to smaller angles (7.5 °2θ) of the (002) plane (shown in de diffraction pattern as GO) indicates an increment in the d-spacing until 1.18 nm due to the exfoliation of graphite sheets caused by the oxidation process. This increase is higher than that reported in literature [7]. It is also possible to observe a small peak in 26.5 °2θ that indicates a small fraction of graphite remains unoxidized.

In Fig. 1c, the experimental diffraction pattern of GO-

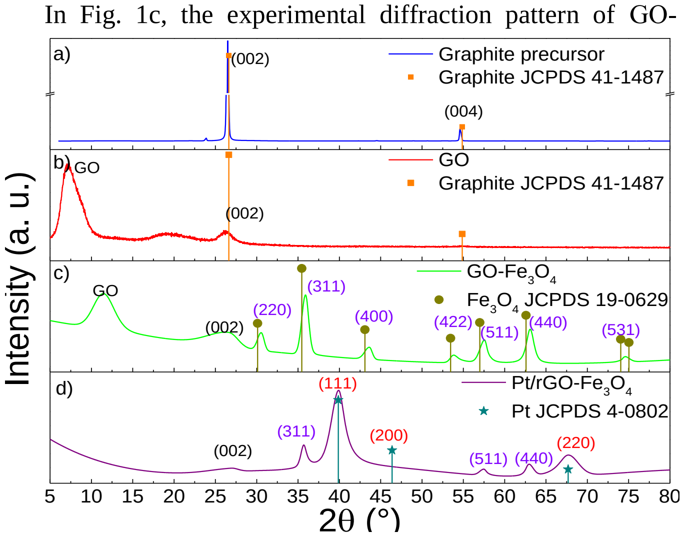

Fig 1. XRD patterns from the graphite precursor (a), the powder as obtained by modified Hummers method, or GO (b), GO-Fe_3O_4 (c) and the catalyst Pt/rGO-Fe_3O_4 (d).

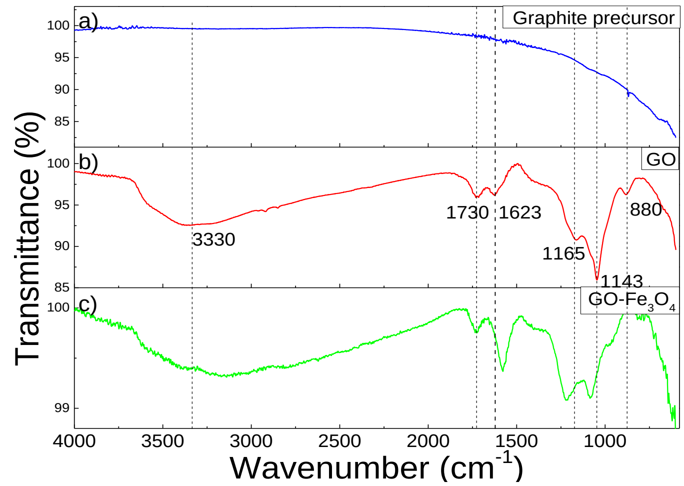

Fig.2. FT-IR spectra of graphite precursor (a), GO (b), GO-Fe_3O_4 (c).

Fe_3O_4 is shown. A displacement of the GO peak to higher angles (11.4 °2θ) respect to GO (Fig. 1b) is observed. The d-spacing calculated is 0.78 nm, which suggest a slight stacking effect over GO promoted by Fe_3O_4 nanoparticles. It is also possible to observe in the same pattern the peaks related to the Fe_3O_4 (FeO•Fe_2O_3, JCPDS 19-0629). Fig. 1d shows the XRD patterns for catalyst Pt/rGO-Fe_3O_4. In the experimental pattern, a broad peak near to 25 °2θ, associated to (002) plane of graphite is observed, which is due to the reduction process that cause a rehybridization $sp^3 \rightarrow sp^2$ from GO to its reduce form (rGO). The other principal peaks located at 39 and 67°, correspond to (111) and (220) planes of metallic Pt with single face-centered-cubic (fcc) structure (Pt, JCPDS 4-0802). The pattern also shows three peaks located at 35, 57 and 63° associated to (311), (511) and (440) planes of Fe_3O_4. The average crystallite size of the catalyst was calculated from difractograms using the Scherrer equation applied to (220) peak from Pt, which were estimated in 3.6 nm.

Fig. 2 shows the FT-IR spectra for graphite precursor and GO. GO-Fe_3O_4 spectrum is also included as a comparative. For the starting material, any bands are observed while for GO powder it can be seen six bands or peaks corresponding to functional groups due to oxidation process. A broad peak between 3000 and 3700 cm^{-1} is commonly attributed to stretching modes from hydroxyl groups (O-H). At 1730 and 1623 cm^{-1} the peaks can be associated to stretching vibration carbonyl (C=O, included either ketones or carboxyl moieties) and stretching modes for C=C or vibration of aromatics related to sp^2 hybridization in GO, respectively [8]. More peaks can be identified including C-OH stretching vibration (at 1165 cm^{-1}), C-O stretching vibrations in C-O-C epoxides (at 1062 cm^{-1}) and the O-H bending in 880 cm^{-1}. For GO-Fe_3O_4 an intensification of the some bands is observed, which suggests an effect of Fe_3O_4 over GO structure.

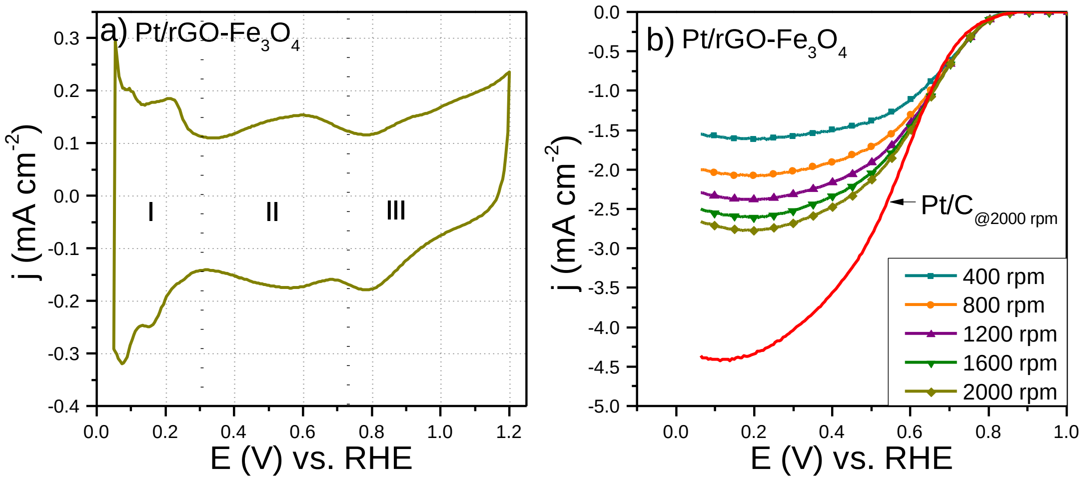

Fig. 2. CV of Pt/rGO-Fe_3O_4 in N_2 saturated 0.5 M H_2SO_4. Scan rate 20 mV s^{-1} (a) and polarization curves of the ORR in 0.5 M H_2SO_4. Scan rate 5 mV s^{-1} in O_2 saturated.

Fig. 3a shows the electrochemical response of Pt/rGO-Fe_3O_4 catalyst in 0.5 M H_2SO_4. The typical voltammetric curve of Pt in acid media for the three catalysts is observed, where three regions are recorded: (I) $H_{ads/des}$, (II) double layer and (III) oxides formation/reduction regions. Fig. 3b shows the polarization curves at different rotation rates and reveal three distinguishable potential regions: kinetic (E > 0.8 V), mixed (0.6 < E < 0.8) and diffusion controlled (E < 0.6 V). The onset potential (E_{ORR}) is near to 0.83 V vs. RHE while the current density at 0.8 and 0.1 V vs. RHE ($j_{RRO}^{0.8\,V}$ and $j_{RRO}^{0.1\,V}$ respectively) are -0.11 and -2.7 mA cm^{-2}, respectively. As comparative, the polarization curve of Pt/C catalyst at 2000 rpm is attached, the E_{ORR} recorded is 0.82 V vs. RHE, while the $j_{RRO}^{0.8\,V}$ and $j_{RRO}^{0.1\,V}$ are -0.10 and -4.4 mA cm^{-2} $j_{RRO}^{0.8\,V}$, respectively. Both catalysts have similar parameters, being Pt/rGO-Fe_3O_4 the material which poses a slightly higher E_{ORR}, however Pt/C has a greater limiting current.

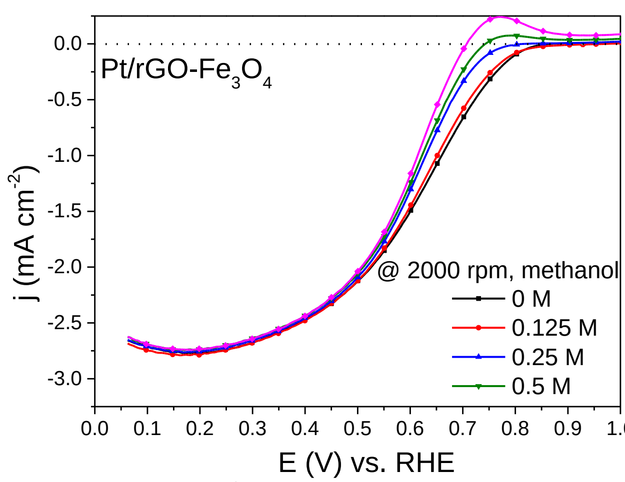

Fig. 4. Polarization curves of Pt/rGO-Fe_3O_4 at 2000 rpm in 0.5 M H_2SO_4 and different concentrations of methanol. Scan rate 5 mV s^{-1} in O_2 saturated.

Methanol-tolerance effects on the ORR activity of Pt/rGO-Fe_3O_4 catalyst were further investigated and the response is show in Fig. 4. At 2000 rpm, an appropriate quantity of methanol was added to the electrochemical cell at four different concentrations (0.125, 0.25, 0.5 and 1 M). Interestingly, the Pt/rGO-Fe_3O_4 display almost constant polarization curves and negligible displacement at the mixed region at 0.125 M. With the increasing of the methanol concentration some displacements of E_{ORR} can be observed. At 0.25 M, the catalyst shows a slight E_{ORR} shift to anodic values (0.76 V) but no positive current densities associated to de oxidation of methanol can be observed. For a 0.5 M concentration the E_{ORR} value is 0.73 V with a small positive current of 0.07 mA cm^{-2}, while for 1 M the E_{ORR} is 0.7 V and current density is barely 0.23 mA cm^{-2}. For the four concentrations the limiting current remains unchanged. These results illustrates the high methanol-tolerance of the catalyst which suggests the high selectivity to the ORR.

IV. Conclussion

A Pt/rGO-Fe_3O_4 catalyst was successfully synthetized with a particle size below of 4 nm. A slightly higher onset potential respect the traditional catalyst Pt/C was observed which suggest a higher electron transfer due to a better interaction Pt-support. Moreover, a high methanol-tolerance is observed for the catalyst, which suggest an improvement of the selectivity for this material for the ORR due to the interactions metal-support.

Acknowledgements

The authors are grateful to the National Council of Science and Technology (Conacyt) through the 259010, 270214 and bilateral Mexico-Brazil projects. NMSP is thankful to Conacyt for the PhD scholarship, to SMH and XVI International Congress of the Mexican Hydrogen Society for the fellowship to assistance to que congress. Authors also are grateful to National Laboratory of Graphene Materials (LNMG) and B. Puente to the facilities provided for the use of some of its installations.

REFERENCES

[1] C.J. Shearer, A. Cherevan, D. Eder, Carbon Nanotubes and Graphene, Elsevier, Massachusetts, 2014.

[2] K.K. Sadasivuni, D. Ponnamma, J. Kim, S. Thomas, Graphene-based polymer nanocomposites in electronics, Elsevier, Switzerland, 2015.

[3] C. Botas, P. Alvarez, P. Blanco, M. Granda, C. Blanco, R. Santamaría, et al., Graphene materials with different structures prepared from the same graphite by the Hummers and Brodie methods, Carbon 65 (2013) 156–164.

[4] G. Shao, Y. Lu, F. Wu, C. Yang, F. Zeng, Q. Wu, Graphene oxide: The mechanisms of oxidation and exfoliation, J. Mater. Sci. 47 (2012) 4400–4409.

[5] N. Sanchez-Padilla, S.M. Montemayor, F.J. Rodriguez Varela, An Easy Route to Synthesize Novel Fe3O4@Pt Core-shell Nanoestructures with High Electrocatalytic Activity, New Mater. Electrochem. Syst. 15 (2012) 171–179.

[6] J.C. Cruz, S. Rivas, D. Beltran, Y. Meas, R. Ornelas, G. Osorio-Monreal, et al., Synthesis and evaluation of ATO as a support for Pt–IrO2 in a unitized regenerative fuel cell, Int. J. Hydrogen Energy. 37 (2012) 13522–13528.

[7] L. Peng, Z. Xu, Z. Liu, Y. Wei, H. Sun, Z. Li, et al., An iron-based green approach to 1-h production of single-layer graphene oxide, Nat Commun. 6 (2015) 5716.

[8] D.C. Marcano, D. V. Kosynkin, J.M. Berlin, A. Sinitskii, Z. Sun, A. Slesarev, et al., Improved synthesis of graphene oxide, ACS Nano. 4 (2010) 4806–4814.

XVI International Congress of the Hydrogen Mexican Society 2016

Hydrogen adsorption and storage in modified nano-toroidal carbon c-120 structures with boron and nitrogen elements through computational molecular simulation analysis

E. López[1], A. García[1], Y. Peña[1], G. González[1], F. Castillo[2], J. Díaz[3], J. Martínez[4]

[1]Universidad Autónoma de la Ciudad de México, Fray Servando Teresa de Mier, México, D. F, 06080.
[*]Tel: +525551349804 Ext. 11110; e-mail: elopezc_h@hotmail.com
[2]Escuela Superior de Física y Matemáticas del Instituto Politécnico Nacional Unidad Adolfo López Mateos, México, D .F, 07738.
[3]Centro de Investigación en Ciencia Aplicada y Tecnología Avanzada, Instituto Politécnico Nacional Legaria, México, D. F.
[4]Instituto Mexicano del Petróleo, Eje Central Lázaro Cárdenas Norte, México, D. F., 07730.

ABSTRACT

The problem of new materials for hydrogen storage has been accounted since many years ago as a major challenge for researchers and scientists. Nowadays, the actual study is over carbon structures such as fullerenes and nanotubes, as promising option because these structures are light, that when they are funtionalized with transition metal atomic elements promize to capture high amounts of atomic or molecular hydrogen atoms. For this reason, we are going to present theoretical studies based on the Density Functional Theory, DFT, over C120 toroidal carbon nanostructures, functionalized with boron and nitrogen atoms in its structures. We study the thermodynamic stability of the functionalized structure, obtaining binding energies, as well as the gravimetric density (wt%) of hydrogen. It is important to say, that we get compativelly results with the ones obtained by other authors in several other carbon structures with some light metal materials. The present results might lead other researchers to be interested in our funzionalized toroidal structures and synthesis them for hydrogen storage.

Keywords: nano-toroidals, Dmol3, hydrogen gravimetric density, DFT.
Correspondence authors: alberto.garcia@uacm.edu.mx, elopezc_h@hotmail.com

Effect of protective agent in the formation of palladium nanoparticles synthesized by sonochemistry

Víctor A. Ortiz-Vergara[1], Patricia Pavón-Orozco[1], B. Fouconnier[1], Ma. Concepción Barerra-Domínguez, L. I. Cabrera-Lara, J. Eduardo Terrazas-Rodríguez[1*]

[1]Universidad Veracruzana, Facultad de Ciencias Químicas-Coatzacoalcos, Av. Universidad Veracruzana km. 7.5, CP 96401, Coatzacoalcos, Veracruz, México.

[2]Laboratorio de electroquímica, Centro Conjunto de Investigación en Química Sustentable UNAM-UAEMex., Km 14.5 Carretera Toluca-Atlacomulco C.P. 50200 Toluca, Estado de México, México.

e-mail: eterrazas@uv.mx

Abstract

The effect of protective agent in the palladium nanoparticles synthesis was investigated. The catalyst was synthetized by sonochemistry technique. Polyvinylpyrrolidone (PVP), Poly(ethylene glycol) (PEG) and citric acid were used as protective agents and particle stabilizers. The particle size was determined by means of Dynamic Light Scattering (DLS) technique at different times of synthesis. Agglomerates of average sizes of 392nm, 228nm and 118nm were obtained for citrate, PEG and PVP, respectively. The particle sizes were also determined by Transmission Electron Microscopy (TEM), and it was observed that the agglomerates were composed of palladium nanoparticles in the size range of 4 to 7 nm. Agglomeration is favored because the pH of the synthesis is near the isoelectric point (pH 1.64 in PVP medium). The catalytic activity towards oxygen reduction in acid was performed using the technique of linear sweep voltammetry and rotating disk electrode. Despite agglomeration, good catalytic activity of the particles was observed, once dispersed on VULCAN carbon.

Keywords— Palladium; Sonochemistry, Protective Agent.

I. Introduction

The limitations of electric power supply increases as the population increases, the sustainability of the current energy systems has emerged as one of the most important concerns, since it is based on the use of fossil fuels. For this reason, fuel cells (FC) arise as an attractive solution to this energy problem and, although they are under experiment stage, they are considered as a form of efficient and clean energy, capable to provide enough energy to stock the industrial, transportation, communication, education, technological sectors, to mention some.

Among the different FC systems, stand the polymer electrolyte membrane fuel cells (PEMFC), which promise to be the most efficient option to generate clean energy since they operate under low temperatures and have high energy conversion efficiency [1-3]. However, one of the most important disadvantages to PEMFC commercialization, is that one of their main components, the catalyst, is based on the use of noble metals, principally platinum nanoparticles (Pt NPs) [2, 4], which increase considerably their acquisition costs.

It is a challenge to generate homogeneous particle size and with high catalytic activity, as with Pt, for its use as a catalyst for PEMFC, since these are limited to oxygen reduction reaction (RRO) taking place at the cathode [1, 5]. Palladium (Pd) has surged as an attractive proposal to substitute Pt [1, 6], which has a high catalytic activity and high electronic conductivity [6-7]. In spite of the diversity of existing synthetic methodology for the generation of metallic NPs, it is the sonochemical assited synthesis [9] which has become a theme of interest, the use of ultrasound [8-9] allows this method to be of simple, economic and versatile application. The sonochemical method has been used to generate new materials with unusual properties, since it allows the formation of particles of smaller size, with higher superficial area, lower particle size distribution and higher catalytic activity tan those reported for other methods [10-15], besides being versatile for its production at industrial scale.

Sonochemistry derives mainly from acoustic cavitation, which concentrates energy by transforming sound diffuse energy to useful chemical energy. Acoustic cavitation consists of three stages: nucleation, growth and violent implosion of a bubble formed in the liquid. The implosion generates a great amount of heat, which can reach high pressures and high temperatures [16-18], which allows the breaking and formation of new molecular bonds, and the creation of nanostructured materials.

Another important factor in the synthesis of NPs is the protector agent, which stabilizes the NPs nuclei once they are formed thanks to ultrasound. With the purpose that these materials will have suitable particle size and morphology for its implementation as catalysts for FCs. Several methods exist for the stabilization of NP, for example the use of polymers [21].

In the present project, ultrasound technique was used for the generation of Pd NPs, where the nature of the protector agent during the synthesis was changed. With the purpose to evaluate the effect of the protector agent during the formation, the morphology and NPs size. Afterwards, their physical characterization was performed by transmission electronic microscopy (MET) and dynamic light scattering (DLS). Finally, cyclic voltammetry (CV) techniques and rotatory disc electrode (RDE) were used to record the kinetic parameters of RRO.

II. Experimental methology

2.1 Shyntesis of Palladium nanoparticles

Three different solutions were prepared for each of the protective agents, using palladium nitrate as a precursor [4 mM $Pd(NO_3)_2$]. All the solutions were prepared with 25% in volume with tetrahidrofurane (THF) and changing the protective agent. The proactive agents used were polyvynilpyrrolidone (2 mM PVP mol wt 10, 000, Sigma-Aldrich), citric acid (16 mM $C_6H_8O_7$, Sigma-Aldrich, 99.5%) and polyethylenglycol (16 mM PEG-600, Sigma-Aldrich).
Ultrasonic irradiation was performed with a sonicator brand QSONICA model Q700, the probe used (diameter 1/2") was immersed within the solution at different amplitudes (40% and 90%) of the total power. The Pd solutions were subjected to ultrasonic pulses (ultrasound time 20 s, standing time 40 s) during 1 h. The latter, was with the purpose to avoid the rise in temperature withing the solution and affect NPs aggregation during their formation.
The solution's temperature was kept constant at 10°C during sonolysis with the help of a thermostat. Later, NPs were filtered, washed with deionized water and isopropanol (C_3H_8O) (Aldrich), to finally dry them at room temperature.

2.2 Electrochemical characterization

The electrochemical characterization was performed with a BioLogic potentiostat/galvanostat model SP-150 and a three electrode cell with a 100 mL volume capacity. As a reference electrode, a saturated calomel electrode was used, and a platinum wire as a counter electrode. All the potentials in this article are reported with respect to the normal hydrogen electrode (NHE). The working electrode (WE) consists of a glassy carbon electrode (diameter 3 mm), covered with Teflon, which is used as a substrate for the catalytic ink. The glassy carbon electrode is polished with 0.05 µm alumina before each experiment. Inks were prepared in a 20%/80% W/W ratio of the catalyst (0.20 mg of the generated NPs, 80 mg Vulcan carbon), 30 µL of C_3H_8O and 10 µL of Nafion (5 wt% in water, Aldrich). The mixture was homogenized by ultrasound during 15 minutes, 10 µL were taken, and placed at the WE surface and left to dry at room temperature.

2.2.1 Linear scan voltammetry

The study of RRO was performed by linear scanning voltammetry technique coupled to a rotating disk electrode (RDE). A 0.5 M H_2SO_4 solution previously saturated with oxygen was used. Constant bubbling of oxygen over the solution surface was kept during the experiment. A potential scanning at 10 mV s^{-1} was performed from the open circuit voltage value to cero (EOC – 0 V) at different rotation rates (200, 400, 600, 1200 and 1600 rpm). Temperature was kept constant at 25°C.

2.3 Physical characterization

The synthesized particles were analyzed by a JEOL-2100 transmission electronic microscope at 200 kV with a LaB6 filament, coupled with a NORAN X-ray detector for energy dispersion spectroscopy. 200 particles were measured in order to record the average diameters and particle size distribution. Nanoparticle size and zeta potential (ξ) was measured by DLS using a Zetasizer nano ZS90 model at different synthesis reaction times.

III. Results and discussion

3.1 Effect of protecting agent

Fig. 1 shows the effect of the nature of the protecting agent (PVP and citric acid) over particle size of Pd NPs generated at pH 1 during a reaction time of 60 minutes with ultrasonic irradiation. It can be observed that, in both media, NPs size presents two characteristic zones in function with irradiation time. The first zone, developed during the first irradiation minutes ($0 < t < 60$ s), it reaches a maximum particle size at $t = 20$ s, to later decrease. During the second stage ($t > 60$ s), the particle is stabilized until it reaches a constant size value. The ultrasonic energy at pH 1 promotes the stages of nucleation and growth to be reached during the first 60 s. During this time, Pd^{2+} ions are reduced to palladium metallic atoms and form nuclei, which act as autocatalyst for the reduction of Pd^{2+} ions. This favors the particle's growth, and at the same times the formation of aggregates (with sizes among 700 nm for H_3Cit and 250 nm for PVP) [26-27, 29]. When ultrasonic irradiation is constantly applied, in the presence of a protecting agent the aggregates tends to decrease their energy by reducing their size until they reach a constant value (ripening stage), which was 300 nm for Pd NPs with H_3Cit and 118 nm with PVP [20]. The Pd-PVP interaction generates higher particles dispersion with lower particle size with respect to the Pd-H_3Cit interaction. Even when both molecules are non-chelating agents, there is a higher adsorption of NPs at the medium with higher molecular weight (PVP). Equally, the synthesis of Pd NPs was performed at a PEG medium at pH 1, where at the end of the reaction, particle size of Pd NPs was of 200 nm (kinetic study of NPs generated in the presence of PEG is not shown in this work).
The particle's aggregation effect on acidic medium was corroborated by performing a zeta potential study in function of pH for particles synthesized in the presence of PVP (insertion in Fig. 1). According to the graph, the isoelectric point is found at pH values below 1. At this highly acidic pH values, Pd NPs newly formed start to aggregate as Brownian movement among particles is favored.

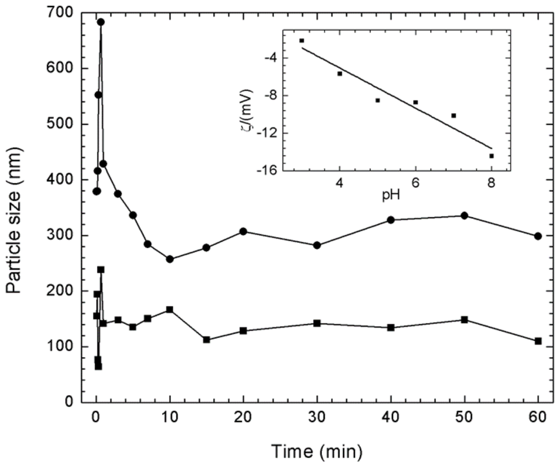

Fig. 1. DLS particle size study at, Pd 90% A; precursor concentration Pd $4x10^{-3}$M: ● Citrate, molar ratio 1:4, ■ PVP molar ratio 2:1.

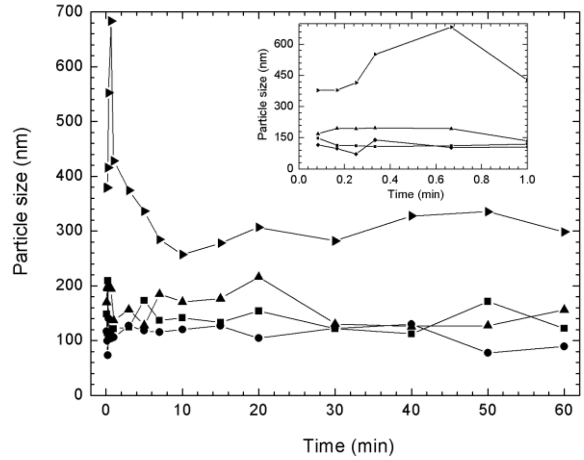

Fig. 2. DLS particle size determination in citrate medium Pd 90% A ($4x10^{-3}$M) molar ratio 1:4; ►pH 1; ■pH 6; ▲pH 7; ● PVP-citrate-pH 6

3.1.2 pH effect

The pH effect during the synthesis of Pd NPs when using H_3Cit as protecting agent (acidic medium) as a function of ultrasonic irradiation reaction time was studied (Fig. 2). The pH selection was based on acid dissociation constant values (pK_a) of H_3Cit: 3.2, 4.8 and 6.4, hence pH values under study in this section were 1, 6 and 7. A difference from the previous section, during the first 60 s of irradiation, at pH 6 and 7, maximum particle size was not observed, avoiding massive aggregation during this time period (insertion in Fig. 2). At pH 6 (above citric acid second pK_a value) NPs with a size among 120 mm were generated, and at pH 7 particle size was of 160 nm. At pH 6, citric acid is found as the deprotonated species $HCit^{2-}$, which defers with the species H_3Cit generated at pH 1. $HCit^{2-}$ acts as a better protecting agent and increases its chelating effect by absorbing itself to the nanoparticle's surface creating a steric barrier. However, this repulsive force is diminished by acidic pH [19-20, 23-25]. Furthermore, the effect in the decrease of particle size has been explained in this media for when using gold precursor by Xiaohui et al. [20], where they mention that at pH values higher than 6.5, NPs follow a traditional growing path, divided in two stages: nucleation followed by growing stage, which is controlled by diffusion [20, 28]. On the other hand, at pH values lower than 6.5, the generation of NPs takes place in three stages: nucleation, aggregation and interparticle ripening.

Likewise, in Fig. 2 can be observed the synthesis of PVP-citrate at pH 6. Under these conditions PVP helps particle dispersion process, since it decreases particle size to 90 nm, which is a smaller than in any other of the systems studied.

3.1.3 Transmission electronic microscopy

Particle size analysis was performed by TEM, in order to compare this value with the one generated by DLS for the synthesis of Pd NPs in the presence of H_3Cit as a protecting agent at pH 1. Fig. 3 shows Pd NPs morphology, size and dispersion when using ultrasonic pulses with 90% A of power. At the micrograph aggregates can be observed with sizes among 350 and 300 nm (Fig. 3a-3c). This agrees with the data generated by DLS. However, aggregates are conformed by Pd NPs which size is around 5.5 and 8.7 nm (Fig. 3d).

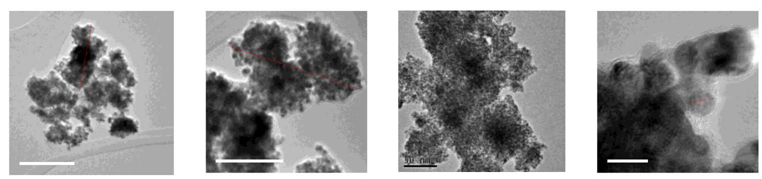

a) b) c) d)

Fig. 3. TEM images of NPs synthesized by ultrasound at 90% A by pulses; for H_3Cit pH 1.

3.2 Ultrasound power effect

The effect of ultrasound power at the probe with a power of 120 W was studied. Amplitude values under study were 40% and 90% of total amplitude (40% A and 90% A, respectively) keeping constant irradiation and at 90% A implementing a pulsed system (90% A-Pulses) irradiating during 20 s and halting irradiation during 40 s for one hour. Voltammograms at 0.5 M H_2SO_4 for the three systems are shown in Fig. 4a. It can be appreciated in the graph that for Pd 40% A a reduction peak is present at 0.67 V, which corresponds to oxygen reduction, while for Pd 90% A this peak is present at 0.64 V. A higher activity is observed towards RRO for particles generated at 40% A than for the ones generated at 90% A. Also, a greater current value can be observed at the double layer region (0.3-0.6 V) associated to particle size. This behavior can be due to a higher ultrasound frequency, the acoustic cavitation takes to a higher formation of •H y OH• highly reactive radicals in aqueous solution

(water sonolysis). These radicals favor thermal decomposition of the protecting agent (which avoids particle aggregation).
On the other hand, particles with higher activity towards RRO were generated by improving the sonochemical reduction system of Pd^{2+} ions by using pulses. According to Fig. 4a, a greater cathodic current magnitude is reached for RRO with the system Pd 90% A-Pulses than the others under study. An indication that these particles are more active, is their smaller size, as shown by the double layer current magnitude (0.27-0.46 V). This higher activity is achieved because by applying ultrasonic pulses, temperature at the interface is kept stable favoring a better covering of NPs surface with the protecting agent, avoiding this way aggregation.
In Fig. 4b is shown a comparison between the voltammograms for the synthesized NPs in the Pd 90%A-Pulses system and these same NPs dispersed on VULCAN carbon (20 % catalyst weight/ VULCAN carbon weight ratio). For this case, faradaic current magnitude corresponding to oxygen reduction is greater than for the Pd massive system, although capacitive current has also been increased due to the presence of VULCAN carbon. The electrocatalytic study of NPs dispersed on VULCAN is studied in the next section.

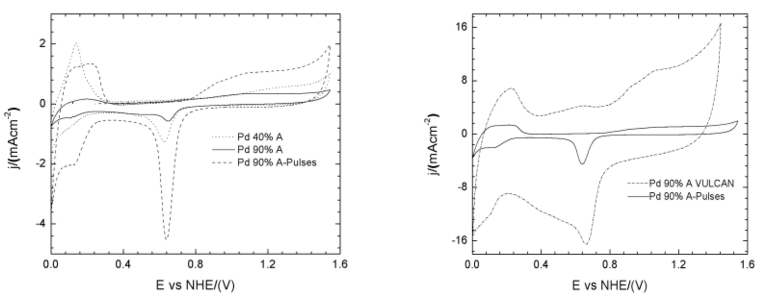

a) b)

Fig. 4. CV performed in 0.5 M H_2SO_4 0.5M oxygen free, v = 100 mV s^{-1}. a) Pd 40 % A, Pd 90 % A, and Pd 90%A-pulses. b) Pd 90 % A, and Pd 90% A –pulses-VULCAN

3.3 Electrocatalytic study in rotating disk electrode

Fig. 5 shows the representative polarization curves for Pd90%A-Pulses NPs dispersed on VULCAN carbon, at 0.5 M H_2SO_4 at a temperature of 25°C, with a RDE. The curves were obtained from open circuit potential, 0.78 V / NHE. Mixed kinetic-diffusion control region is in the range of -0.56 V <E / V vs. NHE <0.48 V and subsequent to this region, diffusional control zone exist. The overall measured oxygen reduction reaction current (i), can be expressed as being dependen ton the kinetic current (i_K), and the boundary layer diffusion-limited current (i_d), which can be expressed in terms of the Koutecky-Levich equation:

$$\frac{1}{i} = \frac{1}{i_k} + \frac{1}{i_d} + \frac{1}{i_f} = \frac{1}{i_k} + \frac{1}{B\omega^{1/2}} \qquad (1)$$

Where B equals the equation $0.2nFAD_j^{2/3}\ v^{-1/6}C_j^*$, where 0.2 is a constant value used when angular speed (ω) is expresed in rpm units, C is the oxygen concentration in the solution (1.1×10^{-6} mol cm^3), D is the diffusion coefficient in the H_2SO_4 solution (1.4×10^{-5} cm^2 /s), F is Faraday's constant (96,500 C mol^{-1}), n express the number of transfered electrons, and υ is the kinematic rate for sulfuric acid (1.0×10^{-2}).

The inset in Fig. 4 represents the inverse current density (i^{-1}) as a function of the inverse of the square root of the rotation rate ($\omega^{-1/2}$), the so-called Koutecky–Levich plot. The linearity and parallelism of these plots indicates first order kinetics with respect to molecular oxygen. It is observed in Tafel graphs, it appears that low overpotential required to perform the cathodic reaction, denoting high catalytic activity towards the RRO. At low currents, the Tafel slope is 23 mV / decade (Fig. inserted in Fig. 4) and the mass transfer coefficient value was 0.64.

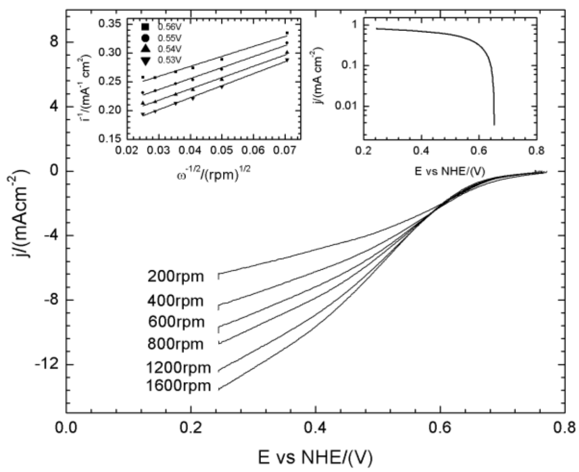

Fig. 5. Polarization curves for Pd 90% A electrocatalyst RRO dispersed on VULCAN carbon at different rotation rates, in 0.5 M H_2SO_4. Inset: Koutecky-Levich plot (i^{-1} vs at differents electrode potentials and Mass transfer-corrected Tafel plots.

IV. Conclusions

In this study the Pd ions reduction by ultrasonic irradiation is a simple and effective method for the generation of Pd NPs. These nanoparticles are useful for the catalytic RRO. The Pd NPs isoelectric point is generated at acidic pH, value that favors particle aggregation. At pH values higher than 6.4 and in the presence of chelating ($HCit^{2-}$) and non-coordinating (PVP) protecting agents, particle dispersion increases as well as particle size. According to TEM micrographies, particle size measured by DLS are Pd NPs aggregates, with an average particles size around 5.5 – 8.7 nm. Because of this, it is important to perform a study, where protecting agent concentration is varied in function with the precursor, in order to modify the nucleation and growing stages, and generate an optimum synthetic method, with high NPs dispersion.

V. Acknowledgments

The authors will like to acknowledge the finantial support for the present work with the project PRODEP UV-PTC-777 y PROFOCIE 30MSU0940B and the interchange program Universidad Veracruzana-Universidad Nacional Autónoma de México.

VI. References

[1] J. Zhao, A. Sarkar, A. Manthiram, "Synthesis and characterization of Pd-Ni nanoalloy electrocatalysts for oxygen reduction reaction in fuel cells", Electrochimica Acta, **55**, 1756–1765 (2010).

[2] R. Huerta, M. Leyva, O. Solorza, "Estudio comparativo de la reducción electrocatalítica de oxígeno sobre rutenio y su desempeño en una celda de combustible con membrana polimérica", Rev. Soc. Quím. Méx., **48,** 1-6 (2004)

[3] V. Murthi, R. Urian, S. Mukerjee, "Oxygen reduction kinetics in low and medium temperature acid environment: Correlation of water activation and surface properties in supported Pt and Pt alloy electrocatalysts", J. Phys. Chem. B, **108**, 11011-11023 (2004).

[4] G. Ramos, M. Bruno, Y. Thomas, H. Corti, O. Solorza, "Mesoporous carbon supported nanoparticulated $PdNi_2$: A methanol tolerant oxygen reduction electrocatalyst", International Journal of Hydrogen Energy, **37**, 31-40 (2012).

[5] J.J. Salvador, S. Citalán, O. Solorza, "Kinetics of oxygen reduction reaction on nanosized Pd electrocatalyst in acid media", Journal of Power Sources, **172**, 229–234 (2007).

[6] N. Alexeyevaa, A. Sarapuua, K. Tammeveskia, F.J. Vidal-Iglesiasb, J. Solla-Gullónb, J.M. Feliu, "Electroreduction of oxygen on Vulcan carbon supported Pd nanoparticles and Pd–M nanoalloys in acid and alkaline solutions", Electrochimica Acta, **56,** 6702–6708 (2011).

[7] Q. Shen, Q. Min, J. Shi, L. Jiang, J. Zhang, W. Hou, J. Zhu, "Morphology-Controlled Synthesis of Palladium Nanostructures by Sonoelectrochemical Method and Their Application in Direct Alcohol Oxidation", J. Phys. Chem. C, **113**, 1267–1273 (2009).

[8] G. Pollet, "The use of ultrasound for the fabrication of fuel cell materials", International Journal of Hydrogen Energy, , **35**, 11986-12004 (2010).

[9] S. Manickam, M. Ashokkumar, "Cavitation A Novel Energy-Efficient Technique for the Generation of Nanomaterials", p. 43,70, 132,174, Cap. 2 (2014).

[10] C.N. R. Rao, A. Müller, A. K. Cheetham, in "The Chemistry of Nanomateriales: Synthesis, Properties and Applications", **1**, 1, C. N. R. Rao, A. Müller, A. K. Cheetham, Editors; Wiley-VCH, Weinheim, (2004).

[11] K.E. Golsalves, H. Li, R. Perez, P. Santiago, M. Jose-Yacaman; Coordination Chemistry Reviews, **607,** 206-207, (2000).

[12] G. B. Sergeev, "Nanochemistry", chapter.2, 2nd ed. Elsevier BV, (2006).

[13] C.P. Poole, F.J. Owens. Jonh Wiley & Sons, "Introduction to Nanotechnology", (2003).

[14] Y. Mastai & A. Gendanken, in "The Chemistry of Nanomateriales: Synthesis, Properties and Applications", **1**, 6; C. N. R. Rao, A. Müller, A. K. Cheetham, Editors,Wiley-VCH, Weinheim, (2004).

[15] K.S. Suslick, T. Hyeon, M. Fang, "Nanostructured Materials Generated by High-Intensity Ultrasound: Sonochemical Synthesis and Catalytic Studies", Chem. Mater., **8**, 2172 (1996).

[16] L.H. Thompson and L.K. Doraiswamy, "Sonochemistry: Science and Engineering", Ind. Eng. Chem. Res., **38**, 1215 (1999).

[17] A.Y. Baranchikov, V. K. Ivanov, Y.D. Tretyakov, "Sonochemical synthesis of inorganic materials" Russian Chemical Reviews, **76** (2), 133-151 (2007).

[18] K. Suárez-Alcántara, O. Solorza-Feria," Evaluation of RuxWySez Catalyst as a Cathode Electrode in a Polymer Electrolyte Membrane Fuel Cell", Fuel Cells, **10**, 84 (2010)

[19] A. Corzo Lucioni, "Sintesis de nanopartículas de oro obtenidas por reducción de $H[AuCl_4]$, **89** (2012)

[20] Xiaohui Ji , Xiangning Song , Jun Li , Yubai Bai , Wensheng Yang , and Xiaogang Peng, "Size Control of Gold Nanocrystals in Citrate Reduction: The Third Role of Citrate", J. Am. Chem. Soc. 13945, **129** N°45 (2007).

[21] M. Ponce, "Síntesis y caracterización de nanopartículas de Ni y NiMo en medio acuoso", p. 105, Tesis de Maestría, Instituto Politécnico Nacional (2011).

[22] M. Contreras, "Electrocatalizadores a Base de Platino, Cobalto y Níquel Preparados por Aleado Mecánico, CVD para la Reacción de Reducción de Oxígeno" p. 180, 181, Tesis Doctoral, Instituto Politécnico Nacional (2007).

[23] Biggs, S.; Chow, M. K.; Zukoski, C. F.; Grieser, "The Role of Colloidal Stability in the Formation of Gold Sols", F. J. Colloid Interface Sci., **160**, 511-513, (1993)

[24] Biggs, S.; Mulvaney, P.; Zukoski, C. F.; Grieser, "Study of Anion Adsorption at the Gold-Aqueous Solution Interface by Atomic Force Microscopy", F. J. Am. Chem. Soc, **116**, 9150-9157. (1994)

[25] Wall, J. F.; Grieser, F.; Zukoski, C. F. J. ,"Monitoring chemical reactions at the gold/solution interface using atomic force microscopy", Chem. Soc., Faraday Trans., **93**, 4017-4020. (1997)

[26] Guozhong Cao, "Nanoestructures & Nanomaterials", 1st ed. Imperial College Press, p. 63-73, (2004)

[27] Tadao Sugimoto, "Fines particles synthesis, characterization, and mechanism of growth", **92** p. 452-456 (2000)

[28] V. K. Lamer, R.H. Dinegar, Theory, Production and Mechanism of Formation of Monodispersed Hydrosols Journal of the American Chemical Society. **72,** 4847. (1950)

[29] Marek Wojnicki , Krzysztof Fitzner, Magdalena Luty-Błocho, Kinetic studies of nucleation and growth of palladium nanoparticles, Journal of Colloid and Interface Science, **465** 190–199. (2016)

Biohydrogen production by anaerobic digestion of corn cob and stem of faba bean hydrolysates

J. C. Gómora-Hernández, D. Alcántara-Díaz, S. M. Ferández-Valverde
Depto. De Química, Depto de Radiobiología, Instituto Nacional de Investigaciones Nucleares,
La Marquesa, Ocoyoacac, México
e-mail: suilma.fernandez@inin.gob.mx

J. C. Gómora-Hernández, M. C. Hernández-Berriel
Depto, de Posgrado e Investigación, Instituto Tecnológico de Toluca
Metepec, Estado de México, México
e-mail: hberriel_1999@yahoo.com

Abstract—One Important research area is the search of biomass waste for hydrogen production. In this paper is reported the research of corn cob and stem of faba bean agricultural waste by hydrolysis for sugar production. Acid hydrolysis was performed in 1 g of dried raw material per 15 mL of different H_3PO_4 acid solutions heated at 100°C and 130°C during 2 h. The sugar yield was determined by dinitro salicylic acid technique. The maximum sugar recovery calculated in g of sugar per g of raw material were 0.43 and 0.17 for corncob and faba bean stalk respectively. For fermentation, hydrolysates were mixed in sealed vials with culture medium in anoxic atmosphere, an inoculum of 0.05 mL of *Clostridium butyricum* and 0.05 mL of *Enterobacter cloacae* was used, the vials were incubated at 37°C, two samples were taken every 2 h. The cell growing was monitored using a Petroff-Hausser counting chamber, hydrogen production was determined by gas chromatography and pH was also determined for each sample. In both substrates the cell growing lag time was 4 hours and after 11 hours hydrogen production was detected. The saccharide-biohydrogen production yields for sugars obtained from the hydrolysates were calculated according to the 2.75 mol H_2 per mol glucose reported experimentally in mexican fruits and vegetable waste. They were 18.9% and 12% for corncob and faba bean stem respectively.

Keywords— Agricultural wastes, dark fermentation, fermentable sugars, pure consortium

Biohydrogen photo-heterotrophic production using dark fermentation effluents from cheese whey

Photo-heterotrophic hydrogen production of fermented cheese whey

K. M. Muñoz- Páez[1], H. M. Poggi-Varaldo[1*]
[1]Environmental Biotechnology and Renewable Energies R&D Group, Dept. Biotechnology and Bioengineering
CINVESTAV-IPN
CDMX, México
r4cepe@yahoo.com *author for all correspondence

***Abstract*—Nowadays, the use of two (or more) biohydrogen production processes could help to achieve better yields and may be part of a biorefinery too. The dark fermentation effluents (*DFE*) are rich on volatile organic acids that could be substrate for purple non-sulphur bacteria and generate more H_2. The feasibility of biohydrogen production from cheese whey (*CW*) has been demonstrated and it is interesting explore the use of the effluents as substrate for photo-heterotrophic fermentation (*PF*). The main objective was to evaluate the *PF* using *DFE* from cheese whey. The dark fermentation (*DF*) was carried out in fluidized bed reactors using activated carbon as support with a hydraulic retention time of 1 day and organic volumetric loading rates of 10 g CW/ L.day. The *PF* was performed in batch reactors of 40 mL of operational volume, incubated at 32 °C and a light intensity of 3 klux. *Rhodopseudomonas palustris* (*Rp*) and a photo-heterotrophic mixed culture were used as inocula. Reactors with Pfennig medium (*Pm*) was used as control. The cumulative H_2 production when cultures of *Rp* were fed with fermented *CW* was 4.7 mmol H_2/L_{LF}.day, nearly 22 fold higher than with the photo-heterotrophic mixed culture. Interestingly, the highest cumulative H_2 production was detected with *DFE* and *Rp*, whereas almost no hydrogen production was detected with *Pm*. The use of *DFE* from *CW* as substrate of *PF* allowed obtaining two fold the H_2 yield of that with only dark fermentation.**

Keywords*— Biohydrogen production, cheese whey, dark fermentation effluents, photo-heterotrophic fermentation, purple non-sulphur bacteria

Design, manufacture and validation of an alkaline hydrogen enrichment reactor for internal combustion engines

Trujillo Olivares, M. Horcasitas Verdiguel, J. M. Sandoval-Pineda
[1]Instituto Politécnico Nacional, ESIME, Sección de Estudios de Posgrado e Investigación Unidad Azcapotzalco, Av. de Las Granjas 682, Azcapotzalco, Santa Catarina, Ciudad de México, México, 02250
hove_lenuma@hotmail.com

R. G. González-Huerta
[2]Instituto Politécnico Nacional, ESIQIE, Laboratorio de Electroquímica y Corrosión, UPALM, Edificio Z-5, Gustavo A. Madero, Lindavista, Ciudad de México, México, 07738
e-mail rosgonzalez_h@yahoo.com.mx

L. F. Terán Balaguer[3]
[3]Xantronic, Rafael Campoy 811, Col. Pitic, C.P. 83150, Hermosillo-Sonora, México
e-mail xantronicmx@gmail.com

***Abstract*— This paper focuses on the description of the design and manufacture of a oxyhydrogen reactor (ROH2) based on the methodology of APQP conjunction with the DFMA and ASHBY methodology for the selection of materials, and whose generation mix is called oxyhydrogen gas (GOH2). The electrical energy required for reactor operation was obtained from a direct current source, which was applied for generating graphs of performance curves (V-I) also the current efficiency ($\eta I - W$), efficiency voltage ($\eta v - W$), temperature and pressure of the electrolytic cell. Validating the prototype with a oxyhydrogen gas production of 1 l / min to 70 amps and 2.47 volts for a connection 20 stainless steel electrodes in parallel.**

Keywords— Oxyhydrogen, DFMA, ASHBY

I. Introduction

Fossil fuel reserves around of the world are somehow limited and severe environmental pollution has promoted the development of several studies on; gasoline economy, their consumption in internal combustion engines (ICE), and the need for alternative clean and renewable energies. Alternative fuels such as ethanol, hydrogen, and some others have been used in automotive systems. Hydrogen generation offers the possibility of reversing the negative impact generated with the use of fossil fuels expelled to the environment and offers an alternative to meet the current demands of fuel and energy [1,2]. Focus now the application of hydrogen in two basic forms; in hydrogen fuel cells and in ICEs. A fuel cell converts the chemical energy of the fuel directly into electricity, however, the cost of a PEM fuel cell is still higher than the one of conventional ICEs. Several global events indicate the fact that we are approaching to start an era which new energy systems will be used; the hydrogen era as a clean and environmentally friendly fuel has started. On the other hand, the limited infrastructure for hydrogen distribution and the high costs for production and storage are obstacles to not allow the popularization of using hydrogen in several types of engines and devises [1,7].

Comparatively, engines that use fuel-hydrogen mixtures have a reduced amount of total fuel consumption providing better combustion and reduced contaminant emissions than the traditional fuel-powered engines [1,3]. Gregory K. Lilik et al [2], investigated the performance effect of hydrogen-oxygen mixtures (oxyhydrogen) injected to diesel engine. Hydrogen assisted diesel combustion was investigated on a DDC/VM Motori 2.5L, 4-cylinder, turbocharged, common rail, direct injection light-duty diesel engine, with a focus on exhaust emissions. Hydrogen was substituted for diesel fuel on an energy basis of 0%, 2.5%, 5%, 7.5%, 10% and 15% by aspiration of hydrogen into the engine's intake air. Four speed and load conditions were investigated. Mohammad O. Hamdan et al. [3], investigated experimentally the behavior of compression ignition engine while boosting the combustion by enriching air-intake manifold with hydrogen supplement at the atmospheric condition, this study reports the engine thermal efficiency, NOx emissions and engine exhaust temperature while varying hydrogen content, engine speed and ignition timing.

According to previous studies [4], the on-board hydrogen storage system adds extra weight to vehicles and increases the need of considering more safety issues. In recent years, the hydrogen generator, which produces gas in-situ with an electrolysis process, provides a suitable solution for the hydrogen implementation on vehicles; the gas produced during the electrolysis contains oxygen which is a combustion promoter. This is beneficial to obtain a fast and complete combustion of the fuel-air mixture [1,10].

Few articles were found in which the integration of an alkaline electrolyzer to an ICE is considered. It is necessary to establish a small-scale manufacturing process for electrolyzers that can offer design security, installation and operation of these devices. Alkaline electrolyzers have several availability advantages, flexibility and high purity. Hydrogen production that use water electrolysis requires improvements in energy efficiency, safety, durability, operability and portability and also reduction in costs of installation and operation.

II. EXPERIMENTAL METHODOLOGY

There are two main electrolyzers groups: alkaline and polymeric [10]. The polymeric electrolyzer allows the use of solid electrolytes, which facilitate the production of high purity hydrogen, but requires expensive components. In this study, water alkaline electrolyzer (WAE) was chosen as the hydrogen generator because the alkaline water electrolysis is one of the easiest way for hydrogen production, offering the advantage of simplicity and lower costs. The challenges to widespread the use of alkaline water electrolysis are: to reduce energy consumption, cost and maintenance and to increase reliability, durability and safety. Figure 1 illustrates the considerations for the electrolyzers manufacturing process, including design, materials and security issues.

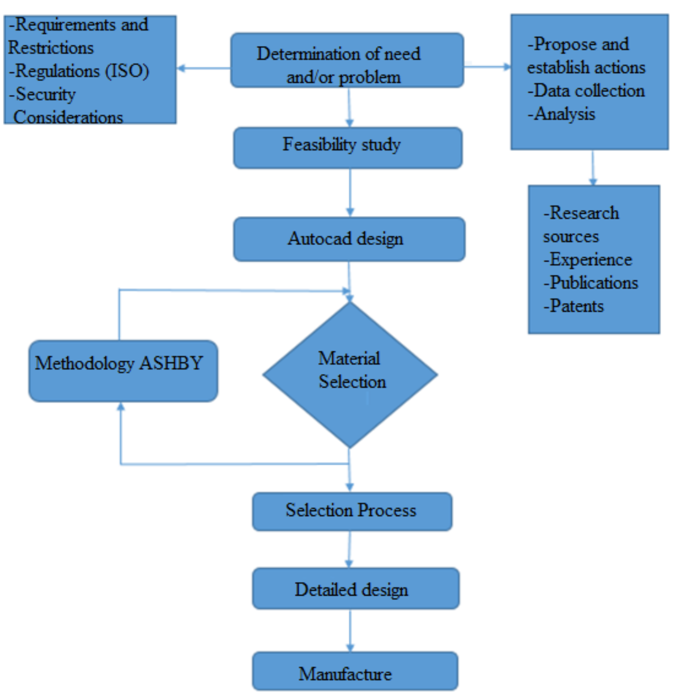

Fig. 1. Electrolyzer manufacturing process

Identify applicable sponsor/s here. If no sponsors, delete this text box (*sponsors*).

A WAE manufacturing process was established by adapting the APQP (Advanced Product Quality Planning) methodology which is an outline of procedures and techniques used to develop products and prototypes. APQP was used as a guide in the alkaline electrolyzer prototype development [6]. Figure 2 shows the selected analytical methodology, potential problems were identified during the development of the final product. Under the APQP analytical methodology, a basic monitoring system was generated to identify each step of the electrolyzer manufacturing process. APQP includes considerations on materials, leaks, corrosion, electrode stacking and the arrangement of the parallel-series configuration.

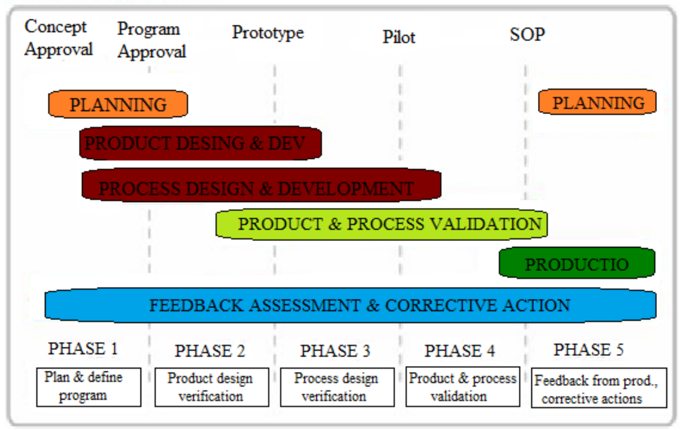

Fig. 2. APQP methodology to design alkaline electrolyzer

The initial electrolyzer design requires a parameters diagram. Figure 3 describes the controlled and uncontrolled aspects that have an influence in the electrolyzer performance; design, inputs and outputs of the system, manufacturing and failures. They will help to identify mistakes, noise and the control variables.

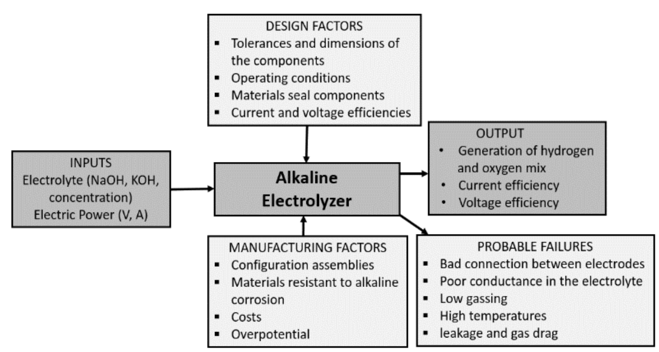

Fig. 3. Parameter diagram

In order to evaluate how acceptable the electrolysis systems are, it is necessary to identify those parameters related to the performance [1,10]. The main parameters should be analyzed. These parameters used for the evaluation of the electrolyzers include:

- Cell configurations: bipolar and monopolar configurations, electrodes gap and flow velocity of the electrolytes.

- Operating conditions: including voltage, current, temperature, pressure, type and electrolytes concentration and the stability of electrode material.
- External requirements: quality of water, gases and safety standards.

A basic water electrolyzer unit is composed by an anode (+), a cathode (-), a power supply, and an electrolyte [6]. After applying the direct current (DC), electrons flow from the negative terminal and the hydrogen production starts. Hydroxide ions (anions) are transferred through the electrolyte solution in direction to the anode taking the electrons back to the positive terminal of the DC source.

The electrolyzer system was designed to support up to 500W (according to the APQP), with 10 cells connected in parallel (20 electrodes connected in parallel). The electrolyzer system is composed by stack of 11.5x16cm in length and diameter respectively, Figure 4 shows the CAD diagram . A total of 20 stainless steel 18 gauge (304) electrodes (12.5 cm ϕ) ad are in contact with a 5% alkaline (NaOH), this concentration was chosen to avoid drag NaOH and that gas purification system was simpler. Stainless steel is considered as one of the most suitable electrodes material for alkaline electrolyzers, since it is relatively chemically stable, cheap and with low overpotential (catalytic material for cathodic and anodic reactions), however stainless steel electrodes not resist high concentration alkaline solutions because they undergo a corrosion process, therefore an electrolyte concentration of 5% was used.

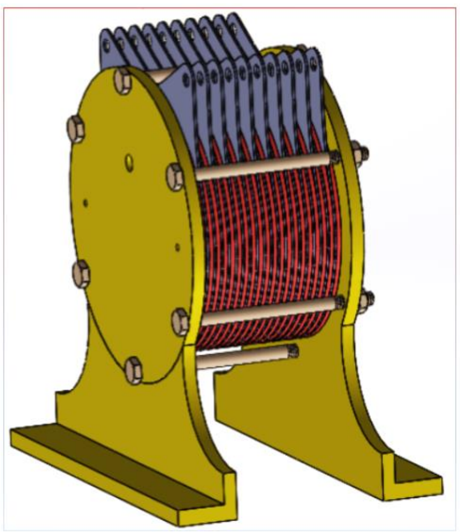

Fig. 4. General control system diagram

The system is connected to a wet trap (electrolyte/bubbles separator) with a volume capacity of 706.8 cm^3. There was no more electrolyte feeding during the electrolyzer operation. The hydrogen gas production ranged from 0.1 L min^{-1} up to 1.0 L min^{-1}. The performance curve was obtained using a controlled current from 0.1 to 80Amps. Water alkaline electrolyzer produces hydrogen-to-oxygen, with a mole ratio of 2:1 (standard oxyhydrogen gas, sOH_2G).

III. Results and Discussions

The arrangement of 20 electrodes connected in parallel was used to create a supply current from 2 to 90 A at 1.81 to 2.47 V. Figure 5 shows the WAE photograph of the parallel stack experimental arrangement.

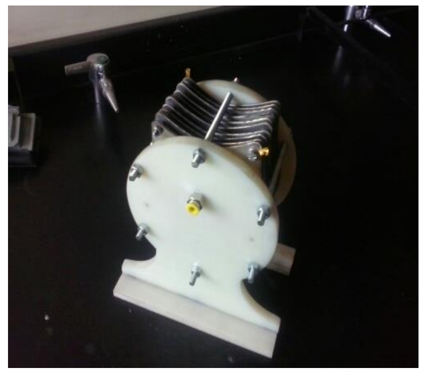

Fig. 5. Electrolyzer integration and photograph of the parallel stack experimental arrangement.

The typical polarization curve was tested at 25 °C. Figure 6 shows the resulting performance curve of the alkaline electrolyzer stack. It is important that test of electrolyzer must be in a ventilated place without flammable materials (solvents, paper, etc.) around the area. The gas produced must be bubbled in distilled water to remove electrolyte dragged.

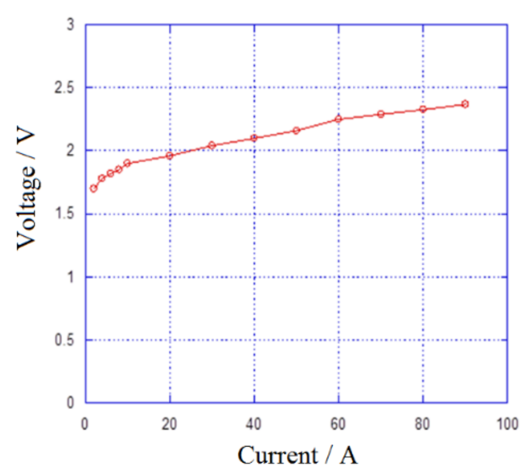

Fig. 6. Typical polarization curve at 25 °C

The amount of oxyhydrogen gas produced was determined with an Agilent Technologies (ADM) Universal Gas Flowmeter. Energy efficiency relates the amount of energy output with respect to energy input. Another way to evaluate the efficacy of the water electrolyzer is to consider the output of hydrogen production with respect to the total electrical energy applied to the system [1,6], the WAE efficiency, η_{WAE}, can be defined by equation 1:

$$\eta_{WAE} = \frac{E_{H_2}}{E_{EC}} \tag{1}$$

Where E_{H2} is the energy produced with the hydrogen and E_{EC} is the energy consumed by the electrolyzer. E_{H2} (kWh) is calculated using the following equation:

$$E_{H_2} = \frac{2}{3} V_{OH_2G} \frac{(P-Pv)}{760} \frac{298}{(T+273)} (0.0899)(33) \tag{2}$$

Where V_{OH2G} is the volume of oxyhydrogen produced (L), 2/3 is a constant for considering only the volume of hydrogen produced, P is local pressure (585 mmHg in México City), Pv is the water vapor pressure (18 mmHg), T is the room temperature (25°C), 0.089 g/L is the hydrogen density and 33Wh/g is the specific energy produced by the hydrogen. The theoretical oxyhydrogen gas produced is calculated assuming the hydrogen and oxygen as ideal gases (using equation 3). E_{EC} is the energy consumed by the electrolyzer in kWh and it was calculated with equation 4:

$$E_{EC} = (V_E)(I_E)(t) \tag{3}$$

Where V_E is the electrolyzer operation voltage, I_E is the applied current and t is the operation time in hours. The efficiency (η_{WAE}) is an important parameter to compare different electrolyzer technologies. It is a critical criterion to observe either energy or hydrogen production [6]. Figure 7 shows the obtained η_{WAE} vs electrolyzer power. An efficiency of around 50% for low temperature (25-60 °C) in alkaline water electrolysis is considered to be good [1].

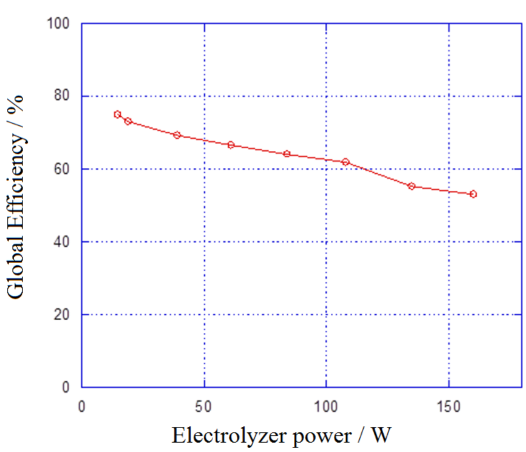

Fig. 7. WAE efficiency vs electrolyzer power

This system will be integrate a diesel test module, figure 8. Increment of gas contaminants from transportation vehicles is motivating researchers for the use of alternative fuels. Hydrogen offers a greatest potential and benefits for the environment and energy supply. The use of hydrogen/hydrocarbon fuel mixtures, reduces storage and combustion challenges presented when using only hydrogen in ICE.

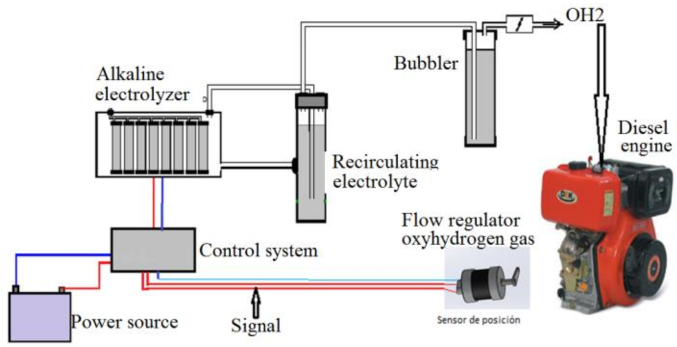

Fig. 8. Diesel test module

IV. Conclusions

The manufacturing process of a WAE prototype was established considering the APQP and ASBY methodology. In the experiment, the oxyhydrogen gas was produced by water alkaline electrolyzer (WAE) connected in parallel. The energy consumption ranged from 30 to 160 W which corresponds to 75 to 50 % of efficiency, a standard oxyhydrogen volume (903 mL min^{-1}) was produced at 160 W (80 A – 2.47 V). This system will be integrate a diesel test module. Increment of gas contaminants from transportation vehicles is motivating researchers for the use of alternative fuels. Hydrogen offers a greatest potential and benefits for the environment and energy supply. The use of hydrogen/hydrocarbon fuel mixtures, reduces storage and combustion challenges presented when using only hydrogen in ICE.

Acknowledgment

This work has been supported by multidisciplinary project IPN-SIP 1683 (2015-2016) and CONACYT: project PEI 231094 (2016) and Programa de Redes Temáticas /RTH2..

References

[1] Shoufeng Wang, Changwei Ji, Jian Zhang, Bo Zhang, Int. J. of Hydrogen Energy 2011; 36; 11164-73.

[2] Gregory K. Lilik, Hedan Zhang, Jose Martin Herreros, Daniel C. Haworth, Andre L. Boehman, Hydrogen assisted diesel combustion, Int. J. of Hydrogen Energy 2010; 35; 4382-4398.

[3] Mohammad O. Hamdan, Mohamed Y.E. Selim, Salah-A.B. Al-Omari, Emad Elnajjar, Hydrogen supplement co-combustion with diesel in compression ignition engine, Renewable Energy 82, 2015; 54-60.

[4] Chenglong Tang, YingjiaZhang, ZuohuaHuang, Renewable and Sustainable Energy Reviews 2014; 30; 195–216.

[5] Abdel HK, Sadik M, Bassyouni M, Shalabi M. Int. J. Hydrogen Energy 2005; 30; 1511-14.

[6] M. Horcasitas-Verdiguel, J. M. Sandoval-Pineda, B. A. Grunstein-Ramírez, L. F. Terán-Balaguer, R. de G. González-Huerta, Design and Manufacture of ICE Test Module to Reduce Gasoline Consumption Using Oxyhydrogen Gas from an Alkaline Electrolyzer, Energy & Fuel, line 2016.

[7] Chenglong Tang, YingjiaZhang, ZuohuaHuang, Renewable and Sustainable Energy Reviews 2014; 30; 195–216.

[8] Abdel HK, Sadik M, Bassyouni M, Shalabi M. Int. J. Hydrogen Energy 2005; 30; 1511-14.

[9] Gregory K. Lilik, Hedan Zhang, Jose Martin Herreros, Daniel C. Haworth, Andre L. Boehman, Int. J. of Hydrogen Energy 2010; 35; 4382–98.

[10] Ji C, Wang S, Zhang B. Int. J. Hydrogen Energy 2010; 35; 5714-22.

[11]

[12] .

Gamma irradiation of polystyrene-co-acrylic acid copolymers to use them as membranes in fuel cells.

R. Urbano, R. Benavides , D. Morales-Acosta
Centro de Investigación en Química Aplicada, Blvd. Enrique Reyna Hermosillo No.140 C.P. 25294 Saltillo, Coahuila México.
Tel.(844)4389830

M.E. Martínez-Pardo, H. Carrasco
Instituto Nacional de Investigaciones Nucleares, Carretera México-Toluca s/n, La Marquesa Ocoyoacac, México
C.P. 52750 - Tel. +52(55) 53297200

Abstract— **Styrene-co-acrylic acid copolymers were synthesized by radical bulk polymerization in a 96:4 molar ratio and subsequently sulphonated with a mixture of sulphuric acid (170% of the molar amount of benzene rings theoretically present in the copolymer) and silver sulphate (0.11% of the sulphuric acid), the latter used as a sulphonation catalyst. Membranes were prepared from the sulphonated copolymers by "casting" their THF solution (0.2 g / mL). Membranes were exposed to γ radiation at several doses (10-100 kGy) in an industrial irradiator, at a dose rate of 10 kGy/h. Membranes were spectrophotometrically characterized by FTIR, thermally by DSC and TGA and mechanically by TMA (including irradiated ones). DSC results show a increase in the glass transition temperature (Tg) of the copolymer, with respect to their homopolymers and further reduction with sulphonation time, which is related with a plasticization effect of the water in the polymer; FTIR show the presence of the characteristic functional groups of the synthesized and sulphonated copolymers. TGA demonstrated a lower thermal stability along sulphonation time. Complex moduli, evaluated by TMA, is greatly enhanced along irradiation dose, however, a lightly reduction for sulphonated copolymers, corroborating the water effect for hydrophilic materials. Gel percentage results observed similar trends for irradiated sulphonated materials.**

Keywords— ***fuel cells; gamma radiation; crosslinking component***

I. INTRODUCTION

There is a worldwide perception related to the reduced availability of non-renewable energy resources (oil and derivatives), and as a consequence an intensive trend for searching new methods for energy generation. The difference is that such methods involve a reduction in environment pollution. Alternatives, from the technical point of view are the fuel cells. They are electrochemical energy generators, using the energy involved into chemical reactions between a fuel and an oxidant. In this way, main components of a fuel cell are the anode, cathode and the electrolyte.

There are various types of fuel cells, however the ones containing a polymeric electrolyte (PEMFC) are some of the most studied and advanced nowadays. The latter have as a key component the proton exchange membrane, which is in charge of transporting protons from the anode to the cathode. Membranes are evaluated by their polyelectrolyte yield, measuring caracteristics as ion exchange conductivity (IEC), water absorption (WU) and proton conductivity [1, 2].

However, it is also of similar importance for membranes to have useful mechanical properties, in order to maintain their properties against the several conditions to which they are exposed: catalyst incorporation, compression forces during assembly of MEA, pressure during PEMFC closing, dimensional changes during hydration en dehydration of the membrane, pressure from the fuel (liquid or gas), temperature, etc. [3].

Nafion is up to now, the prefluorosulphonated ionomer most used as polyelectrolyte; although high fuel permeation (for DMFC), low humidity and low ion conductivity at higher temperatures, limit the performance of such system. There are also Nafion systems based on polymer composites, where the inorganic material is in charge of holding water molecules through the -OH groups they regularly have into their structure. Such systems have improved proton conductivity and enhanced thermal and mechanical properties. However, when Nafion is in contact with water, its Young´s modulus is reduced, since dissolvent has a direct impact in the tension-deformation relationship. Water or any other dissolvent swell the membrane, reduce their intermolecular forces and increase elongation; as a consequence, membrane is more ductile and susceptible to permanent deformation [4, 5]. Considering the previous, control of mechanical properties is of vital importance for new materials pretending to be used as ion exchange membranes, but initial steps consist of preparing a real copolymer, which can be sulphonated without relevant changes in the polymeric structure. Furthermore, must have benefits after treatment with gamma radiation for crosslinking.

II. MATERIALS Y METHODS

A. Materials.

Styrene (St, 99%, Aldrich) purified with NaOH, dried with CaCl2 and finally distilled under reduced pressure. Phenotiazine was added to acrylic acid (AA, 99%, Aldrich) and the monomer distilled under reduced pressure. Benzoyl peroxide as initiator (BPO, Aldrich), sulphuric acid (H2SO4, JTBaker), silver sulphate ⩾99.0% (Aldrich), Tetrahidrofuran ⩾99.9% (THF, Aldrich) and anhydrous dichloromethane ⩾ 99.8% (Aldrich).

B. *Co-polymerization procedure.*

Synthesis was carried out trough a mass copolymerization reaction of styrene and acrylic acid in a 94/6 molar ratio. Benzoyl peroxide was added as initiator (0.05 % mol of total amount of comonomers). Reaction temperature was kept at 100 ºC with a 250 rpm mechanical stirring, under nitrogen atmosphere during 2 hr. Copolymers were dried into a vacuum oven at 40 ºC until constant weight..

C. *Sulphonation procedure.*

Copolymers were sulphonated with sulphuric acid at a 170 % mol (theorethical amount of benzene rings) and 0.055 mol of silver sulphate used as catalyst. Each copolymer was dissolved in dichloromethane using 250 rpm mechanical stirring and 40 ºC under nitrogen atmosphere. Sulphuric acid was mixed with silver sulphate and then added to the copolymer and reaction allowed during 1, 2 and 3 hr. Sulphonation was terminated by removing the solvent and adding cold distilled water. Sulphonated copolymer was washed with abundant distilled water until reach pH $\approx$7 and then dried at ambient temperature with an air stream during 48 hr.

D. *Membrane preparation.*

Films were prepared by casting dissolving 0.2 g/ml of THF and then poured into a glass container; left to dry into a fume cupboard until constant weight.

E. *Irradiation of membranes.*

Membranes were placed into a sample chamber and then placed in a well-known position into the compartment of an industrial gamma irradiator (JS-6500). The irradiator belongs to the Instituto Nacional de Investigaciones Nucleares (ININ). Time was calculated for the samples to obtain doses from 10 to 100 kGy for no sulphonated membranes, and 50, 75 and 100 kGy for sulphonated ones, to evaluate the effect of crosslinking among copolymer chains.

F. *Infrared spectroscopy (FTIR)*

FTIR was used to evaluate presence of functional groups from the synthesized copolymers and compare with sulphonated ones; a ThermoNicolet Avatar 330 instrument was used under following conditions: 25 scans at the region 4000-400 cm-1 and a resolution of 4 cm-1. Samples consisted of thin films from membranes and lecture taken trough transmission.

G. *Thermogravimetric Analysis (TGA).*

Thermal stability of sulphonated copolymers was evaluated by TGA. A thermobalance instrument from DuPont model 951 was used, with a heating rate of 10 ºC/min from ambient temperature up to 700 ºC under nitrogen.

H. *Differential Scanning Calorimetry (DSC).*

In order to evaluate thermal properties of sulphonated membranes calorimetric studies were carried out. A MDSC TA Instruments 2920 under conventional mode was used. A first scan was applied from ambient to 160 ºC to eliminate thermal history, then a second heating was recorded. A heating ramp of 10 ºC/min was used from -30 to 160 ºC.

I. *Thermomechanical Analysis (TMA).*

Complex modulus was evaluated in flexion mode, using rectangular bars obtained from the membranes. Temperature was kept at 30 ºC and a force ramp of 0.001 Nw/min was applied from 0.001-0.01 Nw. Instrument is a TA Instruments 2940. Modulus was calculated by Equation 1:

$$E^* = FL3/4CD3Y \quad (1)$$

where E* = Complex Modulus, F= Force applied (Nw), L= Length of sample (mm), C= Width of sample (mm), D = Thickness of sample (mm), Y =Deflection of the sample under load (mm).

J. *Gel Percentage.*

Irradiated copolymers before and after sulphonation during 1, 2 and 3 hours were extracted in a soxhlet apparatus to evaluate the percentage of insoluble material. THF was used as the solvent and the extraction was carried out during 6 hours. Gel percentage was calculated gravimetrically after keeping cellulose thimbles in a vacuum oven at 60 ºC until constant weight..

III. RESULTS AND DISCUSSION

A. *Infrared spectroscopy (FTIR).*

FTIR was used to evaluate presence of functional groups, either from copolymers as from sulphonation groups in the copolymer. Figure1 show the corresponding spectra from copolymers sulphonated during 1, 2 and 3 hours.

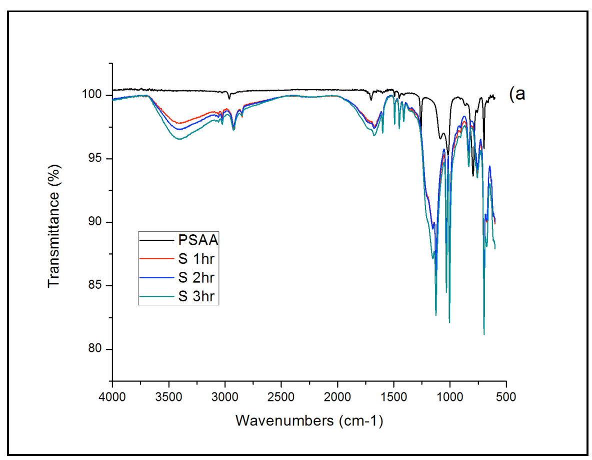

Figure 1. - FT-IR of PSAA copolymers after sulphonation during 1, 2 and 3 hr.

Copolymer show broadening of 3300-2500 cm-1 region due to OH stretching vibrations from the acrylic acid, as well as the 1704 cm-1 from the carbonyl and the out of plane bending at 1430 cm-1 from the same group, all indicating the presence of the acrylic acid in the styrene main structure.

Furthermore, there is a big difference among copolymers before and after sulphonation reaction. Main sign of presence of sulfonic groups is the formation of a broad band at the 3500-3100 cm-1 wavenumber region, corresponding to the OH group from the sulphonic acid. Such band is enhanced along the sulphonation reaction time, suggesting an increasing presence of such groups. Similar band was observed by Proenca [6] during sulphonation reactions with polystyrene and polyaniline for electrodialysis applications.

There are another bands located at the 1400-1000 cm^{-1} region with signals from the sulphonic groups, like the SO_2 asymmetric stretching at 1390-1290 cm^{-1}, and the symmetric one at 1190-1120 cm^{-1}. All mentioned absorption bands indicate that copolymer consist of both comonomers and were effectively sulphonated.

B. Thermal stability (TGA).

Thermogravimetric analysis were carried out in order to evaluate if sulphonated procedure induce changes in thermal stability of copolymers. Figure 2 show thermograms for materials before and after sulphonation during 3 different times; 1,2 and 3 hours.

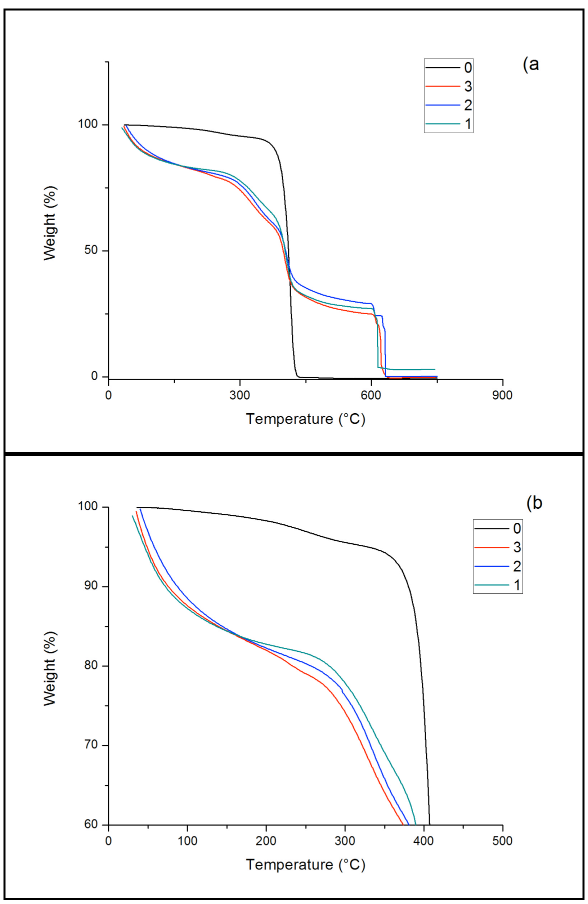

Figure 2. - TGA of sulphonated copolymers, a) full view, b) close view

The copolymer is basically stable up to 400 ºC, to start a fast mass loss representing the destruction of the copolymer structure. The sulphonated copolymers, on the other hand, show an important mass loss from the beginning of the thermogram of about 20 %. Such loss is related with water evaporation from the material, since sulphonic and OH groups from acrylic acid are highly hygroscopic. A following step in mass loss is related with the destruction and evolution of sulphonic groups at around 350 ºC. Such behaviour has been reported previously by De Paoli et al [7], who observed similar trend for pure styrene.

It is important to mention that low temperature behaviour is the most important for this kind of materials, since membranes used in PEM fuel cells work at temperatures below 100 ºC.

C. Differential scanning calorimetry (DSC).

Differential scanning calorimetry was also evaluated for sulphonated copolymers, in order to identify possible changes in vitreous transition (Tg) from copolymers after synthesis and sulphonation reactions. Figure 3 shows thermograms.

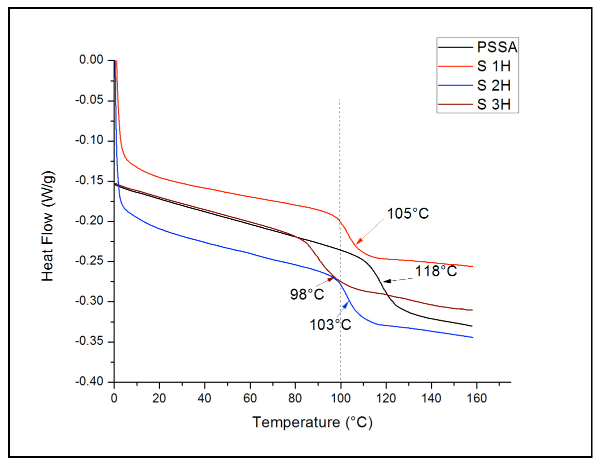

Figure 3. - DSC thermograms from sulphonated copolymers

It is clear to observe that sulphonation reaction change the thermal transition of the copolymer; while the neat copolymer has a transition at 118 ºC, the values is reduced to 98 ºC. The more sulphonation time the lowe the Tg transition for copolymers. It is believed that sulphonic groups enhance chain mobility by more free volume among them. The latter means that lower energy is needed to start macromolecule motion, reducing the transition temperature.

D. Thermomechanical analysis (TMA).

The Young´s Modulus (complex modulus) was calculated according to the equation described in the experimental section, with data from a TMA instrument in flexure mode. Data involve copolymers before and after sulphonation at the 3 different time conditions and also after gamma irradiation at different doses. Figure 4 show results from copolymers synthesized, sulphonated at 1, 2 and 3 hr and then irradiated.

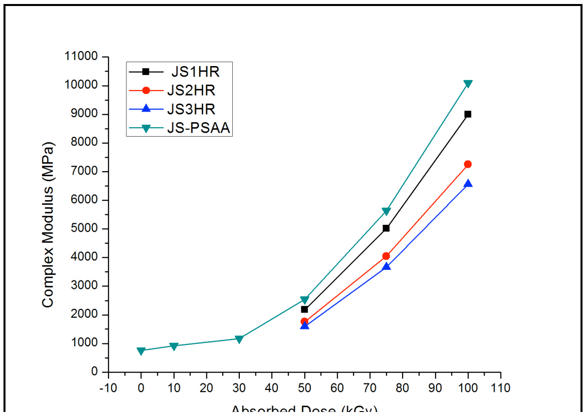

Figure 4. - Modulus values for copolymers with sulphonation and after gamma irradiation at different doses

Results indicate that copolymer by itself gets higher modulus value along the irradiation dose, the increase of E* value is more than a decade between no irradiated and 100 kGy of irradiation dose. Many irradiation doses were applied for copolymer with no sulphonation, since this material was taken as sample for preliminary tests to observe the need of a crosslinking agent in the copolymer; it is clear that E* enhancement along irradiation dose indicates that crosslinking among copolymer chains is going on and no crosslinking agent is needed to improve mechanical properties.

Sulphonated copolymer was only treated at three doses: 50, 75 and 100 kGy and the trend observed is very clearly indicating that higher dose promotes high moduli values; however, it is also clear that the longer sulphonation time the lower E* values are obtained. The latter is indicating that more sulphonated copolymer means more hydrophilic materials, and the water adsorbed into the polymer structure behaves as a plasticizer, corroborating results obtained from TGA and DSC.

Knauth et al [8] reported the existence of a correlation between water adsorption and mechanical properties for proton exchange membranes. They mention that softer membranes are those allowing higher water adsorption, while stronger ones have lower hydrophilicity. They also suggest that water behaves as a plasticizer, reducing the strength among hydrogen bridges from the sulphonic groups in the ionic membrane.

E. Gel Percentage

A simple evaluation for crosslinking level is the measurement of insoluble material in a specific solvent, also known as % gel [9]. The copolymers were extracted in THF and Table 1 show results obtained for copolymer before and after sulphonation during 1,2 and 3 hours, as well as after irradiation at the different doses. It is clear to see that no irradiated copolymer has zero gel %, but the value increases along the irradiation dose, up to 16.5 % for 100 kGy irradiated one; several authors have found similar results for irradiated styrenics [10, 11].

TABLE 1.- GEL PERCENTAGE FOR SULPHONATED COPOLYMER IRRADIATED AT DIFFERENT DOSES

Absorbed Dose (kGy)	**Gel (%)**			
	PSAA	***S-1Hr***	***S-2Hr***	***S-3Hr***
0	0	-	-	-
10	3.10	-	-	-
30	5.67	-	-	-
50	9.25	6.86	6.11	5.55
75	12.95	10.59	8.96	8.47
100	16.45	13.21	12.02	11.30

However, sulphonated copolymer reach lower gel % values, particularly for the more sulphonated material. These results are in agreement with TMA mechanical response, suggesting that crosslinking level is responsible for mechanical properties, although it is not clear why the more sulphonated copolymer reach lower crosslinking level. The latter is perhaps related with the usual degradation observed for copolymers after sulphonation reactions with sulphuric acid [5].

CONCLUSION .

Styrene acrylic acid copolymers were synthesized and then sulphonated at three different time intervals. Chemical structure was evaluated by FTIR and thermally observed less stability after sulphonation. DSC showed a reduction in Tg transition through sulphonation time as a consequence of higher hydrophilicity. Gamma irradiation induce crosslinking among copolymer chains, enhancing mechanical properties, as evaluated by gel % and complex modulus, with and without sulphonation. However, sulphonated copolymer show lower E* values along with sulphonation time, corroborating the effect of higher hdrophilicity. Further characterization is underway to define sulphonation level effect on irradiation crosslinking mechanism.

REFERENCES

[1] Reyna-Valencia A., Kaliaguine S. and Bousmina M, "Tensile Mechanical Properties of Sulfonated Poly(Ether Ether Ketone) (SPEEK) and BPO 4/SPEEK Membranes", Journal of Applied Polymer Science, vol. 98, pp. 2380 –2393, 2005

[2] Zaidi S. M. J. and Matsuura T., "in Polymer Membranes for Fuel Cells", Springer 2009

[3] Kundu S., Simon L. C., Fowler M. and Grot S., "Mechanical properties of Nafione electrolyte membranes under hydrated conditions",Polymer, vol. 46, pp. 11707–11715, 2005.

[4] Kawano Y., Wang Y., Palmer R. A. and Aubuchon S. R., "Stress-strain curves of Nafion membranes in acid and salt forms Polímeros", vol. 12(2), pp. 96–101, 2002.

[5] Melo L., Benavides R., Martínez G., Da Silva L. and Paula M.M.S., "Degradation reactions during sulphonation of poly(styrene-c o-acrylic acid) used as membranes", Polymer Degradation and Stability, vol. 109, pp. 343-352, 2014.

[6] Proença, M. P. "Desenvolvimento de Membranas Íon-Seletivas com Poliestireno Sulfonado e Polianilina dopada para a aplicação em eletrodiálise. Programa de Pós- graduação em Ciência e Engenharia de Materiais", Universidade Federal do Rio Grande do Sul. Porto Alegre, Tese de Doutorado, 2009.

[7] De Paoli, M.A., Martins, C. R. e Ruggeri, G. “Synthesis in Pilot Plant Scale and Physical Properties of Sulfonated Polystyrene”, Journal of Brazilian Chemical Society, vol. 14, pp 5, 2003.

[8] Knauth, P, “Mechanical properties of proton-conducting sulfonated aromatic polymer membranes: Stress–strain tests and dynamical analysis”, Journal of Power Sources, vol. 195, 2010

[9] Castañeda M.C.G., “Uso de radiaciones ionizantes en formulaciones de PVC rígido para incrementar sus propiedades térmicas”, M.C. Thesis, CIQA. Mexico, 2006.

[10] Moustafa A.B., Mounir, A.A.R., Miligy, M.E. and Mohamed B.A., “E□ect of gamma irradiation on the properties of natural rubber/styrene butadiene rubber blends”., Arabian Journal of Chemistry 2011.

[11] Yasin T., Khan S., Shafiq M. and Gill R., “Radiation crosslinking of styrene–butadiene rubber containing waste tire rubber and polyfunctional monomers”, Radiation Physics and Chemistry, vol. 106, pp. 343–347, 2015.

Estimation of a modular control design for applications in a photovoltaic hydrogen system

J. Olmedo González, R de G. González Huerta
Laboratorio de Electroquímica y Corrosión
ESIQIE-IPN
Mexico City
jolmedog0900@alumno.ipn.mx, rosgonzalez_h@yahoo.com

M. Tufiño Velázquez
Laboratorio de Física Avanzada
ESFM-IPN
Mexico City

Abstract

We live in a world where technology and in consequence the demand of electrical energy is growing up very fast and hydrocarbon resources are the principal way to produce it. However, they have not been good for the environment, for this reason it is so important developing new ways to produce energy. Renewable energy sources such as solar or wind energy are cleaner than hydrocarbons and they could satisfy the demand of energy if energy is administered in a correct way. One of the problems of these primary sources are their natural intermittence and hydrogen could be a good solution for this problem.

In the photovoltaic-hydrogen system studied, photovoltaic modules are used to provide energy for a PEM electrolyser producing hydrogen and oxygen gases through the water electrolysis, gases produced are stored in a variable volume tanks, so they are supplied into a PEM fuel cell to generate electrical energy and also the gases are used for other applications like analyses for electrochemical hydrogen compression.

Having a flexible and efficient control system for hydrogen is really important in order to improve the use of it. In this work is studied the feasibility of a modular control system where the different control devices are separated in a strategic modules allowing to have different ways of connection and applications for the hydrogen produced. It exposed the advantages of this structure of control system in comparison with conventional or rigid control systems.

Keywords— Photovoltaic-Hydrogen System; Hydrogen energy; Control System

I. Introduction

At the present time technology is growing rapidly and society increasingly depends on this, it is very important to innovate in sustainable energy sources in order to satisfy the energy demand, therefore it permits to reduce the emissions of pollutant gases that generate problems for the development of environment.

We have the challenge of the optimal development of primary energy sources such as wind and solar energy, which due to its natural intermittency is necessary to develop ways to correct this problem, in relation to a constant demand of electricity by society.

However, it is so important to understand and take into account that society have to learn the correct manage of electricity consumption in relation to the capacity power generation systems with these characteristics compared with power generation systems that is based in hydrocarbons.

Storing the electrical energy produced by the photovoltaic system (PS) promises to be a solution to the intermittence of the primary source, the sun. It is possible to store this energy as a hydrogen (H_2) using, in this case, a PEM electrolyser (PEME) which produces hydrogen and oxygen (O_2 and H_2) of high purity from electrolysis of the water.

In order to have a feasible process at least H_2 and in some cases like this the O_2 must achieve to be stored safely and efficiently under the predetermined conditions of use by the system, which in the proposed system is at conditions of temperature and pressure of Mexico City.

The main goal of storing energy as H_2 is generating electrical energy with PEM fuel cells (PEMFC), according to a predetermined user demand. This system allows to analyse the production of electrical energy to power a PEMFC for two luminaries. However, the system also allows to evaluate and characterize different PEMFC's and other electrochemical devices (ED), helping this to become friendlier with the environment.

In every energetic system one of the most important things is the efficiency of the process and each equipment involved in this. For this reason primary equipment (PS, PEME, and PEMFC) requires efficient secondary equipment or auxiliary equipment such as the supplying gases control system (SGCS).

Having an efficient SGCS improves the global efficiency and it make more feasible this types of energetic systems. In this work is exposed the importance and the way of design a modular control for supply gases in to the PEMFC or other ED which allows you to use only the equipment and the resources for each specific operation.

II. Experimental

A. Hybrid system (photovoltaic-hydrogen)

The PV-hydrogen hybrid system is designed in order to illuminate a work area with a PEM fuel cell (PEMFC) and for the analysis in a test bench of PEMFC´s or other electrochemical devices (ED) that requires hydrogen and oxygen (H_2 and O_2) in the Sustainable Energies laboratory at Escuela Superior de Ingeniería Química e Industrias Extractivas IPN in Mexico City.

The system is composed for five principal stages. The first step is the generation of electricity by a PS that consists in 6 modules of polycrystalline silicon (rigid panels) of 85 W each one, these modules are connected in a series-parallel arrangement to produce 510 W at optimum sunlight and they are able to generate 2.55KWh/day when the irradiance is 1000W m^{-2}.

The second step is the generation of H_2 and O_2, which are produced with a commercial PEME (Peak Scientific PH300), this device produces H_2 in a range of 30 to 300ml min^{-1} at pressures from 7 kPa to 827 kPa, with consumption of 340W, alternant current (AC).

The third stage is the storage of H_2 and O_2. The storage system (SS) was designed in relation with the demand of the PEMFC for illumination and also for a consistent quantity for ED tests, it is worth noting that the H_2 has the highest energy content per unit of weight, but not per unit volume. This relatively low volumetric energy content is an important scientific and technological challenge for store H_2. It was designed a variable volume system which capacity is 15 l of O_2 and 30l of H_2 at Mexico City conditions (25° C, 585 mmHg).

The fourth step is the use of gases for electrical energy production with a PEMFC or for ED analysis tests. The fifth step consists in the electrical charges energized by the PEMFC which in this case are two LED lamps of 25W each one with a predetermined time interval work.

The five principal steps of the global system are showed in the schematic diagram, figure 1, and described in table 1 where the different connections and lines have been detailed that de global system requires for a correct and safe operation.

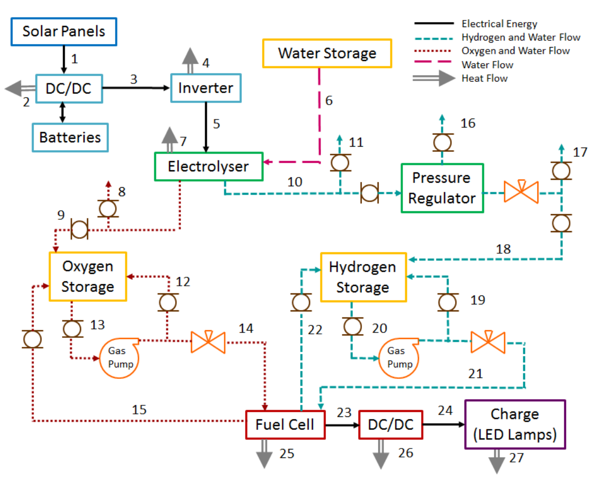

Fig 1. Photovoltaic-hydrogen system schematic diagram

TABLE I. INFORMATION OF PHOTOVOLTAIC-HYDROGEN SYSTEM SCHEMATIC DIAGRAM

Flow	Typology	Flow	Typology	Flow	Typology
1	Electrical Energy	10	H_2	19	H_2 Recirculation
2	Heat Flow	11	Purge	20	H_2
3	Electrical Energy	12	O_2 Recirculation	21	H_2 Regulated
4	Heat Flow	13	O_2	22	H_2 + H_2O Recirculation
5	Electrical Energy	14	O_2 Regulated	23	Electrical Energy
6	H_2O	15	O_2 + H_2O Recirculation	24	Electrical Energy
7	Heat Flow	16	Purge	25	Heat Flow
8	Purge	17	Purge	26	Heat Flow
9	O_2	18	H_2	27	Heat Flow

In colour blue is showed the first step PS, in colour green the second step the PEME, in colour yellow the third step SS, in colour red the fourth step PEMFC and the fifth step in colour purple the charges.

B. *Designing a control system*

The global process requires different control systems in each steps described previously. Some of these steps are commercial equipment such as PS and PEME therefore it is not necessary design a control system or modify them and they are considered rigid control systems, where the energy consumed is constant which is a disadvantage in a hybrid system with hydrogen.

In the step of using H_2 and O_2 is possible to design a control system. It exists several test bench equipment form PEMFC for different capacities that requires considerable electrical energy so it is not feasible this equipment for the proposed applications in this system which has a limited electrical energy.

Designing an efficient supplying gases control system (SGCS) is really important so it is necessary to understand the operating conditions in order to decide which the minimum variables are that the SGCS has to control, reducing the energy consumption.

C. *Operating conditions for hydrogen system*

It is really important that PEMFC or ED work at the correct operating conditions so it is necessary a control system and decide the correct optimal control system is imperative for a correct, safe and efficient operation.

Pressure, temperature, flow rates of H_2 and O_2 and humidity of gases are the principally operating conditions that the control system have to control in a PEMFC and other ED. The SS has the initial parameters (25° C, 585 mmHg, Humidity up to 80% in the tanks), gases are stored in a variable volume tank where the water keep the gases in the tank so gases are in contact with water.

PEMFC operating conditions may change in relation with its power. Typical PEM operating conditions are listed in table 2.

TABLE II. TYPICAL PEM FUEL CELL OPERATING CONDITIONS

Variable	Conditions
Pressure	H2/O2: up to 120kPa
Temperature	50°C to 80°C
Flow Rates	H2: 1 to 1.2 O2: 1.2 to 1.5 Air: 2 to 2.5
Humidity of gases	H2: 0 to 125% O2/air: 0 to 100%

Other ED as electrochemical hydrogen compressors does not work at these conditions but require the control or measure these variables.

It is really important to know initial and desired conditions in order to determinate the way of control. It exist different ways of PEMFC control and it will depend the initial conditions. Most of times H_2 is stored in pressure tanks so it is not required a complex control, but in this case H_2 and O_2 are stored at atmospherically conditions so it is required a more comprehensive control.

It exist three principal modes of reactant supply when H_2 are stored in a pressure tanks and they are showed in figure 2.

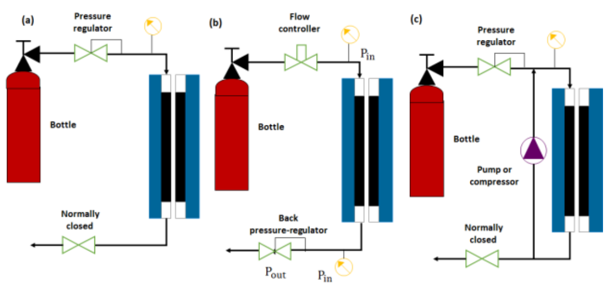

Fig 2. Modes of reactant supply: (a) dead-end mode, (b) flow-through mode, and (c) recirculation mode.

It could seems that in this case is necessary a flow-through mode in relation with initial H_2 pressure, but mode control will depend the type of PEMFC or ED, each mode control has advantages and disadvantages and we have a hydrogen system for producing electricity and for ED tests. We have to remember that SGCS is a hybrid system where it is too important have a flexible control where H_2 and O_2 can be exploited at maximum, increasing the efficacy of the system.

The objective of this project is design a modular control system where H_2 and O_2 can be exploited at maximum for this reason we have to consider different aspects:

- Flexibility of the SGCS (Use of H_2 and O_2 at maximum).
- Have the best efficacy.
- Have a proper control.
- Reduce the energy consumption.
- Have an efficient SGCS

When all variables are controlled is a fact that will have a better performance of the PEMFC's or ED. But it will consumed more energy so it is really important to find a balance between energy consumption and operability. It was developed a diagram where appear the operating conditions of different proposed ED in order to get the proper control system, showed in figure 3.

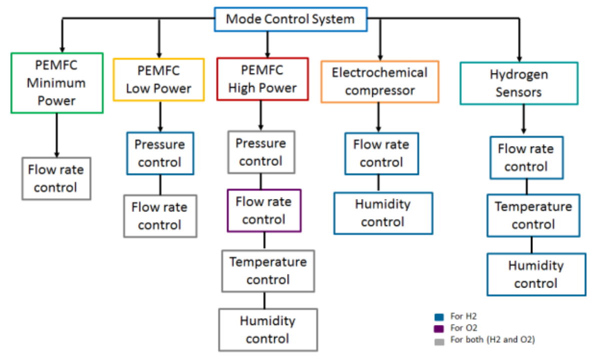

Fig 3. Types of mode control system

The diagram was developed with different information that you can find in the references [3, 4, 5]. It shows the minimum variables that the proposed PEMFC's or ED require for a proper operation. With this diagram it is designed a SGCS for the hybrid system.

III. RESULTS AND DISCUSSION

Taking in consideration different aspects that SGCS has to satisfy it was developed a table where they are shown the principal PEMF's and ED that the SGCS will have to control.

TABLE III. PRINCIPAL PEMFC'S AND ED

PEMFC / ED	Characteristics
PEMFC minimum power	0.3-10W
PEMFC low power	10-100W
PEMFC for Illumination	**55W**
PEMFC high power	none
Electrochemical hydrogen compressor	Low capacity of compression
Hydrogen sensors	Electrochemical Catalytic (Low pressure)

SGCS was designed in relation with the principal PEMFC's and ED that the system will have to control for this reason the SGCS just control pressure and flow rate and measure temperature. It was found that the humidity control is not necessary but some ED require low humidity for these reason it is used a desiccant column so energy consumption is not affected.

The SGCS can control operating conditions for general tests of PEMFC and ED such as characterization curves and the operating conditions for the PEMFC for illumination. In figure 4 appears the structure of the SGCS.

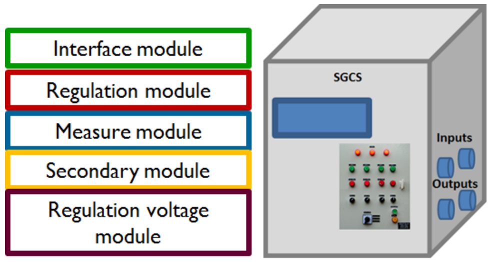

Fig 4. SGCS Structure

It is designed a SGCS named modular control system due to is a flexible control system and it allow you to use only the required devices for specific operations. Each module of the SGCS have their own source power that is connected with the PS batteries. The SGCS just can measure and the regulation module can be disconnected saving energy.

It is really important to understand that some modules cannot function if other modules are not connected, for example if we want an automatic control for a PEMFC for illumination the regulation mode requires measure module and the regulation voltage module.

The aim of SGCS is suppling gases in to the PEMFC or other ED in a specific conditions of pressure and flow rate. The SGCS is composed by a pump that operates in a rage voltage from 5 to 12V and it is used when the storage system is not able to satisfy the selected flow or pressure (depending the mode of control). The system also has an electromechanical valve that control the flow gases, the advantage of this valve between solenoid valves is that requires less energy and the energy consumption is not continual. In figure 5 is shown the principal primary elements and finally elements of control.

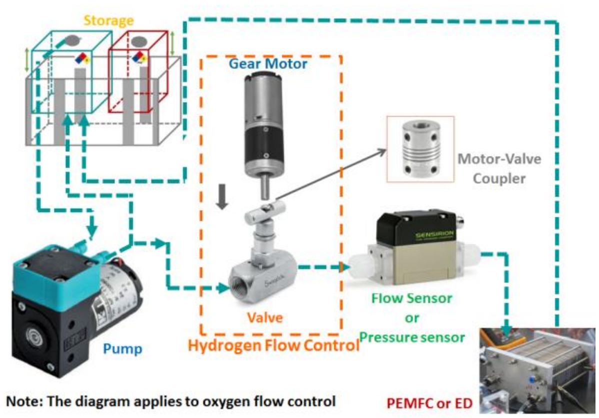

Fig 5. SGCS Schematic diagram

The SGCS is able to operate in a manual or automatic mode. For automatic mode it was developed a closed loop control or feedback control system, this type of control consists in a system that maintains a prescribed relationship between the output and the reference input by comparing them and using the difference as a means of control. In a closed-loop control system the actuating error signal, which is the difference between the input signal and the output signal, is fed to the controller so as to reduce the error and bring the output.

The SGCS energy consumption when all modules are working is estimated in 30Wh. When the system is working with the PEMFC for illumination shown in figure 6.

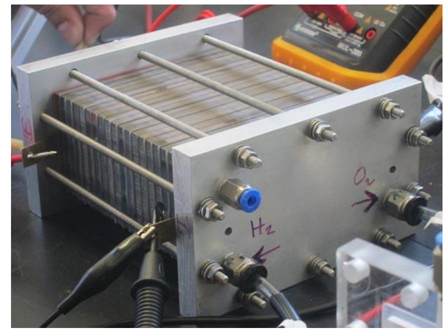

Fig 6. PEMFC for illumination

The energy useful will be calculated with the equation 1 when the energy for the SGCS is from the energy produced for the PEMFC.

$$E_U = E_G - E_{SGCS} \quad (1)$$

Where E_u is the useful energy, E_G is the energy generated by the PEMFC and E_{SGCS} is the energy consumed for the SGCS.

It important to mention that the auxiliary energy or the energy for the SGCS usually come from a battery charged by the PS in order to save H_2 and have a longer time for illumination, in this case the energy useful for the PS is calculated with the equation 2.

$$E_{UPS} = E_{PS} - E_E - E_{AE} - E_{SGCS} \quad (2)$$

Where E_{ups} is the useful energy for the PS, E_{PS} is the energy produced by the PS, E_E is the energy required for water electrolysis to producing H2 and O2 (PEME), E_{AE} is the auxiliary energy required for the PEME and E_{SGCS} is the energy consumed for the SGCS.

In these equations we can see the importance of the efficiency and the energy consumption of the auxiliary equipment or control systems as the SGC and we have to consider in the PS design.

IV. Conclusions

1. Solar-hydrogen-fuel cell technology has an impact on the global energy international scenery. Note further that since the development of hydrogen system is a continuous effort, demonstrative hydrogen system may contribute to improving the role of hydrogen in society. Ignoring the existence of public support and acceptance would definitely lead to a misleading policy towards “green” solar hydrogen planning and its

infrastructure management. Then, experience indicates that greater knowledge about renewables energies and hydrogen system can imply higher political, social and research support. Therefore, with better understanding, imply greater attitude to support a sustainable environment and hydrogen technology, which can consistently involve greater support for the applications of hydrogen and hybrid systems.

2. Design efficient equipment is not enough in order to have an efficient PS-H_2 system, it is really important have an efficient controls systems and auxiliary equipment.
3. It is really important to study and design the correct control in relation with the operation and operating conditions.
4. Modular control improve the efficiency and pretend to reduce the capacity of the PS.
5. It is important to use all the H_2 and O_2 in order to improve the efficacy in the system.
6. Hydrogen technologies only will can have successful growth if we design efficient and intelligent processes.

Acknowledgment

This work has been supported by multidisciplinary project IPN-SIP 1683 (2015-2016).

References

[1] A.Creus, Instrumentation Industrial, 8th ed ., Alfaomega; Mexico, 2011

[2] Birol,F., Cozzi, L., Dorner,D y Gül, T. Energy Climate and Change World Energy Outlook Special Report. International Energy Agency; 2015

[3] Corbo P, Migliardini F, Veneri O. Hydrogen Fuel Cell for Road Vehicles. 1st ed. London: Springer-Verlag; 2011.

[4] F.Barbir, PEM Fuel Cells, Theory and Practice, 2nd ed; Elsevier, Inc; USA; 2013

[5] Hoogers G. Fuell Cell Techonology, Handbook. 1st ed. USA: CRC Press LLC; 2003

[6] K.Ogata, Ingeniería de Control Moderna, 5th ed; Pearson Education; Madrid; 2010

[7] G. Bessarabov,H. Wang, H. Li, and N. Zhao, "PEM electrolysis for hidrogen production principles and aplications," Taylor and Francis group 2016, pp. 269–279.

[8] M.Aguer,A.Miranda, El Hidrógeno, Fundamento de un futuro equilibrado, 1st ed; Ediciones Díaz de Santos; España; 2005

[9] PH User Manual, PEAK Scientific, Scotland., 2011

[10] Sanchez, V.M., Chavez-Ramirez, A.U., Duron Torres, S.M., Hernandez, J., Arriaga, L.G., Ramirez, J.M. (2014). Techno-economical optimization based on swarm intelligence algorithm for a stand-alone wind-photovoltaic-hydrogen power system at south-east region of Mexico, International Journal of Hydrogen Energy, 39 (2014). 16646-6655.

[11] Santarelli, M., Calì,M., Macagno, S. (2004). Design and analysis of stand-alone hydrogen energy systems with different renewable sources. International Association for Hydrogen Energy, 29, 1571 – 1586. doi:10.1016/j.ijhydene.2004.01.014

Sulfonated polystyrene-co-acrylic acid membranes modified by Transmembrane Reduction of platinum.

L. Melo, R. Benavides, G. Martínez, D. Morales-Acosta
Centro de Investigación en Química Aplicada
Enrique Reyna 140, Saltillo, Coah. México.City
e-mail: roberto.benavides@ciqa.edu.mx

Abstract *— The aim of this work is to simplify the process to obtain metal-polymer composite membranes, useful in fuel cells. This was achieved by using the transmembrane reduction method or Takenaka-Torikai method, which was carried out in a device consisting of a cell with two separated compartments by the ion exchange membrane to be modified. One compartment contains the metal precursor solution (H_2PtCl_6) and the other contains the reductor agent solution ($NaBH_4$); once the reductor has diffused through the membrane, it reduces the metal ions found on the other side resulting in metallic platinum particles. Membranes were prepared from copolymers of polystyrene-co-acrylic acid synthesized and sulfonated previously. Once carried out the reduction process, membranes were analyzed by X-ray diffraction (XRD) and scanning electron microscopy (SEM) to determine the nature of the platinum particles formed. XRD results indicated the presence of crystalline metallic platinum with FCC structure, while SEM results showed that the platinum was formed basically on the surface of the membranes, not in the body. The amount of platinum incorporated in each membrane was quantified by plasma emission spectroscopy after acid digestion, yielding platinum concentrations from 0.0243 to 0.3561 mg/cm^2. With these results we can conclude that the Transmembrane Reduction method is effective with the sulfonated polystyrene-co-acrylic acid membranes, is possible to take advantage of the existence of carboxylic and sulfonic groups that could interact with platinum ions, before being reduced to metallic platinum particles on the membrane surface.*

Keywords *— Transmembrane Reduction of Pt; sulfonated polystyrene-co-acrylic acid; fuel cells.*

I. INTRODUCTION

The main component of a fuel cell is the membrane assembly electrode (MEA) which is made up of the gas diffusion layers, the proton exchange membrane and the catalysts which are located on its sides, is in the latter where electrochemical reactions are carried out[1,2].

The MEA can have two basic configurations, one where the catalyst (supported on a porous material) is incorporated in form of catalytic ink on the carbon cloth or paper that, behaving as gas diffusion layer. The other alternative is the incorporation of the catalyst directly on the membrane with a brush, a roller or by printing or spraying the catalyst ink on the membrane [3,4]. The catalyst ink must be a uniform suspension that generally is prepared by dispersing by ultrasonication of a catalyst in a mixture of solvent and a polymeric ionomer, behaving as adhesive, and usually is a Nafion solution. The optimized use of the catalyst is achieved by improving the triple phase boundary (TPB). The latter is the point where the catalyst particles, the proton conducting polymer and the diffusion path reagent match [1,5,6]. Optimization of TPB involves several factors, for example, using small amount of Nafion makes insufficient ionic conductivity of the catalyst layer (generating inactive catalyst), but if too much Nafion is used it can cover the entire surface of the catalyst and/or its support, avoiding for the gas to access the surface of the catalyst, inhibiting its function [3]. To maximize the contact of the catalyst with the ion-conducting polymer, the catalyst particles can be incorporated directly on the membrane by the Takenaka-Torikai method [7]. This method is also known as transmembrane reduction [8], making possible the formation and incorporation of the catalysts metal particles directly on the membrane in one step.

The incorporation of catalyst particles directly on a membrane has application in the field of fuel cells [9,10], in the electrocatalytic synthesis [11-13], in the generation of hydrogen and oxygen gas [14] for ozone generators [15], water purification systems [16] and sensors [17,18]. Therefore, depending of the desired reaction to catalyze and the chemical environment where the catalyst particles will be exposed, the precursor metal used for synthesis is decided.

For fuel cell of proton exchange membrane, type PEMFC or DMFC, the metal particles should catalyze oxidation reactions of the fuel (methanol or hydrogen) and oxygen reduction. In the case of the PEMFC, there are reports of experimental and theoretical results for catalysts used for reactions occurring at the anode and cathode. The most important are those from Nørskov [19] and Greeley [20], involving computer calculations to study pure metals (Ag, As, Au, Bi, Cd, Co, Cu, Fe, Ir, Mo, Ni , Pd, Pt, Re, Rh, Ru, Sb, and W) and some alloys. From these studies, theoretical models were obtained predicting the relationship between the reaction rate of the catalyst and the reagent adsorption and desorption energy of products.

Through these models was found that when the reagent binds strongly to the metal surface or alloy, its catalytic activity is very high at the beginning, but because the reaction products are also strongly adsorbed to the catalyst, they are not removed from the surface so quickly, decreasing the catalyst activity. Otherwise, when the binding energy of the reactant with the catalyst is very weak, it approaches and is adsorbed weakly to the catalyst, but without reacting; so the catalyst activity would be low from the beginning. Among the aforementioned metals, Nørskov and Greeley determined that Pt is the pure metal that keeps the best balance between the reaction rate of the catalyst and the reagent adsorption energy for both: oxygen [19] and hydrogen [20]. However, there is a difference between the oxygen reduction reaction and the hydrogen oxidation reaction when using the same catalyst [3].

In the DMFC the main reaction is the oxidation of methanol, and Pt is a good catalyst for this reaction; however, it is usually quickly poisoned by the strong adsorption of CO on its surface. One way to overcome this disadvantage is to use a second metal as a co-catalyst which is capable of forming species metal-OH that acting as a source of oxygen, which is necessary for the adsorbed CO is oxidized to carbon dioxide, resulting in the release of the active sites on the surface of Pt [21-23].

Platinum is ideal for a membrane in a PEMFC fuel cell type, compared to DMFC type. However, for this work were selected a salt of Pt for modifying the membranes of sulfonated polystyrene-co-acrylic acid, expecting that the results open the field of view of the feasibility of the incorporation of catalytic nanoparticles formed in situ by the transmembrane reduction method.

II. Materials

Styrene (St, 99%, Aldrich) was purified with NaOH, dried with CaCl2 and distilled at reduced pressure. Phenothiazine was added to the acrylic acid (AA, 99%, Aldrich) and distilled at reduced pressure. Benzoyl peroxide (BPO) as initiator. Nafion 117 membrane (Aldrich), H2SO4 (J.T.Baker), chlorihidric acid 36.5-38% (Sigma Aldrich), Nitric acid 70% (CTR Scientific), Silver Nitrate ≥99.0% (CTR Scientific), Sodium chloride (J.T. Baker), sodium hidroxide (Aldrich), inhibitor free tetrahydrofuran ≥99.9% (THF, Aldrich), dimethylsulfoxide ≥99.5% (DMSO, Sigma Aldrich) and anhydride dichloromethane ≥99.8% (Aldrich). Trimethylol propane trimethacrylate (TMPTMA, Aldrich) and Divinyl benzene (DVB, Aldrich) as crosslinking agents.

III. Methods

A. *Polymerization procedure*

Two partially crosslinked copolymers of poly(styrene-co-acrylic acid) (PS-co-AA) were previously synthesized. The reactions were carried out by free radical polymerization in solution, using diethylbenzene as solvent. Employing 0.045 % mol of BPO as radical initiator and 0.25 % mol of crosslinking agent to improve mechanical resistance of the copolymers (divinylbenzene – DVB – or trimethylol propane trimethacrylate –TMPTMA–). The random PS-PAA copolymer D (crosslinked with DVB) exhibits a Mn = 68,012, Mw = 259,095, and the random PS-PAA copolymer T (crosslinked with TMPTMA) presents a Mn = 54,068, Mw = 302,607.

B. *Sulfonation procedure*

D and T copolymers were sulphonated with sulfuric acid (H_2SO_4 = 170% mol) and silver sulfate (Ag_2SO_4 = 0.110% mol). Each copolymer was dissolved under a nitrogen atmosphere at 200 rpm and 40 °C by 40 min in a mixture of dichloromethane and acetic acid. The Ag_2SO_4 was dissolved in the H_2SO_4 and subsequently added to the dissolved copolymer. The sulphonation reaction was left to proceed during 2 or 4 h (for T and D copolymer respectively). The reactions were ended removing the solvent and adding cold distilled water. The sulfonated copolymers were washed with distilled water until reaching the pH ≈ 7. The sulfonated copolymers were dried with room temperature airstream by 48 hours and subsequently at reduced pressure at 40 °C by 72 h.

C. *Casting procedures*

Three different membranes were prepared by casting with each sulfonated copolymer, employing a specific solvent or solvent mixture. The copolymer/solvent/dimension membrane ratio was 0.4g/2mL/16cm^2. The compositions of the solvent or solvent mixture were: THF, THF + DMSO (55% weight) and THF + 110% DMSO. Solvent volatilization proceeded at room temperature during 7 days.

D. *Membrane purification and activation*

After unmolded, the membranes were immersed in distilled water by two days, changing the water each 4 h to eliminate the DMSO. Subsequently the membranes were activated, immersing them in HNO_3 0.5 M (24 h), afterward in H_2O_2 5 %v at 80 °C (1 h), in H_2SO_4 0.5 M at 80 °C (1 h) and in distilled water at 80 °C (1 h).

E. *Deposition of metallic platinum on PEM*

The deposition of metallic Pt on PEM was achieved by reduction of platinum ions using $NaBH_4$ as reductor agent according to the technique known as the Takenaka–Torikai method [6]. According to this method, one surface of a PEM is in contact with a chemical reducing agent, while the other surface is in contact with the metal-ion solution (H_2PtCl_6), this method does not involve the use of a binder. The agent reduces the metal-ion solution to form a metal layer on the membrane surface, which occurs when the agent diffuses through it and encounters the metal-ion solution [7].

Once the membrane was set in the device, 15 mL of the metal-ion solution (3.33 mM) were added in the lower compartment, and left in contact by 30 min. Then, in the upper compartment 50 mL of fresh solution of NaBH4 (100 mM) were added and left in contact by 3 h to allow the reductor diffuse across the membrane by an effective area of 6.7886 cm^2. Bubbles were formed during the reaction and accumulated on the surface of the membrane, so the system was stirred every 15 min during the course of the reaction.

After 3 h, the solutions and membrane were removed from the device; the membrane was rinsed with distilled water, then soaked at ambient temperature in 0.5 M H_2SO_4 for 2 h, subsequently in distilled water by 1 h and finally dried at 80 °C under reduced pressure.

IV. CHARACTERIZATION

A. *X Ray diffraction*

Structural properties of the platinum particles were analyzed by XRD using a Siemens D5000 powder diffractometer (Cu-Kα radiation), scanning 2θ = 15° to 80°, (step size of 0.06°), and tube conditions of 35 kV and 25 mA.

B. *Platinum quantification by Plasma Emission Spectrometry*

To quantify the metallic platinum incorporated, the membranes were dried at 100 °C by 1 h and then they let to cool into a desiccator. After that, the membrane-platinum zones were cut and sized to calculate the area dimension. Acid digestions were performed with each membrane-platinum zone to obtain the platinum ions solutions that were analyzed with a Thermo Jarrell Ash IRIS Advantage Plasma Emission Spectrometer.

Acid digestion was carried out by putting the membrane in a glass with 2 mL H_2SO_4 98%, heating the solution until it turns transparent. Once solution cool down, 1 mL HNO_3 70% and 3 mL HCl 36.5-38 % were added, stirred and heated just to dryness and let the glass to cool. 1 mL HCl 36.5-38 % and 15 mg NaCl were added, heated and evaporated to dryness. Finally, 3 mL HCl 36.5-38 % and 15 mL of desionizated water were added to obtain a solution, that was passed by a Whatman 42 filter paper and completed the volume of the solution to 50 mL with deionized water [23, 24].

The amount of platinum reduced on each membrane were calculated employing the equation (1)

$$Platinun\ on\ the\ membrane\ (mg/cm^2) = \frac{C * 0.05\ L}{área\ de\ la\ membrana\ digerida\ (cm^2)} \quad (1)$$

Where C is the concentration of platinum determined by Plasma Emission Spectrometry in ppm (mg/L). 0.05 L is the total volume of the platinum ions solution prepared by acid digestion.

If all the platinum present in the 15 mL of the H2PtCl6 3.33 mM solution had been reduced and incorporated into the effective surface of the membrane (6.7886 cm2), would be obtained 100% of metal incorporation using the molecular mass of platinum and equation (2).

$$100\%\ Pt\ incorporation\ (mg/cm^2) = \left(0.00333\frac{mol\ Pt}{L}\right)\left(\frac{0.015\ L}{6.7886\ cm^2}\right)\left(195080\frac{mg\ Pt}{mol\ Pt}\right) = 1.4353\ mg/cm^2 \quad (2)$$

Once the 100% platinum concentration is known (1.4352 mg/cm2), it was possible to correlate with the real platinum concentracion incorporated in each membrane

C. Ion-exchange capacity (IEC) and water uptake (U) for membranes

Ion-exchange capacities were measured using a titration method. The cation-exchange membrane was soaked in 1 M HCl solution for 24 h. After washing with deionized water they were immersed into 1 M NaCl solution for 24 hours. The number of displaced protons from the membrane were determined by titration of the NaCl solution with a NaOH 0.005 M solution using a pH-meter.

The membranes were then soaked in 1 M HCl solution for 24 h or more. After that, the membrane was washed with deionized water and the water on the surface was wiped off with tissue paper to measure the wet weight of membrane (W_{wet}). Finally the membranes were placed in an oven at 44 °C for 24 h and then the weight of the dry membrane was measured (W_{dry}). The percentage of water absorption was calculated by differences between dry/wet weights.

The IEC and water uptake (U) of membranes were calculated using ec. (3) [25, 26] and ec. (4) [27, 28].

$$IEC = \frac{ab}{W_{dry}} \quad (3)$$

$$U\ (\%_{mass}) = \frac{(W_{wet} - W_{dry})}{W_{dry}} x100 \quad (4)$$

Where a is the concentration of the NaOH solution (mmol/mL ~ meq/mL), b is the volume of NaOH solution used (mL), Wdry is the dry weight of the membrane (g) and Wwet is the wet weight of the membrane (g).

D. Morphology of the membranes

Morphology surface topography of the membranes was observed using scanning electron microscopy (SEM) JEOL JSM-7401F at 3 kV with a working distance of 5.7 mm.

V. Results and Discussion

A. UV-VIS

The transmembrane reduction or Takenaka-Torikai method consists in the diffusion of the reductor through the membrane to the compartment containing the precursor metal solution, once the reagents come into contact happens the reduction of the metallic ions originating the metallic particles. When $NaBH_4$ is used, it must react with H_2O to generate $H_{2(g)}$ that acts as a reducing agent, which must diffuse and cross the membrane to react with ions at the platinum solution of H_2PtCl_6. The reduction of the ions to metallic platinum can be evidenced by UV-VIS spectrometry, following the intensity of the bands of the $PtCl_6^{2-}$ ions (260 nm [29]) and Pt^{2+} (220 nm [30]) present in the aqueous solution of H_2PtCl_6. Figure 1 show the spectra of solutions of H_2PtCl_6 before and after each experiment performed with membranes of the sulfonated copolymers D and T.

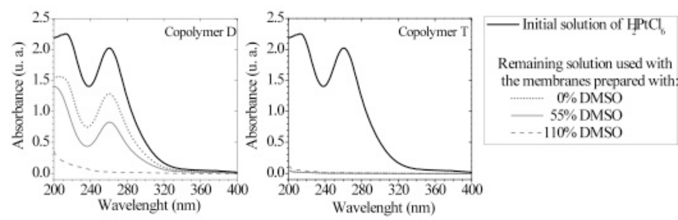

Figure 1. UV-Vis spectra of H_2PtCl_6 solutions before and after their use in the process of Transmembrane Reduction.

Figure 1 shows that using the membranes prepared with THF-DMSO and the copolymer D, the intensity of the bands of metal ions is lower than the signal intensity of the solution used with the membrane of copolymer D prepared in THF. This difference indicates that the diffusion of $H_{2(g)}$ through the membrane of the copolymer D prepared with THF-DMSO mixture is more efficient compared to the diffusion through the membrane prepared with pure THF.

By comparing the spectra of solutions of H_2PtCl_6 employed with the three membranes of copolymer T, the signals corresponding to the metal ions are not observed, which indicates that by using any of these membranes diffusion of $H_{2(g)}$ happens and thereby the total reduction of the ions. The difference in bands intensities, and/or the absence, indicates that the $H_{2(g)}$ diffuses faster through the membranes of the copolymer T compared to membranes of the copolymer D, which may be related to the crosslinking agent. TMPTMA has the characteristic of generating polymers with higher porosity comparing with DVB membranes [31]; even using the same amount of crosslinking agent in the synthesis of both copolymers.

B. *X ray diffraction*

To know the structural nature of the platinum particles formed on the surface of the membrane exposed to Takenaka-Torikai process, the membranes were analyzed by X-ray diffraction. The diffraction patterns obtained are shown Figure 2 .

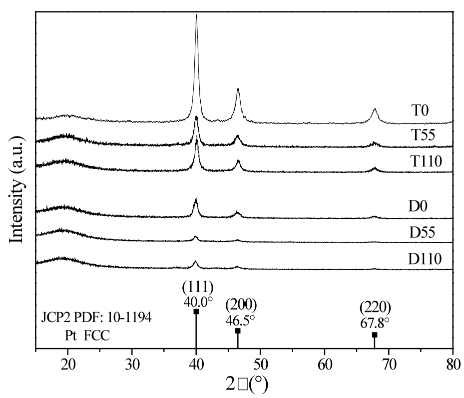

Figure 2. X ray diffraction patterns of the PSS-PAA membranes exposed to the reduction transmembrane process

Signals located at 40.1, 46.6 and 67.8 ° on 2θ scale seen in Figure 2 coincide in position and intensity (relative intensity of 100, 30 and 16) with face cubic centered platinum crystalline structure. Crystallographic planes are (111), (200) and (220) (PDF: 10-1194) reported on the basis of data JCP2. Additionally to the corresponding metal signals, there is a signal at ~ 20 ° of the 2θ scale, this signal may correspond to the Van der Waals interaction forces between styrenic rings [32, 33]. This signal is expected since the main component of the copolymers is styrene (more than 90 % mol), whereby the interaction in the copolymer should be similar to that of pure polystyrene.

Similar to existing reports for Nafion membranes modified by using the Takenaka-Torikai method [16, 34-39], these results confirm that the method is effective for the formation of crystalline metallic platinum particles onto sulfonated PS-co-AA membranes. The advantage of using this method is the use of the precursor metal salt and the reductor agent only, without an additional support for the synthesis of the platinum particles: the particles are formed and incorporated on the membrane in one step. Furthermore, in a PEM the proton conductivity could be favored, the metal particles that act as catalyst layer, and if they are located directly on the proton exchange membrane must facilitate direct contact [2]. Another advantage of using this method is that the lack of an adhesive (usually Nafion solution) for incorporation of particles on the membrane, improving triple phase boundary and avoiding the need of a different polymer, as Nafion.

C. *Quantification of platinum on the membrane by plasma emission spectroscopy*

To quantify the metallic platinum incorporated on the surface of the membranes of sulfonated copolymers D and T, Plasma emission spectrometry was used, so it was necessary to carry out the acid digestion of the areas of the membranes with platinum deposits. Figure 3 shows the appearance of the membranes before and after incorporating the metal, and is indicated by dashed circles the approximate area that was used to carry out the acid digestion.

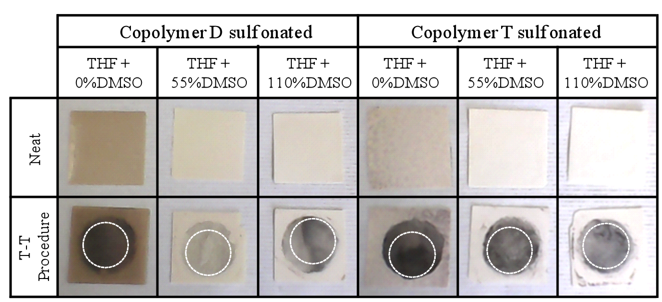

Figure 3. Membranes of sulfonated copolymers D and T before and after incorporation of the metal by transmembrane reduction.

The interaction between positive ions of platinum and sulphonic groups has been reported previously by Waje et al [40]. They reported the deposition of platinum nanoparticles on carbon nanotubes functionalized with sulphonic groups. The acid groups improve the uniformity of platinum particles deposition on the surface of the nanotubes. With the method Takenaka-Torikai the salt $PtCl_6H_2$ was used. The aqueous solution of this salt generates the ions Pt^{2+} and $PtCl_6^{2-}$ (observed by UV-Vis spectroscopy), so it would be expected that the carboxyl groups and sulphonic from the membranes could act as chelators for the ions Pt^{2+}. However, since the complex ion $PtCl_6^{2-}$ has the same charge than the acid groups, when their protons are solvated, hence the importance of verification and quantification of the incorporation of metallic platinum on the membranes.

Table I shows that the percentages of platinum incorporated on our membranes are relative low, comparing with the amount of platinum pretended to incorporate in the membranes (1.4353 mg/cm^2). These percentages could be originated because the $PtCl_6^{2-}$ ions have the same charge as the COO^- and SO_3^- groups, so probably they create metallic platinum far away from the surface of the membranes, in the aqueous solution. This is the reason for UV-VIS results, where a decrease or even absence of the signals corresponding to the metal ions in the solutions was observed for both membranes of the copolymers D and T.

TABLE I. PLATINUM INCORPORATED BY TRANSMEMBRANE REDUCTION PROCEDURE

Membrane	*Platinum (mg/cm2)*	*Platinum (%)*
D0	0.1449	10.1
D55	0.0243	1.7
D110	0.0765	5.3
T0	0.3561	24.8
T55	0.1160	8.1
T110	0.0914	6.4

Although platinum concentrations are low compared to 100% expected (from 0.0243 to 0.3561 mg/cm^2), they are within the values needed in a fuel cell, taking into account that there is a trend to reduce the amount of platinum and that exciting results has been obtained with amounts of 0.1 mg/cm^2 [41].

D. *Scanning Electron Microscopy*

After confirmation and quantification of metallic platinum on the membranes by X-Ray Diffraction and Plasma Emission Spectrometry, characterization was carried out with Scanning Electron microscopy on the surface after cryogenic fracture of the membranes, before and after being exposed to the transmembrane reduction process (Figures 4 and 5).

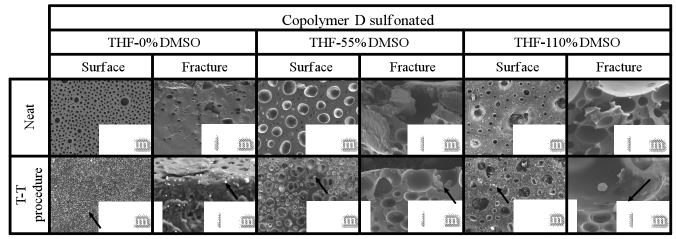

Figure 4. Membranes of the copolymer D before and after the reduction transmembrane process

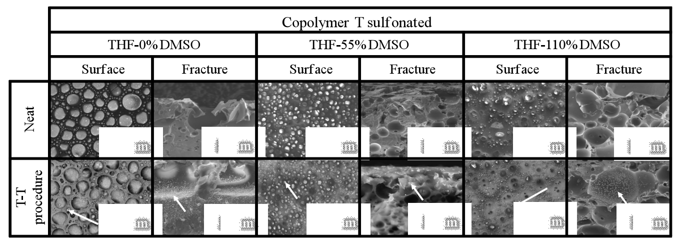

Figure 5. Membranes of the copolymer T before and after the reduction transmembrane process.

Figure 4 shows that the membranes of the sulfonated copolymer D promote the formation of metallic particles of sizes ranging from 1 to 10 µm without good dispersion. Compared to these, formed particles in the membranes of the sulfonated copolymer T (Figure 5), with sizes ranging 100 to 900 nm are better dispersed. This difference of size and dispersion of the particles is related with the more acidic groups of sulfonated copolymer T, compared with the ones from sulfonated copolymer D. The latter must be reflected in the values of ion exchange capacity. It has been reported that the interaction of platinum ions with sulphonic groups allows the formation of metallic platinum particles without aggregation and improved size uniformity [40]. It is also known that the carboxylic groups interact with metal ions as well, before being reduced to form metal nanoparticles [41].

E. *Water uptake (WU)*

The water uptake capacity of the membranes were evaluated before and after to Takenaka-Torikai process procedure, the values obtained are shown in Table II.

TABLE II. THICKNESS AND WATER UPTAKE OF THE MEMBRANES BEFORE AND AFTER MODIFICATION BY THE REDUCTION TRANSMEMBRANE PROCESS

Membrane	*Thickness (mm)*	*Water uptake (% w)*		*Reduction of the water uptake by the presence of platinum (%)*
		Without platinum	*With platinum*	
D0	0.157±0.039	15.2210	15.0673	0.1537
D55	0.207±0.063	64.9186	64.3408	0.5778
D110	0.275±0.057	105.1197	104.4259	0.6938
T0	0.196±0.024	14.9514	14.2666	0.6848
T55	0.205±0.070	83.5415	81.4613	2.0802
T110	0.238±0.080	139.8289	137.0323	2.7966

Values in Table 2 shows that the treatment carried out and/or the presence of platinum on the surface of the membranes reduced the water uptake capacity, however the difference does not exceed 3%. These results may be related to the structure adopted by the membranes prepared with the sulfonated copolymers D and T during casting. SEM results indicated that the presence of DMSO generates pores or cavities in the membranes; particularly higher amount of DMSO induced larger pore formation. Furthermore, including DMSO in the solvent mixture generates thicker membranes (Table 2), even though all were prepared using the same copolymer/solvent/mold area ratio. This difference in thickness is due to the volume occupied by the DMSO, which remained longer in the membranes while THF is volatilized (it was extracted later).

Figure 6 depicts how the use of DMSO during the membranes preparation generates pores inside through a DMSO remaining and a breath mechanism.

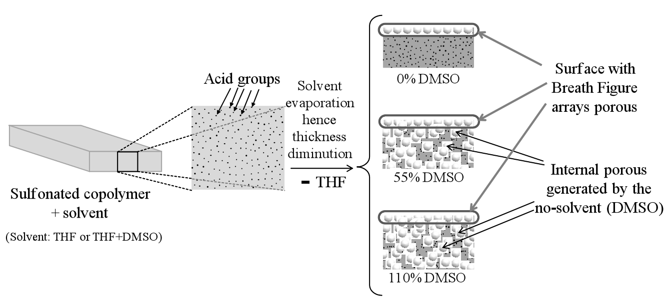

Figure 6. Formation of pores and thickness difference in the membranes because of use of a non-solvent during casting process.

Breath Figure is important since, even in the membranes in which there is no DMSO, pores exist on the surface. Breath Figure is the mechanism where pores are formed by the moisture condensed on it, due to cooling caused by the solvent volatilization (in this case THF). Such a mechanism has been widely studied and explained by Zhang [42] and Escalé [43].

F. *Ionic exchange capacity (IEC)*

Continuing the evaluation of the effect of the platinum incorporation on the membrane, the ion exchange capacity of the sulfonated copolymers D and T membranes, were evaluated before and after being subjected to the process of transmembrane reduction with H_2PtCl_6 and $NaBH_4$, the values obtained are shown in Table III.

TABLE III. ION EXCHANGE CAPACITY OF THE MEMBRANES BEFORE AND AFTER BEING MODIFIED BY THE TRANSMEMBRANE REDUCTION PROCESS.

Membrane	*IEC (meq/g)*		*IEC reduction by the presence of platinum (%)*
	Without platinum	*With platinum*	
D0	0.1436	0.1242	13.51
D55	0.4231	0.4150	1.91
D110	0.5524	0.5434	1.63
T0	0.0783	0.0654	16.47
T55	0.6525	0.6219	4.72
T110	0.9030	0.8844	2.06

Results show a decrease in ion exchange capacity after the addition of platinum on the membranes, especially in membranes prepared only with THF during casting. The latter correspond with the membranes with higher content of platinum on its surface (see Table I), suggesting they are more clogged, and thus the accessibility of the protons is decreased. Figure 7 depicts the effect generated by the pore presence in membranes thickness, water uptake, ionic exchange capacity, and the ratio of these results with the presence of platinum particles on the surface of the membranes.

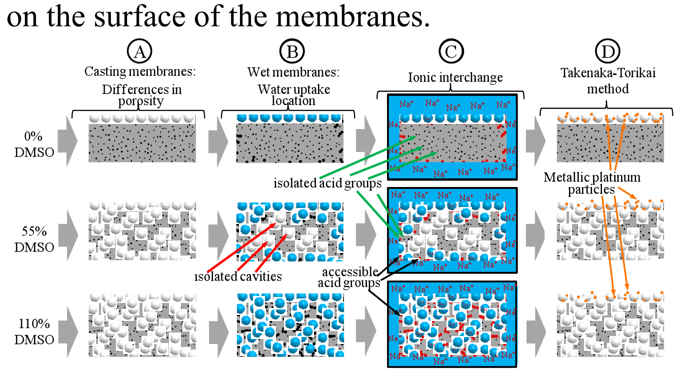

Figure 7. Effect of pores and platinum particles in thickness, water uptake and IEC of the membranes.

Figure 7A represents a possible explanation for the difference in thickness and porosity of the membranes prepared using the same technique and methodology, just varying the composition of the solvent employed. During evaluation of water uptake, change of the weight of the membranes due to absorption of water is compared. The acid groups of the copolymer in the membrane confer their hydrophilicity, however weight change of mass may be attributed to the location of the water within the pores.

Figure 7B show in colored regions the pores that are interconnected from the surface to the body of the membrane. This interconnection may be due to the closeness of pores (direct contact) or through ionic groups (represented with black dots). The more close are the pores more likely to be interconnected, resulting in values of water uptake higher for membranes prepared with THF + DMSO (up to 139.8%, Table II). Once platinum is formed and deposited on the surface of the membranes, the metal does not represent a barrier to the passage of water into its interior. This is the reason for a variation in water uptake of only 2.79% in most cases.

Analyzing the IEC values of the membranes without and with platinum, the most notable decreases are 13.51% and 16.47% (Table III), corresponding to the membranes prepared with the copolymers D and T, with only THF, respectively. This difference is a result of the ionic exchange capacity occurring only between the acid groups of the copolymer and the aqueous saline solution (NaCl). The acidic groups to which the NaCl solution has access are located on the surface of the membranes, so if part of the surface is partially covered by the platinum particles, maybe some of these acid groups are blocked. This effect is not as clear for the membranes having interconnected pores (prepared with THF-DMSO). For this case Na^+ ions can diffuse through the pores into the membrane and have access to the acidic groups located on the inner walls of the pores, exchanging the protons of sulfonic and carboxylic acid groups. The latter results in less variation of IEC between neat membranes and those containing platinum (Figure 7C).

VI. CONCLUSIONS

UV-VIS spectrometry from ions $PtCl_6^{2-}$ and Pt^{2+} from the solutions of H_2PtCl_6 employed in the experiments, corroborated that the membranes of sulfonated polystyrene-co-acrylic acid allow the reductor ($H_{2(g)}$) to diffuse through them. The results of XRD indicated that the platinum formed on the surface of the membranes is crystalline with FCC type structure. The quantification with emission spectrometry plasma indicated that the maximum amount of platinum formed on the membranes of sulfonated copolymer D is 0.1449 mg/cm^2, whereas for the sulfonated copolymer T is of 0.3561 mg/cm^2. The difference in amount of platinum formed on the membranes is possibly related to the amount and acid groups containing each copolymer, as IEC values suggest. It was also observed that the copolymer with greater amount of sulfonated acid groups, copolymer T, generates a better dispersion and lower platinum particle size (100 to 900 nm) on membranes, compared to particles formed in membranes D (1 to 10 μm). Finally, the results of water uptake and IEC indicated that the presence of platinum on the surface of the membrane does not interfere with the process of water uptake, because most of the water retained is located in the pores of the membranes. However, IEC values of membranes are reduced after the Takenaka-Torikar treatment. Eventhough, despite such decrease, the Takenaka-Torikai is a viable method for incorporating metallic platinum particles on the surface of membranes prepared with copolymers of sulfonated polystyrene-co-acrylic acid.

ACKNOWLEDGMENT

The authors would like to thank M.C. María Concepción González Cantú, M. C. Blanca Margarita Huerta Martínez, L. C. Q. Jesús Alejandro Espinosa Muñoz, Q. F. B. Myriam Lozano Estrada and Q. F. B. Jesús Ángel Cepeda Garza for their assistance during characterization. L. Melo would also like to express thanks to CONACYT (National Council of Science and Technology) for her PhD scholarship and for the Hydrogen Network (CONACyT) support.

REFERENCES

[1] Snyder J. D., Elab Y. A. Nafion ® nanofibers and their effect on polymer electrolyte membrane fuel cell performance. *Journal of Power Sources* 2009, 186, 385.

[2] Stolten D., Samsun R. C., Garland N. *Fuel Cells. Data, Facts and Figures.* Wiley-VCH 2016.

[3] Zhang J. *PEM Fuel Cell Electrocatalysts and Catalyst Layers.* Springer. 2008.

[4] Barbir F. *PEM Fuel Cells: Theory and Practice*. Academic Press, 2013.

[5] Brandon N. P., Brett D. J. *Engineering porous materials for fuel cell applications* Phil Trans R Soc A 2006, 364, 147.

[6] Uchida M., Park Y., Kakinuma K., Yano H., Tryk D. A., Kamino T., Uchida H., Watanabe M. *Effect of the state of distribution of supported Pt nanoparticles on effective Pt utilization in polymer electrolyte fuel cells.* Phys Chem Chem Phys 2013, 15, 11236..

[7] Takenaka H., Torikai E., Kawami Y., Wakabayash N. *Solid Polymer Electrolyte Water Electrolysis.* Int J Hydrogen Energy 1982, 7, 397.

[8] Barsukov V., Beck F. *New Promising Electrochemical systems for Rechargeable Batteries.* Kluwer Academic Publishers. 1995..

[9] Lakeman J. B., Mepsted G. O., Adcock P. L., Mitchell P. J., Moore J. M. *Solid polymer fuel-cells for pulse power delivery.* Journal of Power Sources 1997, 65, 179.

[10] Huang L-M., Tang W-R., Wen T-C. Spatially electrodeposited platinum in polyaniline doped with poly(styrene sulfonic acid) for methanol oxidation. J Power Sources 2007, 164, 519.

[11] Ogumi Z., Nishio K., Yoshizana S. Application of the SPE method to organic electrochemistry. II. Electrochemical hydrogenation of olefinic double bonds. Electrochem Acta 1981, 26, 1779.

[12] Jorissen J. Ion exchange membranes as solid polymer elec-trolytes (SPE) in electro-organic synthesis without supporting electrolytes, Electrochem. Acta 1996, 41, 553.

[13] Fedkiw P. S., Potente J. M., Her W-H. Electroreduction of gaseous ethylene on a platinized Nafion Membrane. The Elecrochem Soc 1990, 137, 1451..

[14] Nuttall L. J. Conceptual design of large scale water electro-lysis plant using solid polymer electrolyte technology. Int. J. Hydrogen Energy 1997, 2, 395.

[15] Tatapudi P., Fenton J. M. Synthesis of ozone in a proton exchange membrane electrochemical reactor. J Electrochem Soc 1993, 140, 3527.

[16] Grimm J. H., Bessarabov D. G., Simon U., Sanderson R. D. Characterisation of doped tin dioxide anodes prepared by a sol–gel technique and their application in an SPE-reactor. Journal of Applied Electrochemistry 2000, 30, 293.

[17] Hwang B., Liu Y., Chen Y. Characteristics of Pt/Nafion electrodes prepared by a Takenata–Torikai method in sensing hydrogen. Materials Chemistry and Physics 2001, 69, 267..

[18] Liu Y., Hwang B., Hsu W. Improvement in anti-aging of metallized Nafion hydrogen sensors modified by chemical vapor deposition of polypyrrole. Sensors and Actuators B 2002, 87, 304.

[19] Nørskov J. K., Rossmeisl J., Logadottir A., Lindqvist L., Kitchin J. R., Bligaard T., Jónsson H. Origin of the Overpotential for Oxygen Reduction at a Fuel-Cell Cathode. J Phys Chem B 2004, 108, 17886.

[20] Greeley J., Jaramillo T. F., Bonde J., Chorkendorff I., Nørskov J. K. Computational high-throughput screening of electrocatalytic materials for hydrogen evolution. Nature Materials 2006, 5, 909.

[21] Lin W. F., Iwasita T., Vielstich W. Catalysis of CO Electrooxidation at Pt, Ru, and PtRu Alloy. An in Situ FTIR Study. J Phys Chem B, 1999, 103, 3250.

[22] Pozio A., Giorgi L., Antolini E., Passalacqua E. Electroxidation of H2 on Pt/C Pt–Ru/C and Pt–Mo/C anodes for polymer electrolyte fuel cell. Electrochimica Acta 2000, 46, 555.

[23] Lee S.J., Mukerjee S., Ticianelli E.A., McBreen L. Electrocatalysis of CO tolerance in hydrogen oxidation reaction in PEM fuel cells. Electrochim Acta 1999, 44, 3283.

[24] Clescerl L. S., Greenberg A. E., Eaton A. D. Standard Methods for Examination of Water & Wastewater. 20th Edition, 1999.

[25] Zhou S., Hai S. D., Kim D. Cross-linked Poly(arylene ether ketone) Proton Exchange Membranes with High Ion Exchange Capacity for Fuel Cells. Fuel Cells 2012, 12, 589.

[26] Klaysom C., Ladewig B. P., Lu G. Q. M., Wang L. Preparation and characterization of sulfonated polyethersulfone for cation-exchange membranes. Journal of Membrane Science 2011, 368, 48.

[27] Jun M., Choi Y., Kim J. Solvent casting effects of sulfonated poly(ether ether ketone) for Polymer electrolyte membrane fuel cell. Journal of Membrane Science 2012, 396, 32.

[28] Mikhailenko S. D., Wang K., Kaliaguine S., Xing P., Robertson G. P., Guiver M. D. Proton conducting membranes based on cross-linked sulfonated poly(ether ether ketone) (SPEEK). Journal of Membrane Science 2004, 233, 93.

[29] Analytical Methods for Atomic Absorption Spectroscopy. The PerkinElmer Inc. United States of America. 1996.

[30] Georgieva M., Andonovski B. Determination of platinum(IV) by UV spectrophotometry.Anal Bioanal Chem 2003, 375, 836.

[31] Albright R., U.S. Patent N°: 3,663,467 (1972)

[32] Gharibshahi E., Saion E. Influence of Dose on Particle Size and Optical Properties of Colloidal Platinum Nanoparticles. International Journal of Molecular Sciences 2012, 13, 14723.

[33] Wu N., She X., Yang D., Wu X., Su F., Chen Y. Synthesis of network reduced graphene oxide in polystyrene matrix by a two-step reduction method for superior conductivity of the composite. Journal of Materials Chemistry 2012, 22, 17254.

[34] Sundar P. S., Kal G. P., Ulaganathan M., Arunkumar J. Preparation of durable nanoc atalyzed MEA for PEM fuel cell applica tions. Ionics 2011, 17, 361.

[35] Zhu W., Wu Y., Yan C., Wang C., Zhang M., Wu Z. Facile Synthesis of Mono-Dispersed Polystyrene (PS)/Ag Composite Microspheres via Modified Chemical Reduction. Materials 2013, 6, 5625.

[36] Kita H., Fujikawa K., Nakajima H. Metal electrodes bonded on solid polymer electrolyte membranes (SPE)-II. The polarization resistance of Pt-Nafion electrode. Electrochimica Acta 1984, 29, 1721.

[37] Nakajima H., Kita H. Metal electrodes bonded on solid polymer electrolyte membranes (SPE)-V. Methanol oxidation on Pt-SPE electrode. Electrochimica Acta 1988, 33, 521.

[38] Liu R., Her W., Fedkiw P. S. In Situ Electrode Formation on a Nation Membrane by Chemical Platinization. J Electrochem Soc 1992, 139, 15.

[39] Rajalakshmi N., Ryu H., Dhathathreyan K. S. Platinum catalysed membranes for proton exchange membrane fuel cells – higher performance. Chemical Engineering Journal 2004, 102, 241.

[40] Weissmann M., Coutanceau C., Brault P., Léger J.-M. Direct chemical deposition of platinum on ionic conductive membranes and evaluation of the electrocatalytic activity. Electrochemistry Communications 2007, 9, 1097.

[41] Kongkanand A., Mathias M. F. Mathias. The Priority and Challenge of High-Power Performance of Low-Platinum Proton-Exchange Membrane Fuel Cells. J Phys Chem Lett 2016, 7, 1127.

[42] Zhang A., Bai H., Li L. Breath Figure: A Nature - Inspired Preparation Method for Ordered Porous Films. Chemical Reviews 2015, 115, 9801.

[43] Escalé P., Rubatat L., Billon L., Save M. Recent advances in honeycomb-structured porous polymer films prepared via breath figures. European Polymer Journal 2012, 48, 1001.

Performance Analysis of an Electrochemical Hydrogen Compressor/ Purificator

V. Juárez Casildo, R. de G. González Huerta[1]
[1]ESIQIE-IPN, Lab. Electroquímica y Corrosión, UPALM
CP 07738,
Ciudad de México
rosgonzalez_h@yahoo.com.mx

M. Tufiño Velázquez[2]
[2]ESFM-IPN, Laboratorio de Física Avanzada, UPALM,
CP 07738
Ciudad de México

Abstract— **Today the energy uses is increasing mainly due two factors, the high use of technology and grow of population; therefore it is our duty to develop new energy sources that are friendly to the environment and reduce the use of natural resources. Thanks to the numerous studies on energy development we know about forecast hydrogen as energy storage or energy vector.**

There are several ways to store gaseous hydrogen, however to keep the energy efficiency of the systems high, is important to have an efficient electrochemical hydrogen compressor. The compression of gases in mechanical compressors is often combined with low efficiency and the contamination for the compressed gases. The proton-exchange membrane (PEM) technology is commonly used to produce electrolyzes and reversible fuel cells. It can also be used to create electrochemical hydrogen compressors whose main objective is pressurizing and/ or concentrating gaseous hydrogen.

The aim of this report is to evaluate the characteristics of a monocell compressor and determinate the best operating. In this work a system is described that uses an electrochemical cell for the purification hydrogen. The role of the various parameters (current, gas flow rate in the electrode compartment and the hydration degree of the membrane) has been evaluated and discussed. Results regarding the hydrogen recovery as well as the relation between electrochemical cell voltage and current has been presented.

Keywords: Hydrogen recovery, electrochemical compressor, Hydrogen compression.

I. INTRODUCTION

The use of hydrogen as a secondary energy has two kinds of applications: stationary and mobile. Based on this, they have developed the "Hydrogen technologies". The aim of the research is to find different ways of producing, storing and using hydrogen friendly way with the environment.

Actually hydrogen is produced by electrolysis using two technologies: from the PEM or alkaline technology. The first generate high purity hydrogen (99.999%) but due to use of proton exchange membrane and noble metals in the electrodes is an expensive process compared with alkali which use as electrolyte a solution of potassium hydroxide or sodium, and hydrogen purity is 98%.

Due to the cost of the electrolysis process, today is being given greater application to the hydrogen produced in alkaline electrolyzers, however gas obtained from these systems is a mixture of H_2, O_2, water steam and traces of hexavalent chromium (Cr +6) which limits its application as an energy vector, due to these impurities is not possible to implement in stationary conditions, where fuel cells are involved and they play a very important role in the use of hydrogen to produce electricity.

For the smooth operation and long life time of fuel cells is necessary to feed hydrogen with 99.9999% purity, which is achieved directly if supplied with gas from an electrolyzer PEM, or required of a purification process if the source is an alkali electrolyzer.

For some decades they have developed technologies that allow to treat gas mixtures whose main component is hydrogen in order to purify it; such is the case Electrochemical Hydrogen Compressor (EHC). First accurate publications on the working principle of EHC were published by Sedlak in 1981, electrochemically pumping hydrogen from a low to a high pressure and separation of hydrogen from an inert gas to provide high-purity hydrogen. In 1998, Bessarabov clearly elaborated on the possibilities of hydrogen pumping in a paper on electrochemically aided membrane separation, and in the same year Rohland reported on application of the principle in a hydrogen compressor. The potential ability of EHC to purify and compress hydrogen was recognized, using the general structure of a fuel cell. [1]

This paper describes the first phase of designing a compressor-purifying electrochemical hydrogen whose purpose is to purify the gas from the alkaline reactors expanding the scope of this gas with the possibility of feed to fuel cells while achieving pressure storage eliminating the use of noisy mechanical compressors and low efficiency.

II. MATERIALS AND METHODS

Figure 1. Applying process the electrochemical hydrogen compressor

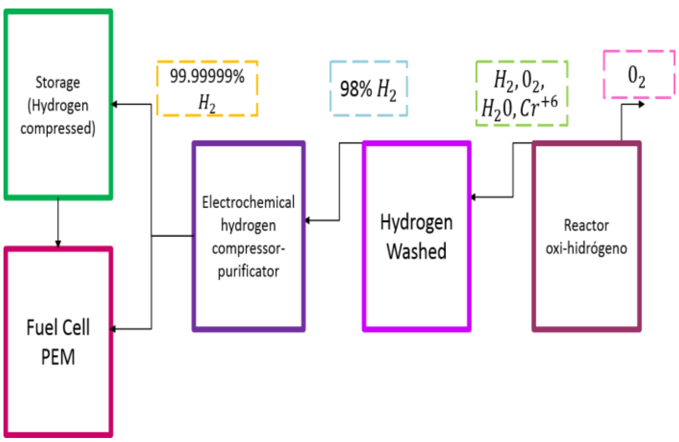

The electrochemical compressor-purificator project consists of several stages, from the description of the principle of operation to its integration and performance analysis. In a first stage, the EHC was fed with pure hydrogen, thus the range of voltage-current which is proper operation thereof, the theoretical operating pressures to be achieved with the cell designed were calculated analyzed. A process for electrochemical characterization compressor designed and integrated into this work was established. Figure 1.

A. *Working Principle.*

The electrochemical hydrogen compressor is a cell in which the membrane electrode assembly is very similar to a fuel cell. The molecular hydrogen is fed by the anode performing anodic oxidation, which are separated protons of electrons, the objective is that the protons are transported through the cation exchange membrane for further reduction in the cathode side; while the electrons are transferred through an external circuit to the catalyst layer located across the membrane, this is achieved by applying a potential difference to the cell. This effectively induces mass transport of hydrogen, and hydrogen only, with simultaneous purification.

Electrochemical reactions taking place at the electrodes is given by the following equations:

Anode $H_2\ (LP) \rightarrow 2H^+ + 2e^-$

Cathode $2H^+ + 2e^- \rightarrow H_2\ (HP)$

Overall reaction $H_2\ (LP) \rightarrow H_2\ (HP)$

Figure 2. Principle of Electrochemical hydrogen compressor.

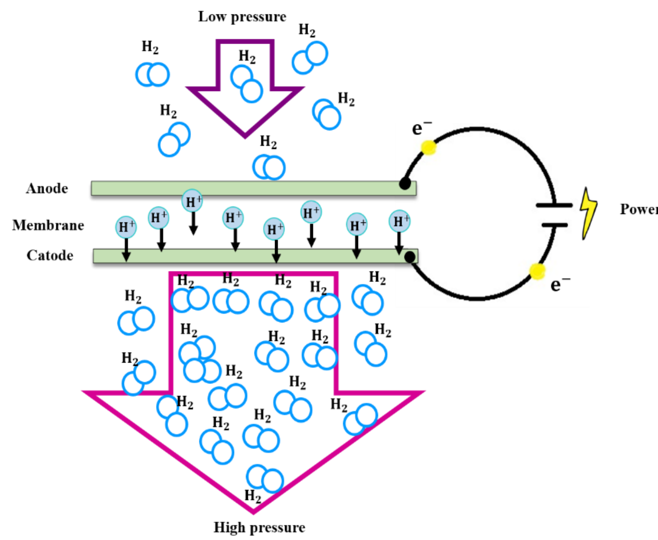

The current drives actively transporting hydrogen from the anode to the cathode, governed by charge neutrality in general, the amount of electrons traveling through the external circuit is directly correlated with the number of protons that pass through the membrane. [2]

The pumping capacity of the compression cell is given by the active area multiplied by the current density, according to the following relationship:

$$J = \frac{j * A * M_W}{n * F} \qquad (1)$$

Where

J is the mass flow (g s−1)
n is the no of electrons in reaction
F is the Faraday constant (C mol−1)
Mw is the Molar weight (g mol−1)
j is the current density (A cm−2)
A is the total active area (cm2)

B. Nernts compression energy.

Assuming that hydrogen is behaves as an ideal gas, the energy required to compress gas under isothermal conditions is dictated through thermodynamic principles. When the compressor cell is in equilibrium, the Gibbs free energy difference between the uncompressed and compressed state translates itself to a voltage difference following the Nernst–Einstein relationship:

$$V = \left(\frac{R*T}{n*F}\right) \ln\left(\frac{P_1}{P_0}\right) \quad (2)$$

Where
G is the Gibbs free energy (work) (J kg−1)
V Nernst is the pressure induced voltage (V)
R is the gas constant (J mol−1 K−1)
T is the temperature (K)
p0 is the pressure on input (Bar)
p1 is the pressure on output (Bar)

The Nernst voltage is a linear relationship with regard to temperature, meaning the energy requirement for compression is lower at lower operating temperatures. [1]

Figure 3. Characterization scheme of an electrochemical hydrogen compressor.

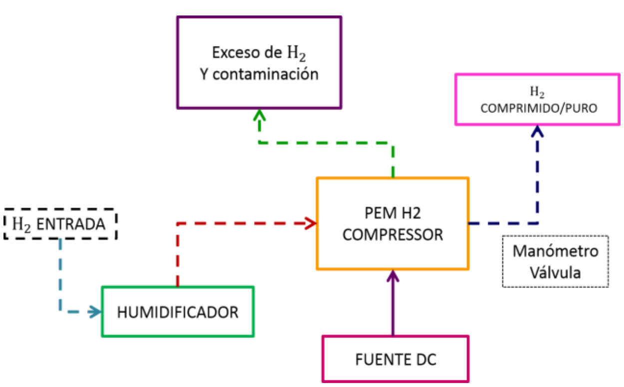

The first stage involved the design and integration of an EHC to analyze cell electrochemical behavior by feeding pure hydrogen. Without performing an experimental measurement of the pressure obtained, only the pumped flow of hydrogen was measured. In Figure 3, the experimental diagram was usted to integrate the EHC is shown. In a second step is contemplated feed contaminated hydrogen to a humidifier in order to give a precleaning to food the cell where carried out the oxidation of hydrogen at the anode and reduction of protons at the cathode from applying a potential difference, excess hydrogen and pollution that does not pass through the membrane and exits the cell by a manometer finally be measured pressure versus time electrolysis.

Figure 4. Compression cell photograph.

The cell's MEA was constructed from Nafion 115 (Thickness 127 µm), mesh carbon was used as a gas diffuser for the anode and cathode; on the other hand, the current collectors employed are 316 stainless steel and teflon seals were used for proper assembly. It was designed to achieve an active area of 6.25 cm2. In Figure 4, the elements of the electrochemical cell shown hydrogen compressor. In Figure 5 the cell which was used in the experiments conducted shown.

The performance analyst of an electrochemical hydrogen compressor-purificator based on pure hydrogen feed streams to different cell where global voltage values were obtained by controlling the current supplied and from a flow meter the flow of hydrogen was determined experimentally reduced.

Figure 5. Single cell of the electrochemical hydrogen compressor

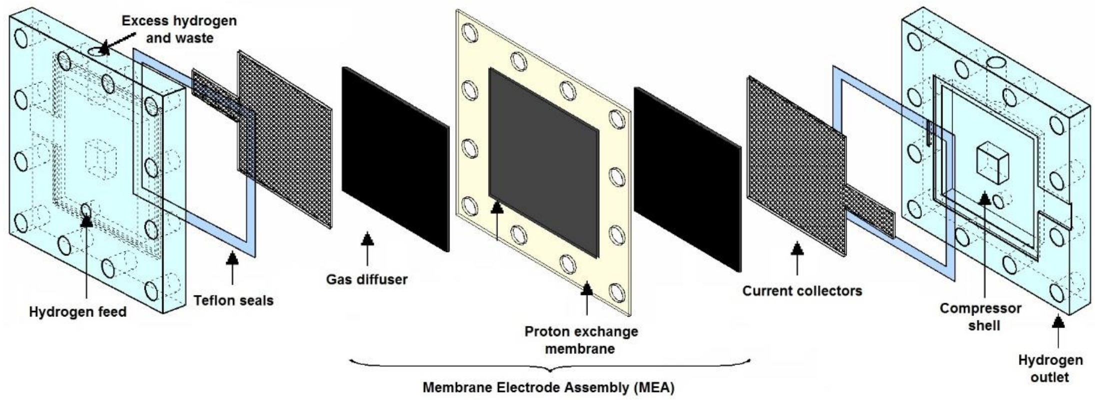

III. RESULTS AND DISCUSSION

Voltage behavior as a function of current flow was analyzed by changing the hydrogen fed, in voltage-current graph which shows relationship that fed hydrogen fewer overall cell voltage decreases shown. Hydrogen oxidation potential is 0 V, however experimentally by the principle of work that may not be possible as to achieve the breaking of molecular hydrogen into protons and electrons, some energy is required to overcome the resistance present which no It should be as large. The flow in which low potential values are obtained is 50 cm^3 / min. For according to the applied current density was the same for all three cases, the same quantity of hydrogen less applied energy is obtained. Figure 6.

Figure 6. V-I relationship to different flows fed.

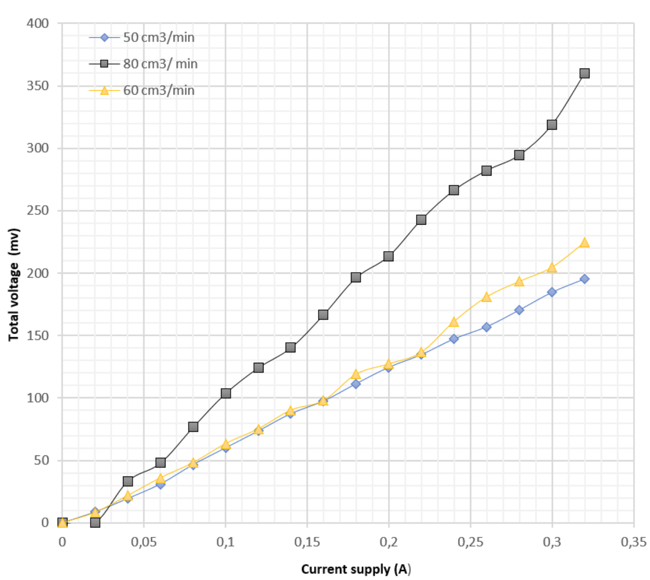

Figure 7. Theorical pressure.

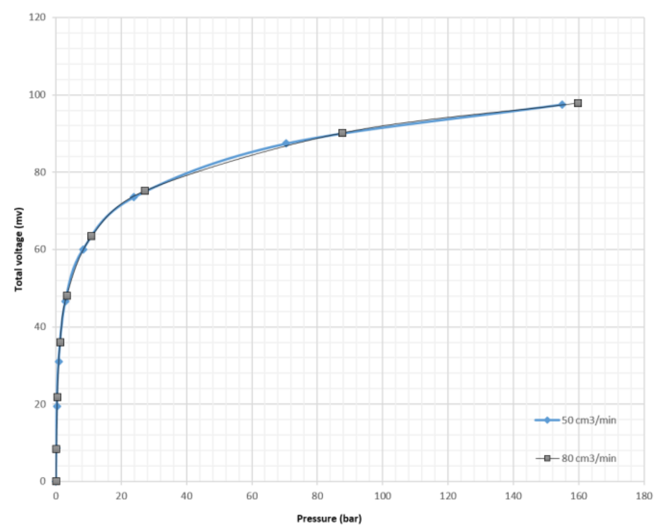

Based on the voltages obtained during experimentation, the theoretical pressure that would be achieved in a given electrolysis`s time according to the active area of the membrane was calculated from the assembly made, 90 mV is sufficient to achieve a pressure of 75 bar. Figure 7.

According to Faraday's law, the flow of hydrogen obtained is directly proportional to the applied current and the active area of the assemblies thus follows a linear behavior, figure 8, where a current of 0.2 A flow of theoretical hydrogen en 5 cm3 / min, while experimentally obtained 2.8 cm3 / min, therefore the integrated cell is has a 20% deviation from the theoretical value.

Figure 8. Real mass production of the cell.

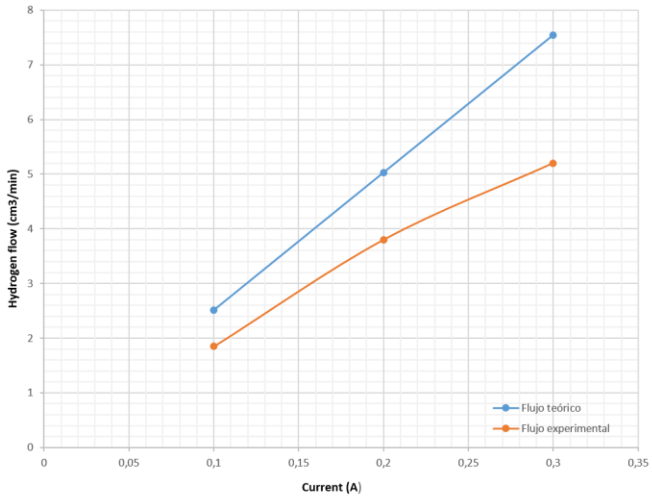

IV. CONCLUSIONS

Based on the results, it is concluded that for the integrated EHC must operate to supply a flow of 50 cm^3/min due thus not feeding the membrane is saturated enough for its pumping capacity.

Due the hydrogen is fed wet is very important to define the limit operating current should be at left of 0.4 A as higher current values can lead to electrolysis of water reaching values of voltage up to 1.6 V, the which causes a high energy consumption and the purpose of the device is the purification of hydrogen is not met.

Is possible to achieve the theoretical pressures calculated by the Nernst equation, however the key variable is the time to produce the amount of hydrogen necessary and can be compressed, which is given by the active area of the cell since this will only oxidize and reduce the number of hydrogen molecules according to their capacity.

V. ACKNOWLEDGEMENTS

This work has been supported by multidisciplinary project IPN-SIP 1683 (2015-2016)

VI. REFERENCES

[1] G. Bessarabov,H. Wang, H. Li, and N. Zhao, “PEM electrolysis for hidrogen production principles and aplications,” Taylor and Francis group 2016, pp. 269–279.

[2] S. Grigoriev, I. Shtatniy, P. Millet, V. Porembsky, and V. Fattev, “Description and characterization of an electrochemical hydrogen compressor/concentrator based on solid polymer”, International Journal of hydrogen and energy 2010.

[3] R. Strobel, M. Oszicipok, M. Fasil, B. Rohland, L. Jorissen and J. Garche, “The compressor of hydrogen in an electrochemical cell based on a pe fuel cell desing,” Journal of power sources 2002.

[4] C. Casati, P. Longhi, L. Znderighi and F. Bianchi, “Some fundamentals aspects in electrochemical hydrogen purification/compression” Journal of power sources 2008.

[5] B. Rohland, K. Eberle, R. Strobel, J. Scholta and J. Garche “Electrochemical hydrogen compressor,” Elsevier science 1998.

Electrochemical evaluation of Pt/GMC and Pt/rGO for the electro-oxidation of methanol

David Macias Ferrer, José Aarón Melo Banda, Ulises Páramo García, Mayda Lam Maldonado, Rebeca Silva Rodrigo
Division of Graduate Studies and Research
Technological Institute of Ciudad Madero
Cd. Madero Tamaulipas, México
e-mail: maestro_macias@hotmail.com

José Ysmael Verde Gomez
Division of Graduate Studies and Research
Technological Institute of Cancún
Cancún Quintana Roo, México

Iván Alziri Estrada Moreno
Department of Engineering and Materials Chemistry
Research Center for Advanced Materials
Chihuahua Chihuahua, México

***Abstract*— In this work, Pt/GMC and Pt/rGO electrocatalysts have been prepared by impregnation reduction method in which Pt precursor is chemically reduced by citric acid, ethanol and Ar-H_2 dynamic atmosphere. Graphitic mesoporous carbon (GMC) sample was synthesized via nanocasting process with anhydrous pyrolysis at 1273 K using SBA-15 as hard template and purified sugar as carbon source. SBA-15 was prepared via sol gel using pluronic P-123 as surfactant and TEOS as silica precursor. Reduced graphene oxide (rGO) was synthesized by modified Hummers method using graphite as carbon precursor. The prepared materials were characterized by means of diffraction (XRD), scanning electron microscopy (SEM), energy-dispersive X-ray spectroscopy (EDS) and high resolution transmission electron microscopy (HRTEM). The performance of electrocatalysts for methanol oxidation reaction (MOR) was measured by cyclic voltammetry (CV). The electrochemical characterization techniques revealed that the mass activity of Pt/GMC, Pt/rGO and the commercial electrocatalyst Pt/C were 627, 332 and 371 mA/mgPt respectively as well as the carbon monoxide tolerance index ICO for these catalysts were 1.07, 1.04 and 0.76 respectively. Therefore, Pt/GMC shows better electrocatalytic performance and best resistance to carbonaceous intermediates species for the electrooxidation of methanol.**

Keywords: Electrocatalysts, Mesoporous carbon, graphene oxide, methanol electrooxidation

I. Introduction

Fuel cells are devices that convert with high efficiency, the power of electrochemical reactions into electricity. In recent years, Polymer electrolyte membrane fuel cells (PEMFC) is one of the most studied devices. The direct methanol fuel cell (DMFC) is a special form of low-temperature fuel cells based on PEM technology [1]. DMFC have attracted significant attention because of their high theoretical power density, high energy conversion efficiency, low environmental pollution and easy refueling, being one of the potential power source for portable electronic devices [2-5]. The high reactivity of methanol with platinum and the excellent catalytic activity for electro-oxidation of methanol on pure Pt especially at low temperature (below 80°C), makes this metal a suitable anodic electrocatalyst in DMFC [6]. However, it is well known that there is a series of technical problems in DMFC that limit their marketing [7]. While Pt, which is generally supported on activated carbon with large surface area such as Vulcan XC-72, is the best catalyst for the electro-oxidation of methanol, it rapidly becomes poisoned because of the intermediate species formed during the oxidation of methanol, mainly CO, since CO molecules can be chemically adsorbed on the surface of Pt and block the active sites, producing a poor kinetic of anodic methanol oxidation due to CO poisoning and a low electrocatalytic activity of electrocatalysts [8-11]. Although electrocatalysts based on Pt and Pt-Ru alloy have shown a good catalytic activity for electro-oxidation of methanol, another of the limitations in the development of DMFC for commercial applications is the high cost of both noble metals [12-13]. Therefore, many efforts have focused on the development of techniques and new electrocatalysts to achieve enhancing the electrocatalytic activity by inhibiting the CO poisoning effect according the bifunctional mechanism and reducing cost of the electrocatalysts [14]. One of the main components of the electrocatalyst that contributes to the high electrocatalytic activity in MOR, is the nature of the carbon material support, which can help in dispersing the metal catalyst and in facilitating electron transport, as well as in promoting mass transfer kinetics at the electrode surface. Thus, several carbon materials such as highly conductive carbon blacks (CBs) of turbostratic structures with high surface areas (Vulcan XC-72R, Shawinigan, Black Pearl 2000, Ketjen Black and Denka Black) and carbon nanostructures like mesoporous carbon, carbon nanotubes (CNTs), nanodiamonds, carbon nanofibers (CNF), ordered mesoporous carbon (OMC), reduced graphene oxide (rGO) and graphene, have been tested [15-16]. In this paper, we propose the use of catalytic supports, graphitic mesoporous carbon (GMC) and reduced graphene oxide (rGO), making the electrocatalysts Pt/GMC and Pt/rGO in order to measure their electrocatalytic activity towards the methanol electro-oxidation in acid media.

II. MATERIAL AND METHODS

A. *Chemicals*

Methanol (CH_4O, 99.9%) was supplied by J.T. Baker. pluronic P123 (non-ionic triblock copolymer, $EO_{20}PO_{70}O_{20}$), tetraethoxysilane ($Si(OC_2H_5)_4$, 98%), platinum (II) acetylacetonate ($Pt(C_5H_7O_2)_2$, 97%), platinum on graphitized carbon 20% wt loading (Pt/C), graphite powder (99.99%), nafion 117 solution, were obtained from Sigma-Aldrich; deionized water, sulfuric acid (H_2SO_4, 98%), hydrofluoric acid (HF, 40%), hydrochloric acid (HCl, 37%), nitric acid (HNO_3, 70%), acetone (C_3H_6O, 99.5%), ethyl Alcohol (C_2H_6O, 99.7%), citric acid ($C_6H_8O_7$, 99.5%), potassium permanganate ($KMnO_4$, 99%), sodium nitrate ($NaNO_3$, 99%), hydrogen peroxide (H_2O_2, 30%) were supplied by Fermont; refined sugar were obtained by Del Marques; ultrapure water (15 $M\Omega cm^{-1}$) was generated by ELGA Purelab Option station.

B. *Synthesis of Pt/GMC*

SBA-15 sample was synthesized according to the standard procedure [17] with some modifications. In a typical synthesis, 2.0 g Pluronic 123 as a structure-directing agent were dissolved in 14 mL deionized water and 60 mL 0.6 M hydrochloric acid by stirring at room temperature for 5 h. Afterwards, 4.3 mL of tetraethoxysilane (TEOS) were added dropwise and the mixture was stirred (700 rpm) at 45 °C for 24 h in the closed glass reactor. After, the mixture was aged in oven at 90 °C for 24 h. The white powder was obtained through filtration, washing and drying in nalgene bottle under vacuum. Finally, the sample was calcined at 550 °C for 6 h under air to remove the surfactant to obtain the silica template. GMC sample was synthesized using a nanocasting pathway using pure silica SBA-15 as hard template and refined sugar as carbon precursor according to the procedure reported in the literature [18-19] with some modifications. In brief: 1 g of refined sugar and 1 g of SBA-15 were dissolved in 5 mL of deionized water by stirring at room temperature for 30 min, during this time 0.05 ml of sulfuric acid were added. The mixture was heated in a oven at 100 °C for 6 h, and subsequently 160 °C for another 6 h. The silica sample, containing partially polymerized and carbonized refined sugar, was carbonized in a quartz furnace at 1000 °C for 1 h under N_2 flow. After pyrolysis, the silica template was removed under vigorous stirring using concentrated HF at the room temperature for 2 h. Afterwards the black powder was obtained through filtration, washing with ultrapure water and drying in a oven at 80 °C for 12 h. The functionalization process for GMC, was carried out in soxhlet equipment by refluxing GMC in 1M HNO_3 + 1M H_2SO_4 at 110 °C by 5 h in order to generate surface oxides such as carboxylic (–COOH), carbonyl (–C=O), and hydroxyl (–C–OH) groups on the support surface. Afterward, the mixture was diluted with ultrapure water, filtered, washed with excess ultrapure water, and dried in N_2 at 150 °C in a tubular furnace by 2 h [20]. Platinum nanoparticles with 20 wt% loading were supported on the GMC by a wet chemical reduction at incipient wetness impregnation method. A detailed procedure is as follows: An appropriate amount of $Pt(C_5H_7O_2)_2$ were dissolved in 20 mL of acetone and simultaneously 0.32 g of GMC (oxidized) were dissolved in 30 mL of ethyl alcohol. Both are mixed under mechanical stirring at room temperature until a homogeneous mixture. Then the dispersion was ultrasonicated for 30 min. Afterwards, the mixture is kept under mechanical stirring for 5 h at room temperature with an Ar-H_2 (90%-10%) atmosphere in order to remove isolate oxygen. After reaction, the obtained products were filtrated, washed with ultrapure water and then vacuum dried. The impregnated carbon sample was heated in a quartz furnace a flowing Ar-H_2 environment while increasing temperature from the room temperature to 250 °C over 1 h then to 400 °C over 2 h. The result sample denoted Pt/GMC electrocatalyst [21-22].

C. *Synthesis of Pt/rGO*

Graphene oxide (GO) was synthesized from graphite powder using modified Hummer's method. In brief, 1 g of graphite and 0.5 g of sodium nitrate were mixed together followed by the addition of 23 mL of concentrate sulphuric acid under constant stirring. After 1 h, 3 g of $KMnO_4$ was added gradually to the above solution while keeping the temperature less than 20°C to prevent overheating and explosion. The mixture was stirred at 35 °C for 12 h and the resulting solution was diluted by adding 500 mL of water under vigorous stirring to ensure the completion of reaction with $KMnO_4$. The suspension was further treated with 30% H_2O_2 solution (5 mL). The resulting mixture was washed with HCl and ethanol respectively, followed by filtration and drying, graphene oxide sheets were thus obtained [23]. For the synthesis of Pt/rGO, it applies exactly the same procedure described for Pt/GMC.

D. *Characterization techniques and electrochemical measurements*

XRD patterns were collected on a Bruker D8 Advance X-ray diffractometer with Cu Kα radiation. SEM characterization was performed using a JEOL model JSM-7100F operating in SEM and GB-Low modes at 20 keV and 2 KeV respectively and EDS detector from Oxford Instruments. The performance of electrocatalysts and commercial catalyst (P/C) for room temperature methanol oxidation reaction was measured in electrochemical work station BASi-epsilon (potentiostat/ galvanostat). A conventional three-electrode cell consisting of the glassy carbon (GC) working electrode, Pt wire as counter electrode and Ag/AgCl reference electrode were used for the cyclic voltammetry studies. A glassy carbon electrode (3 mm in diameter) was sequentially polished with 0.05 μm Al_2O_3 and then washed. The catalyst ink was prepared by ultrasonically dispersing 10 mg catalyst in 1 mL of ethanol and 60μL Nafion/water (25% Nafion) for 45 min. 10 μL of the dispersion was transferred onto the GC and then dried in the air for 30 min. The electrolyte solution for methanol oxidation reaction consists of 0.5 M CH3OH and 0.5 M H_2SO_4 and the CV's were recorded at a scanning rate of 30 mV/s and 20 cycles for each.

III. RESULTS AND DISCUSSION

XRD patterns for Pt/rGO and Pt/GMC electrocatalysts are shown in Fig. 1. For both cases, the diffraction peaks at 39°, 46°, 68°, 81° and 86° were due to Pt (111), (200), (220), (311) and (222) reflections respectively, which confirmed a face centered cubic structure of Pt (JCPDS 071-3756) and are in good agreement with the literature [24-25]. There was no evidence of peaks related to platinum oxide.

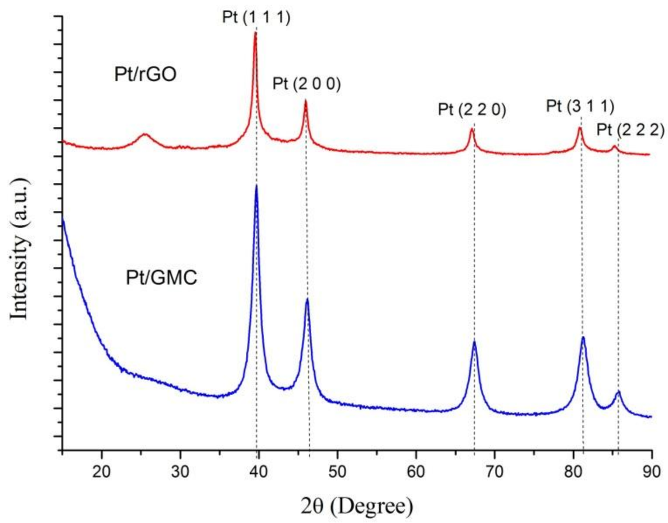

Fig. 1. XRD pattern of Pt/rGO and Pt/GMC

The metal crystallite size were calculated from Pt(111) reflection according to the Debye-Scherrer equation: $D_{XRD} = 0.94\lambda/(B_{2\theta}\cos\theta_{max})$, where DXRD is the crystallite size, λ is the X-ray wavelength (0.154 nm), $B_{2\theta}$ is the full width at half maximum and θmax is the angle at peak maximum. The crystallite size for Pt/rGO and Pt/GMC were 13.7 and 11.7 nm respectively [26].

Fig. 2a, shows an SEM image of GMC illustrating a rope-like morphology that consist in graphene sheets with turbostratic structure and EDS spectrum which shows the elemental chemical composition of the graphitic mesoporous carbon with negligible traces of F (0.78% wt) and Si (0.1% wt). An SEM image of Pt/GMC showing a high dispersion of Pt nanoparticles on the catalyst support, as well as the EDS spectrum revealed the presence of Pt are illustrated in Fig. 2b. The Fig. 2c, shows an SEM image of GO illustrating a laminar morphology that consist in graphene sheets and EDS spectrum which shows the elemental chemical composition of the graphene oxide with negligible traces of K (0.12% wt) and S (0.31% wt). Finally, an SEM image of Pt/rGO showing a high dispersion of Pt nanoparticles on the catalyst support, as well as the EDS spectrum revealed the presence of Pt are illustrated in Fig. 2d. This is in accordance with the reported in literature [27-30]. With respecto to electrocatalysts, the particle size distribution (inset in figures 2b and 2d) were carried out by a count of about 200 particles in both cases, concluding that the average particle size for Pt/rGO and Pt/GMC were 12.46 and 13.8 nm respectively [31-32].

The electrocatalytic activity given by mass activity (the current density is normalized to the platinum loading on the electrodes) of the electrocatalysts Pt/rGO, Pt/GMC and commercial catalysts Pt/C for room temperature methanol oxidation reaction, were obtained by cyclic voltammetry in a conventional three-electrode cell using the conditions described above. In all cases, typically features of methanol oxidation were observed, that is, two oxidation peaks corresponding to the oxidation of methanol and intermediate carbonaceous species (ICS), which occurred at around 0.75 V and 0.55 V respectively (Fig. 3).

The chemisorbed CO specie is considered as a poisoning on pure Pt surface, and are more difficult to oxidize that all intermediate carbonaceous species formed during the methanol oxidation reaction (MOR); to free the pure platinum, is necessary to dissociate the water molecules and cause the oxidation of CO to CO_2, however, this is achieved at high values of potential [33]; it has been shown that the incursion of a second metal (i.e., Ruthenium) [34] or hydroxyl and carboxyl functional groups anchored to the catalytic support [35], can dissociate water molecules at very low potential, and contribute to the release of the active sites of Pt increasing the electrocatalytic activity in the MOR. Currently this process is known as bifunctional mechanism theory [36-37].

On the other hand, the ratio of the forward anodic peak current (I_f) to the reverse anodic peak current (I_b) denoted by I_{CO}, was used to measure the tolerance of electrocatalyst to accumulation of ICS, particularly CO; a higher ratio indicates more effective removal of the poisoning species on the catalyst surface [38].

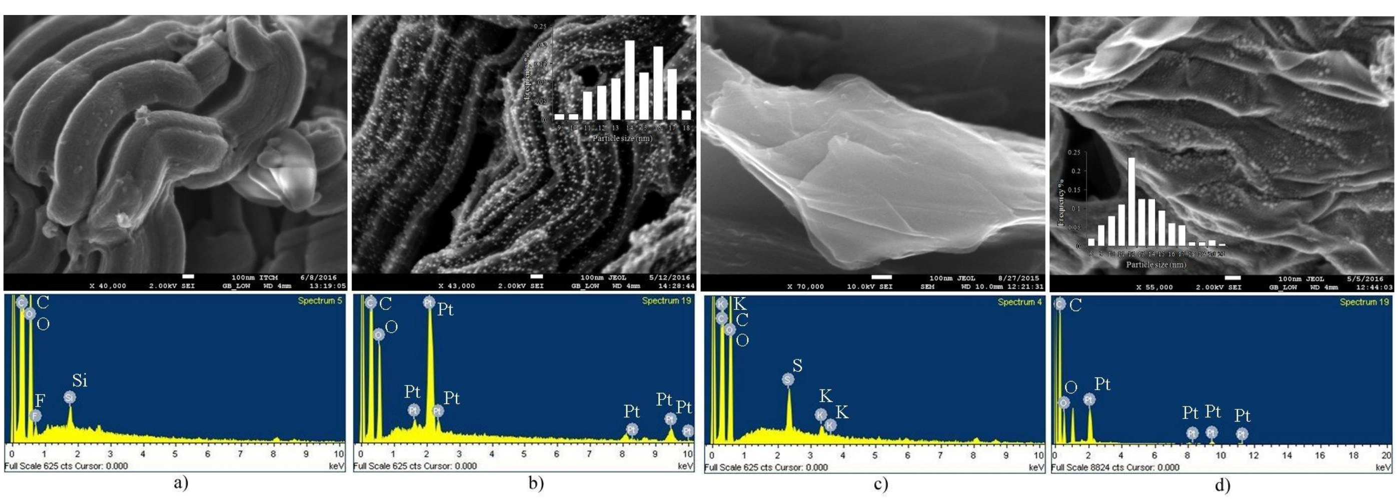

Fig. 2. SEM images and EDS profiles of a) GMC; b) Pt/GMC; c) GO; d) Pt/rGO

According to what explained above and the experimental results, the electrocatalyst Pt/GMC had higher electrocatalytic activity (627 mA/mgPt) and better antipoisoning ability (I_{CO} = 1.07) relative to MOR, than Pt/rGO (332 mA/mgPt, I_{CO} = 1.04) and Pt/C (371 mA/mgPt, I_{CO} = 1.04) catalysts. The improved performance of Pt/GMC toward the MOR, can be explained by the small particle size, high dispersion of the nanoparticles of Pt and the oxygen groups found in the catalyst support due to its preprocessing functionalization. Moreover, the interaction between Pt nanoparticles, with graphitized mesoporous carbon (with a rope-like morphology), promotes free flow of CO_2 molecules improving the electrocatalytic activity towards methanol oxidation [3].

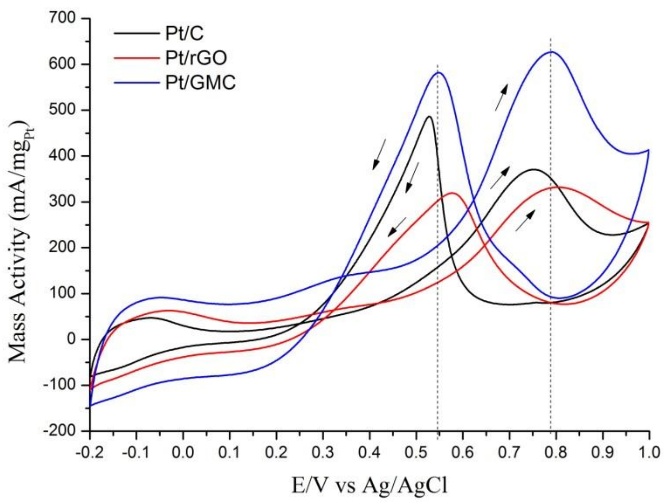

Fig. 3. CV curves of Pt/GMC, Pt/rGO and Pt/C

IV. CONCLUSIONS

The high dispersion of Pt nanoparticles and the oxygenates groups on GMC, were decisive factors in increasing electrocatalytic activity of Pt/GMC, also produced a higher level of CO-tolerance to intermediate carbonaceous species and higher efficiency to remove them. This study shows that the electrocatalyst Pt/GMC deserve a deeper analysis on the development of anodic catalysts for direct methanol fuel cell. Currently they are applied characterization techniques such as: Raman spectoscopy, high resolution transmission electron microscopy, X-ray photoelectron spectroscopy, chronoampero-metric tests and electrochemical impedance spectroscopy, in order to make a more complete study of electrocatalysts.

ACKNOWLEDGMENT

This paper has been supported by the National Council for Science and Technology, México under contract DGEST 4513.12-P; authors also acknowledge the support of Technological Institute of Ciudad Madero, Technological Institute of Cancún, Applied Research Center for Advanced Science and Technology and Research Center for Advanced Materials.

REFERENCES

[1] J. Hagen, Industrial Catalysis. A Practical Approach, 2nd ed., WILEY-VCH Verlag GmbH & Co., 2006, pp. 306-307

[2] F. Ye, Sh. Chen, X. Dong, W. Lin, "Carbon Nanotubes Supported Pt-Ru-Ni as Methanol Electro-Oxidation Catalyst for Direct Methanol Fuel Cells," Journal of Natural Gas Chemistry, vol. 16, pp. 162-166, February 2007.

[3] J. Prabhuram, T.S. Zhao, Z.K. Tang, R. Chen, Z.X. Liang, "Multiwalled Carbon Nanotube Supported PtRu for the Anode of Direct Methanol Fuel Cells," J. Phys. Chem. B, vol. 110, pp. 5245-5252, January 2006 .

[4] H. Zhao, J.P. Dong, S. Xing, Y. Li, J Shen J. Xu, "Electrochemical Oxidation of Small Organic Molecules on Hydrothermal Synthesized Pt and PtCo/ordered Mesoporous Carbon," Int. J. Hydrogen Energy, vol. 36, pp. 9551-9561, June 2011.

[5] Y.-H. Hong, Y.-Ch. Tsai, "Electrodeposition of Platinum and Ruthenium Nanoparticles in Multiwalled Carbon Nanotube-Nafion Nanocomposite for ethanol Electrooxidation," Journal of Nanomaterials, ID 892178, pp. 1-6, August 2009.

[6] J.-H. Choi, K.-W. Park, I.-S. Park, W.-H. Nam, Y.-E. Sung, "Methanol Electro-Oxidation and Direct Methanol Fuel Cell Using Pt/Rh and Pt/Ru/Rh Alloy Catalysts," Electrochimica Acta, vol. 50 (2-3), pp. 787-790, October 2004.

[7] F. Su, Ch.K. Poh, J. Zeng, Z. Zhong, Z. Liu, J. Lin, "Pt Nanoparticles Supported on Mesoporous Carbon Nanocomposites Incorporated with Ni or Co Nanoparticles for Fuel Cells," J Power Sources, vol. 205, pp. 136-144, January 2012

[8] J.W. Guo, T.S. Zhao, J. Prabhuram, R. Chen, C.W. Wong, "Development of PtRu-CeO_2/C Anode Electrocatalyst for Direct Methanol Fuel Cells," J. Power Sources, vol. 156, pp. 345–354, June 2006.

[9] S.-H. Park, H.-M. Jung, S. Um, Y.W. Song, H.S. Kim, "Rapid Synthesis of Pt-based Alloy/Carbon Nanotube Catalysts for a Direct Methanol Fuel Cell using Flash Light Irradiation," Int. J. Hydrogen Energy, vol. 37, pp. 12597-12604, July 2012.

[10] W. Wei, C. Jieming, Ch. Yu, L. Tianhong, "Preparation of Pt/CMK-3 Anode Catalyst for Methanol Fuel Cells Using Paraformaldehyde as Reducing Agent," Chinese Journal of Catalysis, vol. 28(1), pp. 17-21, January 2007.

[11] J.W. Guo, T.S. Zhao, J. Prabhuram, R. Chen, C.W. Wong, "Preparation and Characterization of a PtRu/C Nanocatalyst for Direct Methanol Fuel Cells," Electrochimica Acta, vol. 51(4), pp. 754-763, September 2005.

[12] L. Xiong, X. Yang, M. Xu, Y. Xu, D. Wu, "Pt–Ni Alloy Nanoparticles Supported on Multiwalled Carbon Nanotubes for Methanol Oxidation in Alkaline Media", J. Solid State Electrochem., vol 17, p. 805, March 2013.

[13] M.A. Abdel-Rahim, R.M. Abdel-Hameed, M.W. Khalil, "The Role of a Bimetallic Catalyst in Enhancing the Electro-Catalytic Activity Towards Methanol Oxidation," J. Power Sources, vol. 135, pp. 42-51, July 2004.

[14] X. Wang, H. Wang, R. Wang, Q. Wang, Z. Lei, "Carbon-supported Platinum-decorated Nickel Nanoparticles for Enhanced Methanol Oxidation in Acid Media," J. Solid State Electrochem., vol. 16, pp. 1049-1054, July 2012.

[15] S. Sharma, B.G. Pollet, "Support Materials for PEMFC and DMFC Electrocatalysts. A review," Journal of Power Sources, vol. 208, pp. 96-119, March 2012

[16] Zh. Lei, L. An, L. Dang, M. Zhao, J. Shi, S. Bai, Y. Cao, "Highly Dispersed Platinum Supported on Nitrogen-Containing Ordered Mesoporous Carbon for Methanol Electrochemical Oxidation," Microporous and Mesoporous Materials, vol. 119, pp. 30-38, October 2009.

[17] D. Zhao, J. Feng, Q. Huo, N. Melosh, G.H. Fredrickson, B.F. Chmelka, G.D. Stucky, "Triblock Copolymer Syntheses of Mesoporous Silica with Periodic 50 to 300 Angstrom Pores," Science, vol. 279, pp. 548-552, January 1998.

[18] R. Ryoo, S.H. Joo, S. Jun, "Synthesis of Highly Ordered Carbon Molecular Sieves via Template-Mediated Structural Transformation," J. Phys. Chem. B, vol. 103, pp. 7743-7746, August 1999.

[19] R. Ryoo, S.H. Joo, S. Jun, T. Tsubakiyama, O. Terasaki, "Ordered Mesoporous Carbon Molecular Sieves by Templated Synthesis: the Structural Varieties," Stud. Surf. Sci. Catal., vol. 135, p. 150, September 2007.

[20] A. Santasalo-Aarnio, M. Borghei, I.V. Anoshkin, A.G. Nasibulin, E.I. Kauppinen, V. Ruiz, T. Kallio, "Durability of Different Carbon Nanomaterial Supports with PtRu Catalyst in A Direct Methanol Fuel Cell," Int. J. Hydrogen Energy, vol. 37, pp. 3415-3424, December 2012.

[21] K.-W. Park, K.-S. Ahn, Y.Ch. Nah, J.H. Choi, Y.E. Sung, "Electrocatalytic Enhancement of Methanol Oxidation at Pt-WOx Nanophase Electrodes and In-Situ Observation of Hydrogen Spillover using Electrochromism," J. Phys. Chem. B, vol. 107, pp. 4352-4355, April 2003.

[22] M.S. Saha, R. Li, X. Sun, "High Loading and Monodispersed Pt Nanoparticles on Multiwalled Carbon Nanotubes for High Performance Proton Exchange Membrane Fuel Cells," J. Power Sources, vol. 177, pp. 314–322, November 2008.

[23] L. Shahriary, A.A. Athawale, "Graphene Oxide Synthesized by using Modified Hummers Approach," Int. J. Renewable Energy and Environ. Eng., vol. 2, pp. 58-63, January 2014

[24] L. Calvillo, V. Celorrio, R. Moliner, A.B. Garcia, I. Caméan, M.J. Lazaro, "Comparative study of Pt catalysts supported on different high conductive carbon materials for methanol and ethanol oxidation," Electrochimica Acta, vol. 102, pp. 19-27, April 2013.

[25] J. Park, S. Kim, "Synthesis and electrochemical analysis of Pt-loaded, polypyrroledecorated, graphene-composite electrodes," Carbon Letters, vol. 14, pp. 117-120, February 2013.

[26] F. Ye, X. Cao, L. Yu, S. Chen, W. Lin, "Synthesis and Catalytic Performance of PtRuMo Nanoparticles Supported on Graphene-Carbon Nanotubes Nanocomposites for Methanol Electro-Oxidation," Int. J. Electrochem. Sci., vol. 7, pp. 1251-1265, February 2012.

[27] Sh. Zhou, H. Xu, Q. Yuan, H. Shen, X. Zhu, Y. Liu, W. Gan, "N-Doped Ordered Mesoporous Carbon Originated from a Green Biological Dye for Electrochemical Sensing and High-Pressure CO_2 Storage," ACS Appl. Mater. Interfaces, vol. 8, pp. 918-926, December 2015

[28] S. Gurunathan, J. Han, J.H. Park, J.H. Kim, "An in vitro evaluation of graphene oxide reduced by Ganoderma spp. in human breast cancer cells (MDA-MB-231)," Int. J. Nanomedicine, vol. 9, pp. 1793-1797, November 2013.

[29] A. Liu, S. Huang, "A glucose biosensor based on direct electrochemistry of glucose oxidase immobilized onto platinum nanoparticles modified graphene electrode," Sci. China Phys. Mech. Astron., vol. 55, pp. 1163-1167, July 2012.

[30] Z. Wang, G. Shi, F. Zhang, J. Xia, R. Gui, M. Yang, S. Bi, "Amphoteric surfactant promoted three-dimensional assembly of graphene micro/nanoclusters to accomodate Pt nanoparticles for methanol oxidation," Electrochimica Acta, vol. 160, pp. 288-295, February 2015

[31] Zh. Liu, X. Duan, H. Cheng, J. Zhou, X. Zhou, "Synthesis of platinum/graphene composites by a polyol method: The role of graphite oxide precursor surface chemistry," Carbon, vol. 89, pp. 93-101, March 2015.

[32] R. Zolfaghari, F.-R. Ahmadun, M.R. Othman, W.R.W. Daud, M. Ismail, "Nonionic surfactant-templated mesoporous carbon as an electrocatalyst support for methanol oxidation," Mater. Chem. Phys., vol. 139, pp. 262-269, January 2013

[33] J.B. Goodenough, A. Hamnett, B.J. Kennedy, R. Manoharan, S.A. Weeks, "Methanol Oxidation on Unsupported and Carbon Supported Pt + Ru Anodes," J. Electroanal. Chem., vol. 240, pp. 133-145, 1987

[34] M. Watanabe, S. Motoo, "Electrocatalysis by Ad-Atoms: Part III. Enhancement of the Oxidation of Carbon Monoxide on Platinum by Ruthenium Ad-Atoms," J. Electroanal. Chem., vol. 60, pp. 275-283, 1975

[35] Ch.-T. Hsieh, J.-Y. Lin, "Fabrication of Bimetallic Pt–M (M=Fe, Co, and Ni) Nanoparticle/Carbon Nanotube Electrocatalysts for Direct Methanol Fuel Cells," J. Power Sources, vol. 188, pp. 347–352, 2009

[36] A. Hamnett, "Mechanism and Electrocatalysis in the Direct Methanol Fuel Cell," Catalysis Today, vol. 38, pp. 445-457, 1997

[37] J.B. Goodenough, R. Mancharan, "Methanol Oxidation in Acid on Ordered NiTi," J. Mater. Chem., vol. 2, pp. 875-887, 1992

[38] H. Li, D. Kang, H. Wang, R. Wang, "Carbon-Supported Pt-RuCo Nanoparticles with Low-NobleMetal Content and Superior Catalysis for Ethanol Oxidization," Int. J. Electrochem. Sci., vol. 6, pp. 1058-1065, 2011

Design of a control system for an oxyhydrogen reactor

C. Cedano[1], V. Sánchez[1], R. G. Gonzalez[2], R. Barbosa[1]

[1]Universidad de Quintana Roo, Boulevard Bahía s/n, Chetumal, Q. Roo, México, 77019.
[*]Tel: +529838350300; e-mail: vsanchez@uqroo.edu.mx
[2]ESIQIE, Av. IPN, Gustavo A. Madero, Lindavista, D.F, México, 07738.

ABSTRACT

The fossil fuels that are consumed by the most of the vehicle are non-renewable resources and generate polluting particles that are released into the environment. Currently, there are vehicles with hybrid systems and other technologies that reducing the emission of pollution, however most vehicles do not have them or are not compatible with these new technologies. A viable solution is the enrichment of gasoline with the addition of hydrogen in order to improve the combustion and reduce polluting agents in gasoline motors. This work presents the design of a control system for a low cost oxyhydrogen reactor that produces H2 and O2 with up to 99% purity. A DC-DC power converter is used in order to supply efficiently power to the oxyhydrogen reactor.

Keywords: Oxyhydrogen reactor, hydrogen, power converter, gasoline enrichment.

Spent battery graphite rod as electrode materials for microbial fuel cell application

A.R. Montes-Ochoa[1], C. Frausto Reyes[2], M.O. Morales[2], F. Caballero Briones[3], F. Chalé-Lara[3], S-K. Kamaraj[1]*

[1]Universidad Politécnica de Aguascalientes, Ingeniería en Energía Calle Paseo San Gerardo No. 207. Fracc. San Gerardo. Aguascalientes, Ags. C.P. 20342, México.
[2]Centro de Investigaciones en Óptica, A.C. Prol. Constitución 607, Fracc. Reserva Loma Bonita Aguascalientes, 20200, México.
[3]Instituto Politécnico Nacional, Laboratorio de Materiales Fotovoltaicos, CICATA Altamira. México.
*Tel: +5214491156589; e-mail: sathish.bot@gmail.com,sathish-kumar.kamaraj@upa.edu.mx

ABSTRACT

Usable materials can be recovered from spent battery always attractive of their potential economic and environmental benefits. At this context, we have extracted the graphite rod (GR) from the spend battery and used as electrode materials in the dual chamber microbial fuel cell (MFC), to treat the wastewater collected from Universidad politecnica de Aguascalientes. The maximum volumetric power production of 140.48 mW/m^3, volumetric current density of 341.16 mA/m^3 at the 0.410 V was observed in spent battery graphite rod as electrode materials (anode and cathode) in MFC. Further, the surface of those graphite rod was fractured/irradiated by laser, in order to increase the superficial of electrode. Evaluated systematically this fractured graphite rod (F-GR) as electrode materials in MFCs as follows: 1) F-GR as anodic current collector and GR as cathodic current collector, 2) F-GR as cathodic current collector and GR as anodic current collector, 3) F-GR applied both anode and cathodic current collector. Use of both side F-GR as electrode materials improved 15 times higher volumetric power production (2210.55 mW/m^3).the power generate from this system was used for the low electronic application.

Keywords: graphite rod; microbial fuel cells; wastewater; laser

XVI International Congress of the Mexican Hydrogen Society 2016

Pilot-scale study on novel microbial fuel cell design for wastewater treatment

A. de J. Robledo Ruiz[1]; F. Caballero Briones[2], O. Solorza-Feria[3], K. Sathish-Kumar[1,*], F. Chalé-Lara[2], J. Tapia-Ramírez[4]

[1]Universidad Politécnica de Aguascalientes, Ingeniería en Energía Calle Paseo San Gerardo No. 207. Fracc. San Gerardo. Aguascalientes, Ags. C.P. 20342, México.

[2] Instituto Politécnico Nacional, Laboratorio de Materiales Fotovoltaicos, CICATA Altamira. México.

[3]Centro de Investigación y de Estudios Avanzados del Instituto Politécnico Nacional, Departamento de Química, Av. Instituto Politécnico Nacional 2508, Col. San Pedro Zacatenco, Delegación Gustavo A. Madero, CDMX, C.P. 07360, México.

[4]Centro de Investigación y de Estudios Avanzados del Instituto Politécnico Nacional, Departamento de Genéticas y Biología Molecular, CDMX, México.

[*]Tel: +5214491156589; e-mail: sathish.bot@gmail.com,sathish-kumar.kamaraj@upa.edu.mx

ABSTRACT

Simplifying the microbial fuel cells design is attractive for scaling up the wastewater treatment process along with minimal power production associated cleaning of water. With this context, we have proposed the simplified pilot scale MFC design for consists of vertical integrate clay pipe, where placed the anode at the bottom of the clay tube it was submerged on wastewater (collected from Universidad Politecnica de Aguascalientes). At the top of the clay tube covered with spent battery material act as a cathode, which exposed to open air (Mexican Patent Pending). This configuration was initially implemented on 10 L of wastewater that was separated individually (each holding of 1 L wastewater). One of the compartment produce the maximum volumetric power density of 9.04 mW/m^3, the volumetric current density of 21.71 mW/m^3 at the maximum potential of 0.415 V. Moreover, it exhibits the highest coulombic efficacy. Further, we are in the process of improving the power production by changing the slight configuration on microbial fuel cell design. Remarkably our design of MFC doesn’t require continues flow of wastewater. Therefore it could minimize the power consumption of wastewater.

Keywords: microbial fuel cell; baked Clay tube; Wastewater; pilot scale

XVI International Congress of the Mexican Hydrogen Society 2016

Cantarito (clay cup) modified air cathodic Microbial fuel cell for wastewater treatment

G.J. Bárcenas Durón[1], I. Ieropoulos[2], F. Caballero Briones[3], O. Solarza-feria[4], F. Chalé-Lara[3], J. Tapia Ramírez[5], S-K. Kamaraj[1*]

[1]Universidad Politécnica de Aguascalientes, Ingeniería en Energía, Aguascalientes, Ags. C.P. 20342.
[2]Bristol Robotics Laboratory, Bristol Business Park, Coldharbour Lane, Universities of Bristol and of the West of England, Bristol Business Park, Coldharbour Lane, BS16 1QY, U.K.
[3]Instituto Politécnico Nacional, Laboratorio de Materiales Fotovoltaicos, CICATA Altamira. México.
[4]CINVESTAV-IPN, Departamento de Química, CDMX, México.
[5]CINVESTAV-IPN, Departamento de Genética y Biología Molecular, CDMX, México.
[*]Tel: +5214491156589; e-mail: sathish.bot@gmail.com,sathish-kumar.kamaraj@upa.edu.mx

ABSTRACT

Our work focuses the modification of cantarito (clay cup) used as air cathodic microbial fuel cell system for a treatment of wastewater. Outside of the clay cup was covered by stainless steel mesh coated with spent battery materials act as a cathode. Wastewater collected from the Universidad Politecnica de Aguascalientes was filled inside of the clay cup, served as inocula and waste to be treated, where graphite felt act as an anodic current collector. This configuration produces the maximum volumetric power production of 629.56 mW/m^3, but it was maintained at the short period later tends to reduce the power. Further, we applied the acrylic based varnish and Arabic gum on the both side of the clay cup. Interestingly, acrylic based varnish painted clay cup produced the maximum volumetric power production of 504.11 $mW/m^3$and some way maintained the maximum power production for the long period of operation up to 350 hrs. Finally, energy harvested from the wastewater was powered by the low power electronics.

Keywords: cantarito; microbial fuel cells; wastewater

Bio-hydrogen production by SSF of paper industry wastes using anaerobic biofilms: A comparison of the use of wastes with/without pretreatment.

I.M.M. Moreno-Dávila[1*], E.B. Herrera-Ramirez-[1], M.M. Rodriguez-Garza [1], M.L. Chávez-González, Y. Garza-García [1], L.J. Ríos-Gonzalez[1*]

[1] *Departament of Biotechnology, Facultad de Ciencias Químicas, Universidad Autónoma de Coahuila. Boulevard V. Carranza y José Cárdenas Valdez, Col. Republica Oriente. C.P.25280. Saltillo, Coahuila, México.*

* *contact email: leopoldo.rios@uadec.edu.mx; imayelamorenod@hotmail.com*

***Abstract*—In this research, we carried out the process of simultaneous saccharification and fermentation (SSF) of paper industry wastes (PIW) with/without chemical pretreatment, using reactors in batch with anaerobic biofilms developed in fiber ixtle. This article summarizes the effect of pretreatment of cellulosic wastes on hydrogen production. The key process parameters: pH (4, 5 and 6) and enzyme loading of Celluclast enzyme (10, 40 and 70 FPU) at a temperature of 45 ° C were optimized by the response surface methodology (RSM) based on a two factor-three level central composite design (CCD), respectively. The results showed optimal working conditions, to maximize the production of hydrogen by the SSF process, at a pH of 5.29 and an enzyme load of 70 FPU, the maximum expected value of hydrogen yield was 30.7350 mmol/h*gVS. From the results obtained, the evaluation of the process of SSF was performed with paper industry wastes subjected to chemical pretreatment with H_2SO_4 1.5%. The key process parameters were optimized by the response surface methodology (RSM) based on a two factor-three level central composite design (CCD), using as variables: pH (4.5 and 6), enzyme loading of Celluclast® (10,40 and 70 UPF) and temperature (45°C) .The results showed the optimum working conditions to maximize hydrogen production by SSF process: 4.5051 pH, an enzyme load of 70 FPU and temperature 42.6768 ° C. The maximum expected value of hydrogen yield was 55 844 mmol /h*gVS.**

Keywords—Bio-hydrogen, simultaneous saccharification and fermentation (SSF), response surface methodology (RSM), paper industry wastes.

Dehydrogenation of $LiBH_4$+Al as Hydrogen Storage Reactive Hydride Composite

J. L. Carrillo-Bucio
Unidad Morelia del Instituto de Investigaciones en Materiales de la Universidad Nacional Autónoma de México. Antigua Carretera a Pátzcuaro No. 8701, Col. Ex Hacienda de San José de la Huerta, C.P. 58190, Morelia, Michoacán, México.

K. Suárez-Alcántara
Unidad Morelia del Instituto de Investigaciones en Materiales de la Universidad Nacional Autónoma de México. Antigua Carretera a Pátzcuaro No. 8701, Col. Ex Hacienda de San José de la Huerta, C.P. 58190, Morelia, Michoacán, México.

***Abstract*— The dehydrogenation reaction of $LiBH_4$+Al plus an additive (TiF_3, $TiCl_3$, CeO_2, $PdCl_2$ or Pd) is presented. The mixtures were produced by mechanical milled and characterized by SEM, XRD, and FT-IR. The dehydrogenation reaction was performed in a Sievert´s type reactor at 300°C and between 3.1-3.3 bar initial H_2 pressure. Dehydrogenation products were also characterized by XRD and FT-IR. Among the studied catalyst, the $TiCl_3$ and CeO_2 added-materials presented a reduced dehydrogenation temperature (200°C and 218°C respectively).**

Keywords*— *Hydrogen storage, reactive hydride composites, dehydrogenation temperature

I. Introduction

The $LiBH_4$ is an outstanding material regarding its hydrogen content (18.4 wt.%) [1]. However, its dehydrogenation temperature is too high for any application for hydrogen storage. The $LiBH_4$ presents two dehydrogenation steps at about 350°C and 500°C (maximum peaks of thermal desorption) [1]. In order to reduce the dehydrogenation temperature, the $LiBH_4$ had been mixed with MgH_2 to produce a reactive hydride mixture or composite (RHC). After dehydrogenation, a new mixture of LiH and MgB_2 was observed [2, 3, 4]. The $2LiBH_4+MgH_2 \leftrightarrow 2LiH+MgB_2+4H_2$ RHC had demonstrated a reduction of the dehydrogenation temperature, a change of the hydrogenation/dehydrogenation reactions pathway and an increase of reversibility [4]. Still, further improvements in the dehydrogenation temperatures and kinetics have to be done before any application. The design of new reactive hydride composites (RHCs) is an interesting and active tool in the searching of suitable hydrogen-sorption materials for hydrogen storage. The $LiBH_4$ had been mixed with several compounds in several proportions, producing or not (strictly speaking) new RHCs. A list includes but is not limited to other borohydrides [5], $LiNH_2$ [6], alanates of Li or Na [7, 8], halide salts such as LiCl [9] or LiF [8], metals hydrides such as CaH_2 [10], oxides [11], scaffolds [12], or metals such as Mg or Al [13, 14].

This last system, the $2LiBH_4$+Al, can be of potential interest if complete reversibility is achieved, i.e. the re-hydrogenation to the original mixture. Siegel et al [15] had anticipated, based on first-principles calculations, that the reaction

$$2LiBH_4+Al \rightarrow AlB_2+2LiH+3H_2 \qquad (1)$$

would release 8.6 wt.% hydrogen at 277°C and $p(H_2)$=1 bar. Hansen et al [15] had demonstrated that the dehydrogenation reaction of $2LiBH_4$+Al occurs at 300-500°C and $p(H_2) = 10^{-2}$ bar. The re-hydrogenation demonstrated only partial reversibility. However, it is well-known that the hydrogen pressure or the use of additives (or catalyst) can affect the dehydrogenation products on the related system $2LiBH_4+MgH_2 \leftrightarrow 2LiH+MgB_2+4H_2$ [16]. In turn, dehydrogenation products can affect re-hydrogenation. In the present work, we propose the addition of several materials (TiF_3, $TiCl_3$, CeO_2, $PdCl_2$ or Pd) and to register their effect on the dehydrogenation reaction of $2LiBH_4$+Al at different conditions of temperature and $p(H_2)$ than those reported elsewhere [15]. The selection of additives was performed for covering a wide range of materials from the popular titanium halides to a noble metal.

II. Material and Methods

A. Sample preparation

The mixtures of $2LiBH_4$+Al+additives were produced by mechanical milling. The reactives were purchased to Sigma-Aldrich and used without further purification. The Al was granular, with a particle size roughly of 1 mm and 99.7% purity. The $LiBH_4$ was hydrogen storage grade, meanwhile the rest of materials (additives) were fine powders of high purity. The milling was performed in a planetary mill (Across-International) with the rotation of the jars of 600 rpm. The milling vials were machinated in stainless steel 316L with an internal volume of 100 ml, with bolted lids. The milling balls were made of yttrium stabilized zirconium oxide (1cm diameter). The milling was performed in batches of 1 gram of mixture as needed for performing reactions or characterization. The $LiBH_4$ to Al molar ratio was 2:1. The total amount of the additive in each sample was 5 wt.%. The powder to ball relationship was 1:15. The total milling time was 5 hours divided into periods of 1 hour milling and 10 minutes resting. In each cycle of milling-pause, the rotation direction of the planetary mill was inverted. The handling of materials was performed inside a glove box filled with high purity argon (10 ppm O_2 and H_2O).

B. Dehydrogenation reaction

Dehydrogenations of $2LiBH_4$+Al+additive materials were performed in a Sievert's-type reactor. This reactor was designated and constructed by the research group. It consists basically of a sample holder, a suitable reservoir for H_2, high precision pressure transducers, and control of the reservoir and sample-holder temperatures. It is necessary to mention that the sample holder volume accounts for less than 1% of the reservoir volume for meeting appropriate conditions for hydrogen sorption/ desorption. The dehydrogenation was performed by a thermal-controlled process. The dehydrogenation initial pressure was fixed manually between 3.1-3.3 bar and the reservoir temperature was fixed at 40°C. After the reservoir was at constant temperature, the sample holder valve was opened and the sample temperature was raised from room temperature to 300°C with a heating rate of 5°C/min. The increase of the temperature will produce a small and smooth increase in the registered pressure; however, the dehydrogenation reaction is marked by a significant and sudden increase of the registered pressure beyond the temperature effects. The dehydrogenation time was 5 hours counted at the time of reaching 300°C. Then, the system was cooled down and then the remaining hydrogen was released. Samples were transferred to/from the Sieverts-type reactor without oxygen contact by means of a closing valve at the sample holder. The gases, hydrogen and argon, used during experiments were of chromatographic and high purity grade.

C. Characterization of the ball-milled and dehydrogenated materials

Scanning electron microscopy (SEM) images were obtained in a Jeol JSM-7600F or in a JSM-IT300 microscopes. Samples were dispersed on carbon tape inside the argon glove box; then they were transferred to the SEM chamber reducing the oxygen contact by means of a glove bag, even though partial oxidation could be possible. Unless otherwise indicated, SEM imaged were obtained by backscattered or secondary electrons and 10kV or 20kV of acceleration voltage. The range of conditions was dictated by each sample accordingly its characteristics.

Powder X-ray diffraction (PXRD) were performed in a BrukerB8 or Siemens D500 diffractometers accordingly to availability. Two wavelengths were used Cu K_α (1.540598Å) or Co K_α (1.789007Å) respectively. The powders of as-milled and dehydrogenated materials were compacted in a dedicated sample-holder, then they were covered with a kapton foil for protection against ambient oxygen and moisture.

Fourier transformed infrared spectroscopy (FT-IR). The studied materials were compacted in KBr pellets. The KBr was purchased from Sigma-Aldrich and dried just before the pellet preparation. FT-IR data was collected in a Varian 640-IR, FT-IR Spectrometer in ATR mode.

III. RESULTS AND DISCUSSION

A. Characterization of as-milled materials

Fig. 1 presents the most representative SEM images of the as-milled materials, some descriptions bellow contains remarks about SEM images of lower or bigger magnifications that are not showed in the present manuscript. For comparison purposes, the SEM images of $LiBH_4$ and Al without milling are presented first. Fig.1 (a) shows the $LiBH_4$ material, it is composed of large crystals embedded in an amorphous phase. Meanwhile, Fig.1 (b) shows the Al, it is composed of particles of 50 µm or less, heavily agglomerated to from particles over 1 mm. As-milled $2LBH_4$+Al material, Fig. 1(c), formed a three dimensional, porous structure. Interestingly the surface is fully covered with crystals of less than 1 µm size. Thus a dramatic change in the morphology was observed after ball milling of $LiBH_4$ and Al. The base material ($2LiBH_4$ + Al) plus TiF_3, Fig. 1(d), also presented a three-dimensional structure. The surface was covered with smaller crystals than in the un-catalyzed material. $2LiBH_4$+Al+$TiCl_3$ SEM image is presented in Fig. 1(e), here the surface was also covered with crystals, however in this material the crystals are about 50 µm size.

The addition of CeO_2, Fig. 1(f), to the base material produced an agglomerated, spherical and compacted material of about 50 µm in diameter. Here, clear spots of CeO_2 are distinguishable from the base material. The addition of $PdCl_2$, Fig. 1(g), also produced dramatic changes in the base material; perhaps it is the clearest example of a three-dimensional structure. This structure seems to be formed after the boiling of the $LiBH_4$, i.e. the formation and posterior rupture of bubbles. Fig. 1(h) shows the base material plus Pd, it presents agglomerates of about 50 µm in diameter. $PdCl_2$ is finely distributed along the base material.

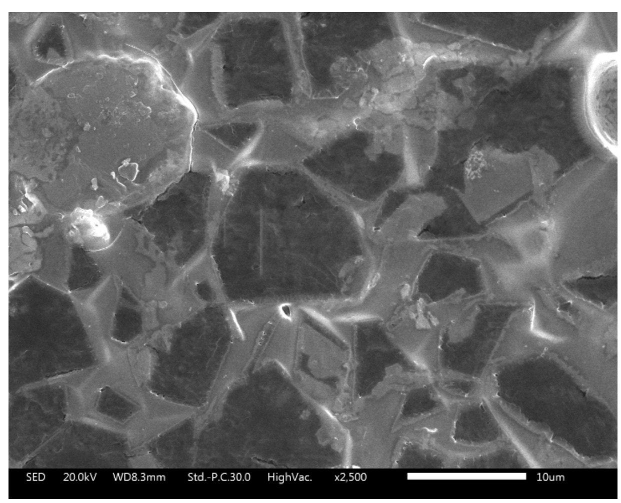

Fig. 1(a). SEM image of $LiBH_4$ (do not ball-milled).

UNAM-DGAPA-PAPIIT IA100415 Nuevos materiales para el almacenamiento de hidrógeno tipo mezclas de hidruro reactivo.

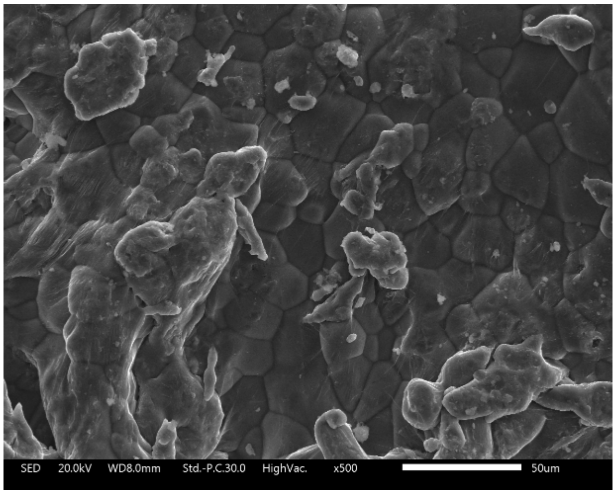

Fig.1(b). SEM image of Al (do not ball-milled).

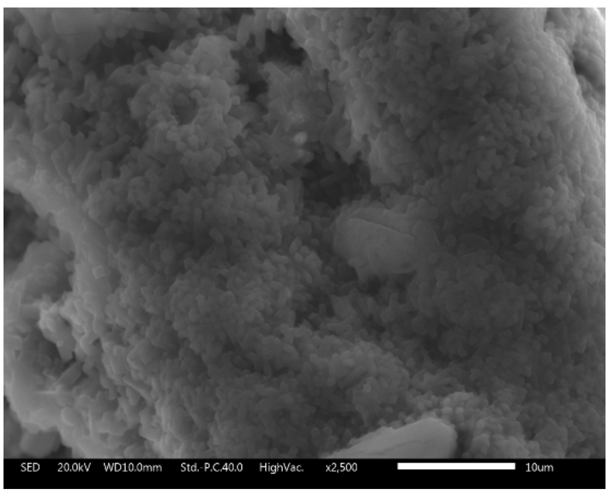

Fig.1(c). SEM image of the as-milled $2LiBH_4$+Al

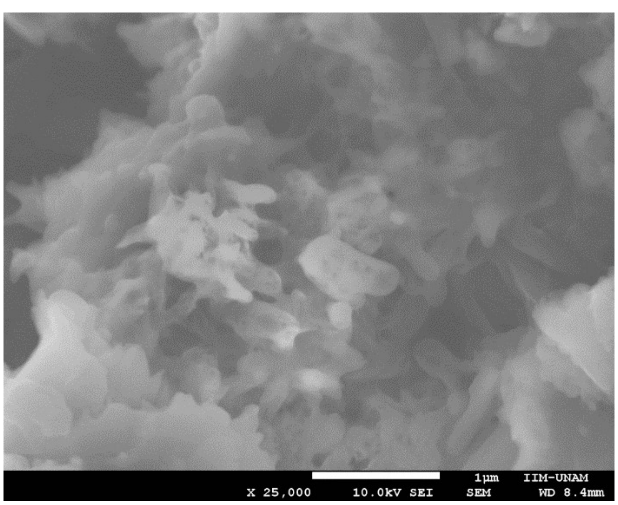

Fig.1(d). SEM image of the as-milled $2LiBH_4$+Al/TiF_3

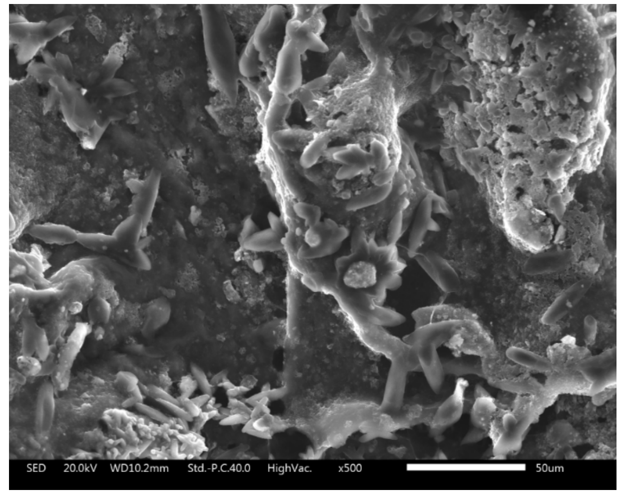

Fig.1(e). SEM image of the as-milled $2LiBH_4$+Al/$TiCl_3$.

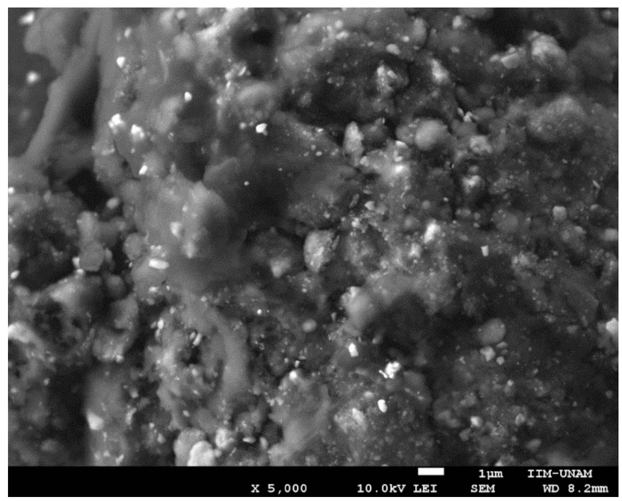

Fig.1(f). SEM image of the as-milled $2LiBH_4$+Al/CeO_2.

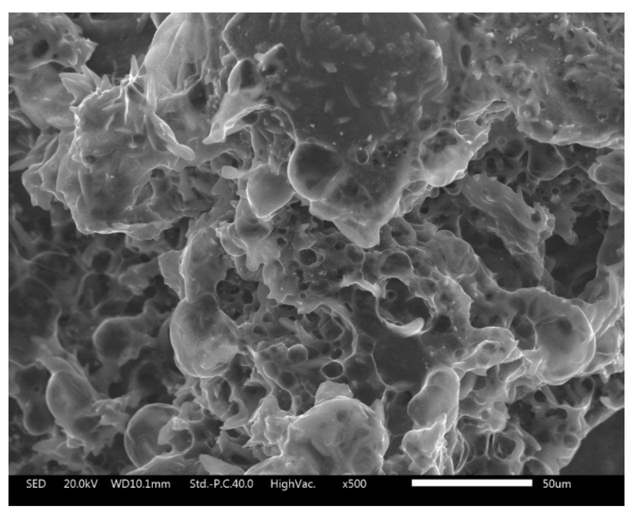

Fig.1 (g). SEM image of the as-milled $2LiBH_4$+Al/$PdCl_2$.

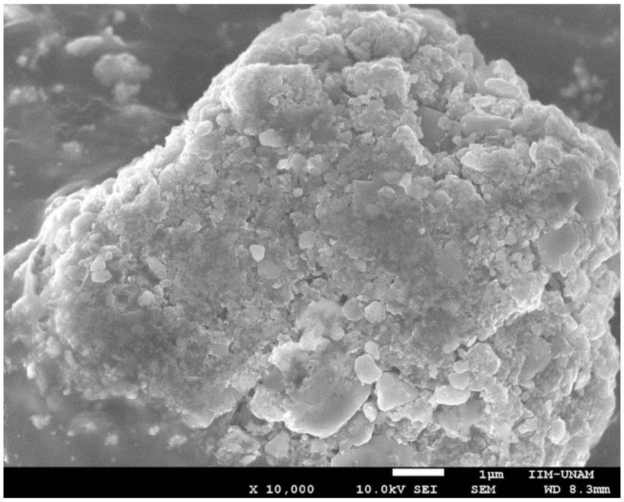

Fig.1(h). SEM image of the as-milled $2LiBH_4$+Al/Pd.

Figure 2 collects the X-ray diffraction patterns of all as-milled materials. Three general characteristics can be observed, the first of them is the clear presence of Al peaks. The second characteristic is that the peaks of $LiBH_4$ are partially obstructed by the kapton broad peaks at low diffraction angles (before 30° in 2theta). The third characteristic is that all additives, but the CeO_2, were well dispersed in the base material, not giving evident peaks. The X-ray diffraction of as-milled materials confirms the formation of fine mixtures of $2LiBH_4$+Al/additive. The broad peaks and the noise/peak ratio point to the formation of crystalline materials in the size range of micro-nano meters. Unfortunately the unavoidable kapton peak and the noise/peak ratio made inconclusive any Rietveld analysis.

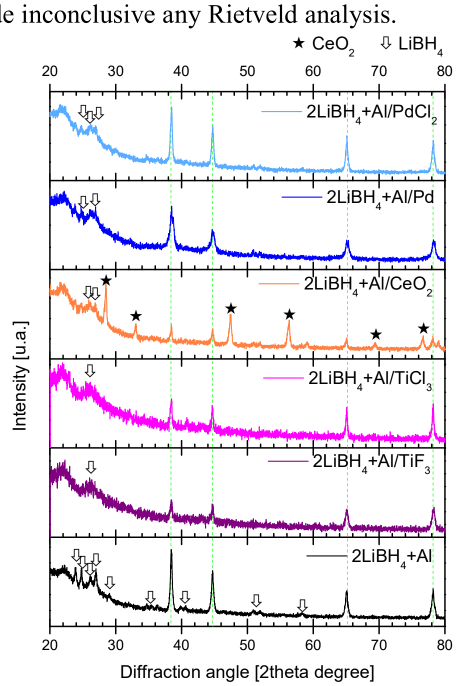

Fig.2. X-ray diffraction of the as-milled materials. λ: Cu K_α (1.540598Å)

A common effect of the local pressure and temperature increase during ball-ball collision is the decomposition of sensitive materials. In the case of the $LiBH_4$, it is intended to decrease the decomposition (dehydrogenation) temperature and preferably do not decompose during ball-milling. Thus FT-IR was performed to check the "survival" of $LiBH_4$ during ball-milling. Borohydrides present two regions of interest B-H bending (1000-1500 cm^{-1}) and H-B-H stretching (2000-2500 cm^{-1}) [17]. Both IR active modes are presented in all the as-milled sampled, indicating a good thermal stability during ball milling. Figure 3 presents the FT-IR data.

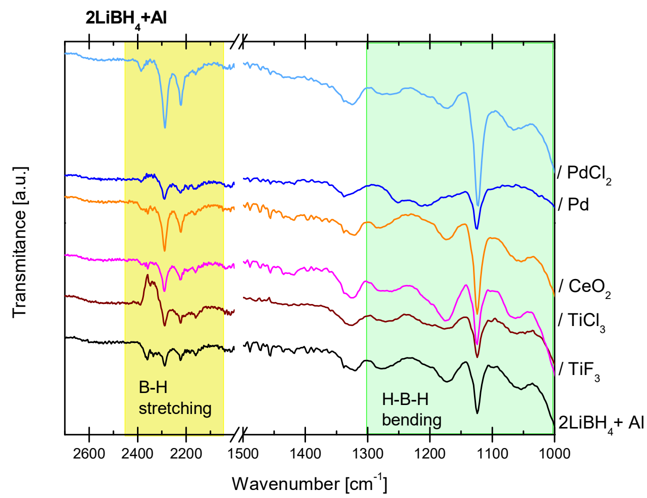

Fig.3. FT-IR of the as-milled materials, $2LiBH_4$+Al as reference and the catalyzed materials.

B. *Dehydrogenation reaction*

Fig. 4 presents the dehydriding reaction traced by thermal-programed control, the $2LiBH_4$+Al as the reference and the catalyzed materials are plotted. The increase of the temperature will produce a small and smooth increase in the registered pressure; however, the dehydrogenation reaction is marked by a significant and sudden increase of the registered pressure beyond the temperature effects. Thus in all frames of Fig. 4, the oven (sample) temperature also was plotted; the oscillations in the registered pressure was due to the small changes in the reservoir temperature (less than 2°C). At the present stage of the own-developed Sieverts type reactor, we only present the dehydriding temperature, the total change in pressure and the mass sample used in each experiment (Table 1). Further development of the reactor, use of state equations, and proper software integration will lead to a direct evaluation of the hydrogen release in wt. %. Still, clear changes due to the different additives can be observed.

The dehydrogenation temperature of $2LiBH_4$+Al without additives is 268°C (Fig. 4 (a)). This value is close to the temperature predicted by Siegel et al, 277°C [15]. $2LiBH_4$+Al without additives seems to dehydrogenate in three steps; the first one was observed below 200°C and produced a small pressure increase. The second and third steps were located at 268°C and 300°C and produced a notable increase in hydrogen pressure. Frames (b) to (f) present the $2LiBH_4$+Al plus additives. Although TiF_3 is a commonly used additive in the hydrogen storage materials research, the $2LiBH_4$+Al/TiF_3 (Fig. 4(b)) material does not represent an improvement in the dehydrogenation temperature, i.e. 276°C. An interesting catalyzed material was the $2LiBH_4$+Al/$TiCl_3$ (Fig. 4(c)). This material combines the lowest dehydrogenation temperature with a moderate increase in hydrogen pressure. The material with CeO_2 (Fig. 4(d)) also is interesting, it combines a good dehydrogenation temperature, 218°C, with the highest increase in hydrogen pressure. $2LiBH_4$+Al/$PdCl_2$ (Fig. 4(e)) material does not represent an improvement as compared with the base material or over the other additives, regarding the pressure increase or the dehydrogenation temperature. $2LiBH_4$+Al/Pd (Fig. 4(f)) material is a special case, it showed essentially no changes, just a very small increase in hydrogen pressure at 300°C.

Another good point founded for the $2LiBH_4$+Al, and the $TiCl_3$ and CeO_2 catalyzed systems, is that the dehydrogenation is rapid, completed within 1 hour. Table 1 summarizes the dehydrogenation temperature and the increase in hydrogen pressure and the mass of samples used. The relationship between the increase of pressure and the used mass is presented as a quick reference. The $2LiBH_4$+Al/$TiCl_3$ and $2LiBH_4$+Al/CeO_2 present good kinetics, a good increase of hydrogen pressure and reduced dehydrogenation temperature.

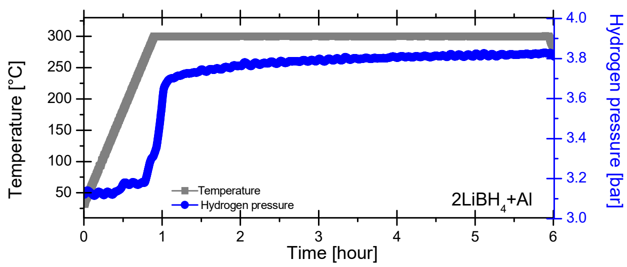

Fig. 4(a). Thermal-programed dehydrogenation of $2LiBH_4$+Al

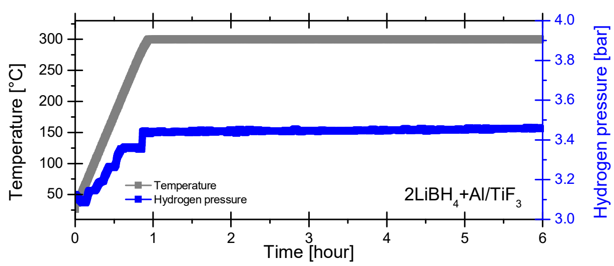

Fig. 4(b). Thermal-programed dehydrogenation of $2LiBH_4$+Al/TiF_3

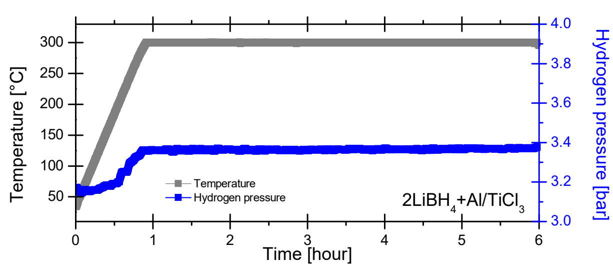

Fig. 4(c). Thermal-programed dehydrogenation of $2LiBH_4$+Al/$TiCl_3$

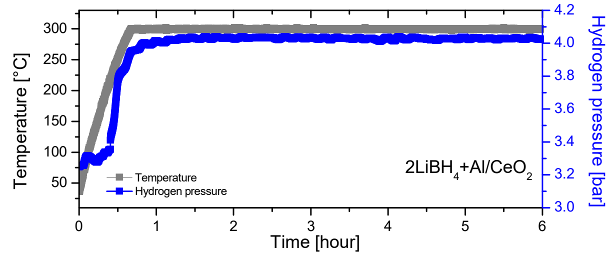

Fig. 4(d). Thermal-programed dehydrogenation of $2LiBH_4$+Al/CeO_2,

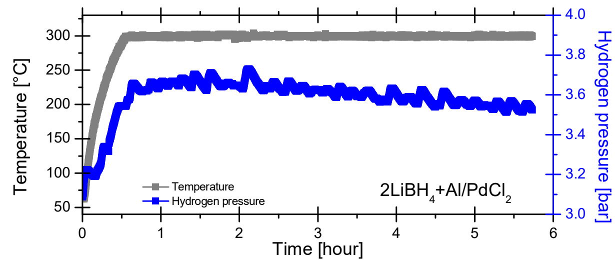

Fig. 4(e). Thermal-programed dehydrogenation of $2LiBH_4$+Al/$PdCl_2$,

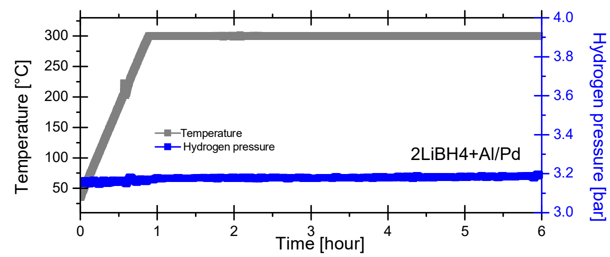

Fig. 4(f). Thermal-programed dehydrogenation of $2LiBH_4$+Al/Pd.

TABLE I. DEHYDROGENATION TEMPERATURE AND INCREASE OF HYDROGEN PRESSURE.

Material	Dehydrogenation temperature [°C]	Increase of pressure [bar]	Mass of sample [g]	Increase of pressure/ Mass of sample [bar/g]
$2LiBH_4$+Al	268	0.51	0.35	1.46
$2LiBH_4$+Al/TiF_3	276	0.09	0.46	0.19
$2LiBH_4$+Al/$TiCl_3$	200	0.16	0.53	0.30
$2LiBH_4$+Al/CeO_2	218	0.64	0.54	1.18
$2LiBH_4$+Al/$PdCl_2$	247	0.33	0.44	0.75
$2LiBH_4$+Al/Pd	300	0.02	0.56	0.004

C. Characterization of dehydrogenated materials

Fig. 5 presents the XRD of the dehydrogenated materials. All materials present the following common characteristics; the peaks of $LiBH_4$ vanished, meanwhile Al and LiH appears at the same diffraction angle (same symmetry and close lattice size). From bottom to top; the first frame presents the dehydrogenated $2LiBH_4$+Al material. This material shows the formation of $LiAlO_2$ as an undesirable product and LiH+ALB_2 as desirable products. The presence of $LiAlO_2$ is related to impurities in the raw materials or small contamination during handling of materials, its main effect is to reduce the hydrogen storage capacity. The 2LiBH$_4$+Al/TiF$_3$ presents very prominent peaks of Al/LiH and AlB$_2$, however, it also presents the LiAlO$_2$ peaks. 2LiBH$_4$+Al/TiCl$_3$ is marked by the formation of an unidentified peak at 53.4°. 2LiBH$_4$+Al/CeO$_2$ is the most interesting material from the XRD characterization, it no longer presents the CeO$_2$ peaks, neither Li, Al nor LiAl oxides. At the 2LiBH4+Al/PdCl$_2$ and 2LiBH$_4$+Al/Pd materials, in addition to the expected Al/LiH and AlB$_2$, PdO was present. Here we re-take the discussion on 2LiBH$_4$+Al/Pd material; thermal-programed desorption indicates no dehydriding reaction meanwhile XRD indicated a successful hydrogenation. Both results can be conciliated if dehydrogenation of 2LiBH$_4$+Al/Pd was carried out in a partial way.

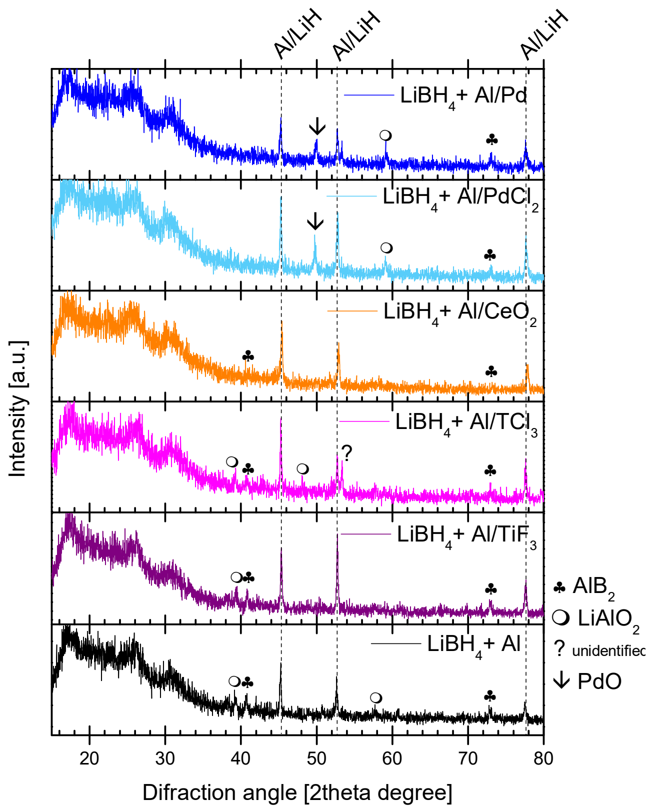

Fig.5. XRD patterns of (bottom to top) 2LiBH$_4$+Al; 2LiBH$_4$+Al/TiF$_3$, 2LiBH$_4$+Al/TiCl$_3$, 2LiBH$_4$+Al/CeO$_2$, 2LiBH$_4$+Al/PdCl$_2$, and 2LiBH$_4$+Al/Pd. or Co K$_\alpha$ (1.789007Å)

FT-IR of the dehydrogenated materials was performed to corroborate the successful dehydrogenation. As observed at the XRD of dehydrogenated samples, this characterization technique is not enough for highly amorphous materials. Fig.6 collects the FT-IR spectra of all samples. The materials added with TiF$_3$, CeO$_2$ and PdCl$_2$ showed a complete depletion of B-H bending (1000-1500 cm^{-1}) and H-B-H stretching (2000-2500 cm^{-1}) signals. On the other hand the un-catalyzed sample and the TiCl$_3$ and PdCl$_2$ added samples showed partial dehydrogenation, i.e. they still presented the bending and stretching peaks.

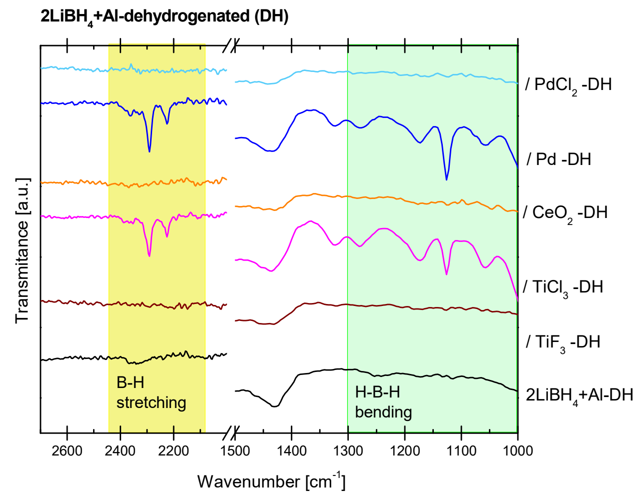

Fig. 6. FT-IR of dehydrogenated samples.

D. *Discussion*

In general, two effects have been observed after ball milling of the studied materials; first a proper integration of LiBH$_4$ and Al in the mixtures. Regarding the milling of Al, it is not so easy, it has the tendency of sintering instead of dispersing unless using proper milling conditions [18]. The milling conditions used here represent a balance between the proper milling of Al and reduced degradation of LiBH$_4$. Also, it is interesting that the additives caused important changes in the morphology of the materials. However, and contrary to other hydrogen storage materials, morphology does not seem to have a direct impact on the dehydrogenation reaction; i.e. the material that presented more agglomerations reacted better.

The multistep nature of the dehydrogenation reaction of the 2LiBH$_4$+Al is shared with the dehydrogenation of LiBH$_4$ [19] and the related RHC LiBH$_4$+MgH$_2$ [16, 20]. The last two dehydrogenations have been recognized as multistep reactions; and in the related MgH$_2$-RHC it had been reported its dependence with dehydrogenation pressure. Related reports on LiBH$_4$-Al at several molar proportions had reported also a multistep mechanism for the dehydriding reaction [21, 22, 23]. In the present work, dehydrogenation reactions of catalyzed materials showed only one step. Thus the use of additives have modified the reaction pathway.

Thermal-programmed desorption and XRD results point to 2LiBH$_4$+Al/TiCl$_3$ and 2LiBH$_4$+Al/CeO$_2$ as interesting materials due to the decreased dehydrogenation temperature. TiCl$_3$ is a moderately well know additive in the hydrogen storage area. CeO$_2$ is not commonly used as additive; however, it has been predicted to interact with hydrogen. Ceria could uptake small amounts of hydrogen below 391°C [24] and CeO$_2$ modified Fe$_2$O$_3$ had been proved adequate for hydrogen production and storage [25]. In the present work CeO$_2$ demonstrated its effectiveness reducing the dehydrogenation temperature and performing a complete reaction.

Additionally, the effect of short exposition to oxygen and moisture must be considered. Relatively recently; it was described that short-term exposure to a moist atmosphere has a very beneficial effect on the desorption reaction of the $2NaBH_4$+MgH_2 mixture [26]. To the best of the author's knowledge, no similar reports for $LiBH_4$ had been published. In the hydrogen storage research, it is normal the use of ultra-high purity argon with oxygen and moisture levels below 0.1 ppm. In our experiments the argon purity was not so high, the supplier-guaranteed argon purity was 10 ppm. This account as short oxygen and moisture exposition.

After the dehydrogenation, a pending question still arises about the absence of CeO_2 and oxides of Li, Al or LiAl in dehydrogenated $2LiBH_4$+Al/CeO_2 material, and to explain the CeO_2 effects on dehydriding reaction of $2LiBH_4$+Al. Further research must be done in that direction; additionally, careful characterization of the reaction exhaust gas (released hydrogen) is highly recommendable due to the possible loss of B. The loss of B is a common drawback for all borohydrides. B can be lost as borane compounds (BH_3, B_2H_6, etc.) or forming B-clusters that are unreactive at moderate pressures and temperature for further re-hydrogenation reaction. B losses are not detectable by FT-IR or XRD.

IV. Conclusions

$2LiBH_4$+Al/additives were prepared by ball milling. The milling conditions were appropriated for the integration of Al and preservation of $2LiBH_4$. The use of additives TiF_3, $TiCl_3$, CeO_2, Pd and $PdCl_2$ produced different morphologies. Among the studied materials $2LiBH_4$+Al/$TiCl_3$ and $2LiBH_4$+Al/CeO_2 materials presented a significant reduction of the dehydrogenation temperature, identified by a sudden increase of the reactor hydrogen pressure. $2LiBH_4$+Al/$TiCl_3$ and $2LiBH_4$+Al/CeO_2 are interesting materials that deserve further characterization.

Acknowledgment

The present work was supported by the UNAM-DGAPA-PAPIIT **IA100415 Nuevos materiales para el almacenamiento de hidrógeno tipo mezclas de hidruro reactivo**.

Authors want to thank Dr. Solaza-Feria and CINVESTAV-DF for facilitating FT-IT characterization. Authors want to thank Dr. Omar Novelo and Dr. Orlando Hernández for SEM characterization.

References

[1] A. Zuttel, P. Wenger, S. Rentsch, P. Sudan, Ph. Mauron, Ch. Emmenegger "$LiBH_4$ a new hydrogen storage material", Int. J. Power Sources 2003;118:1–7.

[2] J.J. Vajo, S.L. Skeith, F. Mertens "Reversible Storage of Hydrogen in Destabilized $LiBH_4$" *J. Phys. Chem. B*, 2005;109:3719–3722.

[3] G. Barkhordarian, T. Klassen, M. Dornheim, R. Bormann "Unexpected kinetic effect of MgB_2 in reactive hydride composites containing complex borohydrides" J. Alloys and Compounds 2007;440:L18–L21.

[4] U. Bösenberg, S. Doppiu, L. Mosegaard, G. Barkhordarian, N. Eigen, A. Borgschulte, T.R. Jensen, Y. Cerenius, O. Gutfleisch, T. Klassen, M. Dornheim, R. Bormann "Hydrogen sorption properties of MgH_2–$LiBH_4$ composites" Acta Materialia 2007;55:3951–3958.

[5] E. Gil-Bardají, Z. Zhao-Karger, N. Boucharat, A. Nale, M. J. van Setten, W. Lohstroh, E. Reohm, M. Catti, M. Fichtner "$LiBH_4$-$Mg(BH_4)_2$: A Physical Mixture of Metal Borohydrides as Hydrogen Storage Material" J. Phys. Chem. C, 2011;115:6095–6101.

[6] M. Aoki, K. Miwa, T. Noritake, G. Kitahara, Y. Nakamori, S. Orimo, S. Towata "Destabilization of $LiBH_4$ by mixing with $LiNH_2$" Appl. Phys. A 2005;80:1409–1412.

[7] A. Borgschulte, A. Jain, A.J. Ramirez-Cuesta, P. Martelli, A. Remhof, O. Friedrichs, R. Gremaud, A. Züttel "Mobility and dynamics in the complex hydrides $LiAlH_4$ and $LiBH_4$" Faraday Discuss.2011;151:213-30.

[8] Q. Shi, X. Yu, R. Feidenhans, T. Vegge "Destabilized $LiBH_4$-$NaAlH_4$ mixtures doped with titanium based catalysts materials research" J. Phys. Chem. C, 2008;112:18244–18248.

[9] O. Zavorotynska, M. Corno, E. Pinatel, L.H. Rude, P. Ugliengo, T. R. Jensen, M. Baricco "Theoretical and experimental study of $LiBH_4$-LiCl solid solution" Crystals 2012;2:144-158.

[10] A. Ibikunle, A.J. Goudy, H. Yang "Hydrogen storage in a CaH_2/$LiBH_4$ destabilized metal hydride system" J. Alloys and Compounds. 2009;475:110-115.

[11] X.B. Yu, D.M. Grant, G.S. Walker. Dehydrogenation of $LiBH_4$ destabilized with various oxides. *J. Phys. Chem. C*, 2009;113:17945–17949.

[12] H.S. Lee, S.J. Hwang, M. To, Y.S. Lee, Y. Whan Cho "Discovery of fluidic $LiBH_4$ on scaffold surfaces and its application for fast co-confinement of $LiBH_4$–$Ca(BH_4)_2$ into mesopores" J. Phys. Chem. C, 2015;119:9025–9035.

[13] J. Yang, A. Sudik, C. Wolverton "Destabilizing $LiBH_4$ with a metal (M) Mg, Al, Ti, V, Cr, or Sc) or metal hydride (MH_2) MgH_2, TiH_2, or CaH_2)" J. Phys. Chem. C 2007;111:19134-19140.

[14] B.R.S. Hansen, D.B. Ravnsbæk, D. Reed, D. Book, C. Gundlach, J. Skibsted, T.R. Jensen "Hydrogen storage capacity loss in a $LiBH_4$–Al composite" *J. Phys. Chem. C*, 2013;117:7423–7432.

[15] D.J. Siegel, C. Wolverton, V. Ozoliņš "Thermodynamic guidelines for the prediction of hydrogen storage reactions and their application to destabilized hydride mixtures" Physical Review B 2007;76:134102.

[16] U. Bosenberg, D. B. Ravnsbæk, H. Hagemann, V. D'Anna, C. Bonatto-Minella, C. Pistidda, W. van Beek, T.R. Jensen, R. Bormann, M. Dornheim "Pressure and temperature influence on the desorption pathway of the $LiBH_4$-MgH_2 composite system" J. Phys. Chem. C 2010;114:15212–15217.

[17] V. D'Anna, A. Spyratou, M. Sharma, H. Hagemann "FT-IR spectra of inorganic borohydrides" Spectrochimica Acta Part A: Molecular and Biomolecular Spectroscopy. 2014;128: 902–906.

[18] M. Ramezani, T. Neitzert "Mechanical milling of aluminum powder using planetary ball milling process" Journal of Achievements in Materials and Manufacturing Engineering 2012;55:790-798.

[19] A. Züttel, S. Rentsch, P. Fischer, P. Wenger, P. Sudan, Ph. Mauron, Ch. Emmenegger. Hydrogen storage properties of $LiBH_4$. J. Alloys and Compounds. 2003;356-357:515-520.

[20] K.B. Kim, J.H. Shim, S.H. Park, I.S. Choi, K.H. Oh, Y. W. Cho "Dehydrogenation reaction pathway of the $LiBH_4$–MgH_2 composite under various pressure conditions" *J. Phys. Chem. C,* 2015;119:9714–9720.

[21] X.D. Kang, P. Wang, L.P. Ma, H.M. Cheng "Reversible hydrogen storage in $LiBH_4$ destabilized by milling with Al" Appl. Phys. A 2007;89:963–966.

[22] O. Friedrichs, J. W. Kim, A. Remhof, F. Buchter, A. Borgschulte, D. Wallacher, Y. W. Cho, M. Fichtner, K. H. Oh, A. Zuttel "The effect of Al on the hydrogen sorption mechanism of $LiBH_4$" Phys. Chem. Chem. Phys. 2009;11:1515–1520.

[23] Y. Zhang, Q. Tian, J. Zhang, S.S. Liu, L.X. Sun "The dehydrogenation reactions and kinetics of $2LiBH_4$-Al composite" J. Phys. Chem. C 2009;113:8424–18430.

[24] K. Sohlberg, S.T. Pantelides, S. J. Pennycook "Interaction of hydrogen with CeO_2" J. Am. Chem. Soc. 2001;123:6609-6611.

[25] X. Zhu, L. Sun, Y. Zheng, H. Wang, Y. Wei, K. Li. CeO_2 modified Fe_2O_3 for the chemical hydrogen storage and production via cyclic water splitting. Int. J. Hydrogen Energy. 2014;39:13381–13388.

[26] C. Pistidda, G. Barkhordarian, A. Rzeszutek, M. Dornheim "Activation of the reactive hydride composite $2NaBH_4 + MgH_2$" Scripta Materialia 2011;64: 1035–1038

From the Can to the Tank: $NaAlH_4$ from Recycled Aluminum

Juan Rogelio Tena-García,
Unidad Morelia del Instituto de Investigaciones en Materiales de la Universidad Nacional Autónoma de México. Antigua Carretera a Pátzcuaro No. 8701, Col. Ex Hacienda de San José de la Huerta, C.P. 58190, Morelia, Michoacán, México.

Ricardo Guerrero-Ortiz,
Escuela Nacional de Estudios Superiores, Universidad Nacional Autónoma de México Unidad Morelia, Antigua Carretera a Pátzcuaro 8701, Col. Ex Hacienda de San José de la Huerta, C. P. 58190, Morelia, Michoacán, México.

Karina Suárez-Alcántara
Unidad Morelia del Instituto de Investigaciones en Materiales de la Universidad Nacional Autónoma de México. Antigua Carretera a Pátzcuaro No. 8701, Col. Ex Hacienda de San José de la Huerta, C.P. 58190, Morelia, Michoacán, México.

***Abstract*— It is presented the recycling of Al-cans (from soft beverages cans) by a ball milling process and its possible use as a main component of a hydrogen storage material. A suitable milling procedure for reducing Al-cans to Al-powders is presented. Then, the Al together with NaH and a suitable catalyst were milled as precursors of a hydrogen storage material. The impurities of the Al cans are well studied (Fe and Si mainly) and probably they have a good effect on the hydriding/dehydriding reactions. It is presented the SEM and DRX characterization of as milled materials.**

***Keywords*— Hydrogen storage; Recycled Al; Sodium alanate**

I. Introduction

The search for renewable and efficient energy sources is one focus of attention in materials science today. Hydrogen steps ahead as one of the most promising energy alternatives and recent research focuses on its storage and performance in optimal conditions for a mobile application [1]. The main goal of any research in hydrogen storage is to develop materials with high storage capacity, good performance, reversibility and rapid reaction kinetics. Research on hydrogen storage materials include, for example, metal hydrides, complex hydrides or metal-organic frameworks [2-4]. However, another aspect to consider for this type of materials is the cost, because raw materials of high purity and elaborate method of synthesis are currently expensive [2-4].

Sodium alanate is one of the most studied materials as potential hydrogen storage. Bogdanovic [5] proposed sodium alanate as hydrogen storage material capable of reversibility, by doping with Ti compounds, according to reactions:

$$3NaAlH_4 \leftrightarrow Na_3AlH_6 + 2Al + 3H_2 \qquad (1)$$

$$2\ Na_3AlH_6 \leftrightarrow 6NaH + 2Al + 3H_2 \qquad (2)$$

Several other researchers agree about the use of Ti-catalysts; however, high purity aluminum had been customary used until Bergemann [6] et al. studied the possibility of producing sodium alanate by reactive ball milling of particles obtained from recycled (wasted and incinerated) Al-slags.

Currenty, the recycling of solid residues is a problem on developing countries like Mexico. Additionally, the purchasing of fine and high purity metal powders such as Ti, Al or Mg is facing increasing restrictions. Thus, the research group have decided to deal both problems by using Al from Al-cans as recycled material. The main goal of the present research is to establish a suitable procedure for recycling of Al-can in order to use it as precursor of a hydrogen storage material.

II. Materials and methods

A. *Al-cans aconditioning and sample preparation*

Al-cans were collected on the university campus and used without washing. The labeling (polymers and inks) of the cans was not removed, thus that was also milled. Both conditions were used to keep circumstances closed to an industrial process. Al cans were cut manually into approximately 0.25 cm^2 area flakes (between 0.3-0.5cm per side). Due to the manually cutting by scissors, only the body of the cans were used, the tops and bottoms were discarded. Perhaps in an industrial process all Al-can could be used. The rest of the materials were NaH (95% purity, Aldrich), $TiCl_3$ (99.995% purity, Aldrich) and, $AlCl_3$ (99.999% purity, Aldrich). The last two materials composed the catalyst mixture: $TiCl_3$ + $AlCl_3$ in 3: 1 ratio. The catalyst mixture was prepared in an agate mortar and then added to the milling vial.

In a first milling procedure, only Al-flakes were milled while visual inspection allowed the determination of optimal milling time. Once the milling time was established, the corresponding amounts of the catalyst mixture, Al-flakes and NaH (10 grams in total) were milled together. The millings were performed in a nylon milling vial of inner volume of 100 ml. The catalyst mixture load accounted for 5 wt.% of the Al-flakes+NaH materials The catalyst mixture preparation and the whole handling of materials were performed in a glovebox with high purity Argon (10 ppm of O_2 and H_2O). The milling vial was closed in Argon atmosphere and transferred to the mill outside the glove box. The design of the milling vial (double cap, one of them a screw-cap) allowed appropriate sealing and avoided contamination. The milling balls were made of yttrium stabilized zirconium oxide (1cm diameter). The ball to powder ratio was 15:1. The milling was performed in a PQ-N04 Ball Mill planetary mill (Across-International) with the rotation of the jars of 600 rpm. The total milling time was 10 hours divided into periods of 1 hour milling and 10 minutes resting. The periods of milling time and pauses where selected to reduce the heating in the nylon vials.

B. *Materials characterization*

The as-milled samples were characterized by X-ray diffraction (XRD) and scanning electron microscopy (SEM). X-ray diffraction was performed in a Siemens D500 diffractometer, with wavelength of Co K_α (1.789007Å). The powders were compacted in a dedicated sample-holder, then they were covered with kapton foil for protection against ambient oxygen and moisture during the measurements.

Scanning electron microscopy (SEM) images were obtained in a JSM-IT300 microscope. Samples were dispersed on carbon tape inside the argon glove box; then they were transferred to the SEM chamber reducing the oxygen contact by means of a glove bag, even though partial oxidation could be possible. Unless otherwise indicated, SEM imaged were obtained by backscattered or secondary electrons and 10kV or 20kV of acceleration voltage. The range of conditions and detector was dictated by each sample accordingly its characteristics. EDS (energy-dispersive X-ray spectroscopy) was performed on both side of Al-flakes to determine their elemental composition.

III. RESULTS AND DISCUSSION

A. *Visual inspection of the milling procedure*

As sated above, the milling time was 10 hours. In a first milling, each hour the milling vial was opened and observed the relative amount of Al-flakes. 10 hours was enough to mill Al-flakes of about 0.25cm per side. Fig. 1 and Fig. 2 present images of the Al recycling process, from the can to the obtaining of Al-powders.

Fig. 1. Al-can and manual cutting to stripes and then to flakes.

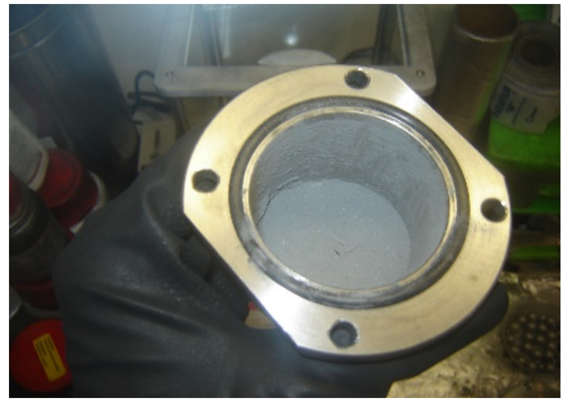

Fig. 2. Physical appearance of recycled Al-powders at 10 hours of ball milling.

B. *XRD of characterization*

Fig. 3 presents the diffractograms of the Al-powders and the NaH+Al/catalyst from recycled Al. Despite that the plot is presented in arbitrary units of intensity of diffracted beam; the intensity of Al peaks is bigger when milled alone compared when milled with the $NaAlH_4$ precursors. In that case (blue diffractogram) the NaH+catalyst can be seen as milling agents that help to reduce the crystallite size of Al. The Al diffractogram (pink) do not present indications of aluminum oxides, hydroxides or other impurities. In contrast, the NaH+Al/catalyst diffractogram evidences the presence of Al_2O_3 and two un-identified peaks.

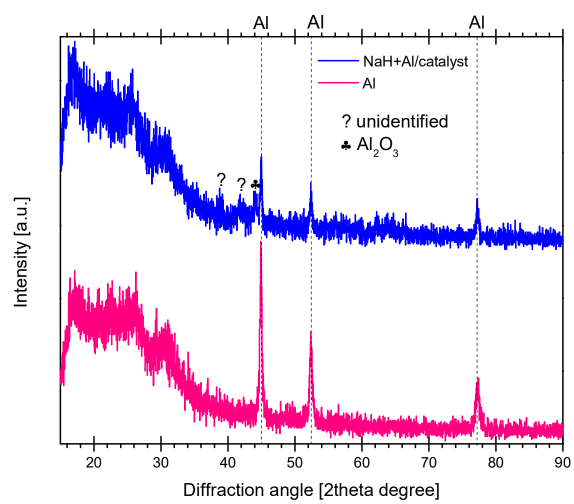

Fig. 3. Powder XRD of as-milled Al and NaH+Al/catalyst from recycled Al.

C. *EDS and SEM characterization*

Al-cans are a wide used product, even though their elemental composition is not wide know. Fig. 4 shows the elemental analysis of the Al-flakes and Table 1 collects the average composition without counting the superficial C and O (from can-labeling). Besides Al, the others important elements in the Al-cans were Fe, and Si. Minor quantities of Mg, Mn, Ti and Cu were also found.

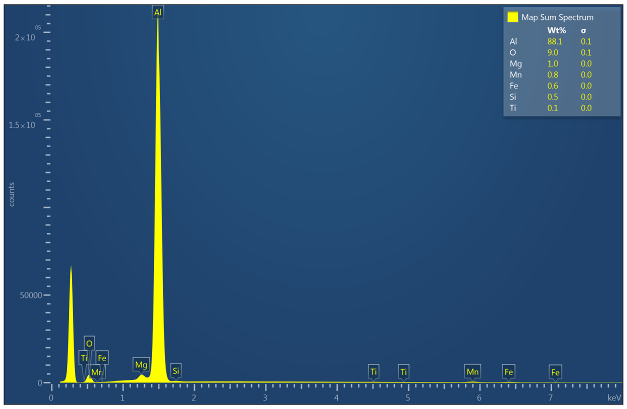

Fig. 4. EDS elemental analysis of the Al-flakes.

TABLE I. ELEMENTAL ANALYSIS OF AL-FLAKES FROM EDS

Element	***Line type***	***Wt %***	***Atomic %***
Mg	K series	0.90	1.04
Al	K series	87.54	91.94
Si	K series	0.90	0.88
Ti	K series	8.56	5.07
Mn	K series	0.90	0.48
Fe	K series	0.61	0.32
Cu	K series	0.57	0.24

Fig. 5 presents a low magnification SEM image of as-milled recycled Al. This recycled material showed particles from 50 μm to few micrometers. Thus the ball milled-recycled Al is equivalent to a -325 mesh commercial material.

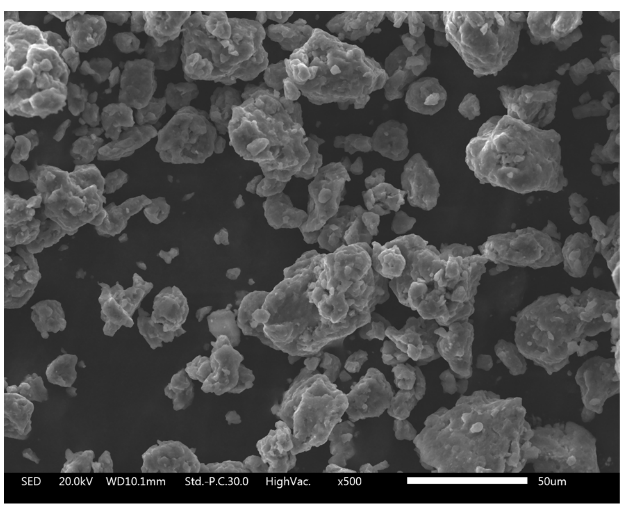

Fig. 5. Low magnification SEM image of as-milled recicled Al

Fig. 6 presents the surface of the as-milled recycled Al. In the material is evident the successive ruptures and cold-welding.

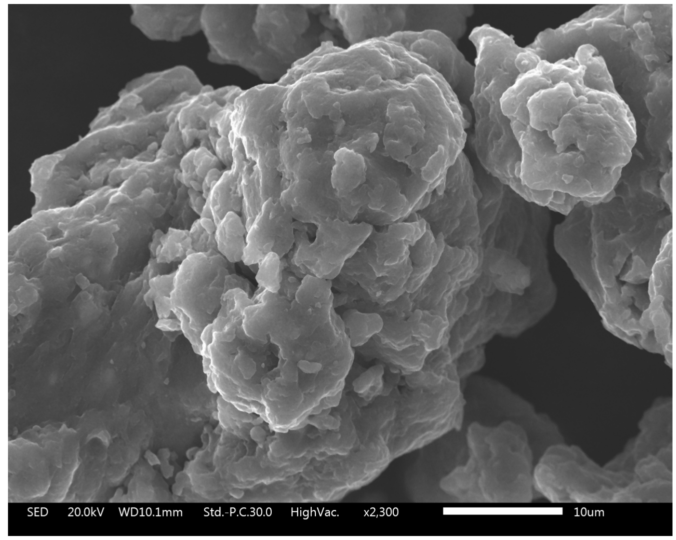

Fig. 6. Medium magnification SEM image of as-milled recicled Al

Intense changes in the material morphology was observed after 10 hours of ball milling of NaH+Al-flakes/catalyst. Fig. 7 present the SEM image of this material. Contrary to the well-defined particles of as-milled recycled Al; the material with NaH and catalyst appear as a fused and continued bed with some particles in its surface (Fig. 8).

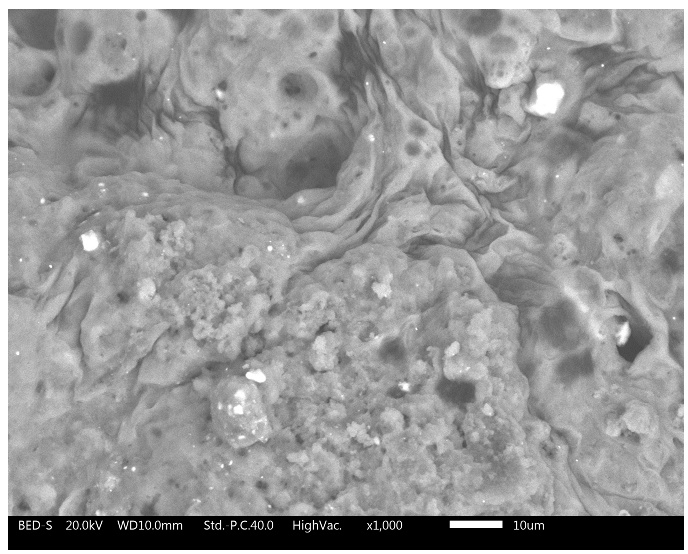

Fig. 7. Low magnification SEM image of as-milled NaH+Al(recycled)/catalyst

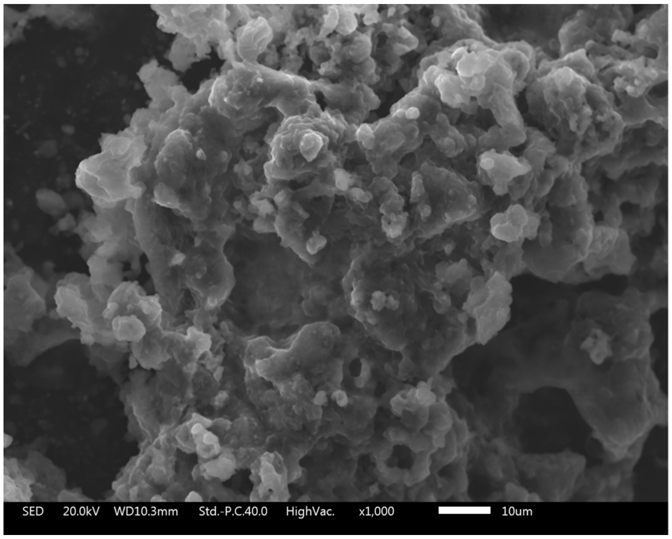

Fig. 8. Medium magnification SEM image of as-milled NaH+Al(recycled)/catalyst

Mechanical milling condition must be enough for dispersing equally the catalyst along the base material. Fig.9 demonstrated that the Ti-catalyst is well dispersed over the milled material. White points indicate the presence of Ti from the catalyst.

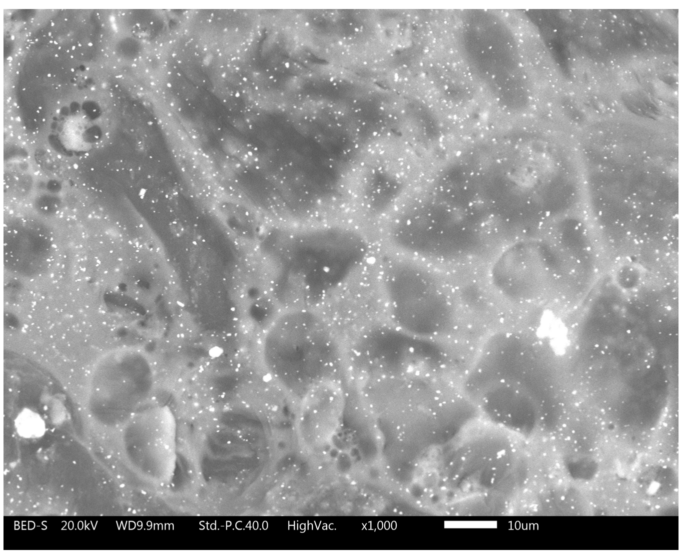

Fig. 9. Medium magnification SEM image of as-milled NaH+Al(recycled)/catalyst. White points indicate Ti presence

D. Discussion

Despite the apparent easiness of the described process for recycling Al and to make it suitable for hydrogen storage purposes, the mechanical milling of Al is not a simple process. Normally Al has the tendency of sintering instead of dispersing unless using proper milling conditions [7]. The milling conditions, particularly the milling time can be considered as soft. This is especially important if an extended or industrial application is intended. Furthermore, the ball milling process of all the precursors of $NaAlH_4$, i.e. NaH+Al/catalyst can be performed in a single step. This also could be of interest for a practical application.

All the elements present in the Al from cans, i.e. Mg, Si, Ti, Mn, Fe, Cu, had been used as catalyst in different materials for hydrogen storage. Particularly when Mg is used as the base element for hydrogen storage. Thus, the presence of all this impurities can be beneficial when the obtained mixture will be subject to hydriding conditions to produce $NaAlH_4$.

NaH is well known for its low melting point, NaH is reported to melt (and decompose) at 426°C [8]. The melting of materials can be responsible of the observed features of the NaH+Al(recycled)/catalyst materials. Locally, during the ball-ball collisions, the temperature and pressure can be raised importantly.

IV. Conlcusions

It was presented a procedure for recycling Al from soft beverage cans. With this procedure, Al powders can be obtained as a suitable precursor of a hydrogen storage material. It was demonstrated that in a single ball milling step all the precursors for $NaAlH_4$ can be obtained. Further work must be done for finding the suitable hydriding conditions.

Acknowledgment

The present work was supported by the UNAM-DGAPA-PAPIIT **IA100415 Nuevos materiales para el almacenamiento de hidrógeno tipo mezclas de hidruro reactivo**.

Authors thank to Dr. Orlando Hernández for SEM characterization.

References

[1] Rifkin, J. (2007). *The Hydrogen Economy*. New York.

[2] Sakintuna , B., Farida, L., & Hirscher , M. (2007). Metal hydride materials for solid hydrogen storage: a review. *Int. J. Hydrogen Energy*.

[3] Samanta , A., Furuta , T., & Li , J. (2006). Theoretical assessment of the elastic constants and hydrogen storage capacity of some metal organic frame work materials. *J. Chem. Phys.*

[4] Orimo, S., Nakamori , Y., Eliseo, J., Zuettel , A., & Jensen , C. (2007). Complex hydrides for hydrogen storage. *Chem. Rev.*

[5] Bogdanovic, B., & Schwickardi, M. (1997). Ti-doped alkali metal aluminium hydrides as potential novel reversible hydrogen storage materials. *Journal of Alloys and Compounds* , 253–254.

[6] Bergemann, N., Pistidda, C., Milanese, C., Girella, A., Bjarne , R., Wurr, J. Dornheim, M. (2014). NaAlH4 production from waste aluminum by reactive ball milling. *International Journal o f Hydrogen energy*, 9877-9882.

[7] Qiu, C.; Opalka, S. M.; Olson, G. B.; Anton, D. L. Thermodynamic Modeling of the Sodium Alanates and the Na-Al-H System. Int. J. Mat. Res. 2006, 97, 1484-1494

[8] M. Ramezani, T. Neitzert "Mechanical milling of aluminum powder using planetary ball milling process" Journal of Achievements in Materials and Manufacturing Engineering 2012, 55, 790-798.

DEVELOPMENT OF A PEMFC PLANT FOR A HYBRID ELECTRIC UTILITY VEHICLE: DESIGN AND CONSTRUCTION

Félix Loyola*, Javier de la Cruz, J. Roberto Flores, I. Lorena Albarrán, Ulises Cano, G. Uriel Ruiz, and I. Adair Prado

Instituto de Investigaciones Eléctricas, Gerencia de Energías Renovables. Calle Reforma 113, Col. Palmira, 62490, Cuernavaca, Morelos, México. * contact email: felix.loyola@iie.org.mx

ABSTRACT

In this work, the outcome of the design and fabrication processes of a proton exchange membrane fuel cell (PEMFC) plant, for a hybrid electric utility vehicle, are presented. The PEMFC plant sizing is based on the current and voltage requirements for the application, hydrogen use efficiency criteria, and mechanical aspects. The resulting PEMFC plant consists of four 100 cell's stack modules. The components design at the cell level take into account the criteria related with: self-humidified systems, open cathode and air-cooled configuration, minimum ohmic contact resistance, fuel sealing system, membrane reinforcement, and porous structures protection (catalyst layer and gas diffusion layer). The PEMFC plant fabrication includes the components manufacturing processes definition and implementation, as well as the cells assembly process into the 4 stack power plant.

Keywords: PEMFC stacks, design, fabrication.

Ni-Pt based nanopolyhedral catalyst to the ORR and PEM single fuel cell performance

J.L. Reyes-Rodríguez[1], D. Bahena-Uribe[2], J. Roque de la Puente[2], M.A. Leyva-Ramírez[1], O. Solorza-Feria[1*]

[1]Departamento de Química, [2]Laboratorio Avanzado de Nanoscopía Electrónica (LANE), Centro de Investigación y de Estudios Avanzados del Instituto Politécnico Nacional, Av. I.P.N. No. 2508, Col. San Pedro Zacatenco, Delegación Gustavo A. Madero, Ciudad de México, 07360.
[*]Tel: +52 (55) 5747 3800 Ext. 3715; e-mail: osolorza@cinvestav.mx

ABSTRACT

The current global trend, followed in several disciplines that use nanotechnology as a tool, is the design of new materials by modifying their composition, size and morphology. The oxygen reduction reaction (ORR) is not an exception and in recent years the trend is no longer seek new alloys or combinations of elements with Platinum, but rather to design more stable catalysts and efficiently exploit the use of the noble metal; i.e. maximizing the catalytic active area. The Ni-Pt based catalysts have been to date the best materials for ORR and recent studies are focusing on the synthesis of catalysts with preferential faceting through colloidal synthesis with controlled parameters. In this paper, we present the electrochemical evaluation toward the oxygen reduction reaction and the PEM single fuel cell performance of Ni-Pt nanopolyhedral catalysts synthetized by a simple colloidal thermal reduction method. The synthesis conditions were optimized to obtain very homogeneous polyhedral nanoparticles, with low polydispersity grade in a range between 30-40 nm and with low Pt content compared with other reports in the literature. For our best knowledge, it is the first time that these nanoparticles are designed under a systematic control of parameters. The materials were characterized by HR-TEM, HR-SEM, EDS, XRD, UV-Vis, and electrochemical evaluation using EDR potentiodynamic techniques. The Ni-Pt nanopolyhedral catalyst reveals a promising catalytic activity towards the ORR compared with commercial Pt/C Etek catalyst. Now it is working in the preparation of MEAs using the synthetized materials as cathodes in single fuel cell test to evaluate their performance.

Keywords: Ni-Pt catalysts, Nanopolyhedral, ORR, Fuel cell

Design of a Production Line of Alkaline Electrolyzer model ECH-001 used for Marine Vessels.

Ing. Maricruz Olalde Pérez
ESIME, SEPI Unidad Azcapotzalco
Instituto Politécnico Nacional
Ciudad de México, México
molaldep29@gmail.com

Dr. Juan Manuel Sandoval Pineda
ESIME, SEPI Unidad Azcapotzalco
Instituto Politécnico Nacional
Ciudad de México, México
jsandovalpineda@gmail.com

M. en I. Marisol Rico Cortéz
ESIME, SEPI Unidad Zacatenco
Instituto Politécnico Nacional
Ciudad de México, México
marisolricocortez@gmail.com

Dra. Rosa de Guadalupe Gonzalez Huerta
ESIQIE, Laboratorio de Electroquímica y Corrosión
Instituto Politécnico Nacional
Ciudad de México, México
rosgonzalez_h@yahoo.com.mx

Dr. Ricardo Gustavo Rodríguez Cañizo
ESIME, SEPI Unidad Azcapotzalco
Instituto Politécnico Nacional
Ciudad de México, México
rgrodriguez@ipn.mx

Luis Fausto Terán Balaguer
Xantronic S.A. de C.V.
Hermosillo Sonora, México
rosgonzalez_h@yahoo.com.mx

Abstract— **This article presents the design of a production line for alkaline electrolyzer model ECH-001 used in marine vessels, this device is integrated to internal combustion engine to reduce fuel consumption. For the development of this work, Methodology Design for Manufacturing and Assembly (DFMA) was applied, because it determines the efficiency of the design by the level of complexity of the components and it establishes the best method of manufacturing and assembly for a quality product with reduced cost. The current conditions of our country concerning air pollution, demand solutions that help reduce greenhouse gas emissions using of alkaline electrolyzers such as model ECH-001, as economizer fuel system is vital to reduce consumption of fossil fuels. As a result it shows the computer simulation of design proposal for alkaline electrolyzer's model ECH-001 production line. It is characterized by the use of a security, quality station and optimization of plant space and material flow.**

Keywords— production line, DFMA; electrolyzer, manufacturing.

I. INTRODUCTION

The environmental situation in our country has been worsening. The authorities have taken corrective measures, such as hardening the program "*Hoy no circula*", with the aim of reducing the emissions of polluting gases into the atmosphere and the situation is not acceptable yet.
At present, fossil fuel consumption in transport is very high. According to the 4th National Emissions Inventory of Greenhouse Gases, which was done by INEGEI (2010), total equivalent emissions of the transport sector in 2010 was 166,412 Gigagrams (Ggr) of carbon dioxide, which represents 35% of total pollution, and the contribution of the maritime sector was 2,341 Ggr. [1].
Because of this, it is of paramount importance the use of alternative energies.
The use of hydrogen as a fuel represents a very promising alternative energy source. The economy of Hydrogen is based on technologies and processes that have existed for many years and have not been widely exploited. In spite of the fact that one of the cleanest methods for obtaining hydrogen is the electrolysis of water Arango [2]. The oxyhydrogen gas can be used to feed a propulsion system, by enriching combustion; since being the oxyhydrogen a flammable gas reduces fossil fuel consumption, which would mean a solution to our environmental problem. Nowadays, researchers of Instituto Politécnico Nacional (IPN), have developed several prototypes of electrolyzers using the principle of electrolysis of water.

Interest in this technology has spread all over the world mainly in Asia and Europe ; and it is very remarkable in the Iceland´s case that has proposed eliminating the consumption of fossil fuels and replace them with hydrogen by 2030. However, in our country this technology is little applied and does not have a scientific and technological basis for its implementation.

II. Background

A. Electrolysis

According to Kreuter [3] History of water electrolysis started as back as the Industrial Revolution. The electrolyzers and fuel cells were invented in the nineteenth century, before the internal combustion engine was invented and the Petroleum was discovered Berry [4]. Between 1972 and 1978 the development of water electrolysis and alkaline advanced systems had already begun to emerge. Sastre [5] relates to an electrolyzer as an electrochemical device which through an electrical current dissociates oxygen and hydrogen of water, this generates a gas called oxyhydrogen, which acts as a power source. Recently, some electrolytic cells, which allow a hydrogen production more efficient, have been developed. An electrolytic cell consists of two electrodes, one of them is an anode and other is a cathode, an electrolyte that facilitates migration of ions and an electrical current source

B. Manufacturing System

Manufacturing systems refer to ways of organizing people and equipment so that production is carried out more efficiently, by means of optimizing resources that allows achieving the production goals. Modern manufacturing systems are dynamic, flexible, lean and looking for a quality production. The word Manufacturing, derives from Latin words: manus (hand) and factus (make). Several centuries ago the production was carried out by manual methods, however modern manufacturing is assisted by automated machinery which is controlled by computer, so its definition has been modified. Kalpakjian [6] defines Manufacturing as the process of converting raw materials into products; further it comprises the activities in which the manufactured product itself is used to make other products. Quoting to Groover [7] the History of Manufacturing can be divided into two parts; the discovery and invention by man of the materials and processes to make things, and the development of the production systems.

C. Production Line

A production line is a manufacturing system with multiple stations and a fixed route system which can be manual, automatic or hybrid. The manufacturing operations are performed sequentially from workstation to workstation and type of product is identical or very similar. For Nahmias [8] a production line is the process of directing resources (people, machinery, raw material) to create a product or service; that is to say, track discrete components that pass from one workstation to another at a controlled rate, following a determined sequence. The advantages of establishing a production line to a manufacturing process is: increment of productivity, quality, easy detection of mistakes in production, reduction of production time, inventories, spaces, and regulates the load work in each station.

III. Methodology

Design for Manufacturing (DFM) is a tool to facilitate manufacturing process used for each component of the product; while Design for Assembly (DFA) facilitates assembly of each of these components. Basing on the merger of these two methodologies it has created a third called Design for Manufacturing and Assembly (DFMA) Krumenauer [9].

A. Application of DFMA

For implementation of the methodology DFMA, to system of electrolyzer production is taken as a basis manufacturing capacity and easy assembly of the final product at the lowest cost.

To apply DFMA in the electrolyzer model ECH- 001, Estorilio [10] recommends the adoption of the following guidelines:

1. Getting of design details. It means to have a physical prototype of which is observed each of its parts, its sequence and assembly .
2. Considering the subassemblies as separate parts and identifying each .
3. Identifying and recording the time of assembly and disassembly .
4. Calculating the design efficiency by Equation (1) where E is the efficiency of the design , NP is the number of parts and TM is assembly time.

$$EP = \frac{3NP}{TM} \qquad (1)$$

According with step 1 of methodology the main components of electrolyzer were identified. The Tab. 1 shows the detail of each of the components, the description of its operation, the number of parts and the estimated assembly time. As a result, Table 1 shows the efficiency of the design is 20%, this value is within design parameters. Based on this result the design of a production system is proposed.

Table 1: Main components of electrolyzer model ECH-001

C1		**C2**	**C3**	**C4**	**C5**	**C6**
Component Number	*Description*	*Component*	*Numbers of Parts*	*Processing timein minutes*	*Operation Timein minutes (C3*C4)*	*Numbers of parts estimated*
1		Cover	3	5	15	2
2		Electrode	3	1	3	2
3		Container	3	5	15	1
4		Pipeline	2	1	2	2
					TM	**NP**
					35	7
		Design Efficiency			0.20	

IV. Development

A. Prototype of Electrolyzer model ECH-001

In Fig. 1 presents the model CH- 001 prototype which was designed by David Flores Hernández BE, and characterized in the laboratory of Electrochemistry of Escuela

Superior de Ingeniería Química e Industrias Extractivas (ESIQIE).
The performance curves of this prototype were obtained to determine its efficiency. It has had excellent results because it is able of generating a volumetric flow of Oxihydrogen gas of 1L/min. spending an electrical current of 80 amperes with 7.8 volts, because of its efficiency has been considered feasible for implementation in marine vessels.

Fig. 1. Electrolyzer model ECH-001.

To have a significant fuel savings, the marine vessels need about 20L/min. of oxyhydrogen gas to feed a diesel engine about 400 HP. Therefore we need to install an array of at least 20 electrolyzers for getting a fuel economizer system.

For the development of production line of this economizer system it is important to consider the market as a key factor, because knowing the optimal market conditions will allow merchandising of the product. Mexico is located in a privileged place. In Fig. 2 Port System Map is shown, and is identified The Guaymas Port in Sonora as the port with the greatest cargo volume. In addition in this port there is a company called Xantronic®, which is interested in acquiring this technology.
They have around 400 marine vessels and if each one requires 20 electrolyzer, the initial demand is estimated in 8000 unites; it means that it is necessary to produce 600 electrolyzer per month.

Fig. 2. Port System Map in Mexico, SCT, 2015

B. Production System

Based on the General Systems Theory developed by German biologist Von Bertalanffy, to define the production system is necessary to note that is an integrative perspective , that is, the components interact together to achieve a final product , such that each of them behaves as a complete and vital unit .

Fig. 3 shows the graphical representation of the Production System with the interrelationships of all units involved , which it consists of identifying the inputs (raw materials, fixed assets , labor, etc.), production process (production line) and Output (final product and its merchandising).

Fig. 3. System design production

C. Proposal of Production Line

The production line must control the discrete components that pass from a workstation to another at a determined rate, following a sequence which carries to manufacture of a product. Chase [11]. In Fig. 4 is shown the proposal of design the production line for electrolyzer model ECH- 001, where manufacturing workstations of the components are determined and external components are detected. Likewise stations subassembly and final assembly is observed. At the end of the process the product passes by a quality analysis and through a safety station, to certify the product attributes and later introduce them to the out station.

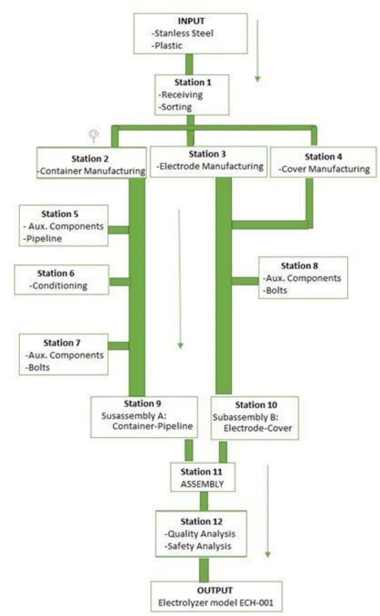

Fig. 4. Production Line

The structure of the production line passed from conceptualization to virtual reality using the Tecnomatix Plant Simulation® software. It is a tool for discrete event simulation that helps create digital models of logistic systems to allow exploration of the characteristics systems and optimizing their performance. Through these digital models can carry out experiments and work with hypothetical scenarios [12].

Fig. 5 is shown the distribution of the production line. It is important to mention that having the design in software allows, testing, modifications and assessments that indicate the level of efficiency of the production line. This tool allows to view 3d virtual line of production, shown in Fig. 6, to obtain a great structure of design proposal.

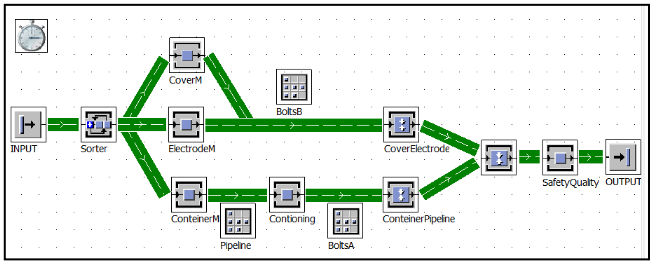

Fig. 5. Simulation of Production Line by Tecnomatix Software®.

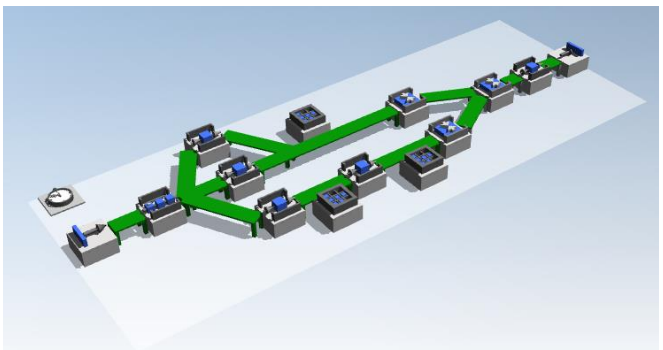

Fig. 6. Simulation of Production Line by Tecnomatix Software®.

V. Results

This proposed design of production line for alkaline electrolyzers is the start of development of a technology little applied in our country, and field is open to research. Thanks to DFMA methodology, the electrolyzer components and design efficiency were identified. Based on these results the principles of the production line were established.

VI. Conclusions

The production line showed in Figure 3 is feasible for implementing, as it respects the principles and characteristics that must have a production line, in addition, the analysis in Tecnomatix Plan Simulation software confirms that the configuration is appropriate, however the software makes several recommendations about configuration, it is necessary to evaluate different scenarios for selecting the best option.

VII. Acknowledgments

To: 1. Government of México, 2. Instituto Politécnico Nacional, 3.Escuela Superior de Ingeniería Mecánica y Eléctrica U-Zacatenco y Azcapotzalco, 4. Escuela Superior de Ingeniería Química e Industrias Extractivas (ESIQIE), 5. Project*: Programa de Estímulos a la Investigación (PEI) CONACYT 231094*, 6. Project SIP No. 20160414-20160416, 7. CONACYT Consejo Nacional de Ciencia y Tecnología, 8. Authors David Flores Hernández BE and Israel Trujillo Olivares BE for their technical support and 9. The organizers of the event by its attentive invitation.

VIII. Bibliography

[1] IV. Inventario Nacional de Emisiones de Gases de Efecto Invernadero (INEGEI), 2013, Secretaría del Medio Ambiente y Recursos Naturales, (1ra ed.) [En línea] Disponible en www.inecc.gob.mx

[2] Mejía Arango Juan Guillermo, Acevedo Álvarez Carlos, "Proyección al año 2015 para el uso del Hidrógeno en el sector de transporte del Valle de Aburrá",Universidad Tecnológica de Pereira, Colombia, Scientia Et Technica, Vol. 18, No. 2, agosto 2013, pp 327-334

[3] W. Kreuter and H. Hoffmann, "Electrolysis: The Important Energy Transformer in a World of Sustainable Energy", Int. J. Hydrogen Energy, 1998, Vol. 23. No 8. pp 661-666.

[4] Berry Gene D., Aceves Salvador M., "La Economía del Hidrógeno como solución al problema de la estabilización del clima mundial", Acta Universitaria, Enero-Abril 2006, Vol. 16. No 1. pp 5-14. [7] Serrano, J. y Muciño, D., "Producción de hidrógeno por electrólisis del agua con energía eoloeléctrica". Disponible: http://132.248.59.12/cu_1_17/Datos/trabajoGHV.pdf

[5] Sastre Soriano, "Aplicación de la energía eólica para la producción de hidrógeno mediante electrólisis", Escola Universitaria d'Enginyeria Técnica Industrial de Barcelona, Universidad Politécnica de Catalunya, 2010. [4] Posso, Fausto, "Energía y ambiente: pasado, presente y futuro", Universidad de los Andes, San Cristóbal, Venezuela, 2003, Vol. 8, No. 1, pp. 49-66.

[6] Kalpakjian S., Manufactura Ingeniería y Tecnología, 2008, Pearson Education de México.

[7] Groover M.P., Fundamentos de Manufactura Moderna, Ciudad de México, 2007, McGraw Hill.

[8] Nahmias S., Analisis de la Producción y las operaciones, Ciudad de México, 2007, McGraw Hill.

[9] Krumenauer, F. Z., Matayoshi, C. T., Da Silva, I., "Concurrent Engineering and DFMA approaches on the development of automative panels and door", 2012, Vol. 6

[10] Estorilio, Carla, Simião, Marcelo César, Schonoski, Cleiton Luis, "Aplicación del método DFMA para la reducción del costo de fabricación de un motor diésel", XII ICIEOM - Fortaleza, Brasil, October 9 - 11, 2006. [13] Vidal Mugica, Ricardo, "Sistemas de Producción", Unidad de Gestión de la Producción Animal, ICATC Universidad Austral de Chile.

[11] Chase, R., Aquilano, N., Jacobs, R., "Administración de producción y operaciones - Manufactura y servicios", McGraw-Hill, 2009, 8va Ed., pp. 4-19.

[12] Siemens PLM, Disponible: https://www.plm.automation.siemens.com/es_mx/plm/index.shtml

Performance of Ni-Pd-Pt catalyst in membrane-electrode assemblies for PEM single fuel cell

C.V. Tinoco-Muñoz[1], J.L. Reyes-Rodríguez[2], D. Bahena-Uribe[3], J.G. Cabañas-Moreno[1], O. Solorza-Feria[2]

[1]Programa de Nanociencias y Nanotecnología, CINVESTAV-IPN. [2]Departamento Química, CINVESTAV-IPN, [3]L.A.N.E. CINVESTAV-IPN.
Av. IPN 2508, Col. Zacatenco, 07360, México D.F., México
[*]Tel: 01 55 5747 3800 Ext. 3715; e-mail: osolorza@cinvestav.mx

ABSTRACT

This paper presents the performance test results of membrane-electrode assemblies (MEAs) for proton exchange membrane (PEM) single fuel cell using a Ni-Pd-Pt catalyst as cathode. The Ni-Pd-Pt catalysts were synthesized from a modified methodology developed in our working group. The electrochemical studies were performed using a classical three-electrode configuration cell employed a 0.1 M $HClO_4$ solution as electrolyte. The physical characterization was performed by X-ray Diffraction (XRD) and High Resolution Transmission Electron Microscopy (HR-TEM). Electrochemical results showed that Ni-Pd-Pt electrocatalyst had an electrochemical surface catalytic area (ESCA) of about 70 m^2/g. Results of the ORR conducted to specific activity (S_A= 0.106 mA/cm^2_{Pt}) and mass activity (MA=0.320 A/mg_{Pt}), both evaluated at 0.9 V vs. RHE. These results were low compared to commercial Pt catalyst (Pt-ETEK; ESCA= 77.11 m^2/g, S_A=0.21 mA/cm^2 and M_A=0.180 A/mg_{Pt} @ 0.9 V vs. NHE). However, the trimetallic catalyst presents an adequate catalytic activity toward the ORR with a low Pt content. The last was considered to make single fuel cell performance tests. Membrane-electrode assembly with an active area of 5cm^2 were prepared using the Ni-Pd-Pt material as cathode and commercial 20%wt. Pt/C catalyst as anode, using the technique of painted with brush and hot pressing (40Kg/cm^2 at 120 °C). Polarization curves were obtained from a single fuel cell after to an activation process of the MEAs operated under humidification conditions at 80°C and 30 PSI of pressure. The preliminary performance results for Ni-Pd-Pt based MEAs were lower than for commercial Pt Etek catalysts based MEAs, used as comparison (@ 0.4V; 462 mW/cm^2) while for Ni-Pd-Pt catalysts it was 50% lower. However, this work showed the possible use of low Pt content catalysts as cathodes in real operating conditions of single fuel cell and opens the research way to continue optimizing these materials.

Keywords: PEM fuel cells, Ni-Pd-Pt catalyst, ORR, Performance

Ni and Ni-Cu core-shell nanoparticles: structural and electrochemical study for ORR

F. Pedro-García, A. M. Bolarín Miró, F. Sánchez de Jesús,
Área Académica de Ciencias de la Tierra y Materiales
Universidad Autónoma del Estado de Hidalgo
Hidalgo, México

C. A. Cortés Escobedo
Centro de Investigación e Innovación Tecnológica
Instituto Politécnico Nacional
Ciudad de México, México
Claudia.alicia.cortes@gmail.com

R. de G. González-Huerta
E. Superior de Ingeniería Química e Industrias Extractivas
Instituto Politécnico Nacional
Ciudad de México, México

G. Torres Villaseñor
Instituto de Investigaciones en Materiales
Universidad Nacional Autónoma de México
Ciudad de México, México

***Abstract*— Ni and Ni-Cu core-shell nanoparticles were synthesized by polyol method. Results of structural, magnetic and morphological characterization are presented. In addition, results of electrocatalytic performance in the oxygen reduction reaction in both, alkaline and acid media are presented. Structural and morphological characterization was performed by means of X-ray diffraction with Rietveld refinement and scanning electron microscopy. Magnetic and electrochemical measurements were made by vibration sample magnetometer and cyclic voltammetry, respectively.**

Keywords—Ni-Cu alloys; core shell; OR

I. Introduction

One of the most worrying problems today are energy sources and their relationship with environmental impact. The main source of fuel for most of the countries are the fossil fuels, but both, extraction and use have an important contribution to the imbalance in carbon cycle and therefore in the availability of this kind of fuels for future generations. This is why is so important to search for more sustainable options in energy generation.Hydrogen is the most promising energy carrier due to its very high energy density of 33.3 kWh kg^{-1} [1], and also, it can be obtained easily from the electrolysis of water, methane and other common products [2]-[4]. Alkaline water electrolysis (AWE) is now-a-days increasingly considered as a promising method for the large-scale production of carbon-free hydrogen and oxygen in view of power grid regulation and large scale energy storage [5]. In spite of this is an promising process, the use of platinum electrocatalysts for having a good performance in the Hydrogen Evolution Reaction (HER) dismisses its commercial use, then, the development of more efficient non-platinum electrocatalysts for HER reaction is still needed.

Hydrogen evolution reaction (HER) occurs through a limited number of steps with only one type of intermediate. The well-known reaction steps in alkaline solutions are represented in equation (1-3) [6]-[7].

$$M + H_2O + e^- \rightleftarrows MH_{ads} + OH^- \quad (1)$$

$$MH_{ads} + H_2O + e^- \rightleftarrows M + H_2 + OH^- \quad (2)$$

$$MH_{ads} + MH_{ads} \rightleftarrows H_2 + 2M \quad (3)$$

HER starts with the proton discharge (Volmer reaction, Eq. (1), and follows either the electrodesorption step (Heyrovsky reaction, Eq. (2), or the H recombination step (Tafel reaction, Eq. (3)). The distinction between steps, (1), (2) and (3) as the rate controlling is usually accomplished in terms of Tafel slopes or by calculating the rate constants of the forward and backward reactions through simultaneous fitting of polarization and impedance data. According to the general model for the HER mechanism, if the Volmer reaction (Eq. (1)) is the rate determining step (rds), the resulting Tafel curve should yield a slope of 118mVdec−1 at 20 ◦C. If the Heyrovsky step is rate determining (Eq. (2)), the measured Tafel slope would yield a value of about 40mVdec−1, or 30mVdec−1 for the Tafel desorption step (Eq. (3)) [8].

During the HER reactions, hydrogen atoms are the intermediate species that are adsorbed on the cathode metal interface. The dependence of the fractional surface coverage and of the electrodeposited species is defined by a pseudocapacitance, CF [9]-[10].

This pseudocapacitance can be improved by modifying surface characteristics in electrocatalyzers, by increasing surface charge or by employing electroactive alloys to promote the adsorption of H into the surface, improving then the performance of the HER.

Some efforts have been made in development of new materials for hydrogen evolution reaction (HER) in the electrolysis of water [6], [11] which, at the same time reduce both platinum content reducing costs and keep adequate efficiency of the HER reaction, by reducing the HER over-potential. To become economically interesting for the large scale hydrogen production, the energy consumption of modern AWE cells should lie somewhere in the 4.2e4.8 kWh/Nm^3 H_2 range, at operating current densities of 0.5 to 1.0 A/cm^2.These can be done by using Ni and Ni alloys as electrocatalyzers [12].

The overpotential can be reduced by alloying Ni with another metal which can increase the electron availability to adsorb H, by increasing specific area diminishing particle size and by modifying the interaction morphology between Ni and other metal [13]-[14].

Among the alloys studied for the hydrogen evolution reaction in alkaline solutions, nickel and some of its alloys could be considered the more active electrode materials. Ni-W films obtained by induced co-deposition were also considered as the most promising catalysts for HER [14]. However, during Ni-M film electrodeposition (where M is a metal), hydrogen evolution secondary reaction (HESR) cannot be avoided due to low current efficiency [15]. In this sense, alloys prepared by polyol process offer two possibilities to enhance the activity of these materials (i) increasing surface area by diminishing grain size (ii) modify the morphology of the Ni-M interaction (core-shell) and (ii) from a catalytic point of view, to combine an active metal with other pure metals to obtain alloys with optimized adsorption characteristics [14].

In the present work the crystal structure, magnetic and physical characterization behavior of Ni, Ni-30Cy and core-shell Ni-Cu powder obtained by polyol process. Besides, the synthesis mechanism during the polyol process is presented.

II. Experimental

A. Synthesis

Stoichiometric amounts of $NiCl_2$ $6H_2O$ (purity 99.995% Sigma Aldrich) and NaOH (purity 99.8% Sigma Aldrich) were dissolved in 125 mL of diethylene glycol ($C_4H_{10}O_3$, purity 99.8% Sigma Aldrich) to achieve the synthesis of powder metallic nickel according to the following equation:

$$\mathrm{NiCl_2.6H_2O + 2NaOH \rightarrow Ni + 2NaCl + 7H_2O} + 1/2\, O_2 \qquad \text{(eq. 4)}$$

NaOH 0.1 M was used as reductor agent of the Ni^{2+} dissolved.

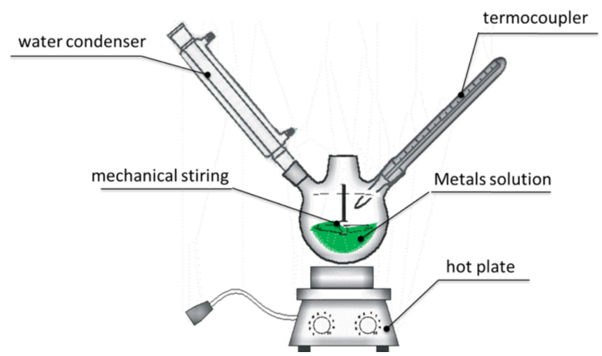

Fig. 1. Schematic representation of the polyol method.

The solution was stirred until a complete solution and then brought to boiling (220°C) under mechanical stirring using a heating rate of 10°C/min. The solution was maintained at boiling temperature in reflux for 2 h. Once cooled, the powders was cleaned by using hot water. To dissolve Na three washing cycles were performed consisting of the following: suspension in ethanol, centrifugation at 12,000 rpm for 15 min, and finally drying at 80°C in air. The Figure 1 show the schematic representation of the experimental setup where are included the experimental parameters.

The same experimental conditions were used to obtain Ni-30Cu powder, using $CuCl_2$ $2H_2O$ (purity 99.995% Sigma Aldrich) as precursor of metallic copper, by following this reaction:

$$\mathrm{NiCl_2.6H_2O + 0.3CuCl_2.2H_2O +}$$
$$\mathrm{2NaOH \rightarrow Ni{+}0.3Cu + 2NaCl + 9H_2O} + 1/2\, O_2 \qquad \text{(eq. 5)}$$

And finally, the last experiment was done to obtain core-shell Ni-30Cu particles. In this case, it was obtained first Ni powder by polyol according to ec. 1, and then, Cu was deposited by polyol, too, the expected powder are show in Figure 2.

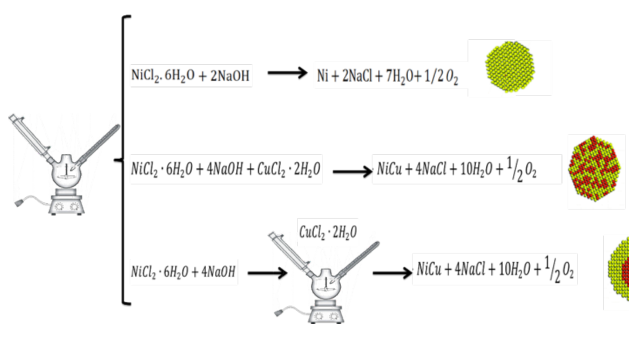

Fig. 2. Schematic representation of Ni, Ni-30 and Ni@30Cu core–shell nanoparticles.

B. Characterization

X-ray diffraction (XRD) of the obtained powders was used to study the phase transformations as a function of the alloy, using a Bruker D2 Phaser. Diffraction parameters were 2θ ranging from 20° to 90°. Cu Kα (λ= 1.5418 A) radiation was used in all experiments. Rietveld refinements were performed on the X-ray diffraction patterns to obtain the percentages of different phases, crystallite sizes and microstrains of the powders. This method considers all collected information in a diffraction pattern and uses a least-squares approach to refine the theoretical line profile until it matches the measured profile [16]. Crystallographic data were obtained from the Crystallography Open Database (COD) [17]. Scanning electron microscopy (SEM) using a JEOL-100-CX II helped determine the morphology and qualitative particle size. Magnetization studies were carried out at room temperature using a MicroSense EV7 vibrating sample magnetometer (VSM) with a maximum field of ±18 kOe.

Electrochemical evaluation was carried out using a Pyrex cell with a working carbon electrode (0.196 cm^2 geometric area), a Hg/Hg_2SO_4, 0.5M H2SO4 (E=0.680 V/NHE) reference electrode and a platinum mesh counter electrode with more than 10 cm^2 of surface area. Potentials are reported with respect to the normal hydrogen electrode unless specified. A rotating disk electrode (RDE) and a 263 A (EG&G PAR) potentiostat/galvanostat with 0.5M H_2SO_4 (acid media) or 0.5M NaOH (basic media) solution as the electrolyte in rotating rates of 100, 200, 400, 900, 1600 and 2500 rpm at a scan velocity of 5 mV seg-1 were used. Electrochemical activation was carried out by 20 successive cycles at 50 mV seg^{-1} in a potential window of 0-1.2 V/NHE to avoid impurities, absorbed oxygen and oxides.

The electrocatalysts were prepared as follows: 1.2 mg of electrocatalyst and 200 µL of ethanol were sonicated for 20 min. The powders were then dried at 40 °C and placed in a closed glass container prior to their utilization. The working electrodes were prepared according to the methodology reported elsewhere [18]. The electrocatalytic thin film deposited on the glassy carbon electrode was prepared by the addition of 16 µL of a uniformly dispersed suspension resulting from the mixture of 60 µL of ethanol, 6 µL of Nafion® (5 wt%, Du Pont 1000EW) and 1.2 mg of electrocatalyst.

Pt mass-specific activity (Im) was calculated at E= 0.90 V/NHE for an ORR polarization curve measured at a scan rate of 5 mV s-1. The mass activities are estimated via calculation of jk (kinetic current) and normalization to LPt (the working electrode Pt loading). Catalyst electrocatalytic activity towards the ORR is quantified at E= 0.90 V because interferences from mass-transport losses cannot be completely excluded at the higher current densities observed below E=0.90 V [19].

III. Results and discussion

In Figure 3, the X-ray diffraction patterns of the obtained metallic powders from the polyol process are presented. As can be observed, in the XRD pattern corresponding to pure Ni, there are peaks corresponding to a mixture of crystal structures hexagonal nickel (PDF#99-101-0883, *P63/mmc*) and cubic nickel (PDF#99-101-2999, *Fm-3m*). It is important to remark that hexagonal structure is not usual in nickel powder since it is not an equilibrium phase, and is expected to observe changes in magnetic and electrochemical properties of the powder, compared to single phase nickel.

The Rietveld refinement corresponding to the XRD patterns are showed in Table I. As can be appreciated, pure nickel is formed by a mixture of two different crystal structures: 82% of bcc-Ni and 18% of hcp-Ni, which is a non-common phase. In spite of Ni-Cu are completely soluble, according to Hume-Rothery´s rules, in our experimental conditions, they do not form a complete solid solution, and only a portion of NiCu (solid solution) is formed. For the case of NiCu mixture, in which both precursors for Ni and Cu were mixed at the same time, cubic Ni and Cu phases are present in almost the same proportions. A different behavior is found for the case in which CuCl2 was added during growth stage in the synthesis. Here, the proportion of single cubic Cu phase is larger than Ni phase and Ni-Cu alloy. This fact should be attributed to the dissociation stage for Ni before crystallization, allowing the NiCu alloy crystallization as Cu were added, as is showed in Fig. 1., while for the first case, Ni and Cu dissociation and crystallization with atoms of the same kind is occurring during growth stage in polyol method.

Table I shows the Rietveld refinement results for the volume percentage of each phase, the crystallite size and the microstrain, all of which were obtained from the XRD pattern analyses (Figure 3). These results confirm that a nanocrystalline material was obtained by using polyol mediated synthesis.

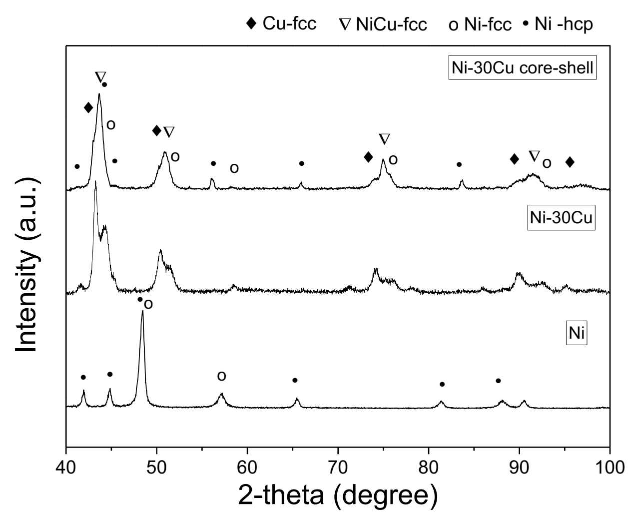

Fig. 3. X-ray diffraction of: (a) Ni (b) Ni-30Cu and Ni-30Cu core-shell.

Sponsors: Center of Nanosciences and micro and nanotechnology of the National Polythecnic Institute; SIP-IPN and CONACYT under grants SIP MULTI-1338, CB-157925, and CB-130413.

Table I: Data from the Rietveld refinements of the XRD patterns of the powders, which were obtained using polyol for obtaining: Ni; Ni-30Cu and Ni-30Cu core-shell.

Parameter	Ni			NiCu			Ni@Cu		
	%v	*Cryst. Size (Å)*	*Micro strain*	*%v*	*Cryst. Size (Å)*	*Micro strain*	*%v*	*Cryst. Size (Å)*	*Micro strain*
Ni *P63mmc*	18.19	225	0.0007	2.37	MNC*	MNC*	0.67	MNC*	MNC*
Ni *Fm3m*	81.81	953	0.0042	29.84	534	0.0027	2.99	MNC*	MNC*
Cu *Fm3m*	0	0	0	30.00	385	0.0027	40.22	880	0.0065
NiCu Alloy Fm3m	0	0	0	37.79	195	0.0067	56.12	660	0.0060

**MNC: Measurement non-confident (%Err>>data)*

Furthermore, these results support the proposed mechanism and quantify the phases that are present. In the cases of NiCu and Ni@Cu samples, for phases with minor proportion, the crystallite size, as well microstrain measurements in Rietveld refienement were non confident, due to calculation of error are too large compared to calculated data.

To evaluate the magnetic behavior, the obtained powders underwent magnetic characterization. Figure 4 shows the magnetic hysteresis loops of powders synthesized by the polyol method. The initial sample (nickel powder) shows a ferrimagnetic behavior typical of this material. The value of specific magnetization at 18 kOe (approximately 17 emu/g at 18 kOe) is lower than the reported value (approximately 55 emu/g at 18 kOe). It is known that magnetization is an intrinsic property, which depends on the components of the mixture; therefore, the lower magnetization can be attributed to the dilution effect of different crystal structure, cubic and hexagonal, which was obtained during the precipitation process. The specific magnetization at 18 kOe of Ni-30Cu and Ni-30Cu core-shell, 8 and 14 emu/g respectively, are lower than the presented by the nickel powder, as a consequence of the presence of copper, due to this element is a diamagnetic. The magnetic behavior is weak ferromagnetic. Therefore, magnetization measurements afford a simple way to estimate the presence of different materials in the mixture.

The coercivity of the obtained material is low (H_c=0.20 kOe) for all the powder, is in good agreement with reported values for Ni and Ni-Cu nanoparticles. However, the particles show low saturation specific magnetization, we consider that is high enough for improving their catalytic properties.

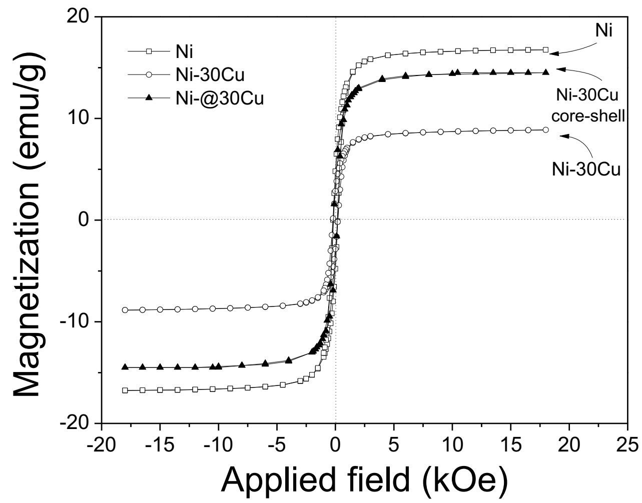

Fig. 4. Magnetic hysteresis loops of Ni; Ni-30Cu and Ni-30Cu core-shell.

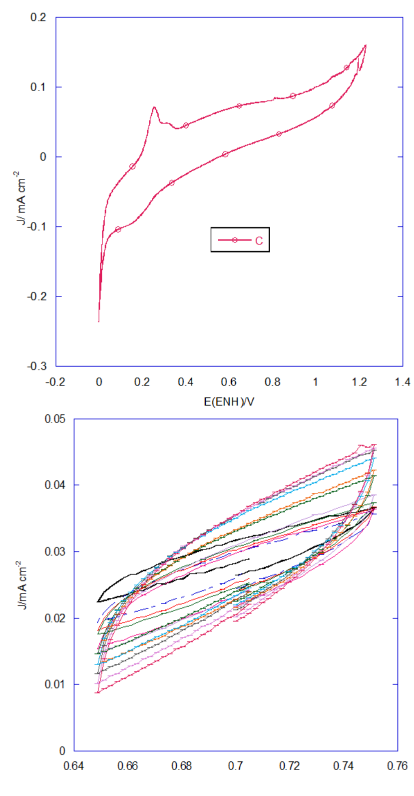

Fig. 5. Cyclic voltammetry for Ni-30Cu core-shell samples in acid media.

In order to understand the effect of the Ni-30Cu core-shell new modifications, cyclic voltammetry of sample was measured in acid and basic media.

In Fig. 5 cyclic voltammogram for acid media is presented, in which both oxidation and reduction signals were found for the same electrochemical reaction, indicating a poor electrocatalyst activity. This result, contrary to expected is associated to stability of Cu crystals which shells the Ni core. Another explanation for this behavior is the electronegative nature of the Cu surface, due to the inductive effect which repels H. Then, cycles from 0.65 mV to 0.75 mV were applied to core-shell sample in order to observe capacitance of the surface. Results are shown in the right side of Fig. 5. Here, a poor capacitance is observed.

This probable electronegative nature of the surface gives potential to act in basic media. In order to evaluate the electrochemical activity of the core-shell Ni@Cu powder, now in basic media, a voltammogram in basic media is presented in Fig. 6. It is observed the unstability of the alloy in basic media.

A study of zeta potential (ζ) versus pH, for all the powder synthesized, was done, the results are shown in Figure 7. As can be observed in Figure 7, the zeta potential (ζ) of all the powders show two different changes, attributed to the formation of different metallic complex.

Ni powders in aqueous medium was determined to be about -32 mV at neutral medium (pH =7). Nevertheless, the zeta potential (ζ) of Ni-Cu at the same pH (7) was fairly increases to +17.0 mV, and it was further moved toward positive charge (+40 mV) by decreasing the pH of the dissolution (acid solution). This fact is a confirmation of Ni and Ni-Cu particles synthesized by polyol, could be a good material as catalyst in HER reaction, however, it is important con control the pH of the aqueous solution.

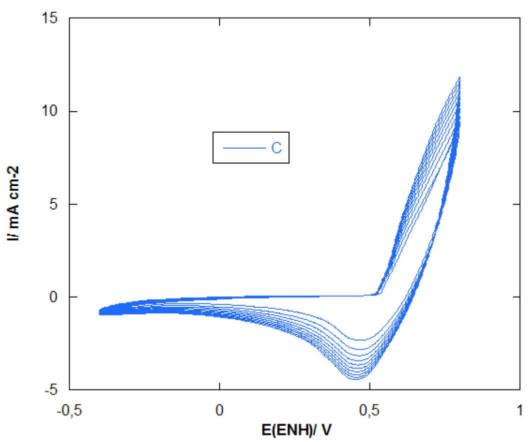

Fig. 6. Cyclic voltammetry for Ni-30Cu core-shell samples in basic media.

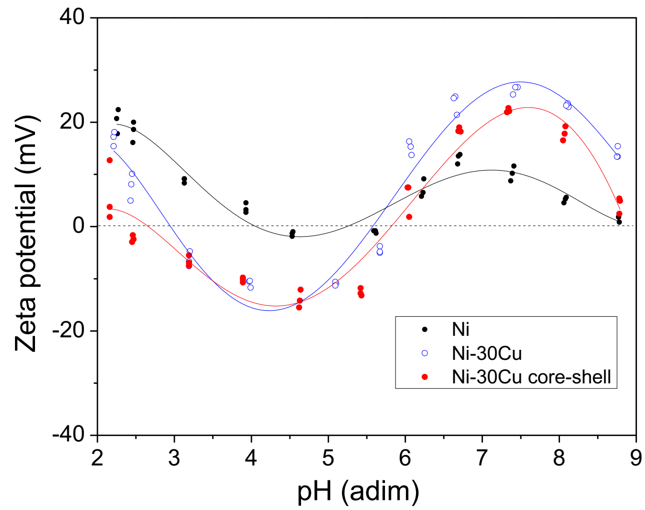

Fig. 7. Zeta potential (ζ) versus pH in aqueous medium of Ni (b) Ni-30Cu and Ni-30Cu core-shell.

For both, Ni-30Cu and Ni-30Cu core-shell samples, the isoelectric point is acid, about pH between 5.5 and 6, then, by associating pH with electrochemical capacitance, both associated with electrical charge of the surface on the particles. On the other hand, at 4 and 7.5 were found the inflection points for curves of the Ni-30Cu and Ni-30Cu core-shell samples, this maximum and minimum in surface charge was found in less potential for Ni sample.

Conclusions

Synthesis of Ni, Ni-30Cu and Ni@30Cu were successful by polyol method, obtaining the non-common hexagonal Ni phase and NiCu alloy rich phase in Ni@30Cu samples.

The presence of hexagonal Ni phase, as well as Cu reduces magnetization saturation in all the samples. Magnetic characterization confirms the presence of diamagnetic phases as hexagonal Ni and Cu.

For better performance in acid and basic media, pH of 4 and 7.5 are recommended for further acid and basic electrochemical measurements, this because the larger ζ potential was found at these pH.

Acknowledgment

Authors thank to Center of Nanosciences and micro and nanotechnology of the National Polythecnic Institute for structural characterization. Thanks are also due to SIP-IPN and CONACYT for financial support under grants SIP MULTI-1338, CB-157925, and CB-130413.

References

[1] Müller CI, Sellschopp K, Tegel M, Rauscher T, Kieback B, Röntzsch L, The activity of nanocrystalline Fe-based alloys as electrode materials for the hydrogen evolution reaction. J Power Sour 2016; 304: 196–206.J. Clerk Maxwell, A Treatise on Electricity and Magnetism, 3rd ed., vol. 2. Oxford: Clarendon, 1892, pp.68–73.

[2] Oliver-Tolentino MA, Arce-Estrada EM, Cortés-Escobedo CA, Bolarín-Miro AM, Sánchez de Jesús F, González-Huerta RG, Manzo-Robledo A, Mechanically activated Pt-Ni and Pt-Co alloys as electrocatalysts in the oxygen reduction reaction. Int J Hyd En 2014; 39:16722-30.

[3] Haüssinger P, Lohmüller R, Watson AM, Hydrogen, 1. Properties and occurence Ullman´s Encyclopedia of Industrial Chemistry, 2011, Wiley-VCH.

[4] Tao Y, Chen Y, Wu Y, He Y, Zhou Z, High hydrogen yield from a two-step process of dark- and photo-fermentation of sucrose, Int J of Hyd En 2007; 32: 200–6.

[5] Navarro RM, Álvarez MC, del Valle F, Villoria JA, Fierro JLG, Water splitting on semiconductor catalysts under visible-light irradiation, Chem Sus Chem 2009; 6: 471-85.

[6] Barbir F, PEM Fuel Cells Theory and Practice, 2005. Elsevier Academic Press.

[7] Tang Y, Gao F, Mu S, Yu S, Zhao Y, Investigation of oxygen reduction reaction and methanol tolerance on the carbon supported Pt-Pd catalysts, Russ J Electrochem 2015; 51:345-52.

[8] Godínez-Salomón F, Hallen-López M, Solorza-Feria O, Enhanced electroactivity for the oxygen reduction on Ni@ Pt core-shell nanocatalysts, Int J Hyd En 2012; 37:14902-10.

[9] Lasia A, Rami A. Kinetics of hydrogen evolution on nickel electrodes. J Electroanal Chem Interfacial Electrochem 1990;294(1):123e41.

[10] Conway BE, Bai L. Determination of the adsorption behaviour of 'overpotential-deposited' hydrogen-atom species in the cathodic hydrogen-evolution reaction by analysis of potential-relaxation transients. J Chem Soc Faraday Trans 1 Phys Chem Condens Phases 1985;81(8):1841e62.

[11] Norskov JK, Rossmeisl J, Logadottir A, Lindqvist L, Kitchin JR, Bligaard T, Jonsson H, Origin of the Overpotential for Oxygen Reduction at a Fuel-Cell Cathode, J Phys Chem B 2004; 108: 17886.

[12] Kuleshov VN, Kuleshov NV, Grigoriev SA, Udris EY, Millet P, Grigoriev AS, Development and characterization of new nickel coatings for application in alkaline water electrolysis 2016; 41:36-45

[13] Zignani, S. C., Antolini, E., Gonzalez, E. R., *J. of Power Sources*, **191**, 344 (2009).

[14] Zhao, J., Jarvis, K., Ferreira, P., Manthiram, A., *J. of Power Sources*, **196**, 4515 (2011).

[15] Zhao, J., Manthiram, A., *App. Cat. B: Enviro.,* 101, 660 (2011).

[16] L. Lutterotti, S. Matthies, and H. R. Wenk, MAUD: A Friendly Java Program For Material Analysis Using Diffraction'', 2114–5, IUCr: Newsletter of the CPD (1999).

[17] http://www.crystallography.net/

[18] A. Ezeta, E.M. Arce, O. Solorza, R.G. Gonzalez Huerta, H. Dorantes, J. of Alloys and Comp., 483 (2009) 429.

[19] G. Liu, H. Zhang, H. Zhong, J. Hu, D. Xu, Z. Shao, Electrochim. Acta 51 (2006) 5710.

Starch-based materials for potential application as catalyst support in fuel cells – a sulfur-doped approach

*Cinthia J. Mena-Durán, B. Escobar**
Unidad de Energía Renovable
Centro de Investigación Científica de Yucatán
Mérida, México
*beatriz.escobar@cicy.mx

P. Quintana
Departamento de Física Aplicada
CINVESTAV-Mérida
Mérida, México

Romeli Barbosa
Universidad de Quintana Roo. Boulevard Bahía s/n,
Chetumal, Q. Roo, México

***Abstract*—*Manihot esculenta* and *Ipomea batata* are starch-derived materials regionally produced in Yucatan. The aim of this study was to evaluate the use of these materials as catalyst support in the search of sustainability during the development of fuel cells. Their synthesis combines the expansion of the starch-derived materials through gelatinization with the use of sonochemistry and solvent interchange. Samples were thermally treated with sulfuric acid to obtain sulfur-doped materials, which were evaluated electrochemically through cyclic voltammetry analysis. As well, the sulfur-doped materials were characterized by elemental analysis, XPS and Raman to correlate their physicochemical properties with their catalytic activity in basic media (0.1 M KOH). Both samples presented sulfonic and reduced sulfur groups. The presence of certain functionalities (more aromatic groups) may affect their catalytic performance.**

Keywords*—*bio-based materials; fuel cells; cyclic voltammetry, sulfur-doped

I. INTRODUCTION

Fuel cells are considered a clean-efficient alternative power source, due to they can directly convert chemicals to electrical energy. For many decades, platinum and other precious metals have been widely used as active catalysts for oxygen reduction reaction (ORR). However, noble metals are expensive, scarce and in some applications are easily poisoned. These problems have promoted an increasing interest to find alternative materials as metal-free electrocatalysts. The use of sulfur as dopant in carbon structures has been reported to have catalytic activity in basic media[1]. On the other hand, the fact that carbon can be derived from abundant precursors through simple processes, constitutes an opportunity to give an added-value to different types of biomass from starch[2]. Our research explores the synthesis and characterization of sulfur-doped starch-based materials, *Manihot esculenta* and *Ipomoea batata,* as potential metal-free electrocatalyst for fuel cells. A general overview of their electrochemical properties was obtained through cyclic voltammetry showing interesting catalytic ability in alkaline media, which motivates further studies to determine its performance in the ORR.

II. MATERIALS AND METHODS

Manihot esculenta and *Ipomoea batata* roots were obtained from a local market and washed with distilled water. Afterwards, samples were cut into cubes of 1 cm per edge and dry at 80 °C overnight in an oven HS60 Prendo. Dry samples were grinded using a coffee grinder and sieved through 100 ASTM sieves. 5 g of grinded material were mixed with 100 mL of distilled water for gelatinization at 72 °C for 1 h. Afterwards samples were put ino a fridge at 4 °C for 48 h to promote retrogradation. Solvent interchange was carried out using 50 mL ethanol (98%), the mixture gel-alcohol was put into an ultrasound bath for 30 minutes. Samples were filtered off and recovered using a Milipore system and dried at 80 °C overnight. i) Thermal treatment, dry samples after gelatinization were carbonized under nitrogen atmosphere at 800 °C for 1h, the heating rate used was 10 °Cmin^{-1}. ii) Treatment with sulfuric acid, raw and carbonized cassava were mixed with sulfuric acid adjusting the methodology proposed elsewhere[3], preserving the ratio 1g to 7 mL of sulfuric acid (95 %) at 95 °C for 3 h. Afterwards sample was extensively washed with hot water until the filtrate washes got a pH around 6. Samples were filtered off and dry at 80 °C overnight.

The elemental analysis was carried out in an Organic Elemental Analyzer ThermoScientific Flash 2000, CHNS-O. The Raman spectra were collected on a ThermoScientific DXR micro-Raman spectrometer using a 633 nm laser. The surface was characterized through X-ray photoelectron spectroscopy (XPS) in a Thermo Scientific spectrophotometer (Mod K-Alpha) with an Al-Ka source at 12 kV. Quantification of the XPS signals and curve fitting of the spectra was carried out using CasaXPS. Spectra calibration was done using C1s at 284.5 eV as reference. The electrochemical activity of the materials was evaluated by cyclic voltammetry (CV) technique. The CV studies were carried out in a computer-controlled workstation VSP Bio-Logic science instruments with a typical three-electrode cell. The carbon ink was formed using 5 mg of catalyst, 20 mL of Nafion® (5% wt) and 10 mL of isopropanol and 1.5 mL from the mixture was deposited over the glassy carbon electrode with 3mm of diameter.

III. Results and discussion

As seen in Fig. 1, the starting materials from *Manihot esculenta* and *Ipomoea batata* present similar composition, with a C:O ratio of 1:1, proper of starch materials[4]. After carbonization at 800 °C, the C:O ratio increased to 7.1 for *Manihot esculenta* and to 6.8 for *Ipomoea batata.* This increasing is due to the deoxygenation of samples and the formation of more graphitic structures and aromatic fused rings, which has been reported for starch-derived materials[5,6]. FTIR studies (Figure 1b) show that both, *Manihot esculenta* and *Ipomoea batata*, present similar functionalities. A broad band is observed in the region 3700-3000 cm^{-1}, assigned to O-H stretching, this corresponds to the hydroxyl groups on the starch molecules[7,8]. The band observed at ca. 2900 cm^{-1} is assigned to CH_2 symmetrical stretching vibrations. The bands at 1150 and 1090 cm^{-1} correspond to C-O stretching and C-OH bending, respectively[7–9]. The band centred at 980 cm-1 is assigned to the skeletal vibrations of glycosidic linkages C-O-C[8].

As described in the methodology section, samples were treated at 800 °C under nitrogen flow and afterwards, they were treated with sulfuric acid at 95 °C for 3 hours. It was found that both samples presented sulfur content in their composition determined by elemental analysis. The samples were named as Sy800 and Sc800 for sulfur-doped *Manihot esculenta* and *Ipomoea batata*, respectively. By elemental analysis, the sulfur content determined (%wt) was 0.92 % for Sy800 and 1.48% for Sc800. For an in-depth knowledge about the chemical composition of samples and determined the species content on samples, XPS analysis was performed and the findings are presented subsequently.

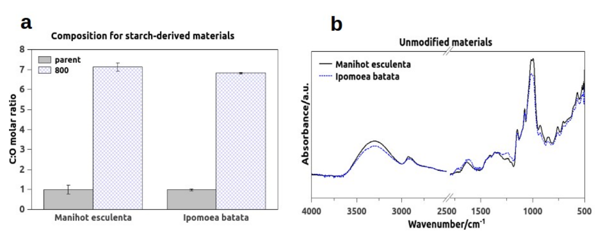

Fig. 1. Composition (a) and FTIR (b) spectra of starch-based materials

A. XPS analysis

Fig. 2 shows the high-resolution spectra for the sulfur-doped materials. All C1s core level regions (a, d) were very similar, implying that materials are close in ther chemical environment of carbon. The shapes of the different core level spectra are asymmetrical and show a broad band at higher values of binding energy between ~286 eV and 290 eV. The presence of these peaks are typical for carbon materials. At ~284.5 eV carbon atoms neighboring other carbon atoms in a sp^2 binding environment[10], while at the higher binding energies, carbon atoms are bound to more electronegative partners. This can be ascribed to the presence of oxygen-bound carbon atoms in different environments. Due to the low concentration of sulphur on the surface, it would be very reckless to assign a C-S bond in the spectra, as it may be hidden. Then, the band centered at 285.6 eV can be assigned to aliphatic carbons[11]. While, the band centred at 287.1 eV can be ascribed to carbon-oxygen bonds in an ether form C-O-C[12] or a carbonyl, carbon with double bond oxygen C=O[10,13]. It is worth mentioning that Sy800 is the only sample which shows a satellite broad attributed to π-π* transitions, proper of fused aromatic rings[14].

As seen in Fig. 2, the high-resolution spectra of O1s for Sy800 and Sc800 present some differences. In the case of Sy800, three components were identified and for Sc800, two components. The component at ca. 531.0 eV was assigned to oxygen atoms from C=O in carboxyl or carbonyl groups; the band centred at 533.2 eV was related to C-O in epoxy, phenol or carboxylic groups and the one at 535.8 eV, to oxygen in H-O-H or OH in carboxylic groups[15,16]. As well, one of the important differences observed in the high-resolution O1s spectra between Sy800 and Sc800 is the proportion of the peak at 533.2 eV, as Sy800 presents at higher percentage 76 % and Sc800, just 31 %.

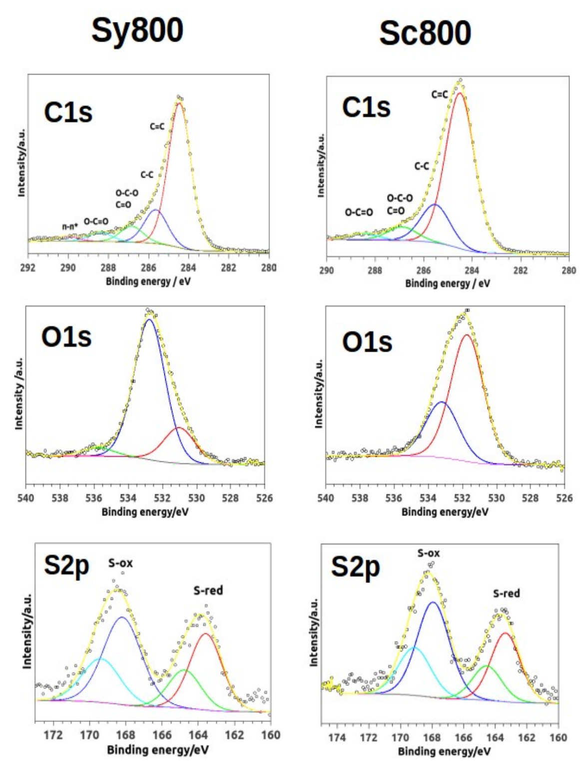

Fig. 2. XPS spectra of C1s, O1s and S2p for Sy800 and Sc800

Hueso *et al*. suggest that peak at 533 eV is related to oxygen groups attached to aromatic carbons and the one at 531 eV, to oxygen groups in aliphatic carbons[17]. Then, according with this information, it seems that Sy800 presents more oxygenated aromatic groups than Sc800. This observation also coincides with the C1s, in which, satellite peaks were observed. For the S2p spectra, both Sy800 and Sc800 presents sulfonic groups (~168 eV) and reduced sulfur (163.5 eV), in the form of R-S-R or thiophenic groups[12,15,18].The proportion of both types of sulfur are very similar in Sy800 and Sc800. The presence of thiophenic groups in the materials may improve the electronic conductivity[19].

B. Raman spectroscopy

Fig. 3 shows micro-photographies of Sy800 (a) and Sc800 (b) and the Raman spectra obtained for both samples. The spectra shows two broad bands at ~1590 cm^{-1} (G band) and ~1328 cm^{-1} (D band). The G band indicates the in-plane vibration of sp^2 carbon atoms and the D band is related to sp^3 carbon vibrations or defect sites, which are attributed to the nonperfect crystalline structure of the material[20]. In our spectra, Sc800 shows a broader D band than Sy800, it is also noticed a small shoulder at the right side of the main peak.

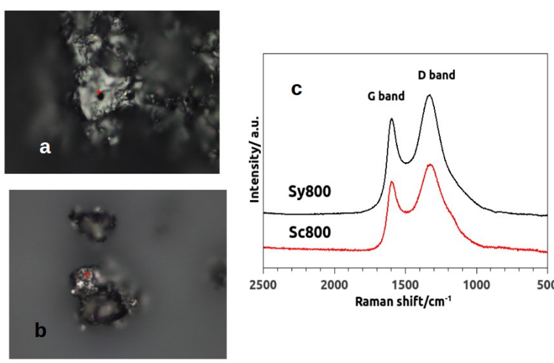

Fig. 3. Raman micro-photographies for Sy800 (a) and Sc800 (b) and Raman spectra (c).

C. Cyclic Voltammetry analysis

A general overview of the catalytic activity of the sulfur-doped materials was obtained through CV analysis. The CV profiles for Sy800 and Sc800 under N_2 and O_2 flow at 20 mVs^{-1} are depicted in Fig. 4, this analysis allowed to determine the reduction potential for the sulfur-doped cassava samples in the alkaline media (0.1 M KOH). A single cathodic reduction peak is observed at -0.24 V for Sy800 and shifted to more negative values for Sc800 at -0.34V. The potential obtained for Sy800 is comparable to the one obtained for S-graphene[21] or S-graphite[22] with a slightly improvement. Respect to the current measured, both Sy800 and Sc800 got current values similar to synthesized S-doped graphene and graphite[21,22].

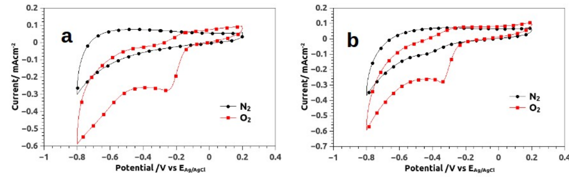

Fig. 4. Cyclic voltammograms for Sy800 (a) and Sc800 (b) under N_2 and O_2 flow at 20mVs^{-1}

IV. CONCLUSIONS

Sulfur-doped materials based on starch-based materials from *Manihot esculenta* and *Ipomoea batata* were prepared using a simple method through thermal treatment with sulfuric acid. The sulfur-doped materials present higher C:O ratio than the starting materials. The XPS analysis showed that both samples present similar composition of sulfonic groups and reduced-sulfur groups (R-S-R and/or thiophenic groups); however the C1s high-resolution spectra show that Sy800 presents satellite peaks p-p*, proper of aromatic fused rings. This observation coincided with the findings in the O1s spectra, which shows that Sy800 presents more oxygen groups attached to aromatic groups. The Raman study showed that Sc800 is more amorphous than Sy800. These physicochemical characteristics may influence the electrochemical performance of the sulfur doped materials, as Sy800 presented a lower cathodic peak than SC800 observed by CV.

ACKNOWLEDGMENT

Thanks to M.C. Martin Baas López for his support during the characterization of the samples by CHONS and Raman analyses. XPS measurements were performed at LANNBIO Cinvestav Mérida, under support from projects FOMIX-Yucatán 2008-108160, and CONACYT LAB-2009-01 (No.123913). Technical help is acknowledged to Eng. W. Cauich. Support to B. Escobar through the Programa de Cátedras - CONACYT is acknowledged.

REFERENCES

[1] Gao S, Li L, Geng K, Wei X, Zhang S. Recycling the biowaste to produce nitrogen and sulfur self-doped porous carbon as an efficient catalyst for oxygen reduction reaction. Nano Energy 2015;16:408–18.

[2] Titirici M-M, White RJ, Brun N, Budarin VL, Su DS, del Monte F, et al. Sustainable carbon materials. Chem Soc Rev 2015;44:250–90.

[3] Mena-Durán Cinthia J., Macquarrie DJ. Esterification of lauric acid with methanol using sulfonated Starbons. Research Journal of Chemistry and Environment 2014;18:1–6.

[4] Tester RF, Karkalas J, Qi X. Starch—composition, fine structure and architecture. Journal of Cereal Science 2004;39:151–65.

[5] Budarin V, Clark JH, Hardy JJE, Luque R, Milkowski K, Tavener SJ, et al. Starbons: new starch-derived mesoporous carbonaceous materials with tunable properties. Angewandte Chemie (International Ed in English) 2006;45:3782–6.

[6] Titirici M-M, Antonietti M, Baccile N. Hydrothermal carbon from biomass: a comparison of the local structure from poly- to monosaccharides and pentoses/hexoses. Green Chemistry 2008;10:1204.
[7] Socrates G. Infrared and Raman Characteristic Groups Frequencies. Tables and Charts. Wiley; 2001.
[8] Kizil R, Irudayaraj J, Seetharaman K. Characterization of irradiated starches by using FT-Raman and FTIR spectroscopy. Journal of Agricultural and Food Chemistry 2002;50:3912–8.
[9] Figueiredo J, Pereira M, Freitas M, Orfao J. Modification of the surface chemistry of activated carbons. Carbon 1999;37:1379–89.
[10] Okpalugo TIT, Papakonstantinou P, Murphy H, McLaughlin J, Brown NMD. High resolution XPS characterization of chemical functionalised MWCNTs and SWCNTs. Carbon 2005;43:153–61.
[11] Desimoni E, Casella G, Salvi A. XPS investigation of ultra-high-vacuum storage effects on carbon fibre surfaces. Carbon 1992;30:527–31.
[12] Zhang L, Ji L, Glans P-A, Zhang Y, Zhu J, Guo J. Electronic structure and chemical bonding of a graphene oxide-sulfur nanocomposite for use in superior performance lithium-sulfur cells. Physical Chemistry Chemical Physics : PCCP 2012;14:13670–5.
[13] Briggs D, Seah MP. Practical Surface Analysis, Auger and X-ray Photoelectron Spectroscopy. 2nd Edition. Wiley; 1990.
[14] Biniak S, Szymański G, Siedlewski J, ŚwiąTkowski a. The characterization of activated carbons with oxygen and nitrogen surface groups. Carbon 1997;35:1799–810.
[15] Petit C, Kante K, Bandosz TJ. The role of sulfur-containing groups in ammonia retention on activated carbons. Carbon 2010;48:654–67.
[16] Martınez M, Callejas M, Benito A. Sensitivity of single wall carbon nanotubes to oxidative processing: structural modification, intercalation and functionalisation. Carbon 2003;41:2247–56.
[17] Hueso JL, Espinós JP, Caballero a., Cotrino J, González-Elipe a. R. XPS investigation of the reaction of carbon with NO, O2, N2 and H2O plasmas. Carbon 2007;45:89–96.
[18] Lindberg BJ, Hamrin G, Gelius U, Fahlman A, Nordling C, Siegbahn K. Molecular spectroscopy by means of ESCA. II. Physica Scripta 1970;1:286–98.
[19] Zotti G, Zecchin S, Schiavon G, Louwet F, Groenendaal L, Crispin X, et al. Electrochemical and XPS Studies toward the Role of Monomeric and Polymeric Sulfonate Counterions in the Synthesis, Composition, and Properties of Poly(3,4-ethylenedioxythiophene). Macromolecules 2003;36:3337–44.
[20] Wang X, Wang H, Dai Q, Li Q, Yang J, Zhang A, et al. Preparation of novel porous carbon spheres from corn starch. Colloids and Surfaces A : Physicochemical and Engineering Aspects 2009;346:213–5.
[21] Yang Z, Yao Z, Li G, Fang G, Nie H, Liu Z, et al. Sulfur-Doped Graphene as an Efficient Metal-free Cathode Catalyst for Oxygen Reduction. ACS Nano 2012;6:205–11.
[22] Jeon I, Choi H, Jung S, Seo J, Kim M, Dai L, et al. Large-Scale Production of Edge-Selectively Functionalized Graphene Nanoplatelets via Ball-Milling and Their Use as Metal-Free Electrocatalysts for Oxygen Reduction Reaction. Journal of the American Chemical Society 2012;135:1386–93.

Characterization of metal hydrides tanks of a hydrogen-based energy storage system

A. Navarro[1], R. Barbosa[1,*], B. Escobar[2,*], V. Sanchez[1]

[1] Universidad de Quintana Roo. Boulevard Bahía s/n, Chetumal, Q.Roo, 77019, México.
[2] Centro de Investigación Científica de Yucatán, Carretera Sierra Papacal– Chuburná Puerto, Km. 5, Sierra Papacal, Mérida, 97302, México.

ABSTRACT

The system is composed of an electrolyzer and a tank of metal hydrides, which was analyzed at different pressures in order to establish a model which predicts and characterizes the actual performance to get feedback for a better implementation. The research consisted of identifying opportunities for the system optimization to generate and store hydrogen. The experimental data allowed the development of an analytical equation, obtained by polynomial regression to relate parameters such as power, pressure and time. This was done through the following scenarios: The system produced and stored hydrogen in tanks of metal hydrides at environmental conditions at checkpoints (CP) pressures of 0.5 bar, 1.5 bar, 2.5 bar, 4.0 bar, 6.5 and 9.0 bar. It was obtained that as the CP increases, the amount of hydrogen generated, the energy required to produce and the potential energy increases linearly from the 4.0 bar; whereas at lower pressures greater amount of energy is required to produce each millilitre of hydrogen. Furthermore, increasing the operating pressure in the charging process, the tank temperature increased in greater proportion and the discharge temperature is reduced proportionally. Finally, it was found that the best energy conversion efficiency was obtained at the CP 4.0 bar, registering a value of 88.45 %, which decreases linearly with increasing CP reaching a value of 72.68 % at CP 9.0 bar.

Keywords: hydrogen; electrolysis; metallic hydrides

XVI International Congress of the Mexican Hydrogen Society
Queretaro, Sep 26-30th, 2016

Green synthesis of nickel nanoparticles using extract of *Sargassum ssp.* and supported onto carbon for the oxygen reduction reaction

B. Escobar[1], K. Salcedo[1], J.M. Baas[1], R. Barbosa[2]

[1] Centro de Investigación Científica de Yucatán, Carretera Sierra Papacal– Chuburná Puerto, Km. 5, Sierra Papacal, Mérida, 97302, México.
[2] Universidad de Quintana Roo, Boulevard Bahía s/n, Chetumal 77019, Q. Roo, México.
[3] Cinvestav Unidad-Saltillo, Saltillo, Coahuila, 25900, México.

ABSTRACT

Green synthesis of nickel nanoparticles (NiNps) is an eco-friendly and low cost route, that has wide benefits over traditional chemical and physical synthesis methods. Our proposal was carried out using the aqueous extract from marine macroalgae *Sargassumm ssp*. This algae is an abundant waste product on the beaches of Quintana Roo, so it can be economically attractive as potential stabilizing and reducing agents for metallic salts in the synthesis of NiNps. The extract was prepared by dissolving 5 g of dry seaweed powder in 50 mL of distilled water. The mixture was kept in an orbital shaker for 3 h and filtered using whatman No. 40 filter paper. Then NiNps were synthesized using 200 μL, 400 μL, 600 μL, 800 μL and 1000 μL of the extract, which were added to 5 mL of 1 mM nickel chloride hexahydrate solution. Lattice parameters of the NiNps were calculated from the electron diffraction pattern to identify the preferential planes. The electrochemical performances of the NiNps supported on carbon obtained from biomass (NiNps/C) were investigated by analyzing their catalytic response to oxygen reduction reaction (ORR). Their use as an electrocatalyst for fuel cell electrode is discussed.

Keywords: green chemistry; biosynthesis; nickel nanoparticles

CONACYT 45 años

Sociedad Mexicana del Hidrógeno A.C.

XVI International Congress of the Hydrogen Mexican Society 2016

Synthesis and functionalization of Ordered Mesoporous Carbon (OMC) for Microbial Fuel Cells applications.

S. García-Mayagoitia[1*], F. Fernández-Luqueño[1], D. Morales-Acosta[2], F.J. Rodríguez-Varela[1]

[1]Sustainbility of Natural Resources and Energy Program, Cinvestav Unidad Saltillo, Av. Industria Metalúrgica No. 1062, Parque Industrial Ramos Arizpe, Ramos Arizpe, Coah., México. C.P.25900
[2]Centro de Investigación en Química Aplicada, Blvd. Enrique Reyna No. 140, San José de los Cerritos, Saltillo, Coah. México. C.P. 25294
[*]E-mail: selviagarciam@hotmail.com

ABSTRACT

Microbial fuel cells (MFCs) are bioelectrochemical devices that use the chemical energy of microorganisms available in a substrate, such as residual water, to produce electric energy. Carbonaceous materials are commonly used as anodes in MFCs because of their properties including biocompatibility with microorganisms and large surface area. Ordered Mesoporous Carbon (OMC) was synthesized via self-assembly in aqueous phase. Was evaluated as anode electrocatalyst for MFCs applications employing *Bacillus subtilis* as biofilm precursor. Its electrochemical performance has been compared to that of commercial Vulcan XC-72 and Graphite flakes. Moreover, some carbonaceous materials samples were functionalized using methanol (MeOH) as chemical agent, in order to evaluate the effect of surface groups on their catalytic activity, while electrodes containing each of the electrocatalysts were fabricated by the painting technique. SEM analysis suggested the formation of a biofilm by *Bacillus subtilis* over the electrodes, while cyclic voltammetry (CV) characterization in residual water showed a higher catalytic activity of the anodes based on OMC, compared to Vulcan and Graphite. Additionally, the catalytic activity of OMC was increased after functionalization and it was found that the MeOH-funtionalized OMC is an attractive alternative as anode electrocatalyst for MFCs applications.

Keywords: Bioelectrochemical devices, Ordered Mesoporous Carbon, Microbial fuel cells, Energetic crisis, Clean water, *Bacillus subtilis*

Development of fuel cell electrodes containing Pt-Sn/C electrocatalyst deposited by the electrophoretic method

D. González-Quijano[1,*], J.I. Escalante-García[1,2], G. Vargas-Gutiérrez[1,2], F.J. Rodríguez-Varela[2,3]
[1]Ingeniería Metalúrgica e Ingeniería Cerámica
[2]Sustentabilidad de los Recursos Naturales y Energía
[3]Programa de Nanociencias y Nanotecnología
CINVESTAV Unidad Saltillo
Ramos Arizpe, Coahuila, México.
[*]diegoxjgq@gmail.com

Abstract*— Catalytic layers of Pt-Sn/C catalyst (Pt:Sn 1:1 atomic ratio) have been grown on commercial carbon cloth by electrophoretic deposition (EPD). The catalyst was synthesized by the polyol method. Three signals were used: i) continuous direct current (CDC); ii) positive pulsed current (PPC); and iii); asymmetric alternating current (AAC). The chemical composition analysis clearly showed the effect of the applied signal on the transport of species to form the catalytic layers. Morphology evaluation by SEM confirmed the effect of deposition signal. The CDC signal formed spherical agglomerates with irregular distribution, along with carbon fibers and cracks over the electrode. A cross-cut view of the electrode showed that the catalyst penetrated into the carbon cloth structure. Meanwhile, the PPC signal promoted a better distribution of the catalytic layer over the carbon cloth. The cross-cut view revealed a thicker and relatively more homogeneous porous layer than CDC. On the other hand, the catalytic layer developed by the AAC signal showed a morphology similar to that by CDC, which suggests the formation of a layer with low metal loading. The cross-cut view of the electrode AAC showed the formation of a highly porous catalytic layer having large areas with apparently limited contact with the carbon cloth fibers. The electrocatalytic activity of the electrodes for the Ethanol Oxidation Reaction (EOR) was studied in acid media. The characterization showed a polarization of the CDC electrode having the typical characteristics of Pt-based catalysts. It showed a higher catalytic activity for the EOR by delivering the highest current density (272 mA mg^{-1}_{Pt}) with the lowest onset potential (341 mV) relative to the PPC and AAC electrodes. These results demonstrated that the EPD technique based on a CDC signal can produce a morphology and a catalytic layer distribution that enhance the EOR.

Keywords—Electrophoretic deposition; fuel cell electrodes; Ethanol Oxidation Reaction.

I. INTRODUCTION

Direct Alcohol Fuel Cells (DAFCs) have been widely investigated worldwide because of their low emissions of pollutants, high conversion efficiency, and high energy density [1,2]. However, some critical issues are the performance, durability and cost of the fuel cell components [3]. The first two issues are influenced by the operating conditions and/or by the selected materials for catalysts, support, membranes, bipolar plates and electrodes [4,5]. Meanwhile, the cost reduction can be achieved by decreasing the amount of Pt anode and cathode electrodes [6–8].

Pt-based alloys such as Pt-Ru/C and Pt-Sn/C contribute to decrease the Pt loading at the electrodes. These alloys have shown high catalytic activity for the oxidation of alcohols, i.e., the onset potential is more negative and the current density is higher during the reaction compared to Pt-alone electrocatalysts [9–15]. The alloys are also more tolerant to the poisoning effect by CO, since the co-catalyst modifies the Pt electronic structure promoting the bi-functional mechanism and the ligand effect [11,12,16]. Moreover, with a suitable synthesis method, the catalyst utilization of the catalyst can be improved, i.e., the particle size is decreased while the electrochemically active surface area becomes higher (ECSA) [9,17].

On the other hand, the electrode manufacturing process influences the performance of the fuel cell by controlling the amount of catalysts deposited and the thickness of the catalyst layer at the electrode's surface. The goal is to achieve a more effective three-phase boundary which enhance the catalyst utilization [8]. EPD is a technique that can achieve a more effective catalyst layer deposition because it has the capability of controlling the morphology and thickness through adjusting the electrochemical deposition parameters [18].

In this work, we investigate the effect of three EPD signals on the morphology and performance of catalytic layers containing Pt-Sn/C catalysts, deposited onto commercial carbon cloth. The chemical composition, morphological and structural characteristics of the electrodeposited catalyst layers are studied by scanning electron microscopy (SEM), Energy-Dispersive Spectroscopy (EDS). The electrodes are electrochemically evaluated for the EOR by cyclic voltammetry (CV).

II. MATERIALS AND METHODS

A. *Reactants and gases*

Analytical grade chemicals were purchased from Aldrich and used as received in this investigation: $H_2PtCl_6{\cdot}6H_2O$, $SnCl_2{\cdot}2H_2O$ as metallic precursors of the catalyst, ethanol (EtOH), ethylene glycol (EG), acetone, 2-propanol, NaOH and H_2SO_4 were used in the catalysts synthesis and electrochemical characterization. Vulcan XC-72 (Cabot Corp) was used as the catalysts support and commercial carbon cloth as the substrate for the electrodes. Ultra-high purity nitrogen gas purchased from Infra gas (purity > 99.999%) was used to control the atmosphere of the electrochemical cell.

B. *Synthesis of the catalysts*

Pt-Sn/C alloy with 20 wt. % metal loading and Pt:Sn atomic ratio (at.) of 1:1, was synthesized by the polyol method with a dispersing solution (EG:EtOH:H_2O) of 96:4:0 volume ratio (v/o) [9,17]. The appropriate amount of Vulcan was dissolved in the dispersing solution. The metal precursors were dissolved separately in 2 mL of pure ethanol. The solutions were sonicated separately for 30 min at room temperature, mixed and stirred for 1 h. Afterwards, a solution of 1 M NaOH was added to the mixture to adjust the pH to 12, the temperature was then increased to 130 °C for 3 h. The solution was then left to cool down to room temperature under stirring conditions for 3 h. Then, 1 M H_2SO_4 was added to set the pH = 2 and the mixture was stirred for another 3 h. The obtained powder was filtered, washed and dried.

C. *Electrode preparation*

Fuel cell electrodes were fabricated by depositing a catalyst layer of the synthesized Pt-Sn/C, on carbon cloth samples (1 cm^2 geometrical area) using EPD. The power source was a Bio Rad Pak 3000 coupled to a Dynatronix DuPR/DPR electrical signal generator. This set up allowed to change the signal type and polarity. Three signals were used, as shown in Fig 1: a) continuous direct current (CDC); b) positive pulsed current (PPC) with a relaxing time of 100 ms; and c) square-shaped asymmetric alternating current (AAC), with an asymmetric factor of 2 and relaxing time of 100 ms at constant frequency of 1.25 Hz.

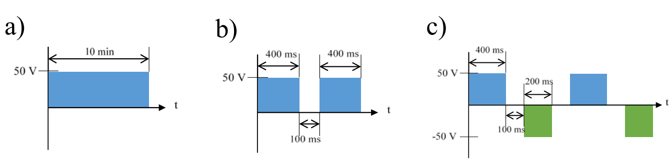

Fig. 1. Schematic representation of EPD signals; a) continuous direct current; b) positive pulsed current; and c) asymmetric alternating current.

The EPD was carried out in a glass cell having two electrode holders with aligned inlets, one with the working electrode (carbon cloth) and one with the counter electrode (stainless steel bar). The distance between electrodes was 1 cm. Carbon cloth samples were mounted in an exposed area of 1 cm^2. The solvent was an acetone:2-propanol mixture (50:50 v/o). Before deposition, the catalysts were dispersed in 50 mL solvent by sonication for 10 min in a beaker. Afterwards, 0.3 mL of Nafion® solution and 0.1 mL of 0.1 M H_2SO_4 were added to the suspension, stirring for 5 min. The obtained suspension was added to the glass cell, in which the carbon cloth and the counter electrode were previously mounted. Then, the different electrical signals were applied separately. The electrode was allowed to dry in a desiccator for 24 h. The catalyst loading was determined by the weight difference between the coated (after drying) and the uncoated carbon cloth sample.

D. *Physicochemical characterization*

The chemical composition of the catalyst and the electrode was determined by EDS analysis and the morphology of the electrode was evaluated by SEM in a Philips XL30 SEM apparatus using an accelerating voltage of 20 keV.

E. *Physicochemical characterization*

The electrochemical measurements were performed with a VoltaLab PGZ 301 potentiostat/galvanostat in a standard three-electrode cell. The working electrode was each of the carbon cloth electrodes prepared by EPD. A Pt foil was the counter-electrode and an Ag/AgCl was the reference electrode, even though all potentials have been referred in this work to the Standard Hydrogen Electrode (SHE).

Cyclic voltammograms (CVs) in 0.5 M H_2SO_4 electrolyte N_2-saturated were obtained at a scan rate of 20 mV s^{-1}. The potential scan was between 50 and 1200 mV/SHE. Afterwards, CVs of the EOR were acquired in the same electrolyte containing 0.5 M C_2H_5OH, in the potential interval 50 - 1200 mV/SHE, maintaining the N_2 atmosphere.

III. RESULTS AND DISCUSSION

Table I shows the chemical composition of the synthesized Pt-Sn/C catalyst and the electrodes manufactured by EPD. The catalyst loading and the amount of Pt deposited are also given. The catalyst shown a chemical composition of the C content close to 80 wt. %, an atomic ratio of 1:1, which approximate the expected values and an O_x content of 5.01 %. The catalyst loading value is higher for CDC, followed closely by PPC (1.1 and 1 mg, respectively). Meanwhile, the deposition by AAC gives the lowest value.

TABLE I. PHYSICOCHEMICAL CHARACTERISTICS OF THE CATALYST AND ELECTRODES PREPARED BY EPD.

Sample	**Catalyst loading (mg)**	**Chemical composition, EDS (wt. %)**				**Pt deposited (mg Pt)**
		Pt	***Sn***	***C***	***O_x***	
Pt-Sn/C	-	8.60	5.18	81.21	5.01	-
CDC	1.1	8.85	4.98	86.17	-	0.095
PPC	1	19.13	11.97	68.90	-	0.086
AAC	0.6	5.43	3.02	91.55	-	0.052

It is clear that there is an effect of the applied signal on the transport of species onto the working electrode while forming the catalyst layer. CDC appears to be the most efficient, since a chemical composition close to that of the deposited RAX0 sample is obtained under such continuous transport conditions (8.85 Pt, 4.98 Sn and 86.17 C, in wt. %). On the contrary, pulsing and reversing the signal limits the simultaneous transport of metallic or carbonaceous species. Under PPC, the value of metals deposited are significantly higher, with the lowest amount of C comparing the three signals (68 wt. %). It is likely that during t_{off} the transport of Vulcan is halted and only the Pt and Sn molecules are moved towards the carbon cloth when the current is pulsed once again, occupying the sites available at the surface. As for the electrode obtained by AAC, the amount of metals is lower than CDC while amount of C is highest among the three samples. It is hypothesized that inversing the current may have promoted the transport of Vulcan over Pt and Sn.

Figure 2 shows the SEM micrographs of the cross-cut section of the carbon cloth samples prepared by CDC, PPC and AAC. A cross cut view of the electrode Figure 2a) reveals the porous characteristic of the catalytic layer of the electrode prepared with CDC signal. It can be observed that the catalyst penetrated into the carbon cloth structure, as an effect of the continuous signal, also the homogeneity of the layer varies along the surface of the electrode when a CDC signal is applied.

The morphology of the electrode prepared by PPC is shown in Figure 2b), and suggests that the cloth is mostly coated by a catalytic layer with high metal content, as seen in the chemical composition of this sample in Table I. The cross-cut view, also reveals a thicker and relatively more homogeneous porous layer formed by PPC related to CDC. Meanwhile, the electrode prepared with the AAC signal, Figure 2c), shows a morphology similar to the CDC electrode. The cross-cut section of the electrode shows the formation of layer having a different morphology compared to CDC and PPC, with higher porosity and large areas with apparently limited contact areas with the carbon cloth fibers. Moreover, the fibers/catalytic layer interphase seems to be modified by the AAC signal as indicated by the presence of wire-like interconnects.

a)

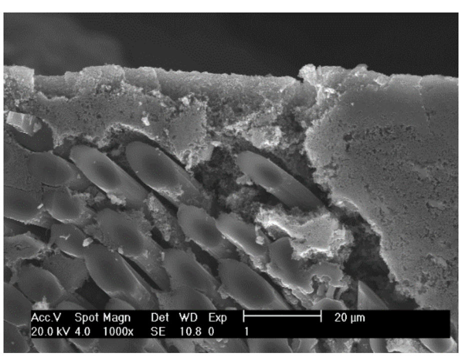

b)

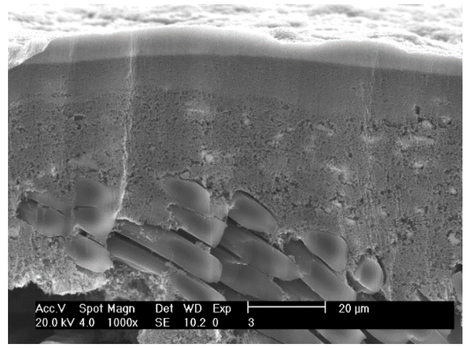

c)

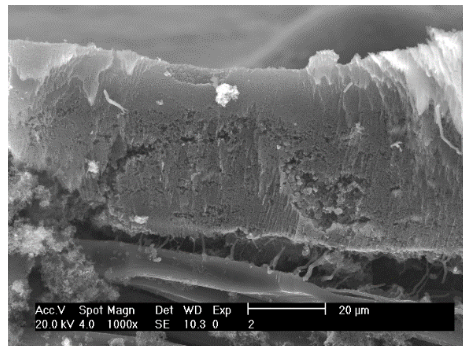

Fig. 2. SEM micrographs of the electrode cross-cut secction prepared by; a) continuous direct current; b) positive pulsed current; and c) asymmetric alternating current.

The electrochemical performance of the electrodes (Figure 3) indicates that the catalytic activity of the CDC electrode clearly surpasses that of the PPC and AAC electrodes by showing: i) lower onset potential of the EOR (341 mV), and ii) higher peak current density in the forward scan (271 mA mg^{-1}_{Pt}). PPC and AAC show onset potentials of 550 mV, with peak current densities of 168.9 and 136.2 mA mg^{-1}_{Pt}, respectively. The electrocatalytic parameters of the EOR at all the electrodes are specified in Table II.

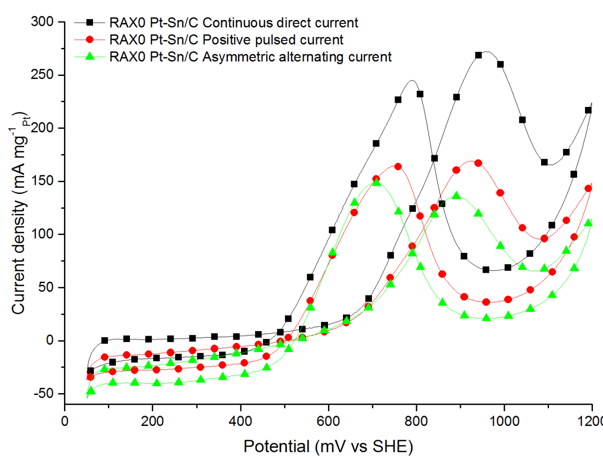

Fig. 3. CVs of the EOR on electrodes prepared by EPD using CDC, PPC and AAC signals. Electrolyte: N_2-saturated 0.5 M H_2SO_4 + 0.5 M C_2H_5OH. Scan rate: 20 mV s^{-1}.

TABLE II. ELECTROCATALYTIC PARAMETERS OF THE EOR AT ELECTRODES PREPARED BY EPD.

Sample	Onset potential (mV)	jf (mg^{-1}_{Pt})
CDC	341	272.1 at 956 mV
PPC	550	168.9 at 923 mV
AAC	550	136.2 at 889 mV

The results indicate that a catalytic layer on carbon cloth electrode prepared by EDP with a CDC signal, has appropriate characteristics to enhance the catalytic activity for the EOR: i) a chemical composition closer to that of the Pt-Sn/C catalyst compared to PPC and AAC (Table I); ii) adequate anchorage of the catalyst at the interstices of the carbon cloth fibers; iii) fair thickness, even though it is not as homogeneous as expected; iv) a porosity that allows the efficient diffusion of the fuel along the catalyst active sites.

IV. CONCLUSIONS

The results showed that the applied signal altered the morphological characteristics and chemical composition of the electrodes.

The EPD using the CDC signal produced a catalytic layer with a good dispersion over the carbon cloth by ensured the attachment of the catalyst in the interstitial spaces of the carbon cloth. Therefore, the electrode fabricated under CDC showed the highest catalytic activity for the EOR in acid media.

Meanwhile, the PPC and AAC signals seems to break the bounds to the carbon support altering the amount, morphology and composition of the alloy deposited leading to a low electrochemical performance and utilization of the catalyst.

ACKNOWLEDGMENT

The authors wish to thank the Mexican National Council for Science and Technology (CONACyT) for financial support of this work through project 241526 and for Doctoral scholarships granted to D.G.Q.

REFERENCES

[1] M. Chatterjee, A. Chatterjee, S. Ghosh, I. Basumallick, Electro-oxidation of ethanol and ethylene glycol on carbon-supported nano-Pt and -PtRu catalyst in acid solution, Electrochim. Acta. 54 (2009) 7299–7304. doi:10.1016/j.electacta.2009.07.054.

[2] J.M. Sieben, M.M.E. Duarte, Methanol, ethanol and ethylene glycol electro-oxidation at Pt and Pt–Ru catalysts electrodeposited over oxidized carbon nanotubes, Int. J. Hydrogen Energy. 37 (2012) 9941–9947. doi:10.1016/j.ijhydene.2012.01.173.

[3] K. Eom, G. Kim, E. Cho, J.H. Jang, H.J. Kim, S.J. Yoo, S.K. Kim, B.K. Hong, Effects of Pt loading in the anode on the durability of a membrane-electrode assembly for polymer electrolyte membrane fuel cells during startup/shutdown cycling, Int. J. Hydrogen Energy. 37 (2012) 18455–18462. doi:10.1016/j.ijhydene.2012.09.077.

[4] S. Hou, R. Chen, H. Zou, T. Shu, J. Ren, X. Li, S. Liao, High-performance membrane electrode assembly with multi-functional $Pt/SnO_2–SiO_2/C$ catalyst for proton exchange membrane fuel cell operated under low-humidity conditions, Int. J. Hydrogen Energy. 41 (2016) 9197–9203. doi:10.1016/j.ijhydene.2015.12.084.

[5] A. BAYRAKCEKEN, S. ERKAN, L. TURKER, I. EROGLU, Effects of membrane electrode assembly components on proton exchange membrane fuel cell performance, Int. J. Hydrogen Energy. 33 (2008) 165–170. doi:10.1016/j.ijhydene.2007.08.021.

[6] H.N. Su, Q. Zeng, S.J. Liao, Y.N. Wu, High performance membrane electrode assembly with ultra-low platinum loading prepared by a novel multi catalyst layer technique, Int. J. Hydrogen Energy. 35 (2010) 10430–10436. doi:10.1016/j.ijhydene.2010.06.070.

[7] H. Su, B.J. Bladergroen, V. Linkov, S. Pasupathi, S. Ji, Study of catalyst sprayed membrane under irradiation method to prepare high performance membrane electrode assemblies for solid polymer electrolyte water electrolysis, Int. J. Hydrogen Energy. 36 (2011) 15081–15088. doi:10.1016/j.ijhydene.2011.08.057.

[8] M.S. Saha, A.F. Gullá, R.J. Allen, S. Mukerjee, High performance polymer electrolyte fuel cells with ultra-low Pt loading electrodes prepared by dual ion-beam assisted deposition, Electrochim. Acta. 51 (2006) 4680–4692. doi:10.1016/j.electacta.2006.01.006.

[9] D. González-Quijano, W.J. Pech-Rodríguez, J.I. Escalante-García, G. Vargas-Gutiérrez, F.J. Rodríguez-Varela, Electrocatalysts for ethanol and ethylene glycol oxidation reactions. Part I: Effects of the polyol synthesis conditions on the characteristics and catalytic activity of Pt–Sn/C anodes, Int. J. Hydrogen Energy. 39 (2014) 16676–16685. doi:10.1016/j.ijhydene.2014.04.125.

[10] A.F.C. Villanueva, A.M. Ramirez, G.V. Gutiérrez, L.A. Torres, F.J.R. Varela, Synthesis of Unsupported Pt-based Electrocatalysts and Evaluation of Their Catalytic Activity for the Ethylene Glycol Oxidation Reaction, J. New Mater. Electrochem. Syst. 16 (2013) 171–176.

[11] E.V. Spinacé, A.O. Neto, M. Linardi, Electro-oxidation of methanol and ethanol using PtRu/C electrocatalysts prepared by spontaneous deposition of platinum on carbon-supported ruthenium nanoparticles, J. Power Sources. 129 (2004) 121–126. doi:10.1016/j.jpowsour.2003.11.056.

[12] F.J. Rodríguez Varela, O. Savadogo, Ethanol-tolerant Pt-alloy cathodes for direct ethanol fuel cell (DEFC) applications, Asia-Pacific J. Chem. Eng. 4 (2009) 17–24. doi:10.1002/apj.193.

[13] J.M. Sieben, M.M.E. Duarte, Nanostructured Pt and Pt–Sn catalysts supported on oxidized carbon nanotubes for ethanol and ethylene glycol electro-oxidation, Int. J. Hydrogen Energy. 36 (2011) 3313–3321. doi:10.1016/j.ijhydene.2010.12.020.

[14] A.O. Neto, T.R.R. Vasconcelos, R.W.R.V. Da Silva, M. Linardi, E.V. Spinacé, Electro-oxidation of ethylene glycol on PtRu/C and PtSn/C electrocatalysts prepared by alcohol-reduction process, J. Appl. Electrochem. 35 (2005) 193–198. doi:10.1007/s10800-004-5824-5.

[15] V. Livshits, E. Peled, Progress in the development of a high-power, direct ethylene glycol fuel cell (DEGFC), J. Power Sources. 161 (2006) 1187–1191. doi:10.1016/j.jpowsour.2006.04.141.

[16] S. Yan, G. Sun, J. Tian, L. Jiang, J. Qi, Q. Xin, Polyol synthesis of highly active PtRu/C catalyst with high metal loading, Electrochim. Acta. 52 (2006) 1692–1696. doi:10.1016/j.electacta.2006.03.101.

[17] D. González-Quijano, W.J. Pech-Rodríguez, J.A. González-Quijano, J.I. Escalante-García, G. Vargas-Gutiérrez, I. Alonso-Lemus, F.J. Rodríguez-Varela, Electrocatalysts for ethanol and ethylene glycol oxidation reactions. Part II: Effects of the polyol synthesis conditions on the characteristics and catalytic activity of Pt–Ru/C anodes, Int. J. Hydrogen Energy. 40 (2015) 17291–17299. doi:10.1016/j.ijhydene.2015.06.154.

[18] P. Yu, J. Yan, J. Zhang, L. Mao, Cost-effective electrodeposition of platinum nanoparticles with ionic liquid droplet confined onto electrode surface as micro-media, Electrochem. Commun. 9 (2007) 1139–1144. doi:10.1016/j.elecom.2007.01.022.

XVI International Congress of the Mexican Hydrogen Society 2016

Effects of the chemical composition on the catalytic activity of Pt-Sn/C alloys for the EOR

D. González-Quijano[1,*], J.I. Escalante-García[1,2], G. Vargas-Gutiérrez[1,2], F.J. Rodriguez-Varela[2,3]

[1]Ingeniería Metalúrgica e Ingeniería Cerámica
[2]Sustentabilidad de los Recursos Naturales y Energía
[3]Programa de Nanociencias y Nanotecnología
[*] Tel: +52(844)236-7292; e-mail: diegoxjgq@gmail.com
Cinvestav Unidad Saltillo, Av. Industria Metalúrgica 1062, Parque Industrial Ramos Arizpe.
Ramos Arizpe, Coahuila, C.P. 25900, México.

ABSTRACT

Pt-Sn/C catalysts with nominal Pt:M atomic ratio of 1:1, 2:1 and 3:1 were synthesized by a polyol reduction process. The Metal:Vulcan support ratio was 20:80 (wt. %). XRD characterization showed reflection peaks ascribed to carbon, fcc Pt and SnO_x. The crystallite size calculated with the Scherrer equation was almost 2.2 nm. Chemical analysis by EDS indicated that the atomic ratios were 1:1, 1.6:1 and 2.4:1, close to the nominally expected. The electrocatalytic activity of the alloys for the Ethanol Oxidation Reaction (EOR) was studied in acid media. Accelerated degradation test shown ECSA losses for the Pt-Sn/C alloys comparable to that of Pt/C catalyst. The CO stripping experiments indicated that the catalysts desorb the CO_{ads} at lower potentials than Pt/C, generating smaller current densities. The electrochemical characterization showed that the EOR starts on Pt-Sn/C catalysts at more negative onset potential, with higher mass current density, in comparison with Pt/C. SPAIRS analyses revealed that the ethanol reaction mechanism at Pt/C preferentially proceeds via the formation of CO, followed by CO_2 production. Meanwhile, the reaction mechanism at Pt-Sn/C proceeds through a parallel pathway that involves, besides CO oxidation to CO_2, the formation of acetaldehyde(AAL) and acetic acid (AA) that produce CO_2. These results demonstrated that the Pt-Sn/C alloyed catalysts have better performance and stability during the EOR than Pt/C catalyst, particularly with a Pt:Sn atomic ratio of 1:1.

Keywords: Pt-Sn alloys; Ethanol Oxidation Reaction; acid media; Fuel Cells

The oxygen reduction reaction onnitrogen-doped carbon supportedCoSe_2

I.J. García-Rosado[1,2], J. Uribe-Calderón[1,*], N. Alonso-Vante[2].

[1]Centro de Investigación Científica de Yucatán (CICY), Calle 43 No. 130 x 32 y 34,Chuburná de Hidalgo, CP 97205, Mérida, Yucatán, México.
*Email: jorge.uribe@cicy.mx
[2]IC2MP - UMR-CNRS 7285 Université de Poitiers, 4, rue Michel Brunet - B27 BP 633 - TSA 51106, F-86022 Poitiers Cedex, France.

ABSTRACT

The oxygen reduction reaction (ORR) in aFuel Cell (FC) represents a large part of the power loss in the system. The use of traditional, high cost, platinum-based catalytic materials is one of the obstacles for successful large-scale applicationof FCs in the energy market;in consequence, there is an important interest fordeveloping alternative, low-cost, catalytic materials. In this communication, a novel catalytic system is proposed. First, graphite oxide (GO) was prepared by a modified Brodie method [1], followed by the polymerization *in-situ* of polypyrrole nanoparticles at the GO surface, as a nitrogen source. This composite was thermally reduced (rGO) under Argon atmosphere at 800-1000°C for 30 min. The same procedure was carried out for carbon Vulcan® in order to determine the morphological and doping effect of the support towards the ORR. Cobaltselenide ($CoSe_2$), a catalytic center [2], was synthesized onto the composites in order to increase the ORR activity. The nitrogen-doped carbon supports show an increase in the activity towards ORR in alkaline medium. This system could be an interesting metal-free catalyst. The X-Ray Diffraction (XRD) patterns show a signal corresponding to hexagonal structureof $CoSe_2$ on the composite, in agreement with the HR-SEM morphology observations. EDX, FTIR and XPS results show the decrease of oxygen bonding species amount after thermal treatment, and the formation of new nitrogen bonds, besides the polymer backbone structure. BET results show an increase in the surface area for the rGO support; and XRD and TEM reveal a reduced number of layers in the rGO after thermal treatment. Finally, the positive effect of the nitrogen-doped carbons supports, in a H_2/O_2 alkaline micro laminar flow fuel cells (µLFFC) system over conventional carbon supports, was assessed.

Keywords: ORR; Graphite Oxide; Nitrogen doping.

Acknowledgements: Ismael JesúsGarcíaRosado acknowledges CONACyT for the financial support with scholarship and Basic Science project No. 181106; Dr. Ysmael Verde and InstitutoTecnológico de Cancún, Dra. Karina Cuentas and IER-UNAM, as well as the University of Poitiers for the use of infrastructure, equipment and facilities during my doctoral studies.

References.
[1] Cristina Botas, *et al*. Graphene materials with different structures prepared from the same graphite by the Hummers and Brodie methods. Carbon 65 (2013) 156–164.
[2]Yongjun Feng, Nicolas Alonso-Vante. Carbon-supported cubic $CoSe_2$ catalysts for oxygen reduction reaction inalkaline medium. Electrochimica Acta. 72 (2012) 129– 133.

Organometallic functionalization of graphene: Novel route to form Pt-Ru alloys as electrocatalyst for Methanol Oxidation Reaction

A. A. Siller-Ceniceros[1], M. E. Sánchez-Castro[1,2], F. J. Rodríguez-Varela[1.2]
[1]Programa de Nanociencias y Nanotecnología
[2] Grupo de Sustentabilidad de los Recursos Naturales y Energía
CINVESTAV-IPN Unidad Saltillo
Ramos Arizpe, Coah., México
adriana.siller@cinvestav.mx

D. Morales-Acosta, J.R. Torres-Lubián
CIQA
Saltillo, Coah., México
diana.morales@ciqa.edu.mx

E. Martínez-Guerra
CIMAV Unidad Monterrey
Apodaca, N L., México
eduardo.martinez@cimav.edu.mx

Abstract

Graphene is a nanostructured carbon material with excellent properties to support Pt nanoparticles as electrocatalysts for fuel cells applications. Nevertheless, graphene surface must be activated to anchor homogeneously distributed metal nanoparticles. Typically, the activation involves aggressive acid media such as aqua regia, to chemically modify the carbon surface, forming functional groups and generating lattice distortion. In this work, the functionalization of graphene with the ruthenium organometallic complex $[(\eta^6\text{-}C_6H_5OCH_2CH_2OH)RuCl_2]_2$ (Ru-dim) and ruthenium chloride $RuCl_3{\cdot}XH_2O$ (Ru-com) to obtain the functionalized $G_{Ru\text{-}dim}$ and $G_{Ru\text{-}com}$ supports is reported. $G_{Ru\text{-}dim}$ and $G_{Ru\text{-}com}$ are used to synthesize $Pt/G_{Ru\text{-}dim}$ and $Pt/G_{Ru\text{-}com}$ electrocatalysts with the polyol method. For comparison, Pt/G (on non-functionalized graphene) has been obtained. Raman spectroscopy characterization shows an increase in the intensity of the G-band of $G_{Ru\text{-}dim}$ and $G_{Ru\text{-}com}$ compared with G, demonstrating a graphitic constructive rehybridization because of ruthenium complexation over the graphene surface, preserving the sp^2 hybridization. XRD analysis strongly suggests the formation of Pt-Ru alloys on $Pt/G_{Ru\text{-}dim}$ and $Pt/G_{Ru\text{-}com}$. Evaluation of catalytic activity for Methanol Oxidation Reaction (MOR) shows an enhanced performance of $Pt/G_{Ru\text{-}dim}$ due to a synergistic effect between Pt and Ru atoms. $Pt/G_{Ru\text{-}dim}$ generates superior electrocatalytic parameters than $Pt/G_{Ru\text{-}com}$ and Pt/G. The results confirm that $Pt/G_{Ru\text{-}dim}$ is a high-performance anode electrocatalyst for Direct Methanol Fuel Cells (DMFC).

Keywords: Ru organometallic complex; functionalization; graphene; Pt-Ru alloys; fuel cell; electrocatalyst.

I. INTRODUCTION

Direct methanol fuel cells (DMFCs) exhibit enormous potential to be implemented on the field of rechargeable batteries, due to low operating temperature and the advantages that methanol displays, such as: practical transportation, handling, storage and high energy density [1].

However, the use of platinum (Pt) evaluated specifically such as anode during methanol oxidation reaction (MOR), demonstrate lower catalytic activity due to poisoning effect from sub-product CO adhered on Pt surface, this fact avoid the Pt implementation such as anode in DMFCs [2-3]. Nevertheless, investigations have been reported the interaction of Pt with the co-catalyst ruthenium (Ru), increase significantly the catalytic activity during MOR [4].

In addition, an important effect in the efficiency on the electrocatalyst is the selection of an adequate carbon support; this material is necessary to attach the metal nanoparticles with effective dispersion to generate wide active sites during fuel oxidation. Graphene (G) has been demonstrated an interesting electronic contribution used such as support to Pt electrocatalyst increasing their catalytic activity [5-6].

The purpose of this work is to study the electrocatalytic effect of Pt nanoparticles supported over previous organometallic functionalization of graphene. Previous reports have demonstrated the functionalization of graphene with chrome (Cr) organometallic complexes [7], those reports showed an excellent organic affinity between Cr and graphitic structure of graphene which gave a high chemical stability by metal-carbon fragment [8-10].

In this work, the functionalization of G was carried out using an arene-ruthenium organometallic complex (Ru-dim). The hypothesis of ruthenium-carbon (Ru-C) interaction presence could be explained such as coordination interaction present in support functionalized. The product obtained from functionalization process was labeled $G_{Ru\text{-}dim}$, the possible Ru-C coordination was corroborated by Raman spectroscopy.

$G_{Ru\text{-}dim}$ support was employed to obtain electrocatalyst via conventional polyol method. The electrocatalyst synthetized was denominated $Pt/G_{Ru\text{-}dim}$, with the objective to compare electrochemical properties were generated two electrocatalyst: a) $Pt/G_{Ru\text{-}com}$ where was implemented a support functionalized with ruthenium commercial precursor $RuCl_3{\cdot}XH_2O$ (Ru-com),

denominated G_{Ru-com} and b) Pt/G nanoparticles of platinum attached on non-functionalized graphene.
The electrocatalysts were characterized by XRD, SEM-EDS, HR-TEM and electrochemically. XRD analysis strongly suggests the formation of Pt-Ru alloys on Pt/G_{Ru-dim} and Pt/$G_{Ru-com.}$ Evaluation of catalytic activity for Methanol Oxidation Reaction (MOR) confirm that Pt/G_{Ru-dim} is a high-performance anode electrocatalyst for Direct Methanol Fuel Cells (DMFC`s).

II. Methodology

Graphene was obtained from X, ruthenium chloride ($RuCl_3 \cdot XH_2O$), ethylene glycol, 1-metoxy-1,4-ciclohexadiene, ethanol, chloroplatinic acid hexahydrate, Nafion solution (5 wt. %), sulfuric acid, nitric acid, sodium hydroxide, were purchased from Sigma Aldrich.

A. *Synthesis of $[(\eta^6\text{-}C_6H_5OCH_2CH_2OH)RuCl_2]_2$ (Ru-dim).*

Ru-dim was obtained following the methodology reported in [11], with slight modifications as follows: methoxy-1,4-cyclohexadiene (2.25 mL, 19.2 mmol) was added to a 1,2-ethanediol solution (15 mL) of ruthenium trichloride trihydrate (1.0 g, 3.82 mmol), followed by heating at 120 °C for 3 h. Yield: 59.26% (702 mg, X mmol) of brilliant orange solid. Ru-dim: $[(\eta^6\text{-}C_6H_5OCH_2CH_2OH)RuCl_2]_2$, ^{1}H-NMR (500 MHz, D_2O, δppm): 3.94 (t, 4 H, CH_2, J = 7.1 Hz), 4.32 (t, 4 H, CH_2), 5.52 (m, 2 H, *Ph*), 5.54 (m, 4 H, *Ph*), 6.07 (t, 4 H, A *Ph*, J= 9.2 Hz).

B. *Synthesis of G_{Ru-dim} and G_{Ru-com}.*

Graphene (G) support was functionalized with organometallic complex Ru-dim to obtain G_{Ru-dim}, under conditions established in [12] with slight modifications. Preserving a molar ratio of Ru-dim:G (1:10), corresponding to 104.16 mg (0.168 mmol) of Ru-dim and 20 mg (1.68 mmol) of G were stirred in 8 mL of THF under Ar atmosphere and refluxing conditions for 24 h at 130 °C. The black solution generated was transferred into a Schlenk tube, filtered through a cannula, washed with dried THF and finally dried in vacuum for 12 h, resulting in a brown powder.

G_{Ru-com} was obtained following the same procedure, starting with 43.93 mg (0.168 mmol) of $RuCl_3 \cdot XH_2O$ and 20 mg (1.68 mmol) of G, resulting in a black powder.

C. *Synthesis of Pt/C electrocatalysts*

The electrocatalysts Pt/G_{Ru-dim}, Pt/G_{Ru-com} and Pt/G were synthesized via the polyol method with ethylene glycol (EG) as reducing agent. The nominal concentrations (% wt.) to all electrocatalyst were 20:80 correlation of Pt:G [13]. Separately, 80 mg of G_{Ru-dim}, G_{Ru-com} or G were dispersed for 30 min by ultrasound in 48 mL of EG. The appropriate amount of $H_2PtCl_6 \cdot 6H_2O$ (20 wt. % of Pt) was dispersed in an ultrasonic bath for 30 min in 2 mL of EG and added to the graphene solution. The mixture was subjected to magnetic stirring for 1 h, followed by the adjustment of the pH to 12 by adding 2 mL of NaOH (1 mol L^{-1}). Then the temperature was increased to 130 ºC under refluxing and stirring conditions, kept constant for 3 h and left to cool down to room temperature. Afterwards, 4 mL of H_2SO_4 (1 mol L^{-1}) were used to adjust the pH to 2, maintaining stirring for another 3 h. The solution was filtered and the dark powder obtained was washed and dried under vacuum atmosphere.

D. *Phyisicochemical Characterization*

-Nuclear Magnetic Resonance (NMR) analysis was obtained in a 500 MHz Bruker Advance III (using a 5 mm direct broad band with Z-grad (PABBO-1H/D Z-GRAD). The ^{1}H chemical shifts were referenced to residual no deuterated solvent.

- Raman micro-analysis was performed in a confocal μ-Surf explorer microscope (Horiba) equipped with a 532 nm laser. The spectra were recorded over the 4000-400 cm^{-1} range.

- X-Ray Diffraction (XRD) patterns were recorded in an Empyrean PANalytical diffractometer with a Bragg–Brentano geometry operated at 40 kV and 45 mA, using a Cu-K_α radiation source (λ=1.5406 Å) in the 2θ range of 5–100° with a step scan of 0.0167 and 59 s per step.

- The chemical composition of the carbon supports and the Pt electrocatalysts was determined in a Philips XL30 Scanning Electronic Microscope (SEM), equipped with the Energy Dispersive Spectroscopic (EDS) technique, under an accelerating voltage of 20 kV. The morphology of the supports was determined with the same apparatus.

- The electrocatalysts were characterized by HR-TEM, HAADF-STEM and chemical mapping in a Jeol JEM-ARM200F microscope, operating at 30 kV.

E. *Electrochemical Characterization*

The electrochemical measurements were carried out in a three-electrode electrochemical cell using a VoltaLab PGZ301 potentiostat/galvanostat. The counter-electrode was a Pt foil, while the reference electrode was of the Ag/AgCl type, although the potentials have been referred to the Standard Hydrogen Electrode (SHE). To build the thin-film working electrodes, a mirror-finished glassy carbon disk (5 mm diameter) was used. Catalytic inks were prepared by separately sonication 10 mg of each electrocatalyst for 30 min, in a mixture containing 2 mL isopropyl alcohol and 5 μL Nafion solution. Then, aliquots of 10 μL of each electrocatalyst were deposited over the glassy carbon and let to dry.

Cyclic voltammograms (CVs) were acquired in N_2-saturated 0.5 mol L^{-1} H_2SO_4, in the 0.05 to 1.2 V (vs. SHE) potential range, at a scan rate of 20 mV s^{-1}. In order to evaluate their catalytic activity for the MOR, polarization curves were acquired in the same conditions, adding 0.5 mol L^{-1} CH_3OH to the electrolyte. CO-stripping measurements were carried out bubbling CO into the cell for 10 min while polarizing the electrode at 0.075 V (vs. SHE), followed by Ar purging for 20 min. Then, CVs were recorded at 20 mV s^{-1} in the 0.05 to 1.2 V range (vs. SHE).

III. RESULTS AND DISCUSSION

The formation of $[(\eta^6\text{-}C_6H_5OCH_2CH_2OH)RuCl_2]_2$ (Ru-dim) was confirmed by ^{1}H-NMR spectroscopy; chemical shifts are characteristic for functionalized-arene-ruthenium compound. [11]

Raman spectra of functionalized supports $G_{Ru\text{-}dim}$, $G_{Ru\text{-}com}$ and pristine graphene are current in Fig. 1. All the supports display the expected signals for carbon materials: i) the D band at ca. 1349 cm^{-1} related to lattice disorder, attributed to the C–C vibrations of the sp^3 defect sites; and ii) the G signal at ca. 1570 cm^{-1} corresponding to sp^2 hybridization from C=C bonds (graphitized lattice), due to π interactions [14].

Other important parameter to quantify disorder due to a shift from sp^2 to sp^3 orbitals can be determined from the ratio of the intensities of the G and D bands, I_D/I_G [15]. In Fig. 1 the decrease of I_D/I_G correlation to Pt/$G_{Ru\text{-}dim}$ and Pt/$G_{Ru\text{-}com}$ respect to graphene are evident, this behavior suggest a strong interaction between d-orbitals of ruthenium from Ru-dim complex and π orbitals from sp^2 hybridization of benzenoid aromatic ring of graphene, where is possible the formation of metal-carbon coordination that avoid lattice disorder with sp^3 hybridization. A comparable metal coordination behavior has been reported to different chromium organometallic complex with nano-structured carbon systems [7]. Nevertheless, this hypothesis needs to be elucidated with other elemental characterization techniques such as XPS with inert conditions or theoretical DFT calculations.

The chemical composition of the functionalized supports obtained from EDS analysis is shown in TABLE I. Ru concentration of 21.47 wt. % from $G_{Ru\text{-}dim}$ is about three times higher than $G_{Ru\text{-}com}$ (6.62 wt. %), this results exhibit the remarkable affinity between Ru-dim and graphene, considering the same molar ratio in both synthesis (10:1) Ru-dim:G and (10:1) Ru-com:G. Additionally, the carbon concentration decrease drastically to $G_{Ru\text{-}dim}$ wich is in relation to possible superficial functionalization of Ru-dim covering the carbon lattices. The presence of O and Cl are showed in TABLE I, these elements are in the structure of ruthenium precursors.

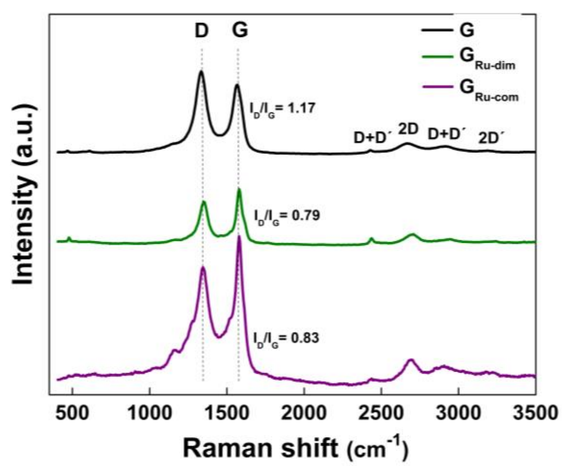

Fig. 1. Raman spectra of $G_{Ru\text{-}dim}$, $G_{Ru\text{-}com}$ and G.

TABLE I. Chemical composition of $G_{Ru\text{-}dim}$ and $G_{Ru\text{-}com}$.

Support	wt. %			
	C	***Ru***	***O***	***Cl***
$G_{Ru\text{-}dim}$	53.54	21.47	7.83	17.61
$G_{Ru\text{-}com}$	71.29	6.62	10.53	11.56

In Fig. 2. a) the XRD spectrum of pristine graphene shows the main characteristic signal to graphitic matrix in 2θ= 26.50 corresponds to 002 crystal reflection (JCPDS 41-1487). In all electrocatalysts the graphitic crystal reflection (002) are present, however, the intensity decrease remarkably to platinum electrocatalyst anchored on functionalized supports confirming the superficial Ru-C interaction. XRD spectra to reference material Pt/G shows the platium inherent crystal structure fcc (JCPDS 04-0802) corresponding to (111), (200), (220) and (311) reflections at 39.91°, 46.48°, 67.94° and 81.74° respectively (in 2θ scale).

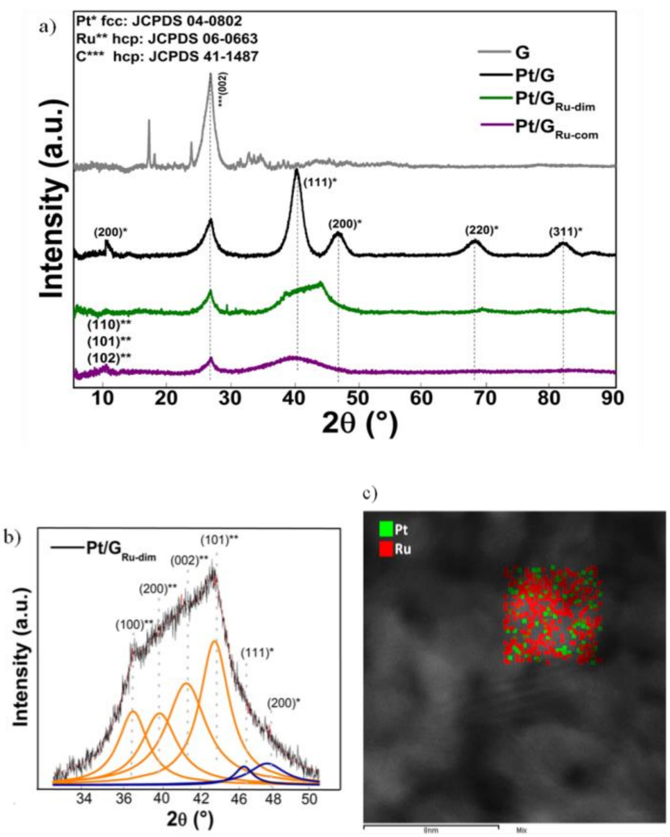

Fig. 2. XRD patterns of G, Pt/G, Pt/$G_{Ru\text{-}dim}$ and Pt/$G_{Ru\text{-}com}$. b) Deconvolution of the peak in 34-50° (2θ) of Pt/$G_{Ru\text{-}dim}$. c) HR-TEM micrograph and elemental mapping of Pt/$G_{Ru\text{-}dim}$.

The Pt:Ru interaction in Pt/$G_{Ru\text{-}dim}$ and Pt/$G_{Ru\text{-}com}$ is elucidate with vanish of typical platinum crystal reflections in (200), (220) and (311) in 2θ. Furthermore, the Pt:Ru alloy formation is possible due a overlaping of Pt and Ru signals of crystal reflections, demostated in the deconvolution of the peak in 2θ range from 34° to 50° shown in Fig. 2. b), acording to reported in the literature [16]. Addicionally, HR-TEM information defines the reduction in crystallite size of 2.59, 2.28 and 2.04 nm to Pt/G, Pt/G_{Ru-com} and Pt/G_{Ru-dim}, respectively (study not presented in this work). Finally, the Pt-Ru superficial interactions over G surface are showing HR-TEM mapping in Fig. 2. c) to Pt/G_{Ru-dim} where is possible demonstrate the higher Pt-Ru interactions are recovering G surface.

TABLE II. Chemical composition of Pt/G_{Ru-dim}, Pt/G_{Ru-com} and Pt/G.

Support	wt. %				
	C	*Pt*	*Ru*	*O*	*Cl*
Pt/G	79.48	20.52	-	-	-
Pt/G_{Ru-dim}	52.09	18.01	16.98	12.04	0.88
Pt/G_{Ru-com}	54.37	22.52	11.43	10.83	0.85

In TABLE II is shown the chemical composition to Pt/G electrocatalyst that has values approximates (80:20 wt. %) corresponding to calculate nominally, with 79.48 and 20.52 wt. % attributed to C and Pt, respectively. Pt/G_{Ru-dim} and Pt/G_{Ru-com} are presenting a considerable decrease of carbon concentration, due to Pt-Ru interactions covering G surface. Pt wt. % is lightly similar to 20 wt. % calculated. The concentration of ruthenium is 16.98 wt. % to Pt/G_{Ru-dim} the most higher compared with 11.43 wt. % of Pt/G_{Ru-com}. The oxygen and chlorine concentration are determined, it is important to note that the strong decrease in the chloride concentration indicate the lost of this ligands in ruthenium structures, this effect produce better superficial accessibility of ruthenium to interact with platinum atoms or carbon support.

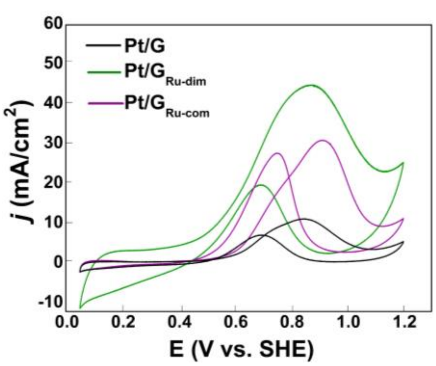

Fig. 3. Polarization curves of the MOR at the electrocatalysts. Electrolyte: Ar-saturated 0.5 M H_2SO_4 + 0.5 M CH_3OH. Scan rate: 20 mV s^{-1}.

The polarization curves in Fig. 3., to evaluate the electrocatalyts during MOR, determine that the Pt/G_{Ru-dim} electrocatalyst generates a maximum current density of 40.07 mA cm^{-2} with an on-set potential of 262.97 mV, significantly more negative than Pt/G_{Ru-com} and Pt/G with 380.49 and 402.04 mV, respectively, the correspondent current density is reported in TABLE III.

Furthermore the CV of the Pt/G electrocatalyst in Fig. 4 a) show slightly the characteristic regions of platinum materials: i) hydrogen adsorption and desorption ($H_{ads/des}$) in the potential range of 50-250 mV vs. SHE; ii) double layer (250-700 mV vs. SHE); iii) Pt-oxides formation/reduction (700-1200 mV vs. SHE). The weak definition of three peaks in hydrogen desorption region (H_{des}) to Pt/G reveals a possible electronic effect from graphene support. However, the onset potential of the Pt-oxides formation and the peak current density due to their reduction are distinguishable.

Moreover, the ruthenium presence and interaction with platinum in electrocatalysts Pt/G_{Ru-dim} and Pt/G_{Ru-com} is evident, vanishing peaks in H_{des} and exposing a current density slope up to the Pt-oxides region. However, the Pt-oxides formation/reduction region to Pt/G_{Ru-dim} and Pt/G_{Ru-com} is no clearly detected, suggesting the Pt-Ru alloy present in both electrocatalysts, similar behavior are attributed to the presence of Ru and the formation of RuOH species on Pt–Ru/C alloys [17]. Pt/G_{Ru-dim} demonstrates a drastic wide in double layer region due to remarkable effect between metal-support electronic interaction, analogous effect is reported to platinum nanoparticles supported in graphene [18]

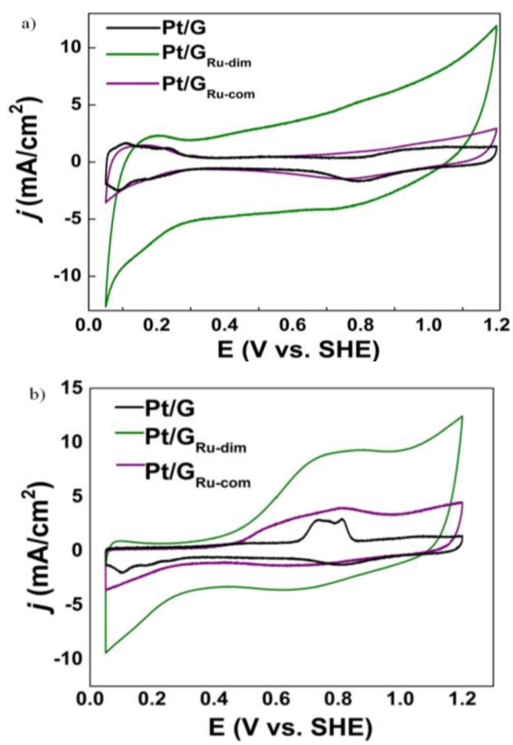

Fig. 4. a) CVs and b) CO-stripping curves of the electrocatalyts. Electrolyte: 0.5 M H_2SO_4. Scan rate: 20 mV s^{-1}.

TABLE III. Electrochemical parameters for Pt/G, Pt/C_{Ru-dim} and Pt/C_{Ru-com}.

Electrocatalyst	MOR			CO-stripping
	j *(mA cm^{-2})*	*E_{onset}* *(V)*	*j_f/j_b* *ratio*	*E_{onset}* *(V)*
Pt/G	11.31	0.40	1.54	0.65
Pt/G_{Ru-dim}	45.07	0.26	2.27	0.28
Pt/G_{Ru-com}	31.15	0.38	1.12	0.37

In addition, CO-stripping analysis has demonstrated an on-set potential for CO-oxidation of 287.73 mV for Pt/G_{Ru-dim}, lower compared to Pt/G_{Ru-com} and Pt/G (373.87 and 648.65 mV, respectively, parameters reported in TABLE III). Pt/G_{Ru-dim} demonstrates a synergistic effect from Pt-Ru alloy and metal-C interaction; these contributions could be produce different CO-adsorbed species over platinum surface to increase the CO oxidation and high catalytic activity during MOR. It was also observed Pt/G exhibit more than only a CO-specie oxidized during CO-stripping analysis, corroborating the synergistic effect metal-support, behavior reported to platinum nanoparticles supported on carbon nanostructured systems such as graphene and carbon nanotubes [19].

IV. CONCLUSIONS

The graphene functionalization with ruthenium compounds Ru-dim and Ru-com was confirmed through Raman spectroscopy. The intensity increase of the G-band corresponds to sp^2 hybridization from π bond of benzoic ring that conform the lattice graphene. The carbon sp^2 hybridization preservation is not affected in G_{Ru-dim} and G_{Ru-com} with ruthenium interaction, suggesting the bond coordination between affinities of d-orbital from ruthenium and p orbital of aromatic ring.

The results obtained from EDS analysis of chemical composition, X-ray patterns and grain size determined by HR-TEM, confirm the alloy Pt-Ru formation to G_{Ru-dim} and G_{Ru-com}. In addition, TEM mapping analysis exhibits extensive Pt-Ru interactions covering the graphene surface in the case of Pt/G_{Ru-dim}.

The Pt/G_{Ru-dim} electrocatalyst exhibit the higher J_f/J_b correlation 2.27 and current density value of 45.07 mA/cm^2 during the MOR with the lowest onset potential of 262.97 mV, compared with Pt/G_{Ru-com} and Pt/G (31.15 31 mA/cm^2 at 380.49 mV and 11.31 mA/cm^2 at and 402.04 mV, respectively). Finally, CO-stripping analysis the Pt/G_{Ru-dim} showed the lowest on set potential to CO-oxidation at 287.73mV.

The results demonstrated a remarkable positive effect to use previous functionalized supports with organometallic co-catalysts, with excellent potential to synthesis novel kind Pt/G electrocatalyst increasing the catalytic activity.

ACKNOWLEDGMENT

To CONACYT for project 241526 and PhD scholarship granted to A.A.S.C. Special thanks to CIMAV-Monterrey and CIQA for the use of facilities and resources.

REFERENCES

[1] M. P. Hogarth, G. A. Hards. "Direct Methanol Fuel Cells technological advances and further requeriments," Platin Met Rev., vol. 40, pp. 150-159, October 1996.

[2] A.S Arico, P.L Antonucci, E. Modica, V. Baglio, H. Kim, V. Antonucci, "Effect of Pt-Ru alloy composition on high-temperature methanol electro-oxidation," Electrochim Acta., vol. 47, pp. 3723-3732, August 2002.

[3] Y-C. Hsieh, Y. Zhang, D. Su, V. Volkov, R. Si, L. Wu, Y. Zhu, W. An, P. Liu, P. He, S. Ye, R. R. Adzic, J. X. Wang, "Ordered bilayer ruthenium–platinum core-shell nanoparticles as carbon monoxide-tolerant fuel cell catalysts". Nat Commun., vol. 4, pp.24661-24669, August 2013.

[4] M. Marques-Tusi, N. Soares-Polanco, M. Brandalise, O. Vercino-Correa, J. C. Villalba, F. Jacó-Anaissi, A. Oliveira-Neto, E. Vitorio-Spinacé, "PtRu/Carbon Hybrids With Different Pt:Ru Atomic Ratios Prepared by Hydrothermal Carbonization for Methanol Electro-Oxidation," Int J Electrochem. Sci. vol. 6, pp. 484-491, January 2011.

[5] Q-Y. Wang, Y-H. Ding, "Mechanism of methanol oxidation on graphene-supported Pt: Defect is better or not?," Electrochimi Acta, http://dx.doi.org/10.1016/j.electacta.2016.08.052, August 2016.

[6] H. Kim, A. W. Robertson, S. O. Kim, J. M. Kim, J. H. Warner, "Resilient High Catalytic Performance of Platinum Nanocatalysts with Porous Graphene Envelope," ACS Nano, vol. 9, pp 5947–5957, June 2015.

[7] S. Sarkar, S. Niyogi, E. Bekyarova, R. C Haddon, "Organometallic chemistry of extended periodic π-electron systems: hexahapto-chromium complexes of graphene and single-walled carbon nanotubes," Chem Sci.,vol. 2, pp. 1326-1333, March 2011.

[8] E. Bekyarova, S. Sarkar, F. Wang, M. E. Itkis, I. Kalinina, X. Tian, R. C. Haddon, "Effect of Covalent Chemistry on the Electronic Structure and Properties of Carbon Nanotubes and Graphene". Acc. Chem. Res., vol. 46, pp 65–76, January 2013.

[9] E. Bekyarova, S. Sarkar, S. Niyogi, R. C. Haddon, "Advances in the chemical modification of epitaxial graphene". J Phys D Appl Phys, vol. 45, pp. 18 (154009), March 2012.

[10] S. Sarkar, H. Zhang, J-W. Huang, F. Wang, E. Bekyarova, Ch. N. Lau, R. C. Haddon, "Organometallic hexahapto functionalization of single layer graphene as a route to high mobility graphene devices," Adv. Mater., vol. 25, pp. 1131−1136, February 2013.

[11] J. Soleimannejad, C. A. White, "A Convenient One-Pot Synthesis of a Functionalized-Arene Ruthenium Half-Sandwich Compound $[RuCl_2(\eta^6\text{-}C_6H_5OCH_2CH_2OH)]_2$,", Organometallics, vol. 24, pp. 2538-2541, April 2005.

[12] R. C. Haddon, S. Sarkar, S. Niyogi, E. Bekyarova, M. E. Itkis, X. Tian, F. Wang, "Organometallic Chemistry of Extended Periodic II-electron Systems". U.S. Patent 0202515, issued August 8, 2013.

[13] D. González-Quijano, W. J. Pech-Rodríguez, J. I. Escalante-García, G. Vargas-Gutiérrez, F. J. Rodríguez-Varela, "Electrocatalysts for ethanol and ethylene glycol oxidation reactions. Part I: Effects of the poliol synthesis conditions on the characteristics and catalytic activity of Pt-Sn/C anodes," Int. J. Hydrogen Energy, vol. 39, pp. 16676-16685, May 2014.

[14] A. C. Ferrari, "Raman spectroscopy of graphene and graphite: Disorder, electron–phonon coupling, doping and nonadiabatic effects," Solid State Commun., vol. 143, pp. 47-57, April 2007.

[15] M. S. Dresselhaus, A. Jorio, A. G. Souza-Filho, R. Saito, "Defect characterization in graphene and carbon nanotubes using Raman spectroscopy," Phil. Trans. R Soc. A, vol. 368, pp. 5355-5377, 2010.

[16] J. W. Long, R. M. Stroud, K. E.Swider-Lyons, D. R. Rolison, "How to make electrocatalysts more active for direct methanol oxidation avoid PtRu bimetallic alloys" J. of Phys. Chem. B, vol. 104, pp. 9772-9776. 2000.

[17] Y. Cheng, S. P. Jiang, "Highly effective and CO-tolerant PtRu electrocatalysts supported on poly(ethyleneimine) functionalized carbon nanotubes for direct methanol fuel cells," Electrochimica Acta, vol. 99, pp. 124–132, March 2013.

[18] D. C. Azevedo, W. H. Lizcano-Valbuena, E. R. Gonzalez, "An Impedance Study of the Rate Determining Step for Methanol Oxidation on Platinum and Platinum-Ruthenium Supported on High Surface Area Carbon," J. New Mat. Electr. Sys., vol. 7, pp. 191-196, May 2004.

[19] Yu-Ch. Chiang, Ch-Ch. Liang, Ch-P. Chung, "Characterization of Platinum Nanoparticles Deposited on Functionalized Graphene Sheets" Materials, vol. 8, pp. 6484-6497, September 2015.

MCFC technology for clean energy generation, carbon capture and CO_2 valorization.

A. Meléndez-Ceballos, V. Albin, V. Lair, A. Ringuede, M. Cassir
Chimie ParisTech, PSL Research University, CNRS, Institut de Recherche de Chimie Paris (IRCP)
F-75005 Paris, France
arturo.melendez@chimie-paristech.fr

S.M. Fernández-Valverde
Depto. de Química
Instituto Nacional de Investigaciones Nucleares
A.P.18-1027, México D.F. C.P.11801, México.

Abstract— **The Molten Carbonate Fuel Cell technology (MCFC) has a great potential in terms of stationary energy generation with an installation of up to 60 MW in South Korea. Nevertheless, lifetime and performance issues are not enough to allow a large commercialization of this technology. One of the major problems is Ni cathode degradation through Ni dissolution in the molten carbonate media. To reduce cathode dissolution, atomic layer deposition technique is used to deposit nano-scaled layers of a metal oxide onto the state-of-the-art porous Ni cathode. TiO_2, CeO_2, Nb_2O_5 and Co_3O_4 are studied by means of open circuit potential (OCP) and electrochemical impedance spectroscopy (EIS). Interesting results are obtained, reducing Ni dissolution almost in half and keeping high cathode electrochemical performance. Further on, a molten carbonate eutectic serving as MCFC electrolyte is analyzed in presence of additives, such as with the addition of Cs or Rb carbonates. The kinetic study performed with a gold flag electrode and EIS by variation of PCO_2 and PO_2 with 0, 3 and 5 mol% additions of Cs_2CO_3 reveals a significant increase in the CO_2 diffusion coefficient. In order to investigate the impact of electrolyte modification in the state-of-the-art Ni cathode, we tested it in Li-K and Li-Na carbonate eutectics modified with the addition of 5 mol% Rb_2CO_3 or Cs_2CO_3. OCP and EIS reveal a significant decrease in cathode total resistance, which may represent an increase in power output in real conditions. Besides, molten carbonates constitute performing media for capturing the CO_2 released to the environment by industrial processes such as cement production and carbon or hydrocarbon power plants among others. Thermodynamic calculations show that CO_2 and H_2O can be directly transformed into CO + H_2 (syngas) by means of a co-electrolysis process into a molten carbonate electrolyzer cell (MCEC) due to the important solubility of CO_2 in carbonate media, which is two orders of magnitude higher than in the most advanced ionic liquids. Contrarily to other solvents, CO_2 dissolution is enhanced in molten carbonates by increasing the temperature. Chronopotentiometry is used to study the feasibility of the direct CO_2 reduction into CO in carbonate media.**

Keywords— Molten Carbonates; MCFC; MCEC; electrolyzer; Carbon capture and storage; CO_2 reduction.

I. INTRODUCTION

The environmental issue of global warming is one of the biggest concerns of mankind, a good part of the research around the world contribute in different ways to attain the problem. Among the research fields that have as goal reducing CO_2 emissions, the main ones are renewable-energy related and CO_2 management related. In this aspect, high temperature fuel cells (HTFC) are involved in both approaches not only from a clean energy generation point of view but also as a medium to capture, storage and valorize CO_2. Among the HTFC technologies that could achieve an efficient power generation, molten carbonate fuel cells (MCFC) are outstanding since they can also serve as CO_2 sequestration systems. MCFC technology has reached commercialization mainly as stationary power plants ranging from 1.4 MW up to 60MW the world largest fuel cell facility built in Hwasung City in South Korea [1]. Nevertheless, MCFC technology still has some drawbacks regarding stack lifetime. Stack degradation is mainly due to cathode dissolution in molten carbonate media, a phenomena that causes Ni^{2+} dissolved at cathode to reach the anode side where the presence of H_2 reduces it to metallic Ni, then it precipitates into the electrolyte matrix forming a conductive path that in long term operation causes a short-circuit between anode and cathode reducing considerably the performance of the MCFC [2–5]. Hence, reducing cathode dissolution without affecting the electrochemical performance is necessary to increase stack lifetime from the current 5 years to 10 years objective [6]. This can be achieved by cathode material modification or electrolyte modification. Both approaches were investigated by means of ultra-thin layer deposition of various metal oxides (TiO_2, CeO_2, Co_3O_4 and Nb_2O_5) onto the state-of-the-art Ni cathode by using atomic layer deposition technique (ALD) [7–10] and by electrolyte modification with additives such as Cs and Rb [11]. A comparative study of the most significant results obtained from these approaches is presented in this paper in a brief manner.

TABLE I. DEPOSITION PARAMETERS OF ALD-PROCESSED COATINGS.

Deposited Material	Precursor	Temperature (°C)	Pulse time (s)	Purge time (s)	Oxidant	Pulse time (s)	Purge time (s)	Chamber T (°C)
TiO_2	$Ti(OCH(CH_3)_2)_4$	60	0.5	2	H_2O	0.5	2	250
CeO_2	$Ce(TMHD)_4$	180	3	2.5	O_3	4	2.5	300
Co_3O_4	$Co(TMHD)_3$	160	1.5	3	O_3	1.5	6	240
Nb_2O_5	$Nb(OCH_2CH_3)_5$	80	0.5	3	H_2O	0.1	3	300

Regarding CO_2 capture and storage (CCS) technology, MCFC is capable of capturing CO_2 from the cathode infeed gases, Rexed *et al.* [12] evaluated this possibility and recently, it has been shown by the authors [13–15] and by our research group [16,17] that CO_2 electrochemical reduction can be achieved in molten carbonate media. CO_2 in molten carbonates is 400 times more soluble than in water and 4 times more soluble than in ionic liquids [18], due to the high solubility of this gas in the molten carbonates the process could be more efficient than other technologies. This fact could make possible CO_2 reduction by using the same MCFC technology used for power generation. As shown by the thermodynamic studies of CO_2 and H_2O electrolysis both reactions could take place in parallel at the same time [19,20], if this could be achieved, the co-electrolysis of CO_2 and H_2O will produce a mixture of CO and CH_4 (syngas), in this way CO_2 could be valorized and reused for other processes including hydrocarbons synthesis. Following previous studies from our research group, we investigated CO_2 reduction in molten carbonate eutectics of Li-Na, Li-K and Na-K by means of chronopotentiometry at a golden flag electrode, the results obtained will be briefly discussed in this paper..

II. EXPERIMENTAL

A. Atomic Layer Deposition of Metal Oxide Layers

Atomic layer deposition (ALD) is a chemical gas phase deposition technique developed in Finland in the 1970s by T. Suntola [21]. In ALD, reactant gas pulses are separately introduced to reach the substrates to be coated. Growth is achieved through self-terminating surface reactions. Self-terminating means that only one monolayer of reactant gas species can be adsorbed to the surface during a pulse. The pulses containing reactant gases are separated by purging pulses where the ALD reactor is flushed with an inert gas. The purging pulses ensure that the reactant gas pulses do not mix. Mixing of the reactant gas pulses would lead to continuous growth and the accurate thickness control of the deposition process would be lost. By-products like detached ligands and excess reactants are also flushed away by the purging pulses. A complete set of reactant gas pulses and purging pulses needed to deposit a certain compound are referred to as a cycle. If the deposition parameters have been chosen properly, the number of cycles rather than the concentration of the reactant species determines the film thickness [22]. A known deposition route was followed using halide-free and non-corrosive precursors. Thin layers of TiO_2, CeO_2 or Co_3O_4 were deposited on a commercial porous nickel substrate (produced by Doosan, South-Korea) by means of ALD technique using a vertical flow type reactor (Picosun SUNALE™ R-series). Titanium isopropoxide [$Ti(OCH(CH_3)_2)_4$], $Ce(TMHD)_4$ [tetrakis(2,2,6,6-tetramethyl-3,5 heptanedionato)cerium(IV)], $Co(TMHD)_3$ [tris(2,2,6,6-tetramethyl-3,5-heptanedionato)cobalt(III)] or Nb ethoxide were used as precursors while distilled water or O_3 were used as oxidizing agents. In order to prepare the thin layers [7–10], precursor and oxidant on each case were introduced into the reactor chamber using the parameters given in Table 1 and the thickness of each deposit are depicted in Fig. 1.

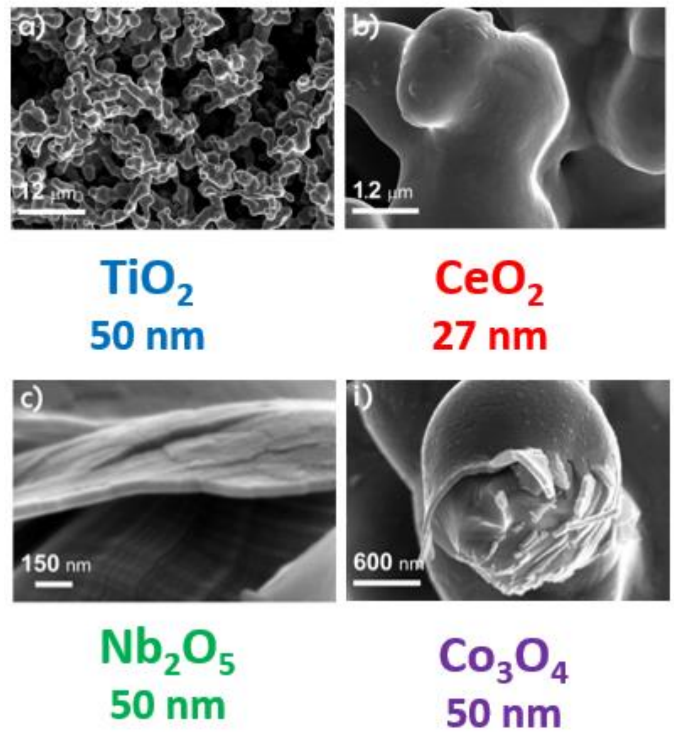

Figure 1. Thicknesses of as-deposited oxides on to porous Ni cathode [8,10].

B. Electrochemical Tests

All experiments were carried out in the same type of half-cell reactor as shown in Fig. 2 This high-temperature electrochemical cell was a single-compartment crucible of dimensions 70 x 50 mm^2 contained in an alumina Al_2O_3 reactor of dimensions 250 x 60 mm^2, hermetically sealed by a stainless steel cover with a Viton O-ring. The whole electrochemical set-up was fully described in a previous paper [24]. Temperature controlled by means of a calibrated chromel/alumel thermocouple was maintained constant at 650 °C. The electrolyte was a mixture of lithium and potassium carbonates of high grade purity > 98 % (Sigma-Aldrich®), in a proportion of 62:38 mol %. The standard cathode atmosphere was a mixture of Air/CO_2 (70:30 mol %) of high grades purity (Air Liquide®) at 650 °C and a pressure of 1 atm.

This work was supported by the French program PLANEX ANR11-EQPX-0-01 and benefited of a Mexican CONACY T Ph.D. scholarship 314518 and the project number 2520 03.

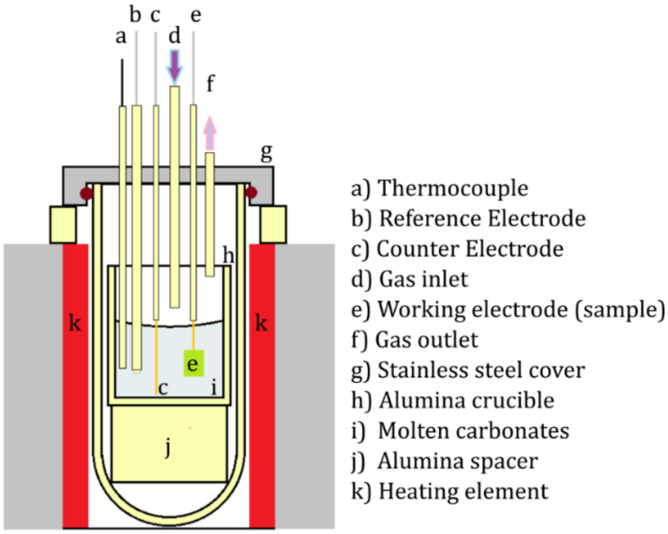

Figure 2. Electrochemical set up used for all the experiments.

A carbonate melt was prepared and stabilized 24 h at 650 °C for each TiO_2, CeO_2, Nb_2O_5 and Co_3O_4 coated samples. After stabilizing the molten carbonate eutectic under the selected cathode atmosphere, samples were immersed in the melt and electrochemical measurements were performed for 230 h. After electrochemical tests, samples were rinsed with deionized water to remove the carbonates, dried at 100 °C in an oven and kept in small plastic boxes to prevent contamination before further analysis. In the case of Cs and Rb improved electrolytes as well as chronopotentiometric studies of CO_2 reduction, the working electrode was a gold flag electrode polished to grain 4000 with SiC polishing paper. The electrolyte was modified by the addition of 3 and 5 mol% of Cs or Rb carbonates, the electrolyte was a eutectic mixture of Li-K or Li-Na carbonates. For the CO_2 reduction, eutectic mixtures of Li-K, Li-Na and Na-K carbonates were used with no further modification. The atmosphere was modified to study oxygen and CO_2 kinetics by variating the partial pressure of the gases according to Table 2. For chonopotentiometric studies only CO_2 was used as reactant gas, the balance gas was Ar, the partial pressure of CO_2 was varied between 0.05 and 1 atm.

III. Results and Discussion

A. *Cathode mofication by ALD of metal oxides*

The detailed study of each metal oxide behavior was already reported by Melendez-Ceballos et al. [7–10] therefore in this section we will compare the most interesting results from those already reported. In Fig. 3, the open circuit potentiometric measures for 50 nm TiO_2, Co_3O_4, Nb_2O_5 and 27 nm CeO_2 are presented. The black line in the graph representing the standard porous Ni cathode shows the typical behavior of Ni immersed in eutectic Li-K molten carbonates, before Ni reaches its balance potential around 0 V where it is ready to work as cathode in a MCFC, it goes through an oxidation/lithiation process. This can be observed as two plateaus, the first present around -0.7 V *vs* Ag/Ag^+ (I), characteristic of Ni oxidation process. A second plateau at around -0.4 V *vs* Ag/Ag^+ (I I) associated with NiO lithiation process and finally, the third plateau at around 0 V *vs* Ag/Ag^+ (I I I) where it stabilizes. The whole process of in-situ oxidation lithiation is about 230 h in our experimental conditions.

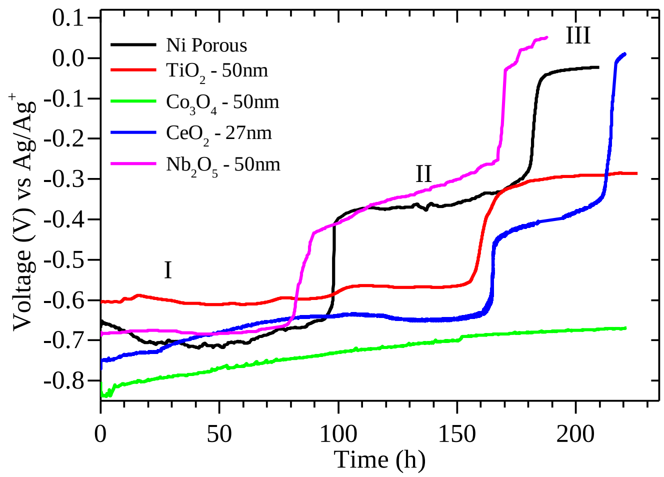

Figure 3. Open circuit potentiometry of selected metal oxide covered samples.

Once the cathode has been protected with an oxide layer the OCP evolves in a different manner, indication that the oxidation/lithiation process have changed, this can be observed in Fig. 3, where the presence of a thin Nb_2O_5 layer seems to accelerate oxidation and lithiation of Ni, reaching the balance potential before standard porous Ni. Contrarily, Co_3O_4 thin layer seems to completely stop oxidation and lithiation process, this is confirmed by XRD where a big amount of metallic Ni is present in the sample after 230 h immersion, which was not the case on the other samples [10]. This can be due to the formation of $LiCoO_2$ that stops further oxygen and lithium penetration in the material. On the other hand, CeO_2 behaves similarly to standard porous Ni, reaching the balance potential about 30 h after.

TABLE II. Gas compositions tested.

O2/CO2/Ar Atm. %	O2/CO2/Ar Atm. %
7/30/63	14/20/66
14/30/56	14/30/56
21/30/49	14/40/46
28/30/42	14/50/36

TiO_2 has a first and second plateau, but it did not showed the third plateau during the 230 h immersion, nevertheless it could reach the balance potential if the experiment is extended. Together with the OCP data, electrochemical impedance spectroscopy (EIS) data were collected, from EIS information such as electrolyte resistance (R1), charge transfer resistance (R2) and mass transfer resistance (R3) can be deduced.In Fig. 4 a Nyquist representation diagram together with the equivalent circuit used to deduce that information is shown. From the fitting, total resistance Rtot (Rtot = R1 + R2 + R3) was deduced for all samples, total resistance evolution in time is shown in Fig. 5. As it can be observed, Co_3O_4 presents the lower resistance from all the samples, this is in agreement with the formation of $LiCoO_2$ which is much more conductive than NiO. CeO_2 presents a lower resistance than NiO around 320 ohms, while TiO_2 shows a total resistance of 540 ohms that is 60 % higher than standard porous Ni. Unfortunately Nb_2O_5 showed such a high resistance (over 2500 ohms) that is not shown in the graph for comparison, this high resistance is not surprising since Nb_2O_5 is highly resistive what is impressive is that even though total resistance is very high, the OCP showed a fast evolution to balance potential. This could be due to a catalytic or electrocatalytic behavior that has not been completely understood [8].

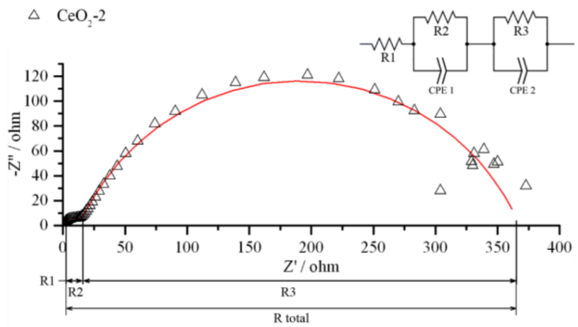

Figure 4: EIS Nyquist representation of CeO2 coated sample and the equivalent circuit used to fit the data, the fitting is shown in red [7].

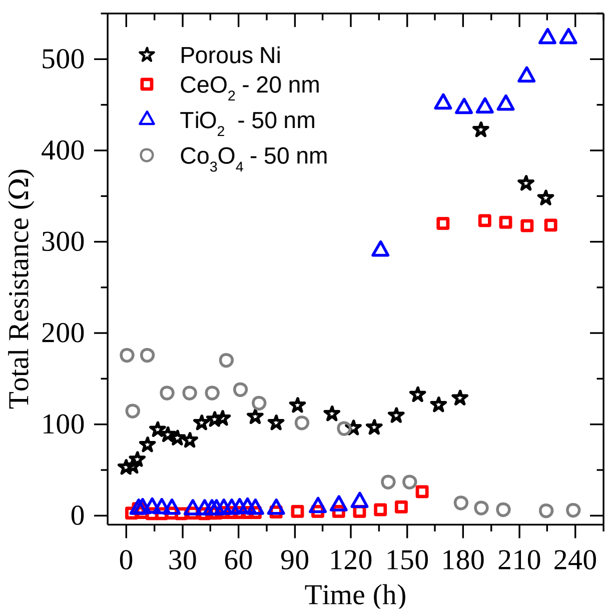

Figure 5: Total resistance evolution over immersion time [10].

Ni dissolution in the molten carbonates was measured after each electrochemical test by ICP-AES, the amount of nickel dissolved in the carbonates for each sample is shown in Table 3. We can observe that the best material in terms of cathode protection is TiO_2, which is explained by the formation of a very stable Li_2TiO_3 phase which protects NiO from dissolution. CeO_2 is not far in terms of protection which as Nb_2O_5 got 30 % reduction of Ni dissolution.

TABLE III. NI DISSOLUTION IN LI-K MOLTEN CARBONATES AT 650 °C FOR EACH TESTED PROTECTIVE COATING.

Sample	Bare Ni	TiO2	CeO2	Nb2O5	Co3O4
Ni content (wt. ppm)	15	8.6	10	10	12

B. *Electrolyte Modification*

Li-K molten carbonate eutectic mixture modified with 3 and 5 mol% addition of Cs_2CO_3 was studied by EIS and from which, a reaction order analysis was performed to obtain valuable information such as the diffusion coefficients D_{CO_2} and $D_{O_2^-}$. It is not the objective of this paper to go into details about the method used, a detailed description of this type of analysis can be found in references [11,23]. Figure 6 shows the variation of diffusion coefficients D_{CO_2} and $D_{O_2^-}$ with the addition of Cs, as can be noted, a beneficial effect is obtained specially for D_{CO_2} which doubles its value from 1.1 10^{-5} to 2.2 10^{-5}. The presence of Cs increases the oxo-acidity of the carbonates which favours CO_2 solubility. On the other hand, $D_{O_2^-}$ decreases slightly with 3 mol % Cs addition, but increases again with 5 mol % Cs to 2.1 10^{-5} a value almost two times that of non-modified electrolyte.

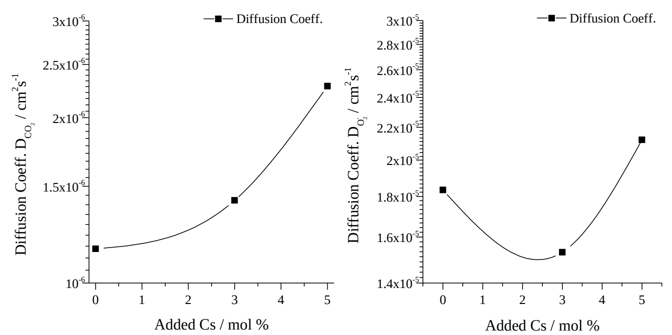

Figure 6: variation of D_{CO_2} and $D_{O_2^-}$ diffusion coefficients with added Cs [11].

C. *CO_2 reduction*

Chronopotentiometry was used to elucidate more details about the possible mechanism that could dominate the CO_2 reduction reaction. From previous studies by cyclic voltammetry carried out by our research team [16,19,20] a 4 electron mechanism was proposed. It is not our objective to go deep into the details of the chronopotentiometry and we will discuss some preliminary results only. Fig. 7 shows the cyclic voltamperogram obtained previously by our research team in previous studies: two peaks appear on the cyclic voltammetry one at -0.8 V *vs* Ag/Ag^+ and the second appearing at -1.2 V *vs* Ag/Ag^+. These two potentials should be detected by chronopotentiometry since they are related to a reaction at the electrode; hence, the transition time τ could be estimated and applying the Sand's equation (1) the number of electrons could be deduced.

$$i\tau^{1/2} = (nFS\pi^{1/2}\, C_0\, D_0^{1/2}) / 2 \qquad (1)$$

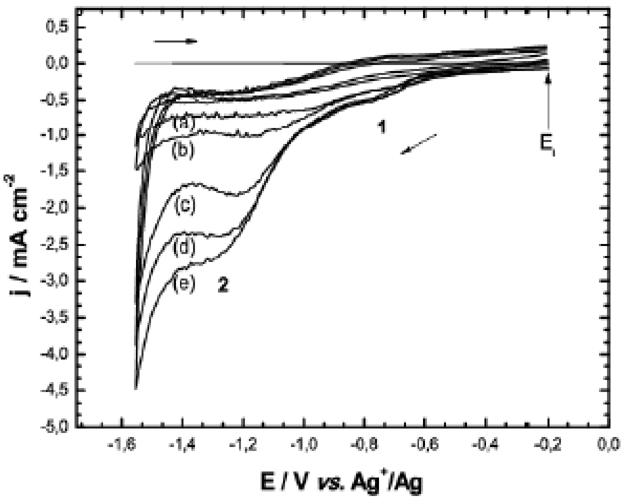

Figure 7: Cyclic voltammetry of gold electrode in Li2CO3-K2CO3 (62:38 mol%) at 575°C, p(CO2)=1 bar, for different scanning rates: (a) 10mV/s, (b) 20 mV/s, (c) 100 mV/s, (d) 150 mV/s, (e) 200 mV/s [19].

An example of the chronopotentiograms obtained is shown in Fig. 8, where a series of curves can be observed , showing a single plateau that does not end abruptly as could be expected; instead, the plateau ends in a slope which makes difficult to measure the transition time. Nevertheless, the plateau observed appears around -1.2 V *vs* Ag/Ag$^+$ which corresponds to CO_2 reduction potential. Expectedly, the length of the plateau decreases with increasing current which is due to the faster consumption of the specie reacting at the electrode at higher currents.

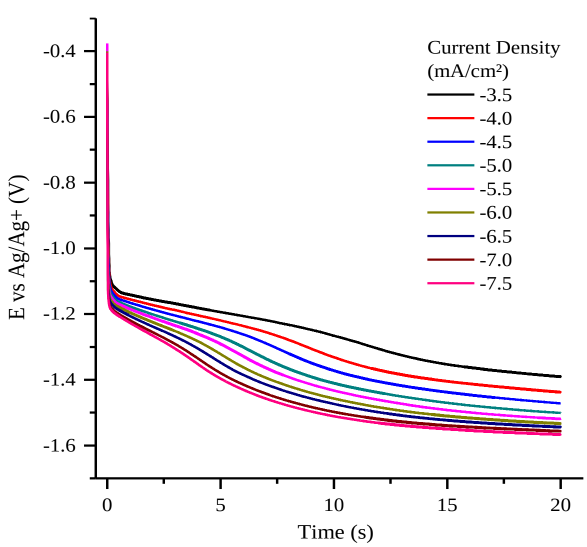

Figure 8: Chronopotentiograms on gold flag electrode immersed in Li_2CO_3-Na_2CO_3 eutectic at 650°C, p(CO_2)=0,5 atm, for different current densities; Ei = 0 V vs Ag/Ag$^+$

The slow transition could be due to a non-stationary regime in the molten carbonates, which is possible due to the high convection movement of the melt caused by the temperature difference between the surface of the liquid and the bottom of the crucible. Better estimations of transition time could be obtained by restricting the carbonate convection to make the system stationary. We will continue with experiments to get better results. If the number of electrons could be confirmed a good insight on the CO_2 reduction reaction could be achieved.

IV. Conclusions

Ultra-thin layers deposited by atomic layer deposition are an effective way for reducing cathode dissolution where TiO_2 and CeO_2 demonstrated to be good candidates as protective coatings for state-of-the-art cathode material. A good improvement of TiO_2 protective coating could be achieved by adding Co_3O_4 to reduce electrode total resistance without compromising electrochemical performance and maintaining the excellent protective properties of TiO_2 layer. Further tests in complete fuel cell mode will be necessary to test these promising materials in real working conditions. On the other hand, Cs addition to molten Li-K carbonates showed to improve diffusion of D_{CO_2} and $D_{O_2^-}$ which are the main species involved in the oxygen reduction reaction, thus demonstrating that additives such as Cs could improve cell efficiency, this hypothesis should also be tested in real working conditions.

Chronopotentiometry is a promising technique to study CO_2 reduction in molten carbonate media, the results obtained up to now could be improved by reducing convection in the cell. Testing this method with a confined electrolyte could solve the problem of convection, this could be achieved by using commercial electrolyte matrix and gold electrodes in a symmetrical cell configuration.

Acknowledgment

Authors would like to acknowledge Camille Crapart for her contributions on the CO_2 reduction experiments.

References

[1] FuelCell Energy's Korean Growth Continues: 60 MW for Power Park in Hwaseong, 8.4 MW for Samcheok n.d. http://www.fuelcelltoday.com /news-archive/2012/may/fuelcell-energy%E2%80%99s-korean-growth-continues-60-mw-for-power-park-in-hwaseong,-84-mw-for-samcheok (accessed August 26, 2016).

[2] Orfield ML, Shores DA. Solubility of NiO in molten Li_2CO_3, Na_2CO_3, K_2CO_3, and Rb_2CO_3 at 910°C. J Electrochem Soc 1988;135:1662–8. doi:10.1149/1.2096093.

[3] Orfield ML, Shores DA. The Solubility of NiO in binary mixtures of molten carbonates. J Electrochem Soc 1989;136:2862–6. doi:10.1149/1.2096301.

[4] Makkus RC. Electrochemical studies on the oxygen reduction and NiO(Li) dissolution in molten carbonate fuel cells. Delft: 1991.

[5] Ota K, Mitsushima S, Kato S, Asano S, Yoshitake H, Kamiya N. Solubilities of nickel oxide in molten carbonate. J Electrochem Soc 1992;139:667–71. doi:10.1149/1.2069282.

[6] McPhail S, Leto L, Della Pietra M, Cigolotti V, Moreno A. International status of molten carbonate fuel cells technology - 2015. ENEA; 2015.

[7] Meléndez-Ceballos A, Albin V, Fernández-Valverde SM, Ringuedé A, Cassir M. Electrochemical properties of atomic layer deposition processed CeO_2 as a protective layer for the molten carbonate fuel cell cathode. Electrochimica Acta 2014;140:174–81. doi:10.1016/j.electacta.2014.05.025.

[8] Meléndez-Ceballos A, Fernández-Valverde SM, Albin V, Lair V, Chávez-Carvayar JÁ, Ringuedé A, et al. Investigation on niobium oxide coatings for protecting and enhancing the performance of Ni cathode in the MCFC. Int J Hydrog Energy 2016. doi:10.1016/j.ijhydene.2016.04.045.

[9] Meléndez-Ceballos A, Fernández-Valverde SM, Barrera-Díaz C, Albin V, Lair V, Ringuedé A, Cassir M. TiO_2 protective coating processed by atomic layer deposition for the improvement of MCFC cathode. Int J Hydrog Energy 2013;38:13443–52. doi:10.1016/j.ijhydene.2013.07.083.

[10] Meléndez-Ceballos A, Albin V, Ringuedé A, Fernández-Valverde SM, Cassir M. Electrochemical behavior of $M_{x-1}O_x$ (M = Ti, Ce and Co) ultra-thin protective layers for MCFC cathode. Int J Hydrog Energy 2014;39:12233–41. doi:10.1016/j.ijhydene.2014.03.213.

[11] Meléndez-Ceballos A, Albin V, Lair V, Ringuedé A, Cassir M. A kinetic approach on the effect of Cs addition on oxygen reduction for MCFC application. Electrochimica Acta 2015;184:295–300. doi:10.1016/j.electacta.2015.10.057.

[12] Rexed I, della Pietra M, McPhail S, Lindbergh G, Lagergren C. Molten carbonate fuel cells for CO_2 separation and segregation by retrofitting existing plants – An analysis of feasible operating windows and first experimental findings. Int J Greenh Gas Control 2015;35:120–30. doi:10.1016/j.ijggc.2015.01.012.

[13] Yin H, Mao X, Tang D, Xiao W, Xing L, Zhu H, et al. Capture and electrochemical conversion of CO_2 to value-added carbon and oxygen by molten salt electrolysis. Energy Environ Sci 2013;6:1538. doi:10.1039/c3ee24132g.

[14] Kaplan V, Wachtel E, Gartsman K, Feldman Y, Lubomirsky I. Conversion of CO_2 to CO by electrolysis of molten lithium carbonate. J Electrochem Soc 2010;157:B552–6. doi:10.1149/1.3308596.

[15] Licht S. Efficient Solar-Driven Synthesis, carbon capture, and desalinization, STEP: solar thermal electrochemical production of fuels, metals, bleach. Adv Mater 2011;23:5592–612. doi:10.1002/adma.201103198.

[16] Chery D, Lair V, Cassir M. CO_2 electrochemical reduction into CO or C in molten carbonates: a thermodynamic point of view. Electrochimica Acta 2015;160:74–81. doi:10.1016/j.electacta.2015.01.216.

[17] Chery D. Approche prévisionnelle de la valorisation électrochimique du CO2 dans les carbonates fondus. Disertation. Universite Pierre et Marie Curie-Paris VI, 2015.

[18] Jones AP, Genge M, Carmody L. Carbonate Melts and Carbonatites. Rev Mineral Geochem 2013;75:289–322. doi:10.2138/rmg.2013.75.10.

[19] Chery D, Albin V, Lair V, Cassir M. Thermodynamic and experimental approach of electrochemical reduction of CO_2 in molten carbonates. Int J Hydrog Energy 2014;39:12330–9. doi:10.1016/j.ijhydene.2014.03.113.

[20] Chery D, Albin V, Meléndez-Ceballos A, Lair V, Cassir M. Mechanistic approach of the electrochemical reduction of CO_2 into CO at a gold electrode in molten carbonates by cyclic voltammetry. Int J Hydrog Energy 2016. doi:10.1016/j.ijhydene.2016.06.094.

[21] Haukka S, Kytökivi A, Lakomaa E-L, Lehtovirta U, Lindblad M, Lujala V, et al. The utilization of saturated gas-solid reactions in the preparation of heterogeneous catalysts. In: G. Poncelet JM B Delmon, PA Jacobs and P Grange, editor. Stud. Surf. Sci. Catal., vol. 91, Elsevier; 1995, p. 957–66.

[22] Leskelä M, Ritala M. Atomic layer deposition (ALD): from precursors to thin film structures. Thin Solid Films 2002;409:138–46. doi:10.1016/S0040-6090(02)00117-7.

[23] Nishina T, Uchida I, Selman JR. Gas electrode reactions in molten carbonate media part V . electrochemical analysis of the oxygen reduction mechanism at a fully immersed gold electrode. J Electrochem Soc 1994;141:1191–8. doi:10.1149/1.2054895.

XVI International Congress of the Hydrogen Mexican Society 2016

Sonochemical synthesis of graphene by liquid exfoliation and its electrochemical performance for oxygen reduction reaction.

I. Alonso-Lemus[1,*,ǂ], M.Z. Figueroa-Torres[2], B. Escobar-Morales[3,ǂ], F.J. Rodríguez-Varela[1], A. Fernandez-Fuentes[1], E. Montes-Bocanegra[1].

[1]Centro de Investigación y Estudios Avanzados del Instituto Politécnico Nacional Unidad Saltillo, (CINVESTAV-Saltillo). Parque Industrial Saltillo-Ramos Arizpe. Ramos Arizpe, Coahuila, México, C.P. 25900.
[2]Facultad de Ingeniería Civil, Universidad Autónoma de Nuevo León (UANL), Av. Universidad s/n, Ciudad Universitaria, San Nicolás de los Garza, Nuevo León C.P. 66451, México
[3]Centro de Investigación Científica de Yucatán (CICY). Unidad de Energía Renovable. Calle 43 No. 130 Col. Chuburná de Hidalgo, Mérida, Yucatán, México. C. P. 97200
[ǂ] Conacyt Research Fellow
[*]Tel: +528444389626; e-mail: ivalemus@gmail.com

ABSTRACT

This work reported a fast and simple synthesis of graphene sheets from graphite flakes through ultrasound assisted method. The effect of liquid media and ultrasonication time in the characteristics of the obtained graphene was investigated. Pure dimethylformamide (DMF) and an aqueous solution of Pluronics (P123®) were used as solvents. Ultrasound time was evaluated in a range of 30 to 120 minutes. The quality of exfoliation and the morphology were determined by Scanning Electron Microscopy (SEM), Raman Spectroscopy (RS) and X-Ray diffraction (XRD). Additionally, graphene was functionalized by hydrothermal treatment in order to obtain nitrogen doped graphene. Metal-free electrocatalyst were also obtained. The total nitrogen and carbon were determined using a CHNS analyzer. The functional groups determinates by FTIR found in graphene are carboxyl and amine groups. Preliminary results obtained by Raman spectroscopy indicates that nanocarbon materials has a molecular structure composed by a mixture of graphene and exfoliated graphite. The electrochemical performance of the material for the oxygen reduction reaction (ORR) was tested by rotation disk electrode technique (RDE). It was observed that stable graphene suspensions could be prepared using both solvents. However, DMF showed a higher exfoliation degree. Results demonstrate that ultrasonication time is a key parameter to control the yield and size of graphene, when sonication time was higher than 60 minutes the production of graphene decreased. Electrochemical evaluation revealed that these materials are electroactive for ORR in alkaline media. Therefore, the sonochemical synthesis is an attractive massively scalable and simple method for preparation of graphene to energy applications.

Keywords: metal-free electrocatalyst; nitrogen doped-graphene; fuel cells, ORR; Ultrasound; Exfoliation

Design, manufacture and experimental validation of a miniaturized air breathing PEMFC for portable applications

Kuan-Wen Kuo[1], Romeli Barbosa[1], B. Escobar[2], F. Matera[3], I. Gatto[3]

[1]Universidad de Quintana Roo, Boulevard Bahía s/n, Chetumal, Q. Roo, México, 77019.
[*]Tel: +529831566032; e-mail: romelix1@gmail.com
[2]Centro de Investigación Científica de Yucatán, C. 43 No 130, Chuburná de Hidalgo, Mérida, Yucatán, México, 97200.
[3]CNR-ITAE, via S. Lucia sopra Contesse 5, 98126, Messina, Italy.

ABSTRACT

Fuel cells are one of the applications of renewable energy that convert chemical energy directly into electric energy. Proton Exchange Membrane Fuel Cell (PEMFC) is the most versatile of all types due to its light weight and easy transport. The present work focuses on designing and fabricating a PEMFC prototype which can offer greater flexibility for portable systems whose design provides a high specific power density considering the former conventional designs. The fabrication of the miniaturized air breathing PEMFC process includes the deposition of the components by layers: 1) flat polymer composite bipolar plate with micro platinum wires, 2) gas diffusion layer with flow field, 3) membrane electrode assembly with high platinum load. The performance of the manufactured cell is experimentally studied in order to validate the feasibility of the open-cathode design. The performance of the single air-breathing cell under different conditions (pressure, mass flow of fuel and the reactant, humidity of fuel) was compared (Figure 1). Moreover, different diffusive materials were implemented for further studies. In addition to that, the designs of the entrance for the reactant gas, air, also contribute significantly in the performance of the cell. The results, so far, only serve as conceptual suggestion aiming for a more developed prototype and systems in electrochemical and economic aspects of the design.

Keywords: Fuel cells; Portable Applications; Bipolar Plate.

XVI International Congress of the Hydrogen Mexican Society 2016

Hydrogenolysis of glycerol to produce valuable chemicals: A review

I. Pala-Rosas[1,*], E. A. de la Rosa-Reyna[2], A. A. Fragoso-Montes de Oca[1], J. Horáček[2], M. A. Valdes-Madrigal[3].

[1] ESIQIE-SEPI, Instituto Politécnico Nacional, UPALM, Av. Instituto Politécnico Nacional s/n, Col. San Pedro Zacatenco, Del. Gustavo A. Madero, Ciudad de México, México, C.P.07738.

[*]e-mail: ipalar@hotmail.com

[2]Research Institute of Inorganic Chemistry, RENTECH-UniCRE, Chempark Litvínov, Záluží-Litvínov, Czech Republic, C.P. 43670.

[3]Programa de Doctorado en Nanociencias y Nanotecnología, CINVESTAV, Av. Instituto Politécnico Nacional 2508, Col. San Pedro Zacatenco, Del. Gustavo A. Madero, Ciudad de México, México, C.P. 07360.

ABSTRACT

In the last decades, the depletion of fossil fuel deposits due to the large demand has led to the research and development of sustainable technologies for production of valuable chemicals, among which biomass processing by means of heterogeneous catalysis seems to be a promissory option.

Under this approach, the glycerol obtained as a by-product in the manufacture of biodiesel may be subjected to variety of catalytic processes among which hydrogenolysis in the presence of a catalyst and hydrogen is one of the most important because it turns out in the production of compounds of technological interest, such as α-propylene glycol (1,2-propanediol), β-propylene glycol (1,3-propanediol) and minor alcohols, depending on the reaction conditions and on the type of active sites present on the catalyst surface, offering a route to their renewable production contrasting to the current processes of synthesis from petroleum derivatives.

This paper deals with the fundamentals and advances of the glycerol hydrogenolysis regarding to the chemical principles, the chemical thermodynamics and the catalytic systems applied for this process.

Keywords: glycerol hydrogenolysis, propylene glycol, propanediol, valuable chemicals.

Synthesis of graphene and nitrogen-doped graphene with electrocatalytic activity towards Oxygen Reduction Reaction

J. C. Carrillo-Rodríguez, I. L. Alonso-Lemus, A. A. Siller-Ceniceros, F. J. Rodríguez-Varela
Sustentabilidad de los Recursos Naturales y Energía
CINVESTAV-IPN Unidad Saltillo
Ramos Arizpe, Coahuila, México
ivonne.alonso@cinvestav.edu.mx

E. Martínez-Guerra
Departamento de Física de Materiales
CIMAV Unidad Monterrey
Apodaca, Nuevo Leon, México

***Abstract*— We report the novel synthesis of graphene (G) by mechanical milling using graphite flakes as the precursor and aluminum as exfoliating agent. Graphene has been doped with hydrazine as nitrogen precursor ex situ under hydrothermal treatment to form the G_{D1} sample. Characterization by XPS shows the formation of Pyrrolic, Pyridinic, Amine Graphitic and Oxidized nitrogen in G_{D1}. The electrochemical results demonstrate a higher catalytic activity of G_{D1} for the Oxygen Reduction Reaction (ORR) relative to G in 0.5 M KOH. The enhanced performance of G_{D1} is attributed to the formation of the several types of nitrogen bonds, particularly the quaternary and pyridinic species.**

Keywords—nitrogen doped graphene, Oxygen reduction reaction and electrocatalysts.

I. Introduction

It is acknowledged that the relatively slow kinetics of the oxygen reduction reaction (ORR) limits the performance of Fuel Cell devices [1]. Therefore, materials that can improve the kinetics of such reaction are required. Moreover, current strategies to reduce the costs of cathode electrocatalysts include the development of alternative ORR electrocatalysts based on non-precious metal or even metal-free materials [2, 3]. Recently, N-doped graphene nanomaterials have been proposed as candidate electrocatalysts for the ORR, because they exhibit catalytic activity similar to commercial Pt/C [4].

Mainly, graphene and N-doped graphene are synthesized by the Chemical Vapour Deposition (CVD) method [5-7]. However, this process has important drawbacks such as high production costs, it requires high temperature and inert atmosphere, it often needs the use of corrosive precursors, and its scalability is limited [8, 9].

One easy alternative route to synthesize graphene and doped-graphene, with relatively low cost and environmental impact, is mechanical milling. It consists of mixing graphite with an inorganic salt, while using mechanical forces to promote the displacement of the graphite layers [9-12].

In this work, we propose the synthesis of graphene (G) by mechanical milling, followed by hydrothermal post-treatment with hydrazine as nitrogen precursor, in order to form N-doped graphene (G_{D1}). The electrocatalysts are characterized by X-ray diffraction (XRD) and X-ray photoelectron spectroscopy (XPS), as well as tested for the ORR in alkaline media.

II. Experimental

A. *Synthesis of graphene*

Graphene (G) was obtained by mechanical exfoliation of graphite flakes (Sigma-Aldrich, 99.99%) using aluminium powder (Alfa Aesar, 99.97%) as exfoliating agent at 2:1 mass ratio. Ball milling was carried out in a planetary ball-mill machine (Retsch PM100 mill) for 8 hours, at 300 rpm. The obtained powders were sequentially washed in 1 M HCl solution and deionized water, to be dried under vacuum.

To obtain G_{D1} metal-free electrocatalysts by the hydrothermal method, 1 g of G was dispersed in 30 mL of hydrazine (Sigma-Aldrich, 65%), sealed stainless steel autoclave and heated at 180 °C for 24 h. The resulting powder was filtered, washed with deionized water and dried under vacuum.

B. *Physicochemical and electrochemical characterization*

X-ray diffraction (XRD) patterns were recorder with a Philips X´Pert (PANalaytical) diffractometer with a Ni-filtered Cu Kα radiation. X-ray photoelectron spectroscopy (XPS) analysis was carried out in a Thermo Scientific ESCALAB 250Xi (Al-Kα, 20 eV). Their catalytic activity for the ORR was evaluated with the aid of a Pine Wavedrive 20 potentiostat, connected to a RDE apparatus. Cyclic voltammograms (CV) were obtained in N_2-saturated 0.5 M KOH at scan rate of 20 mV s^{-1}, while linear sweep voltammograms (LSV) were acquired in O_2-saturated electrolyte at several rotating rates (ω) in the 0.05 to 1.2 potential range at scan rate of 5 mV s^{-1}.

Identify applicable sponsor/s here. If no sponsors, delete this text box (*sponsors*).

III. RESULTS AND DISCUSSION

The XRD patterns of G_{D1} and G are shown in Figs. 1a) and b), respectively. The diffraction peaks at 2θ = 26.4, 43.1, 54.1 and 77.4 for G, correspond to the (002), (101), (004) and (110) carbon planes, which demonstrates that the as synthesized G nanosheets possess graphitic structure [8]. The XRD pattern of G_{D1} shows the same reflections. Nevertheless, the widening of the peaks is attributed to a higher disorder of the graphitic structure caused by the incorporation of nitrogen in the structure.

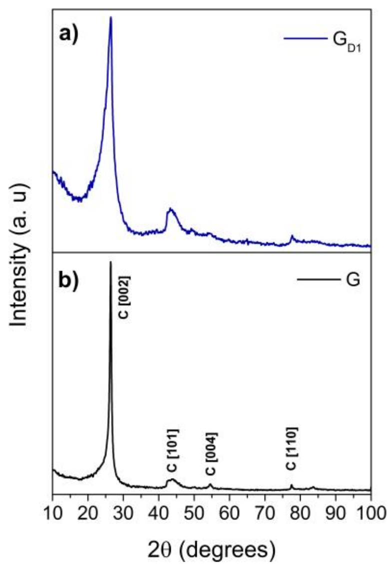

Fig. 1. XRD patterns of a) G_{D1} and b) G).

Fig. 2 shows the deconvoluted high resolution N 1s spectrum of G_{D1}. Five peaks are observed at 398.8, 399.4, 400.3, 402.5 and 405.3 eV, ascribed to pyridinic N , amine N, pyrrolic N, quaternary N and N oxidized of pyridinic N, respectively [13, 14].

The spectrum confirms the incorporation of nitrogen species into the graphene structure after hydrothermal treatment, since the spectrum of G no signs that can be attributed to the presence of N species are observed.

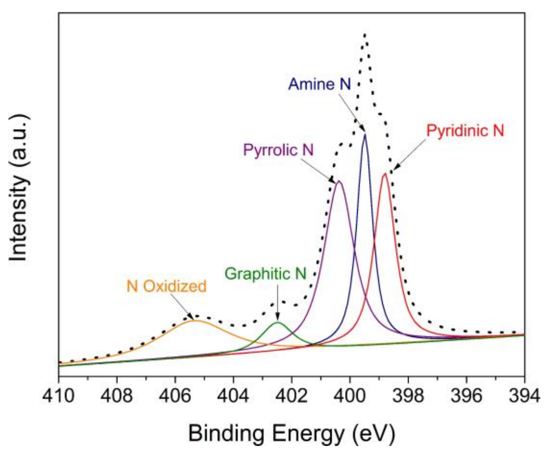

Fig. 2. N 1s high resolution XPS spectrum of G_{D1}.

Previous reports in the literature indicate that the catalytic activity of carbon-based electrocatalysts towards species RRO is enhanced by the presence of pyridine N, quaternary N [13].

Some works show that pyridine N improves the onset potential (E_{onset}), while quaternary N increases the limiting current density of the ORR [15, 16].

However, the specific contribution of each N species in enhancing the catalytic activity for the ORR is not clearly elucidated yet.

Fig. 3 shows the CVs of G and G_{D1}. The shape is quasi-rectangular, with no redox peaks and fast voltage reversal at each end potential, characteristics that exhibit an electrical double-layer capacitance [17, 18]. G_{D1} shows an increase in current density probably caused by the presence of N.

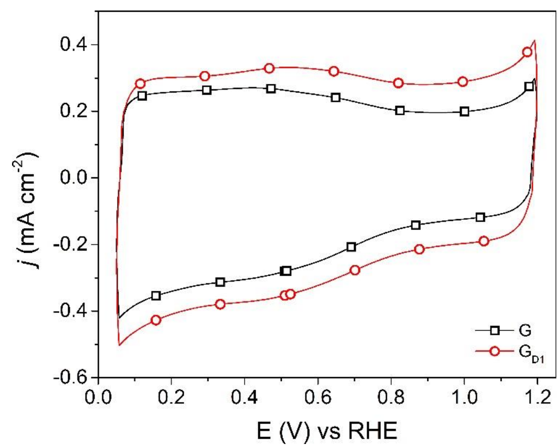

Fig. 3. CVs of G and G_{D1}. Electrolyte: N_2-saturated, 0.5 M KOH. Scan rate: 20 mV s^{-1}.

Fig. 4 shows the LSVs of the ORR at G_{D1}, with three typical regions: i) kinetic (0.85 - 1.2 V vs. RHE); ii) mixed (0.85 to 0.7 V vs. RHE); and iii) diffusion limited (0.7 to 0.3 V vs. RHE). The E_{onset} of the ORR at the electrocatalyst is 0.88 V vs. RHE. On the other hand, the current density at 0.3 V is 2.24 mA cm^{-2}.

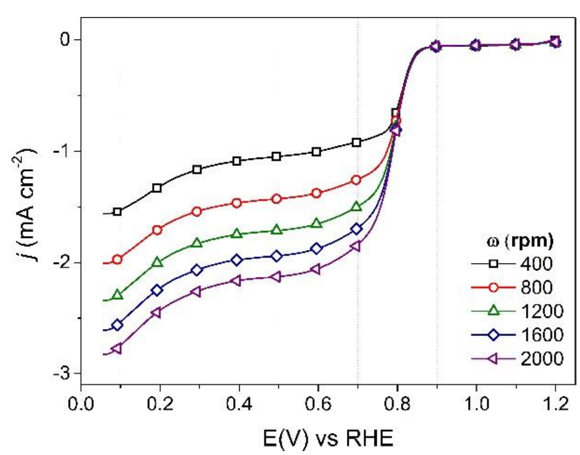

Fig. 4. LSVs of the ORR at G_{D1}. Electrolyte: O_2-saturated 0.5 M KOH. Scan rate 10 mV s^{-1}, at different rotation rates..

The values reported here are comparable to those of Wu et. al., who obtained a E_{onset} values between 0.8 and 0.85 V vs. RHE, with limiting current densities of around 2.4 - 3.2 mA cm^{-2}, using nitrogen doped-graphene as the electrocatalyst [19].

IV. Conclusions

We developed an easy and scalable synthesis method of graphene and N-doped graphene by mechanical milling and hydrothermal treatment. The G_{D1} electrocatalyst exhibited a good performance for the ORR in alkaline media. The results indicate that the catalytic activity for the ORR of G_{D1} is promoted by the nitrogen incorporation in the graphene structure. This makes graphene obtained by mechanical milling a promising alternative cathode material for fuel cells.

Acknowledgment

The authors wish to thank to CONACYT by financial support through 250632, 251603 grants Catedras CONACyT program.

References

[1] X. Ge, A. Sumboja, D. Wuu, T. An, B. Li, T. Goh, A. Hor, Y. Zong and Z. Liu, "Oxygen Reduction in Alkaline Media: From Mechanisms to Recent Advances of Catalysts," ACS Catal. vol. 5, pp. 4643–4667, 2015.

[2] D. Geng, N. Ding, T. S. Andy Hor, Z. Liu, X. Sun and Y. Zong, "Potential of metal-free "graphene alloy" as electrocatalysts for oxygen reduction reaction," J. Mater. Chem. vol. A3, pp. 1795–1810, 2015.

[3] L. Lai, J. R. Potts, D. Zhan, L. Wang, C. K. Poh, C. Tang, H. Gong, Z. Shen, J. Lin and R. S. Ruoff, "Exploration of the active center structure of nitrogen-doped graphene-based catalysts for oxygen reduction reaction," Energy Environ. Sci. vol. 5, pp. 7936-7942, 2012.

[4] H. P. Cong, P. Wang, M. Gong and S. H. Yu, "Facile synthesis of mesoporous nitrogen-doped graphene: An efficient methanol-tolerant cathodic catalyst for oxygen reduction reaction," Nano Energy, vol. 3, pp. 55–63, 2014.

[5] E. Del Rio, C. Merino, E. Díez and E. Vázquez, "Selective suspension of single layer graphene mechanochemically exfoliated from carbon nanofibres," Nano Res. vol. 7, pp. 963–972, 2014.

[6] A. Gupta, T. Sakthivel and S. Seal, "Recent Development in 2D Materials Beyond Graphene," Prog. Mater. Sci. vol. 73 pp. 44–126, 2015.

[7] F. Wang, Z. Wang, Q. Wang, F. Wang, L. Yin, K. Xu, Y. Huang and J. He, "Synthesis, properties and applications of 2D non-graphene materials" Nanotechnology, vol. 26; pp. 1-26 , 2015.

[8] F. Pan, J. Jin, X. Fu, Q. Liu and J. Zhang, "Advanced oxygen reduction electrocatalyst based on nitrogen-doped graphene derived from edible sugar and urea," ACS Appl. Mater. Interfaces, vol. 5 pp. 11108–14, 2013.

[9] T. J. Nacken, C. Damm, H. Xing, A. Rüger and W. Peukert, "Determination of quantitative structure-property and structure-process relationships for graphene production in water," Nano Res. vol. 8 pp. 1865–1881, 2015.

[10] T. Lin, Y. Tang, Y. Wang, H. Bi, Z. Liu, F. Huang, X. Xie and M. Jiang, "Scotch-tape-like exfoliation of graphite assisted with elemental sulfur and graphene–sulfur composites for high-performance lithium-sulfur batteries," Energy Environ. Sci. vol. 6, pp. 1283-1290, 2013.

[11] L. Dai, Y. Xue, L. Qu, H. J. Choi and J.B. Baek, "Metal-Free Catalysts for Oxygen Reduction Reaction," Chem. Rev. vol. 115, pp. 4823–4892, 2015.

[12] J. H. Warner, F. Schäffel, A. Bachmatiuk, M. H. Rümmeli, J. H. Warner, F. Schäffel, A. Bachmatiuk and M. H. Rümmeli, "Chapter 4 Methods for Obtaining," in Graphene, Elsevier Inc., 2013, pp. 129–228.

[13] H. Wang, T. Maiyalagan and X. Wang, "Review on Recent Progress in Nitrogen-Doped Graphene: Synthesis, Characterization, and Its Potential Applications," vol. 2, pp. 781-794, 2012.

[14] N. Mahmood, C. Zhang, H. Yin and Y. Hou, "Graphene-based nanocomposites for energy storage and conversion in lithium batteries, supercapacitors and fuel cells," J. Mater. Chem. vol. A2, pp. 15–32, 2014.

[15] C. Zhang, R. Hao, H. Liao and Y. Hou, "Synthesis of amino-functionalized graphene as metal-free catalyst and exploration of the roles of various nitrogen states in oxygen reduction reaction" Nano Energy, vol. 2, pp. 88–97, 2013.

[16] L. Qu, Y. Liu, J. B. Baek and L. Dai, "Nitrogen-doped graphene as efficient metal-free electrocatalyst for oxygen reduction in fuel cells," ACS Nano, vol. 4, pp. 1321–1326, 2010.

[17] J. Yan, T. Wei, B. Shao, Z. Fan, W. Qian, M. Zhang and F. Wei, "Preparation of a graphene nanosheet/polyaniline composite with high specific capacitance," Carbon, vol. 48, pp. 487–493, 2010.

[18] C. Zheng, X. Zhou, H. Cao, G. Wang, and Z. Liu, "Synthesis of porous graphene/activated carbon composite with high packing density and large specific surface area for supercapacitor electrode material," J. Power Sources, vol. 258 pp. 290–296, 2014.

[19] J. Wu, D. Zhang, Y. Wang, and B. Hou, "Electrocatalytic activity of nitrogen-doped graphene synthesized via a one-pot hydrothermal process towards oxygen reduction reaction," J. Power Sources, vol. 227, pp. 185–190, 2013.

Effect of the scaling-up the reactions synthesis of the poly(styrene-co-acrylic acid) polyelectrolyte at laboratory level

L. Melo, R. Benavides, G. Martínez, D. Morales-Acosta
Centro de Investigación en Química Aplicada
Enrique Reyna 140, Saltillo, Coah. México.City
e-mail: roberto.benavides@ciqa.edu.mx

Abstract *— Sulfonated styrene-acrylic acid copolymers have been used as an alternative polyelectrolyte membrane for applications in fuel cells. In this work, the raw copolymer has been prepared by a well studied solution copolymerization reaction method, but at two different capacity reactor conditions: 100 mL and 3 L. The main idea was to scale up the copolymer production for having enough material for future sulfonation reactions. The reaction conditions consisted of styrene/acrylic acid in a 94/6 % mol, BPO as radical initiator in a 0.045 % mol, divinyl benzene (DVB) as crosslinking agent at 0.25 %mol and the solvent diethyl benzene (DEB) in a 50/50 volume ratio with monomers. Temperature was kept at 90 °C and the system stirred at 200 rpm during 2 hours, for both reactors. Molecular weight of copolymers was obtained by means of GPC, glass transition (Tg) by DSC and decomposition temperature (Td) through TGA analysis.*

Keywords *— scaling-up, copolymers, polyelectrolytes.*

Thermodynamic Analysis and Process Simulation of Syngas Production from Methane using $CoWO_4$ as Oxygen Carrier

P. E. González-Vargas, M. J. Meléndez-Zaragoza, V. Collins-Martínez, A. López-Ortiz*
Centro de Investigación en Materiales Avanzados, S.C., Miguel de Cervantes 120, Complejo Industrial Chihuahua Chihuahua, Chih. México.
*Tel: +52 6144394815; e-mail: alejandro.lopez@cimav.edu.mx

***Abstract*— For the production of synthesis gas (syngas), the partial oxidation (POX) of methane is a reaction that is more efficient than the steam reforming process (SMR), currently the dominant technology in hydrogen production. To overcome one of the most important disadvantages of POX reaction, which deals with the use of pure oxygen, a metal oxide ($CoWO_4$) is proposed as an oxygen carrier (POX-MeO). Using a thermodynamic analysis of an arrangement of two reactors, here is presented. In the first reactor POX-MeO reactions ($4CH_4 + CoWO_4 = 8H_2 + 4CO + Co + W$; $2CH_4 + CoWO_4 = 4H_2 + 2CO_2 + Co + W$) and the undesirable coal formation ($CH4 = C + 2H_2$) are carried out, while in the second reactor solid products of the first reactor are combined with steam to gasify the previously deposited coal ($C + H_2O = H_2 + CO$; $C + 2H_2O = 2H_2 + CO_2$) and simultaneously regenerate the metal oxide to produce syngas ($Co + W + 4H_2O = CoWO_4 + 4H_2$). Then, the regenerated oxide is recycled back to the first reactor to make a continuous process. A simulation of this process in Aspen Plus was performed taking into account an initial flow rate of 4 kmol/hr of methane. Four sensitivity analyses were performed to determine optimal operating process conditions. The first one was aimed to determine the $CoWO_4/CH_4$ feed molar ratio to carry out the reduction of the oxygen carrier, which was 1.1:4. The second sensitivity analysis determined 800°C as the optimal operating temperature of the first reactor to produce the highest yield to syngas. The third sensitivity analysis was carried out in the second reactor studying the variation of the operating temperature at which regeneration of $CoWO_4$ occurred, being 590°C. And finally, the fourth sensitivity analysis found the molar feed of steam to complete the regeneration of $CoWO_4$. At this established conditions a 96% of methane conversion was found and the production of one gas stream of syngas and another with 100% hydrogen purity.**

Keywords*— syngas; partial oxidation; CoWO₄; hydrogen; process simulation.

I. Introduction

Today, energy demand in the world is constantly growing, and a significant amount of this is covered by fossil fuels. Due to the reduction of these fuel reserves and the impact on the environment and health, nations worldwide are looking for alternative energy sources and sustainable raw materials [1].

In recent decades, there has been a great interest in hydrogen as a raw material for a variety of processes, for example, in ammonia synthesis, pharmaceutical manufacture, production of hydrogen peroxide and the electronics and petrochemical industries [1, 2]. Of comparable importance to hydrogen, the mixture of hydrogen and carbon monoxide (H_2 + CO), commonly called synthesis gas or syngas [3-5] is a valuable raw material for various industrial applications.

In principle, syngas may be generated from any hydrocarbon feedstocks [5]. However, in most applications, natural gas is the predominant raw material [3].

The steam reforming of methane (SMR, reaction 1) is the dominant technology for the production of syngas [6-9]. However, it has been suggested that the partial oxidation (POX, reaction 2) for the production of syngas presents greater efficiencies than the SMR. Furthermore, POX has other advantages such as: it needs less investment and still is able to produce a syngas with a H_2/CO molar ratio of 2, also is based on an exothermic reaction (which infers substantial energy savings), uses small reactors and exhibits high methane conversions (≈90%) and selectivities to hydrogen (94~99%). But, this process also has some disadvantages such as high operating temperatures (900~ 1000°C), and the need for an oxygen plant in place, which makes this a very expensive process [10].

Reaction 1: $CH_{4(g)} + H_2O_{(g)} = 3H_{2(g)} + CO_{(g)}$

Reaction 2: $2CH_{4(g)} + O_{2(g)} = 4H_{2(g)} + 2CO_{(g)}$

To solve these disadvantages research has been conducted in order to reduce production costs of syngas through POX and to lower operating temperatures. A proposed strategy is the elimination of the oxygen plant, which represents about half of the investment [10]. An example of such achievements is the use of metal oxides as oxygen carriers, based on a variation of the partial oxidation of methane to produce syngas and/or hydrogen involving two steps: first, the necessary oxygen for partial oxidation is provided by a metal oxide (MeO) containing oxygen, which is released under a reducing atmosphere to produce syngas and the reduced metal (Me) (Reaction 3); while in the second, the reduced metal is reoxidized with steam to produce hydrogen and the MeO (Reaction 4).

Reaction 3: $CH_{4(g)} + MeO = 2H_{2(g)} + CO_{(g)} + Me$

Reaction 4: $H_2O_{(g)} + Me = MeO + H_{2(g)}$

The MeO is recirculated to the initial reactor completing a full cycle, this process is called POX-MeO [4, 10]. It is important to notice that the overall reaction of this process is comparatively equal to the SMR [11].

Partial oxidation of methane under this concept was proposed by De los Rios et. al [2, 10, 12], and suggests the use of a nickel catalyst and cobalt tungstate ($CoWO_4$) as the oxygen carrier, since this material is very stable to cyclic tests subjected to partial oxidation of methane to syngas production. Reduction reactions of methane and reoxidation of the metals involved in this approach are presented in Table 1 as POX-MeO (1), POX-MeO (2) and reoxidation (3), respectively.

In any hydrocarbon combustion process undesirable coal generation is presented, in this case through the reactions 4a and 4b shown in Table 1.

This research aims to evaluate the technical feasibility of a process for the production of syngas that involves the partial oxidation of methane using $CoWO_4$ as oxygen carrier. For this work a simulation model of the process consists in two reactors, one where the partial oxidation occurs and another where the metal oxide is regenerated and the residual carbon is removed with steam.

Table 1. Chemical reactions in the proposed process.

POX-MeO (1)	$4CH_{4(g)} + CoWO_4 \rightarrow 8H_{2(g)} + 4CO_{(g)} + Co + W$
POX-MeO (2)	$CH_{4(g)} + CoWO_4 \rightarrow 2H_2O_{(g)} + CO_{2(g)} + Co + W$
Reoxidation (3)	$4H_2O_{(g)} + Co + W \rightarrow CoWO_4 + 4H_{2(g)}$
Coal Formation (Methane decomposition and Boudard reaction) (4)	(a) $CH_{4(g)} \rightarrow C + 2H_{2(g)}$ (b) $2CO_{(g)} \rightarrow C + CO_{2(g)}$
Coal gasification (5)	$C + H_2O_{(g)} \rightarrow H_{2(g)} + CO_{(g)}$
Coal gasification (6)	$C + 2H_2O_{(g)} \rightarrow 2H_{2(g)} + CO_{2(g)}$

II. METHODS

Simulation programs are useful because they allow performing material and energy balances, cost analysis, sizing estimates of equipment and process cycle time, quickly and easily [1]. In this research a process simulation is carried out in Aspen Plus, which is a simulation program that can be used for a variety of thermodynamic calculations and process analyses [13].

The Gibbs reactor system (RGibbs) can efficiently calculate the chemical equilibrium in multiphase and multistep reaction systems. To achieve this, the program finds a solution using an algorithm that minimizes the Gibbs free energy of the thermodynamic system (Gibbs free energy minimization technique) [13].

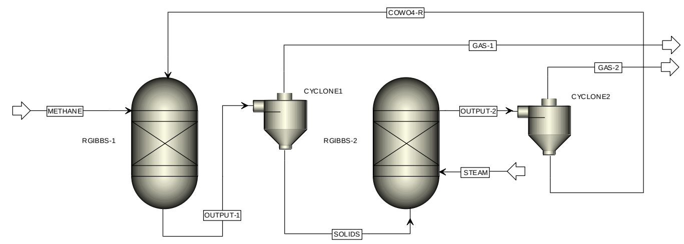

Figure 1. Process simulation flowsheet.

The process scheme shown in Figure 1, consists of two Gibbs reactors. In the first one (RGIBBS-1) the oxidation of methane in the presence of tungstate cobalt ($CoWO_4$) as oxygen carrier is carried out, while in the second reactor (RGIBBS-2) tungsten and cobalt reoxidation reactions are carried out in the presence of steam, thus regenerating cobalt tungstate and producing hydrogen, as well as removing any carbon deposits on this oxygen carrier. 4 kmol/hr of methane are fed in the first reactor. A thermodynamic system based on the Redlich-Kwong-Aspen equation of state was used in this simulation, which is aimed for processes that involve hydrocarbons and their mixtures with polar components for medium and high pressures [14].

Similarly, cyclones at the outlet of each reactor (CYCLONE1 and CYCLONE2) are used to separate the solid and gaseous products resulting from both reactors. In the case of the first separation the resulting solids (cobalt, tungsten, and a small fraction of deposited carbon) are disposed as reagents for the second reactor and the separated gas (GAS-1) constitutes the rich hydrogen product. In the second reactor, according to reactions (3), (5) and (6), the solid products, which are separated by the second cyclone comprise cobalt tungstate (COWO4-R), and this is recirculated to the first reactor, whereas the separated gas (GAS-2) is the hydrogen-rich product.

On the other hand, in this paper four sensitivity analyses were performed to determine optimal operating process conditions. The first one was aimed to determine the $CoWO_4/CH_4$ feed molar ratio to carry out the reduction of the oxygen carrier. The second sensitivity analysis will determine the optimal operating temperature of the first reactor to produce the highest yield to syngas. The third sensitivity analysis will be carried out in the second reactor aiming to study the variation of the operating temperature at which regeneration of $CoWO_4$ is expected to occurr. And finally, the fourth sensitivity analysis will find the molar feed of steam to complete the regeneration of $CoWO_4$.

III. RESULTS AND DISCUSSION

A. *Sensitivity Analyses*

Figure 2 (a) shows results for the first sensitivity analysis, where a minimum molar flow of 1.1 kmol/hr of $CoWO_4$ and 4 kmol/hr of methane are needed ($CoWO_4/CH_4$ molar ratio = 1.1:4) to prevent carbon deposition by methane decomposition and Boudard reactions (reactions 4a and 4b), which is of great importance, because will avoid coal gasification at RGIBBS-2. Likewise in Figure 2 (b), a considerable amount of hydrogen of

7.29 kmol/hr is produced together with small amounts of carbon dioxide and residual methane and a maximum flow of 3.6 kmol/hr of carbon monoxide, this represents a H_2/CO molar ratio of approximately 2.

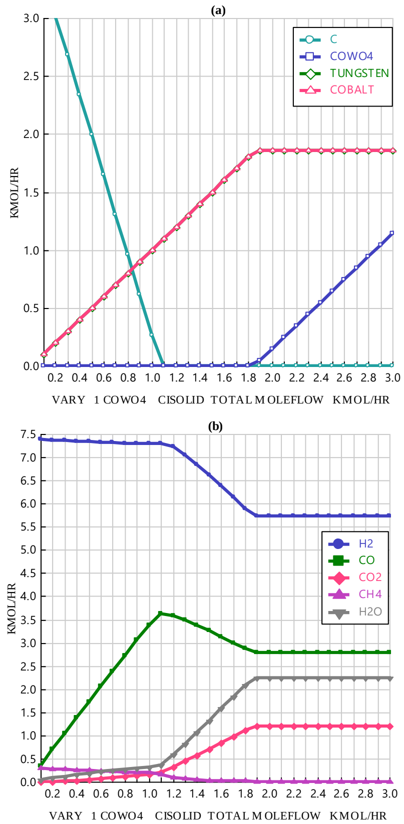

Figure 2. Sensitivity analysis of $CoWO_4$ mole inflow in the first Gibbs reactor, results of solid (a) and gas products (b).

The first sensitivity analysis is directly related to the second analysis, since the variation of the operating temperature (300 to 900°C) in RGIBBS-1 resulted in a wide range of gas equilibrium compositions. According to the results, it was found that in an approximate temperature range between 750 and 800°C the greatest amount of hydrogen is produced. Considering the increase in operating temperature, this range can be seen as a "unnecessary energy expense" compared to the hydrogen yields obtained in this temperature range, as shown in Figure 3 (b). At the same time, it can be seen in Figure 3 (a) that the possibility of carbon formation at 740°C and higher is null. For these reasons a temperature of 800°C was selected as the operating temperature of the first reactor, where the first sensitivity analysis was performed.

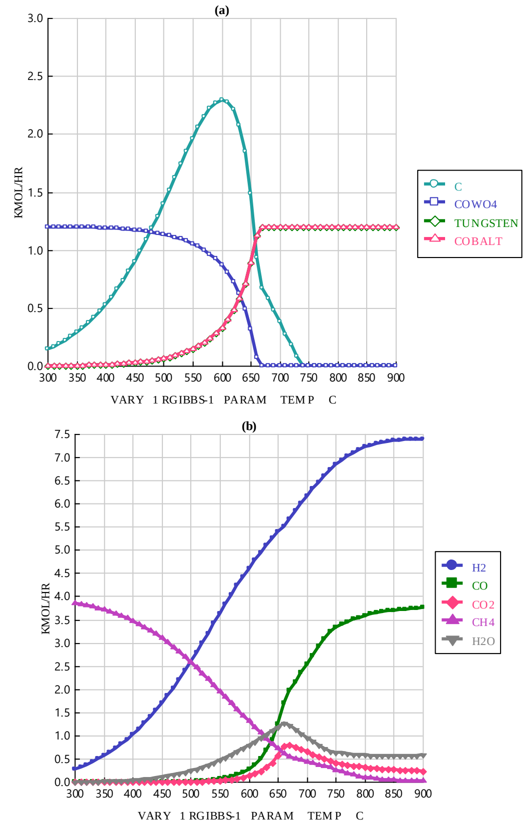

Figure 3. Sensitivity analysis of temperature in the first Gibbs reactor, results of solid (a) and gas products (b).

For the case of the sensitivity analysis in the second reactor, shown in Figure 4, it was observed that the most suitable operating temperature is 590°C, because it is the maximum temperature at which cobalt tungstate is stable together with a high hydrogen production (4.4 kmol/hr), without the formation of tungsten and cobalt (Figure 4 (a)) or the use of hydrogen to form water (Figure 4 (b)). Also, because cobalt tungstate regeneration kinetics with steam is slow at low temperatures [2]. Therefore, at a higher temperature it is possible to carry out the reaction (3), while being benefiting from faster kinetics.

At the fourth sensitivity analysis shown in Figure 5, it was found that a feed value of 5.6 kmol/hr of steam is needed in the second reactor to achieve a total regeneration of cobalt tungstate. Furthermore, this analysis shows no significant presence of carbon compounds (traces), whereby the gaseous product of this operation is only composed of hydrogen and water vapor, which in turn, by condensing water, a high purity hydrogen stream can be obtained.

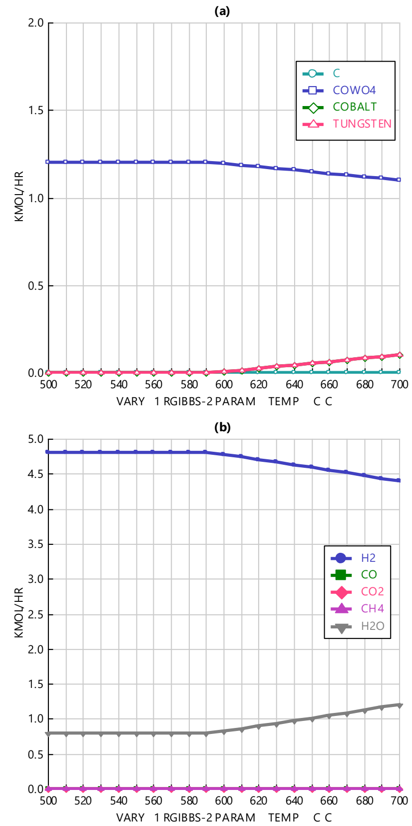

Figure 4. Sensitivity analysis of temperature in the second Gibbs reactor, results of solid (a) and gas products (b).

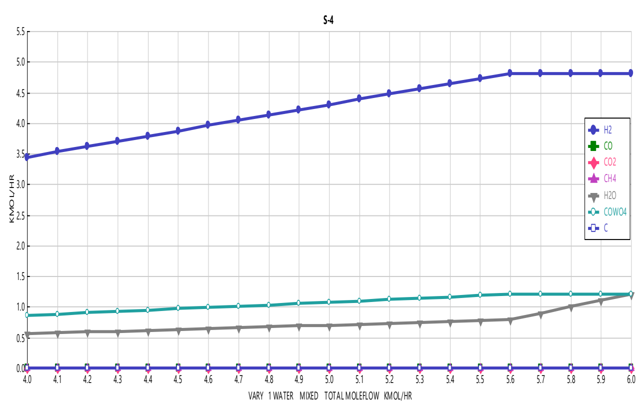

Figure 5. Sensitivity analysis of molar inflow of steam to the second reactor.

B. Simulation

Having established the appropriate parameters for the simulation of the entire process through the sensitivity analyses, it was possible to obtain the results shown in Table 2. These results show the successful production of syngas in the first reactor with 96% conversion of methane and a full recovery of the oxygen carrier in the second reactor, leading to a direct hydrogen production.

Table 2. Simulation results.

Heat and Material Balance Table									
Stream ID		COWO4-R	GAS-1	GAS-2	METHANE	OUTPUT-1	OUTPUT-2	SOLIDS	STEAM
Temperature	C		800.0	590.0	700.0	800.0	590.0		590.0
Pressure	bar		1.013	1.013	1.013	1.013	1.013		1.013
Vapor Frac			1.000	1.000	1.000	1.000	1.000		1.000
Mole Flow	kmol/hr	0.000	11.661	5.600	4.000	11.661	5.600	0.000	5.600
Mass Flow	kg/hr	0.000	134.568	30.488	64.171	134.568	30.488	0.000	100.886
Volume Flow	cum/hr	0.000	1027.106	396.718	319.523	1027.106	396.718	0.000	396.443
Enthalpy	Gcal/hr		-0.072	-0.046	-0.036	-0.072	-0.046		-0.296
Mole Flow	kmol/hr								
CH4			0.169		4.000	0.169			
CO			3.630			3.630			
CO2			0.201			0.201			
H2			7.293	4.400		7.293	4.400		
H2O			0.368	1.200		0.368	1.200		5.600
COWO4									
COBALT									
TUNGSTEN									
C									
Mass Flow	kg/hr	337.459	134.568	30.488	64.171	401.630	367.947	267.062	100.886
Enthalpy	Gcal/hr	-0.277	-0.072	-0.046	-0.036	-0.061	-0.323	0.012	-0.296
Temperature	C	590.0				800.0	590.0	800.0	
Pressure	bar	1.013			1.013	1.013	1.013	1.013	1.013
Vapor Frac		0.000				0.000	0.000	0.000	
Mole Flow	kmol/hr	1.100	0.000	0.000	0.000	2.200	1.100	2.200	0.000
Mass Flow	kg/hr	337.459	0.000	0.000	0.000	267.062	337.459	267.062	0.000
Volume Flow	cum/hr	0.033	0.000	0.000	0.000	0.018	0.033	0.018	0.000
Enthalpy	Gcal/hr	-0.277				0.012	-0.277	0.012	
Mole Flow	kmol/hr								
CH4									
CO									
CO2									
H2									
H2O									
COWO4		1.100					1.100		
COBALT						1.100		1.100	
TUNGSTEN						1.100		1.100	
C									

Gaseous product from RGIBBS-1 (GAS-1) resulted in unreacted methane (0.04 fraction of the original feed), water vapor and carbon dioxide as byproducts. On the other hand, in the same stream, syngas of interest has a molar H_2/CO ratio of 2.01, which satisfies the relationship that has been previously reported including impurities, besides this relationship it is suitable for gas to liquid processes (GTL) [10, 15].

The established operating temperature of 800°C in the first reactor, where the partial oxidation of methane occurs, is relatively lower than those reported with other materials as oxygen carriers such as transition metal oxides (Ni, Cu, Fe and Mn), whose operating temperature conditions can be up to 1200°C [15], and this represent significant energy savings.

The solid products obtained from RGIBBS-1 (SOLIDS), consisted of a cobalt and tungsten molar ratio of 1:1 due to the reduction of the metal oxide, and these are the solids products that enter as reagents into the second reactor (RGIBBS-2) along with a stream of steam of 5.6 kmol/hr (STEAM) for the regeneration of the metal oxide.

Results from RIBBS-2, consisted in only pure cobalt tungstate (COWO4-R), which shows the complete recovery of the original oxygen carrier at a flowrate of 1.1 kmol/hr for subsequent recirculation to RGIBBS- 1, thus closing the cycle. In the case of gaseous product (GAS-2), this shows that 4.4 kmol/hr hydrogen and 1.2 kmol/hr of steam is produced, which represents a high purity hydrogen stream in the gaseous product of this operation, our main compound of interest.

Comparing the gaseous current generated in the first reactor in dry basis (65% H_2, 32% CO, 2% CO_2 and 1% CH_4) with a typical gas product from a steam reforming process (approximately 75% H_2, 12% CO, 6% CO_2, and 7% CH_4) [16], i.e. POX-MeO and SMR, it can be observed that the syngas molar ratio from the two different processes is markedly different. Even though the H_2 mole fraction obtained in POX-MeO is smaller than the one obtained for SMR, POX-MeO generates a higher methane conversion, a syngas with less impurities with similar hydrogen contents reported in other researches.

Nevertheless, at the cyclical operating conditions suggested in the process of this study, the cyclic experimental behavior of cobalt tungstate has not been tested so far. Therefore, appropriate testing to determine the experimental viability of the proposed process in this research it is recommended as a future work.

IV. Conclussions

A simulation of a POX-MeO process using $CoWO_4$ as oxygen carrier was performed, the advantage of this process over other previously reported research lies on the stability of cobalt tungstate to a cyclic exposure at high temperatures (800°C) and various reactive atmospheres (CH_4, H_2O, etc.).

Simulation results found optimal reaction conditions to favorably carry out the POX-MeO process. At a temperature of 800°C in the first reactor a conversion of 96% methane without carbon formation can be obtained. This in turn, benefited the second reactor performance, because only the metal oxide regeneration is achieved, together with a carbon-free hydrogen gas.

Results show that a syngas stream with a molar H_2/CO ratio of 2.01 and a high purity hydrogen in the second reactor can be obtained.

Finally, an experimental assessment of the cobalt tungstate regeneration at certain conditions in the present work is recommended, in order to evaluate the results obtained here and the viability of the process.

Acknowledgment

The authors of this paper wish to thank the Mexican Society of Hydrogen for accepting the proposed research for dissemination and discussion, as well as the scholarship. We thank equally to CONACYT for scholarships awarded to students involved in the project.

References

[1] Sunny, A., P.A. Solomon, and K. Aparna, Syngas production from regasified liquefied natural gas and its simulation using Aspen HYSYS. Journal of Natural Gas Science and Engineering, 2016. 30: p. 176-181.

[2] De Los Ríos, T., et al., Synthesis, characterization and stability performance of CoWO4 as an oxygen carrier under redox cycles towards syngas production. International Journal of Chemical Reactor Engineering, 2007. 5(1).

[3] Wilhelm, D.J., et al., Syngas production for gas-to-liquids applications: technologies, issues and outlook. Fuel Processing Technology, 2001. 71(1–3): p. 139-148.

[4] Vázquez, M.S., et al., Synthesis gas production through redox cycles of bimetallic oxides and methane. Journal of New Materials for Electrochemical Systems, 2009. 12: p. 029-034.

[5] Haarlemmer, G. and T. Bensabath, Comprehensive Fischer–Tropsch reactor model with non-ideal plug flow and detailed reaction kinetics. Computers & Chemical Engineering, 2016. 84: p. 281-289.

[6] Dincer, I. and C. Acar, Review and evaluation of hydrogen production methods for better sustainability. International Journal of Hydrogen Energy, 2015. 40(34): p. 11094-11111.

[7] Jansen, D., et al., Pre-combustion CO2 capture. International Journal of Greenhouse Gas Control, 2015. 40: p. 167-187.

[8] Makarshin, L.L., et al., Syngas production by partial oxidation of methane in a microchannel reactor over a Ni–Pt/La0.2Zr0.4Ce0.4Ox catalyst. Fuel Processing Technology, 2015. 131: p. 21-28.

[9] Voldsund, M., K. Jordal, and R. Anantharaman, Hydrogen production with CO2 capture. International Journal of Hydrogen Energy, 2016. 41(9): p. 4969-4992.

[10] De los Ríos Castillo, T., et al., Global kinetic evaluation during the reduction of CoWO4 with methane for the production of hydrogen. International Journal of Hydrogen Energy, 2013. 38(28): p. 12519-12526.

[11] Protasova, L. and F. Snijkers, Recent developments in oxygen carrier materials for hydrogen production via chemical looping processes. Fuel, 2016. 181: p. 75-93.

[12] De Los Ríos-Castillo, T., et al., Study of CoWO4 as an Oxygen Carrier for the Production of Hydrogen from Methane. Journal of New Materials for Electrochemical Systems, 2009. 12(1): p. 55-61.

[13] Sandler, S.I., Using Aspen Plus in thermodynamics instruction: a step-by-step guide. 2015: John Wiley & Sons.

[14] Mathias, P.M., A versatile phase equilibrium equation of state. Industrial & Engineering Chemistry Process Design and Development, 1983. 22(3): p. 385-391.

[15] Tang, M., L. Xu, and M. Fan, Progress in oxygen carrier development of methane-based chemical-looping reforming: A review. Applied Energy, 2015. 151: p. 143-156.

[16] Gupta, R.B., Hydrogen Fuel: Production, Transport, and Storage. 2008: CRC Press.

Synthesis and Characterization of Graphene Supported Pt-CoTiO$_3$ Catalyst for the ORR in Alkaline Media

A. Hernández-Ramírez[1], M. E. Sánchez-Castro[1,2], F. J. Rodríguez-Varela[1,2]
[1]Programa de Nanociencias y Nanotecnología, [2]Grupo de Sustentabilidad de los Recursos Naturales y Energía
Cinvestav, Unidad Saltillo, Ramos Arizpe, Coahuila, México
yatzin_1228@hotmail.com, javier.varela@cinvestav.edu.mx

***Abstract*— The Oxygen Reduction Reaction (ORR) has been studied on graphene (G) supported Pt-CoTiO$_3$/G catalyst in 0.5 M KOH electrolyte. In a first step, CoTiO$_3$ nanoparticles were synthesized by the citrate gel method. Then, 20% Pt-CoTiO$_3$/G catalyst (Pt:CoTiO$_3$ at. ratio of 1:1) was obtained by the microwave-assisted polyol method. As a reference, a 20% Pt/G catalyst was synthesized by the same experimental procedure. XRD analysis confirmed the polycrystallinity of CoTiO$_3$ (crystallite size of ca. 42 nm) and the formation of nanostructured Pt-CoTiO$_3$/G with crystallite size around 2.3 nm. The electrochemical behavior of the Pt-CoTiO$_3$/G and Pt/G catalysts was evaluated by cyclic voltammetry using a rotating disk electrode configuration. Pt-CoTiO$_3$/G showed a lower performance for the ORR compared to Pt/G in terms of current density (-4.3 and -5.2 mA cm^{-2} at 0.1 V vs. RHE, respectively) and mass activity. However, Pt-CoTiO$_3$/G demonstrated a higher specific activity and more important tolerance to methanol than the monometallic cathode. The results suggest that Pt-CoTiO$_3$/G is a good candidate as cathode material for Alkaline Direct Methanol Fuel Cells applications.**

***Keywords*—Cobalt titanate, CoTiO$_3$; graphene supported Pt-CoTiO$_3$/G catalyst; Oxygen Reduction Reaction**

I. INTRODUCTION

Polymer Electrolyte Membrane Fuel Cells (PEMFCs) are being considered as a promising technology for sustainable energy production with very low emission of pollutants. Recent advances in the synthesis of chemically stable anion-exchange membranes have resulted in the development of Alkaline Direct Alcohol Fuel Cells (ADAFCs), which are promising devices since the kinetics of the electrochemical reactions is faster than in acid media [1-4]. Moreover, under alkaline conditions, the catalytic activity of different type of catalysts is considerably higher than that in acid conditions [1-4].

Pt-based materials are still widely used as anode and cathode electrodes due to their high catalytic activity for fuel cell reactions. Nevertheless it is necessary to reduce the amount of noble metal on the electrodes in order to decrease the cost of the fuel cell devices. Moreover, the cathode in ADAFCs must show a high tolerance to liquid fuels to limit the negative effects due to the crossover phenomena [5-10].

On this context, this study focuses in the development of cobalt titanate (CoTiO$_3$) as co-catalyst of Pt, and graphene as support, to obtain the Pt-CoTiO$_3$/G nanocatalyst. The material has been evaluated for the ORR in alkaline media.

II. MATERIALS AND METHODS

A. Reactants and gases

Chemicals of analytical grade were used as acquired without any further purification or pretreatment: $CoCl_2 \cdot 6H_2O$, $Ti[OCH(CH_3)_2]_4$, citric acid (CA), $H_2PtCl_6 \cdot H_2O$, ethylene glycol (EG), 2-propanol, Nafion, KOH and CH_3OH from Aldrich. UHP N_2 and O_2 from Infra (purity ≥ 99.999%). Graphene powder was obtained from IDnano.

B. Physicochemical characterization

Structural phases and crystallite sizes were determined by X-ray diffraction (XRD) analysis in a PANalaytical X´Pert apparatus with a Ni-filtered Cu Kα radiation. Chemical composition by EDS was obtained in a Philips XL30 SEM equipment.

C. Synthesis of CoTiO$_3$ nanoparticles and Pt-CoTiO$_3$/G catalyst

CoTiO$_3$ nanoparticles were obtained by a wet-chemical procedure, as reported elsewhere [11-12]. The precursor was calcinated in air atmosphere for 3 h at 900 °C.

The 20% Pt-CoTiO$_3$/G catalyst with Pt:CoTiO$_3$ nominal ratio 1:1 (at. %) was synthesized by the microwave-assisted polyol method following the procedure described in [12]. For comparison, a 20% Pt/G electrocatalyst was synthesized under the same conditions.

D. Electrode preparation and electrochemical set-up

Catalytic inks were prepared separately by sonicating for 30 min 10 mg of the catalyst, 1 mL 2-propanol and 5 µL Nafion® solution. To prepare the working electrodes, an aliquot of 10 µL of each ink was dispersed on a glassy carbon electrode (5 mm in diameter), which is placed in a rotating disc set-up. Electrochemical measurements were carried out in a standard three-electrode cell using a potensiostat (Pine Inst.). A Pt wire was used as the counter electrode while a Ag/AgCl (sat. KCl) electrode was employed as the reference electrode. The potentials have been reported with respect to the Reversible Hydrogen Electrode (RHE) according to the Nernst equation:

$$E_{RHE} = E_{Ag/AgCl} + 0.059\ pH + E°_{Ag/AgCl}$$

where $E_{Ag/AgCl}$ is the potential measured, pH of the 0.5 M KOH electrolyte is 13.96 and $E°_{Ag/AgCl}$ = 0.197 V.

Cyclic voltammetry (CV) measurements were performed in N_2-satured 0.5 M KOH. The CVs were obtained at a scan rate of 20 mV s^{-1} in the 0.5 to 1.2 V range (vs. RHE). Afterwards, to evaluate the catalytic activity of the synthesized electrocatalysts for the ORR, CV curves in O_2-satured electrolyte were obtained at different rotation rates (400, 800, 1200, 1600 and 2000 rpm), at the scan rate of 5 mV s^{-1} in the same potential range.

To correct for the contribution of capacitive current, CVs in N_2-satured electrolyte at a scan rate of 5 mV s^{-1} at 2000 rpm were obtained. Then, the background current was substracted from the experimental ORR current.

Plots of mass and specific catalytic activities were obtained by normalizing the current with respect to the Pt content from EDS and the Pt real surface area after measuring the charge in the H_{des} region from the CVs, respectively. The tolerance behavior of the nanomaterials was studied obtaining polarization curves at 2000 rpm in the presence of 0.1 and 0.5 M CH_3OH under O_2 atmosphere.

III. Results and Discussion

A. Physicochemical characterization

Fig. 1a shows the XRD patterns of the cobalt titanate. The nano-material displays narrow and intense peaks indicating the high crystallinity of the $CoTiO_3$ phase.

The crystallite size determined by the Scherrer equation is 42 nm. Figs. 1b-c show the diffraction patterns of the Pt/G and Pt-$CoTiO_3$/G catalysts, respectively. The (111), (220) and (311) planes characteristic of crystalline fcc structure of Pt can be observed in both diffractograms. The peak located at 25° (2θ) is attributed to (002) crystalline graphite plane of the carbon support. The cystallite sizes of Pt/G and Pt-$CoTiO_3$/G are 3.9 and 2.3 nm, respectively (Table 1).

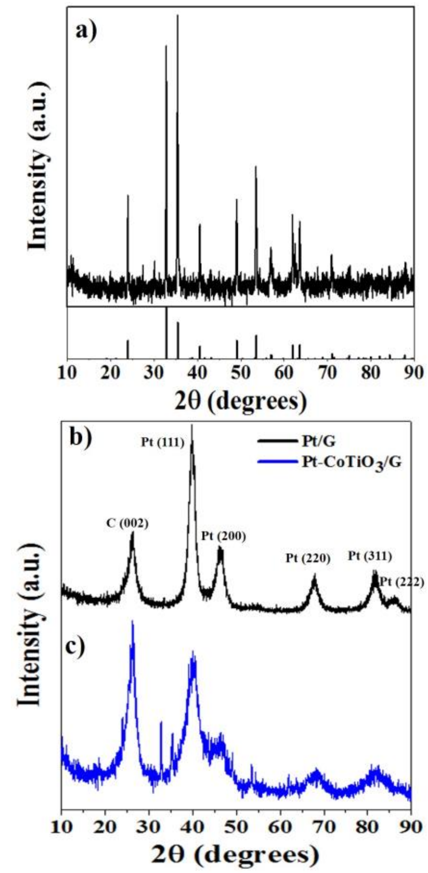

Fig. 1. XRD patterns of a) $CoTiO_3$, b) Pt/G and c) Pt-$CoTiO_3$/G.

The EDS analysis demonstrates that the experimental chemical composition of Pt/G is very close to the nominally calculated. On the other hand, the experimental catalyst content is higher than the theoretical at Pt-$CoTiO_3$/G (i.e., C content of 67.3 wt. %). Also, the Pt:$CoTiO_3$ ratio is 1:0.72, slightly higher than the expected value of 1:1.

TABLE I. PHYSICOCHEMICAL CHARACTERISTICS OF PT/C AND PT-$CoTiO_3$/G

Catalyst	*Crystallite size, XRD (nm)*	*Chemical composition (wt. %)*			*Pt:$CoTiO_3$ ratio*
		Pt	$CoTiO_3$	C	
Pt/G	3.9	19.9	-	80.0	
Pt-$CoTiO_3$/G	2.3	21.0	12.1	67.3	1:0.72

B. Electrochemical characterization and catalytic activity for the ORR

Fig. 2 shows the CVs of Pt/G and Pt-$CoTiO_3$/G, with typical electrochemical behavior of platinum-based materials: in the region of 0.05 to 0.43 V, the hydrogen adsorption process is represented by a negative current signal, while its desorption generates a positive current (I); from 0.43 to 0.63 V the double layer is identified (II); and the formation (positive current) and subsequent reduction (negative current) of metal-oxides (III) is observed from 0.63 to 1.2 V. The current density is higher for the monometallic catalyst, relative to Pt-$CoTiO_3$/G, because the metaltitanate inhibited the surface processes occurring on the composite catalyst. However, this is not necessarily an indication of a lower catalytic activity to perform the ORR.

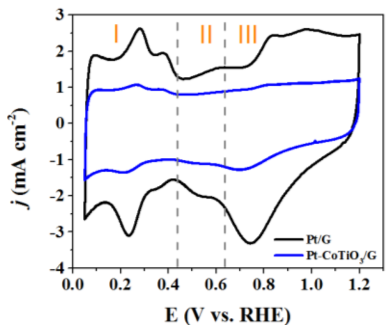

Fig. 2. CVs of the Pt/G and Pt-$CoTiO_3$/G catalysts. Electrolyte: N_2-saturated 0.5 M KOH. Scan rate: 20 mV s^{-1}.

The polarization curves of the ORR at Pt/G and Pt-$CoTiO_3$/G are shown in Figs. 3a and b, respectively. The titanate-containing catalyst has a slightly lower catalytic activity than the monometallic material. The onset potential (E_{onset}) for the ORR is 1.08 V for both catalysts.

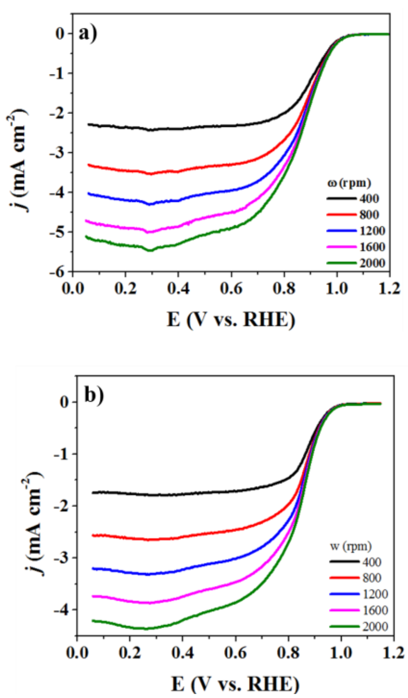

Fig. 3. Polarization curves for the ORR on: a) Pt/G and b) Pt-$CoTiO_3$/G. Electrolyte: O_2-saturated 0.5 M KOH. Scan rate: 5 mV s^{-1}.

The plots of mass and specific catalytic activity are shown in Figs. 4a and b, respectively. The mass activity is higher in the case of Pt/G, particularly at low overpotentials. However, it should be noticed that Pt-$CoTiO_3$/G exhibits superior specific activity, with a threefold increase relative to Pt/G at 0.85 V. Thus, the metaltitanate has a positive effect, enhancing the performance of the catalyst for the ORR per real area of Pt nanoparticles.

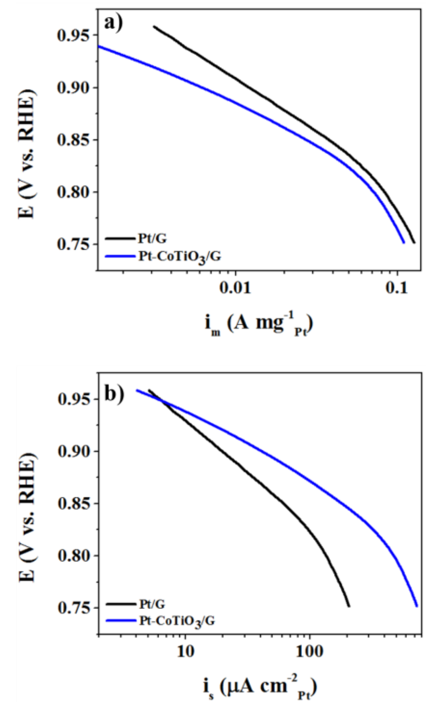

Fig. 4. a) Mass and b) specific activity plots of the ORR on Pt/G and Pt-$CoTiO_3$/G. Electrolyte: 0.5 M KOH saturated with O_2, ω = 2000 rpm.

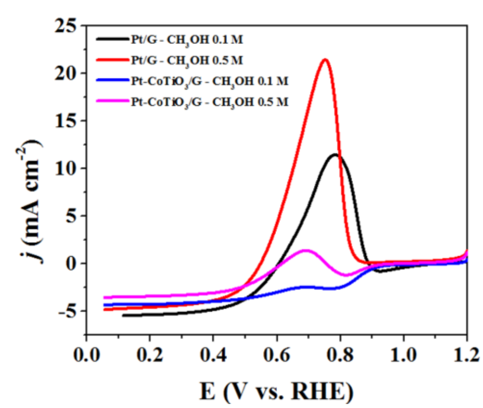

Fig. 5. Polarization curves for the ORR at Pt/G and Pt-$CoTiO_3$/G in the presence of 0.1 and 0.5 M CH_3OH. Electrolyte: 0.5 M KOH. Scan rate: 5 mV s^{-1}.

It is well known that the Pt-alone cathodes are depolarized by the presence of organic molecules, with a loss of catalytic activity. Then, it is important to study the electrochemical behavior of the catalysts in the presence of such substances. Fig. 5 shows the polarization curves of Pt/G and Pt-$CoTiO_3$/G catalysts during the ORR in the presence of 0.1 and 0.5 M CH_3OH.

It is evident that the use of $CoTiO_3$ as co-catalyst increases the selectivity towards the ORR, since the methanol oxidation current densities are much lower compared to Pt/G. With 0.1 M CH_3OH, Pt-$CoTiO_3$/G is fully tolerant and selective for the ORR.

IV. Conclusions

XRD analysis confirmed the polycristallinity of $CoTiO_3$ (crystallite size ca. 42 nm). Nanostructured graphene supported Pt-$CoTiO_3$/G catalyst was successfully synthesized by the microwave-assisted polyol method having a crystallite size around 2.3 nm.

The catalytic activity of Pt-$CoTiO_3$/G for the ORR in 0.5 M KOH was slightly lower than that of Pt/G in terms of diffusion-limited current density. E_{onset} of Pt-$CoTiO_3$/G was the same with respect to Pt/G (1.08 V vs. RHE).

Even though the mass catalytic activity of Pt/G was higher, specific activity plots indicated an enhanced performance of Pt-$CoTiO_3$/C.

Meanwhile, Pt-$CoTiO_3$/G showed a higher tolerance to methanol compared to Pt/G, in terms of significantly lower oxidation current densities. With 0.1 M CH_3OH, Pt-$CoTiO_3$/G was fully tolerant to the organic molecule.

Acknowledgments

To CONACYT for financial support (project 241526) and PhD scholarship granted to AHR.

References

[1] M. Perry and T. Fuller, "A historical perspective of fuel cell technology in the 20th century" J. Electrochem. Soc. vol. 149, pp. S59-S67, 2002.

[2] G. Merle, M. Wessling and K.J. Nijmeijer, "Anion exchange membranes for alkaline fuel cells: A review" Membrane Sci. vol. 377, pp. 1-35, 2011.

[3] B. Lin B, D. Kirk and S. Thorpe, "Performance of alkaline fuel cells: A possible future energy system?" J. Power Sources. vol. 161, pp. 474-483, 2006.

[4] H. Corti and E. Gonzalez, Direct Alcohol Fuel Cells. Materials, Performance, Durability and Applications. New York. Springer, 2014, pp. 1-6.

[5] E. Yu and K. Scott, "Development of direct methanol alkaline fuel cells using anion exchange membranes" J. Power Sources. vol. 137, pp. 248-256, 2004.

[6] L. Carrete, K. Friedrich and U. Stimming, Fuel Cells – Fundamentals and applications. Fuel Cells, vol. 1, Wiley-VCH, 2001, pp. 5-39.

[7] L. An and T. Zhao, "An alkaline direct ethanol fuel cell with a cation exchange membrane" Energy Environm. Sci. vol. 4, pp. 2213-2217, 2011.

[8] J. Varcoe and R. Slade, "Prospects for alkaline anion-exchange membranes in low temperature fuel cells" Fuell Cells. vol. 5, pp. 187-200, 2005.

[9] R. Sigh, R. Awasthi and C. Sharma, "Review: An overview of recent development of platinum-based cathode materials for direct methanol fuel cells" Int. J. Electrochem. Sci. vol. 9, pp. 5607-5639, 2014.

[10] E. Yu, U. Krewer and K. Scott, "Principles and materials aspects for direct alkaline alcohol fuel cells" Energies. vol. 3, pp. 1499-1528, 2010.

[11] R. Vijayalakshimi and V. Rajendran, "Effect of the reaction temperatura on size and optical properties of $NiTiO_3$ nanoparticles", E-Journal of Chemistry, vol. 9, pp. 282-288, 2012.

[12] A. Hernández, M. E. Sánchez, I. Alonso, A. Kalasapuyaril, P. Karthikeyan, R. Manoharan and F. J. Rodríguez, "Evaluation of the nickel titanate-modified Pt nanostrcutured catalyst for the ORR in alkaline media", Journal of the Electrochemical Society, vol. 163, pp. F16-F24, 2016.

Electroless Nickel Plating Process in Electrodes for Use in Oxi-hydrogen Reactors

L. F. Contreras-López, E.M. Hernández-Hernández, C. A. Cortés-Escobedo, J. Santa Ana-Téllez, W. Martínez-Velazco

Laboratorio de Energías Limpias
Centro de Investigación e Innovación Tecnológica, IPN
Ciudad de México, México
luisfe.con@gmail.com

***Abstract*— It was found that when a mixture of hydrogen and oxygen in the fuel gas stream is injected, either gasoline or diesel, it increases its combustion efficiency decreasing at the same time the pollutant emissions of fuels without burning into the atmosphere and saving from 10 up to 30% on fuel. In order to obtain this gaseous mixture, reactors oxyhydrogen operating in conditions in which the engine operates has been developed. A part important of these reactors are the electrodes that should count with characteristics as high resistance to the corrosion, high electronic conductivity and high surface area. This work presents the construction of electrodes for oxyhydrogen reactors with different characteristics, allowing to increase life time while maintaining the efficiency of the reactors. For this electroless nickel plating method was select to deposit a thick coating on aluminum and brass substrates at different bath times. Structural and morphological characterization is presented and discussed. The results obtained by X-ray diffraction and optical microscopy, showed that both materials to favor the deposition of nickel. It can be concluded that the time of deposition of 4, 6 and 8 hours not significantly influences the amount of nickel deposited on the material in reference with X-ray analysis.**

Keywords*— nickel plating process; reactor oxi-hydrogen, coating, electrodes.

ALD processed ceria-based layers for SOFC and micro SOFC applications

A. Grishin, D. Dallel, A. Marizy, A. Ringuedé, M. Cassir
PSL Research University, Chimie ParisTech - CNRS
Institut de Recherche de Chimie Paris (IRCP)
Paris, France
michel.cassir@chimie-paristech.fr

J. Chávez-Carvayar
Instituto de Investigaciones en Materiales
Universidad Nacional Autónoma de México (UNAM)
México, D. F. México

***Abstract*— Optimization of high temperature fuel cells is still facing delicate problems, such as yields, durability and costs, which must be solved in terms of accelerated kinetics, degradation protection and new materials, controlling their nature and morphology. The modular and compact "all solid" solid oxide fuel cell (SOFC) is one of the most promising next-generation fuel cell regarding stationary power generation. However, combining solid electrodes, electrolyte and interconnects at very high temperatures requires a perfect control of interfaces. Serious developments are going on, but SOFC systems should work at lower temperatures (<650°C) without additional overpotentials at the electrodes and with stable and efficient materials. In this case, thin functional layers constitute a key issue for improving interface reactions and building new architectures. The role of micro- or nanostructured thin films for SOFC applications can be diverse: protective layers (diffusion or electronic barriers), bond layers between electrodes and interconnects and catalytic layers. Furthermore, for SOFCs, thin-layered electrolytes can be envisaged for micro fuel cells systems as well as active electrolyte or electrode layers to improve both charge and mass transport. Atomic Layer Deposition (ALD), processing conformal, adherent and homogeneous layers is one of the most adapted technique for the high quality films required in SOFCs' [1]. Crystalline layers can be obtained by ALD at T<300°C without any additional annealing treatments. Thus, we recently fabricated an orientated ceria layer up to 100 nm thin; moreover, we demonstrated that it is an epitaxial layer up to its top surface [2]. In this paper, we will focus on yttria-doped ceria layers processed by Atomic Layer Deposition technique (ALD) in order to produce both epitaxial and polycrystalline thin films. The impact of the crystallinity as well as the Y-doping level, towards the hydrogen oxidation reaction will be discussed principally from Electrochemical Impedance Spectroscopy (EIS) data. This work constitutes an important step in the reactional mechanisms and catalytic properties understanding towards on ceria-based layers.**

Keywords—ceria-based materials; yttria-doped ceria (YDC); ALD; thin layers; epitaxial layers; SOFC; micro SOFC

Location of hydrogen refueling stations methodology. Modeling of the behavior of H_2 vehicle users.

C. Herradón[1], C. Fúnez Guerra[2], L. Rodriguez Mayor[2], E. Angulo Sánchez-Herrera[3], D. Verastegui Rayo[3], R. García Ródenas[4], C. Clemente-Jul[5], L. Reyes-Bozo[6] and H. Valdés-González[6].

[1] Departamento de Ciencias de la Ingeniería, Antonio Varas 880, Universidad Andres Bello, Santiago, Chile.
[*]Tel: +56226618255; e-mail: carolina.herradon@unab.cl
[2] National Hydrogen Center, Prolongación Fernando el Santo S/N, Puertollano, Ciudad Real, Spain.
[3] Mining and Industrial Engineering School of Almaden, Castilla la Mancha University, Plaza Manuel Meca S/N, Almadén, Ciudad Real, Spain.
[4] Graduate Informatics School, Castilla la Mancha University, Paseo de la Universidad, 4, Ciudad Real, Spain.
[5] Departament of energy and fuels. School of Mining and Energy Technical University of Madrid (UPM), Rios Rosas, 21, Madrid, Spain.
[6] Universidad Central de Chile. Toesca 1783, Santiago. Chile.

***Abstract*— The use of Alternative Fuel Vehicles (AFV), and of those based on hydrogen fed fuel cells (Fuel Cell Vehicles – FCV), to replace vehicles powered by internal combustion, is an alternative form of road transport that may provide, in the long term, security in energy supply, reduction in greenhouse gas emissions and improvement in air quality in cities. For these purpose in order to guarantee market penetration of environmentally friendly cars there are five areas that should be addressed: (a) the purchase price, (b) running costs, (c) vehicle range before refueling, (d) refueling time and (e) availability of refueling stations. Location models for hydrogen based vehicles are intended to accelerate market penetration of these vehicles, making efficient decisions about infrastructure design. In this work, we describe a bi-level model for the optimum definition of subsidy policies for the promotion of hydrogen infrastructure. The model includes the behavior of hydrogen station owners in a competitive environment, modeling of user behavior (buying of Fuel Cell Vehicles, choice of trips, routes), station coverage and subsidy policy, determining the optimum policy which allows a certain level of coverage to be achieved by a network in a given year. The model are based on genetic algorithm consisting in five sub-models (traffic modelling, nested logic model, behavior of Fuel Cell Electric Vehicles, subsidies policies and behavior of hydrogen refueling stations owners) and the optimization process is carried out using Matlab. Infrastructure (supply) leads to demand, but in order for the infrastructure to be economically viable, there must already exist a given level of demand. A model is described which allows, by Stackelberg equilibrium, a "road map" to be modeled for the optimal development of future infrastructure of hydrogen filling stations, so as to achieve the set objectives with minimum consumption of public resources. In this work, we describe one part of the bi-level developed model, simulating the behavior of H2 vehicle users. We use a discrete choice model to represent how users acquire FCV during the study period. The hierarchic nested logit model chosen for this study has been widely used in the field of transport.**

***Keywords*— nested logit; fuel cell vehicles; refueling stations; behavior; conventional vehicles.**

I. INTRODUCTION

The use of Alternative Fuel Vehicles (AFV) to replace vehicles powered by internal combustion, is an alternative form of road transport that may provide, in the long term, security in energy supply, reduction in greenhouse gas emissions and improvement in air quality in cities [1, 2, 3]. Reference [4] points out five areas which should be addressed in order to guarantee market penetration of environmentally friendly cars: (a) the purchase price, (b) running costs, (c) vehicle range before refueling, (d) refueling time and (e) availability of refueling stations.

Location models are intended to accelerate market acceptance of AFVs, making efficient decisions about infrastructure design. One of the main problems which must be addressed in the roll-out of the necessary infrastructure for the use of alternative fuels in transport is the so-called chicken and egg problem [5]. Infrastructure (supply) leads to demand, but in order for the infrastructure to be economically viable, there must already exist a given level of demand. Fig. 1. shows the essential elements of this vicious circle involving supply and demand.

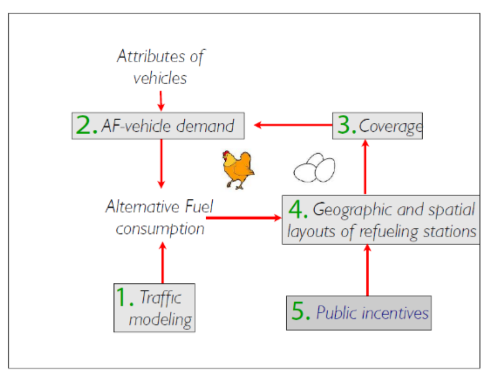

Fig. 1. Simplified representation of the elements in the supply, demand and market process of AF-vehicles.

This problem requires public-private partnerships to overcome the initial stage in the AFV market. A temporary policy of government subsidies can change this situation.

This policy can aim to: i) design a preliminary network of coordinated locations of stations, which will minimize the government subsidies required by maximizing the utility of stations constructed or ii) design policies for existing gasoline stations so they have an incentive to include alternative fuels among their products. This aid should be given to the most convenient stations, and so part of the subsidy should be used to reward the amount of alternative fuel served by each station, and the other part to subsidize the investment costs, and both parts should be time-dependent, to take advantage of dynamic mechanisms until the AFV market becomes mature.

The problem reflects viewpoint ii) and considers the five elements mentioned in Fig. 1. It in established a Stackelberg equilibrium model to design and assess optimal subsidy policies to favor the growth of AF infrastructure. The State plays the role of leader and the owners of AF stations are the followers. The leader wishes to design a subsidy policy to minimize the investment necessary to roll out the infrastructure effectively. On the other hand, the owners of the potential alternative fuel stations decide dynamically whether to install an AF station (lower level variables) as a function of the estimated profit from the investment based on the current subsidy policy and AF demand. The model incorporates the behavior of the agents of the process (The State, the owners of AF stations and owners of Fuel Cell Vehicles (FCV's)) in a dynamic context of competition between AF stations. The competition aspect is new in the literature, as most studies assume coordinated placement, that is, a monopoly in the ownership of AF stations, or equivalently, the existence of a State which can force an owner to set up an AF station; the objective is to maximize the profit of the sole corporate owner or to maximize overall coverage of the network. In the model described in this paper the change in the number of AF stations and their location depends on the change in the subsidies that the owners of the AF stations receive from the State and on the change in the number and special distribution of AFV's, which in turn depends on the deployment of the infrastructure.

The infrastructure for alternative fuel focuses on hydrogen fuel cells, and so Fuel Cell Vehicles (FCV) are considered.

This work focuses to the behavior model of alternative vehicles users.

II. Methodology

A. Selecting a Template (Heading 2)

In this section, we use a discrete choice model to represent how users acquire FCV vehicles during the study period. The hierarchic nested logit model has been widely used in the field of transport, [5, 6, 7], and it is the model chosen for this study.

The nested logit model in figure 2 shows the process of choosing an FCV-vehicle. At the higher level a user chooses to purchase a conventional vehicle (alternative b) or an AFV (alternative a). At the lower level AFV users choose the type of fuel.

Let $\overline{g_j^t}$ be vehicle sales prevision during period t in town j. The model disaggregates total vehicle sales by type of alternative fuel. In the first decision a person in town j at instant t has two alternatives when buying a vehicle: (a) AFV or (b) conventional vehicle. The first level model splits the vehicles sold between alternatives (a) and (b) thus:

$$g_j^{a,t} = \frac{\exp(\beta_1 U_j^{m,t})}{\sum_{m\in\{a,b\}} \exp(\beta_1 U_j^{m,t})} \cdot \bar{g}_j^t \qquad m \in \{a,b\}, \tag{1}$$

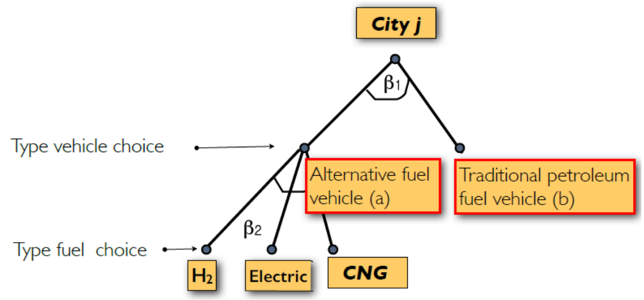

Fig. 2. Nested logit model for choice in vehicle purchase.

The second level of the nested logit model disaggregates the AFV into alternative fuel types S by:

$$g_{j,s}^{a,t} = \frac{\exp(\beta_2 U_{j,s}^{a,t})}{\sum_{s'\in\mathcal{S}} \exp(\beta_2 U_{j,s'}^{a,t})} \cdot g_j^{a,t} \qquad s \in \mathcal{S} \tag{2}$$

Nested logit models calculate the utility of alternative $U_j^{a,t}$ as the "log-sum" of the utilities of ecological type:

$$U_j^{a,t} = \frac{1}{\beta_2} \ln\left(\sum_{s\in\mathcal{S}} \exp(\beta_2 U_{j,s}^{a,t})\right) \tag{3}$$

Reference [4] gives an overview of the various attributes used in previous choice experiments on AFV preferences. These authors point out the purchase price and operating costs, driving range, recharge time and fuel availability may have substantial effects on consumer preferences for AFVs. Emission reduction is also signaled as an important factor. For this reason, this paper considers linear utility.

$$U_{j,s}^{a,t} = \alpha_1 \mathrm{pv}_s^t + \alpha_2 \mathrm{pc}_s^t + \alpha_3 \mathrm{co}_{j,s}^t + \alpha_4 \mathrm{dr}_s^t + \alpha_5 \mathrm{rt}_s^t + \alpha_6 \mathrm{e}_s^t \tag{4}$$

where:

-pv_s^t is the purchase price of vehicle type s in period t,

-pc_s^t is the price of fuel in period t and for vehicle type s

-$co_{j,s}^t$ is the coverage from town j for vehicle type s in period t (we have considered as an index the maximum number of kilometers that this user must travel between consecutive filling stations).

- dr_s^t is the driving range in period t and for vehicle type s.

- rt_s^t is the recharge time in period t and for vehicle type s.

- e_s^t is the emissions of vehicle type s in period t.
- α_r, β_r, parameters used in the modeling of the vehicle sales.

Reference [4] suggests attributes such as limited driving range, long refueling times and limited availability of refueling opportunities are to a large extent responsible for consumers' preferences in the early years. These attributes are taken into account by the model.
Finally, the total number of FCV vehicles (we assume the obsolescence period of the vehicle is greater than the study period) present in town j in period t is

$$G_j^t = \sum_{t'=0}^{t} g_{j,H_2}^{a,t'} \qquad (5)$$

The dynamic evolution of the attributes, excepting the coverage of the infrastructure, is exogenous to the proposed model and it introduces assumptions about technological progress and energy prices into the model.

Not all relevant uncertainties have been included in the analysis. The goal is the dynamic design of early subsidies for insuring adequate provision of refueling infrastructure. These subsides should be designed in accordance with the evolution of technological factors and the evolution of economies of scale in AF vehicle production.

III. Results and Discussion

This test looks at the problem developed five Spanish cities (nodes) with the largest population and 6 highways (arcs) used for communication, all belonging to the Trans-European transport network. The graph of the test problem is shown in Fig. 3.

Nested logit model predicting the evolution of vehicles sales. It has conducted an exercise in reverse engineering to calibrate the model. Match prospective studies it is for the determination of the evolution of sales of vehicles and for the determination of the attributes of each type of vehicle.
The model requires the estimation of total vehicle sales. It was found that the number of vehicle sales is correlated to the GDP and there have been estimates for GDP by 2030.

It has made the calibration model by Conditional Normalized Maximum Likelihood model (CNML), with the aim that the nested logit model fits with the greatest possible precision to prospective studies.

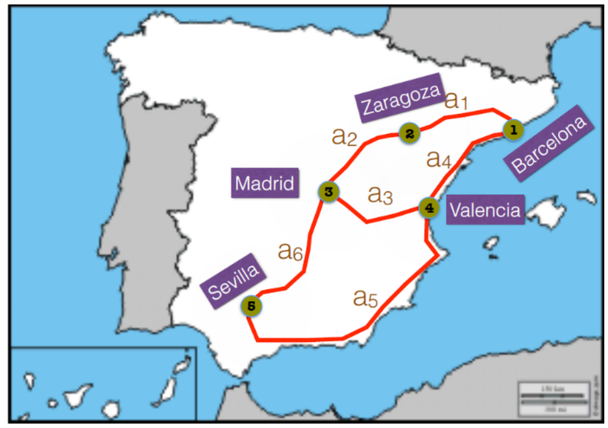

Fig. 3. Test problem.

Fig. 4 shows the results. It is observed that the model reproduces the prospective behavior for the four types of vehicles (conventional, electrical, hydrogen and Compressed Natural Gas).
In model calibration each attribute model was standardized between 0 and 1 and has performed an analysis model calibrated with respect to attribute coverage (all attributes have been obtained from literature, except for coverage attribute that comes from another part of the model).
The data used for attributes have been obtained from prospective reports of United Kingong H_2 mobility and National Innovation Programme (NIP) in Germany.

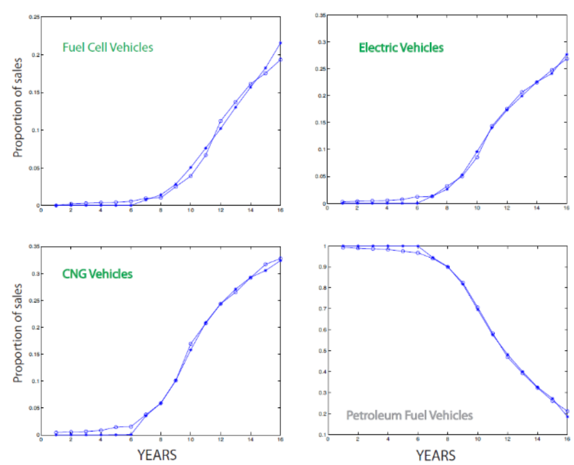

Fig. 4: Estimation of the Nested Logit Model. Predicted and observed sales by the CNML model.

Fig. 5 shows that in the current period t = 1 the coverage attributes has no effect on the sale of hydrogen vehicles. At t = 15 with their respective attributes, the coverage has an effect on sales ranging from about 2% with a coverage network 1 (the worst) to over 30% with the most extensive coverage possible.

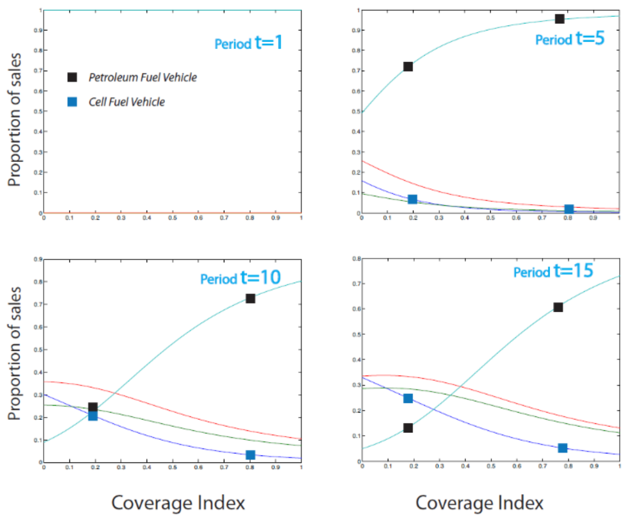

Fig. 5: Sensibility analysis of the attribute coverage.

IV. Conclusions

After the problem analysis test shows that the model works well. Consistent results according to prospective studies taken as reference are obtained.

The behavior of vehicle users to attributes change are analyzed. Specifically, it has changed the coverage attribute observed changes in penetration of different vehicles.

In the test problem can be seen as a low coverage (few filling stations) makes the hydrogen car sales are low and as high coverage (many filling stations) makes hydrogen vehicles sales are high.

References

[1] Y. Huang, Y. Fan, and N. Johnson, “Multistage system planning for hydrogen production and distribution”. Networks and Spatial Economics, vol. 10(4), pp. 455-472, 2009.

[2] Y. Wang and C. Wang, “Locating passenger vehicle refueling stations”. Transportation Research Part E Logistics and Transportation Review, vol. 46(5), pp. 791-801, 2010.

[3] S. D. Stephens-Romero, T. M. Brown, J. E. Kang, W. W. Recker, and G. S. Samuelsen, “Systematic planning to optimize investments in hydrogen infrastructure deployment”. International Journal of Hydrogen Energy vol. 35(10), pp. 4652-4667, 2010.

[4] A. Hoen and M. J. Koetse, “A choice experiment on alternative fuel vehicle preferences of private car owners in the Netherlands”. Transportation Research Part A: Policy and Practice vol. 61, pp. 199-215, 2014.

[5] M. Ben-Akiva and S. R. Lerman, “Discrete Choice Analysis: Theory and Application to Travel Demand”. MIT Press, 1987.

[6] N. Oppenheim, “Urban Travel Demand Modeling: From Individual Choices to General Equilibrium”. A Wiley-Interscience Publication. Wiley, 1995.

[7] R. García-Ródenas, and A. Marín, “Network equilibrium with combined modes: models and solution algorithms”. Transportation Research Part B Methodological vol. 39(3), pp. 223-254, 2005.

New low-Pt loading electrocatalysts using N-doped carbon nanotubes as support

A. M. Valenzuela-Muñiz[1,*], I. Paniagua[2], H. A. Lara-Romero[2] and Y. Verde-Gómez[2]

[1] CONACYT- Instituto Tecnológico de Cancún, Av. Kabah Km. 3, Cancún, Q.R., México, 77500.
[2]Instituto Tecnológico de Cancún, Av. Kabah Km. 3, Cancún, Q.R., México, 77500.
[*]Tel: +529888807432 ext. 1040; e-mail: anavalenzuelam@yahoo.com

ABSTRACT

One way to approach the Pt scarcity and high cost related to its use as catalysts in PEM fuel cells is the utilization of tailored supports. With this it is possible to decrease the Pt loading and at the same time offer interesting properties to the electrocatalyst. An adequate support provides high contact area for the reactants, as well as a good Pt particle distribution, optimizing in consequence the metal utilization. The carbon nanotubes in specific the multiwall carbon nanotubes have been studied extensively in recent times to be utilized as support to Pt particles. Its great electrical conductivity and the stability that show either in acidic or alkaline media, makes it an ideal candidates to be used as support. Moreover, the doped CNT, specially the N-doped CNT, have shown interesting and unique characteristics that can maximize the activity of the electrocatalyst for PEM fuel cells. In this research group there have been different approaches to the synthesis of Pt electrocatalysts using CNT, achieving high electrochemical activities; at the same time the group has been working in the development of N-doped CNT reaching interesting and promising results regarding the oxygen reduction reaction. In the present research work, Pt particles of small size were deposited over N-doped CNT in order to maximize the utilization of the active metal. Also, materials with the same loading of Pt but using pristine CNT were synthesized in order to compare the behavior. The obtained electrocatalysts were characterized physic and chemically using scanning and transmission microscopy, x-ray diffraction and energy dispersive x-ray spectroscopy. On the other hand, the nanomaterials were studied electrochemically in a conventional three electrodes cell, using a glassy carbon rod as working electrode, a Pt wire as counter electrode, a Ag/AgCl (KCl Sat) electrode as reference. Acidic and basic electrolytes were used separately in order to analyze the behavior of the novel materials. Interesting results have been found, and will be presented at the conference.

Keywords: Low-Pt electrocatalysts; N-doped carbon nanotubes; PEM fuel cells

BINDING ENERGY OF H_2 MOLECULE ON Mg_xM_{1-x} ALLOYS (M= Al, Ni, Zn; $0.8 \leq x \leq 1.0$)

E. Ramírez-Platón
email address: ismael.rplaton@gmail.com
G. Ramírez-Dámaso
SEPI ESIA TICOMAN
Instituto Politécnico Nacional
Del. Gustavo A. Madero, Ciudad de México
email address: gramirezd@ipn.mx
E. Rojas-Hernádez
SEPI ESIA TICOMAN
Instituto Politécnico Nacional
Del. Gustavo A. Madero, Ciudad de México
F. L. Castillo-Alvarado
Departamento de Física del Estado Sólido, ESFM
Instituto Politécnico Nacional
Edificio 9, Zacatenco, Ciudad de México
F. Caballero
División de Ingeniería Química y Bioquímica
Tecnológico de Estudios Superiores de Ecatepec
Ecatepec, Estado de México
O. Ramírez-Rodríguez
SEPI ESIA TICOMAN
Instituto Politécnico Nacional
Del. Gustavo A. Madero, Ciudad de México
C. E. González-Olguín
SEPI ESIA TICOMAN
Instituto Politécnico Nacional
Del. Gustavo A. Madero, Ciudad de México
G. Ramírez-Dámaso
División de Ingeniería Química y Bioquímica
Tecnológico de Estudios Superiores de Ecatepec
Ecatepec, Estado de México
F. L. Castillo-Alvarado
Becario COFAA-IPN, EDD IPN
Instituto Politécnico Nacional
Ciudad de México

***Abstract*—It is a theoretical work oriented to the study of metal hydride with applications to hydrogen storage in solid state phase. Magnesium (Mg) is a metal used for hydrogen storage with 7.6 % hydrogen in weight, but the temperatures of adsorption and desorption are about 300 ºC, then the objective of this work is to find a magnesium alloy with less value of adsorption/desorption temperature. By using Density Functional Theory (DFT) was possible obtain the enthalpies of formation of three kinds of magnesium alloys, magnesium-aluminum, magnesium-nickel and magnesium-zinc (Mg_xM_{1-x}), for different magnesium concentrations x = 1.00, 0.98,…, 0.80. The strategy used, was build bulk crystal structure and then this structures were cleaved in the direction of the plane (110). Hydrogen molecules were supplying on this surface in order to obtain their enthalpies; finally, these enthalpies values are used to calculate the binding energy of hydrogen molecule on the surface of the metallic alloys. By analyzing the behavior of different alloys studied, it was possible to conclude, that the magnesium-aluminum alloy is the best candidate for hydrogen storage. The enthalpies were calculated by applied the generalized gradient approximations (GGA) in CASTEP module, of the molecular simulation program Materials Studio 6.0.**

Keywords—Binding energy; magnesium-aluminum alloy; magnesium-nickel alloy; magnesium-zinc alloy

I. INTRODUCTION

In the past three decades, the study of new sources of energy, different from those of the fossil fuels, called clean energy, opened a new branch of generation of energy; one of those are that refers to the energy obtained of hydrogen. As is known, hydrogen is the most abundant of universe, with about the 75 %. It is widely believed that within few decades hydrogen will become the means of storing and transporting energy, as in projects in which hydrogen fuel cells will provide the energy. One of the reasons is the depletion of oil and the other is the relatively easy production of hydrogen from various renewable sources of energy with water as the only raw material needed. While hydrogen has many advantages, there remains a problem with his storage and transportation, the problem to use hydrogen in gaseous state is that in a volume of 45 m^3 contains only 5 kg of hydrogen [1], that difficult his use in gaseous state almost that is highly explosive in combination with O_2; condensed hydrogen is about ten times denser, but is too expensive to produce and maintain. Those are some reasons to find different forms for hydrogen storage, in solid state. Metal hydrides represents an alternative and an excellent method of hydrogen storage, which thereby can act as sponges. Many experimental [2-5] and theoretical works [6-8] have been published about hydrogen storage on metals as magnesium, aluminum, nickel, lanthanum, zinc, iron, titanium or their alloys.

II. THEORY AND COMPUTATIONAL DETAILS

The setup parameters in data collections obtained by CASTEP of density functional theory (DFT) method, available in the software package the Material Studio, was used in the calculations: for geometry optimization, density of states and final enthalpy as are shown in Table 1.

TABLE I. SETUP PARAMETERS IN THE CASTEP CALCULATIONS.

	Final enthalpies calculation
Basis Set	Plane waves
Functional	GGA (PW91)
SCF convergence	10^{-6}
k-point separation (1 Å)	0.04 (fine)
Core treatment	All electron
Hamiltonian integration accuracy	Fine

We construct the surface of Mg_xM_{1-x} alloy (x= 0.80, 0.82,…, 1.00) by cleaving in the direction (110), the bulk Mg_xM_{1-x}. Then we construct a surface (1x1) and a supercell (2x1) interacting with hydrogen molecule.
The set of optimizations calculate the enthalpies of formation of every one alloy, whose values are used to obtain repulsion and chemisorption energy of H_2 molecule on Mg_xZn_{1-x} [9]:

$$E_{rep} = \frac{1}{2}E_{(2x1)\ H2\ on\ MgAl(110)} - E_{(1x1)H2\ on\ MgAl(110)} \tag{1}$$

and

$$E_{chem} = \frac{1}{2}E_{(2x1)\ H2\ on\ MgAl(110)} - E_{MgAl\ (110)} - E_{H2\ molecule} \tag{2}$$

III. RESULTS AND DISCUSSION

Hydrogen storage on metal hydrides has been object of a wide range of theoretical studies, with different alloys, which also react readily with hydrogen. However, in spite of improved kinetics in hydrogen uptake, the required reactions temperatures in most cases were not lowered significantly. The allowing approach also suffers a sharply lowered mass percentage of hydrogen in the hydrides. In this studies, we worked with three alloys: MgAl, MgNi and MgZn.

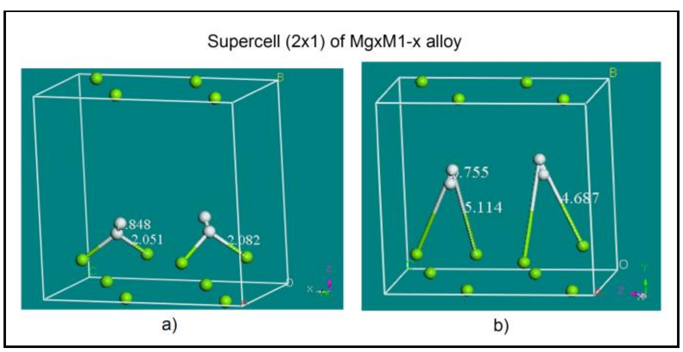

Fig. 1. Supercell (2x1) a) before be optimized and b) after be optimized with hydrogen molecule.

Fig. 1, corresponds to $Mg_{0.9}Zn_{0.1}$ and we observe that the distance of H_2 molecule to atop atoms increases from 2.05 $\dot{A}$ to 5.11 $\dot{A}$, or 2.08 $\dot{A}$ to 4.68 $\dot{A}$. The interaction between H_2 molecule and (2x1) supercell, after be optimized, has a value 0.755 $\dot{A}$, which suggest us that H_2 molecules do not are dissociated when are adsorbed on the surface of the alloy; this result is similar to the result reported by Wang, who mention that optimum distance for H-H bond is between 0.74 $\dot{A}$ and 0.757 $\dot{A}$ [10].

In Fig. 2, we show the results of MgAl alloy, where repulsion energies goes to zero and chemisorption is maintained constant with a value of 1.4 eV. We consider the difference between chemisorption and repulsion energies as the binding energy, E bind. Binding energy of H_2 in the surface is between -0.2 and 0 eV, that corresponds to concentrations of Al between 0.06 and 0.08 such as we have obtained in [8].

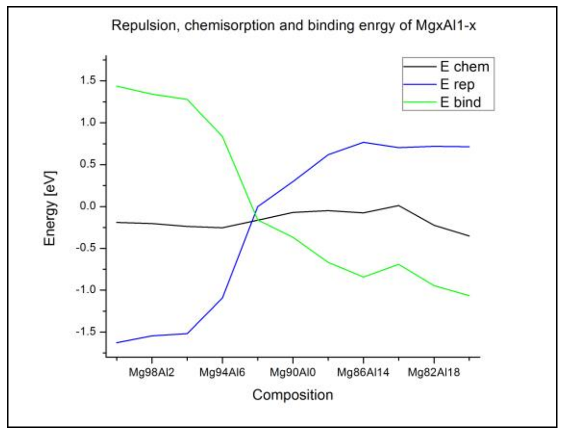

Fig. 2. Repulsion, chemisorption and binding energy of Mg_xAl_{1-x}

Repulsion, chemisorption and binding energy of MgNi alloy is shown in Fig. 3. The value of repulsion energy is maintained constant around -1.6 eV, the value of chemisorption energy is maintained constant around -0.1 eV. Binding energy doesn't experiment changes and his value is maintained constant with a value of 1.5 eV.

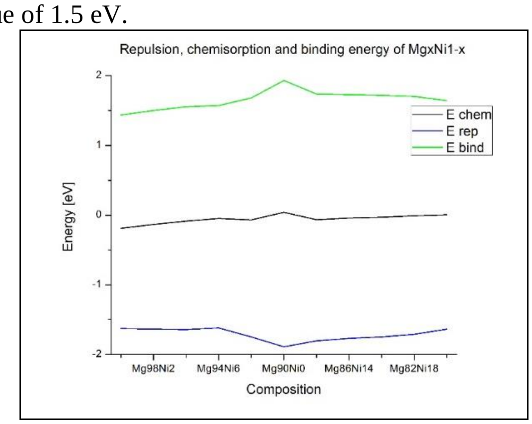

Fig. 3. Repulsion, chemisorption and binding energy of Mg_xNi_{1-x}

In Fig. 4, we observe the results of repulsion, chemisorption and binding energy of MgZn. In this case repulsion, chemisorption and binding energy are maintained with a value constant, similar to MgNi alloy.

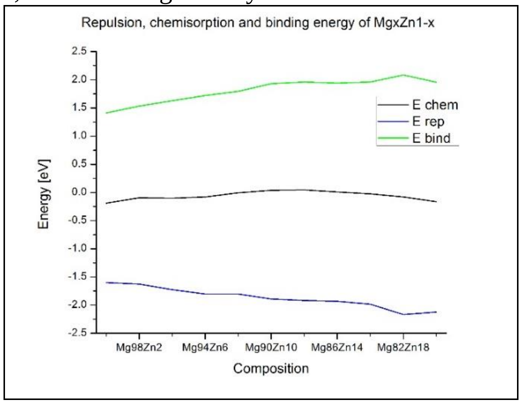

Fig. 4. Repulsion, chemisorption and binding energy of Mg_xZn_{1-x}.

IV. CONCLUSIONS

Of the three metals with which we have worked, the results shown that the MgAl alloy is a good material to be used for hydrogen storage. A clear trend is observed for MgAl alloy, such that, when the concentration of Al increases, repulsion energy decreases; it means that the H_2 molecule binds to the surface with higher intensity. Binding energy in the case of MgZn and MgNi doesn't change with concentration of nickel or zinc.

ACKNOWLEDGEMENT

I am grateful with Professor G. Ramírez-Dámaso and Professor E. Rojas-Hernádez by their time for scientific discussions and help for this manuscript.

F. L. Castillo-Alvarado acknowledges the partial support provided by COFAA-Instituto Politécnico Nacional, EDD-Instituto Politécnico Nacional, MEXICO.

REFERENCES

[1] Schlapbach L, Züttel A, Hydrogen-storage materials for mobile applications. Nature (2001) 414: 353-358.

[2] Zaluska A, Zaluski L, Strom-Olsen JO. Structure, catalysis and atomic reactions on the nano-scale: a systematic approach to metal hydrides for hydrogen storage. Appl. Phys. A (2001) 72: 157-165.

[3] Zaluska A, Zaluski L, Strom-Olsen JO. Nanocrystalline magnesium for hydrogen storage, J. Alloys Comp. (1999) 288: 217–225.

[4] Bououdina M, Gou ZX, Comparative study of mechanical alloying of (Mg+Al) and (Mg+Al+Ni) mixtures for hydrogen storage. Journal of Alloys and Compounds (2011) 336, 222-231.

[5] Bouaricha S, Dodelet JP, Guay D, Huot J, Boily S, Schulz R. Simple Metal and Intermetallic Hydrides, J. Alloys Compd. (2000) 297: 282–293.

[6] Norskov JK, Houmoller A, Johansson PK, Lundqvist BI, Adsorption and Dissociation of H_2 on Mg surfaces, Physical Review Letters, (1981) Volume 46, Number 4, 257-260.

[7] Liang JJ. Theoretical insight on tailoring energetics of Mg hydrogen absorption/desorption through nano-engineering. Appl. Phys. A (2005) 80(1): 173–178.

[8] Ramírez-Dámaso G, Ramírez-Platón IE, López-Chávez E, Castillo-Alvarado FL, Cruz-Torres A, Caballero F, Mondragón-Guzmán R and Rojas-Hernández, A DFT study of hydrogen storage on surface (110) of $Mg_{1-x}Al_x$ $(0 \leq x \leq 1.0)$, International Journal of Hydrogen Energy, (2016) in press.

[9] Web page: www.accelrys.com.

[10] Wang Q, Sun Q, Jena P, Kawazoe Y. Theoretical Study of Hydrogen Storage in Ca-Coated Fullerenes J. Chem. Theory Comput. (2009) 5(2): 374-379.

Electrical conductivity and performance in SPEWE single cell of Ir-Sn-Sb-O (40) mixed oxide powder catalyst

N. J. Pérez-Viramontes, I. L. Escalante-García, R. Espinosa-Lumbreras, M. Galván-Valencia, S. M. Durón-Torres*
UACQ, Universidad Autónoma de Zacatecas
Zacatecas, Zac. México, 98160
e-mail: duronsm@prodigy.net.mx

J.R. Flores-Hernández,
Gerencia de Energías Renovables
Instituto Nacional de Electricidad y Energías Limpias
Cuernavaca, Morelos, México

***Abstract-* The electrical conductivity of a mixed oxide powder with general formula Ir-Sn-Sb-O, whit properties both as a support and an electrocatalyst for OER, was obtained from four-point electrical resistivity (ER) and impedance spectroscopy (IS) measurements. The conductivity obtained for this material was compared with those obtained under the same conditions for Vulcan Carbon (VC) and tin oxide (SnO2), which are materials commonly used as supports in water electrolysers. The conductivity measurements were performed in a steel cylinder-piston cell with a constant area of 0.2165 cm2, maintaining the initial volume of the material constant. All the measurements were performed at room temperature under a constant pressure by using a mechanical press. The results showed that the conductivity of commercial tin oxide was 0.028 S m-1, 484.26 S m-1 for the Vulcan Carbon and 154882 S m-1 for the Ir-Sn-Sb-O material at a pressure of 150 lbf. The conductivity value of the mixed oxide is close to those found in metallic materials. The main electronic conductivity behavior of Ir-Sn-Sb-O material was confirmed by IS. In order to evaluate the performance of the electroactivity of Ir-Sn-Sb-O material for oxygen evolution, a SPEWE single cell test was carried out, employing a mixture of Pt-VC as catalyst in the cathode and the mixed oxide in the anode. The results show that the synthesized materials are suitable for their use as anode for SPE water electrolyser.**

Keywords: Catalyst powder, conductivity, impedance, SPEWE.

I. INTRODUCTION

There are different processes for H_2 production, such as hydrocarbon reforming, photocatalytic products, biodigesters, water thermolysis, electrolysis of water, etc. The water electrolysis is one of the most striking, because in H_2 production, the secondary reaction product is O_2, unlike the others, which are obtained as byproducts pollutants such as CO and CO_2. Solid-polymer-electrolyte water electrolyzer (SPEWE) it´s one of the most studied today.[1–3]

Water electrolysis is a process in which water molecule is separated into hydrogen molecules and oxygen through the use of electrical energy, where hydrogen evolution occurs at the cathode, while the evolution of oxygen takes place in the anode side. Electrolysis of water requires excess of energy in the form of overpotential to overcome activation barriers. No excess energy in water electrolysis, hydrogen and oxygen are produced slowly.[4]

The limiting reaction in the process of electrolysis is the oxygen evolution reaction (OER), have been used for this purpose different types of catalysts. There have been found to precious metal oxides with rutile structure, such as ruthenium and iridium oxide are those with higher electrocatalytic activity for this reaction. [5–7]

However, the materials used as catalysts for this reaction are of low abundance in the earth's crust, raising the price of such materials. For this reason, new materials are investigated on which disperse the active material to reduce the content of it, trying to get similar results to those that would be obtained if the pure material were used.[8]

Tin oxide doped with antimony (ATO) has been used in multiple applications, as in the case of fuel cells, batteries, gas sensors, solar cells. Recently has been invsestigate its use as a support for catalysts in water electrolyzers for OER due to their corrosion resistance in acidic media.[9–11] SnO_2-IrO_2 mixtures have been extensively investigated for the oxygen evolution reaction in acidic environment. In recent years we have studied the synthesis methods for obtaining multimetal materials to reduce precious metals in the anode, waiting for the electrocatalytic activity is not affected.[12–16] Thermal decomposition mixed oxide presents high activity for OER[7,12,17–20], however, the preparation of these mixed oxide prepared by thermal decomposition involving the presence of a substrate, which limits their use in SPEWE.[20–22] Different synthesis methods has been evaluated for obtaining catalyst powder for it use in water electrolyser.[23,24]

This study shows the synthesis of composite with general formula Ir-Sn-Sb-O (40), IrO_2 and ATO by the thermal decomposition of the chloride precursors in ethanol. Also shown the electrical conductivity of the materials obtained by electrical resistivity (ER) and impedance spectroscopy (IS), the conductivity was compared with commercial supports. The performance in single cell electrolyser of the Ir-Sn-Sb-O (40) was evaluated and compared with the equivalence mixture of IrO_2 and ATO synthetized by thermal decomposition.

II. MATERIAL AND METHODS

A. Mixed oxide synthesis

The catalysts for oxygen evolution reaction were prepared by a conventional thermal decomposition using as precursors H_2IrCl_6, $SnCl_4 \cdot 5H_2O$ and $SbCl_3$ (Aldrich). The metal precursor proportions in the preparation calculated in atomic percentages corresponded to (1) 40 at. % Ir, 57 at. % Sn, 3 at. % Sb, (2) 100 at. % Ir (called IrO_2) and (3) 95 at. % Sn, 5 at. % Sb (ATO). The synthesis was previous reported.

B. Electrical conductivity in powder

The electrical conductivity (σ) were performed in a steel cylinder-piston cell with a constant area of 0.2165 cm^2, maintaining the initial volume of the material constant. Table 1 show the mass of different materials used. All the measurements were performed at room temperature. For each measurement, the samples were placed in a hollow cylinder and compressed with by a mechanical press (Carver) since 0 lb_f in^{-2} to 200 lb_f in^{-2} with a step of 50 lb_f in^{-2}. In a first step, the electrical conductivity was measured using a miliohmeter Agilent 4338B. The electrical conductivity is given by (1).

$$\sigma = \frac{l}{RA} \tag{1}$$

The electrical conductivity was also measured by impedance spectroscopy over a frequency range 1 Hz to 10^6 Hz with a voltage of 0.005 V vs Ref using a Potentiostat Gamry.

C. Membrane electrode assembly

The membrane electrode assemblies (MEA) was prepared using Nafion® 117 membrane as solid polymer electrolyte. As cathode was used a Pt/C mixture (5 we % of platinum) with 0.2 mg of $Ptcm^{-2}$, and as anode the mixed oxide Ir-Sn-Sb-O (40), additionally assembly using IrO_2 supported on ATO, both synthetized by thermal composition for comparison was prepared. The inks were composed of Ir-Sn-Sb-O (40) mixed oxide (2.6 $mgcm^{-2}$) material and 10 wt.% Nafion® (5 wt.%, DuPont) dispersed in etanol, and a mechanical mixture of IrO_2-ATO (40 at. % of IrO_2), with 2.6 $mgcm^{-2}$ in the mixture.[7,12,17,19,20,23]

Table 1. Mass of materials used to measure electrical conductivity.

Material	Mass (mg)	Material	Mass (mg)
Ir-Sn-Sb-O (40)	40.7	IrO_2+ATO	17
IrO_2	22.3	Carbon	10
ATO	15.3	SnO_2	15

.

D. Electrochemical characterization

The electrocatalytic activity if the Ir-Sn-Sb-O (40) and mechanical mixture of IrO_2-ATO (40 at. % of IrO_2) was evaluated in single cell PEMWE with an active area of 4 cm^2, the single cell body was made of stell, and as gas diffusers were used two plates of sintered titanium. The electrochemical properties of the catalysts were characterized by cyclic voltammetry (CV) and electrochemical impedance spectroscopy (EIS) in single cell, using as work electrode Ir-Sn-Sb-O (40) catalyst (anode) and as counter electrode Pt/C catalyst (cathode), at the same time, was employed a carbon mesh as gas diffusor at the cathode. The scan rate of CV was 100 mVs^{-1} for all test a scan range of 1 V to 1.8 V before and after chronopotentiometry test. The chronopotentiometry test was conducted with a current density range of 0 $mAcm^{-2}$ to 150 $mAcm^{-2}$ for both assemblies Ir-Sn-Sb-O (40) and 0 $mAcm^{-2}$ to 160 $mAcm^{-2}$ for IrO_2-ATO (40 at. % of IrO_2), the time of potential stabilization was 1 min. The EIS measurements were conducted at a range of 10^5 Hz to 1 Hz at open circuit (OC), 1.5 V, 1.6 V, 1.7 V and 1.8 V for Ir-Sn-Sb-O (40) and (OC), 1.5 V, 1.6 V, 1.7 V, 1.8 V, 1.9 V, 2.0 V and 2.4 V for IrO_2-ATO mixture. Open circuit EIS were realized before and after chronopotentiometry The single cell test were performed with a Potentiostat/Galvanostat/ZRA Gamry Instruments. The operation temperature in the cell operation was 70 °C.

III. RESULTS AND DISCUSSION

A. Electrical conductivity in powder

The electrical conductivity of mixed oxide synthetized by thermal decomposition was obtained by electrical resistivity measurements. At 150 psi in^{-2} of pressure, Ir-Sn-Sb-O (40) material present an electrical conductivity of 154882 Sm^{-1}, the values of Vulcan carbon and SnO_2 commercial was 484.26 S m^{-1} and 0.028 S m^{-1}.[11] The Table 2 show the values of electrical conductivity of the materials measured by electrical resistivity (ER) an impedance spectroscopy (IS) at different pressures P (psi in^{-2}). The electrical conductivity of the materials decreases as Ir-Sn-Sb-O (40) >IrO_2>ATO+IrO_2>ATO. The higher electrical conductivity for Ir-Sn-Sb-O (40) may be due to the presence of metallic iridium, besides the combination with other metals favor electron transport within the material. In the case of iridium oxide synthetized by thermal decomposition has a lower conductivity than mixed oxide, however, it has metallic conductivity type.[17,24] ATO synthetized by thermal decomposition have less conductivity than other materials, at 150 psia in^{-2}, ATO presents higher conductivity than SnO_2 commercial and other prepared with different synthesis mechanism,[11,25] showing that the synthesis method and the presence of an additional metal promotes the conductivity of the support. There can see that σ increase with the pressure, this could be because the piston pressing, the material density increase, allowing to the particles be closer, and favors electron transport.

The conductivity of the materials obtained by IS was measured at different frequencies (form 0.1 Hz to 1 MHz), they show that the impedance it´s independent of the frequency, at 1 kHz, the conductivity of the material decrease as follows: Ir-Sn-Sb-O (40) >IrO_2>ATO+IrO_2>ATO (see Table 2), but the conductivity obtained by this technique are lower than the obtained by ER. The σ of Ir-Sn-Sb-O (40) and IrO_2 suggest metallic type conductivity.[26]

Table 2. Electrical conductivity of materials synthetized by thermal decomposition obtained by electrical resistivity (ER) and impedance spectroscopy (IS) at different pressures.

P (psi in^{-2})	σ (Sm^{-1}) Ir-Sn-Sb-O (40)		IrO_2		ATO		ATO+IrO_2	
	ER	*IS*	*ER*	*IS*	*ER*	*IS*	*ER*	*IS*
0	10329	3.85	88.50	7.98	3.01	-	0.09	0.57
50	82190	429	20099	86.50	5.81	-	0.07	11.49
100	117616	3070	40905	647	135.5	-	20.11	30.88
150	154882	14645	78614	10903	252.2	-	337.8	100.1
200	24068	65904	122330	13121	558.7	-	786.4	196.1

B. Single cell test

All electrochemical experiments were carried out at 70 °C with a flow rate of water of 7 mL s^{-1}. The resistance of the cell was measured, showing a low resistance (0.24 Ω). Cyclic voltammetry (CV) of Ir-Sn-Sb-O (40) membrane electrode assembly before and after of the chronopotentiometry (CP) are show in Figure 1. In Figure 2 show cyclic voltammogram of the IrO_2-ATO anode before and after CP. The curve corresponding to Ir-Sn-Sb-O (40) anode before CP shows that the oxygen evolution reaction starts close to 1.5 V, and at 1.8 V a current density of 60 mAcm^{-2}. In Figure 2, the curve of IrO2-ATO anode show a start of OER at 1.5 V, a difference with Ir-Sn-Sb-O (40) anode show a current density at 1.8 V of 35 mAcm^{-2}. Then the Ir-Sn-Sb-O (40) catalyst show a less over potential for OER. The cyclic voltammogram of Ir-Sn-Sb-O (40) after CP show a decrease in the electroactivity of the mixed oxide, the current density decreases under 40 mAcm^{-2} at 1.8 V. In the same way, the electroactivity of IrO_2 synthetized by thermal decomposition show a decrease, close to 15 mAcm^{-2}. The decrease in the current density for both materials suggest a passivation of catalyst, or a detachment of catalyst. Among that suggest that the mechanical mixture of IrO_2-ATO are less stable than Ir-Sn-Sb-O (40).

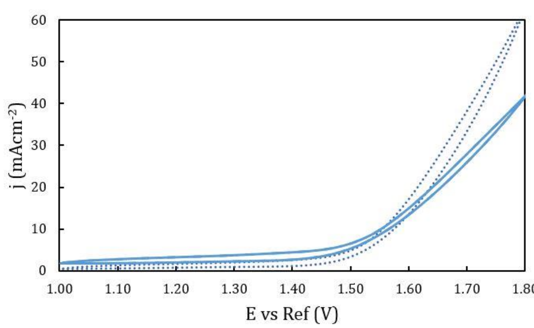

Figure 1. Cyclic voltammetry of Ir-Sn-Sb-O (40) assembly. (· · ·) Ir-Sn-Sb-O (40) before chronopotenciometry, (——) Ir-Sn-Sb-O (40) after chronopotenciometry.

In the same way, electrochemical impedance spectroscopy (EIS) for the two assemblies was realized at open circuit, before and after CP, the typical Nyquist plots are show in Figure 3. In Figure 3 (a) illustrate an electrochemical impedance specter for Ir-Sn-Sb-O (40) assembly and the IrO_2-ATO assembly are illustrate in Figure 3 (b). The resistance for both assemblies at the cell before CP are close to 1 Ωcm^2. The specters of both materials show an increase in cell resistance.

Electrochemical impedance spectroscopy was realized for both assemblies at different potential. The specters of EIS for Ir-Sn-Sb-O (40) anode are illustrate in Figure 4. The resistance obtained at that different potential was used to correct ohmic drop correction in the polarization curve, the cross in the real plane of all specters are close (2 Ωcm^2), it´s observed that the cell resistance increased as the potential was applied. The depressed semicircle represents the charge transfer resistance (R_{ct}), which reduce according the increase of the overpotential. The Figure 5 show the EIS specters for IrO_2-ATO assembly. The cross line in the real plane are close to 2 Ωcm^2, the variation with the potential is minimum. The resistance of the cell was used to correct ohmic drop in polarization curve. The size (Ωcm^2) of the semicircle corroborate that the mixed oxide has higher electroactivity than mechanical mixture of IrO_2-ATO. The depressed semicircle for Ir-Sn-Sb-O (40) assembly at 1.8 V, has a similar diameter than IrO2+ATO assembly at 2.4 V. That show a higher overpotential (lower charge transfer resistance) for the mechanical mixture than for the catalyst-support synthetized in one step.

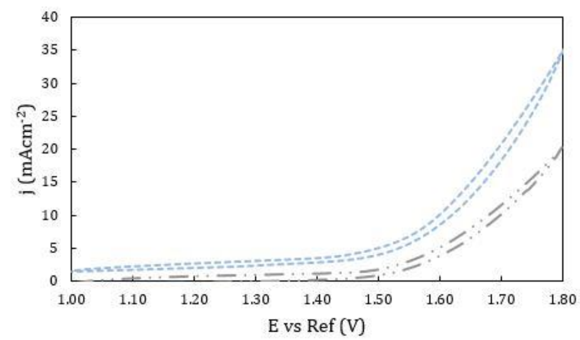

Figure 2 Cyclic voltammetry of IrO_2+ATO assembly. (– – –) IrO_2+ATO before chronopotenciometry, (–· ·–) IrO_2+ATO after chronopotenciometry.

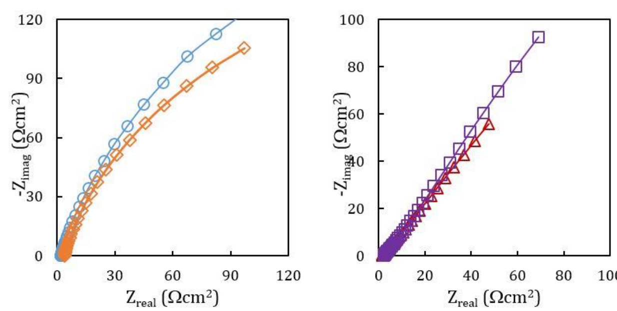

Figure 3. Electrochemical impedance specters. (a) Ir-Sn-Sb-O (40) assembly, (o) before and (◊) after CP. (b) IrO_2-ATO assebly.(□) before and (Δ)after CP.

The polarization curves before and after ohmic drop correction are show in Figure 6 for Ir-Sn-Sb-O (40) assembly, and in Figure 7 for IrO_2+ATO assembly. There show that the potential at start the OER (E_{OER}) for Ir-Sn-Sb-O (40) starts at 1.5 V after and before ohmic drop correction, with increasing current demand also increase the resistance of the cell, therefore, the difference between the two curves is evident at higher overpotential. The correction in overpotential it´s close to 0.5 V. The higher current density obtained with this assembly is 150 mAcm^{-2}.

In Figure 7, is show the polarization curve for IrO2+ATO mechanical mixture assembly in single cell. The OER starts at a potential of 1.5 V after and before ohmic drop correction, in this assembly, we can see a less change in polarization curve with ohmic drop correction, the change in resistance of the cell wasn´t notorious. The potential in the crhonopotentiometry was more stable than for Ir-Sn-Sb-O (40) assembly.

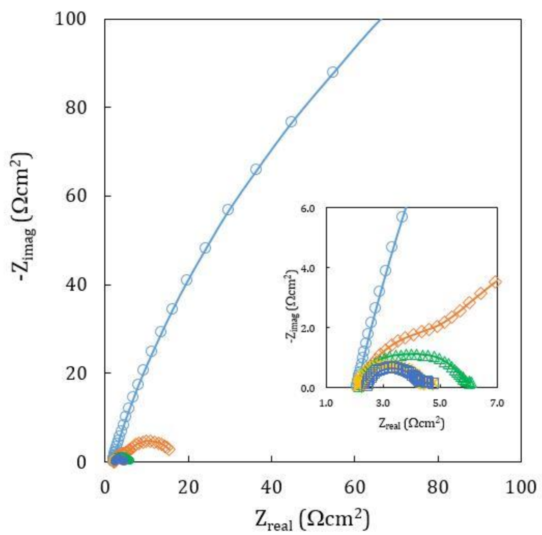

Figure 4. EIS specterws of Ir-Sn-Sb-O (40) catalyst at: (o) OC, (◊) 1.5 V, (Δ) 1.6 V, (×)1.7 V, (□)1.8 V.

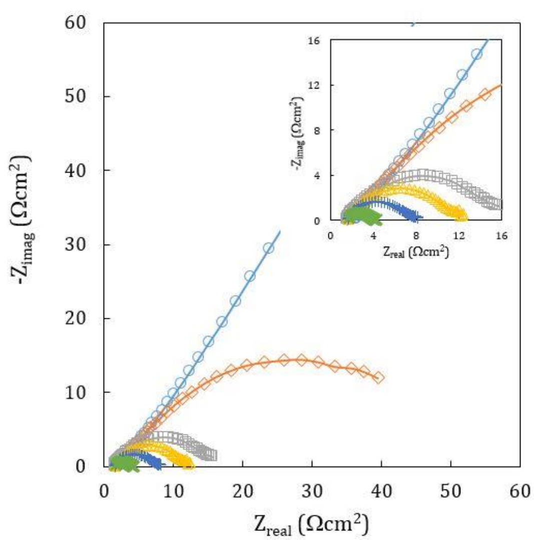

Figure 5. EIS specters of IrO2-ATO assembly at: (o) OC, (◊) 1.5 V, (□)1.6 V, (Δ) 1.7 V, (×)1.8 V, (+)2.4 V.

In comparison, both polarization curves were similar after ohmic drop correction, only it should be noted stability in the potential applied in the assembly of mechanical mixture of catalyst and support.

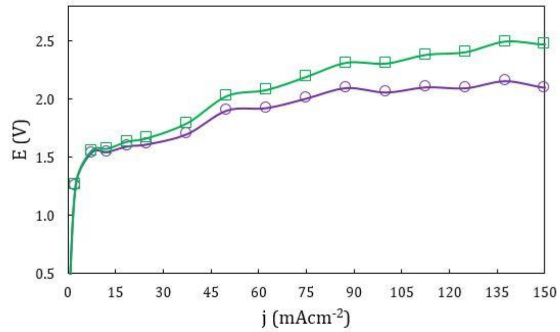

Figure 6. Polarization curve of Ir-Sn-Sb-O (40) (□) before ohmic drop and (o) after ohmic drop.

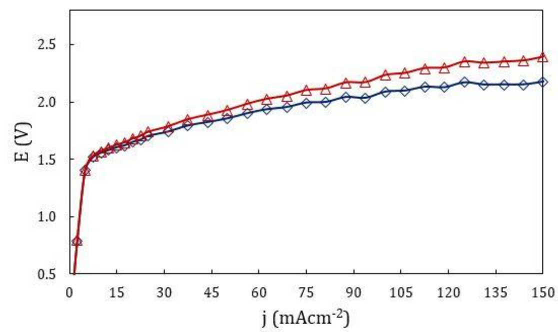

Figure 7. Polarization curve of IrO_2+ATO assembly (Δ) before ohmic drop correction and (◊) after ohmic drop correction.

IV. CONCLUSIONS

In this work, was synthetized electrocatalyst for oxygen evolution reaction by thermal decomposition method. The electrical conductivity of the mixed oxide show a metallic conductivity,[24] 2.4x10^5 Sm^{-1} at 200 lbf in^{-2} for Ir-Sn-Sb-O (40) and 1.2x10^5 Sm^{-1} for IrO_2. Cyclic voltammetry shows the typical shape of IrO_2 in both materials, suggesting the presence of active phase. In preliminary results, the mixed oxide shows a higher electroactivity, but, in polarization curve, show same overpotential for mechanical mixture than mixed oxide. Cyclic voltammogram of Ir-Sn-Sb-O (40) after chronopotentiometric test suggest a pasivation of catalytic film. Then the stability of the material can be committed by operation conditions.

V. ACKNOWLEDGMENTS

The authors acknowledge financial support from the Mexican Council for Science and Technology (CONACyT, Project 167012). SMH and XVI International Congress of the Mexican Hydrogen Society for your attention for the participation in this congress.

VI. REFERENCES

[1] Millet P, Ngameni R, Grigoriev SA, Mbemba N, Brisset F, Ranjbari A, et al. PEM water electrolyzers: From electrocatalysis to stack development. Int J Hydrog Energy 2010;35:5043–52. doi:10.1016/j.ijhydene.2009.09.015.

[2] Grigoriev SA, Porembsky VI, Fateev VN. Pure hydrogen production by PEM electrolysis for hydrogen energy. Int J Hydrog Energy 2006;31:171–5. doi:10.1016/j.ijhydene.2005.04.038.

[3] Chaubey R, Sahu S, James OO, Maity S. A review on development of industrial processes and emerging techniques for production of hydrogen from renewable and sustainable sources. Renew Sustain Energy Rev 2013;23:443–62. doi:10.1016/j.rser.2013.02.019.

[4] Lee J, Jeong B, Ocon JD. Oxygen electrocatalysis in chemical energy conversion and storage technologies. Curr Appl Phys 2013;13:309–21. doi:10.1016/j.cap.2012.08.008.

[5] Audichon T, Mayousse E, Napporn TW, Morais C, Comminges C, Kokoh KB. Elaboration and characterization of ruthenium nano-oxides for the oxygen evolution reaction in a Proton Exchange Membrane Water Electrolyzer supplied by a solar profile. Electrochimica Acta 2014;132:284–91. doi:10.1016/j.electacta.2014.03.141.

[6] Audichon T, Mayousse E, Morisset S, Morais C, Comminges C, Napporn TW, et al. Electroactivity of RuO2–IrO2 mixed nanocatalysts toward the oxygen evolution reaction in a water electrolyzer supplied by a solar profile. Int J Hydrog Energy 2014;39:16785–96. doi:10.1016/j.ijhydene.2014.07.170.

[7] Ardizzone S, Bianchi CL, Cappelletti G, Ionita M, Minguzzi A, Rondinini S, et al. Composite ternary SnO2–IrO2–Ta2O5 oxide electrocatalysts. J Electroanal Chem 2006;589:160–6. doi:10.1016/j.jelechem.2006.02.004.

[8] Antolini E. Iridium as catalyst and cocatalyst for oxygen evolution/reduction in acidic polymer electrolyte membrane electrolyzers and fuel cells. ACS Catal 2014;4:1426–40. doi:10.1021/cs4011875.

[9] Xu J, Li Q, Hansen MK, Christensen E, Tomás García AL, Liu G, et al. Antimony doped tin oxides and their composites with tin pyrophosphates as catalyst supports for oxygen evolution reaction in proton exchange membrane water electrolysis. Int J Hydrog Energy 2012;37:18629–40. doi:10.1016/j.ijhydene.2012.09.156.

[10] Hu Y, Zhang H, Yang H. Synthesis and electrical property of antimony-doped tin oxide powders with barite matrix. J Alloys Compd 2008;453:292–7. doi:10.1016/j.jallcom.2006.11.062.

[11] Oh H-S, Nong HN, Strasser P. Preparation of Mesoporous Sb-, F-, and In-Doped SnO2 Bulk Powder with High Surface Area for Use as Catalyst Supports in Electrolytic Cells. Adv Funct Mater 2015;25:1074–81. doi:10.1002/adfm.201401919.

[12] Marshall A, Børresen B, Hagen G, Tsypkin M, Tunold R. Electrochemical characterisation of IrxSn1−xO2 powders as oxygen evolution electrocatalysts. Electrochimica Acta 2006;51:3161–7. doi:10.1016/j.electacta.2005.09.004.

[13] De Pauli CP, Trasatti S. Composite materials for electrocatalysis of O2 evolution: IrO2+SnO2 in acid solution. J Electroanal Chem 2002;538–539:145–51. doi:10.1016/S0022-0728(02)01055-0.

[14] De Pauli CP, Trasatti S. Electrochemical surface characterization of IrO2 + SnO2 mixed oxide electrocatalysts. J Electroanal Chem 1995;396:161–8. doi:10.1016/0022-0728(95)03950-L.

[15] Kadakia K, Datta MK, Velikokhatnyi OI, Jampani P, Park SK, Saha P, et al. Novel (Ir,Sn,Nb)O2 anode electrocatalysts with reduced noble metal content for PEM based water electrolysis. Int J Hydrog Energy 2012;37:3001–13. doi:10.1016/j.ijhydene.2011.11.055.

[16] Li G, Yu H, Wang X, Yang D, Li Y, Shao Z, et al. Triblock polymer mediated synthesis of Ir–Sn oxide electrocatalysts for oxygen evolution reaction. J Power Sources 2014;249:175–84. doi:10.1016/j.jpowsour.2013.10.088.

[17] Marshall A, Børresen B, Hagen G, Tsypkin M, Tunold R. Hydrogen production by advanced proton exchange membrane (PEM) water electrolysers—Reduced energy consumption by improved electrocatalysis. Energy 2007;32:431–6. doi:10.1016/j.energy.2006.07.014.

[18] Marshall A, Tsypkin M, Boørresen B, Hagen G, Tunold R. Nanocrystalline IrxSn(1-X)O2 electrocatalysts for oxygen evolution in water electrolysis with polymer electrolyte - Effect of heat treatment. J New Mater Electrochem Syst 2004;7:197–204.

[19] Su H, Linkov V, Bladergroen BJ. Membrane electrode assemblies with low noble metal loadings for hydrogen production from solid polymer electrolyte water electrolysis. Int J Hydrog Energy 2013;38:9601–8. doi:10.1016/j.ijhydene.2013.05.099.

[20] Hu J-M, Zhang J-Q, Cao C-N. Oxygen evolution reaction on IrO2-based DSA® type electrodes: kinetics analysis of Tafel lines and EIS. Int J Hydrog Energy 2004;29:791–7. doi:10.1016/j.ijhydene.2003.09.007.

[21] Cornell A, Håkansson1 B, Lindbergh1 G. Ruthenium based DSA® in chlorate electrolysis—critical anode potential and reaction kinetics. Electrochimica Acta 2003;48:473–81. doi:10.1016/S0013-4686(02)00679-5.

[22] Trasatti S. Electrocatalysis: understanding the success of DSA®. Electrochimica Acta 2000;45:2377–85. doi:10.1016/S0013-4686(00)00338-8.

[23] Hu C-C, Wang C-C, Chang K-H. A comparison study of the capacitive behavior for sol–gel-derived and co-annealed ruthenium–tin oxide composites. Electrochimica Acta 2007;52:2691–700. doi:10.1016/j.electacta.2006.09.026.

[24] Marshall A, Børresen B, Hagen G, Tsypkin M, Tunold R. Preparation and characterisation of nanocrystalline IrxSn1−xO2 electrocatalytic powders. Mater Chem Phys 2005;94:226–32. doi:10.1016/j.matchemphys.2005.04.039.

[25] Jeon H-J, Jeon M-K, Kang M, Lee S-G, Lee Y-L, Hong Y-K, et al. Synthesis and characterization of antimony-doped tin oxide (ATO) with nanometer-sized particles and their conductivities. Mater Lett 2005;59:1801–10. doi:10.1016/j.matlet.2005.01.070.

[26] Egil Rasten - Thesis.pdf - FULLTEXT01.pdf n.d.

Electrochemical water Oxidation by Cobalt-Iron Cyanide effect of Mix Valance State

M.A. Oliver-Tolentino, J. Vázquez-Samperio, I. Zumeta-Dubé, A. Guzman-Vargas, E. Reguera*
CICATA Legaría
IPN
México City
*edilso.reguera@gmail.com

Cobalt-Iron Cyanide was synthetized by precipitation method, whereas the sample with Mix Valance State was prepared by temperature annealing. The films of Co-Fe cyanide were obtained by spin coating deposition on FTO electrode. The electrocatalytic activity towards Oxygen Evolution Reaction (OER) is discussed in terms of the effect of internal and external metal in prussian blue analogues and the amount of Co (III) exposed in electrode / electrolyte interface, which promote the oxidation of water.

Keywords: Mix Valance Material, Oxygen Evolution Reaction, electrocatalysis

I. INTRODUCTION (*HEADING 1*)

Cobalt hexacyanoferrate (CoHCF), among the PBAs, is one of the more interesting inorganic material and shows switching properties caused by the CoII(HS)-FeIII ↔ CoIII(LS)-FeII (HS and LS stand for high and low spin) electron transfer.[1] This material is very attractive because of the peculiar physicochemical properties: electrochromism,[2] thermochromism,[3] photochemical magnetism,[4] and electrocatalytic and sensing properties.[5]

The redox process in CoHCF involves two different metal transition ions (Fe and Co), unlike other materials of the same class; the phenomenon is driven by a metal-to-metal charge transfer. The contemporary occurrence of FeIII and CoIII makes it possible to observe both the redox couples, FeIII/FeII and CoIII/CoII, in the same material.[1]

Recently, the Co-Fe Prussian blue with $Fe^{II} - C{\equiv}N - Co^{II}$ chain has been used as electrocatalyst in electrochemical water oxidation, shows that water oxidation occurs in the Co^{3+} [6], which are produced during cathodic sweep.

Based on the electrocatalityc properties of this material over oxygen evolution reaction, in the present work are obtained thin films by spin coating method of CoHCF with Fe(CN)6 vacant sites, where the cobalt atoms are found at the surface, completing their coordination environment with water molecules.

II. EXPERIMENTAL SECTION

Firstly the sample with the fallowing compositions: $Co^{2+}K_2[Fe^{II}(CN)6]$ H_2O (S1) was obtained mixing aqueous solutions of $Co(SO_4)$ and $K_4[Fe^{II}(CN)_6]$ prepared in situ under stirring, the precipitated solid separated, washed and dried, this sample was labeled as S1.
Subsequently the powder with the composition: $KCo^{2+}[Fe^{III}(CN)_6]$ (S2), were preparing an aqueous solution of appropriate molar mixtures of $K_3[Fe^{III}(CN)_6]$ and $Co(SO_4)$ and it then added under stirring at room temperature, labeled S2. The formed precipitate was aged within the mother liquor for 24 h. The obtained solid is isolated by filtration, washed several times with distilled water and then air dried up to constant weight. After obtaining S2 powder, this heated at the temperatures 100 °C (labeled S3) and 150 °C (labeled S4), thus obtaining the S3 and S4 powders respectively.
The electrochemical measurements were carried out in a three-electrode quartz cell. The working electode was the thin films of CoHCF deposited on FTO surface area of 1.0 cm^2. A Pt wire and an Ag/AgCl, were used as the counter and the reference electrode respectively. A scanning potentiostat (Autolab) was used for the potentiometric and chronoamperometric measurements. The electrolyte solution used for the electrochemical measurements was 1.0 M KNO_3.

III. RESULTS AND DISCUSSION

The Linear sweep voltammetry in 1M KNO_3 solution at $1mVs^{-1}$ of CoHCF are display in Figure not show. According to these results, the current magnitude order during oxygen evolution was as follows: S4 > S1 > S3 > S2, indicating that sample S4 exhibits the best electrocatalytic activity towards OER. With the aim to understand the effect of inner metal and external metal in the OER, experiment using $Co^{II}_3[Co^{III}(CN)_6]_2$ (M1), $Mn^{II}_3[Co^{III}(CN)_6]_2$ (M2), $Ni^{II}_3[Co^{III}(CN)_6]_2$ (M3) this system exhibited $Co(CN)_6$ vacant site and $KFe^{III}[Fe^{II}(CN)_6]$ (M4), were carried out; the cyclic voltammery for every samples are shows in the inset of Figure 1. M1, M2 and M3 not exhibited any redox process, this is associated to the insertion/desertion of K+ not occurs, additional, the $Co(CN)_6$ are not expected to participate in the oxidation or reduction processes [7] due to the Co^{III}-CN ion in low spin state has six electrons in the t_{2g} orbitals, which provides a high stability. Whereas, the M4 present two redox process Ea1 and Ec1 assigned to Fe^{III}/Fe^{II} in high spin, and

Ea2 and Ec2 attributed to Fe^{III}/Fe^{II} in low spin this faradic process are accompanied by potassium ion diffusion.

The Linear sweep voltammetry (Fig 1) showed a poor catalytic activity of M3 and M4, due to any metal change the oxidation state and the OER not occurs; whereas M4 exhibited activity toward water oxidation, this behavior is associated to Fe^{III} (LS) produced during anodic sweep which catalyzed the water oxidation as was report before [8]. On the other hand, the M1 showed a peak c.a. 1.46 V attributed to oxidation of Co^{III} to Co^{IV} [9], due to the no obvious participation of the hexacyanocobaltate (III) anion in oxidation or reduction processes is expected as was demonstrated in M2 and M3; the oxidation process observed in M1 is associated to external Cobalt, which need to complete their coordination environment with water molecules, in average, $CoN_4(H_2O)_2$, due to the $Co(CN)_6$ vacant, these open metal sites being available to absorb water and promote the oxygen evolution reaction.

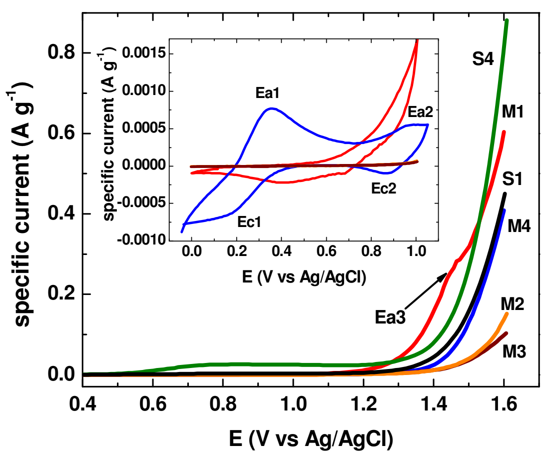

Figure 1. Linear Sweep at 1 mV s-1 in KNO3 (1mol L^{-1}) of the samples M1, M2, M3 and M4, inset: Cyclic Voltammetry.

The current magnitude of S1 is a little higher than M4 indicating that catalytic activity of S1 is mainly associated to presence of Fe^{III} (LS) which catalyzed the water oxidation; whereas the S4 is higher than S1 and M1 suggesting that OER occurs mainly by the high amount of Co^{III} in low spin configuration which are found at the surface of their large pores and are completing their coordination environment with water molecules, due to $Fe(CN)_6$ vacant; in this Co^{III} (LS) the eg orbitals are free to receive electrons from CN ligands or for coordinating water; and can be oxidized to Co^{IV} (S= ½), which promotes the water oxidation.[10], however the water oxidation catalyzed by Fe^{III} (LS) and charge transfer mechanism from Co^{II} (HS) to Fe^{III} (LS) can be contributing to enhance of oxygen evolution reaction. The tafel plots calculated from inset in Figure 1, are near to 90 mV dec-1, as was reported by Pintado et. al. [11], suggesting that OER occurs by a catalytic process with the same mechanism for four samples.

IV. CONCLUSIONS

In the present work was obtained thin films of CoHCF with different composition on conducting glass (FTO), from spin coating method. The oxidation state of the metallic cations presented in each compound after and before the oxidations processes are identify by Raman Spectroscopy. The oxidations processes in the samples were fallows by cyclic voltammetry and the linear Sweep curves shows which the current magnitude order during oxygen evolution was as follows: S4 > S1 > S3 > S2, indicating that sample S4 exhibits the best electrocatalytic activity towards OER, the S4 shows a PCET mechanism, suggesting that this system can be used in acidic conditions, where no cobalt leaching occurs.

V. REFERECNES

References

[1] S. Pintado, S. Goberna-Ferrón, E.C. Escudero-Adán, J.R. Galán-Mascarós, Fast and Persistent Electrocatalytic Water Oxidation by Co–Fe Prussian Blue Coordination Polymers, Journal of the Am. Chem. Soc., 2013,135,13270-13273.

[2]R. Martinez-Garcia, M. Knobel, J. Balmaseda, H.Yee-Madeira, E. Reguera, Mixed valence states in cobalt iron cyanide, J. Phys. Chem. Solids, 2007,68,290-298.

[3] R. Martinez-Garcia, M. Knobel, G. Goya, M. Gimenez, F. Romero, E. Reguera, Heat-induced charge transfer in cobalt iron cyanide, J. Phys. Chem. Solids., 2006,67,2289-2299.

[4] E. Manuel, M. Evangelisti, M. Affronte, M. Okubo, C. Train, M. Verdaguer, Magnetocaloric effect in hexacyanochromate Prussian blue analogs, Phys. Review B., 2006,73,172406.

[5] R.O. Lezna, R. Romagnoli, N.R. de Tacconi, K. Rajeshwar, Cobalt hexacyanoferrate: compound stoichiometry, infrared spectroelectrochemistry, and photoinduced electron transfer, J. Phys. Chem. B., 2002,106,3612-3621.

[6] R. Mažeikienė, G. Niaura, A. Malinauskas, Electrochemical redox processes at cobalt hexacyanoferrate modified electrodes: An in situ Raman spectroelectrochemical study, J. Electroana. Chem., 2014,719,60-71

[7] S.F. Kettle, E. Diana, E. Marchese, E. Boccaleri, P.L. Stanghellini, The vibrational spectra of the cyanide ligand revisited: the ν (CN) infrared and Raman spectroscopy of Prussian blue and its analogues, J. Raman Spec. 2011,42,2006-2014.

[8] F. Scholz, A. Dostal, The formal potentials of solid metal hexacyanometalates, Angew. Chem. Int. Ed. Eng., 1996,34,2685-2687.

[9] O. Sato, Y. Einaga, A. Fujishima, K. Hashimoto, Photoinduced long-range magnetic ordering of a cobalt-iron cyanide, Inorg. chem., 1999,38,4405-4412.

[10] J.G. McAlpin, Y. Surendranath, M. Dinca, T.A. Stich, S.A. Stoian, W.H. Casey, D.G. Nocera, R.D. Britt, EPR evidence for Co (IV) species produced during water oxidation at neutral pH, J. Am. Chem. Soc., 2010,132,6882-6883.

[11] Y. Surendranath, M. Dinca, D.G. Nocera, Electrolyte-Dependent Electrosynthesis and Activity of Cobalt-Based Water Oxidation Catalysts, J. Am. Chem. Soc., 2009,131,2615-2620.

[12] Y. Lu, L. Wang, J. Cheng, and J. B. Goodenough, Prussian blue: A new framework of electrode materials for sodium batteries, Chem. Commun., 2012, 48, 6544-6546.

[13] M.W. Kanan, D.G. Nocera, In Situ Formation of an Oxygen-Evolving Catalyst in Neutral Water Containing Phosphate and Co2+, Science, 2008, 321, 1072-1075.

[14] S.-i. Ohkoshi, K. Nakagawa, K. Tomono, K. Imoto, Y. Tsunobuchi, H. Tokoro, High Proton Conductivity in Prussian Blue Analogues and the Interference Effect by Magnetic Ordering, J. Am. Chem. Soc., 2010, 132, 6620–6621

XVI International Congress of the Hydrogen Mexican Society
2016

INFLUENCE OF THE S CONTENT IN FORMATION OF SULFUR-DOPED CARBON NANOMATERIALS

E. Montiel-Macias[1]*, P. B. Balbuena[2], A. M. Valenzuela-Muñiz[1], Y. Verde-Gómez[1]

[1]Instituto Tecnológico de Cancún, Av. Kabah Km 3, Cancún Q. Roo, México, 77500
[2]Department of Chemical Engineering, Texas A&M University, TAMU 3122, College Station, TX, USA, 77843
[3]CONACYT-Instituto Tecnológico de Cancún, Av. Kabah Km 3, Cancún Q. Roo, México, 77500
*Tel: +52998807432 ex. 1012, e-mail: elizabethmontielmacias@hotmail.com

ABSTRACT

One of the most important components of a proton exchange membrane fuel cells (PEMFC) are the membrane electrode assemblies (MEA). It is here where the electrochemical reactions to produce the electrical energy are performed. Usually electrocatalysts based on noble metals such as platinum (Pt) or Pt with other metals supported on carbon materials have been manufactured, due to its stability and high electrocatalytic activity. However, due to the limited availability of Pt and its high cost, there have been efforts to investigate non-platinum materials, which allow alternatives to replace or decrease this material in the electrodes. As a promising alternative, new carbon nanomaterials doped with heteroatoms as N, B, P and S have been investigated. In this research work sulfur-doped carbon nanomaterials were synthesized by a modified chemical vapor deposition method. Previously, we have determined the optimal synthesis parameters such as reaction temperature, carrier gas flow and preheating temperature. Ferrocene was used as a catalytic agent; toluene and thiophene were used as sources of carbon and carbon-sulfur, respectively. The influence in the relation of carbon-sulfur source on the formation of sulfur doped nanocarbons was investigated. Physical and chemical characterization was performed by X-Ray Diffraction and Scanning Electron Microscopy, in order to determinate the structural and morphological properties. In addition, the chemical elemental analysis was done by energy dispersive spectroscopy. The interesting results obtained, as well as the discussion will be presented at the conference.

Keywords: Sulfur doped carbon nanomaterials, Electrocatalysts, Fuel Cells.

Design of a photobioreactor for the production of hydrogen from microalgae

E.M. Hernández-Hernández[1], C. A. Cortés-Escobedo[1], H.A. Velasco-Bedrán[2]
[1]Centro de Investigación e Innovación Tecnológica, Cda. Cecati S/N Col. Santa Catarina, Azcapotzalco, México, 02250.
[*]Tel: +5255 5729 6000; e-mail: mariana.hernandez2703@outlook.com
[2]Escuela Nacional de Ciencias Biológicas, Wilfrido Massieu 399 Nueva Industrial Vallejo, Gustavo A. Madero, México, 07738.

***Abstract*— Today humanity has increased quasi exponentially the rate of use of fossil fuels, which has indirectly caused adverse environmental effects besides its progressive depletion is getting closer. Because of the international scientific community confront the urgent task of finding alternative fuels, with the profile to replace today's energy so that it is possible to obtain them from more environmentally friendly sources. H_2 production by biological species (Bio hydrogen) has a number of advantages and could be a cost effective alternative to current industrial methods of H_2 production. In this fact, the bioreactors are essential for bio hydrogen production by cyanobacteria and green microalgae, such production is linked to photosynthetic reactions of dissociation of water and it is possible to use solar energy (light) for this process. The main challenges in the design of a photobioreactor for these purposes are to design a simple and inexpensive system, which has high productivity and efficiency, which is scalable to industrial capabilities. Particularly the design of a photobioreactor to produce hydrogen represents additional features such as phase separation during gas production, establishing appropriate conditions to induce the H_2 production and scaling for sunlight systems. This document describes the choice process of the design bases and the final design of the photobioreactor medium scale, which has dimensions of 1x0.70 x 0.03 m and a nominal volume of 0.021m3 and 0.35L per hour production of hydrogen expected.**

Keywords— biohydrogen, photobioreactor, flat-plate, *Chlamydomonas reinhardtii*.

I. INTRODUCTION (*HEADING 1*)

Today conventional industrial methods for the production of H_2 are expensive and the most of this methods use fossil or other energy source. So that the problem that prevails is to find a cheaper way to produce clean hydrogen [1]. It should be mentioned that there is a great diversity of microorganisms having the ability to produce H_2 using different biochemical mechanisms[2]. They may occur through the use of organic materials (ej. sugar or biomass) or simply by using water through reactions hydrogenase enzyme catalyzed or nitrogenase in photosynthetic microorganisms. Particularly in the latter case the process involve a CO_2 absorption, giving an environmental advantage, in addition the culture of these organisms is relatively cheaper and its management on a large scale could have benefits of greater impact given the current demand for functional food.

For the exploitation of such microorganisms the use of tools that allow the growth of large quantities of biomass may have higher performance, one of these tools are the bioreactors. Therefore, bioreactors are indispensable for biohydrogen production scale and ideal for practical cell growth under controlled conditions purposes. Specifically H_2 production is linked to water dissociation reactions through light energy therefore it is possible to use solar energy (light) for this purpose [3].

Particularly the design of a photobioreactor (FBR) to produce hydrogen imply challenges, such as phase separation during gas production, establishment of suitable conditions to induce the H_2 production and easy operation [3] [4].

Biohydrogen can occur through different biological pathways, these are grouped into two distinct categories: light dependent or not light dependent processes, both of them include direct or indirect fotofermentación, dark fermentation and biophotolysis [4]. The advantage of direct photolysis is the requirements are only water and light, which is relatively available and economic. In particular this project is guide to direct biophotolysis.

II. MICROALGAE-HYDROGEN BACKGROUND

In 1942 Gaffron y Rubin discover the hydrogen photoproduction in anaerobic conditions of *Scenedesmus* sp. [4].

Stuart y Gaffron in 1972 describe the kinetics of hydrogen photoproduction in two phases: an initial phase (dehydrogenation) and a slower phase which is limited by the flow of electrons. [5]

Subsequently in 1982 Bothe report the conversion of solar energy by green algae is extremely sensitivity of the hydrogenase with respect to O_2 and emphasizes that the ability to produce H_2 is completely lost when the O_2 level in the test exceeds 1% concentration [6].

Later in 2002 Melis y cols. Investigate into absence of sulfur in the medium favors H_2 production, expression of hydrogenase in the presence of light, suggest an H_2/O_2 temporary separation processes in two stages [7].

In the same year Zhang, Happe y Melis work in biochemical characterization of H_2 production induced absence of sulfur in the culture medium with *Chlamydomonas reinhardtii* [8].

In 2005, Fedorov y cols. test H_2 photoproduction continuous, two-stage system that physically separates the photosynthetic growth of H_2 production, and incorporates two photobioreactors [9].

In summary, several reviews have examined the potential of biological hydrogen production. Although microorganisms produce hydrogen by different mechanisms, the step can be represented by the simple chemical reaction

$$2H^{+} + 2e \rightarrow H_2.$$

This reaction is known to be catalyzed by either nitrogenase or hydrogenase enzymes. For example, in Chlamydomonas reinhardtii the process is as shown in Figure 1.

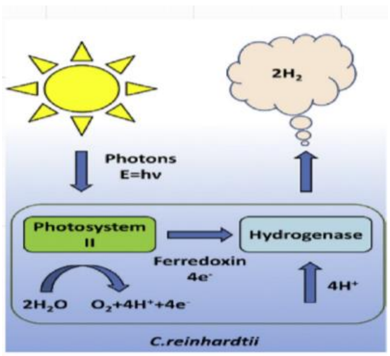

Fig. 1. General scheme hydrogen production. Modified Azwar, 2014.[15]

Direct photobiological hydrogen production by photosynthetic microorganisms is an active, developing field nowadays. Realization of technical processes for large-scale photobiological hydrogen production from water, using solar energy, would result in a major, novel source of sustainable, environmentally friendly and renewable energy [16].

Is important to emphasize that the research work carried out in the identification and description of the biological process with different microalgae, identify or design less oxygen sensitive microorganisms, isolate cycles hydrogen and oxygen, or change the ratio of photosynthesis to respiration to prevent accumulation of oxygen [10]. However existing developments around the engineering design of the reactor, or the phenomenological kinetic modeling that describes the biochemical process that is, to find the best operating conditions of a FBR for hydrogen production are minimal or nonexistent and there come from isolated workgroups.

While this technology has significant promise, its escalation also presents enormous challenges, such as obtain a suitable surface to absorb enough light, facilitate the establishment of appropriate conditions to induce hydrogen production. The aim of this work was to design and build a FBR in order to produce biohydrogen from the green microalgae *Chlamydomonas reinhardtii.*

III. Material and Methods

First, the choice of the type of reactor to be built, was made as a function of operability and easy to measure for the kinetic of the growth of the microorganism and the consecuent hydrogen production kinetic. Then the system choice was batch reactor. After considering such restrictions proceeded to define the design bases, for which a contribution of 0.35L was established as a requirement.

This requirement was assumed according to maximum hydrogen production in a continuous FBR reported, which is 0.60 mL (h * L) [20]. In the same way, the minimum hydrogen demand in a PEM Fuel Cell is 0.5L/min and 40% efficiency and performance of 14.4 V [17].

The design of the device was using the software SOLID WORKS ® 2016 and proceeded to its construction, for this acrylic 6mm was used for the side faces and 12mm for the frame structure. They were assembled with screws and nuts, ensuring the tightness of the system with a teflon^{R} seal between the faces. A sprinkler stainless steel tube 13mm in diameter was also placed at the bottom of the structure to conduce air flow as asperger tube.

Chlamydomonas reinhardtii strain CC-125 wild type mt + [137c], which was provided by the Laboratory of Molecular Biotechnology graduate (UPIBI-IPN) was used. It was replicated in solid medium BG-11 (agar 15%) and subsequently mounted a culture in liquid medium for growth kinetics.

Preliminary tests were conducted in small flasks 250 mL and using the sulphur deprived techinque.

IV. Results and discussions

Biophotolysis as direct hydrogen production process that will take place in the photobioreactor according to the characteristics of the most common FBR's. Flat-plate type was established as the most suitable design, because the agitation should be gentle, given the fragility of the cellular material. In addition, the sun-exposed area, thus more light available was considered, resulting in increased energy available, and optimized light path within the device.

For the design of the dimensions it was taken into account as an important factor in the light path of no more than 5cm [11], since it is used as a light source projected sunlight.

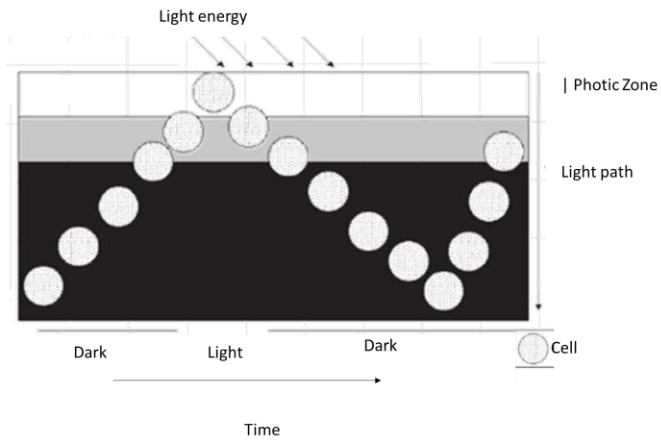

Fig. 2. Escheme of light path in a PBR. Modified Contreras, 2003 [11].

For volume control FBR were taken into account references of hydrogen production in small scale [12] and references of energy expenditure considering common devices that run on hydrogen technologies. Then, a volume control 21L and 14.7L volume operation was established.

The final dimensions of the device were 1x.70x.03 m. A gas valve was also installed, for taking gas samples with type Tedlar bags. It also has two outputs fill and drain. rigid transparent hose connections for liquid and gas was used. The sprinkler pipe was drilled with 10 holes 0.003m in diameter along the tube.

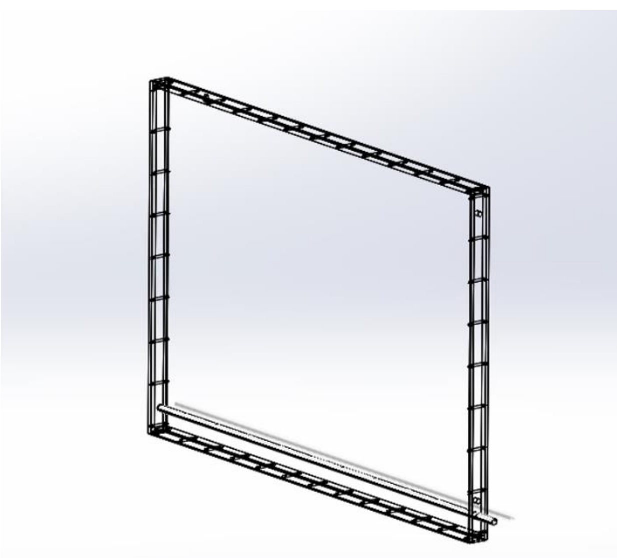

Fig. 3. Isometric View of FBR.

Fig. 4. Flat Plate PBR

A flat-plate vertical one-litre photobioreactor that facilitates the biophotolytic H_2 production process was designed and constructed. The flat-plate reactor geometry was subsequently chosen due to its superior surface-tovolume ratio, which results in the highest observed photochemical efficiencies for H_2 production [14]. Because of we can say the design choice can feasible for an adecuate scale H_2 production.

Fig. 5. Valve for gas sampling.

In Figure 5 shows the gas valve installed in the FBR, likewise the position of screw holes and teflon seal used.

In leak testing and filling a small trickle was observed, because of this more drilling were performed to securing the tightness of the system.

Finally is important to analyze the temperature effect on the H_2 production process, because it directly influences the process of biophotolysis, addition to a weathering process it have a significant effect on the microorganisms mantenance. To avoid this problem an infrared filter is used to reduce the temperature rise by solar radiation in subsequent test. In adition an air flux and water flux analysis will be performed in SOLID WORKS.

V. Conclusions

The design and dimensions were operable an feasible for H_2 production, however there are some features that can be improved. Such as the distance between the screw joints and the seal for sealing within the device. Is necessary evaluate the temperature effect on H_2 photoproduction in outdoor conditions.

Acknowledgments

This work was supported by the Laboratory of Clean Energy at Research Center and Technological Innovation, at IPN. The authors wish to acknowledge the financial support granted by project SIP 20160415, México.

References

[1] Zúñiga A.,Reza C., Manríquez M.,"Propiedades fisicoquímicas del hidrógeno gaseoso". In: González, H.R. Oliver, M.A. Rodríguez, F.J. Hidrógeno, producción y almacenamiento: Retos hacia su uso como vector energético sustentable, Estados Unidos de América: CreateSpace. 2013.

[2] Valenzuela, M.A. Zapata, B. Alfaro, S. "*Procesos para la producción y purificación de hidrógeno mediante hidrocarburos líquidos y gaseosos"* En: González, R. de G. Solórza, F. O. Valenzuela, M.A. Tecnologías de Hidrógeno y Celdas de Combustible de Fuentes Renovables,2011.

[3] Markov, S.A. "Hydrogen production in bioreactors: current " Energy Procedia,2012,29 394–400.

[4] Gaffron, H. y Rubin, J. "Fermentative and Photochemical Production Of Hydrogen In Algae". The Journal of General Physiology, 1942.. 219-241.

[5] Stuart, T. S. y Gaffron, H. The Mechanism of Hydrogen Photoproduction by Several Algae. Planta, 1972:91-100.

[6] Bothe, H. "Hydrogen production by algae" Verlag Experentia,1982:. (38) 59-65.

[7] Melis, A., Zhang, L., Forestier, M., Ghirardi, M. L. y Seibert, M. "Sustained Photobiological Hydrogen Gas Production upon Reversible Inactivation of Oxygen Evolution in the Green Alga Chlamydomonas reinhardtii" Plant Physiology, 2002, (122), 127-136.

[8] Zhang, L., Happe, T. y Melis, A. "Biochemical and morphological characterization of sulfur-deprived and H2-producing Chlamydomonas reinhardtii (green alga)" Planta, 2002, (214), 552-561.

[9] Fedorov, A. S., Sergey, K., Ghirardi, M. y Seibert, M. Continuous "Hydrogen Photoproduction by Chlamydomonas reinhardtii using a novel Two-Stage, Sulfate-Limited Chemostat System" Applied Biochemistry and Biotechnology. Humana Press Inc., 2005, 121-124, 403-413.

[10] Ghirardi, M. L., Togasaki, R. K. y Seibert , M. "Oxygen sensitivity of algal H2-Production" Applied Biochemistry and Biotechnology, 1997, Vol. 63-65, 142-151.

[11] Contreras-Flores, C. et al. "Avances en el diseño conceptual de fotobiorreactores para el cultivo de microalgas". Interciencia, 2003, 28-8.

[12] Show, K.Y. Lee, D.J. Tay, J.H. Lin, C.Y. y J.S. Chang, 2012 International Journal of Hydrogen energy.37:15616-15631.

[13] Lehr, F. Morweiser, M. Rosello, S. R. Kruse, O. y C. Postens, 2012, Journal of Biotechnology.162:89– 96.

[14] Bojan T., Zemichael F. W., Crudge P., G. C. Maitland, Hellgardt K. "Design of a novel flat-plate photobioreactor system for green algal hydrogen production". International journal of hydrogen energy, 2011, 36: 6578-6591.

[15] Azwar, M.Y., M.A. Hussain y A.K. Abdul-Wahab. "Development of biohydrogen production by photobiological, fermentation and electrochemicalprocesses: A review" Renewable and Sustainable Energy Reviews, 2014, (31) 158–173.

[16] Demirbas, A. Biohydrogen. En Demirbas. A., Biohydrogen for Future Engine Fuel Demands. Londres.Springer, 2009, 163-174.

[17] Yunez, A. "Implementación de un sistema híbrido Solar-Hidrógeno". Tesis Maestría en Tecnología Avanzada. CIITEC-IPN, 2016.

[18] Show, K.Y. Lee, D.J. Tay, J.H. Lin, C.Y. y J.S. Chang. International Journal of Hydrogen energy, 2012;. 37:15616-15631.

[19] Lehr, F. Morweiser, M. Rosello, S. R. Kruse, O. y C. Postens. Journal of Biotechnology, 2012, 162:89– 96.

[20] Torzillo A., Scoma A., Faralonia C., Enaa A., Johanningmeier U.. "Increased hydrogen photoproduction by means of a sulfur-deprived Chlamydomonas reinhardtii D1 protein mutant" International journal of Hidrogen Energy. 2008, 1-8.

XVI International Congress of the Hydrogen Mexican Society 2016

Design and Preparation of Electrodes by Alkaline Water Electrolyser for Production of Hydrogen and Oxygen.

S. Citalán-Cigarroa[1], O. Solorza-Feria[1]

[1]Depto. Química, Centro de Investigación y de Estudios Avanzados del IPN
Av. Instituto Politecnico Nacional # 2508
C.P. 07360, México D.F. México.
Tel : +5257473800 ext. 4473.
e-mail: scitalan@cinvestav.mx

ABSTRACT

Recent years have marked great interest in the production of hydrogen by alkaline water electrolysis (AWE). Hydrogen is an excellent energy carrier and is quickly becoming one of the best solutions for renewable energy generation. Nickel-cobalt nanoparticles with an atomic ratio of 1:1 were synthesized from elemental powders by mechanical alloying. The structural characterization and composition of the nanoparticles was conducted by X-ray diffraction and Scanning Electron Microscopy (SEM). An electrolyzer cell (20 cm^2 active area) was designed and constructed. The membrane used is anion exchange membrane (AEM) and was prepared using nanoparticles of NiCo as a cathode for hydrogen evolution reaction (HER), and nanoparticles of Co_3O_4 oxide as the anode for oxygen evolution reaction (OER). The analysis was carried out in a 1M KOH solution with the help of a d.c. galvanostatic electrochemical measurement technique. The electrochemical parameters were presented for the HER, OER, and the electrolysis performed.

Keywords: alkaline water electrolysis; anion exchange membrane; hydrogen; oxygen

XVI International Congress of the Hydrogen Mexican Society 2016

Nanostructured A-Zeolite Containing Rb^+ and Cs^+ Cations for CO_2/H_2 Separation: DFT Calculations

D. Barraza-Jimenez[1], M.A. Flores-Hidalgo[1], L.M. Pulido-Jaquez[1], M.A. Escobedo-Bretado[1], V. Collins-Martinez[2], A. Lopez-Ortiz[2]

[1] Facultad de Ciencias Químicas, Universidad Juárez del Estado de Durango, Av. Veterinaria S/N, Circuito Universitario, Durango, Dgo. México, C.P. 34120.
*Tel: +526181301120; e-mail: dianabarraza@ujed.mx
[2]Departamento de Ingeniería y Química de Materiales, Centro de Investigación en Materiales Avanzados, S.C., Miguel de Cervantes 120, Chihuahua, Chih., México, 31109.

Zeolites are sieve molecular type materials with high silica content or silica dioxide possess great potential for gases separation. These zeolites offer low cost and good H_2 selectivity due to their hydrophobic character. Separation due to size differences has better effectiveness potential at high temperature than in competitive adsorption. Within the more employed zeolites are type-A (LTA) with a pore diameter of 0.41 nm [1]. Theoretical and experimental studies have showed that incorporating extraframework cations affects supercavities accessibility, also these cations are required to balance the framework charge and may coordinate in the 8MRs (small pores in the structure, eightmembered rings which additional tri-dimensional typical zeolites framework) [3]. In this work we present an electronic structure study using Density Functional Theory (DFT). Our study started with geometric optimization for LTA structure, CO_2 and H_2 molecule, then we performed vibrational frequencies calculations and obtain the IR. After optimized geometry calculations, the energy barrier calculations show the energy profile for migration of a single cation where Rb^+ and Cs^+ were used. Theoretical method used B3LYP [2] functional and 6-311+G (d, p) basis set [4]. All calculations were carried out using program suite Gaussian 09 [5]. This computational study allows to identify the electronic structure behind CO_2/H_2 separation as a result in hydrogen bioproduction using cheese whey

---

Keywords: Keywords: nanostructured A-zeolite, DFT, CO_2/H_2 separation

References:

[1] Michalkiewicz, B; Koren, ZC; Zeolite membranes for hydrogen production from natural gas: state of the art. J Porous Mater 22 (2015) 635–646.
[2]. Becke, AD. Density-functional thermochemistry. III. The role of exact exchange. J. Chem. Phys. 98 (1993) 5648-52.
[3] Shang J, Li G, Singh R et al, Discriminative Separation of Gases by a “Molecular Trapdoor” Mechanism in Chabazite Zeolites . JACS. 134 (2012) 19246-19253
[4] McLean, AD. and. Chandler, GS. Contracted Gaussian-basis sets for molecular calculations. 1. 2nd row atoms, Z=11-18. J. Chem. Phys. 72 (1980) 5639-5648.
[5] Gaussian 09, Revision D.01, M. J. Frisch, et al. Gaussian, Inc., Wallingford CT, 2013.

Presenting author’s email:
dianabarraza@ujed.mx

Effect of operational perturbations on H_2 production in a microbial electrolysis cell: voltage and concentration variations

R. Cardeña[1], G. Buitrón[1]
[1]Laboratory for Research on Advanced Processes for Water Treatment, Instituto de Ingeniería, Unidad Académica Juriquilla, Universidad Nacional Autónoma de México, Querétaro, México
*Tel: +524421926165; e-mail: gbuitronm@iingen.unam.mx

***Abstract*— The biohydrogen yield can be increased when dark fermentation is coupled to microbial electrolysis cells (MEC). In this work we focused on the effect of variation of applied voltage and initial concentration on the performance of a single-chamber MEC. The substrate was a mixture of volatile fatty acids as produced in a dark fermentation effluent (30% acetate, 13% propionate and 57% butyrate respect to COD). The anode was made of graphite felt whereas the cathode was made of nickel foam. The experiment was conducted varying the applied voltage (Eap) (3 cycles per condition) following the next order: 0.5, 0.2, 0.5, 0.7 and 0.3 V, and maintaining the initial COD concentration constant at 2g/L. Another set of experiments were carried out varying the initial concentration at 0.6, 1.0, 2.0, 1.0 and 0.6 mg-COD/L, maintain the Eap constant at 0.5 V. High hydrogen production rates (up to 1.51 m3 H2/m3 -d) were observed. The H2 purity was 84%. No effect on the MEC performances was observed when the Eap was varied up to 0.5 V. At 0.7 the performance decreased. It was observed that the initial substrate had no significant effect of the MEC performances. It was found that the major effect is the operating time of the cell. For both cases, irrespectively of the initial condition the MEC performances decreased after 32 days. These low performances are result to the consumption of acetate and H2-produced by methanogenic microorganisms and is compounded by the oxidation of hydrogen at electrons in the anode leading to increased coulombic efficiencies (CE) over 100 %. All experiments presented a CE higher than 100% (151-541 %).**

***Keywords*—** *Microbial fuel cells; hydrogen; dark fermentation; perturbations*

Acknowledgment

The authors gratefully acknowledge the financial support of the project Fondo de Sustentabilidad Energética SENER-CONACYT, Clúster Biocombustibles Gaseosos, project 247006. Technical assistance of Gloria Moreno and Jaime Pérez is also acknowledged..

Influence of the irradiance intensity on a biofilm photobioreactor for hydrogen production

E. Guevara-López[1], A. Díaz[1], G. Buitrón[1]
[1] Laboratory for Research on Advanced Processes for Water Treatment, Instituto de Ingeniería, Unidad Académica Juriquilla, Universidad Nacional Autónoma de México, Blvd. Juriquilla 3001, Querétaro, Qro., México, 76230
Tel: +524421926165; e-mail: gbuitronm@iingen.unam.mx

***Abstract*—Purple non-sulfur (PNS) photosynthetic bacteria have been investigated widely to hydrogen production. It has been observed that the illumination conditions affect the hydrogen production. Furthermore, it has been observed that immobilization of bacteria helps to avoid inhibition effects and can increase hydrogen production. The objective of this work is to determine the influence of light intensity and the kind of light on the hydrogen production using an immobilized PNS consortium. Luffa fibers were used for support to immobilize the consortium. The light intensity experiments were carried out by using as substrate 1200 mg/L of acetic acid, 1571 mg/L of butyric acid and 715 mg/L of propionic acid. Two different lamps were used (tungsten and fluorescent) with continuous illumination at 90 and 125 W/m^2. It was observed that tungsten lamps at 125 W/m^2 promoted the highest hydrogen production (3709 mL H_2/L). Moreover, the highest yield (3.5 mol H_2/mol of VFA) was also obtained with this lamp. Hydrogen production was also evaluated with light/dark cycles of 12 h/12 h in a tubular reactor. It was possible to increase the light intensity up to 500 W/m^2 without a significant decrease of the hydrogen production rate.**

Keywords—Hydrogen, Rhodpseudomonas palustris, immobilized cells, light intensity.

I. INTRODUCTION

Photofermentation is mainly perform by Purple Non Sulfur Bacteria (PNSB), that include genera as *Rhodobacter and Rhodopseudomonas* [1]. This group of microorganism can produce hydrogen using light and a carbon source as Volatile Fatty Acids (VFA's) [1]. In the photofermentative process, hydrogen is produced mainly by the action of nitrogenase in conditions of absence of oxygen and molecular nitrogen [2]. The process also requires the synthesis of pigments: bacteriochlorophylls (absorbing to 590, 805, 855 and 875 nm) and carotenoids (absorbing to 450, 477 and 510 nm) [3]. Illumination conditions influence the synthesis of both, nitrogenase and pigments [3], [4].

The effect of the light source and light intensity on hydrogen production by photofermentation has been evaluated by different authors. In a study with *Rhodobacter sphaeroides*, different kind of lamps were tested [5] (tungsten, fluorescent, halogen and infrared) and it was found that halogen and fluorescent lamps allowed to reach hydrogen production rates (R_{max}) higher than the other lamps tested (8.7 and 6.3 mL H_2/L/h). Using tungsten lamps at 277 W/m^2, it was possible to reach a R_{max} of 33 mL/L/h from malate [6]. These lamps were also used by Lazaro et al. [7] with a mixed carbon source and a microbial consortium. A R_{max} of 24.6 mL H_2/L/h were reached to a light intensity of 276 W/m^2.

However, there are few studies evaluating the effect of these variables with microbial consortia and immobilized cells. Cell immobilization can help to increase hydrogen production [8]and microbial consortia may be useful for avoid sterilization [9]. The aim of this work is to determine the effect of the illumination source and light intensity on H_2 production and substrate consumption using an immobilized consortium of purple non-sulfur bacteria (PNS).

II. EXPERIMENTAL

A. Bacterial consortium and media

The hydrogen producing bacterial consortium was isolated from bioelectrochemial system. Three different species of PNSB were previously identified in the consortium (*Rhodopseudomonas palustris, Rubrivivax gelatinosus* and *Rhodobacter sphaeroides*) [10]. Bacteria were grown on basal medium used by Ying Li, et al. [11] and it was supplemented with sodium acetate (1480 mg/L), sodium butyrate (3300 mg/L) and sodium glutamate (370 mg/L). The initial pH was of 6.7. Oxygen in the cultures was displaced using vacuum. The cultures were conducted to 32±2°C with continuous incandescent illumination to 5 klux. The biomass was collected by centrifugation (Centrifuge Solbat C-40) to 3500 rpm for 15 min. Recovered cells were immobilized on luffa fibers according to Guevara-López and Buitrón [10].

B. Effect of the illumination conditions

Experiments to evaluate the hydrogen production, were done with the same basal medium described in the Section II.B. Carbon source consisted of 1640 mg/L of sodium acetate, 1960 mg/L of sodium butyrate and 930 mg/L of sodium propionate [9] and nitrogen source was sodium glutamate (1880 mg/L). Serum bottles of 120 mL were used as reactors. Bottles were filled with 90 mL of culture media and inoculated with 300 mg/L of SV as immobilized biomass. Oxygen was displaced by applying vacuum to the bottles. Cultures were conducted to 32±2°C. Two lamps were tested: fluorescent (peaks to 435, 488, 545 and 611 nm) and tungsten (continuous spectrum, 300-900 nm) to 90 and 125 W/m^2. Cultures were done in batch mode. Results of biogas produced were converted to standard temperature and pressure and fitted to Gompertz modified equation (1).

$$H = H_{max} \exp\left\{-\exp\left[\frac{R_{max} e}{H_{max}}(\lambda - t) + 1\right]\right\} \qquad (1)$$

where H (mL H_2/L) is the cumulative amount of hydrogen produced at culture time t (h), H_{max} (mL H_2/L) is the maximum amount of hydrogen produced, R_{max} (mL H_2/L/h) is the maximum hydrogen production rate and λ (h) is the lag phase time.

Additionally, hydrogen production was evaluated in a tubular reactor of 300 mL. Light/dark cycles of 12 h/12 h were used to simulate environmental conditions. Tungsten lamps were used and light intensity was increased to 333 and 500 W/m^2.

C. Analytical methods

Cell concentration, COD and biogas composition were measured as described by Guevara-López and Buitrón [10]. For pH measurement a pH meter (OAKTON 510, probe Orion 9156BNWP) and for light intensity a luxmeter (Extech LT300) and pH.

III. RESULTS

Table 1 shows the effect of light intensity and kind of light on H_{max}, R_{max}, the percentage of the Chemical Oxygen Demand removal (%COD_{rem}) and the yield (mol H_2/mol VFA) with the two kind of lamps and two light intensities. [3]. For fluorescent lamps, hydrogen production and hydrogen production rates were lower than they reached with tungsten lamps. The absorption spectrum of fluorescent lamps shows peaks near to 435, 488, 545 and 611 nm [3]. Hydrogen production can be related to the peaks of 435 and 438 nm, where carotenoid pigments show absorption peaks, too. However, tungsten lamps were more efficient to hydrogen production. The explanation of these results is that these lamps provide a continuous spectrum (300-900 nm) which covers the entire absorption spectrum of photosynthetic pigments for PNSB. With fluorescent and tungsten lamps, it was observed that when light intensity was increased, H_{max}, R_{max} and %COD_{rem} were improved. The production of hydrogen with tungsten lamps were four-fold than those achieved with fluorescent lamps. The highest yield (3.5 mol H_2/mol of VFA) was obtained with tungsten lamps to 125 W/m^2.

TABLE 1. HYDROGEN PRODUCTION AND SUSTRATE CONSUMPTION WITH FLUORESCENT AND TUNGSTEN LAMPS.

Lamp	**Fluorescent**		**Tungsten**	
Light intensity (W/m^2)	**90**	**125**	**90**	**125**
H_{max} (mL/L)	80	2666	3350	3709
R_{max} (mL/L/h)	0.5	2.92	11.4	11.9
%COD_{rem}	55	71	89.3	91.4
mol H_2/mol VFA	0.1	2.5	3.1	3.5

Results of hydrogen production and Gompertz fit in tubular reactor can be observed in Fig. 1. Gompertz parameters and yields are displayed in Table 2. It can be observed that H_{max} was similar for three light intensities tested. Nevertheless, R_{max} increased four times when light intensity increased from 125 to 333 W/m^2. It is important to note that the most of the studies report optimal light intensities for hydrogen production below 300 W/m^2 [5], [7]. The increase in light intensity is associated with photoinhibition [6]. Nevertheless, in this study there was no significant decrease in the hydrogen production rate between 333 and 500 W/m^2. The results suggest that immobilization can confer protection against photoinhibition. Being able to produce hydrogen at high intensities is an advantage considering that the aim is to produce hydrogen with sunlight, where the light intensity can reach 1000 W/ m^2.

Maximal hydrogen production yield was 2.2 mol H_2/mol VFA. The results are lower that the reached in serum bottles, however, in this case light/dark cycles were used.

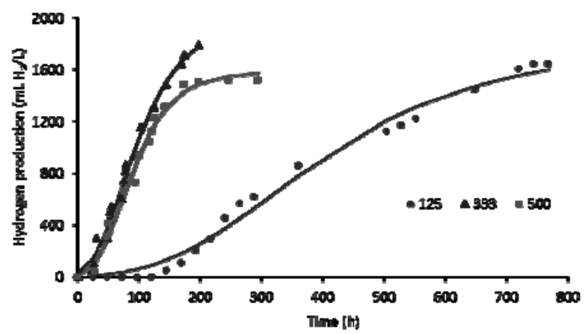

Fig. 1. Hydrogen production with tubular reactor and Gompertz fit.

TABLE 2. GOMPERTZ PARAMETERS AND YIELD IN TUBULAR REACTOR.

Light intensity (W/m^2)	**H_{max} (mL/L)**	**R_{max} (mL/L/h)**	**λ (h)**	**mol H_2/mol VFA**
125	1750	135	3.5	1.9
333	1940	22	14.1	2.2
500	1580	27	13.2	1.8

Several authors have reported higher hydrogen production rates than the values reached in this study [12], [7], [13], but those studies were mainly conducted with pure strains, requiring sterilization. It is impractical for actual applications. The use of a microbial consortium avoid sterilization. Furthermore, the immobilization permitted the recovery of the biomass and the production of hydrogen with high light intensity.

IV. CONCLUSIONS

The evaluation of the kind of light and light intensity showed that both factors have an effect on hydrogen production with the immobilized microbial consortium.

Tungsten lamps permitted to increase hydrogen production due to these lamps provided a continuous spectrum that cover the complete absorption spectrum of the pigments used for PNSB for hydrogen production. Maximal hydrogen production of 3709 mL H_2/L and hydrogen production rates of 11.9 mL H_2/L/h were obtained with tungsten lamps to 125 W/m^2. When hydrogen production was evaluated in a tubular reactor and light/dark cycles of 12 h/12 h, it was observed that hydrogen production rate was not severely affected when the light intensity was increased to 500 W/m^2. This shows that the immobilization can protect against photoinhibition and it is possible to produce hydrogen at high light intensities with the immobilized microbial consortium.

Acknowledgment

This research was supported through CONACYT CIENCIA BÁSICA, 251718. The authors are grateful to Jaime Perez and Dr. Isaac Monroy for the technical support and fruitful discussions.

References

[1] H. Sakurai, H. Masukawa, M. Kitashima, and K. Inoue, “Photobiological hydrogen production: Bioenergetics and challenges for its practical application,” *J. Photochem. Photobiol. C Photochem. Rev.*, vol. 17, pp. 1–25, Dec. 2013.

[2] N. Basak, A. K. Jana, D. Das, and D. Saikia, “Photofermentative molecular biohydrogen production by purple-non-sulfur (PNS) bacteria in various modes: The present progress and future perspective,” *Int. J. Hydrog. Energy*, vol. 39, no. 13, pp. 6853–6871, Apr. 2014.

[3] A. Adessi and R. De Philippis, “Photobioreactor design and illumination systems for H2 production with anoxygenic photosynthetic bacteria: A review,” *Int. J. Hydrog. Energy*, vol. 39, no. 7, pp. 3127–3141, Feb. 2014.

[4] J. Meyer, B. C. Kelley, and P. M. Vignais, “Effect of light nitrogenase function and synthesis in Rhodopseudomonas capsulata.,” *J. Bacteriol.*, vol. 136, no. 1, pp. 201–208, Oct. 1978.

[5] H. Argun and F. Kargi, “Photo-fermentative hydrogen gas production from dark fermentation effluent of ground wheat solution: Effects of light source and light intensity,” *Int. J. Hydrog. Energy*, vol. 35, no. 4, pp. 1595–1603, Feb. 2010.

[6] B. Uyar, I. Eroglu, M. Yücel, U. Gündüz, and L. Türker, “Effect of light intensity, wavelength and illumination protocol on hydrogen production in photobioreactors,” *Int. J. Hydrog. Energy*, vol. 32, no. 18, pp. 4670–4677, Dec. 2007.

[7] C. Z. Lazaro, M. B. A. Varesche, and E. L. Silva, “Effect of inoculum concentration, pH, light intensity and lighting regime on hydrogen production by phototrophic microbial consortium,” *Renew. Energy*, vol. 75, pp. 1–7, Mar. 2015.

[8] C.-Y. Chen and J.-S. Chang, “Enhancing phototropic hydrogen production by solid-carrier assisted fermentation and internal optical-fiber illumination,” *Process Biochem.*, vol. 41, no. 9, pp. 2041–2049, Sep. 2006.

[9] R. Cardeña, G. Moreno, I. Valdez-Vazquez, and G. Buitrón, “Optimization of volatile fatty acids concentration for photofermentative hydrogen production by a consortium,” *Int. J. Hydrog. Energy*, vol. 40, no. 48, pp. 17212–17223, Dec. 2015.

[10] E. Guevara-López and G. Buitrón, “Evaluation of different support materials used with a photo-fermentative consortium for hydrogen production,” *Int. J. Hydrog. Energy*, vol. 40, no. 48, pp. 17231–17238, Dec. 2015.

[11] R. Ying Li, T. Zhang, and H. H. P. Fang, “Characteristics of a phototrophic sludge producing hydrogen from acetate and butyrate,” *Int. J. Hydrog. Energy*, vol. 33, no. 9, pp. 2147–2155, May 2008.

[12] Y.-Z. Wang, Q. Liao, X. Zhu, R. Chen, C.-L. Guo, and J. Zhou, “Bioconversion characteristics of Rhodopseudomonas palustris CQK 01 entrapped in a photobioreactor for hydrogen production,” *Bioresour. Technol.*, vol. 135, pp. 331–338, May 2013.

[13] C.-Y. Chen, W.-B. Lu, J.-F. Wu, and J.-S. Chang, “Enhancing phototrophic hydrogen production of Rhodopseudomonas palustris via statistical experimental design,” *Int. J. Hydrog. Energy*, vol. 32, no. 8, pp. 940–949, Jun. 2007.

Mechanistic models for hydrogen production by photo-fermentation using an immobilized consortium of photobacteria

I. Monroy, G. Buitrón, E. Guevara
Laboratory for Research on Advanced Processes for Water Treatment, Unidad Académica Juriquilla.
Instituto de Ingeniería. UNAM
Querétaro, México
Boulevard Juriquilla 3001, 76230

***Abstract*— This research work addresses a set of mechanistic models that describe the hydrogen production through photo-fermentation with an immobilized consortium of purple non-sulfur bacteria and using either artificial or solar light sources. The first model is based on batch operation and using tungsten artificial light. Kinetic profiles obtained from this model fitted the corresponding experimental kinetics and therefore, this model on batch operation was extended to be used in outdoor solar light conditions. The corresponding kinetic parameters were obtained from experimental outdoor photo-fermentations and several simulations validated the constructed model. However, the time profiles suggested to pre-process the experimental data by taking into account only the light period so that both experimental and modeled kinetics were equivalent.**

Keywords*— *Mechanistic models; hydrogen production; outdoor photo-fermentation

I. Introduction

Hydrogen is a green fuel with the highest energetic content per weight that can be produced using renewable materials such as biomass [1-2] and water [3] and whose combustion only generates water without carbon-based emissions. These traits support the relevance to look for more sustainable processes to produce it in large scale.

Among biological processes, photo-fermentation can be found, which is mainly carried out by a group of purple-non-sulfur (PNS) bacteria, capable of converting volatile fatty acids (VFA's), organic acids and sugars into hydrogen with the aid of light energy [4].

It is still common to find in literature the use of pure cultures in hydrogen-producing fermentations, which is impractical in terms of wastewater treatment and energy cost. In contrast, mixed cultures or consortiums represent great advantages in these terms even though only few applications on the bio-hydrogen production have been reported [5-6]. Even less efforts have been made on investigating photo-bacteria consortium immobilization despite its advantage in terms of higher biomass concentrations, homogeneous light distribution [7], and higher H_2 productivities [8-9].

Modeling photo-fermentation and bioprocesses in general is a difficult task that is required in order to decrease experimental work that is time-consuming and costly [10]. In fact it has been documented as one of the most critical requirements for improving the ability to predict the hydrogen yield [11-12].

Mechanistic models are aimed to expressing the variation in substrate, biomass and product concentration through process time by differential equations. These equations involve kinetic parameters, already reported or calculated from experimental fermentations.

There are also several process variables that control the hydrogen production in photo-fermentation such as light source, light intensity, lighting protocol, temperature, pH, among others, which should be considered in the models.

Research about hydrogen production modeling by photo-fermentation is scarce. Most of the reported models are based on batch operation using artificial light source and pure cultures either suspended [10,13-14] or immobilized [15-16]. Only few are based on batch operation with mixed cultures [5-6,17], and most of them have been carried out with suspended cultures rather than with immobilized cells, which is still found in literature.

This work addresses the construction of mathematical models for hydrogen production through photo-fermentation with an immobilized PNS bacteria consortium and using either artificial or solar light. Batch model under solar light conditions will be further improved and used for developing a continuous model as future work.

II. Materials and Methods

In order to construct the different mechanistic models, several photo-fermentations were performed in a 400 mL tubular lab reactor irradiated with tungsten lamps as artificial light source at four light intensities (125.3, 333.3, 366.7 and 500 W/m^2), as well as with solar light in outdoor conditions. Simulations obtained from the constructed models were used to compare experimental kinetics.

A. *Experimental procedure*

A PNS bacteria consortium, composed mainly of Rhodopseudomonas palustris, was immobilized on luffa fiber and used as biological source in all the experimental fermentations. Initial concentration of volatile solids (VS) was 300 mg/L. Isolation and identification of the microbial consortium, as well as the culture medium preparation and immobilization, are described in a previous work [7].

The same basal medium for colonization was used as culture medium for this photo-fermentation, supplemented with acetic acid (1200 mg/L), butyric acid (1570 mg/L), propionic acid (720 mg/L) and sodium glutamate (1760 mg/L) according to Cardeña et al [18]. Fermentations were set up in a 400-mL tubular photo-bioreactor with 300 mL of culture medium. The reactor was illuminated with tungsten lamps (light efficacy of 15 lm/W) at four different light intensities: 125.3, 333.3, 366.7 and 500 W/m^2.

A lighting protocol of 12 h light/12 h dark cycles was applied and all the fermentations were replicated three times. Operating conditions were as follows: Initial pH of 6.7, average pH of 7.0 along fermentations, and 30±2°C. The highest hydrogen production among the four light intensities was obtained at 366.7 W/m^2 and then considered as the optimal light intensity for modeling purposes.

B. *Analytical methods*

Biogas production during all photo-fermentations was quantified by the water displacement method. Besides, the biogas composition was determined on a gas chromatograph (SRI 8610C) equipped with thermal conductivity detector (TCD) [19].

Using tungsten lamps, the light intensity was measured at the fermenter wall with a lux meter (Extech LT300), and the pH with a potentiometer (OAKTON 510, probe Orion 9156BNWP). Suspended cell concentration was determined by optical density at 660 nm using a spectrophotometer (HACH DR/2010) and the biomass attached to the support was determined by protein concentration [20].

COD was measured by the dichromate method, total sugars by phenol-sulfuric acid method [21], and ethanol, acetic acid, butyric acid and propionic acid concentrations measured by GC (Agilent Technologies 7890B).

C. *Batch mechanistic models*

First, a mathematical model for batch hydrogen production with an immobilized PNS bacteria consortium and artificial light provided by tungsten lamps was developed based on the Monod equations for batch fermentation [22-23], and the constructed model for the same bacteria consortium using fluorescent light [18].

In this study, one part of the experimental data using tungsten artificial light is extracted from the research work documented by Guevara-López and Buitrón in 2015 [7] so as to obtain the kinetic parameters for the batch photo-fermentation mechanistic model.

The reason to start with batch photo-fermentations and using tungsten light is because its absorption spectrum is the most resembled to the solar light spectrum, from 400 to 900 nm wavelength. In comparison to the tungsten light spectrum, sunlight intensity entails a wide wavelength range, from 400 to 1000 nm [24].

Therefore, the batch mechanistic model from using artificial light source could be extrapolated for sunlight in outdoor conditions, expecting that the resulting model simulates the corresponding experimental kinetics appropriately.

The differential equations for biomass (X), chemical oxygen demand (S), and product (P) concentration that represent the batch fermentation dynamics for hydrogen production are next presented.

$$\frac{dX}{dt} = \mu^* X \tag{1}$$

$$\frac{dS}{dt} = -\frac{\mu^* X}{Y_G} - m^* X \tag{2}$$

$$\frac{dP}{dt} = \alpha^* \frac{dX}{dt} + \beta X \tag{3}$$

Some kinetic parameters (marked with *) are modified by process variables such as temperature (T), pH and light intensity (I) according to Liao et al. [15].

The maximum specific growth rate (μmax) was calculated for the experimented light intensities and it was found a relationship between μmax and light intensity according to Equation 4. It is important to note that the μmax value in Equation 4 corresponds to the optimal light intensity (I_{op}) which was set to 366.7 W/m^2 (5500 lx) for tungsten light source, where the maximum hydrogen yield was obtained. Optimal values for T and pH (T_{op}, pH_{op}) were 303.15 K and 7.0 respectively according to literature [10,25-27].

$$\mu^*_{max} = \mu_{max} \times \exp\left[-0.324\left(\frac{I}{I_{op}} - 1\right)^2\right] \tag{4}$$

It has been investigated and proved that the dependency between the specific growth rate (μ*) and the maintenance coefficient (m*) with T and pH can be explained by the relationships reported by Liao et al., in 2011 [15], as it is shown in Equations 5 and 6, which also fitted the experimental data in this research work.

$$\mu^* = \frac{\mu^*_{max} S}{Ks + S} \times \exp\left[-10.8\left(\frac{pH}{pH_{op}} - 1\right)^2\right] \times \exp\left[-10.5\left(\frac{T}{T_{op}} - 1\right)^2\right] \tag{5}$$

$$m^* = m \times \exp\left[-2.8\left(\frac{I}{I_{op}} - 1\right)^2\right] \times \exp\left[-5.1\left(\frac{pH}{pH_{op}} - 1\right)^2\right] \times \exp\left[-4.5\left(\frac{T}{T_{op}} - 1\right)^2\right] \tag{6}$$

Besides, we found an expression that better fits the growth-associated kinetic parameter (α*) to light intensity (I) for the tungsten light source used in this work according to the Equation 7.

$$\alpha^* = 2.779E-06\, I^2 - 6.645E-04\, I + 0.0449 \times \exp\left[-21.2\left(\frac{pH}{pH_{op}} - 1\right)^2\right] \times \exp\left[-8.1\left(\frac{T}{T_{op}} - 1\right)^2\right] \tag{7}$$

The original kinetic parameters α and m were calculated experimentally, as Ks and μ_{max}, under the optimal conditions in this work, and the values for all the kinetic parameters are shown in Table 1.

TABLE I. KINETIC PARAMETERS FOR THE PHOTO-BACTERIA CONSORTIUM, DETERMINED EXPERIMENTALLY WITH DATA FROM GUEVARA-LÓPEZ AND BUITRÓN (2015) AND USED IN THE BATCH MECHANISTIC MODEL

Kinetic parameter	Unit	Parameter value
Ks (Monod constant)	g COD/L	0.077
μmax (Maximum growth rate)	h^{-1}	4.68 x10^{-3}
m (Maintenance coefficient)	gCOD/g biomass.h	7.7 x10^{-3}
α_{opt} (Growth-associated kinetic constant)	g hydrogen/g biomass	0.175
β (Non-growth associated kinetic constant)	g hydrogen/g biomass. h	6×10^{-4}
$Y_{X/S}$ (Observed biomass – substrate yield)	g biomass/g COD	0.17
Y_G (True yield)	g biomass/g COD	0.24
I_{opt} (Optimal light intensity)	W/m^2	366.7
T_{opt} (Optimal temperature)	K	303.15
pH_{opt} (Optimal pH)	-	7.0

Some of these values are close to the kinetic parameters reported by Zhang et al., 2015 [14] for a hydrogen production dynamic model with *Rhodopseudomonas palustris*, using glycerol as carbon source and an incandescent light source, which makes them more reliable and valid.

The resulting mechanistic model in Matlab was performed considering as input variables X_0= 0.3 g/L, S_0= 6.82 g/L and P_0= 0 g/L, and the optimal values for T, pH and I, previously mentioned and listed in the Tungsten light column from Table 1.

Next, a batch mechanistic model for photo-fermentations with solar light has been developed from the previous model for tungsten light. A preliminary simulation was run according to the initial conditions in the outdoor reactor (X_0= 0.3 g/L, S_0= 8.8 g COD/L).

III. RESULTS AND DISCUSSION

First of all, the batch-operating mechanistic model for hydrogen production by photo-fermentation with an immobilized consortium of PNS bacteria and using a tungsten artificial light was constructed. The kinetic parameters were determined experimentally and it was observed that the growth associated product constant (α) changed sharply when modifying the light intensity (I). Due to this dependency, a mathematical equation of α as function of I for the experimental range was fitted and taken into account in the product differential equation.

Figure 1 shows α value for three light intensities proved, as well as the equation that fits this range, from 125.3 W/m^2 (corresponding to a 1880 lx irradiance) to 500 W/m^2 (7500 lx).

Next, some simulations were run with the model encoded in Matlab under these conditions so that both experimental and modeled kinetics were compared. For this purpose, the hydrogen production time profile was plotted in mL of accumulated hydrogen per liter of culture, as depicted in Figure 2.

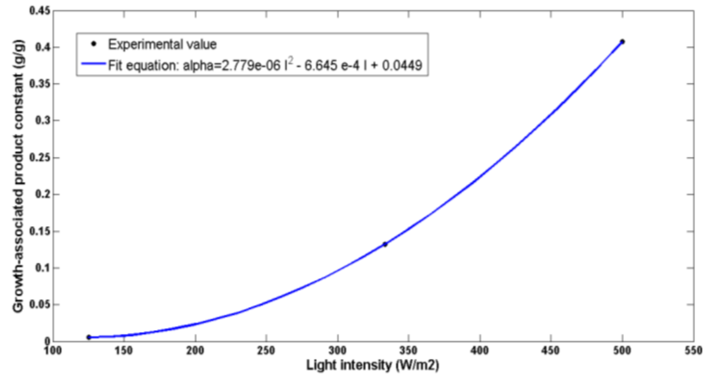

Fig. 1. Dependency of growth associated product constant (α) on light intensity (I) for tungsten lamps

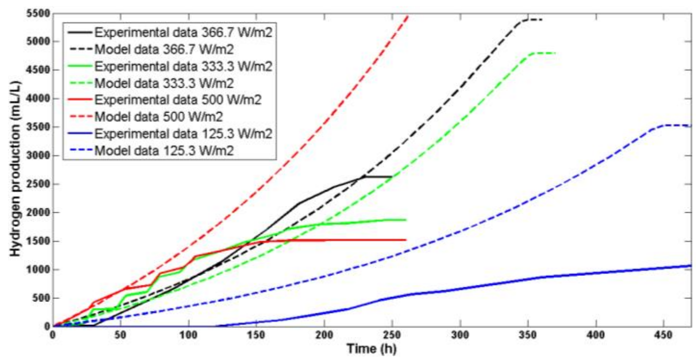

Fig. 2. Batch hydrogen production kinetics from all the experimental and modeled scenarios using tungsten lamps as artificial light source

First, it is observed that the maximum experimental hydrogen production was obtained at 366.7 W/m^2, which was then considered as the optimal light intensity in the maximum growth rate expression, as stated before. In contrast to the experimental kinetics, the modeled time-trajectory (black dash line) ended up at a higher hydrogen concentration, and the same situation occurred at 333.3 W/m^2 (green lines). Nevertheless, it is important to highlight that the model kept running up to the COD total consumption, which not necessarily has to occur in reality.

Time profiles for 500 W/m^2 were also similar even though the hydrogen production stopped after 150 hours of batch photo-fermentation. It is assumed that due to the high light intensity biomass increases quickly at the beginning, but at some point the immobilized biomass hinders the pass of light through the culture medium and hence the hydrogen production. This behavior has been explained and documented as an enzymatic capacity saturation of nitrogenase due to excessive production of ATP and Fd_{red} [24,28].

Furthermore, it is observed at 125 W/m^2 a close tendency during the first 300 hours ignoring the lag time in the experimental kinetics which is not considered in the model; nonetheless, after this period of time hydrogen production turned out out to be slow. Indeed, it has been documented that using acetate as substrate and a low light intensity with tungsten lamps (135 W/m^2 in the reported study) results in high polyhydroxybutyrate (PHB) accumulation with low hydrogen production [29], which explains the experimental behavior and the final COD concentration, which was around 1 g/L.

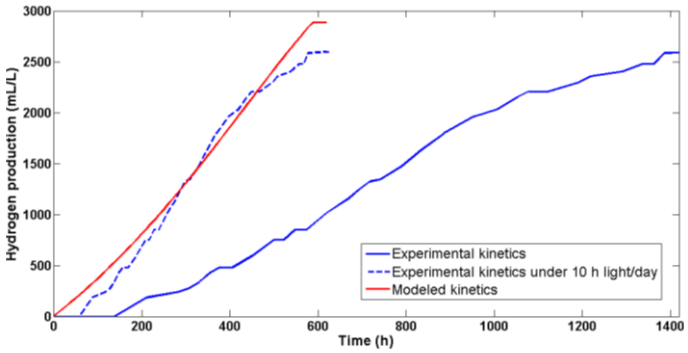

Fig. 3. Batch hydrogen production kinetics from both experimental and modeled scenarios using solar light source in an outdoor photobioreactor

Concerning the batch-operating mechanistic model for photo-fermentations with solar light, Figure 3 shows a comparison between the hydrogen production experimental kinetics and the simulated profile from the model. Specifically, the blue line shows the experimental kinetics.

In comparison, the proposed model is run at optimal light intensity (320 W/m^2) and the kinetics is depicted in black line. Final hydrogen concentration is close to the experimental concentration but obtained approximately at half of process time. For this reason, it was then considered a real period of 10 light hours from 24 hours a day in the experimental kinetics. The profile under this lighting protocol is shown in blue dash line and it is quite similar to the modeled kinetics.

It has been previously reported a study with *Rhodopseudomonas palustris* in a photo-bioreactor operated in alternating cycles of 10 h light/14 h dark in order to mimic the natural situation of sunlight irradiation with tungsten lamps at 50 W/m^2 [26], which supports this study.

IV. Conclusions

Batch mechanistic models for hydrogen production through photo-fermentation with both artificial and solar light and an immobilized consortium of PNS bacteria have been proposed and performed in this work.

A relationship between light intensity and the growth-associated product constant for tungsten artificial light was found and fitted through a mathematical equation, which was also applied to the batch model for solar light. Kinetics obtained from both models reveal their reliability when compared to the experimental kinetics.

Regarding to the solar batch model, preliminary results show that the model can fit the experimental kinetics by preprocessing the experimental data taking into account a cycle of 10 hours light/14 hours dark and running the model at optimal light conditions. Further improvements to this mechanistic model are being developed and the resulting research will be reported onwards.

Acknowledgments

Financial support from CONACYT through the National Postdoctoral Fellowship Program (2015-290941) is fully appreciated. This research has also been supported through the funded projects DGAPA-UNAM (PAPIITIT100113) and CONACYT (251718).

References

[1] I. K. Kapdan, F. Kargi, “Bio-hydrogen production from waste materials,” Enzym Microb Technology, vol. 38, pp. 569-582, 2006.

[2] X. M. Guo, E. Trably, E. Latrille, H. Carrère H, J. P. Steyer, “Hydrogen production from agricultural waste by dark fermentation: a review,” Int J Hydrogen Energy, vol. 35, 10660-73, 2010.

[3] J. R. Bartels, M. B. Pate, N. K. Olson, “An economic survey of hydrogen production from conventional and alternative energy sources,” Int J Hydrogen Energy, vol. 35, pp. 8371-84, 2010.

[4] C-Y. Chen, C-H Liu, Y-C Lo, J-S. Chang, “Perspectives on cultivation strategies and photobioreactor designs for photo-fermentative hydrogen production,” Bioresour Technol, pp. 102: 8484–92, 2011.

[5] W. JianLong, W. Wei, “The effect of substrate concentration on biohydrogen production by using kinetic models,” Sci. China Ser B: Chem, vol. 51, pp. 1110–1117, 2008.

[6] T. Assawamongkholsiri, A. Reungsang, “Photo-fermentational hydrogen production of *Rhodobacter sp. KKU-PS1* isolated from an UASB reactor,” Electronic Journal of Biotechnology, vol. 18, pp. 221-230, 2015.

[7] E. Guevara-López E, G. Buitrón, “Evaluation of different support materials used with a photo-fermentative consortium for hydrogen production,” Int J Hydrogen Energy, vol. 40, pp. 17231–17238, 2015.

[8] H. Argun, F. Kargi, “Bio-hydrogen production by different operational modes of dark and photo-fermentation. An overview,” Int J Hydrogen Energy, vol. 36, pp. 7443-7459, 2011.

[9] D. B. Levin, L. Pitt, M. Love, “Bio-hydrogen production: prospects and limitations to practical application,” Int J Hydrogen Energy, vol. 29, pp. 173-85, 2004.

[10] Y-Z. Wang, Q. Liao, X. Zhu, J. Li, D-J Lee, “Effect of culture conditions on the kinetics of hydrogen production by photosynthetic bacteria in batch culture,” Int J Hydrogen Energy, vol. 36, pp. 14004-14013, 2011.

[11] R. S. Prakasham, T. Sathish, P. Brahmaiah, “Imperative role of neural networks coupled genetic algorithm on optimization of biohydrogen yield,” Int J Hydrogen Energy, vol. 36, pp. 4332-9, 2011.

[12] N. Nasr, H. Hafez, M. Hesham El Naggar, G. Nakhla, “Application of artificial neural networks for modeling of biohydrogen production,” Int J Hydrogen Energy, vol. 38, pp. 3189-3195, 2013.

[13] J. Obeid, J-P Magnin, J-M Flaus, “Modelling of hydrogen production in batch cultures of the photosynthetic bacterium in batch cultures of the photosynthetic bacterium *Rhodobacter capsulatus*,” Int. J of Hydrogen Energy, vol. 34, pp. 180-185, 2009.

[14] D. Zhang, N. Xiao, K. T. Mahbubani, E. A. Del Rio-Chanona, N. K. H. Slater, V. S. Vassiliadis, “Bioprocess modelling of biohydrogen production by *Rhodopseudomonas palustris*: Model developmenr and effects of operating conditions on hydrogen yield and glycerol conversion efficiency,” Chemical Engineering Science, vol. 130, pp. 68-78, 2015.

[15] Q. Liao, D-M. Liu, D-D Ye, X. Zhu, D-J. Lee, “Mathematical modeling of two-phase flow and transport in an immobilized-cell photobioreactor,” Int. J of Hydrogen Energy, vol. 36, pp. I3939-I3948, 2011.

[16] C-L. Guo, H-X. Cao, H-S. Pei, F-Q. Guo, D-M. Liu, “A multiphase mixture model for substrate concentration distribution characteristics

and photo-hydrogen production performance of the entrapped-cell photobioreactor," Bioresource Technology, vol. 181, pp. 40-46, 2015.

[17] I. Monroy, E. Guevara, G. Buitrón, "A mechanistic model supported by data-based classification models for hydrogen production with an immobilized photo-bacteria consortium," unpublished.

[18] R. Cardeña, G. Moreno, I. Valdez-Vazquez, G. Buitrón, "Optimization of volatile fatty acids concentration for photofermentative hydrogen production by a consortium," Int J Hydrogen Energy, vol. 40, pp. 17212–17223, 2015.

[19] G. Buitrón, C. Carvajal, "Biohydrogen production from Tequila vinasses in an anaerobic sequencing batch reactor: Effect of initial substrate concentration, temperature and hydraulic retention time," Bioresour Technol, vol. 101, pp. 9071–9077, 2010.

[20] O. H. Lowry, N. J. Rosebrough, A. L. Farr, R. J. Randall, "Protein measurement with the Folin phenol reagent," J Biol Chem, vol. 193, pp. 265-275, 1951.

[21] M. DuBois, K. A. Gilles, J. K. Hamilton, P. A. Rebers, F. Smith. Colorimetric Method for Determination of Sugars and Related Substances," Anal Chem, vol. 28, pp. 350–356, 1956.

[22] J. M. Lee, Biochemical Engineering. New Jersey: Prentice Hall, 1992.

[23] M. L. Shuler, F. Kargi, Bioprocess Engineering. Basic Concepts. 2nd Edition. Saddle River, New Jersey: Prentice Hall, 2002.

[24] I. Akkerman, M. Janssen, J. Rocha, R. H. Wijffels, "Photobiological hydrogen production: photochemical efficiency and bioreactor design," Int J Hydrog Energy, vol. 27, pp. 1195-1208, 2002.

[25] H. Koku, I. Eroglu I, U. Gunduz, M. Yucel, L. Turker, "Kinetics of biological hydrogen production by the photoproduction bacterium *Rhodobacter sphaeroides O.U. 001*," Int J Hydrogen Energy, vol. 28, pp. 381-388, 2003.

[26] Y-Z. Wang, Q. Liao, X. Zhu, X. Tian, C. Zhang, "Characteristics of hydrogen production and substrate consumption of *Rhodopseudomonas palustris CQK 01* in an immobilized-cell photobioreactor," Bioresource Technology, vol. 101, pp. 4034-4041, 2010.

[27] X-Y Shi, W-W Li, H-Q Yu, "Optimization of H_2 photo-fermentation from benzoate by *Rhodopseudomonas palustris* using a desirability function approach," Int J Hydrog Energy, vol. 39, pp. 4244-4251, 2014.

[28] N. J. Kim, L. K. Lee, C. G. Lee, "Pigment reduction to improve photosynthetic productivity of *Rhodobacter sphaeroides*," J Microbiol Biotechnol, vol. 14, pp. 442–9, 2004.

[29] I. Ero-glu, A. Tabano_glu, U. Gündüz, E. Ero_glu, M. Yücel, "Hydrogen production by *Rhodobacter sphaeroides O.U. 001* in a flat plate solar bioreactor," Int J Hydrogen Energy, vol. 34, pp. 180-5, 2008.

Biohydrogen production from wine vinasses by dark fermentation: effect of substrate concentration and pH

B. A. Albarrán-Contreras[1], J. Carrillo-Reyes[1], G. Buitrón[1]
[1]Laboratory for Research on Advanced Processes for Water Treatment, Instituto de Ingeniería, Unidad Académica Juriquilla, Universidad Nacional Autónoma de México, Querétaro, México
*Tel: +524421926165; e-mail: gbuitronm@iingen.unam.mx

***Abstract*— Vinasses are an acidic effluent from the wine industry, with a high content of organic matter and nutrients. Vinasses could be an environmental concern if these are disposed without any treatment. In this work for the first time, the energetic valorization of wine vinasses was evaluated as a potential substrate for the biological hydrogen production. Because of the high organic content and acidic pH of vinasses, the effect of initial pH values of 5 and 6, as well as chemical oxygen demand (COD) values ranging from 4 to 50 g/L, were tested in batch assays. The best hydrogen potential was obtained at an initial pH value of 6 and a COD concentration of 50 g/L, producing 26 mL H2 in a working volume of 80 mL. Regarding the pH, the initial value of 6 doubled the hydrogen obtained at pH of 5. Even though the hydrogen potential increased in response of the COD increments, the best yield was observed at 10 g COD/L, achieving a maximum value of 2 mL H2/g CODinitial. Hydrogen molar yields range from 1.0 – 1.5 mol H2/mol hexoseconsumed, indicating that hydrogen was produced only by the soluble sugars fermentation. At the end of hydrogen production batch assays, the volatile fatty acids concentrations yield were around 0.5 g CODequivalent/g CODinitial. This value indicates that dark fermentation played a stabilization role in the vinasses fermentation. The present work demonstrates the potential valorization of wine vinasses, by biohydrogen production. Indeed, the effluent generated by vinasses fermentation has an ideal composition for a subsequent energy production, either more hydrogen or methane.**

Keywords—Hydrogen, Batch tests; biohydrogen; dark fermentation; wine vinasses.

ACKNOWLEDGMENT

The authors gratefully acknowledge the financial support of the projects Fondo de Sustentabilidad Energética SENER-CONACYT, Clúster Biocombustibles Gaseosos, project 247006 and CONACYT 255537. Technical assistance of Gloria Moreno, Jaime Pérez and Karen Daniela Ramírez Martínez is also acknowledged.

$W_{1-X}Mo_xO_3 \cdot 0.33H_2O$ semiconductor oxides for photocatalytic H_2 production: A physical approach

A. Arzola-Rubio, B. González-Raigoza, F. Paraguay-Delgado, V. Collins-Martínez*
Laboratorio Nacional de Nanotecnología
Centro de Investigación en Materiales Avanzados, S. C.,
Chihuahua, Chih., México
*email:virginia.collins@cimav.edu.mx

J. Camarillo-Cisneros
Facultad de Medicina
Universidad Autónoma de Chihuahua
Chihuahua, Chih., México.

***Abstract*—A series of solid solutions of $W_{1-X}Mo_xO_3 \cdot 0.33H_2O$ (X = 0, 5, 10, 15, 20, 25, 50, 75 and 100%) semiconductor oxides were synthetized by conventional hydrothermal techniques. The compounds were characterized by transmission electron microscopy, scanning electron microscopy, X-ray diffraction, RAMAN spectroscopy and UV-Vis spectroscopy. These oxides were evaluated photocatalytically for hydrogen production using a photo reactor, a mercury lamp and a gas chromatograph. The $W_{0.25}Mo_{0.75}O_3$•$0.33H_2O$ (WM75) compound shows the highest hydrogen production of 20 µmoles H_2/g_{cat}. Additionally, through a theoretical study of all chemical compositions employing first principles and in a framework of DFT calculations; the WM75 compound demonstrated the highest activity. Both experimental and theoretical results categorized the compounds as indirect semiconductor; however, this conclusion was against measures obtained by ultra violet spectrum radiation which categorizes as direct semiconductors. We explained the switch from direct/indirect nature of the material at the moment of photocatalytic activity due to highest quantity of free-states available; showed by density-of-state diagram.**

Keywords—Band-structure,Crystallography, Optical properties, Band gap tunable, Hydrogen

I. INTRODUCTION

Metal-oxide semiconductors could be utilized in a widespread assortment of functions counting photocatalytic degradation of organic molecules and gas checking [1, 3].

Tungsten oxide-based compounds, counting tungsten oxides and tungsten oxide hydrates have been placed as photocatalytic compounds for the degradation of organic disposal water and highly susceptible compounds for the diagnosis of both reducing and oxidizing gases [4, 6].

Metallic oxide WO_3 with a low energy gap (e.g., Eg ≈ 2.6 eV for monoclinic WO_3) [2] offers the chance to collect visible light [2, 8, 9]. WO_3 has been employed for the photocatalytic degradation of organic compounds, such as methyl orange using visible light irradiation [7, 8]. Nevertheless, pure $WO_3 \cdot 0.33H_2O$ is not an effective photocatalyst because of its quite low conduction band level (0.5 V vs NHE, normal hydrogen electrode).

This is because most of the available states are at 4 eV, which is at the UV region.

II. EXPERIMENTAL

For this synthesis it used Ammonium Heptamolybdate Tetrahydrate ($(NH_4)_6Mo_7O_{24}$•$4H_2O$), Ammonium Metatungstate Hydrate ($(NH_4)_6H_2W_{12}O_{40}$•xH_2O), Hydrogen peroxide (H_2O_2, 30 wt.%), and Nitric acid (HNO_3, 70 wt.%).

The solutions ‘‘x’’ mmol (x = 0, 2.5, 5.0, 7.5, and 10.0 of Ammonium heptamolybdate tetrahydrate and 10-x mmol of Ammonium metatungstate hydrate) are determined for the synthesis technique. All the precursors and solvents for the method technique were incorporated in a mixture of 21 ml of tridistilled H_2O, 9 ml of 30 wt.% H_2O_2, and 3 ml of 2.2 M HNO_3. Then all content was moved into a Teflon vial and placed in a stainless-steel autoclave, sealed and hydrothermally treated at 180°C for 24 h. The final product was gathered via centrifugation, decanted and centrifuged again twice, and finally dried over a hot plate at 100°C. The resultant products with x = 0, 2.5, 5.0, 7.5, and 10.0 are designated as WO_3•$0.33H_2O$ (WH_1), $W_{0.75}Mo_{0.25}O_3$•$0.33H_2O$ (WM25), $W_{0.50}Mo_{0.50}O_3$•$0.33H_2O$ (WM50), to $W_{0.25}Mo_{0.75}O_3$•$0.33H_2O$ (WM75), and MoO_3•$0.55H_2O$ (MH_1).

Raman spectroscopy was done using Micro RAMAN Labram VIS-63 operated at room temperature; with a 632.8 nm wavelength standard He–Ne laser. The UV–Vis diffusive reflectance spectra (DRS) were obtained on a Lambda 10 UV–Vis spectrometer. All ab initio calculations were performed using the Quantum Espresso code in the frame-work of density functional theory (DFT). Due to the known band gap sub estimation in DFT treatments [10, 11] (by the presence of ‘‘d’’ orbitals in W and Mo atoms) DFT + U method was employed. The models for calculating WH1 and MH1 oxides were used to reduce the unit cells from conventional to primitive, while the solid solutions WM25, WM50 and WM75 were calculated by means of 2x2x1 supercells. In all systems, the hydrated unit cell, was employed (to XRD pattern fitting and to DFT calculations), however, in both theoretical approach the presence of H atoms were excluded.

III. RESULTS AND DISCUSSION

The optical properties of all compounds were analyzed from their DRS. In Fig. 1, it is observed that as Mo substitutes W, this makes the materials´ reflectance edge substituted with molybdenum (WM25, WM50 and WM75) that absorbed in the UV region (250-390 nm), now move to the visible area of electromagnetic light spectrum around 440 nm (Fig. 1-a). The shifts are from the UV to the visible light spectral region and can be attributed to the Mo substitution of W. The effective reduction in the band gap (BG) of these solid solutions was then ascertained due to the incorporation of Mo. Figure 1-b show the band gap of the as-synthetized samples. For the energy gap calculation of the synthesis techniques, $[F(R)h\nu]n$ is placed against hν. For materials with indirect gap such as $W_{1-x}Mo_xO_3$•$0.33H_2O$, the value n has to be 1/2 or n = 2 for direct gap.

To get the energy gap values, a tangent line has to be placed on the rectilinear zone of $[F(R)h\nu]^{1/2}$ against hν axis at $[F(R)h\nu]^{1/2} = 0$. In the crystal lattice of the host structure, WO_3•$0.33H_2O$, the electronic shift occurs from VB to CB. Effects for the compounds $W_{1-x}Mo_xO_3$•$0.33H_2O$ are quite comparable to the crystal host (WO_3•$0.33H_2O$) only that they display extra activity in the visible area (~400 nm). As the Mo atoms start to substitute the W atoms, a substantial shift is detected (matched with the crystal host WO_3•$0.33H_2O$), pointing out a contraction of the energy gap. With the controlled and percentual substitution of W atoms by Mo atoms (25, 50, and 75 %), important displacements in direction to the visible area can be noticed. For x = 25, 50, and 75%, the energy gaps of the hydrothermal compounds are 2.37, 2.35, and 2.15 eV. The MH1´s energy gap (2.25eV), does not follow the behavior of the W1-xMoxO3•0.33H2O compounds because of their crystal lattice structural differences. The DRS results clearly demonstrate the importance of the crystalline phase in exploring the configuration-property relationship of the solid solution $W_{1-x}Mo_xO_3$ materials and the successive shifting in the energy gap values. Consequently, this demonstrate that band gap can be adjusted for precise applications by varying the Mo content on the compound.

Fig. 2 (Raman) reveals that all solid solutions (all Raman bands were normalized), except MH1, displays two strong bands at 720 and 813 cm^{-1} and one medium band at 280 cm^{-1} and one weak band positioned at 336 cm^{-1}.

There are weak peaks at 450 and 1000 cm^{-1}. The two strong bands situated at 720 and 813 cm^{-1} are related to stretching vibrations ν(W-O-W) of the bridging oxygen atoms.

The band at 336 cm^{-1} is typical of ς(O-W-O) deformation mode, and the weak band at 1025 cm^{-1} can be associated to the stretching mode of the terminal W=O double bond [12]. As a result, the compounds having X = 0.25, 0.50, and 0.75 (WM25, WM50 and WM75 are relatively comparable to the X = 0 (WH1), the Raman spectra demonstrate structural comparison of these compounds.

After Mo substitutes W in the host crystal structure, there is a change in the location of some peaks. The signals positioned at 720 and 813 cm^{-1} slowly change to 750 and 845 cm^{-1}. Simultaneously, these bands grew broader, that could be because of either disarrangement or loss of enlarged area translational periodicity (of high atomic number atoms). For MH1 the characteristic Raman signals of MoO_3•$0.55H_2O$ are at magnitude of 200–1000 cm^{-1}. At 900 and 1000 cm^{-1} two weak signals can be detected, that correspond to ν(O=Mo=O) and ν(Mo=O) stretching. The peak located at 700 cm^{-1} could belong to ν(OMo2) and ν(OMo3). The signals positioned at 400 and 500 cm^{-1} could belong to deformation modes. Also the signal at 340 cm^{-1} belongs to a ν(Mo-OH2) stretching. Under 300 cm^{-1}, there are signals that correspond to deformation and lattice modes. Nano size effects like phonon confinement, strain and non-stoichiometry can add up to the detected adjustments in Raman bands profile [13]. As Mo atoms in the host structure are substituting W atoms, the Raman mode is being moved to bigger frequencies for both methods. Their line thickness turned broader and symmetrical, therefore corroborating that the fractional addition of Mo get to grain increase in grain size and improved arranged structure.

The photocatalytic activity evaluation of the compounds was monitored through the evolution of the hydrogen produced by the dissociation reaction of the water molecule via photocatalysis. There was very little production of hydrogen and we believe that is because of the nature of WO_3 itself.

We found reports that have shown that WO_3 is a visible light responsive photocatalyst with a relatively narrow band-gap energy and a VB potential similar to that of TiO_2 [14].

However, pure WO_3 is not an efficient photocatalyst because of its low CB level, which limits the photocatalyst's ability to react with electron acceptors such as oxygen [15].

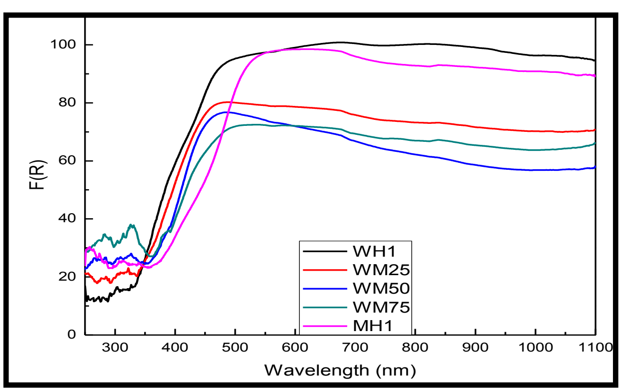

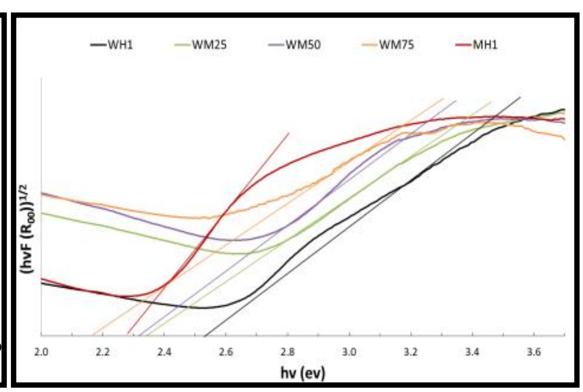

Fig. 1. a) DRS of hydrothermal and MW compounds. b) Tauc plot of all compounds were a tangent line is drawn to get the energy gap values.

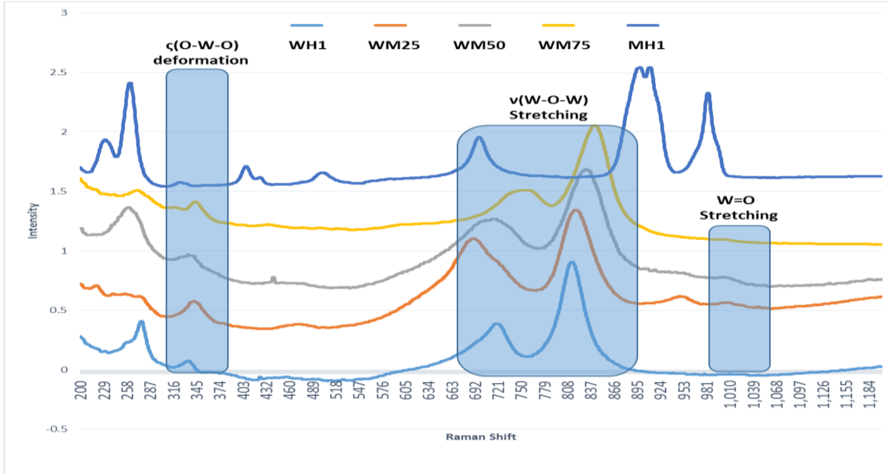

Fig. 2. Raman bands of hydrothermal synthesis.

TABLE I. H_2 PRODUCTION THROUGH PHOTOCATALYTIC DISSOCIATION WATER MOLECULE UNDER MERCURY LIGHT (250W)

Compound	Surface area	µmoles H_2/gcat	µmoles H_2/m^2
WM25	46	11	2.3
WM50	40	15	3.7
WM75	15	20	13
MH1	1	5	5
Ag-TiO2	140	180	13

A comparison among previous publications by us [16] in which the hydrothermal method was employed, it revealed a clear tendency in lattice parameters compared to microwave method.

For compound WH1, all three-cell lattice parameters are smaller, in contrast to the 0.5 and 0.75 doping samples where all parameters are higher and close similar to 0.25 Mo. We created a DFT model starting from Rietveld lattice parameters, and then a quasi-harmonic method was employed to optimize DFT lattices. As expected, DFT results were close similar to previously calculated hydrothermal method [16], with an electronic gap in the range of 0.44 eV and metallic character equal to MH1, contrary to experimental results. We systematically tested Coulomb potential values by the Hubbard method determining U = 9 eV to be comparable with experimental values. The gap tendency decreases function of the Mo amount, obtaining 2.63 eV for WH_1, 2.26 eV for WM25, 2.04 eV for WM50 and 1.98 eV for WM75 and indirect gaps employing hydrothermal synthesis. Mo positions it was not defining gap values, this was concluded after several tested configurations. Fig. 3 concentrate the densities of state of DFT computational models for compounds synthetized by hydrothermal method.

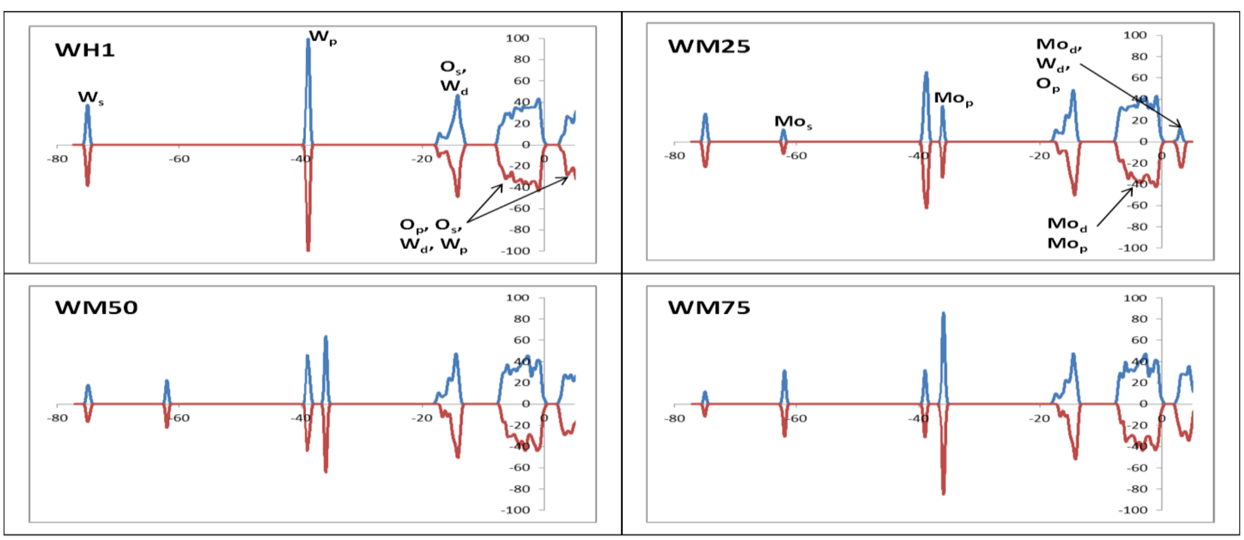

Fig. 3. Density of states for WH1 to WM75 tungsten compositions. The presence of Mo create states at low energies at -60 and -38 eV due to orbitals Mos and Mop, respectively. Greater the number of Mo the electronic gap is reduces from 2.26 eV to 1.98 eV for the compound synthesized by hydrothermal method
.

The presence of the Mo in the chemical composition replaces W atoms within the crystal and creates additional bands or states around -60 and -38 eV due to s and p orbitals. The presence of Mo practically eliminates the contribution of Os and Wp orbitals from conduction bands, leaving just Mod, Wd and Op. The decrease of available states provided by W atoms in d orbital is the reason why the electronic gap reduces proportional to the quantity of W atoms.

IV. Conclusion

With the hydrothermal method, it was possible to obtain a series of solid solutions with controlled Mo content (0, 25, 50, 75 and 100%).

The compound that showed the most H_2 production was compound WM75 but low in comparison with photocatalyst Ag/TiO_2.

It can be observed that as the molybdenum percentage increment, the energy gap of the compounds decreased from 2.55 to 2.15 eV. DFT + U studies demonstrated that gap decrease was because additional bands under conductions level of the initial WO_3•$0.33H_2O$ material.

According to our experimental data, all compounds should have activity in the visible area (approx. 400 to 760nm) because of their gap energy of 2.63 to 1.98 eV, but theoretical data proves that all compounds have activity in the UV region since they have a large quantity of available states suited at 4 eV.

This approach could explain the behavior of this type of materials that although possessing the energy gap suited at the visible region, the available states at the UV region make these compounds work at that region.

References

[1] Zeng J, Hu M, Wang W, Chen H, Qin Y. Sens Actuators B 2012;161:447–52.

[2] Tong H, Ouyang S, Bi Y, Umezawa N, Oshikiri M, Ye J. Adv Mater 2012;24:229–51.

[3] Kowsari E, Ghezelbash MR. Mater Lett2012;68:17–20.

[4] D'Arienzo M, Armelao L, Mari CM, Polizzi S, Ruffo R, Scotti R, et al. JAmChem Soc 2011;133:5296–304.

[5] Xie Z, Zhu Y, Xu J, Huang H, Chen D, Shen G. Chem Eng Commun 2011;13:6393–8.

[6] He X, Hu C, Yi Q, Wang X, Hua H, Li X. Catal Lett 2012;142:637–45.

[7] Jiao, Z. H.; Wang, J. M.; Ke, L.; Sun, X. W.; Demir, H. V. ACS Appl. Mater. Interfaces 2011, 3, 229.

[8] Li, L.; Krissanasaeranee, M.; Pattinson, S. W.; Stefik, M.; Wiesner, U.; Steiner, U.; Eder, D. Chem. Commun. 2010, 46, 7620.

[9] Bamwenda, G. R.; Arakawa, H. Appl. Catal., A 2001, 210, 181.

[10] J. Ruiz-Fuertes, S. Lopez´-Moreno, J. Lopez-Solano, D. Errandonea, A. Segura, R. Lacomba-Perales, A. Munoz, S. Radescu, P. Rodriguez-Hernandez, M. Gospodinov, L. Nagornaya, C. Tu, Phys. Rev. B 86 (September) (2012) 125202.

[11] V. Panchal, D. Errandonea, A. Segura, P. Rodriguez-Hernandez, A. Muñoz, S. Lopez-Moreno, M. Bettinelli, J. Appl. Phys. 110 (2011).

[12] Ph. Colomban, Stress- and nanostructure-imaging of ceramic fibers and abradable thermal barrier coatings by Raman microspectrometry: state of the art and perspectives, Ceram. Eng. Sci. Proc. 21 (2000) 143.

[13] E. Spanier, R.D. Robinson, F. Zhang, S.W. Chan, I.P. Herman, Phys. Rev. B 64, 245407 (2001)

[14] M. Miyauchi, M. Shibuya, Z. G. Zhao and Z. Liu, J. Phys. Chem. C, 2009, 113, 10642.

[15] M. Miyauchi, Phys. Chem. Chem. Phys., 2008, 10, 6258.

[16] A. Arzola-Rubio, J. Camarillo-Cisneros, L. Fuentes-Cobas, V. Collins-Martı´nez, L. De la Torre-Sa´enz, F. Paraguay-Delgado, Superlattices Microstruct. 81, 175–184 (2015).

XVI International Congress of the Hydrogen Mexican Society 2016

Excited States of Cyanidin as Dye Sensitizer on Small TiO_2 Nanoclusters Used as Photocatalyst in Hydrogen Production: A DFT Study

M.A. Flores-Hidalgo[1], D. Barraza-Jiménez[1], M.A. Escobedo-Bretado[1] V. Collins-Martinez[2], A. López Ortiz[2]

[1] Universidad Juárez del Estado de Durango, Facultad de Ciencias Químicas, Av. Veterinaria S/N, Circuito Universitario, Durango, Dgo. México, C.P. 34120. *Tel: +526181881941; e-mail: maflores.hidalgo@gmail.com

[2] Centro de Investigación en Materiales Avanzados, S.C., Departamento de Ingeniería y Química de Materiales, Miguel de Cervantes 120, Chihuahua, Chih., México, 31109.

ABSTRACT

Based in prior work within our research team, we use anthocyanidin molecule cyanidin as a pigment water soluble widely distributed in plants interacting with $(TiO_2)_n$ nanoclusters. Using our prior results with nanostructures formed with pristine cyanidin and $(TiO_2)_n$ we gathered data about ground states. Using these basis we carry out a study involving these same nanostructures to compute excited state energies, as well as absorption wavelength using Time Dependent-Density Functional Theory (TDDFT) for both nanostructures in its pristine form and also for the different variants formed by one out of four nanoclusters, in particular, when there is interaction with cyanidin. All calculations were developed using DFT theoretical methods performed at the Gaussian09 programs suite. Ground states calculations for pristine nanoparticles, including geometries, atomization energies, HOMO-LUMO and other properties, were obtained using B3LYP/6311+G(d, p). For the emission wavelength, the excited state geometry optimization was carried out with Hartree–Fock Configuration Interaction Singles (HF/CIS). Our theoretical results are new data related to the geometry as well as to the spectral absorption/emission properties of the proposed nanostructures. These cluster variants present features interesting for solar technology and optical applications. Our work generates data to learn more about the interaction of cyanidin with $(TiO_2)_n$ nanostructures which is a topic of interest for the application of natural dyes in solar cells and photocatalysis.

Keywords: Titanium dioxide nanoclusters, cyanidin, photocatalysis, hydrogen generation

A Photocatalyst Based in Pelargonidin 3-Glucoside as Dye Sensitizer on Small TiO_2 Nanoclusters

M.A. Flores-Hidalgo[1], D. Barraza-Jiménez[1], L.F. Lozano-Silva[1], M.A. Escobedo-Bretado[1] V. Collins- Martinez[2], A. López Ortiz[2]

[1] Universidad Juárez del Estado de Durango, Facultad de Ciencias Químicas, Av. Veterinaria S/N, Circuito Universitario, Durango, Dgo. México, C.P. 34120. *Tel: +526181881941; e-mail: maflores.hidalgo@gmail.com
[2] Centro de Investigación en Materiales Avanzados, S.C., Departamento de Ingeniería y Química de Materiales, Miguel de Cervantes 120, Chihuahua, Chih., México, 31109.

ABSTRACT

Anthocyanins are pigments water soluble widely distributed in plants that may appear in different colors. These natural colorants have become a subject of great interest experimentally and theoretically. We use pelargonidin 3-glucoside $(C_{21}H_{21}O_{10})^{+}$, commonly known as pelargonidin, a known anthocyanin, as a sensitizer on four small $(TiO_2)_n$ nanoclusters with (n=2-5) reported stable. Results reported by other teams related to our nanoclusters and dye selection are compared with our results for the individual particles. Our contribution relies in the study of the interaction between pelargonidin and the nanoclusters aimed to understand their electronic structure using DFT methods. Pelargonidin is known for its orange or red colors in some flowers and fruits and may benefit $(TiO_2)_n$ nanoclusters properties for solar technology applications. DFT theoretical calculations were performed in the Gaussian09 programs suite. Pelargonidin as a (+1) cation initial structure as well as $(TiO_2)_n$ nanoclusters were relaxed using B3LYP/6311+G(d, p). DFT calculations include geometry, vibrational frequencies and atomization energies and HOMO-LUMO parameters for the individual pelargonidin and nanoclusters. Conceptual DFT was used for individual particles to calculate ionization potential, electronic affinity, softness, hardness, and Fukui functions. The reactive sites of the individual particles were used to define how the particles can interact better during the docking process. Four nanostructures were formed with pelargonidin and a particular variant out of four $(TiO_2)_n$ nanoclusters. To simulate the interaction, the structures were located at different distances between 1.8-3 Å and performed geometric optimization and vibrational frequency calculations. Atomization energy and HOMO-LUMO parameters were calculated for each one of these nanostructures with the interacting particles. This work intends to generate data so we learn more about the interaction of anthocyanins, particularly pelargonidin, with $(TiO_2)_n$ nanostructures which is a topic of interest for the application of natural dyes in renewable energy and photocatalysis.

Keywords: Titanium dioxide nanoclusters, pelargonidin, photocatalysis, hydrogen generation

XVI International Congress of the Hydrogen Mexican Society 2016

TiO_2 Nanostructures with Sulfur Substitution and Sensitization with Pelargonidin for Hydrogen Generation Employing DFT

M.A. Flores-Hidalgo[1], D. Barraza-Jiménez[1], L.E. Vargas-Durón[1], M.A. Escobedo-Bretado[1] V. Collins- Martinez[2], A. López Ortiz[2]

[1] Universidad Juárez del Estado de Durango, Facultad de Ciencias Químicas, Av. Veterinaria S/N, Circuito Universitario, Durango, Dgo. México, C.P. 34120. *Tel: +526181881941; e-mail: maflores.hidalgo@gmail.com
[2] Centro de Investigación en Materiales Avanzados, S.C., Departamento de Ingeniería y Química de Materiales, Miguel de Cervantes 120, Chihuahua, Chih., México, 31109.

ABSTRACT

Small $(TiO_2)_n$ nanoclusters with (n=2-5) used in prior research within our team were optimized using Density Functional Theory (DFT) and a sulfur atom was introduced on the nanostructure in substitution of oxygen. Sulfur addition has been reported as a photocatalytic activity increase material when added as dopant in TiO_2. The nanoclusters with sulfur substitution were sensitized with pelargonidin 3-glucoside, common name pelargonidin, which is a known anthocyanidin dye. Pelargonidin is an interesting dye due to their natural properties in colors such as red and orange. DFT theoretical calculations were performed in the Gaussian09 programs suite. Atomization energy and HOMO-LUMO parameters are calculated for as a (+1) cation using as well as for $(TiO_2)_n$ with B3LYP/6-31+G(d,p). $(TiO_2)_n$ nanostructures and S-TiO_2 structures atomization energies and HOMO-LUMO parameters were calculated using the same theory level. Conceptual DFT was used for individual particles to calculate ionization potential, electronic affinity, softness, hardness, and Fukui functions. Our contribution within this work relies in the substitution with sulfur on TiO_2 nanoclusters and the interaction between pelargonidin and the S-TiO_2 structures. Reactive sites were used to understand how the particles can interact better. Several cluster variants were built depending on the symmetry and oxygen location to develop the sulfur substitution and then we carried out the interaction between pelargonidin and S-TiO_2 structures. Individual nanoparticles were located at different distances each time and performed geometric optimization and vibrational frequency calculations. This work intends to generate data so we learn more about the interaction of pelargonidin with S-TiO_2 nanostructures which is a topic of interest for the application of natural dyes in renewable energy and photocatalysis.

Keywords: Titanium dioxide nanoclusters, pelargonidin, photocatalysis, hydrogen generation

Photocatalytic Properties of TiO_2 Nanostructures Sensitized with Delphinidin 3-Glucoside for Hydrogen Generation: A DFT Study

M.A. Flores-Hidalgo[1], D. Barraza-Jiménez[1], A.Carrasco-Estrada[1], M.A. Escobedo-Bretado[1] V. Collins- Martinez[2], A. López Ortiz[2]

[1] Universidad Juárez del Estado de Durango, Facultad de Ciencias Químicas, Av. Veterinaria S/N, Circuito Universitario, Durango, Dgo. México, C.P. 34120. *Tel: +526181881941; e-mail: maflores.hidalgo@gmail.com
[2] Centro de Investigación en Materiales Avanzados, S.C., Departamento de Ingeniería y Química de Materiales, Miguel de Cervantes 120, Chihuahua, Chih., México, 31109.

ABSTRACT

Anthocyanins are pigments obtained from plants that may appear in different colors and because of this, they have become a subject of great interest. We use delphinidin 3-glucoside $(C_{21}H_{21}O_{12})^+$, known as delphinidin, as a sensitizer on four small $(TiO_2)_n$ nanoclusters with (n=2-5) used in prior research within our team. Results within the literature are compared with our results for the individual particles. Our contribution relies in the study of the interaction between delphinidin and the nanoclusters aimed to understand their electronic structure for applications in hydrogen generation employing photocatalysis. Delphinidin is known for its blue-red colors in some flowers and fruits and may benefit $(TiO_2)_n$ nanoclusters properties for solar technology applications. DFT theoretical calculations were performed in the Gaussian09 programs suite. Delphinidin as a (+1) cation initial structure as well as $(TiO_2)_n$ nanoclusters were relaxed using B3LYP/6311+G(d, p). DFT calculations include geometry, vibrational frequencies and atomization energies and HOMO-LUMO parameters for the individual delphinidin and nanoclusters. Conceptual DFT was used for individual particles to calculate ionization potential, electronic affinity, softness, hardness, and Fukui functions. Four nanostructures were formed with delphinidin and a particular variant out of four $(TiO_2)_n$ nanoclusters. This work generates data to learn more about the feasibility of using nanostructured $(TiO_2)_n$ sensitized with delphinidin for the application in photocatalysis within a hydrogen generation process.

Keywords: Titanium dioxide nanoclusters, delphinidin, photocatalysis, hydrogen generation

Photocatalytic Properties of TiO_2 Nanostructures with Sulfur Substitution and Sensitized with Delphinidin 3-Glucoside for Hydrogen Generation: A DFT Study

M.A. Flores-Hidalgo[1], D. Barraza-Jiménez[1], G. Núñez-Lares[1], M.A. Escobedo-Bretado[1]
V. Collins- Martinez[2], A. López Ortiz[2]

[1] Universidad Juárez del Estado de Durango, Facultad de Ciencias Químicas, Av. Veterinaria S/N, Circuito Universitario, Durango, Dgo. México, C.P. 34120. *Tel: +526181881941; e-mail: maflores.hidalgo@gmail.com
[2] Centro de Investigación en Materiales Avanzados, S.C., Departamento de Ingeniería y Química de Materiales, Miguel de Cervantes 120, Chihuahua, Chih., México, 31109.

ABSTRACT

Small $(TiO_2)_n$ nanoclusters with (n=2-5) used before in our prior research were optimized using Density Functional Theory (DFT) and a sulfur atom was used in the nanostructure instead of an oxygen. Sulfur addition may increase photocatalytic activity in the nanomaterial, particularly, when added as dopant in TiO_2. Nanoclusters with sulfur substitution were sensitized with delphinidin 3-glucoside, commonly known as delphinidin. This pigment´s family is interesting due to its natural properties in colors such as blue-red. All theoretical calculations were performed in Gaussian09 programs suite. Geometries and nanoestrucures atomization energies were calculated for the individual nanoparticles with B3LYP/6-31+G(d,p). S-TiO_2 structures parameters were calculated using the same theoretical level. Conceptual DFT was used to learn more about properties of these nanostructured materials. The idea of this work relies in the substitution with sulfur on $(TiO_2)_n$ nanoclusters interacting with delphinidin and the S-TiO_2 structures. Our results are compared with data reported within different assemblies to produce hydrogen using photocatalysis. This work intends to generate data so we learn more about the interaction of delphinidin with S-TiO_2 nanostructures for their application in hydrogen generation using green photocatalysis processes.

Keywords: Titanium dioxide nanoclusters, sulfur substitution, delphinidin, photocatalysis, hydrogen generation

Hydrogen Production by a Fe-based Oxygen Carrier and Methane-Steam Redox Process: Thermodynamic Analysis

M. J. Meléndez-Zaragoza, J. L. Domingez-Arvizu, J. M. Salinas-Gutierrez, V. Collins-Martínez, A. López-Ortiz*
Centro de Investigación en Materiales Avanzados, S.C., Miguel de Cervantes 120, Complejo Industrial Chihuahua Chihuahua, Chih. México.
*Tel: +52 6144394815; e-mail: alejandro.lopez@cimav.edu.mx

***Abstract*— The redox performance of iron oxide magnetite (Fe_3O_4) as an oxygen carrier was investigated for hydrogen (H_2) and/or syngas (H_2+CO) production through a methane-steam redox process using a thermodynamic analysis and process simulation to find most favorable reactions conditions (MFRC). The reaction system was divided in two reactors. In the first reduction step the following reactions were targeted: ¼ CH_4(g) + Fe_3O_4 = 3FeO + ¼ CO_2(g) + ½ H_2O(g) and CH_4(g) + Fe_3O_4 = 3FeO + $2H_2$(g) + CO(g), which both represent complete and partial oxidation of methane by an oxygen carrier (Fe_3O_4). While several other reactions were allowed to proceed such as the carbon formation by methane decomposition as well as further iron reduction to Fe. The CH_4/Fe_3O_4 molar ratio was varied from 0.25-1 in a temperature range from 300-900 °C. In the second oxidation reactor the solid products from the first reactor were combined with steam to regenerate the oxygen carrier by: 3FeO + H_2O(g) = Fe_3O_4 + H_2(g) using a fixed feed of 5.5 mols of H_2O in a temperature range of 300-900 °C. Thermodynamic analysis by the Gibbs free energy minimization technique and process simulation were performed in Aspen Plus. Criteria used to find MFRC were: carbon-free formation conditions, reduction and oxidation carrier phases as FeO and Fe_3O_4, respectively, avoiding the formation of metallic Fe (carbon formation promoter) and the minimum possible operating temperatures for energy saving reasons. Results indicate that in the reduction reactor the MFRC consist in T = 650-700°C and CH_4/Fe_3O_4 = 0.75-1, While for the regenerator were: T = 520-600 °C. Details of the mass and heat balances are also presented.**

***Keywords*— Methane-Steam Redox Process; Oxygen carrier, Thermodynamic Analysis.**

I. Introduction

Hydrogen, apart from being an important industrial chemical worldwide, can be considered as the choice of carrier for the emerging renewable energy generation technologies. However, today hydrogen production relies on the use of fossil fuels, being steam methane reforming (SMR) the preferred route for the industrial production of hydrogen, since it accounts for more than a half of the world hydrogen production. SMR is a highly endothermic catalytic reaction ($\Delta H°_{298}$ = 206 kJ/mol), which takes place in a temperature range of 700-850°C according to:

Reaction 1: $$CH_{4(g)} + H_2O_{(g)} = 3H_{2(g)} + CO_{(g)}$$

The economic feasibility of SMR units are restricted by scale, since small-scale plants make hydrogen production uneconomical. Therefore, large centralized industrial plants have been found to be the most cost-effective [1]. World consumption of hydrogen is projected to increase 3.5 percent annually through 2018 to more than 300 billion cubic meters and is expected to grow to about 5-6% in the next five years [2]. Therefore, an alternate approach that may include the use of near and remote natural gas reserves, especially those coming from the recent shale gas sites being explored worldwide, is needed for more cost-effective small scale H_2 production. Consequently, there is a renewed interest in the old and mature steam-iron process [3]. This process, in principle, is one of the few processes that do not require the step of gas separation to produce a high purity hydrogen stream at small scale. This process involves a series of the redox reactions, where the reduction of iron oxide with syngas (a mixture of CO and H_2) is followed by the oxidation of the reduced metallic iron with steam according to the following reactions:

Reaction 2: $$Fe_3O_4 + 4CO_{(g)} = 3Fe + 4CO_{2(g)}$$

Reaction 3: $$Fe_3O_4 + 4H_{2(g)} = 3Fe + 4H_2O_{(g)}$$

Reaction 4: $$3Fe + 4H_2O_{(g)} = Fe_3O_4 + 4H_{2(g)}$$

This process make use of a metal oxide (Fe_3O_4) as an oxygen carrier to perform the redox reactions (2-4) and at the same time serves as a heat transfer medium between the two reactors (reduction and oxidation) in a cycle reaction loop in order to make a continuous process and to increase energy efficiency. Gaseous carbon oxides rich stream is achieved after steam condensation from the reduction reactor (reactions 2 and 3) and a high purity hydrogen stream can be obtained after steam condensation from the oxidation reactor (reaction 4). Due to the significant characteristics of this process, this has been used as a reference for the production of H_2 in the chemical looping combustion [4] and H_2 storage [5].

For the specific case of the reduction of iron oxide with a gas fuel such as methane and the redox iron pair being Fe_3O_4/FeO the following reaction applies:

Reaction 5: $$Fe_3O_4 + \frac{1}{4}CH_{4(g)} = 3FeO + \frac{1}{4}CO_{2(g)} + \frac{1}{4}H_2O$$

Even though several other metal oxides have been proposed under the chemical looping concept for hydrogen production, the Fe_3O_4/Fe redox system is one of the most studied systems due to the fact that employs inexpensive materials and because it produces a high yield of H_2 per mass of iron (48 g H_2/kg Fe, from equation 4). One of the main challenges of a looping operation of the steam-iron process lies in the temperature swings and different gaseous atmospheres that the material needs to be exposed in order to perform a cycle operation in the process. This operation mode, performed at high temperatures, often produce sintering in the material with the consequent loss of activity and this being reflected in a significant decrease of lifetime, thus reducing the overall efficiency of the process.

In order to overcome this problematic, several studies have concentrated in improving reactor kinetics and the stability of the materials by modifying iron oxide with the addition of metals like Al, Mo and Ce as reported by Otsuka et al [6]. Takenaka et al [7] employed a mixture of Ni–Cr–FeO*x* reacted with methane followed by reaction with steam to produce pure hydrogen, where Cr species in Ni–Cr–FeO*x* were stabilized as octahedral $Cr^{3+}O_6$ in the ferrites $Cr_xFe_{3-x}O_4$ during the redox reactions. It was concluded that Cr helped to inhibit sintering of iron species. While Urasaki et al [8] added palladium and zirconia to the iron-based oxygen carrier to accelerate both the reduction and oxidation rates and also found that zirconia enhanced structural and thermal stability in iron oxides. Zafar et al [9] used SiO_2 and $MgAl_2O_4$ as supports to reduce the sintering of iron oxide, while Galvita and Sundmacher [10] proposed the use of Cr_2O_3–Fe_3O_4–CeO_2–ZrO_2 to provide stability to the oxygen carrier up to 100 redox cycles. However, some carbon monoxide in the hydrogen product stream was observed during the re-oxidation phase, whereas Liotta et al [11] examined the redox behavior and structural stabilization of ceria-zirconia solid solutions supported on alumina towards the CO oxidation catalysis. The unique oxygen storage capacity of the CeO_2–ZrO_2 combined with iron oxides produced an oxygen carrier that combines this important feature with the thermal stability and activity as confirmed by several research studies [12-14].

Moreover, several researchers [15-19] have proposed a novel two-step SMR process for hydrogen production based on the chemical looping concept and a scheme of this is presented in in Figure 1.

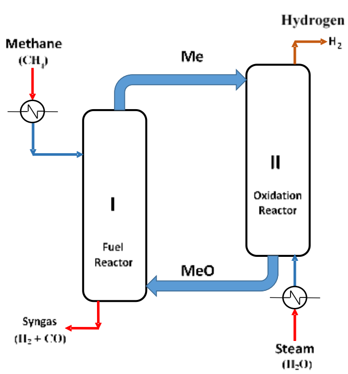

Figure 1. Conceptual scheme of the SMR chemical looping

In the fuel reactor (I) the oxygen carrier, typically a metal oxide (MeO), is reacted with methane to produce syngas and the reduced metal (Me) according to:

Reaction 6: $CH_{4(g)} + MeO = Me + 2H_{2(g)} + CO_{(g)}$

Reaction 7: $H_2O_{(g)} + Me = MeO + H_{2(g)}$

Finally, the regenerated oxygen carrier is sent back to the fuel reactor to complete one full loop or reaction cycle. The combination of reactions (6) and (7) leads to reaction (1), which is the SMR reaction. The reaction process indicated in Figure 1 is usually called as chemical looping steam methane reforming (CL-SMR). This process separate the feed of methane and steam in two step reactors thus, producing a syngas stream in the first and a H_2 gas product in the second that needs no further purification.

One critical issue of this proposed reaction scheme deals with the relatively low reactivity of the oxygen carrier towards the reoxidation of the reduced metal (reaction 6). Several metal oxides have been reported as oxygen carriers for the CL-SMR such as Fe_3O_4, WO_3, SnO_2, Ni–Fe, (Zn, Mn)–Fe, Cu–Fe and Ce-based oxides [15] . Among all these oxygen carriers such as Fe-oxides have proven to be suitable for the CL-SMR. Nevertheless, thermodynamic constrains for the hydrogen evolution make this oxygen carrier to behave in a complex way, since in some cases the complete reduced Fe phase is required for a high H_2 production yield, while the complete oxidation with steam beyond Fe_3O_4 is thermodynamically limited [20]. However, this oxygen carrier can be considered ideal for CL-SMR applications and this is based on its reduced propensity to carbon formation and resistance to form agglomerates. These last features are critical for an oxygen carrier to retain its activity over continuous redox cycles. Furthermore, iron oxide oxygen carriers are not susceptible to form sulfide or sulfate compounds under sulfur-containing atmospheres [21], while large natural reserves and low cost make them suitable for implementation at large scales [22-24]. Some drawbacks of these Fe-based oxygen carriers include weak redox characteristics, relatively low oxygen storage capacity (OSC), and limited reactivity towards gaseous fuels like methane [25].

Additionally, Fe presents multiple oxidation states such as Fe_2O_3, Fe_3O_4, FeO and Fe and as indicated above it presents thermodynamic limitations, since only the transformation from Fe_2O_3 to Fe_3O_4 is feasible for the total oxidation of methane, whereas partial oxidation of methane (POX) is favored in the transition reduction from FeO to Fe according to Monzam et al [26].

Thermodynamic Considerations

Several thermodynamic analyses have studied different approaches to the CL-SMR process. Fraser et al. [26] performed a thermodynamic analysis of the reformer sponge iron cycle (RESC) process that consisted in the hydrogen production including a hydrocarbon reformer and a sponge iron reactor (SIR). The reformer output gas (H_2 and CO) reduces the pellets from magnetite (Fe_3O_4) and wuestite (FeO) into iron metal (Fe) through reactions (2) and (3) and the reduced Fe is reoxidized with steam by reaction (4). They found that the process offers hydrocarbon to hydrogen conversion efficiencies in the order of

75% vs LHV for methane and at a temperature range of 750 °C and above. Steinfeld and Kuhn [27] presented a high temperature thermochemistry analysis of the Fe_3O_4 reduction with methane for the production of syngas. They studied the reaction system at temperatures above 1000 °C aimed for the use of concentrated solar radiation as the energy source. They found that a mixture of 66.7% H_2 and 33.3% CO can be achieved with complete reduction to metallic Fe. Kang et al [28] performed a Thermodynamic analysis of the three-reactor chemical-looping process (TRCL), which consisted in a fuel reactor, a steam reactor, and an air reactor. In the fuel reactor, natural gas (mainly CH_4) is oxidized to CO_2 and H_2O by the lattice oxygen of the oxygen carrier (Fe_2O_3, WO_3, and CeO_2). In the steam reactor, the steam is reduced to hydrogen through oxidation of the reduced oxygen carrier, while in the air reactor; the oxygen carrier is fully oxidized by air. Results indicate that an expected hydrogen production of 2.64 mol H_2 per mol CH_4 under thermo-neutral conditions can be achieved and this was affected mainly by the steam-conversion rate. Bohn et al [29] studied the hydrogen production with simultaneous capture of CO_2 using the redox reactions of iron oxides in packed beds. They examined the thermodynamics of exposing Fe_2O_3 to a syngas to produce a high purity CO_2 stream ready for sequestration, while the oxidation of FeO to Fe_3O_4 with steam produced a high purity hydrogen stream. They found that reduction to Fe, rather than FeO, in step 1 gave low levels of H_2 and after 10 cycles of reduction and oxidation led to the deposition of carbon at lower temperatures. Furthermore, Svoboda et al [30] studied the thermodynamic and chemical equilibrium of the reduction of Fe_3O_4 by CH_4 and oxidation of iron by steam. The study was concentrated on finding convenient conditions for reduction of Fe_3O_4 to iron at temperatures from 400- 800 K, but also on the possible formation of undesired soot, Fe_3C and iron carbonate. Reduction of magnetite with methane did not produce iron carbides or carbonates, whereas conditions favored the formation of Fe and CO_2, and H_2O as gas products.

From all previous thermodynamic studies related to the use of iron oxides as oxygen carrier for the complete oxidation of methane (reactions 2 and 3) or the partial oxidation of methane, which is a special case of the so called chemical looping steam methane reforming (CL-SMR) that involve the partial oxidation of methane through:

Reaction 8: $3Fe_2O_3 + CH_{4(g)} = 2Fe_3O_4 + 2\mathrm{H}_{2(g)} + \mathrm{CO}_{(g)}$

Reaction 9: $Fe_3O_4 + CH_{4(g)} = 3FeO + 2\mathrm{H}_{2(g)} + \mathrm{CO}_{(g)}$

Reaction 10: $FeO + CH_{4(g)} = Fe + 2\mathrm{H}_{2(g)} + \mathrm{CO}_{(g)}$

Reaction 11: $3FeO + \mathrm{H_2O}_{(g)} = Fe_3O_4 + \mathrm{H}_{2(g)}$

This last reactions present the advantage to produce a syngas mixture in the iron reduction reactor (reactions 8-10), while the regeneration of the reduced Fe with steam is able to produce a high purity H_2 stream. However, this regeneration will only produce Fe_3O_4 as reaction (11) is thermodynamically limited. Therefore, in a cyclic operation the redox reaction between the two reactors of Figure 1 will only be reactions (9) and (11). However, carbon deposition during the operation is another important aspect to be considered in this process through the Boudouard and methane pyrolysis reactions:

Reaction 12: $2\mathrm{CO}_{(g)} = \mathrm{CO}_{2(g)} + \mathrm{C}$

Reaction 13: $\mathrm{CH}_{4(g)} = 2\mathrm{H}_{2(g)} + \mathrm{C}$

Galvita and Sundmacher [31] studied the CL-SMR reaction system and concluded that at a reduction of approximately 60% of the Fe_2O_3 carbon formation was avoided. Further reduction towards Fe produced carbon deposits on the oxygen carrier. Therefore, the restrictions in order to avoid carbon formation and the steam oxidation of the reduced iron lead to select the Fe_3O_4/FeO as the ideal redox pair for the CL-SMR process.

Up to date, no thermodynamic analysis have been performed to explore optimal reactions conditions. From one end: complete oxidation of methane by Fe_3O_4 (steam iron process, SIP, which produce only CO_2 and FeO in the reduction reactor) to the other end: partial oxidation of methane (POX-MeO or CL-SMR, where syngas and FeO is produced) and subsequent hydrogen production from reoxidation of FeO. This proposed process operation aims to restrict the oxidation states between the two reactors of Figure 1 to the Fe_3O_4/FeO redox pair, while avoiding carbon formation to insuring a high purity hydrogen stream from the steam oxidation reactor.

Therefore, the aim of the present investigation is to perform a thermodynamic and process simulation studies to find optimal operating conditions (avoiding carbon formation) close to equilibrium for a high H_2 and/or syngas production. In addition, these under the SIP/CL-SMR reaction system using methane as a feed (for the fuel reactor) and steam (for the oxidation reactor), while employing the Fe_3O_4/FeO redox pair between the reduction and oxidation reactors. This analysis will include the evaluation of the thermodynamic equilibrium composition of the reaction system, the behavior of the Fe_3O_4/CH_4 and H_2O/FeO feed molar ratios as a function of temperature and products composition for the reduction and oxidation reactors, respectively. Furthermore, it is expected that the feed molar ratio of Fe_3O_4 to CH_4 will determine the operation mode of the process from complete oxidation (SIP) to a partial oxidation of methane (CL-SMR). Consequently, a process simulation will examine oxygen carrier recirculation from the oxidation to the reduction reactors and its influence on the process operating conditions.

II. METHODS

Thermodynamics Method

Thermodynamic calculations in the present study were performed by the Gibbs free energy minimization technique. In a reaction system where many simultaneous reactions take place, equilibrium calculations can be performed through the Gibbs energy minimization approach (also called the nonstoichiometric method). Details of this technique can be found elsewhere [32]. All calculations were performed using the ASPEN Plus® RGIBBS reactor model and the Redlich–Kwong equation of state for correction of non-ideal conditions. In a RGIBBS reactor the equilibrium composition of all possible combination of reactions that are able to take place within the thermodynamic system. The RGIBBS program of this reactor finds the most stable phase combination and establish the phase compositions where the Gibbs free energy of the reaction system reaches its minimum at a fixed mass balance, constant pressure, and temperature. For the oxidation of methane and regeneration of the iron oxide species the gaseous species included were: CH_4, CO, CO_2, H_2, and H_2O, while solid species were: C, Fe, FeO, Fe_2O_3, F_3C, and $FeCO_3$.

For the fuel reactor the temperature was varied in the range of 300-900 °C at 1 atm. While, the CH_4/Fe_3O_4 feed molar ratio was varied from 0.25 (stoichiometric value according to reaction (5)) to 1 (stoichiometric value according to reaction (9)). Whereas, for the oxidation reactor the temperature was also varied in the range of 300-900 °C at 1 atm. The solid product of the fuel reactor was fed to the steam oxidation reactor. In this reactor, the FeO is to be reacted with steam according to reaction (11). In this reactor the FeO/H_2O feed molar ratio was varied from 3 (stoichiometric value according to reaction (11)) to 0.546. This represents a gradual increase from 1 kmol/h of H_2O per 3 kmol/h of FeO up 6 kmol/h of H_2O per 3 kmol/h of FeO. This feed steam variation was intended to find the minimum amount of steam needed in order to regenerate FeO to Fe_3O_4 at a reasonable oxidation temperature, where kinetics are favorable (500-600 °C) [39]. It is important to notice that all the present simulation calculations are based on theoretical thermodynamic considerations and these are to be taken as a guide to further experimental evaluation of the reaction systems, since no heat and mass diffusional limitations as well as kinetics effects were taken into account for the conformation of the present thermodynamic analysis.

Process Simulation Method

Process simulation calculations was performed using the Aspen-Plus© Engineering Process Simulator. This is a program for simulation of chemical processes in which the analysis of chemical processes as well as heat integration can be made. This simulator was employed for the analysis of the process scheme of Fig. 2. The module of Aspen-Plus that was used to evaluate the reaction systems were: the RGibbs (Gibbs Reactor), wherein RGibbs method is based on the Gibbs free energy minimization technique for multiphase reactions and material balance, cyclone units were used to separate solid and gas streams.

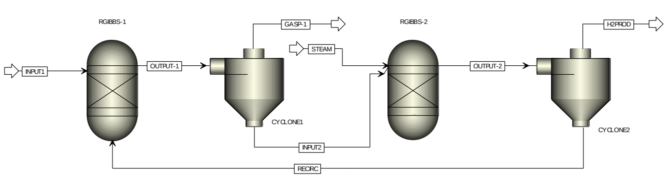

Figure 2. Process simulation flowsheet.

III. Results And Discussion

A. Thermodynamic Analysis

The Fuel Reactor

This section presents results from the equilibrium amounts of H_2, CO, CO_2, CH_4 and C, Fe, FeO, Fe_2O_3 and Fe_3O_4 from the fuel reactor in a temperature range of 300-900 °C and CH_4/Fe_3O_4 feed molar ratios from 0.25 to 1. At the studied conditions the conversion of methane was gradually increased from about 4% at 300 °C, 90% at 500 °C and up to 99.9% at 600°C. This is associated to the intrinsic equilibrium reactivity of a solid Fe_3O_4 with respect to a gaseous fuel such as CH_4 and availability of the metal oxide lattice oxygen into the gas phase. Fig. 3 shows the equilibrium production of H_2 (3a) and CO (3b) from the fuel reactor (dry basis) in kmol/h as a function of temperature and CH_4/Fe_3O_4 feed molar ratio.

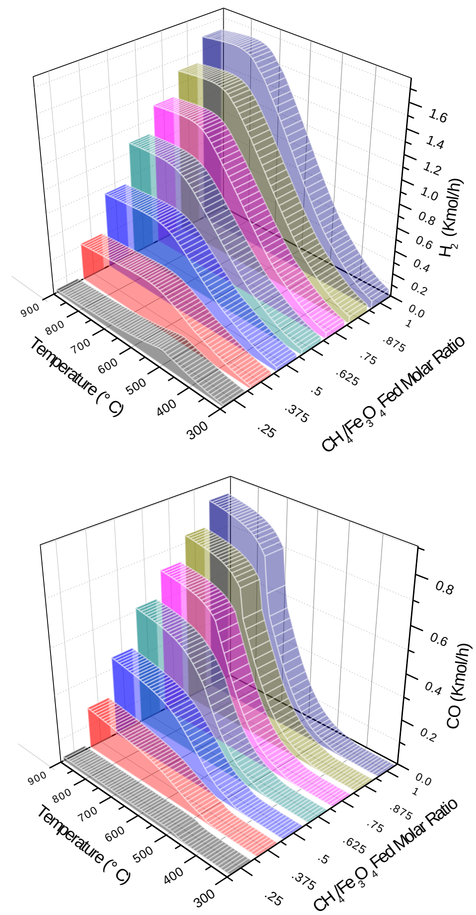

Figure 3. Equilibrium content of H_2 (a) and CO (b) for the fuel reactor

At low temperatures (300-500 °C) and where CH_4/Fe_3O_4 ratio is small (below 0.5), there is no enough temperature and/or oxygen available for the reaction between Fe_3O_4 and methane to produce syngas (CO + H_2) and therefore, this metal oxide is poorly reactive towards reaction (9). However, the small reactivity in this region is attributed to the complete oxidation of methane by Fe_3O_4 (reaction 5) where at the SIP conditions (CH_4/Fe_3O_4 = 0.25 and higher but not greater than 0.5) the production of CO_2 and H_2O dominate. Greater temperatures than 500 °C and CH_4/Fe_3O_4 ratios than 0.5 will lead to the promotion of the partial oxidation of methane by Fe_3O_4 to form syngas through reaction (9) according to results presented in Figures 3(a) and 3(b).

Figures 4(a) and 4(b) present results of unreacted CH_4 and formed CO_2 contents in the gas product from the fuel reactor.

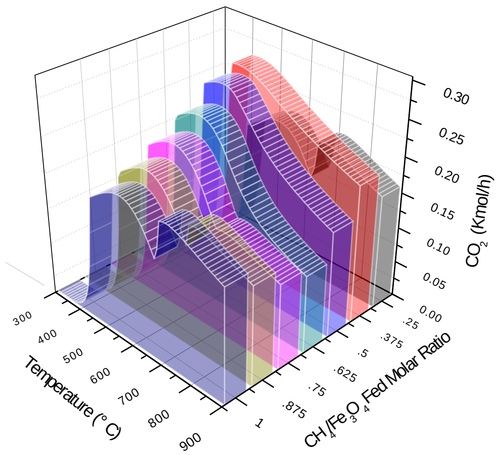

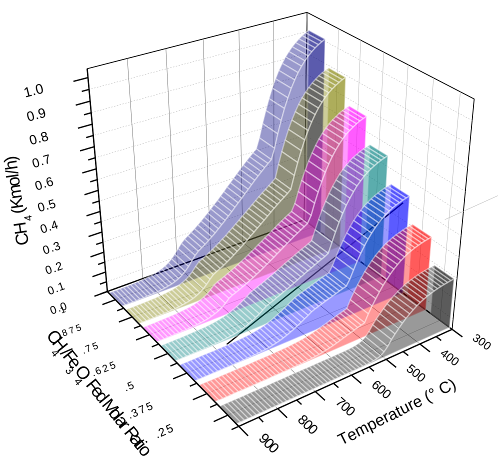

Figure 4. Equilibrium content of CO_2 (a) and CH_4 (b) for the fuel reactor

In this Figure it is evident that low temperatures (T < 500 °C) and small CH_4/Fe_3O_4 ratios, CO_2 formation is favored, which is the region where complete oxidation of methane is promoted and the CO_2 content is reduced as the available oxygen content is increased as the CH_4/Fe_3O_4 ratio is also grown. Also in Figure 4(b) it is evident that methane reactivity is high at low oxygen lattice content (Fe_3O_4) and this is reflected in small methane content in the product gas at temperatures greater than around 500 °C and small CH_4/Fe_3O_4 ratios (smaller than 0.5). Here in this plot the gradual increase in methane conversion is clear that increases as temperature rises and the CH_4/Fe_3O_4 ratio decrease, which is translated in the promotion of the partial oxidation of methane reaction with Fe_3O_4 (oxygen starving conditions, reaction 9)

Moreover, Figure 5 describe de behaviors of the FeO and C solid content at the effluent stream from the fuel reactor of Figure 1.

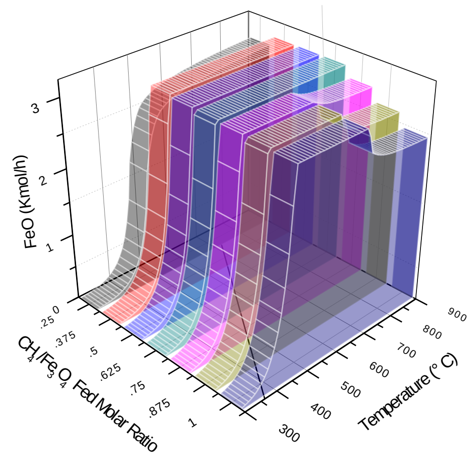

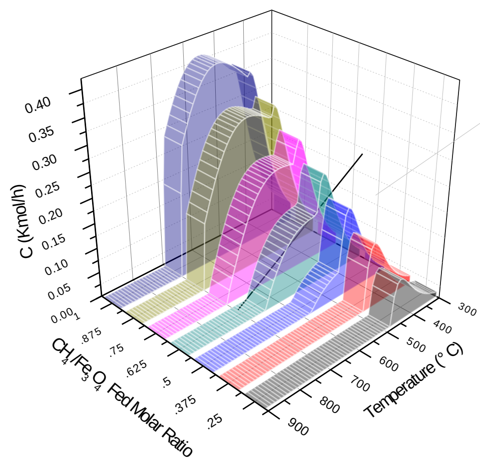

Figure 5. Equilibrium content of FeO (a) and C (b) for the fuel reactor

In this plot the maximum conversion from Fe_3O_4 to FeO at a feed of 1 kmol/h of Fe_3O_4 is according to reaction (5) of 3 kmol/h and that means that the iron oxide is in the oxidation state where in the next reactor can be combined with the appropriate amount of steam to produce a pure hydrogen stream. Therefore, optimal reaction conditions will be those which complete conversion of Fe_3O_4 to FeO is achieved and those are where the amount of FeO in Figure 5 (a) is 3 kmol/h. From this figure, it is clear that those conditions are achieved at temperatures between 500 to 700 °C at all CH_4/Fe_3O_4 ratios. At those conditions, methane is able to reduce iron oxide to magnetite either through complete or partial oxidation of methane. However, not only at those conditions magnetite is also thermodynamically stable, greater temperatures from 700 up to 900 °C in a CH_4/Fe_3O_4 range from 0.375 to 0.625 will also insure the production of magnetite and these last conditions coincide with partial oxidation of methane through equation (9).

Also important in the present investigation is to find operating conditions where no carbon formation is feasible, since any carbon contamination over the oxygen carrier will be gasified in the oxidation reactor, thus producing carbon dioxide gases that will ultimately combine with the expected hydrogen production and consequently become a gaseous byproduct. Figure 5(b) show that the carbon free operating windows of the fuel reactor are as follows: from CH_4/Fe_3O_4 = 0.25-0.375 no carbon is present in a temperature range of 480-900 °C, CH_4/Fe_3O_4 = 0.5 from 580-900 °C, CH_4/Fe_3O_4 = 0.625 from 660-900 °C and CH_4/Fe_3O_4 = 0.75-1 from 700-900 °C. These free carbon regions that can be seen in Figure 5(b) is where either the Boudouard and/or the methane decomposition reactions (12 and 13) are not thermodynamically favorable. These results agree well with experimental results reported by Tang et al [40].

A more careful analysis of the generated data allows to conclude that according to the previous thermodynamic analysis optimum conditions in order to produce a maximum hydrogen production and carbon free operation is at T = 650-700°C and CH_4/Fe_3O_4 = 0.75-1. It is important to indicate that no metallic iron (Fe) was present at the studied fuel reactor conditions.

The Oxidation Reactor

This section presents results from the equilibrium amounts of H_2 and Fe_3O_4 from the oxidation reactor in a temperature range of 500-600 °C and H_2O feed molar flowrate range from 1-6 kmol/h. At the studied conditions, it is expected to find the minimum amount of steam per three kmols of FeO at a reasonable temperature from 500-600 °C, where the reaction kinetics are reported to be favorable [39]. Figure 6 (a) and (b) presents results from the oxidation reactor at conditions above described.

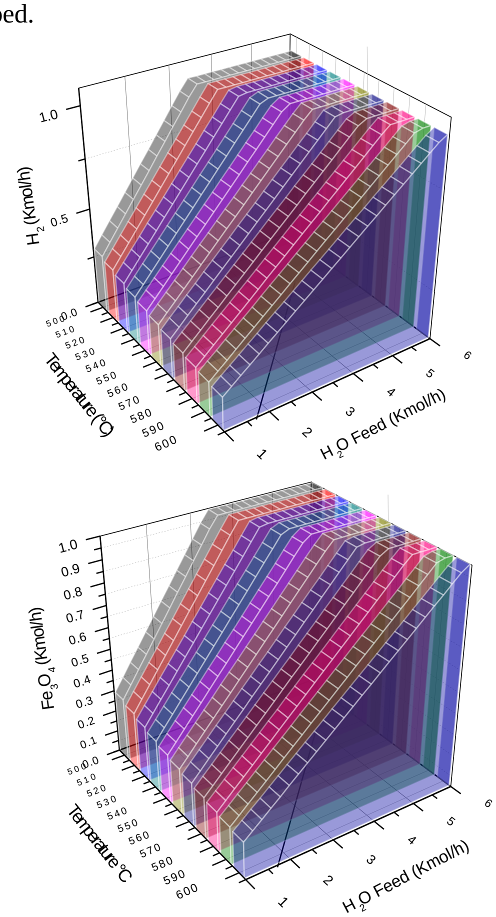

Figure 5. Equilibrium content of H_2 (a) and H_2O (b) for the oxidation reactor.

In plot 5 (a) the maximum hydrogen production can be seen as a function of temperature and the feed molar flow to the reactor. From this figure, it is evident that there is a defined region where the maximum hydrogen production is achieved which happens to be of 1 kmol/h. These conditions increase as the amount of steam and temperature both increase. For example, at 500 °C a minimum range of 3.4 to 6 kmol/h of steam is needed in order to produce the maximum amount of hydrogen according to reaction (11), while at 550 °C a range of steam of 4.6-6 kmol/h are needed to obtain the maximum possible H_2 production. Finally, at 600 °C 6 kmol/h of steam or greater are needed for this purpose. However, research points out that H_2 evolution via water the splitting reaction (11) requires Fe phase to be as fully reduced as possible, while it is difficult for Fe phase to be completely oxidized beyond Fe_3O_4 by using steam [40]. Moreover, other research indicate that the reduction from Fe_3O_4 to Fe promotes carbon deposition [31].

Furthermore, Figure 5(b) presents the Fe_3O_4 content at different steam feed to the oxidation reactor. Here in this plot it can be seen that the only conditions where complete conversion of FeO to Fe_3O_4 is achieved at regions where the amount of steam and temperature both increase. These results mimic the same conditions where the maximum hydrogen production is achieved from Figure 5(a). Therefore, this regenerated 1 kmol/h is expected to be recirculated back to the fuel reactor.

Process Simulation

Fig. 1 presented a diagram of the process scheme employed during the simulation of the SIP/CL-SMR reaction system with either the production of pure CO_2 or a syngas stream from the fuel reactor, while in the oxidation reactor the H_2 evolution and iron oxide regeneration is achieved. While, Table 1 summarizes results from the process simulation of selected streams from Figure 1.

Table 1. Summary of process simulation results of the SIP process

Stream Nane	INPUT1	RECIRC	OUTPUT-1	GASP-1	INPUT2	STEAM	OUTPUT-2	H2PROD
Mole Flow, Kmol/h								
CH4	0.25	0	4.1329E-07	4.13E-07	0	0	0	0
CO	0	0	0.0174931	0.017493	0	0	0	0
CO2	0	0	0.2325064	0.232506	0	0	0	0
H2	0	0	0.0505711	0.050571	0	0	0.9319341	0.9319341
H2O	0	0	0.449428	0.449428	0	6	5.068066	5.068066
FE3O4	0	1	0.0680659	0	0.068066	0	1	0
FEO	0	0	2.795802	0	2.795802	0	0	0
FE	0	0	0	0	0	0	0	0
Mole Flow, Kmol/h	0.25	1	3.6138672	0.749999	2.863868	6	7	6
Mass Flow, Kg/h	4.01069	231.5386	235.54928	18.92108	216.6282	108.0917	324.71989	93.18129
Volume Flow, m^3/h	20.38051	0.044524	61.1744308	61.1246	0.049831	429.693	429.823224	429.7787
Temperature,°C	720	600	720	720	720	600	600	600

In this Table, the extreme case where complete production of CO_2 is targeted (SIP) and therefore the CH_4/Fe_3O_4 feed molar ratio is equal to 0.25. Here in this table stream INPUT-1 denotes the fresh CH_4 feed of 0.25 kmol/h, while the RECIRC stream contains the 1 kmol/h of Fe_3O_4. Stream OUTPUT-1 contains the products from the fuel reactor at a temperature of 700 °C where no carbon formation is possible and the complete oxidation of methane by magnetite is favored. In this stream, a methane conversion of 99.99% is reflected with the production of 0.23 kmol/h of CO_2 compared to the theoretical 0.25 kmol/h according to reaction (5) makes these operating conditions very convenient, while the other carbon specie produced is CO with 0.017 kmol/h accompanied with the production of water. Furthermore, in this stream only 2.79 kmol/h of FeO is produced, while only a small amount of unreacted Fe_3O_4 is present (0.068 kmol/h). Gases and solids are separated in streams GASP-1 and INPUT-2, where this last is fed to the oxidation reactor together with stream STEAM, which consist of 6 kmol/h at a reactor temperature of 600 °C. Stream OUTPUT-2 contains the products from the oxidation reactor where 0.93 kmol/h of H_2 combined with 1 kmol/h of Fe_3O_4 and 5 kmols/h of excess steam are produced. This stream is separated in H2PROD and RECIRC streams, where this last one is stent back to the fuel reactor. The yield of this process based on the hydrogen product is of 3.72 mols of H_2 produced per mols of methane being fed.

Moreover, Table 2 presents results from the simulation of the other process (CL-SMR), which represents the other mode of operation of the process described in Figure 1. In this simulation a CH_4/Fe_3O_4 feed molar ratio is equal to 1 was employed in the fuel reactor.

Table 2. Summary of process simulation results of the CL-SMR process

Stream Nane	INPUT1	RECIRC	OUTPUT-1	GASP-1	INPUT2	STEAM	OUTPUT-2	H2PROD
Mole Flow, Kmol/h								
CH4	1	0	0.100206	0.100206	0	0	0	0
CO	0	0	0.7035638	0.7035638	0	0	0	0
CO2	0	0	0.1962302	0.1962302	0	0	0	0
H2	0	0	1.536961	1.536961	0	0	1.358652	1.358652
H2O	0	0	0.2626274	0.2626274	0	8.2	6.841348	6.841348
FE3O4	0	1	0	0	0	0	1	0
FEO	0	0	2.641348	0	2.641348	0	0	0
FE	0	0	0.3586516	0	0.3586516	0	0	0
Mole Flow, Kmol/h	1	1	5.799588	2.799588	3	8.2	9.2	8.2
Mass Flow, Kg/h	16.0	231.5	247.6	37.8	209.8	147.7	357.5	126.0
Volume Flow, m^3/h	81.5	0.0	223.7	223.6	0.0	587.2	587.4	587.4
Temperature,°C	720	0	700	700	700	600	600	600

In this table stream INPUT-1 contains the fresh CH_4 feed of 1 kmol/h, while the RECIRC stream contains also 1 kmol/h of Fe_3O_4. Stream OUTPUT-1 comprises the products from the fuel reactor at a temperature of 700 °C where no carbon formation is possible and the complete oxidation of methane by magnetite is favored. In this stream a methane conversion of 90% is reflected with the production of 1.53 kmol/h of H_2 compared to the theoretical 2 kmol/h according to reaction (9), while the production of CO was 0.7 kmol/h compared to the theoretical value of 1 kmol/h of the same reaction. With respect to the reaction of the Fe_3O_4 with methane, it is significant that two reduced iron species were produced with a combination of 2.64 and 0.36 kmol/h of FeO and Fe_3O_4, respectively. Here, it is possible that the syngas formed (H_2 + CO) is able to further reduce the FeO to a small extent.

Gases and solids are separated in streams GASP-1 (syngas) and INPUT-2 (solid product), where this last is fed to the oxidation reactor together with stream STEAM, which consist of 8.2 kmol/h at a reactor temperature of 600 °C. This excess of steam being fed at the oxidation reactor in further needed to re-oxide FeO and Fe reduced species back to Fe_3O_4. Stream OUTPUT-2 contains the products from the oxidation reactor where 1.36 kmol/h of H_2 combined with 1 kmol/h of Fe_3O_4 and 6.8 kmols/h of excess steam are found. This stream is separated in H2PROD and RECIRC streams, where this last one is stent back to the fuel reactor. The yield of this process based on the hydrogen product is of 1.35 mols of H_2 produced per mols of methane being fed. While based on the syngas produced is 2.24 mols of syngas (CO+H2) per mol of methane fed at a H_2/CO product ratio of 2.19, which is very convenient, since this streams can be used in the Fischer-Tropsch process for the production of liquid fuels (GTL).

IV. Conclussions

In the present research, the redox performance of iron oxide magnetite (Fe_3O_4) as an oxygen carrier was investigated for hydrogen (H_2) and/or syngas (H_2+CO) production through a methane-steam redox process using a thermodynamic analysis and process simulation to find most favorable reactions conditions. The studied reaction system was divided in two reactors. In the fuel reactor the complete or the partial oxidation of methane with Fe_3O_4 were studied. . Results indicate that in the reduction reactor the most favorable reactions conditions consisted in T = 650-700°C and CH_4/Fe_3O_4 = 0.75-1, While for the regenerator were: T = 520-600 °C. Finally, these results can be taken as a basis for future experimental and theoretical studies in search for a suitable catalyst and conditions to evaluate the present proposed technology.

Acknowledgment

The authors of this paper wish to thank the Mexican Society of Hydrogen for accepting the proposed research for dissemination and discussion, as well as the scholarship. We thank equally to CONACYT for scholarships awarded to students involved in the project.

References

[1] Mueller-Langer F, Tzimas E, Kaltschmitt M, Peteves S. Techno-economic assessment of hydrogen production processes for the hydrogen economy for the short and medium term. Int J Hydrogen Energy 2007; 32(16):3797-810.

[2] HIS Markit, Hydrogen, Chemical Economics Handbook, June 2015, available at: https://www.ihs.com/products/hydrogen-chemical-economics-handbook.html.

[3] Yang J. Cai N. Li Z., Hydrogen Production from the Steam-Iron Process with Direct Reduction of Iron Oxide by Chemical Looping Combustion of Coal Char, Energy & Fuels 2008, 22, 2570–2579.

[4] Bayham S C., Kim H R., Wang D, Tong A, Zeng L, McGiveron O, Kathe M V., Chung E, Wang W, Wang A, Majumder A, Fan L. Iron-Based Coal Direct Chemical Looping Combustion Process: 200-h Continuous Operation of a 25-kWth Subpilot Unit, Energy Fuels, 2013, 27 (3), pp 1347–1356.

[5] Lee DH, Cha KS, Lee YS, Kang KS, Park CS, Kim YH. Effects of CeO_2 additive on redox characteristics of Fe-based mixed oxide mediums for storage and production of hydrogen. Int J Hydrogen Energy 2009; 34(3):1417-22.

[6] Otsuka K, Kaburagi T, Yamada C, Takenaka S. Chemical storage of hydrogen by modified iron oxides. J Power Sources 2003;122(2):111-21.

[7] Takenaka S, Hanaizumi N, Son VTD, Otsuka K. Production of pure hydrogen from methane mediated by the redox of Ni- and Cr-added iron oxides. J Catal 2004; 228(2):405-16.

[8] Urasaki K, Tanimoto N, Hayashi T, Sekine Y, Kikuchi E, Matsukata M. Hydrogen production via steam-iron reaction using iron oxide modified

with very small amounts of palladium and zirconia. Appl Catal, A 2005; 288(1e2):143-8.

[9] Zafar Q, Mattisson T, Gevert B. Redox investigation of some oxides of transition-state metals Ni, Cu, Fe, and Mn supported on SiO_2 and $MgAl_2O_4$. Energy Fuels 2006; 20(1):34-44.

[10] Galvita V, Sundmacher K. Cyclic water gas shift reactor (CWGS) for carbon monoxide removal from hydrogen feed gas for PEM fuel cells. Chem Eng J 2007; 134(1-3):168-74.

[11] Liotta LF, Longo A, Pantaleo G, Di Carlo G, Martorana A, Cimino S, et al. Alumina supported Pt (1%)/$Ce_{0.6}Zr_{0.4}O_2$ monolith: remarkable stabilization of ceria-zirconia solution towards $CeAlO_3$ formation operated by Pt under redox conditions. Appl Catal, B 2009; 90(3-4):470-7.

[12] Sim A, Cant NW, Trimm DL. Ceria-zirconia stabilized tungsten oxides for the production of hydrogen by the methane-water redox cycle. Int J Hydrogen Energy 2010; 35(17):8953-61.

[13] Trovarelli A. Catalytic properties of ceria and CeO_2-containing materials. Catal Rev Sci Eng 1996; 38(4):439-520.

[14] Sosa Vázquez M I, Delgado Vigil M D., Salinas Gutiérrez J, Collins-Martínez V, López Ortiz A. Synthesis Gas Production through Redox Cycles of Bimetallic Oxides and Methane, Journal of New Materials for Electrochemical Systems 12, 29-34 (2009).

[15] Zhu X, Wei Y, Wang H, Li K. Ce–Fe oxygen carriers for chemical-looping steam methane reforming. Int J Hydrogen Energy 2013; 38:4492–501.

[16] Zheng Y, Zhu X, Wang H, Li K, Wang Y, Wei Y. Characteristic of macroporous CeO_2–ZrO_2 oxygen carrier for chemical-looping steam methane reforming. J Rare Earths 2014; 32:842–8.

[17] Zhu X, Li K, Wei Y, Wang H, Sun L. Chemical-looping steam methane reforming over a CeO_2–Fe_2O_3 oxygen carrier: evolution of its structure and reducibility. Energy Fuels 2014; 28:754–60.

[18] Lee DH, Cha KS, Kim HS, Park CS, Kim YH. Syngas and hydrogen production via stepwise methane reforming over Cu-ferrite/YSZ. Int J Energy Res 2014; 38:1522–30.

[19] He F, Wei Y, Li H, Wang H. Synthesis gas generation by Chemical-looping reforming using Ce-based oxygen carriers modified with Fe, Cu, and Mn oxides. Energy Fuels 2009; 23:2095–102.

[20] Zhu X, Li K, Wei Y, Wang H, Sun L. Chemical-looping steam methane reforming over a CeO_2–Fe_2O_3 oxygen carrier: evolution of its structure and reducibility. Energy Fuels 2014; 28:754–60.

[21] Adanez J, Abad A, Garcia-Labiano F, Gayan P, De Diego LF. Progress in chemical-looping combustion and reforming technologies. Prog Energy Combust Sci 2012; 38:215–82.

[22] Mattisson T, Johansson M, Lyngfelt A. Multicycle reduction and oxidation of different types of iron oxide particles – application to chemical-looping combustion. Energy Fuels 2004; 18:628–37.

[23] Mattisson T, Lyngfelt A, Cho P. The use of iron oxide as an oxygen carrier in chemical-looping combustion of methane with inherent separation of CO_2. Fuel 2001; 80:1953–62.

[24] Nasr S, Plucknett K. Kinetics of iron ore reduction by methane for chemical looping combustion. Energy Fuels 2014; 28:1387–95.

[25] Cabello A, Abad A, García-Labiano F, Gayán P, de Diego LF, Adánez J. Kinetic determination of a highly reactive impregnated Fe_2O3/Al_2O_3 oxygen carrier for use in gas-fueled chemical looping combustion. Chem Eng J 2014; 258:265–80.

[26] Monazam ER, Breault RW, Siriwardane R. Kinetics of magnetite (Fe_3O_4) oxidation to hematite (Fe2O3) in air for chemical looping combustion. Ind Eng Chem Res 2014; 53:13320–8.

[27] Fraser S.D. Monsberger M., Hacker V. A thermodynamic analysis of the reformer sponge iron cycle. Journal of Power Sources 161 (2006) 420–43.

[28] Steinfeld A. and Kuhn P. High-Temperature Solar Thermochemistry: Production of Iron and Synthesis Gas by Fe_3O_4-Reduction with Methane. Energy Vol. 18, No. 3, pp. 239-249, 1993.

[29] Kang K. Kim C. Bae K. Cho W. Kim S. Park C. Oxygen-carrier selection and thermal analysis of the chemical-looping process for hydrogen production. Int J. Hydrogen Energy 35 (2010) 12246-12254.

[30] Bohn C. D. Muller C. R. Cleeton J. P. Hayhurst A. N. Davidson J. F. Scott S. A. Dennis J. S. Production of Very Pure Hydrogen with Simultaneous Capture of Carbon Dioxide using the Redox Reactions of Iron Oxides in Packed Beds. Ind. Eng. Chem. Res. 2008, 47, 7623–7630.

[31] Svoboda K. Slowinski G. Rogut J. Baxter D. Thermodynamic possibilities and constraints for pure hydrogen production by iron based chemical looping process at lower temperatures, Energy Conversion and Management 48 (2007) 3063-3073.

[32] Galvita V and Sundmacher K. Hydrogen production from methane by steam reforming in a periodically operated two-layer catalytic reactor. Applied Catalysis A: General 289 (2005) 121–127.

[33] Collins-Martínez V, Escobedo Bretado M, Meléndez Zaragoza M, Salinas Gutiérrez J, López Ortiz A. Absorption enhanced reforming of light alcohols (methanol and ethanol) for the production of hydrogen: thermodynamic modeling. Int J Hydrogen Energy 2013; 38:12539-53.

[34] Yamaguchi D. Tang L. Wonga L. Burke N. Trimm D. Nguyen K. Chiang K. Hydrogen production through methane-steam cyclic redox processes with iron-based metal oxides. Int J. Hydrogen Energy 36 (2011) 6646-6656.

[35] Tang M. Xu L. Fan M. Progress in oxygen carrier development of methane-based chemical-looping reforming: A review. Applied Energy 151 (2015) 143–156.

.

Water effect in the stability of a non-aqueous vanadium flow battery for energy storage applications

I. L. Escalante-García*, S. M. Durón - Torres
Unidad Académica de Ciencias Químicas
Universidad Autónoma de Zacatecas
Zacatecas, Zac. México
ileg@uaz.edu.mx

J. S. Wainright, R. F. Savinell
Department of Chemical Engineering
Case Western Reserve University
Cleveland, OH, United State of America

***Abstract*— Non-aqueous redox flow batteries are recently being considered an attractive option for energy storage applications since they have exhibited redox reactions with cell potentials >2 V. , and therefore hold promise for enabling high energy and power density systems. Despite the advantages of the non-aqueous redox chemistries (large potentials, fast kinetics and reversible reactions, etc.), a fundamental understanding of the factors limiting the cell performance, energy storage capacity and the long-term stability in a realistic flow battery design is needed for practical applications. In this research, the single metal vanadium (III) acetylacetonate ($V(acac)_3$) in acetonitrile redox system with a cell potential of 2.2 V was considered as the flow battery electrolyte. The overall performance and stability of the non-aqueous vanadium system were investigated in an inert atmosphere chamber with a water vapor concentrations of 250 ppm. The performance of a standard flow-through $V(acac)_3$ RFB system using Daramic was acceptable (80% CE and 73 % EE) at 10 mA cm^{-2}. The battery capacity of the $V(acac)_3$ was studied by investigating ohmic, kinetics and concentration overpotentials during battery cycling using Electrochemical Impedance Spectroscopy. The EIS results showed that battery capacity fade was associated to a decrease in the surface area of the electrodes due to the formation of a resistive film. Hydrogen evolution from trace amounts of water limited the stability of the supporting electrolyte originating undesired species that react with the electrodes.**

Keywords*— renewable energy; redox flow battery; energy storage system

I. Introduction

Redox flow batteries (RFB) are a very attractive technology for energy storage applications that can efficiently maximize the use of energy from renewable sources. A RFB is an electrochemical device that stores electrical energy as soluble electro-active species in a liquid electrolyte. The electro-active species and electrolyte are stored externally in two separate reservoir tanks and are continuously pumped to flow-through carbon electrodes in the battery stack during operation. The energy is stored or delivered by means of the redox reaction at the surface of carbon electrodes of the two electro-active species with different reduction potentials, separated by an ion exchange membrane [1, 2]. Unlike conventional batteries, redox flow battery systems are more attractive for large scale energy storage because they offer more flexible operation, simple electrode reactions, electrochemically reversible reactions, operation at low temperature, longer cycle life, higher overall energy efficiencies and easier scale-up [3].

Aqueous redox flow batteries are the state-of-the-art with some practical demonstrations [4, 5]. However, non-aqueous redox flow batteries are recently being considered since they have exhibited redox reactions with cell potentials >2 V, and therefore hold promise for enabling high energy and power density systems. The increased cell potential is considered the primary advantage of non-aqueous electrolytes over aqueous electrolytes, which are constrained to cell potentials ~1.6 V due to the electrolysis of water. There exist several reports of non-aqueous redox flow battery systems. For instance, a non-aqueous chemistry based on ruthenium acetylacetonate and ruthenium bypiridine complexes in acetonitrile was first proposed for RFBs applications in the late 1980s by Matsuda et al. [6]. In more recent years, non-aqueous chemistries based on transition metals complexed with ligand molecules (such as β-diketonate, bis(acetylacetonate)ethylenediamine, or bipyridine ligands) [7-12], redox non-innocent ligands [13], and all-organic redox active molecules [14] have all been explored for RFB applications. In addition, non-aqueous redox systems based on lithium ion (Li-ion) or Li-metal battery chemistries have been proposed for higher energy density RFB systems [15-18]. Among all these systems above, the vanadium acetylacetonate, the iron – nickel bipyridine, and the Li-organic systems have been considered in ongoing research as possibilities for RFB applications [18-20].

The vanadium (III) acetylacetonate ($V(acac)_3$), a simple β-diketonate ligand, with $TEABF_4$ in acetonitrile was proposed as a possibility for high-energy density RFB applications by the Thompson group [7, 19]. The $[V(III)(acac)_3]/[V(IV)(acac)_3]^+$ redox couple at 0.44 V *vs.* Ag/Ag^+ is associated with the positive electrode reaction, shown for battery charging in Eq. (1), whereas the $[V(II)(acac)_3]^-/[V(III)(acac)_3]$ redox couple at -1.76 V *vs.* Ag/Ag^+ is related to the negative electrode reaction, shown for battery charging in Eq. (2). The redox reactions associated with the $V(acac)_3$ chemistry in acetonitrile have exhibited a cell potential of ~2.2 V high electrochemical reversibility and very fast kinetics as estimated by cyclic voltammetry [7, 19]. The $V(acac)_3$ system has the characteristic that it is a single active species electrolyte which involve only three oxidations states, thus during discharge the redox couples in the positive and/or negative electrolyte are reverted to the same oxidation state (Eq.1 and 2).

Positive electrode:

$$[V(III)(acac)_3] \leftrightarrow [V(IV)(acac)_3]^+ + e^- \qquad 0.44\ V\ vs.\ Ag/Ag^+ \qquad (1)$$

Negative electrode:

$$[V(III)(acac)_3] + e^- \leftrightarrow [V(II)(acac)_3]^- \qquad -1.76\ V\ vs.\ Ag/Ag^+ \qquad (2)$$

Despite the many advantages that different non-aqueous $V(acac)_3$ redox electrolyte offers and the research efforts that have been done to increase its power and energy density, there are several challenges in the $V(acac)_3$ RFB cell design that still must be overcome in order to obtain a viable RFB systems for energy storage applications. The prototype vanadium acetylacetonate ($V(acac)_3$) RFB cells with TEA-Nafion and Daramic as separators exhibit promising performance for flow battery applications [21]. However, it was observed that the performance of the $V(acac)_3$ RFB cells decreased over battery cycling and time, particularly, the loss of battery capacity was observed. The loss of capacity was associated to the cell overpotentials effects (ohmic, kinetics and concentration overpotentials) in the RFB due to chemical degradation of the redox electrolyte in the positive half-cell during cycling. Additionally, it has been reported that capacity fade may occur by a) undesired transport of active species from the positive and/or negative half–cell through the separator (so-called crossover), b) deterioration of cell components (e.g. electrodes or membrane aging) and c) degradation of electrolyte due to parasitic side reactions (e.g. poor chemical stability of electrolyte) [2, 22-24].

In this work, the mechanisms of capacity fade in a $V(acac)_3$ RFB were examined by obtaining an understanding of the potential losses associated with the different cell overpotential (ohmics, kinetics and concentration overpotentials) effects during battery cycling and time (battery aging) in a controlled N_2-atmosphere glove box with a water vapor content of 250 ppm. Electrochemical Impedance Spectroscopy (EIS) was performed at the end of charge during battery cycling. EIS parameters of the $V(acac)_3$ RFB cells were obtained by fitting the impedance responses to an equivalent circuit model. Subsequently, a correlation of EIS parameters with cell overpotentials and capacity fade was discussed.

II. Experimental Methodology

A. *Charge – Discharge Battery Cycling Test*

The performance of a flow battery was studied by galvanostatic charge-discharge cycles of the $V(acac)_3$redox electrolyte in a single flow-through configuration flow cell. The flow cell was assembled as previously reported in the literature [21].

For the charge-discharge experiments, the positive and negative electrolytes consisted of a solution of 0.1 M vanadium (III) acetylacetonate ($V(acac)_3$, 98% Aldrich, US) in 0.5 M $TEABF_4$ dissolved in anhydrous CH_3CN unless other indicated. As received $V(acac)_3$ and $TEABF_4$ were used without further purification or drying processes. Each electrolyte reservoir contained a volume of 25 ml of electrolyte. Prior to any experiments, the RFB cell and the electrolyte solutions were individually purged with ultra-high purity N_2 for 30 min. Subsequently, the electrolyte was pumped into the RFB cell at a flow rate of 25 ml/min. The electrolyte was under a N_2-flowing blanket throughout the experiments to minimize any environmental contamination.

Galvanostatic charge-discharge cycles were performed at constant current mode using a standard flow-through configuration RFB cell using a Daramic separator as follows. An applied current density of 10 mA cm^{-2} was chosen unless otherwise specified. The first charge was performed up to 75% of the theoretical maximum state of charge (SOC). Then, the RFB cells were cycled within 50% of the theoretical SOC swings (25-75%) unless the potential reached the cutoff potential. The cutoff potentials were ~ 2.27 V for charging, and 1 V for discharge unless otherwise specified. Twenty charge-discharge cycles were initially programed at the fore mention experimental conditions. A standard flow-through configuration RFB cell using a TEA-Nafion separator was also considered as comparison.

At the end of the first charge, the RFB cells were stopped and were allowed to relax at the open circuit potential (OCP_{cell}) for one minute. Measurements of the OCP_{cell} after charge showed that the RFB cells reached a potential equilibrium within one minute.

B. *Electrochemical Impedance Spectroscopy*

Electrochemical Impedance Spectroscopy (EIS) was carried out at the OCP_{cell} bias at eight points per decade for frequencies ranging from 0.1 Hz to 250 kHz using an AC potential perturbation of 10 mV. Cell resistance (R_{HF}) was taken to be the high frequency intercept of the Nyquist plot. Additionally, EIS measurements were performed during battery cycling at the end of charge of charge 1, 11 and 21 in a similar manner as described above. After the EIS measurement, a cell polarization curve was obtained using cyclic voltammetry (CV) between 300 mV and -800 mV *vs.* OCP_{cell} at a scan rate of 10 mV s^{-1}. The slope of the polarization curve (R_{slope}) in the linear region was calculated and compared with the DC limit (R_{DC}) of the impedance response of the $V(acac)_3$ RFB cell as a further check of the EIS analysis. In this work, R_{DC} was considered to be $R_{HF} + R_E + R_{MT}$ as estimated by the fitting of the equivalent circuit model.

All charge-discharge battery experiments were carried out at room temperature in a N_2-filled glove box with 250 ppm water unless other specified. A Solartron SI 1287A potentiostat/galvanostat coupled with a Solartron 1260 impedance/gain phase analyzer was employed to conduct the battery cycle tests and EIS measurements. An equivalent circuit model was proposed to estimate the physical and electrochemical parameters of the $V(acac)_3$ RFB cell as described below. The equivalent circuit analysis of the impedance response was done using Zview software (Scribner Associated, Inc). Solartron 1260 impedance/gain phase analyzer was employed to conduct the battery cycle tests and EIS measurements.

III. Results and Discussion

A. Charge – Discharge Battery Cycling Test

The performance of the $V(acac)_3$ redox system was investigated in a traditional flow-through electrolyte/electrode configuration RFB cell (the most common flow cell design used among the RFB community research) with daramic as separator, Fig. 1a. The first seven charge-discharge cycles are presented. The charge-discharge cycles exhibited high electrochemical reversibility as anticipated for the $V(acac)_3$ redox electrolyte using cyclic voltammetry as reported by Shinkle *et al.* [19]. Single charge and discharge potential plateaus were observed indicating, that a single reaction was occurring in each half-cell of the flow battery (V(II)/V(III) at the negative and V(III)/V(IV) at the positive half-cell). An OCP_{cell} of ~2.2 V was measured at the end of the first charge. Overall, this value is in good agreement with the cell potential estimated by the difference in half-wave potentials between the positive and negative redox couples of the $V(acac)_3$ electrolyte measured using cyclic voltammetry (~2.2 V)[19].

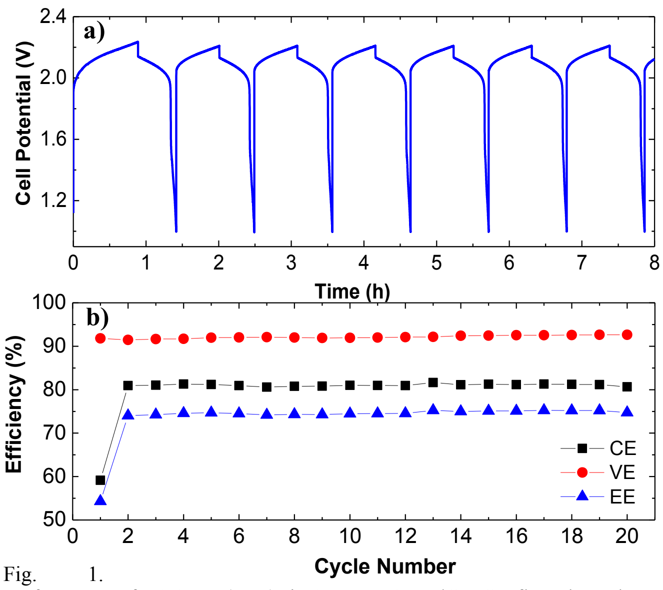

Fig. 1. Performance of a 0.1M $V(acac)_3$ in 0.5M $TEABF_4/CH_3CN$ flow-through RFB cell with Daramic as separator. a) Charge-discharge cycles. Cycles 1 to 7 are shown. b) Efficiencies for charge-discharge cycles. Current density: 10 mA cm^{-2}. Flow rate: 25 ml/min. Active area: 5.65 cm^2. Room temperature.

The charge-discharge cycling performance of the $V(acac)_3$ RFB cell employing Daramic separator was evaluated by calculating coulombic (CE), voltaic (VE) and energy (EE) efficiencies. The average CE, VE and EE efficiencies for the $V(acac)_3$ RFB/Daramic were ~80%, ~92% and ~73%, respectively, for twenty cycles at 10 mA cm^{-2} (Fig. 1b). As a reference, the $V(acac)_3$ RFB/TEA-Nafion exhibited a CE of ~90%, VE of ~ 92% and EE of ~83% for twenty charge-discharge cycles at 10 mA/cm^2 (Table 1). The 20 % CE losses in the RFB with Daramic separator were likely associated to a decrease in the concentration of active species due to cross-over through the separator and also to parallel side as compared to 10% CE losses registered for the $V(acac)_3$ RFB with TEA-Nafion. The TEA-Nafion separator is more ion permselective than the daramic separator thus much less crossover of active species was expected. Consequently, the energy efficiency for the RFB with Daramic separator was lower as compared to that of the RFB/TEA-Nafion. Note that the voltaic efficiency of both flow-through RFB with different separators was comparable (~ 92 %) which was expected since these cells exhibited a similar R_{HF} value (Table 1).

Table 1. Summary of the performance parameters of 0.1 M $V(acac)_3$ in 0.5 M $TEABF_4$/acetonitrile RFB cells at 10 mA cm^{-2}.

Separator	OCP_{cell}[1] (V)	R_{HF}[1] (Ω cm^2)	CE (%)	VE (%)	EE (%)
Daramic	2.20	2.2	80.0	92.0	73.0
TEA^+ - Nafion	2.22	2.4	89.9	92.6	83.2

[1] OCP_{cell} and R_{HF} are reported at the end of the first charge.

The $V(acac)_3$ RFB with daramic exhibited constant energy efficiency (EE) over the battery cycling test presented in Fig. 1. This is of great importance because EE is directly linked to the battery capacity. The battery capacity of a RFB system is critical to be considered as an energy storage option for practical applications. However, battery capacity can be diminished by potential losses related to kinetic, concentration (mass transfer) and ohmic overpotentials over cycling and time, which will affect the voltaic efficiency, thus limiting the long – term stability of the RFB system for practical applications.

B. Battery Capacity Study by EIS

The battery capacity of the $V(acac)_3$ system with Daramic was investigated using Electrochemical Impedance Spectroscopy (EIS) at the end of charges 1, 11 and 21 (as described in Section IIB) in order to determine changes in the cell characteristics (potential losses) caused by charge-discharge cycling as shown in Fig. 1. Typical Nyquist response plots for the $V(acac)_3$ flow-through RFBs with Daramic separator exhibited two time constants (Fig. 2). At high frequency, a semicircle (10^4 to 10^1 Hz) associated with the coupling of the electrode resistance (R_E) and a constant phase element (CPE_E) (10^2 to 10^1 Hz) was observed. At low frequency, R_{MT} (10^0 to 10^{-1} Hz) was associated with a finite Warburg diffusion impedance. The $V(acac)_3$ flow-through RFB/Daramic exhibited similar Nyquist impedance response independent of cycle number. The equivalent circuit in Fig. 2 was used to perform the impedance analysis. The parameters R_{HF}, R_E and R_{MT} are related to ohmic, activation and concentration overpotentials, respectively. A constant phase element (CPE_E) was considered since the impedance response of the electrodes sometimes did not show the ideal response expected for single electrochemical reactions (ideally capacitive behavior). For this study, the equivalent circuit fit the individual impedance responses with good accuracy as discussed below (Fig. 2, black line and Table 2).

The EIS parameters used in the equivalent circuit model can be determined with good accuracy (Table 2). The fitting result exhibited that R_{HF} did not increase over battery cycling. The Daramic separator exhibited good chemical and mechanical stability in the $V(acac)_3$ in $TEABF_4$/acetonitrile electrolyte during the cycling test. The ohmic losses (iR_{HF}) at 10 mA cm^2 were constant over time (23 mV for the flow-through RFB). The ohmic losses were mostly associated to the areal resistance of the separator, ~ 68% of the total ohmic losses for the flow-through (based on the separator conductivity, 17.2 mS/cm) [21]. The remaining of the iR_H losses were associated with electric contact resistance between cell components (~32%).

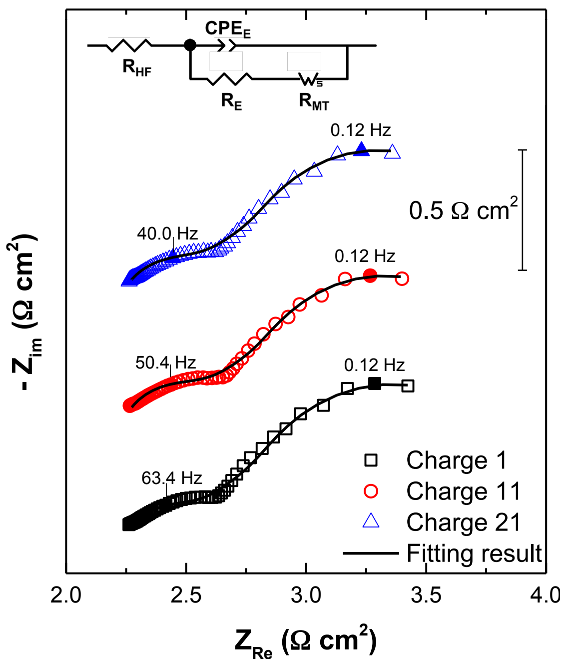

Fig. 2. Nyquist plots recorded at the end of charge for 0.1 M $V(acac)_3$ in 0.5 M $TEABF_4/CH_3CN$ in a flow-through RFB with Daramic as separator (Fig. 1). Inset: equivalent circuit model used to fit the impedance response. Membrane active area: 5.65 cm^2.

TABLE 2. PARAMETERS FOR 0.1 M $V(ACAC)_3$ IN 0.5 M $TEABF_4/CH_3CN$ FLOW-THROUGH RFB USING DARAMIC.

Parameter	Charge 1	Charge 11	Charge 21
L (1×10^{-8} H)	-	-	-
R_{HF} (Ω cm^2)	2.27 ± 0.01	2.27 ± 0.01	2.27 ± 0.01
R_E (Ω cm^2)	0.31 ± 0.01	0.36 ± 0.01	0.35 ± 0.01
R_{MT} (Ω cm^2)	1.43 ± 0.02	1.30 ± 0.01	1.32 ± 0.02
CPE_E-Q (1×10^{-2} $s^{(\alpha-1)}$ F $\cdot cm^{-2}$)	7.90 ± 1.14	9.2 ± 1.0	11.8 ± 1.3
CPE_E-α	0.62 ± 0.02	0.60± 0.02	0.57 ± 0.02
$C_{dl,E}^{eff}$ (mF/cm^2)	28.0 ± 7.0	32.0 ± 6.6	43.0 ± 9.0
R_{DC}(Ω cm^2)	4.01	3.94	3.94
R_{slope} (Ω cm^2)	3.98	3.89	3.84

The $V(acac)_3$ flow-through RFB/Daramic separator experienced minimal increases in R_E and R_{MT} as reported in Table 2. Therefore, the activation and concentration overpotential were practically constant over cycling test indicating a constant cell polarization. This is consistent with no loss in battery capacity. Although R_E showed an increase of 10% by charge 21 as compared to after charge 1 (Table 2), $C^{eff}_{dl,E}$ shows a slight increase over time indicating that the redox reactions are more distributed within the porous structure of electrode rather than the loss of active surface area. Here, the effective capacitance ($C^{eff}_{dl,E}$) was estimated from the CPE parameters (CPE-Q and CPE-α) using the Brug model as reported in [25-27]. In addition, it is suggested that the constancy of R_{MT} was associated with a balanced re-mixing of electrolyte due to crossover between the active species in the negative and positive half-cell occurring during battery cycling test. Recall that Daramic separator allow higher rates of crossover than TEA-Nafion membrane as reported by coulombic efficiency at 10 mA cm^{-2}. Consequently, the RFB cell did not exhibit a polarization due to mass transfer limitation. In addition, the charges at 10 mA cm^2 did not occur a 100% current efficiency since the OCP_{cell} at the end of charge 11 and 21 was measured to be ~ 2.17 V corresponding to a 37% actual SOC as compared to an OCP_{cell} of 2.2 V expected for the 50% theoretical SOC swings in the battery cycling test. This also suggests that some of the applied current loss can be due to crossover. It is expected that battery cycling at higher current densities (>10 mA cm^{-2}) would decrease observed crossover effects of active species and, probably, will lead to increased cell polarization effects as discussed below.

The 0.1 M $V(acac)_3$ in 0.5 M $TEABF_4$/acetonitrile flow-through RFB with Daramic separator was considered for further investigation to pursue insight of additional factors that may cause battery capacity decay at other experimental conditions than those described in Fig. 2. First, the $V(acac)_3$ flow-through RFB/daramic was driven to a high cell polarization to simulate an aging process, i.e. physical degradation of cell components, as described below. To increase the cell polarization, a charge-discharge cycling test was performed at higher applied current density, first at 100 mA cm^{-2} and, then at 80 mA cm^{-2}. For this test, 50% theoretical SOC swings were carried out. A charging cutoff potential of 3.5 V and a discharging cutoff potential of 1 V were used (data not shown). Ten cycles were performed at each charge-discharge current density. Subsequently, EIS measurements were performed at the end of charge in a similar manner as described in Section IIB.

The Nyquist impedance responses of the $V(acac)_3$ RFB/Daramic cell at the end of the 10^{th} charge at both 100 mA cm^{-2} and 80 mA cm^{-2} are shown in Fig. 3. Conversely to low current density charge – discharge cycles, the impedance responses exhibited three time constants. A Voigt element was added to the equivalent circuit in Fig. 2 in order to describe the capacitive semicircle at high frequency which is associated with the coupling of R_F and C_F. The overlapping semicircle at middle and low frequencies were related to the resistance of the electrode reaction (R_E) and to a mass transfer resistance (R_{MT}). The equivalent circuit model in Fig. 3 was used to fit the impedance response and estimate the RFB cell characteristics at the end of charge.

To gain additional insight, the $V(acac)_3$ flow-through RFB/Daramic cell was aged by performing a discharge at 10 mA cm^{-2} for ~ 3 h (right after the last charge at 80 mA cm^{-2}). The $V(acac)_3$ RFB cell reached an extreme cell potential of ~-4.5 V. At this potential, the decomposition of both the $V(acac)_3$ redox active species and the $TEABF_4$/acetonitrile system would be expected. The electrochemical potential window of the $TEABF_4$/acetonitrile system is reported to be stable below ~3.3 V *vs.* SCE [28]. Trace amounts of water also reduce the chemical stability of both the redox electrolyte and the $TEABF_4$/acetonitrile system at high potentials [29, 30].

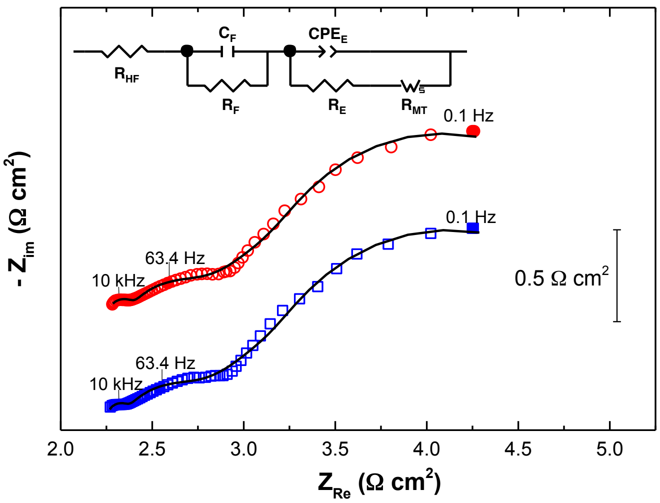

Fig. 3. Nyquist plots recorded for 0.1 M $V(acac)_3$ in 0.5 M $TEABF_4/CH_3CN$ RFB with Daramic at the end of the 10th charge at after cycling at a) 100 mA cm^{-2} (blue squares) and b) 80 mA cm^{-2} (red circles). Fitting result (black line). Insert: equivalent circuit model used to fit the impedance response. Membrane active area: 5.65 cm^2.

After the aging process, the health condition of the battery was investigated by performing a charge-discharge cycling test at low current density (20 mA cm^{-2}) with a time corresponding to 50% theoretical SOC swings. In addition, EIS measurements were carried out at the end of the last charge in order to track the evolution of R_F and the cell overpotential effects.

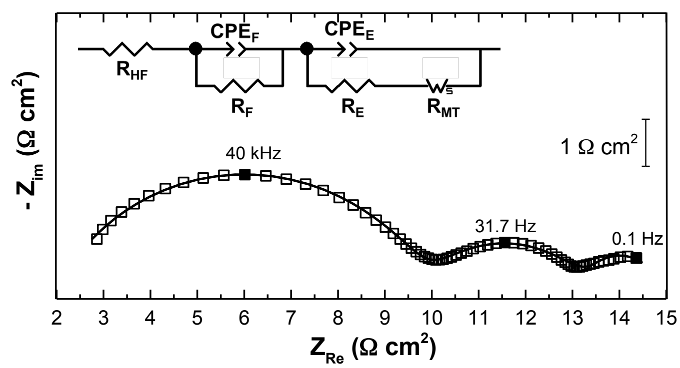

Fig. 4. Nyquist plot recorded for an aged 0.1 M $V(acac)_3$ in 0.5 M $TEABF_4/CH_3CN$ in a flow-through RFB/ Daramic (black squares) and the fitting result (solid line). Insert: equivalent circuit model used to fit the individual impedance response. Membrane Active area: 5.65 cm^2.

The Nyquist impedance response of the aged $V(acac)_3$ RFB/Daramic at the end of the last charge is shown in Fig. 4. The impedance response displayed three time constants which were associated with the processes described above (R_F, R_E and R_{MT} at high, middle and low frequencies, respectively). The impedance response was fit to the equivalent circuit depicted in Fig. 4 very well. The Characteristic parameters of the $V(acac)_3$ RFB/Daramic before (at the end of the initial charge, Table 2) and after aging obtained by equivalent circuit analysis are reported in Table 3. As a reference, the EIS parameters after the charge-discharge cycles at 80 mA cm^{-2} (Fig. 3) are reported in Table 3 (refer to column "after high *i*") since the RFB/Daramic at high polarization started to revealed R_F.

TABLE 3. PARAMETERS FOR 0.1 M $V(ACAC)_3$ IN 0.5 M $TEABF_4$ /CH_3CN FLOW-THROUGH RFB USING DARAMIC BEFORE AND AFTER BATTERY AGING.

Parameter	Before aging	After high *i*	After aging
R_{HF} (Ω cm^2)	2.27 ± 0.01	2.28 ± 0.01	1.96 ± 0.01
R_F (Ω cm^2)	-	0.10 ± 0.01	7.99 ± 0.03
R_E (Ω cm^2)	0.31 ± 0.01	0.47 ± 0.02	3.24 ± 0.04
R_{MT} (Ω cm^2)	1.43 ± 0.02	2.29 ± 0.02	1.64 ± 0.01
CPE_F-Q (1×10^{-4} $s^{(\alpha-1)}$ F $\cdot cm^{-2}$)	-	-	0.19 ± 0.01
CPE_F-α	-	-	0.71 ± < 0.01
CPE_E-Q (1×10^{-2} $s^{(\alpha-1)}$ F $\cdot cm^{-2}$)	7.9 ± 1.14	4.6 ± 0.64	0.79 ± 0.04
CPE_E-α	0.62 ± 0.02	0.65 ± 0.02	0.68 ± 0.01
C_F^{eff} (μF/cm^2)	-	118.2 ± 14.3	0.27 ± 0.02
$C_{dl,E}^{eff}$ (mF/cm^2)	28.0 ± 7.0	13.4 ± 3.4	1.17 ± 0.10
R_{DC}(Ω cm^2)	4.01	5.10	14.84
R_{slope} (Ω cm^2)	3.98	5.08	14.71

In Table 3, the process associated with R_F dramatically increased after the aging process (by a factor of ~ 78 times as compared with the value estimated "after high *i*"). R_E increased by a factor of ~10 as compared before aging (first charge at 10 mA cm^{-2}) whereas the effective double layer capacitance, $C_{dl,E}^{eff}$, decreased before and after aging by a factor of 25, consequently, the active surface area of the electrode decreased. These results support the hypothesis that a surface film was formed (such as salt film/layer, adsorption layer, or a polymeric layer) on either the negative or positive electrode. Moreover, the ability to measure the capacitive semicircle at high frequencies (associated with a surface film, R_F) does not depend on film thickness, but it is sensitive to the effective conductivity of the film [31]. Thus, the resistive surface film in the $V(acac)_3$ RFB cells can be related to accumulation of conductive ions/aggregates from the species in the electrolyte solution (e.g. TEA^+, BF_4^+ and/or vanadium species). Additionally, the effective capacitance (C_F^{eff}) associated with R_F as determined by equivalent circuit analysis was small as compared with the double layer capacitance after aging (< 1μF cm^{-2} *vs.* ~1 mF cm^{-2}), suggesting that this is linked to a different physical process (Table 3). Typically, a dielectric material (such as salt film, oxide film, and/or polymer film) exhibits very small capacitance which can be negligible as compared to the double layer capacitance of the electrode[31]. Also, a dielectric material can be polarized contributing to the potential losses such as in the $V(acac)_3$ RFB/Daramic as discussed below.

According with these results, the potential losses associated with a resistive film (R_F) and the activation overpotential would have a faster effect in the decay of the energy performance (which is related to voltaic efficiency fade) than the ohmic and concentration overpotential as reported for R_{HF} and R_{MT} before and after aging (Table 3) of a

$V(acac)_3$ RFB/Daramic at high operational conditions (high applied current densities). However, the potential loss due to the resistive film would depend on the concentration of the conductive species/aggregates at the surface of the electrode over time as reported elsewhere[32]. For instance, if a very small amount of conductive specie is adsorbed at the surface of the electrode, the current path maintained through this species is negligible. However, it becomes polarizable as the accumulation of conductive species increases. In this case, the impedance of the $V(acac)_3$ RFB/Daramic will include a third time constant ($\tau=R_F C^{eff}_F$) as reveled in Fig 3.

A better understanding of the chemical/physical mechanism that causes the formation of the passive film on the electrodes in the $V(acac)_3$ RFB cell will require further work that was not pursued here. However, it is suggested that it may occur by similar mechanisms as reported for electrochemical double layer capacitors (EDLC) [28, 33-36]. Although, for a $V(acac)_3$ in $TEABF_4$/acetonitrile RFB cell, the mechanism may be more complex since vanadium redox species are also involved. Briefly, in the electrochemical double layer capacitors (another energy-storage technology which compromise high-surface area carbon electrodes and the $TEABF_4$/acetonitrile electrolyte), the loss in capacitance (e.g. aging of carbon electrodes) has been associated with the blockage of pores by trapped ions or decomposition products of the organic electrolyte [28,33-36]. The electrolyte decomposition has been related with the trace amounts of water which reduced its electrochemical potential window and hydrogen evolution [28, 30].

IV. CONCLUSIONS

The $V(acac)_3$ in a prototype RFB cell using Daramic showed excellent performance for flow battery applications. The use of Daramic as separator allowed charge-discharge current densities two order of magnitude larger than previous literature (10 mA/cm^2 *vs.* $\leq$ 0.14 mA/cm^2) [19]. Much higher electrochemical reversibility was observed during battery cycling than previous literature.

Electrochemical Impedance Spectroscopy analysis was used to estimate the contribution of the cell overpotentials leading toward an understanding of the battery capacity of a $V(acac)_3$ RFB with Daramic over time. Capacity fade was associated with increases in the activation overpotentials due to passivation of the high surface area carbon electrodes.

A growing film (R_F) (either on the positive or negative electrode) was revealed by equivalent circuit analysis to decreased the surface area of the electrodes in the $V(acac)_3$ RFB increasing the apparent activation overpotential. The film was formed as a function of cell polarization and time. It is proposed that the film formation was due to accumulation of conductive ions species from the decomposition of the electrolyte in presence of trace amounts of water. In addition, it is suggested that the potential loss associated with the surface film might not play a significant role toward the loss in capacity at low cell polarization and at the early cycle life of the battery. However, the effect of the resistive film may be significant if the cell polarization increases either by overpotential effects increases or by high applied current densities. In such cases, the resistive surface film would contribute much faster in the performance decay of the RFB system in the long-term operation (specifically, voltaic efficiency will decrease) and, perhaps, the film effect would be more detrimental to the battery capacity than the cell overpotential effects (activation, concentration and ohmic overpotential).

V. ACKNOWLEDGEMENTS

This work was supported by the National Science Foundation, Sustainable Energy Pathways Program (NSF-1230236). I.L.E.-G. gratefully acknowledges to the Electrochemical Enginering and Energy Lab at Case for all the support and use of the facilities to carry this work. I.L.E.-G. also thanks to the Mexican Council for Science and Technology (CONACyT) and the Autonomous University of Zacatecas (UAZ–México) for financial support.

REFERENCES

[1] T. Nguyen and R. F. Savinell, "Flow batteries," *Interface,* vol. 19, pp. 54-56, 2010.

[2] H. Vafiadis and M. Skyllas-Kazacos, "Evaluation of membranes for the novel vanadium bromine redox flow cell," *Journal of Membrane Science,* vol. 279, pp. 394-402, 2006.

[3] C. Ponce de León, A. Frías-Ferrer, J. González-García, D. A. Szánto, and F. C. Walsh, "Redox flow cells for energy conversion," *Journal of Power Sources,* vol. 160, pp. 716-732, 2006.

[4] P. Alotto, M. Guarnieri, and F. Moro, "Redox flow batteries for the storage of renewable energy: A review," *Renewable and Sustainable Energy Reviews,* vol. 29, pp. 325-335, 2014.

[5] M. Skyllas-Kazacos, G. Kazacos, G. Poon, and H. Verseema, "Recent advances with UNSW vanadium-based redox flow batteries," *International Journal of Energy Research,* vol. 34, pp. 182-189, 2010.

[6] Y. Matsuda, K. Tanaka, M. Okada, Y. Takasu, M. Morita, and T. Matsumura-Inoue, "A rechargeable redox battery utilizing ruthenium complexes with non-aqueous organic electrolyte," *Journal of Applied Electrochemistry,* vol. 18, pp. 909-914, 1988.

[7] Q. Liu, A. E. S. Sleightholme, A. A. Shinkle, Y. Li, and L. T. Thompson, "Non-aqueous vanadium acetylacetonate electrolyte for redox flow batteries," *Electrochemistry Communications,* vol. 11, pp. 2312-2315, 2009.

[8] A. E. S. Sleightholme, A. A. Shinkle, Q. Liu, Y. Li, C. W. Monroe, and L. T. Thompson, "Non-aqueous manganese acetylacetonate electrolyte for redox flow batteries," *Journal of Power Sources,* vol. 196, pp. 5742-5745, 2011.

[9] M.-J. L. Junyoung Mun, z, Joung-Won Park, Duk-Jin Oh, Doo-Yeon Lee and Seok-Gwang Doo, "Non-aqueous redox flow batteries with nickel and iron tris(2,2′-bipyridine) complex electrolyte," *The Electrochemical Society, Electrochemical and Solid-State Letters,* vol. 15, pp. A80-A82, 2012.

[10] M. H. Chakrabarti, E. P. L. Roberts, C. Bae, and M. Saleem, "Ruthenium based redox flow battery for solar energy storage," *Energy Conversion and Management,* vol. 52, pp. 2501-2508, 2011.

[11] Q. Liu, A. A. Shinkle, Y. Li, C. W. Monroe, L. T. Thompson, and A. E. S. Sleightholme, "Non-aqueous chromium acetylacetonate electrolyte for redox flow batteries," *Electrochemistry Communications,* vol. 12, pp. 1634-1637, 2010.

[12] D. Zhang, H. Lan, and Y. Li, "The application of a non-aqueous bis(acetylacetone)ethylenediamine cobalt electrolyte in redox flow battery," *Journal of Power Sources,* vol. 217, pp. 199-203, 2012.

[13] P. J. Cappillino, H. D. Pratt, N. S. Hudak, N. C. Tomson, T. M. Anderson, and M. R. Anstey, "Application of redox non-innocent ligands to non-aqueous flow battery electrolytes," *Advanced Energy Materials,* vol. 4, pp. 1300566, 2014.

[14] Z. Li, S. Li, S. Liu, K. Huang, D. Fang, F. Wang, *et al.*, "Electrochemical properties of an all-organic redox flow battery using 2,2,6,6-tetramethyl-1-piperidinyloxy and n-methylphthalimide," *Electrochemical and Solid-State Letters,* vol. 14, pp. A171-A173, 2011.

[15] F. R. Brushett, J. T. Vaughey, and A. N. Jansen, "An all-organic non-aqueous lithium-ion redox flow battery," *Advanced Energy Materials,* vol. 2, pp. 1390-1396, 2012.

[16] S. Hamelet, T. Tzedakis, J. B. Leriche, S. Sailler, D. Larcher, P. L. Taberna*, et al.*, "Non-Aqueous Li-Based Redox Flow Batteries," *Journal of The Electrochemical Society,* vol. 159, pp. A1360-A1367, 2012.

[17] X. L. Wei, W. Xu, M. Vijayakumar, L. Cosimbescu, T. B. Liu, V. Sprenkle*, et al.*, "TEMPO-Based Catholyte for High-Energy Density Nonaqueous Redox Flow Batteries," *Advanced Materials,* vol. 26, pp. 7649-7653, 2014.

[18] X. Wei, L. Cosimbescu, W. Xu, J. Z. Hu, M. Vijayakumar, J. Feng*, et al.*, "Towards high-performance nonaqueous redox flow electrolyte via ionic modification of active species," *Advanced Energy Materials,* vol. 5, pp. 1400678, 2015.

[19] A. A. Shinkle, A. E. S. Sleightholme, L. T. Thompson, and C. W. Monroe, "Electrode kinetics in non-aqueous vanadium acetylacetonate redox flow batteries," *Journal of Applied Electrochemistry,* vol. 41, pp. 1191-1199, 2011.

[20] D.-H. Kim, S.-J. Seo, M.-J. Lee, J.-S. Park, S.-H. Moon, Y. S. Kang*, et al.*, "Pore-filled anion-exchange membranes for non-aqueous redox flow batteries with dual-metal-complex redox shuttles," *Journal of Membrane Science,* vol. 454, pp. 44-50, 2014.

[21] I. Escalante-García, J. Wainright, R. Savinell, T. Thompson, "Performance of a non-aqueous vanadium acetylacetonate prototype redox flow battery: examination of separators and capacity decay", *Journal of The Electrochemical Society*, vol. 162, pp. A363-A372, 2015.

[22] W. Wang, Q. Luo, B. Li, X. Wei, L. Li, and Z. Yang, "Recent progress in redox flow battery research and development," *Advanced Functional Materials,* vol. 23, pp. 970-986, 2013.

[23] E. Agar, A. Benjamin, C. R. Dennison, D. Chen, M. A. Hickner, and E. C. Kumbur, "Reducing capacity fade in vanadium redox flow batteries by altering charging and discharging currents," *Journal of Power Sources,* vol. 246, pp. 767-774, 2014.

[24] V. Pop, *Battery management systems: accurate state-of-charge indication for battery powered applications*. Springer, Netherlands, 2008.

[25] B. Hirschorn, M. E. Orazem, B. Tribollet, V. Vivier, I. Frateur, and M. Musiani, "Determination of effective capacitance and film thickness from constant-phase-element parameters," *Electrochimica Acta,* vol. 55, pp. 6218-6227, 2010.

[26] M. E. Orazem and B. Tribollet, "Time-constant dispersion," in *Electrochemical Impedance Spectroscopy*, ed: John Wiley & Sons, Inc., 2008, pp. 233-263.

[27] Teisis Isma

[28] K. I. Makoto Ue, Shoichiro Mori, "Electrochemical properties of organic liquid electrolytes based on quaternary onium salts for electrical double-layer capacitiors," *Journal of the Electrochemical Society,* vol. 141, p. 2989, November 1994.

[29] A. A. Shinkle, A. E. S. Sleightholme, L. D. Griffith, L. T. Thompson, and C. W. Monroe, "Degradation mechanisms in the non-aqueous vanadium acetylacetonate redox flow battery," *Journal of Power Sources,* vol. 206, pp. 490-496, 2012.

[30] P. Kurzweil and M. Chwistek, "Electrochemical stability of organic electrolytes in supercapacitors: spectroscopy and gas analysis of decomposition products," *Journal of Power Sources,* vol. 176, pp. 555-567, 2008.

[31] M. E. Orazem and B. Tribollet, "Equivalent Circuit Analogs," in *Electrochemical Impedance Spectroscopy*, ed: John Wiley & Sons, Inc., 2008, pp. 153-162.

[32] V. F. Lvovich, "Impedance analysis of complex systems," in *Impedance Spectroscopy*, ed: John Wiley & Sons, Inc., 2012, pp. 113-161.

[33] M. Zhu, C. J. Weber, Y. Yang, M. Konuma, U. Starke, K. Kern*, et al.*, "Chemical and electrochemical ageing of carbon materials used in supercapacitor electrodes," *Carbon,* vol. 46, pp. 1829-1840, 2008.

[34] P. Azaïs, L. Duclaux, P. Florian, D. Massiot, M.-A. Lillo-Rodenas, A. Linares-Solano*, et al.*, "Causes of supercapacitors ageing in organic electrolyte," *Journal of Power Sources,* vol. 171, pp. 1046-1053, 9/27/2007.

[35] D. Aurbach, M. D. Levi, G. Salitra, N. Levy, E. Pollak, and J. Muthu, "Cation trapping in highly porous carbon electrodes for EDLC cells," *Journal of The Electrochemical Society,* vol. 155, pp. A745-A753, 2008.

[36] M. Deschamps, E. Gilbert, P. Azais, E. Raymundo-Piñero, M. R. Ammar, P. Simon*, et al.*, "Exploring electrolyte organization in supercapacitor electrodes with solid-state NMR," *Nat Mater,* vol. 12, pp. 351-358, 2013.

Photocatalytic Hydrogen generation by oxide based nanostructures

P. Pizá-Ruiz, A. Sáenz-Trevizo, P. Amézaga-Madrid, V. Collins-Martínez, M. Meléndez-Zaragoza, J. Salinas-Gutiérrez, S. Olive-Méndez, T. Holguín-Momaca and M. Miki-Yoshida.*

Centro de Investigación en Materiales Avanzados S.C.

Chihuahua, Chihuahua, C.P. 31136, Mexico,

*Corresponding author: mario.miki@cimav.edu.mx

***Abstract*—Oxide based nanostructures were grown by aerosol assisted chemical vapor deposition onto borosilicate glass substrates. Experimental setup and general synthesis conditions were reported elsewhere. Nanostructures were coatings of: Ti oxide, composites of Ti-Fe and Cu-Fe oxides and multilayers of TiOx-FeOx and CuFeOx-SnOx. All nanostructures were covered with a layer of Pt nanoparticles. Microstructure of the samples was analyzed by electron microscopy and x-ray diffraction. Optical properties were also determined in the UV-visible-near IR interval. Photocatalytic generation of Hydrogen was evaluated in a batch reactor under visible light irradiation, using a filtered low vapor pressure Hg lamp of 250 W. Hydrogen evolution was tested every hour by gas chromatography.**

Keywords—direct water splitting, Hydrogen generation, metal oxide heterostructures

I. INTRODUCTION

Solar water splitting represents a promising alternative for energy generation [1-5]. This, since the resulting molecular H_2 can be used as a sustainable and clean power source [1-3]. However, physical limitations related to the efficient energy conversion have been found [2]. From existing methods, direct water splitting [1] and photo-electrochemical processes [4, 5] using semiconductors, are being extensively studied and in some cases, efficiently applied [1]. Thus, in search for effective and stable materials, this work focus on the development of composite and hetero-structured metal oxide layers with Pt nanoparticles for direct oxidation of water.

II. EXPERIMENTAL

Samples comprising metal oxide based materials were synthesized onto borosilicate glass substrates (BGS) using the aerosol assisted chemical vapor deposition (AACVD) technique as in [6]. The layers' structure of the samples appears summarized in Table 1. The microstructure, including elemental composition of the synthesized coatings, was analyzed by X-ray diffraction (XRD) and scanning electron microscopy (SEM), involving energy dispersive x-ray spectroscopy (EDXS). The total transmittance and reflectance spectra of the samples were measured in the UV-visible- near IR interval. Moreover, the generation of H_2 was evaluated using each sample inside a customized radiation chamber. A solution of distilled water and 2% of methanol was used for the generation of H_2. All samples were irradiated with a filtered low vapor pressure Hg lamp of 250 W. The evolution of the generated H_2 was monitored every hour, up to 24 h, using gas chromatography (GC).

TABLE I. CONFIGURATION OF THE METAL OXIDES USED FOR THE GENERATION OF H_2

Oxide layers	Sample				
	A	***B***	***C***	***D***	***E***
First layer	TiO_2	TiO_2	TiO_2	TiO_2	TiO_2
Second layer	nano Pt	FeO_x	TiO_2/FeO_x	$CuFeO_2$	$CuFeO_2$
Third layer		nano Pt	nano Pt	nano Pt	SnOx
Fourth layer					nano Pt

III. RESULTS AND DISCUSSION

A. *Morphology, chemical composition, crystalline structure and optical properties*

Secondary electron micrographs revealing the surface morphology of representative samples are shown in Fig. 1. All micrographs show well distributed grains covering the surface. No cracks or defects were evident. Micrograph for sample A, obtained using backscattered electrons at high magnification (Fig. 1 a), shows the existence of a layer formed of irregular nanoparticles of around 20 - 30 nm. According to synthesis configuration, this layer corresponded to the formation of Pt nanoparticles. Fig. 1 e) shows the elemental composition determined by EDXS of samples C, D and E. Results prove the existence of the different metals oxides in the nanostructures.

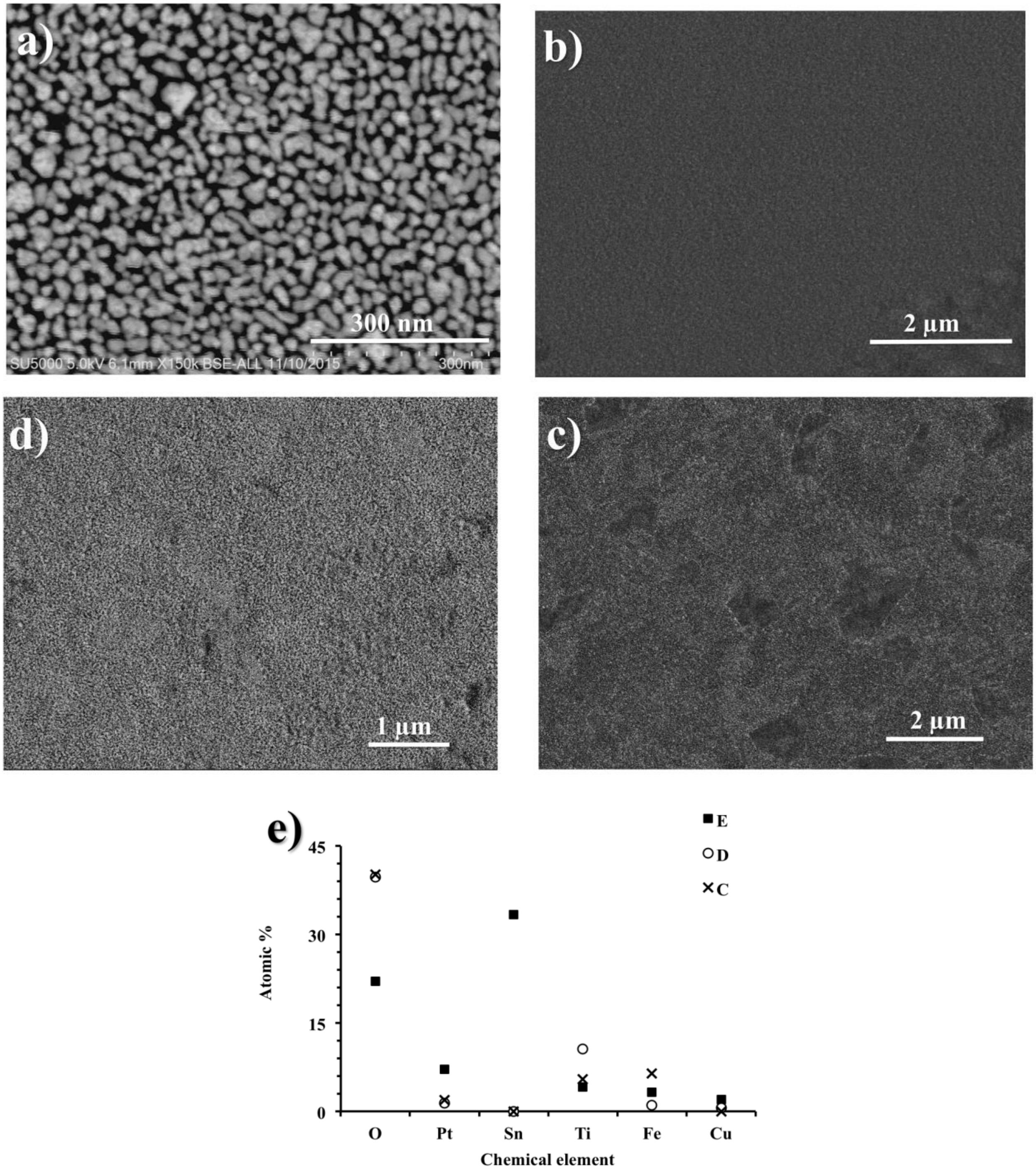

Fig. 1 a) Backscattered SEM micrograph of sample A showing the uniform distribution of Pt nanoparticles. b), c) and d) Secondary SEM micrographs of samples C, D and E, respectively. e) Elemental composition of samples C, D and E proving the existence of different metal oxide layers. All images reveal the surface topography of the developed materials. Most of the images exhibit smooth and uniform coatings.

The crystalline structure and optical absorptance of selected samples appear in Fig. 2. Diffractograms in Fig. 2 a) evidenced the existence of amorphous and crystalline phases on the developed materials. Interestingly, the presence of crystalline TiO_2 as anatase was identified in all cases using the peak at around 25.2º (PDF 021-1272). For sample C, mostly amorphous components were detected. For samples D and E, the formation of crystalline Pt nanoparticles accompanying the layer of TiO_2 (peaks at around 39.7º and 46.2º, PDF 01-071-6560), was observed.

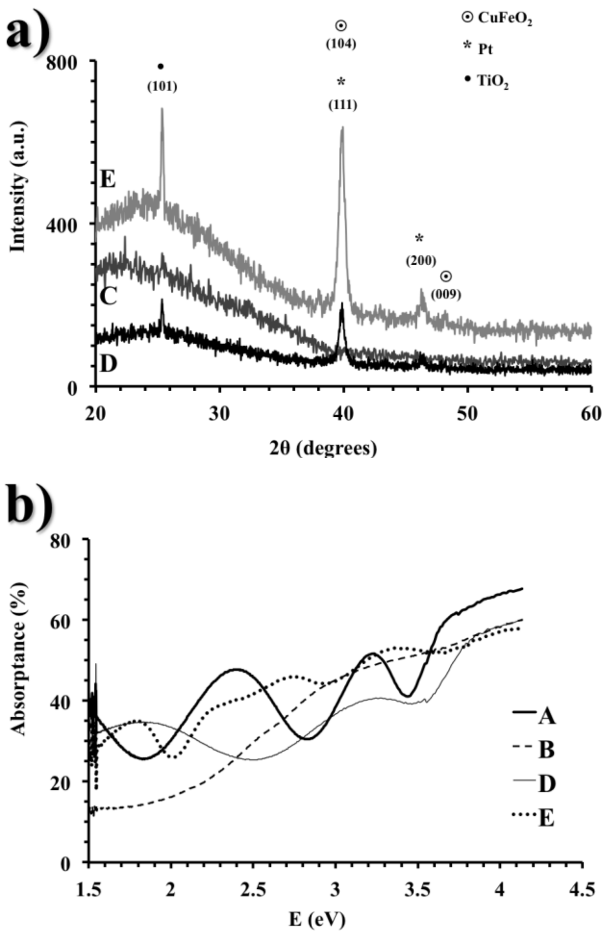

Fig. 2. a) diffractograms of samples C, D and E exhibiting the crystalline structure of the samples. b) absorptance spectra of selected samples.

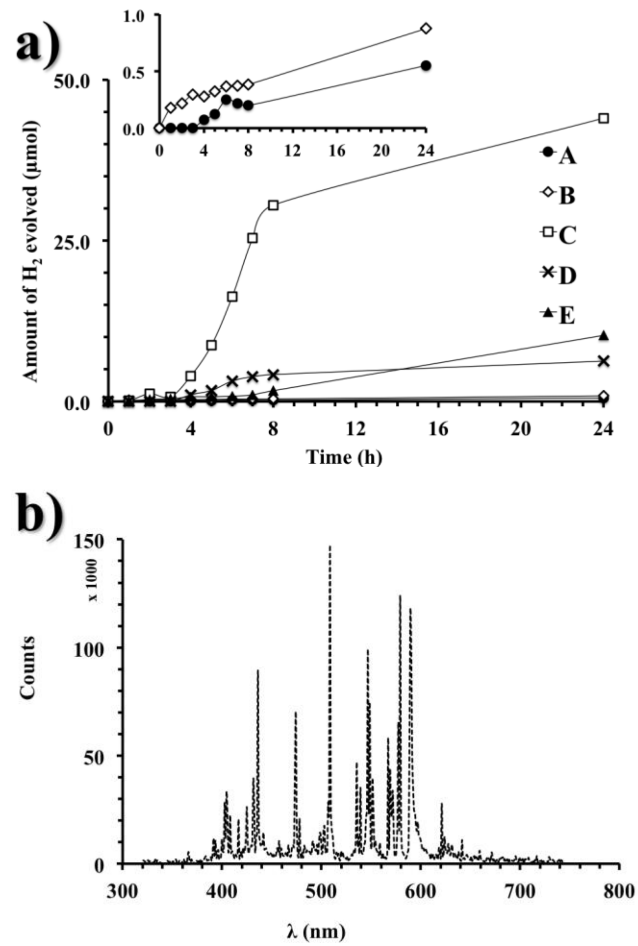

Fig. 3. a) Photoassisted generation of H_2 as a function of time, obtained inside the irradiation chamber. b) Qualitative emission spectrum of the filtered lamp used as excitation source (Hg lamp of 250 W).

Also, a barely detected peak at around 47.6º suggests the existence of delafossite phase of $CuFeO_2$ (PDF 01-075-2146). No crystalline Sn or Fe oxides were identified. Absorptance spectra in Fig. 2 b) was calculated from the total transmittance and reflectance measurements. Outcomes reveal that all materials are able to absorb photons in the UV-Vis region. For most of the cases, absorption in the Vis region was more than 30% and up to 65% in the UV interval (above 3.1 eV). The modulations observed in the absorptance spectra are associated with smooth interfaces and uniform layers' thickness.

B. H_2 generation

The photoassisted generation of H_2 was monitored in a batch reactor under visible light irradiation, using a customized reaction chamber. Outcomes summarized in Fig. 3 a) show that, after 24 h of continuous irradiation with the multiple wavelengths emitted by the lamp (Fig. 3 b), significant generation of H_2 was achieved with most of the samples. Individual layers of TiO_2 and FeO_x in samples A and B, presented the less satisfactory outcomes (0.55 and 0.9 µmol, respectively). However, a marked increase resulted within the incorporation of a composite material ($CuFeO_2$), as in samples D and E. In fact, within the incorporation of an additional amorphous layer of SnO_x (sample E), it was noted that the H_2 generation augmented from 6.26 (sample D) to 10.25 µmol, after 24 h. Moreover, a noteworthy increases of the amount of H_2 (44 µmol) was observed using sample C, which incorporated a composite amorphous layer of Ti and Fe oxides. Since no clear differences among the samples was established, further tests to determine the influence of other parameters, such as the thickness of the layers, stoichiometry of the components, mobility of the carriers, etc., have to be studied in detail.

IV. CONCLUSIONS

Outcomes show that hetero-structures comprising metal oxide based materials can be used effectively for H_2 generation.

ACKNOWLEDGMENT

The authors would like to thank to W. Antúnez-Flores and C. Ornelas-Gutiérrez for the assistance they provided during the undertaking of this work. The authors would also like to thank SEP-CONACYT (project N° 242612) for partial financial support.

REFERENCES

[1] K. Maeda, D. Lu and K. Damen, “Direct Water Splitting into Hydrogen and Oxygen under Visible Light by using Modified TaON Photocatalysts with d0 Electronic Configuration”, Chem. Eur. J. 2013, 19, 4986-4991.

[2] Kleidon, L. Miller and F. Gans, “Physical Limits of Solar Energy Conversion in the Earth System”, Top Curr. Chem. 2016, 371, 1-22.

[3] R.Marschall, “Heterojunctions in Composite Photocatalyst”, Top Curr. Chem. 2016, 371, 143-172.

[4] C.G. Read, Y. Park and K.S. Choi, “Electrochemichal synthesis of p-type CuFeO2 electrodes for use in an electrochemical cell”, J. Phys. Chem Lett. 2012, 3, 1876-1876.

[5] Derbal, S. Omeiri, A. Bouguelia, M. Trari, “Characterization of new heterosystem $CuFeO_2/SnO_2$ application to visible-light induced hydrogen evolution”, Int. J. Hydrogen Energ. 2008, 33, 4274-4282.

[6] M. Miki-Yoshida et al, Aerosol processing of nanostructured oxides for environmental applications. Ch. 3 in Aerosols, Ed. A. Yanick Pearson, Nova Science Publishers Inc., (2014) New York.

XVI International Congress of the Hydrogen Mexican Society 2016

Synthesis and characterization of TiO_2/graphene oxide composite and photocatalytic evaluation for H_2 production

P. Mendoza-Correa[1], J.A. Colín-García[2], M. J. Meléndez-Zaragoza[3], J. M. Salinas-Gutiérrez[3], B.C. Hernández-Majalca[3], M. Hinojosa-Rivera[1], A. López-Ortiz[3], V. Collins-Martínez[3]*

[1] Universidad Autónoma de Nuevo León, Facultad de Ingeniería Mecánica y Eléctrica, Pedro de Alba S/N, Ciudad Universitaria, San Nicolás de Los Garza, N.L., Mex. 66450
[2] Instituto Politécnico Nacional, Escuela Superior de Ingeniería Química e Industrias Extractivas, AV. Miguel Othón de Mendizábal La Escalera, Cd. de México, Mex. 07738
[3] Centro de Investigación en Materiales Avanzados, S.C., Depto. de Ingeniería y Química de Materiales, Miguel de Cervantes 120, Complejo Industrial Chihuahua, Chih., Mex. 31136.
*Tel: +526144391129; e-mail: virginia.collins@cimav.edu.mx

ABSTRACT

Titanium dioxide (TiO_2) is most widely used photocatalyst. However, its band gap is found on the ultraviolet light spectrum. Graphene oxide (GO) can absorb photons from the visible to the infrared spectrum range with a fast response[i]. TiO_2P25 on graphene oxide (TiO_2/GO)[ii] was obtained through photo-assisted anchoring. XRD results show the oxidation of graphite (GrO) produced from the Hummer´s method, which subsequently is thermally exfoliated to become graphene oxide (GO). The diffraction pattern of TiO_2/GO shows the disappearance of GO signal and P25 signals (anatase and rutile) being present. A slight shift in the band gap in its diffuse reflectance spectrum was detected, which was attributed to the interaction of GO with TiO_2P25. Scanning Electron Microscopy images show evidence of the dispersion of TiO_2 on GO. photocatalytic H_2 production evaluation used a 250 W mercury lamp and 2% methanol as sacrificial agent. Results showed that after 8 hours of irradiation TiO_2/GO generated almost twice hydrogen than that of pure TiO_2P25 as photocatalysts.

Keywords: graphene oxide; photocatalysis; hydrogen production; titanium dioxide

[i] Shen, Y., Yang, S., Zhou, P., Sun, Q., Wang, P., & Wan, L. et al. (2013). Evolution of the band-gap and optical properties of graphene oxide with controllable reduction level. Carbon, 62, 157-164.

[ii] Williams, G., Seger, B., & Kamat, P. (2008). TiO_2 -Graphene Nanocomposites. UV-Assisted Photocatalytic Reduction of Graphene Oxide. ACS Nano, 2(7), 1487-1491.

Water splitting activity evaluation of photocatalytic $CoFe_2O_4$ nanoparticles synthesized by a self-combustion route

J.L. Domínguez-Arvizu, M. J. Meléndez-Zaragoza, J. M. Salinas-Gutiérrez, B.C. Hernández-Majalca[1], A. López-Ortiz, V. Collins-Martínez *

Departamento de Ingeniería y Química de Materiales
Centro de Investigación en Materiales Avanzados, S.C.
Chihuahua, Chih. México
*Tel: +52 6144391129; e-mail: virginia.collins@cimav.edu.mx

***Abstract*— Self-combustion technique has proven to be an efficient route to synthetize spinel-type nanoparticles. In particular, cobalt ferrite ($CoFe_2O_4$) has been employed in the past for a wide variety of applications and this has been the object of numerous research studies. However, self-combustion (SC) synthesis of $CoFe_2O_4$ has not been reported in the literature towards its evaluation as a visible light photocatalyst for water splitting hydrogen production. Therefore, the present research is aimed to synthesize $CoFe_2O_4$ nanoparticles by the SC route. Characterization of the material consisted in X-Ray diffraction (XRD), Scanning electron microscopy (SEM) and UV-Vis spectroscopy. Evaluation of $CoFe_2O_4$ photocatalytic activity was performed in a laboratory photoreactor under visible light irradiation using a 250 W mercurial lamp. Results indicate that after 8 hours of irradiation 6911.4 μmol H_2/g_{cat} were achieved, which is about 27 times greater than the photocatalytic activity of commercial TiO_2 P-25 under the same experimental conditions.**

Keywords*—*Self-combustion; $CoFe_2O_4$; Water splitting

I. Introduction

According to a U.S.-EIA (Energy information administration) report, a continuous increase in world energy consumption of 56% between 2010 and 2040 is predicted, with fossil fuels comprising to about 78%, and the remaining is expected to come from nuclear energy. The massive utilization of fossil fuels is responsible for climate change, greenhouse gas emissions and pollutants (e.g. CO, SOx, NOx, ashes, etc.) [1].

Hydrogen is a clean fuel, which does not produce toxic emissions as well as CO_2, since its only product is water. Hydrogen can be used in transportation systems, fuel cells and combustion engines. Indeed, hydrogen energy yield is approximately 2.75 times greater than hydrocarbon fuels (122 kJ/g). However, there is a general perception that hydrogen can be obtained only by clean technologies, but this is not necessarily true. Nowadays near the 95% of hydrogen production comes from fossil fuels, mainly by natural gas steam reforming. In order to avoid CO_2 generation and high energy consumption, hydraulic, wind and solar together with water splitting technologies, can be good options for hydrogen production, whereas, solar water splitting is the most promising approach, since energy and space limitations are less demanding in comparison with the other ones [2-4].

The research in the field of photocatalytic water splitting initiated using monocrystalline TiO_2 (rutile) as photoanode and a Pt cathode by applying an external current, this photoelectrochemical phenomena is known as the Honda-Fujishima effect. When a TiO_2 anode, n-type semiconductor, is illuminated by light with an energy greater than the TiO_2 band gap, electrons and holes are generated in conduction and valence bands, respectively. The migrating electrons, which will reach the Pt counter electrode reduce the H+ generated from water into H_2. Meanwhile, the holes that were left behind on the TiO_2 surface oxidize water forming O_2. TiO_2 is the most common and widely studied photocatalyst and this is due to its high stability and photocorrosion resistance, which commonly occurs with semiconductor materials. However, its efficiency is very low due to the fact that the process is limited to the high energy radiation (UV) coupled to a band gap energy of ~3.2 eV, which can be only provided from an artificial source and happens to be expensive. For this reason one of the main objectives in this area is to develop efficient photocatalytic materials, which work under visible light irradiation [4-6].

Ferrites with the general formula MFe_2O_4, where (M) represents a metal cation are used in various applications due to its chemical and thermal stability such as electronic devices and circuits, besides their use as absorbers of toxic and harmful substances to health. Spinel ferrites have shown to be effective photocatalysts due to fact that their wide band gap falls under the visible light spectrum and therefore are able to generate hole-electron pairs on the semiconductor surface, apart from their low cost and high corrosion resistance. Its photocatalytic activity is based on their redox potentials, ability to store oxygen on their crystalline lattice, and tendency to form oxygen-vacancy compounds, when synthesized under reducing atmospheres [4, 7].

Different spinel ferrite nanoparticle synthesis have been developed having a common feature that all reagents are mixed in stoichiometric amounts of precursors. Most popular methods are co-precipitation, sol-gel, micro-emulsion, hydrothermal, spray pyrolysis, reverse micelle etc. Complex procedures and low production rates are common problems of these wet chemical methods. On the other hand, self-combustion method, where the chemical sol-gel and combustion process is combined has shown great potential in the preparation of spinel-type ferrite nanomaterials [8]. This synthesis has been employed for the preparation of MFe_2O_4 type materials using different cations such Li, Ni, Zn, Cd, Mg or their combinations [9-12]. Furthermore, this method have also been employed in obtaining nano-structures, exhibiting photocatalytic properties [13]. However, self-combustion (SC) synthesis of CoFe2O4 has not been reported so far in the literature towards its evaluation as a visible light photocatalyst for water splitting hydrogen production. Therefore, the present research is aimed to synthesize CoFe2O4 nanoparticles by the SC route.

II. Experimental

A. Preparation

Stoichiometric amounts of $Co(NO_3)_2.6H_2O$, $Fe(NO_3)_3.9H_2O$ and $C_6H_8O_7$ (citric acid) analytical grade reagents were used to prepare three solutions adding minimum quantities of tri-distilled water in order to obtain a final 1:2:2.22 molar ratio mixture. A small amount of NH_4OH was added dropwise to adjust the pH value to about 6, during this procedure the mixture was continuously stirred in a hot plate using a magnetic stirrer. Then, the solution was heated at 80°C and constantly stirred in the hot plate for 1 hour until a very viscous brown solid was obtained. Finally, the material was burnt in a self-propagating combustion manner until complete combustion to form a dark gray loose product, which was pulverized in an agate mortar and later annealed in a muffle at 450°C by 4 hours.

B. Characterization

Characterization of the ferrite was performed by X-ray diffraction (XRD) by using a PANalytical X'Pert PRO diffractometer with X'Celerator model detector, scanning electron microscopy (SEM) with a HITACHI SU3500 and UV-visible spectroscopy on a Cary 5000 Varian/Agilent.

C. Photocatalytic Evaluation

The photocatalytic activity of water splitting was evaluated using a 250 W mercurial lamp and methanol as a sacrificial agent (2% vol). Reaction monitoring was performed by gas chromatography using a Clarus 500 Perkin Elmer GC taking gas samples at regular time intervals using a 1ml syringe through a septum located at the top of the reactor. The system configuration employed was composed of a photoreactor, artificial lighting, and CG analysis with PC data acquisition as shown in Fig. 1.

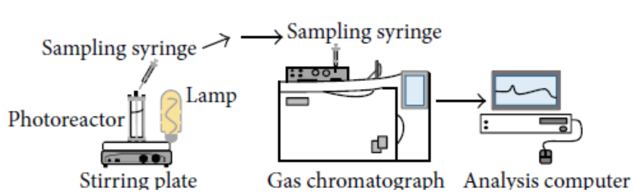

Fig. 1. Schematic experimental evaluation of the material, 0.2 g of $CoFe_2O_4$, H_2O and methanol as sacrificial agent.

A sample under darkness was taken at the beginning of the experiment, then a sample was taken every hour for a total of 8 hour irradiation time.

III. Results and Discussion

A. Characterization

1) X-Ray diffraction: Fig. 2 presents the X-Ray diffraction pattern of the synthesized sample. Data processing of this pattern was performed using the Match! Program from Crystal Impact Inc. using the PDF-2 database. Analysis of the diffraction pattern indicates that the material has crystalline nature and the peaks had coincidence with the spinel phase of cobalt ferrite (IPCC 00-022-1086). Moreover, average crystal size calculation was performed using the Scherrer's equation (1)

$$D = 0.9\lambda/\beta cos\theta \quad (1)$$

Where D is the crystal average size, λ is the X-Ray wavelength, β is the full width at half maximum (FWHM) and θ is the Brag's angle, the FWHM was calculated using OriginPro 8.0 and the estimated crystal size value was about 32 nm. Kanagesan et al. [13] obtained similar sizes in the range 20-40nm for $CoFe_2O_4$ nanoparticles synthesized by the same method.

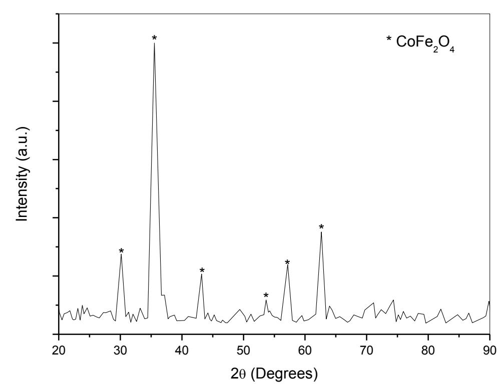

Fig. 2. X-Ray pattern from synthesized sample.

2) Scanning electron microscopy (SEM): Fig. 3 presents a SEM image showing the morphology of the synthesized material where nanoparticles agglomerates can be observed with an approximate size of around < 0.1 µm (100 nm). Also energy dispersive X-Ray spectroscopy (EDS) mapping through SEM was performed in order to observe if the element distribution, and therefore the phase formed was uniform. Trough the image presented in the Fig. 4 it is evident that the composition of the material is fairly uniform, thus suggesting that the unique crystal phase being formed is the $CoFe_2O_4$

spinel and confirming the previous X-ray results presented above.

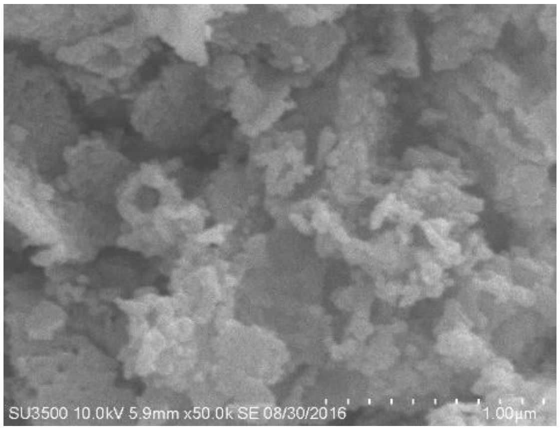

Fig. 3. SEM image of $CoFe_2O_4$ nanoparticle agglomerates.

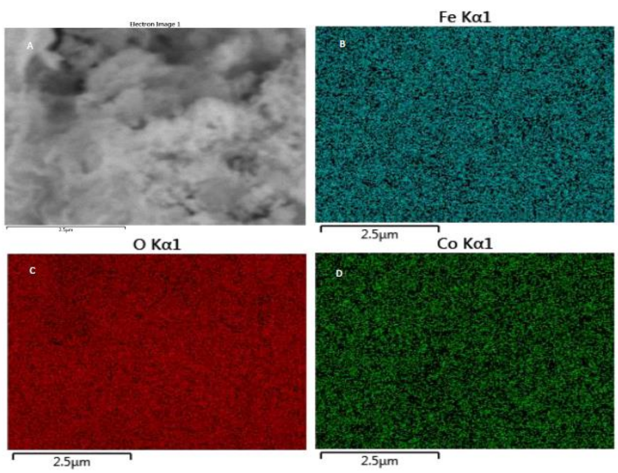

Fig. 4. EDS mapping of $CoFe_2O_4$ synthesized, A) Selected area for the mapping, B), C) and D) element distribution of Fe, O and Co, respectively.

3) UV/Visible spectroscopy: The UV/Vis spectra results are shown in Fig. 5, where a plot of energy vs transformed reflectance by the Kubelka-Munk function is presented. The linear proportion of the diffuse reflectance function cuts the abscissa axis in about a band gap energy value of 1.55 eV.

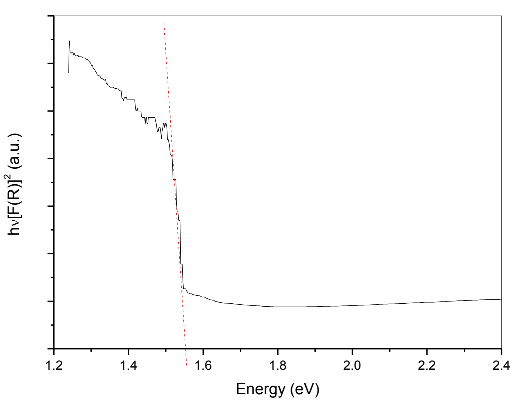

Fig. 5. UV/Visible reflectance spectra for the $CoFe_2O_4$

The obtained value is similar to values reported by Limei et al. (~1.55 eV) [14]. Also, another work by López et al. [4] reported $CoFe_2O_4$ nanoparticles synthesized by ball milling and coprecipitation methods obtaining values of ~1.1 and ~1.4 eV respectively.

B. Photocatalytic Activity

Photocatalytic activity obtained by self-combustion method (SC) is shown in Fig. 6. A comparison was performed respect to the commercial TiO_2 P-25 under the same experimental conditions. Hydrogen produced by $CoFe_2O_4$ by SC was 6911.4 μmol H_2/g_{cat}, while only 253.6 μmol H_2/g_{cat} was generated by TiO_2 P-25 indicating a higher photocatalytic activity of $CoFe_2O_4$ under visible light irradiation. This is expected, because the $CoFe_2O_4$ band gap energy value of 1.55 eV is more suitable to work under visible light, rather than TiO_2, which band gap energy is 3.2 eV and at this value UV light is more adequate for TiO_2 high photocatalytic activity.

Moreover, reported photocatalytic evaluation of $CoFe_2O_4$ towards water splitting hydrogen production performed by López et al. [4] using ball milling (BM) synthesis method showed an important photocatalytic activity. They claim that this activity was due to a significant increase of oxygen vacancies in the solid sample during the ball milling process. They reported a hydrogen production of 3309.42 μmol H_2/g_{cat} under similar conditions. The superior hydrogen production through the SC synthesis technique found in the present investigation compared to previous reported research by Ortega-Lopez et al can be explained by the findings from Feng Gu et al. [15] who suggest that due to a rapid combustion, oxygen vacancies can be generated at a greater degree, and this directly affecting the photocatalytic activity for water splitting, because they serve as electrons traps that prevent the electron-

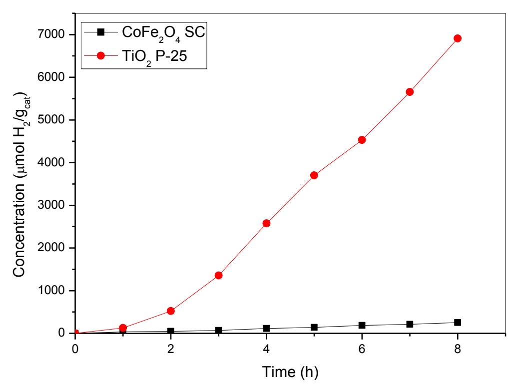

hole pair recombination [16].

Fig. 6. Comparison of $CoFe_2O_4$ photocatalytic activity with respect to commercial P-25

IV. CONCLUSIONS

Cobalt ferrite nanoparticles were successfully synthetized by the sol-gel self-combustion method reaching a <100nm particle size, a band gap energy of 1.55 eV with a highly pure $CoFe_2O_4$ spinel phase. These features confer to the material the needed properties to work as a photocatalyst for water splitting hydrogen production under visible light. This photocatalytic activity was found to be superior to the one presented by theTiO_2 P-25 under the same experimental conditions. These results can be presumably explained by a high combustion rate, which generate a greater degree of oxygen vacancies on the material thus, directly affecting the photocatalytic activity for water splitting, and these serving as electrons traps that prevent the electron-hole pair recombination.

ACKNOWLEDGMENT

The authors of this paper wish to thank the Mexican Society of Hydrogen for accepting the proposed research for dissemination and discussion, as well as the scholarship. We thank equally to CONACYT for scholarships awarded to students involved in the project.

REFERENCES

[1] Suleman, F., Dincer, I., and Agelin-Chaab, "Environmental impact assessment and comparison of some hydrogen production options," International Journal of Hydrogen Energy, vol. 40(21), pp. 6976-6987, June 2015.

[2] Hosseini, S. E., and Wahid, M. A, "Hydrogen production from renewable and sustainable energy resources: Promising green energy carrier for clean development," Renewable and Sustainable Energy Reviews, vol. 57, pp. 850-866, May 2016.

[3] Rostrup-Nielsen, J. R., "Fuels and energy for the future: the role of catalysis," Catalysis Reviews, vol. 46(3-4), pp. 247-270, December 2004.

[4] Ortega-Lóprez Y., Medina-Vázquez H., Salinas-Gutiérrez J., S., Guzmán-Velderrain V., López-Ortiz A. and Collins-Martínez V., "Synthesis method effect of $CoFe_2O_4$ on its photocatalytic properties for H_2 production from water and visible light," Journal of Nanomaterials, vol. 76, pp. 1-9, December 2015.

[5] Maeda, K., "Photocatalytic water splitting using semiconductor particles: history and recent developments," Journal of Photochemistry and Photobiology C: Photochemistry Reviews, vol. 12(4), pp. 237-268. December 2011.

[6] Zazoua, H., Boudjemaa, A., Chebout, R., and Bachari, K. (2014). "Enhanced photocatalytic hydrogen production under visible light over a material based on magnesium ferrite derived from layered double hydroxides (LDHs)," International Journal of Energy Research, vol. 38(15), pp. 2010-2018, may 2014.

[7] Casbeer E., Sharma-Virender K. and Xiang-Zhong L., "Synthesis and photocatalytic activity of ferrites under visible light: a review," Separation and Purification Technology, vol. 87, pp. 1-14, March 2012.

[8] Sutka, A., and Mezinskis, G., "Sol-gel auto-combustion synthesis of spinel-type ferrite nanomaterials". Frontiers of Materials Science, vol. 6(2), pp. 128-141, June 2012.

[9] Randhawa, B., Dosanjh, H., and Kumar, N., "Synthesis of lithium ferrite by precursor and combustion methods: a comparative study," Journal of Radioanalytical and Nuclear Chemistry, vol. 274(3), pp. 581-591, August 2007.

[10] Sutka, A., Gross, K. A., Mezinskis, G., Bebris, G., and Knite, M., "The effect of heating conditions on the properties of nano-and microstructured Ni-Zn ferrite," Physica Scripta, vol. 83(2), 025601, January 2011.

[11] Nayak, P. K., "Synthesis and characterization of cadmium ferrite," Materials Chemistry and Physics, vol. 112(1), pp. 24-26, November 2008.

[12] Thant, A. A., Srimala, S., Kaung, P., Itoh, M., Radzali, O. and Fauzi, M. A., "Low temperature synthesis of $MgFe_2O_4$ soft ferrite nanocrystallites," Journal of the Australian Ceramic Society, vol. 46(1), pp. 11-14, July 2010.

[13] Kanagesan, S., Hashim, M., Tamilselvan, S., Alitheen, N. B., Ismail, I., Syazwan, M., and Zuikimi, M. M. M., "Sol-gel auto combustion synthesis of cobalt ferrite and its cytotoxitity properties," Digest Journal of Nanomaterials & Biostructures (DJNB), vol. 8(4), pp. 1601-1610, December 2013.

[14] Limei, X., Fenghua, Z., Bin, C., and Xuefeng, B., "Preparation of light-driven spinel nanoparticles $CoAl_2O_4$, $MgFe_2O_4$ and $CoFe_2O_4$ and their photocatalytic reduction of carbon dioxide," IEEE Computer Society, pp. 2153-2156, February 2011, [International Conference on Computer Distributed Control and Intelligent Environmental Monitoring (CDCIEM)].

[15] Gu, F., Wang, S. F., Lü, M. K., Zhou, G. J., Xu, D., and Yuan, D. R., "Structure evaluation and highly enhanced luminescence of Dy3+-doped ZnO nanocrystals by Li+ doping via combustion method," Langmuir, vol. 20(9), pp. 3528-3531, April 2004.

[16] Qin, Y., Xiong, J., Zhang, W., Liu, L., Cui, Y., & Gu, H., "Facile synthesis and photocatalytic performance of Mg2SnO4/SnO2 heterostructures," Journal of Materials Science, vol. 50(17), pp. 5865-5872, September 2015.

A Photocatalyst Based in Pelargonidin 3-Glucoside as Dye Sensitizer on Small TiO_2 Nanoclusters

M.A. Flores-Hidalgo[1**], D. Barraza-Jiménez[1], L.F. Lozano-Silva[1], M.A. Escobedo-Bretado[1], V. Collins- Martinez[2], A. López Ortiz[2], A.Martínez de la Cruz[3]

[1]Universidad Juárez del Estado de Durango, Facultad de Ciencias Químicas, Av. Veterinaria S/N, Circuito Universitario, Durango, Dgo. México, C.P. 34120. *Tel: +526181881941

email: maflores.hidalgo@gmail.com

[2]Centro de Investigación en Materiales Avanzados, S.C., Departamento de Ingeniería y Química de Materiales, Miguel de Cervantes 120, Chihuahua, Chih., México, 31109

[3]Facultad de Ingeniería Mecánica y Eléctrica, Universidad Autónoma de Nuevo León, Ciudad Universitaria, C.P. 66451, San Nicolás de los Garza, N.L., México

Four small TiO_2 nanoclusters sensitized with pelargonidin 3-glucoside ($C_{21}H_{21}O_{10}^{+}$), a natural pigment derived from anthocyanidin. A model of the sensitization interaction between the nanoclusters and the natural pigment was developed and its geometric features as well as its electronic structure properties are studied. DFT methods were used to obtain geometries and a frequencies analysis was carried out to assure global minima. Ground states were calculated for the individual nanostructures and pelargonidin. Next the interaction between a nanocluster with the pigment was studied and its geometric parameters for better results are proposed. Energies were obtained for the individual nanoclusters and pigment at their ground state and the same methodology was applied to the interacting systems. HOMO, LUMO, band gap, chemical properties and other features are discussed. The sensitization process output is several interesting dye sensitized nanoclusters for photocatalysis applications with strong attraction to negative charge and a reduction on their band gap.

Keywords—TiO_2 nanoclusters; sensitized; photocatalysis; DFT.

I. INTRODUCTION

It is an undergoing task the search for cleaner methods to produce hydrogen. For this process, the use of alternative energy such as solar, eolic, geothermic, among others etc. as precursor to obtain hydrogen is a good possibility as cleaner technology [1]. Within these alternative energy options our work focuses in solar energy using photocatalysis. In photocatalysis the photocatalyzer plays a major role and the its critical success factors depend on properties such as chemical stability, creep resistance, visible light absorption, appropriate energy bands, etc,[2] It is well known the more used photocatalyzer is titanium dioxide (TiO_2) due to its better features for this application and there is a lot of work in this matter either trying to improve its properties or finding alternative semiconducting metal oxides that may perform similarly [3-4]. Due to its outstanding performance the use of TiO_2 as photocatalyzer has extended to water dissociation, pollutants degradation, organic selective transformations, CO_2 sequestration for fuel generation, etc. [5-6] There are several techniques to improve TiO_2 properties, in this work we will use nanostructured TiO_2 in its cluster presentation and a sensitization of the semiconducting oxide using a natural pigment. A model of the sensitized nanostructure was built and density functional theory is used to carry out electronic structure calculations. The sensitized material properties are discussed. Properties such us band gap, HOMO, LUMO, IP, EA, among others are displayed within this work and insights on the potential on this material for photocatalysis applications.

II. THEORY AND COMPUTATIONAL DETAILS

Theoretical calculations were performed in Gaussian09 programs suite [7]. $(TiO_2)_n$ nanostructures, pelargonidin and nanostructured systems containing both molecules were relaxed. Pelargonidin is used as a (+1) cation and was treated with B3LYP/6-311+g(d,p). $(TiO_2)_n$ nanostructures were built resembling previously reported geometric parameters [8-10]. Energy calculations were performed for all molecules to find the electronic properties such as HOMO, LUMO, gap, ionization potential (IP), electronic affinity (EA), electrophilicity (ω), electronegativity (χ), hardness (η), and Fukui functions with the same theoretical method.

Geometry optimizations and vibrational frequency analyses were carried out using DFT with the well-known B3LYP approach, which includes the interchange hybrid functional from Becke [11] in combination with the correlation functional three parameter by Lee-Yang-Parr [12], and 6-311g(d) basis set as implemented in Gaussian09 program package. Based on literature and our method validation results, we propose B3LYP/6-311+g(d,p) theoretical method provides good results with a good level of accuracy for these systems and will be used to carry on with the rest of the work. We considered some variants of $(TiO_2)_n$, nanoclusters already studied theoretically and used the same geometric parameters to build the input structures. The work was done this way under the assumption that the structure feasibility was already proved by Hamad et al. and other research teams [8-10]. In their works when these $(TiO_2)_n$ were proposed. Then we made the geometry optimization of $(TiO_2)_n$ nanoclusters and applied the sensitization by bonding a single pelargonidin molecule at each nanocluster to create new structures. Our theoretical calculations used a different theoretical method since we used DFT in contrast to the genetic algorithm used on the referred works. We present a single variant for each size of the $(TiO_2)_n$ nanoclusters as shown in Fig. 1, all of them optimized at the same theoretical level in its pure form. Then we used the optimized nanocluster to add the pelargonidin molecule as sensitizer material and relaxed the new geometry with the same theoretical method. Each geometry optimization was followed by a calculation of harmonic vibrational frequencies to confirm that the optimized geometry corresponds to a local minimum. The zero-point vibrational energy (ZPVE) scaling and the thermal correction (TC) at 298.15 K were also performed. Our results are compared with the literature to verify the geometric parameters for the nanostructures in their pristine form. We also used as reference the generally accepted TiO_2 in its bulk presentation as basis to compare how much the bond length and angles in our study differ from a commonly known bond or angle within TiO_2 simple crystals.

III. RESULTS AND DISCUSSION

Four nanocluster geometries were modeled according to recommended parameters within the literature. This nanostructures were relaxed and treated for energy computations with B3LYP/6-311+g(d,p). With this theoretical method it was achieved good accuracy in comparison with computational time. Nanocluster geometries showed bond length values near 1.8 Å for Ti-O. Dihedral angles values were near to the reported 113°+/-5° [13]. Pigment geometry behaved similarly to nanoclusters with bond length and angles in agreement with known values for these organic molecules. Pristine TiO_2 nanoclusters and pelargonidin geometry calculations agreed with literature reported parameters in general, without any relevant additional insight.

Pristine nanoclusters and pigment and its ground states were used to build a model to represent interactions between them. Variants of the nanosystems formed by the nanocluster and the natural dye are displayed in Fig. 2.

During the exercise of finding the best location for nanostructures interaction with the organic molecules we calculated the Fukui functions (Tables 5 and 6). However, our best approach during the search process for best location was based on attempting to locate the nanocluster more accessible Ti atom with the outer pigment oxygens. For pelargonidin the dangling oxygens are good places for interactions with the selected semiconductor oxide.

Different external oxygens around the pigment allowed us to locate the interaction atoms in different places. The more accessible Ti atom was selected to interact with the pigment oxygens. It was observed weak interactions were possible between pigment molecule and nanostructures for the sensitized nanosystems with a Ti-O bond size near 2.0 Å. We tested interactions with other bond lengths, distances were increased in 0.1 Å increments over the 2.0 Å with unsuccessful results because resulting structures were unstable.

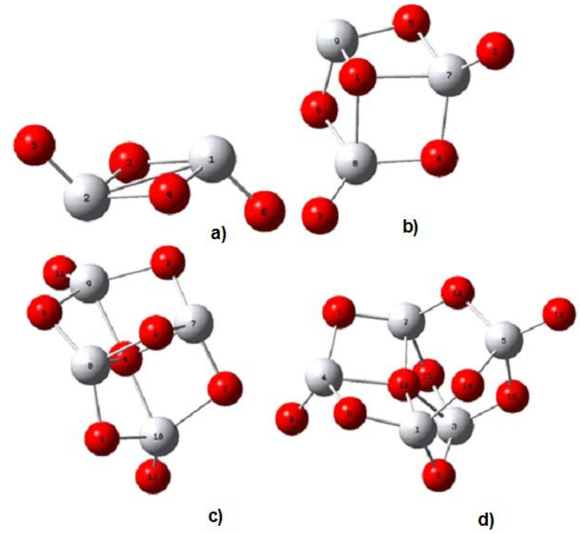

Fig. 1. Nanostructures sensitized. In light grey Ti atoms in red oxygen atom

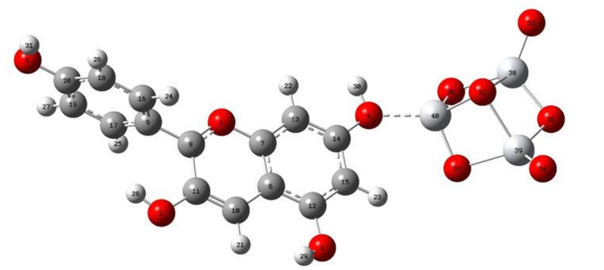

Fig. 2. Interaction model of $(TiO_2)_3$ (right side) nanocluster with pelargonidin (left side).

Table 1. Energy calculations. Emin is minimum energy and Eg is HOMO-LUMO gap. All units in eV.

Nanocluster	Emin	Eg	HOMO	LUMO
$(TiO_2)_2$	-25961.62	2.881	-10.080	-7.200
$(TiO_2)_3$	-54423.40	5.021	-8.076	-3.054
$(TiO_2)_4$	-81637.60	3.753	-7.952	-4.199
$(TiO_2)_5$	-108852.00	5.159	-8.717	-3.558
$(C_{15}H_{11}O_5)^+$	-136066.20	4.889	-8.608	-3.719

Table 2. Chemical properties obtained with conceptual DFT. All units in eV.

Cluster/Molec	PI	EA	χ	η	μ	ω	S
$(TiO_2)_2$	10.416	1.516	5.966	4.450	0.225	0.670	0.225
$(TiO_2)_3$	9.915	2.588	6.251	3.664	0.273	0.853	0.273
$(TiO_2)_4$	10.501	1.786	6.143	4.357	0.229	0.705	0.230
$(TiO_2)_5$	10.221	2.215	6.218	4.003	0.250	0.777	0.250
$(C_{15}H_{11}O_5)^+$	11.653	5.701	8.677	2.976	-8.677	12.649	0.336

Table 3. Energy calculations for interacting nanoclusters and pelargonidin. *a*=$(TiO_2)_2$, *b*=$(TiO_2)_3$, *c*=$(TiO_2)_4$, *d*=$(TiO_2)_5$. All units in eV.

Variant	Emin	Eg	HOMO	LUMO
Variant^a 1	-80389.625	2.749	-9.794	-7.045
Variant^a 2	-80393.835	2.967	-9.694	-6.728
Variant^a 3	-80390.120	3.027	-9.861	-6.833
Variant^a 4	-80389.430	2.401	-9.592	-7.191
Variant^b 1	-107605.452	2.910	-9.805	-6.896
Variant^b 2	-107605.740	2.778	-9.496	-6.718
Variant^b 3	-107605.392	3.026	-9.990	-6.964
Variant^b 4	-107605.056	2.912	-9.881	-6.968
Variant^c 1	-134820.511	2.898	-9.948	-7.050
Variant^c 2	-134820.588	2.932	-9.867	-6.935
Variant^c 3	-134820.645	3.015	-10.025	-7.010
Variant^c 4	-134820.545	2.918	-10.115	-7.197
Variant^d 1	-162036.180	2.620	-9.914	-7.294
Variant^d 2	-162036.458	2.864	-9.699	-6.835
Variant^d 3	-162036.165	3.071	-9.804	-6.733
Variant^d 4	-162036.244	3.035	-10.086	-7.051

Table 4. Chemical properties obtained with conceptual DFT corresponding to interacting nanoclusters and pelargonidin. All units in eV.

Cluster/Molec	PI	EA	χ	η	μ	ω	S
Variant^a 1	11.073	5.628	8.351	2.723	-8.351	12.806	0.367
Variant^a 2	11.115	6.191	8.653	2.462	-8.653	15.206	0.406
Variant^a 3	11.226	5.437	8.332	2.895	-8.332	11.991	0.346
Variant^a 4	11.087	5.736	8.412	2.675	-8.412	13.224	0.374
Variant^b 1	11.072	5.513	8.293	2.778	-8.293	12.369	0.360
Variant^b 2	10.846	5.381	8.113	2.732	-8.113	12.046	0.366
Variant^b 3	11.299	5.603	8.451	2.848	-8.451	12.537	0.351
Variant^b 4	11.211	5.502	8.356	2.855	-8.356	12.231	0.350
Variant^c 1	11.208	5.666	8.437	2.771	-8.437	12.844	0.361
Variant^c 2	11.153	5.569	8.361	2.792	-8.361	12.518	0.358
Variant^c 3	11.326	5.654	8.490	2.836	-8.490	12.709	0.353
Variant^c 4	11.243	5.760	8.506	2.742	-8.502	13.182	0.365
Variant^d 1	11.097	5.893	8.495	2.602	-8.495	13.865	0.384
Variant^d 2	11.030	5.498	8.264	2.766	-8.264	12.346	0.362
Variant^d 3	11.097	5.893	8.495	2.602	-8.495	13.865	0.384
Variant^d 4	11.271	5.630	8.450	2.820	-8.450	12.660	0.355

Energy calculations were carried out to understand the newly formed sensitized nanostructures using B3LYP/6-311+g(d,p). We calculated the minimum energy for pristine TiO_2 nanoclusters at its ground states and then applied a similar theoretical method for dye sensitized nanoclusters.

Table 5. Fukui functions for nanoclusters. Units in eV.

Nanocluster	fk$^+$		fk$^-$		fk^0	
$(TiO_2)_2$	0.389	O3, O4	0.202	O5, O6	0.284	Ti1, Ti2
$(TiO_2)_3$	0.556	Ti9	0.185	O2, O3	0.327	Ti9
$(TiO_2)_4$	0.199	Ti7, Ti8	0.121	O11, O12	0.141	Ti7, Ti8
$(TiO_2)_5$	0.325	Ti2	0.161	O13	0.191	Ti2

Table 6. Fukui functions for pelargonidin. Units in eV.

Pelargonidin	fk$^+$		fk$^-$		fk^0	
(C15H11O5)+	0.100	C13	0.140	C9	0.074	C13
	0.068	C14	0.131	C6	0.058	C9
	0.063	C13	0.104	C20	0.053	C20
	0.059	C7	0.076	O2	0.053	O2
	0.058	C19	0.061	O5	0.046	C6

Dye sensitization has a favorable effect in nanoclusters minimum energy without exception by decreasing its values. Minimum energy, HOMO-LUMO gap, HOMO and LUMO are shown in Tables 1 and 2.

Band gap for pristine nanoclusters are wide with $(TiO_2)_2$ and $(TiO_2)_4$ having the narrower values with 2.881 and 3.753 eV. Pigment has a wide band gap aswell with a resulting value for pelargonidin of 4.889 eV. In order to obtain a reduction in TiO_2 band gap energy levels of nanocluster and pigment to mix and complement each other. With the proposed model all nanocluster variants reduce their band gap but depend largely in the nanocluster interaction location. The narrower band gap calculated with our DFT results was found in $(TiO_2)_2$ nanocluster variant with 2.401 eV. With the proposed model all nanocluster variants reduce their band gap but depend largely in the nanocluster interaction location. The narrower band gap found was found in $(TiO_2)_2$ with 2.401 eV. Pigment molecular orbitals have an effect on HOMO but the effect in LUMO is stronger and this contribution is the more significant to determine the gap. This is true for three nanocluster variants but $(TiO_2)_2$ is an exception. In $(TiO_2)_2$ pigment effect on its electronic structure is less and changes in HOMO and LUMO are smaller than in the other nanostructures.

Conceptual DFT was used to calculate chemical properties. These calculations indicate an increase in ionization potential, electron affinity and electronegativity of nanoclusters when dye sensitization was carried out. This effect may be due to the cation feature contributed by pelargonidin to the system. This positive charge provided by the pigment has also a noticeable effect in hardness and softness and it is even more evident in the electrophilicity index which shows a clear trend of the sensitized materials to attract electrons. Tables 3 and 4 display conceptual DFT.

Our research within these proceedings indicate sensitization of TiO_2 nanoclusters increase the potential of the nanoclusters for photocatalysis applications. Further calculations will be performed in the short term to continue analyzing electronic structure and charge transfer.

IV. CONCLUSIONS

Four nanocluster geometries were sensitized with pelargonidin. This work provides data to make the sensitization process more efficient from geometric parameters to electronic structure data. Sensitization process may work well with this nanoclusrters and pelargonidin but the cation character of the pigment is present in the final systems. If attraction to electron charge is needed, then these nanomaterials may be a good option. Further research to calculate charge transfer and more electronic structure data will aid to learn more about this photocatalyzer.

Acknowledgment

MAFH, DBJ and MAEB are researchers at FCQ-UJED and CONACYT. ALO and VHCM are researchers at CIMAV-CONACYT. AdelaCM is a researcher at FIME-UANL and CONACYT. This work was financed by SEP-CONACYT with DSA/103.5/15/7028 project supported by 2015 National PRODEP funding. Thanks to Dr. D. Glossman-Mitnik for his technical contribution.

References

[1] U.S. Department of Energy Hydrogen, Fuel Cells and Infrastructure Technologies Program, Hydrogen Posture Plan, U.S. Department of Energy, 2006. U.S.

[2] J. Zhu, M. Zach, “Nanostructured materials for photocatalytic hydrogen production”, current opinion in colloid interface science, [2009].

[3] Chen X B, Mao S S. Chem Rev, 2007, 107: 2891.

[4] Fujishima A, Honda K. Nature, 1972, 238: 37.

[5] Wen, J.; Li, X.; Liu, W.; Fang, Y.; Xie, J.; Xu, Y. Photocatalysis fundamentals and surface modification of TiO_2 nanomaterials. Chinese Journal of Catalysis 2015, 36, 2049-2070.

[6] Jenny Schneider, Masaya Matsuoka, Masato Takeuchi, Jinlong Zhang, Yu Horiuchi, Masakazu Anpo, and Detlef W. Bahnemann. Understanding TiO_2 Photocatalysis: Mechanisms and Materials. Chem. Rev. 2014, 114, 9919−9986.

[7] Gaussian 09, Revision D.01, M. J. Frisch, G. W. Trucks, H. B. Schlegel, G. E. Scuseria, M. A. Robb, J. R. Cheeseman, G. Scalmani, V. Barone, B. Mennucci, G. A. Petersson, H. Nakatsuji, M. Caricato, X. Li, H. P. Hratchian, A. F. Izmaylov, J. Bloino, G. Zheng, J. L. Sonnenberg, M. Hada, M. Ehara, K. Toyota, R. Fukuda, J. Hasegawa, M. Ishida, T. Nakajima, Y. Honda, O. Kitao, H. Nakai, T. Vreven, J. A. Montgomery, Jr., J. E. Peralta, F. Ogliaro, M. Bearpark, J. J. Heyd, E. Brothers, K. N. Kudin, V. N. Staroverov, T. Keith, R. Kobayashi, J. Normand, K. Raghavachari, A. Rendell, J. C. Burant, S. S. Iyengar, J. Tomasi, M. Cossi, N. Rega, J. M. Millam, M. Klene, J. E. Knox, J. B. Cross, V. Bakken, C. Adamo, J. Jaramillo, R. Gomperts, R. E. Stratmann, O. Yazyev, A. J. Austin, R. Cammi, C. Pomelli, J. W. Ochterski, R. L. Martin, K. Morokuma, V. G. Zakrzewski, G. A. Voth, P. Salvador, J. J. Dannenberg, S. Dapprich, A. D. Daniels, O. Farkas, J. B. Foresman, J. V. Ortiz, J. Cioslowski, and D. J. Fox, Gaussian, Inc., Wallingford CT, 2013.

[8] Woodley S.M., Hamad S., Mejías J. A. and Catlow C.R.A. Properties of small TiO_2, ZrO_2 and HfO_2 nanoparticles. J. Mater. Chem., 2006, 16, 1927–1933.

[9] Syzgantseva O.A., Gonzalez-Navarrete P., Calatayud M., Bromley S., and Minot C. Theoretical Investigation of the Hydrogenation of $(TiO_2)_N$ Clusters (N = 1-10). J. Phys. Chem. C 2011, 115, 15890.

[10] Hamad, S.; Catlow, C. R. A.; Woodley, S. M.; Lago, S.; Mejias, J. A. Structure and Stability of Small TiO_2 Nanoparticles. J. Phys. Chem. B 2005, 109, 15741.

[11] A.D. Becke. J.Chem Phys. 104 (1993) 5648.

[12] C. Lee, R. Yang, G. Parr. Phys. Rev B, 37 (1988) 785.

[13] Gribb, A.A. and Banfield, J.F. “Particle size effects on transformation kinetics and phase stability in nanocrystalline TiO_2” American Mineralogy (82) 717-728..

Hydrogen production improved mixed oxide TiO_2-ZrO_2 photocatalyst as semiconductor

H2 production with mixed oxide

Alejandro Pérez-Larios
Universidad de Guadalajara, CUAltos, Depto. Ciencias Biológicas, Carretera a Yahualica km. 7.5, Tepatitlán de Morelos, Jalisco, México. 47600.
alarios@cualtos.udg.mx

Ricardo Gomez Romero
[2]Universidad Autónoma Metropolitana-Iztapalapa, Depto. de Química, Área de Catálisis, Grupo ECOCATAL, Av. San Rafael Atlixco No 189, D.F., México 09340

Abstract— In this study the synthesis of the semiconductor oxide TiO_2 doped with ZrO_2 varying concentrations was using for hydrogen production. The photocatalysts were characterized by N2 phisisortion studies, scanning electron microscopic-energy dispersive analysis, X-ray diffraction studies, UV-vis and Raman spectroscopy. The anatase phase in these materials showed high superficial area, the studies of UV-Vis absorption showed a diminish in the energy band gap in function of the zirconium content. The Raman spectrum indicates that crystalline structure of TiO_2 was modified for the presence of cerium. In the photocatalytic activity, the materials showed an increase in the hydrogen production, where, the maximum hydrogen production was achieved at 10 wt. % of the zirconium content.

Keywords— Hydrogen; photocatalysts; semiconductor; TiO₂; Mixed oxide

Introduction

Hydrogen is an attractive alternative sustainable clean energy carrier because of the depletion of fossil fuel reserves and the environmental pollution caused by continuous burning of fossil [1,3]. Hydrogen is currently obtained from nonrenewable natural gas, naphta, heavy oil, methanol, biomass, wastes, coal, petroleum and water, but could be generated from renewable resources such as biomass [4,8]. Water decomposition by means of sunlight mimics photosynthesis by converting water into H_2 and O_2 using inorganic photo-semiconductors that catalyze the water-splitting reaction [9,10]:

$$H_2O \rightarrow \frac{1}{2}O_2 + H_2 \quad \text{(g)}$$

Water decomposition using sunlight on semiconductor photocatalysts has attracted intense research interest since the pioneering work on a photo-electrochemical cell conducted [11]. This work has stimulated the research for the overall water splitting reaction using particulate photocatalysts that was first realized in 1980 [12] who reported stoichiometric evolution of hydrogen and oxygen. Since these ground-breaking works, many papers have been published on the impact of different semiconductor materials on photocatalytic water splitting performance [13-14]. These studies clearly prove that the energy conversion efficiency of water splitting is principally determined by the properties of the semiconductors used as photocatalysts. Light-driven water splitting is initiated when a photo-semiconductor absorbs light photons with energies greater than its band gap energy (Eg). This absorption creates excited photoelectrons in the conduction band (CB) and holes in the valence band (VB) of the semiconductor. After that, the second step in photochemical water splitting consists of charge separation and the migration of photogenerated electron–hole pairs from the bulk of the semiconductor towards the reaction sites on the photocatalysts surface. The final step of the photocatalytic process involves the surface chemical reactions. The photo-generated electrons (e^-) and holes (h^+) that migrate to the surface of the photocatalysts without recombination can reduce and oxidize, respectively, water molecules adsorbed onto the surface of the semiconductor to produce gaseous oxygen and hydrogen by the following reactions:

Oxidation: $H_2O + 2h^+ \rightarrow 2H^+ + \frac{1}{2}O_2$

Reduction: $2H^+ + 2e^- \rightarrow H_2$

Overall reaction: $H_2O \rightarrow \frac{1}{2}O_2 + H_2$

This phenomenon explains the slow hydrogen production by photocatalytic water splitting using TiO_2 alone [15,16]. Some oxide in combine with TiO_2 in the formation of mixed oxide is also known to increase photocatalytic performance via inhibiting the recombination of electrons and holes for the evolution of H_2 [17].

It was recently suggested by Verykios and co-workers, that decomposition of organics and H_2-production can be used in tandem [18, 19]. The idea is that H_2-production efficiency is increased by using an electron-donor contaminant (sacrificial reagent), which will ultimately result in enhancement of the H_2 production rate with simultaneous degradation of the organic substrate'' [18]. In the majority of the studies published in the literature, methanol was used as sacrificial

reagent [19–23], further examples include the decomposition of various azo-dyes [18], glucose [24], glycerol [25] and formic acid [26], etc.
In the present study we have prepared mixed oxide TiO_2-ZrO_2 photocatalysts using sol-gel method and tested their efficiency for hydrogen generation. Thus, the principal objective of the work is to develop TiO_2-ZrO_2 mixed oxide photocatalysts for hydrogen production from aqueous solution ethanol-water under irradiation with UV-visible light. Characterization of the catalysts was done following standard procedures.

EXPERIMENTAL

2.1 Synthesis and Characterization of Materials

The mixed oxide TiO_2-ZrO_2 nanostructures were prepared by the sol-gel method using titanium butoxide (IV) (Aldrich 97%) and their respective salt as precursor: 44 mL of 1-butanol (Aldrich 99.4 %) and 18 mL of distilled wáter containing the appropriate average $C_{20}H_{28}O_8Zr$ (Strem Chemicals 99%), In the preparation of each of the series of obtaining materils with 1.0, 3.0, 5.0 y 10.0 wt %, were mixed and added few drops of HNO_3 to obtain a pH=3 in the solution. 44 mL were prepared butoxide titanium (IV) to add the above solution at 70°C under reflux (with a molar ratio of 8) this solution was mixed under magnetic stirring to form the gel. The gel was dried at 100 °C for 24h and the solid was ground to a fine powder in an agate mortar. The xerogel obtained was calcined at 500° C for 5 h in an air atmosphere with a heating rate of 1°C/min; finally the product was ground again. As a reference the sample of pure TiO_2 was prepared in the same manner described but not added salt as precursors.

2.2 Materials Characterization

2.2.1 Thermal Analysis (TGA)

Thermograms for thermogravimetric analysis (TGA) were determined on a Perkin Elmer Analyse, modelo Diamond TG/DTA instrument. It was operated un der static atmosphere of air, covering the range from room temperature to 800º C with a heating rate of 10 ºC/min. Samples of about 50 mg of dry gel were analized [27].

2.2.2 Energy dispersive X-ray spectroscopy (EDS)

Energy dispersive X-ray spectroscopy, EDS best known, is an analytical technique used for the elemental analysis or chemical characterization of a simple. Analysis were carried out in a JEOL JSM-6390LV Scanning Electron Microscope instrument.

2.2.3 Nitrogen adsorption

Nitrogen adsorption-desorption isotherms were obtained with an automatic Quantachrome Autosorb 3B instrument. Prior to the nitrogen adsorption, all the samples were outgassed overnight at 200° C. The specific surface areas of the samples were calculated from the nitrogen adsorption-desorption isotherms using the BET method, and the mean pore size diameter from the desorption isotherms using the BJH method.

2.2.4 X-ray diffraction

The obtained TiO_2 and TiO_2-ZrO_2 powders were analyzed by X-ray diffraction using a Bruker D-8 Advance apparatus. The diffraction intensity as a function of the diffraction angle (2θ) was measured between 4 and 70°, using a step of 0.03° and a counting time of 0.3 s per step [30,31].

2.2.5 RAMAN Spectroscopy

Raman spectra ewre obtained using a renishaw spectrometer model Invia MicroRaman using 100x objective and as radiation source an argón laser monochromatic with wavelength 514.5 nm wmission corresponding to green light and a power of 25 mW. In the analysis equipment were placed 10 mg of powdered sample of solids. The Raman shift range for analysis was of 0 a 1200 cm^{-1}[30,32].

3.2.6 UV-Visible Spectroscopy by reflactance difusse.

The UV–Vis absorption spectra were obtained with a Cary 100 UV–Vis spectrophotometer (VARIAN) coupled with an integration sphere for diffuse reflectance studies. A sample of MgO with 100% of reflectance was used as a reference. The diffuse reflectance spectrum was obtained and transformed to a magnitude proportional to the extinction coefficient (α) through the Kubelka-Munk function, equation (a):

$$F(R) = \frac{(1-R)^2}{2R} \qquad \text{(a)}$$

Eg value was calculated from the plot of Kubelka-Munk function F(R) vs wavelength of the absorbed light.

2.2.7 Hydrogen production

The schematic reactor system is described in a previous report. The photo-activity for the hydrogen generation was evaluated using a homemade Pyrex reactor of 250 mL containing 200 mL of water-ethanol solution (1:1 vol/vol) and 0.1 g of catalysts. The irradiation was made using a high pressure Hg pen-lamp (with a radiation of 254 nm and intensity of 2.2 mW/cm^2) encapsulated in a quartz tube immersed in the water solution. The amount of hydrogen produced was followed by using a gas chromatograph (VARIAN CP-3800) equipped with a thermal conductivity detector and with a 5A column molecular sieve (30m length, 0.35mm ID and 50 mm OD).

Result and discussion

3.1 Thermogravimetric analysis (TGA-DTA)

The principal analysis of thermogravimetric (TGA) of the samples of TiO_2-ZrO_2 (1.0, 3.0, 5.0 and 10.0 wt %) it can show in the figures 2 and 3.

The Fig. 2 and 3shown the lost weight (Tg) and the curves of analysis differential thermal (DTA) of the mixed oxide TiO_2-ZrO_2 without thermal treatment. For the sample with 1 % de Zr in the figure 2 shown the curves of TG at 1 % wt of Zr, where it show a peak endothermic a low temperatures of 80° C, with a lost weight of 1.0 %, that go associates to lost residual water and trapped solvent in the particles. of 80° C to

250° C, 250° C to 270° C, 270° C to 350° C and 350° C to 460° C, it has tree peaks exothermic corresponding to 8.9 %, 10.5 % and 18.42 % of lost weight respectively, that could be atribuirse to the combustion of organic residual strong retained, same that it evidence of calcination of gel. After of 460° C it has a sintering of material that suggest a crystallization to anatase phase [27].

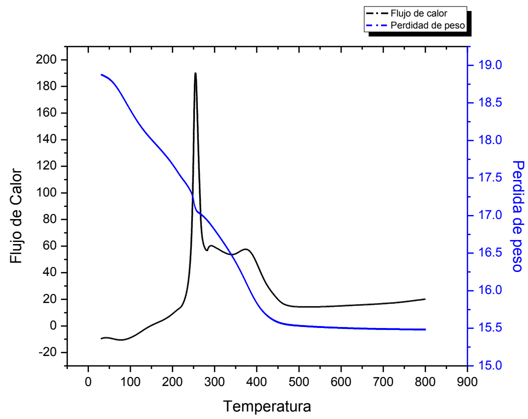

Figure 2. TGA-DTA of mixed oxide of TiO_2-ZrO_2 at 1 %.

Figure 3 show the lost weigth (TG) and the curves of the analysis differential thermal (DTA) of mixed oxide TiO_2-ZrO_2 at 5 % wt. of Zr, without thermal treatment. The curves of TG show the lost endothermic weight to small temperature of 50° C to 100° C it has a peak, with lost weight of 4.76 %, that ranging associated to residual water and trapped solvent in the particles. Of 100° C to 220° C, 220° C to 400° C, it has two exothermic peaks corresponding to 9.0 % and 19.04 % of lost weight respectively that go associated at organic material. After of the 450° C it has a winterization of material that suggest more stability of anatase phase [27].

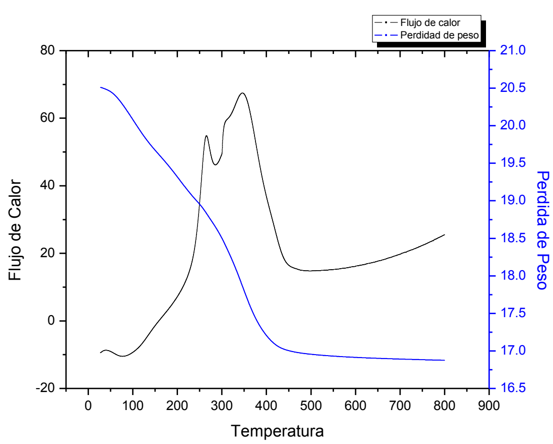

Figura 3. TGA-DTA of mixed oxide TiO_2-ZrO_2 at 10 %.

3.2 Energy Dispersive Spectroscopy (EDS)

Spectra EDS were obtained, which are shown in table 1, it can be seen the presence of ZrO_2, these results can be observed the presence of Zr^{4+}, which is not identifiable by X-ray technique, will be appreciated that the material surface has unevennes, you can also be seen in the micrographs some agglomerates granular appearance. The presence of particles with large unevenness is likely due to the fact that the formation of mixed oxide, in this cases TiO_2-ZrO_2, are in the Surface of TiO_2.

Tabla 1. Elemental Analysis EDS of mixed oxide TiO_2-ZrO_2

Percent	Ti	Zr
1	98.68	1.32
3	96.72	3.28
5	93.42	6.42
10	91.68	8.32

3.3 N_2 Physisorption

The data of the specific áreas of the samples which were calcined at 500° C are reported in table 2. The results show that the specific área by the BET method when the % Zr increases, increased respect to reference of TiO_2 (64 m^2/g). the profiles of the isotherms and the distribution of pore size respectively, we suggest that are type 4 [2], this adsorption isotherm perfectly corresponds to that determined by Hackley and Anderson [3], with hysteresis type 2 (IUPAC), accordingto the classification of de boer [4] which are in solid matrices with uniform pores having capillary condensation and have mesoporous structure and is attributed to the monolayer adsorption data distribution pore size are reported in table 2 (1.0, 3.0, 5.0 and 10.0 % wt of Zr) although wide is unimodal with maximum (4 nm) located in the mesoporous region [5].

Tabla 2. Textural properties, Band gap (Eg) of mixed oxide of TiO_2-ZrO_2.

ZrO_2 (% Wt)	Área (m^2/g)	Pore diameter (nm)	Eg (eV)	Cell Parameters a (nm)	c (nm)	Cristalite size D (nm)
1.0	91	5.6	3.05	0.56	0.948	7.8
3.0	147	7.7	3.14	0.58	0.956	7.9
5.0	157	7.8	3.20	0.66	0.950	8.7
10.0	138	6.5	3.15	0.78	0.156	9.9
TiO_2	64	6.5	3.20	0.377	0.943	5.7

3.4 X-ray Difracction (XRD)

Figure 4 XRD patterns of the samples of TiO_2 and mixed oxide TiO_2-ZrO_2. XRD patterns show the anatase phase (JCPDD: 21-1272) formed in the TiO_2. Peaks appear in 2ϴ=25.4°, 38°, 48°, 54°, 63°, corresponding to the diffraction patterns of (101), (112), (200), (211) and (204) respectively of anatase phase. It has been reported that ZrO_2 peaks does not appear in the present study in 2ϴ: 30°, 35°, 50° y 60°, corresponding to the diffraction patterns of (101), (002), (112) and (211). The tetragonal phase of ZrO_2 not appear in the present study [6]. Vishwanathan et al. Has been reported that 10 % by weight does not contribute to any change in morphology in the mixed oxide, as well as high crystallinity in the existing particles [7]. These results suggest that some of Zr^{4+} cations were incorporated within the network of titania, as evidence increase in cell parameter with respect to Zr (Table 2). However, high specific area shown in the mixed oxide is highly likely that the ZrO_2 was sufficiently dispersed to form clusters on the Surface of titania and not detectable by

XRD [8] these data are supported with RAMAN and EDS spectroscopy.

The cristal size, D, of the samples was estimated from half with (β) of the peak 2θ = 25.4° by the Scherrer formula:

$$D = \frac{K\lambda}{\beta \cos\theta}$$

The values are reported in table 2, the cristal size is in the range of nanometers (7.8 to 9.9 nm) which was obtained in all samples.

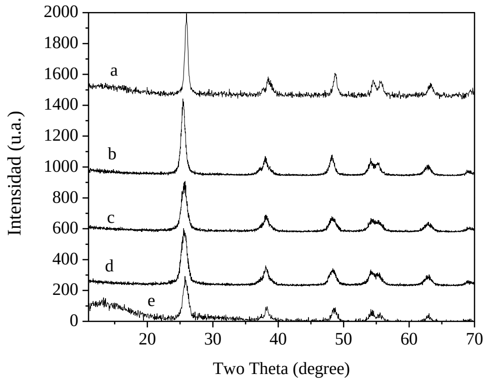

Figure 4. X-Ray diffractograms for mixed oxide TiO_2-ZrO_2

3.5 RAMAN Spepctroscopy

Figure 5 shows the RAMAN spectra of the samples TiO_2-ZrO_2, with concentrations of Zr^{2+} (1.0, 3.0, 5.0 and 10.0 %). Al peaks are characteristic signs of the anatase phase which has a shift in wavelength of 145 cm^{-1}, 395 cm^{-1}, 513 cm^{-1} and 640 cm^{-1} [9], these peaks correspond to the 5 modes of absorption of this active phase Raman of which overlapped two of the located at 519 cm^{-1} [10], which suggest that the ZrO_2 be embedded in the network of the titania. On the other hand these peaks decrease as the content of Zr^{2+} is increased, indicating a significant decrease in the cristalilinity of the mixed oxide. These result are consistent with XRD, not corresponding to the rutile phase (240 cm^{-1}, 442 cm^{-1} and 606 cm^{-1}) [11] or broquita (450 cm^{-1}, 365cm^{-1}, 320 cm^{-1} and 245 cm^{-1}) [12], where smalls crystal size correspond to smaples with high content of Zr.

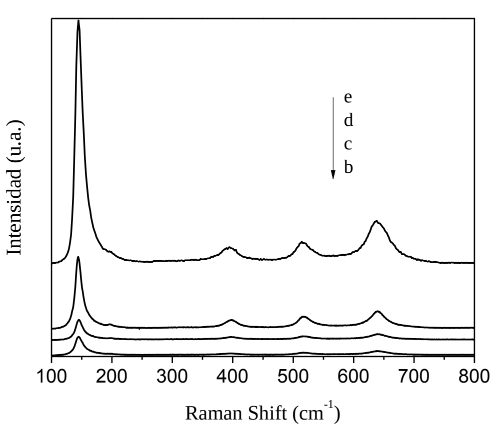

Figura 5. Raman spectra of the simple TiO_2-ZrO_2

3.6 UV-Vis spectroscopy

As to UV-visible spectrum of the sol-gel TiO2 calcined at 500° C (Fig. 6) is observed (at ~ 356 nm) corresponding to electronic transitions of Ti-O-Ti bonds in octahedral coordination absorption. It has been reported [13] that the anatase phase is characterized by an absorption starting near 450 nm with an inflexion near 370 nm accompanied by a plateau between 330 and 230 nm. This signal originates from the charge transfer transition → O2- Ti^{4+} corresponding to the excitation of electrons from the valence band (O2p with character) to the conduction band (with Ti 3d character) [14]. The position of this band with an energy gap of 3.2 eV characterizes in the TiO2 anatase phase as a semiconductor.

The UV-Vis studies were conducted in order to investigate the effect of ZrO_2 in the photophysical properties of TiO_2-ZrO_2 semiconductors. All samples a shift between these wavelengths, which can be attributed to the transitions of the Ti-O electrons TiO_2 nanocrystals TiO_2-ZrO_2 and the results show small bands in the red region (3.05-3.2 eV) for TiO_2-ZrO_2 samples of 1% to 10% by weight of Zr, compared to TiO_2 in anatase phase reference (3.2 eV) (Fig. 6) .

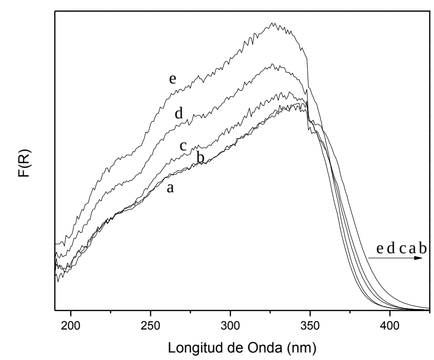

Figure 6. UV-Vis spectra by diffuse reflactance, samples TiO_2-ZrO_2

3.7 Hydrogen Production

In Figure 9, the hydrogen production is shown as a function of irradiation time for samples of TiO_2 and TiO_2-ZrO_2. It can be seen that the formation of hydrogen increases with respect to the weight percent of Zr^{4+}. Hydrogen production for titanium dioxide was 190 mol / h. an important effect of ZrO_2, regarding the content is observed. Forming TiO_2-ZrO_2 to 1% and TiO_2-ZrO_2 to 3% was 387 and 910 μmol/h, respectively, an increase of approximately 100% and for each of the catalysts 500%. H_2 production for TiO_2-ZrO_2 5% was 1600 μmol/h, while the maximum formation was obtained for TiO2-ZrO_2 catalyst 10% to 1,990 μmol/h, Fig. 7 The ZrO2 disappears as the reaction proceeds in the samples d and e (graph 7). These results are very interesting compared when used Au/TiO_2 [16] Pt-TiO_2 [17,18] Ag/TiO_2. [19].

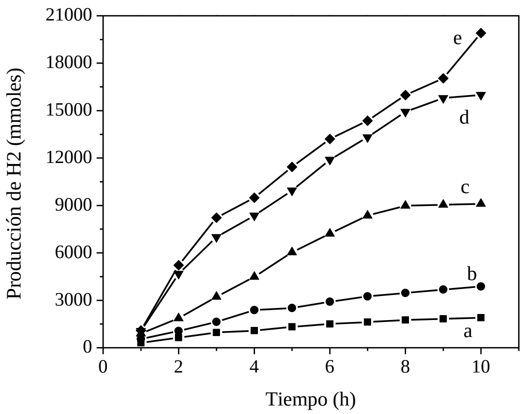

Figure 7. Profile of hydrogen production of mixed oxide TiO_2-ZrO_2

4. Conclusion

This study clearly demonstrates the advantages of the formation of mixed oxides such as ZrO_2-TiO_2, for photocatalytic hydrogen generation. Most TiO_2 parameters such as particle size, surface area, the anatase phase, OH groups on the surface and the thermal stability can be controlled in the formation of the mixed oxides by sol-gel method.

Although high ZrO_2 content of the specific area increases and crystallite sizes suffer the same effect. The photocatalytic activity was good from 5% ZrO_2, this is due to the number of transfers electrons to TiO_2 at ZrO_2. Chemical interactions of Zr-O-Ti in the mixed oxide is a major factor by which a high photocatalytic activity was taken into H_2 production. The study of UV-vis by diffuse reflectance can give strong evidence of changes in the transition states, and there are changes on the surface of oxides, so we suggest that there is a change of CB ZrO_2 of the CB surface of TiO_2 and facilitate the exchange of electrons between them. And preventing recombination of electrons and holes to increase the photocatalytic efficiency of TiO_2. Electron generation proves to be the most important in the photocatalytic activity of the mixed oxides as evidenced by UV-vis analysis after reaction factor.

Acknowledgment

A. Pérez-Larios, thanks to Conacyt for scholarships and 63053 Grant supporting this research.

REFERENCIAS

[1] Gratzel M. Photoelectrochemical cells.Nature 2001;414:338-44.

[2] Rostrup-Nielsen JR. Conversion of hydrocarbons and alcohols for fuel cells. Phys Chem Chem Phys 2001;3:283-8.

[3] Service RF. Hydrogen economy? Let sunlight do the work. Science 2007;315:789.

[4] Cortright RD, Davda RR, Dumesic JA. Hydrogen from catalytic reforming of biomass-derived hydrocarbons in liquid water. Nature 2002;418:964-7.

[5] Woodward J, Orr M, Cordray K, Greenbaum E. Biotechnology: enzymatic production of biohydrogen. Nature 2000;405: 1014-5.

[6] Bard AJ, Fox MA. Artificial photosynthesis: solar splitting of water to hydrogen and oxygen. Acc Chem Res 1995;28:141-5.

[7] Fujishima A, Honda K. Electrochemical photolysis of water at a semiconductor electrode. Nature 1972;238:37-8.

[8] Khan SUM, Al-shahry M, Ingler Jr WB. Efficient photochemical water splitting by a chemically modified n-TiO_2. Science 2002;279:2243-5.

[9] Maeda K, Teramura K, Lu D, Takata T, Saito N, Inoue Y, et al. Photocatalyst releasing hydrogen from water. Nature 2006; 440:295.

[10] Ishikawa A, Takata T, Kondo JN, Hara M, Kobayashi H, Domen K. Oxysulfide $Sm_2Ti_2S_2O_5$ as a stable photocatalyst for water oxidation and reduction under visible light irradiation (λ= 650 nm). J Am Chem Soc 2002;124:13547-53.

[11] Ashokkumar M. An overview on semiconductor particulate systems for photoproduction of hydrogen. Int J Hydrogen Energy 1998;23:427-38.

[12] Meissner D, Memming R, Kastening B. Photoelectrochemistry of cadmium sulfide. 1. Reanalysis of photocorrosion and flatband potential. J Phys Chem 1988;92:3476-83.

[13] J. Jitputti, Y. Suzuki, S. Yoshikawa. Synthesis of TiO_2 nanowires and their photocatalytic activity for hydrogen evolution.

[14] L.S. Yoong, E.K. Chong, B.K. Dutta. Development of copper doped TiO2 photocatalyst for hydrogen production under visible light. Energy 34 (2008) 1652-1661.

[15] Ha SP, Dong HK, Sun JK, Kyung SL. The photocatalytic activity of 2.5 wt.% Cu doped TiO_2 nano powder synthesized by mechanical alloying. J Alloy Compounds 2005;415:51–5.

[16] Ni M, Micheal KH, Dennis YCL, Leung KS. A review and recent development in photocatalytic water-splitting using TiO2 for hydrogen production. Renew Sust Energ Rev 2007;11:401–25.

[17] K. Maeda, H. Terashima, K. Kase, K. Domen. Nanoparticulate precursor route to fine particles of TaON and ZrO2-TaON solid solution and their photocatalytic activity for hydrogen evolution. App. Catal. A: Gral. 357 (2009) 206-212.

[18] Patsoura A, Kondraides DI, Verykios XE Appl Catal B 64 (2006) 171.

[19] Patsoura A, Kondraides DI, Verykios XE Catal Today 124 (2007) 94.

[20] Sreethawong T, Suzuki Y, Yoshikawa S C R Chimie 9 (2006) 307.

[21] Dubey N, Rayalu SS, Labhsetwar NK, Devotta S Int J Hydrogen Energy 33 (2008) 5958.

[22] Yin S, Sato T. J Photochem Photobiol A 169 (2005) 89.

[23] Khan MA, Akhtar MS, Woo SI, Yang O-B. Catal Commun 10 (2008) 1.

[24] Fu X, Long J, Wang X, Leung DYC, Ding Z, Wu L, Zhang Z, Li Z, Fu X. Int J Hydrogen Energy 33 (2008) 6484.

[25] Daskalaki VM, Kondarides DI (in press) Catal Today. 144 (2009) 75-80.

[26] Chen T, Wu G, Feng Z, Hu G, Su W, Ying P, Li C. Chin J Catal 29 (2008) 105.

[27] Xu Q., Anderson M. A., *J. Am. Ceram. Soc*. **77** (1994) 1939

[28] Brunauer S., Deming L. S., Deming W. E., Teller E., *J. Am. Chem. Soc*. **62** (1940) 1723.

[29] Hackley V. A., Anderson M. A., Spooner S., *J. Mater. Res*. **7** (1992) 2555

[30] de Boer J. H., van den Heuvel A., Linsen B. G., *J. Catal*. **3** (1964) 268

[31] Bosch G. P., Domínguez J. M., Zénith J., Rouffignac E., Guzmán O.,Tejeda J., "Técnicas Experimentales en la Caracterización de Catalizadores", Series Científicas IMP, México (1986).

[32] Dzwigaj S., Louis C., Breysse M., Cattenot M., Bellière V., Geantet C., Vrinat M., Blanchard P., Payen E., Inoue S., Kudo H., Yoshimura Y., *Appl. Catal.* B **41** (2003) 181.